Energy and water exchange of permafrost patterned ground - towards a scaling concept

Habilitation thesis

submitted by
Dr. rer. nat. Julia Boike
to the

Faculty of Chemistry and Earth Sciences
Ruperto-Carola University of Heidelberg, Germany

January 2011

Table of contents

Zusammenfassung

Ein wesentliches Merkmal von Permafrostlandschaften ist die Oberflächenstrukturierung durch Frostbodenformen, wie z.B. Polygone, Kreise, Streifen oder Thermokarstseen. Die Bildung dieser Formen wird in erster Linie durch das Klima bestimmt, das eine Vielzahl kryopedogener Prozesse zur Folge hat. Weitere Faktoren sind Bodeneigenschaften, die Verfügbarkeit von Wasser, Zeit und Topografie. Die Ziele dieser Arbeit sind (i) die Prozesse in den Strukturen und zwischen den Strukturen und der Atmosphäre zu bestimmen und (ii) ihren Einfluss auf unterschiedlichen (räumlichen und zeitlichen) Skalen von Zentimetern bis Kilometern zu bestimmen. Hochauflösende, mehrjährige Datensätze von drei unterschiedlichen arktischen von Permafrost geprägten Standorten werden detailliert untersucht: Sibirien (Lena Delta), Spitzbergen (Ny-Ålesund) und Alaska (North Slope). Diese drei Standorte unterscheiden sich in ihrer Vereisungsgeschichte, ihrem vergangenen und zur Zeit herrschenden Klima, ihrer Topografie, und ihren Eigenschaften an der Oberfläche und im Untergrund. Permafroststrukturen mit unterschiedlichen Größen liegen an allen drei Standorten vor: nicht sortierte Feinerdekreise (Spitsbergen), Polygone und Thermokarstseen (Sibirien) und „water tracks“ (Alaska). Die hydrologischen, thermischen und geochemischen Transportprozesse werden mit experimentellen Daten untersucht und weiterhin mit ein- und zwei-dimensionalen Modellen simuliert. Während des Sommers sind die Unterschiede zwischen den Standorten in den Energiebilanzen (sensibler und latenter Wärmestrom, Bodenwärmefluss) klein. Die Wasserbilanz dagegen variiert stark zwischen den Standorten und wird in erster Linie durch die Menge und zeitliche Abfolge des Niederschlags (Schnee und Regen) bestimmt. An allen Standorten beeinflussen die Strukturen maßgeblich die Wasser- und Energieflüsse. An dem Spitsbergen-Standort führen kleinräumige Unterschiede in der Oberfläche und in den Bodeneigenschaften zur Bildung und Erhaltung von Unterschieden, z.B. einer tieferen Auftautiefe im Zentrum des Feinerdekreises. In größeren Strukturen, z.B. den polygonalen Tümpeln in Sibirien, erfolgt durch die frei werdende Wärme während des winterlichen Rückfrierens eine Änderung der Oberflächentemperatur. In den kleinen, hydrologischen Einzugsgebieten in Alaska und Sibirien wird der Wasserspeicher und Abfluss weitgehend durch Topografie und Strukturen, „water tracks“ und Polygone beeinflusst. Um Änderungen des Energie- und Wasserhaushaltes arktischer Landschaften vorherzusagen, sind daher Landschaftsmodelle notwendig, die Schlüsselprozesse, hauptsächlich Tauen und Transport („Routing“) des Wassers, korrekt wiedergeben.

Summary

A specific characteristic of permafrost landscapes is the occurrence of patterned ground, such as polygons, circles, stripes, and thermokarst lakes. The formation of these patterns through periglacial processes is primarily determined by the climate as one factor, but soil characteristics and availability of water, time (duration of formation) and topography are others. The goals of this project are to (i) to determine which processes in and across the ground-atmosphere surfaces are significant and (ii) investigate their relative importance on scales from centimetres to hundreds of kilometres. Three contrasting arctic permafrost sites are studied in detail: Siberia (Lena Delta), Spitsbergen (Ny-Ålesund) and Alaska (North Slope). These sites differ in their history (glaciation record), past and current climate, topography, surface and subsurface characteristics. Patterned ground is dominant at all three sites at varying scales from meters to kilometres: non sorted circles (Spitsbergen), polygons and thermokarst lakes (Siberia) and water tracks (Alaska). The hydrologic, thermal and solute dynamic processes are analysed using experimental data of these fluxes as well as one and two dimensional modelling. It is found that, differences between the sites in radiative, atmospheric fluxes and ground heat fluxes are relatively small during the summer. The summer water budget, however, varies significantly between the sites and depends largely on the precipitation (snow/rain) input and timing. At all sites, patterned ground exerts a major influence on the heat and water budget. At the Spitsbergen site, small scale differences in surface and subsurface heat budget induce and maintain small scale differences such as greater thaw depths underneath the centre of a mud boil. On a larger unit, such as polygonal pond in Siberia, the heat release during fall freeze-back affects the surface temperature. At the watershed scale (Alaska, Siberia) the water storage and runoff depends on topography and patterned ground features, such as water tracks and polygonal ponds and lakes. Thus, predicting changes in surface energy and water budget requires landscapes models where key processes, mainly thawing and routing of water, are accurately predicted.

Acknowledgements

While working in the Arctic for more than 20 years, I have always been amazed by the striking and beautiful surface patterns which are now central in this thesis.

The thesis was written when I lead my Helmholtz University Young Investigator research team on "Sensitivity of the permafrost system's water and energy balance under changing climate: A multiscale perspective" (*SPARC)* based at AWI and the University of Heidelberg. This provided me with the freedom to work with a great team. It included the brightest PhD students (Torsten Sachs, Sebastian Westermann, Moritz Langer, Sina Muster, Anna Abnizova in Canada), diploma students that withstand field and modeling challenges (Imke Schramm, Britta Kattenstroth, Anne Ludin, Katrin Fröb, Niko Bornemann) and the superb engineer (Konstanze Piel). Many discussions and expeditions were shared as group tasks, as well as fun times!

I would like to thank my mentor Kurt Roth for his ongoing support and scientific exchange for more than 15 years and the final push towards this thesis. I found that there was much more to discover scientifically which is not yet included in this thesis!

At AWI Potsdam I especially thank my director, Hans-Wolfgang Hubberten, who supported the *SPARC* team in many ways and for also leaving me the space to be (scientifically) creative. Furthermore, I thank Ute Bastian and Antje Eulenburg for laboratory and Molo Stoof and Waldemar Schneider for expedition support. Many other people contributed to productive discussion, along with some great expedition times!

Larry Hinzman provided scientific exchange and support during my almost 3 year research visit at the University of Alaska, Fairbanks.

Special thanks go to Klaus Töpfer and Moritz Remig at the Institute for Advanced Sustainability Studies in Potsdam to provide an office space during the final writing phase.

Finally, the biggest thanks go to my family, my sons Emil and Finn and my husband Paul. Although they spent long times without me, they always supported my dedication to science. Sharing their life is a great gift and helps to concentrate on issues that really matter!

Chapter 1

1.1 Introducing the research- state of the art on permafrost

Significance of permafrost and patterned ground as indicators of past and current conditions

Permafrost is defined as ground that remains below 0°C for at least two consecutive years (Brown *et al.*, 1997). Permafrost may be comprised of bedrock, sediment, soils, or organic materials, and may or may not contain liquid water and ground ice. Its distribution, temperature and extent depend on past (for example glaciation periods) and current environmental conditions (surface and subsurface energy balance). For example, the deepest permafrost with depths of about 1600 m in Central Yakutia is the result of past and present cold climates with no indication of glaciation.

A typical feature of permafrost landscapes is that they are heterogeneously structured, with both large-scale elements, such as thermokarst lakes, as well as small-scale elements such as circles (Figure 1). Patterned ground features result from the interplay between a variety of periglacial processes, dominated mainly by climate, and operating in polar, subpolar and alpine areas. Periglacial processes include freezing/thawing, frost heave and sorting, physical volume changes, migration of water as a result of gradients (matric potential, temperature, vapour pressure, solutes concentrations) and mechanical mixing through cryoturbation and cracking. These processes are highly complex and patterned ground is usually the combination of many individual processes (Washburn, 1979a).

For example, cryoturbation mobilizes soil carbon up and downward. Tarnocai *et al.* (2009) and Ping *et al.* (2008) show that non-sorted circles in permafrost soils are the main mechanism of carbon sequestration in the Alaskan tundra. In Finnish wetlands, peat circles are the landform-feature that emits the highest N_2O fluxes to the atmosphere (Repo *et al.*, 2009). In Siberia, the highest CH_4 fluxes are measured in the Yedoma thermokarst lakes (Walter *et al.*, 2006). Ice wedge polygon and thermokarst lakes increase surface storage in watersheds with low topographic gradients and thus affect carbon discharge (Kane *et al.*, 2003) and vertical fluxes (Rouse *et al.*, 2005; Krinner and Boike, 2010). Nonetheless, our understanding of how patterned ground features are formed in time and space and, in turn, what their role has been and is, in regulating lateral and horizontal fluxes, is still evolving.

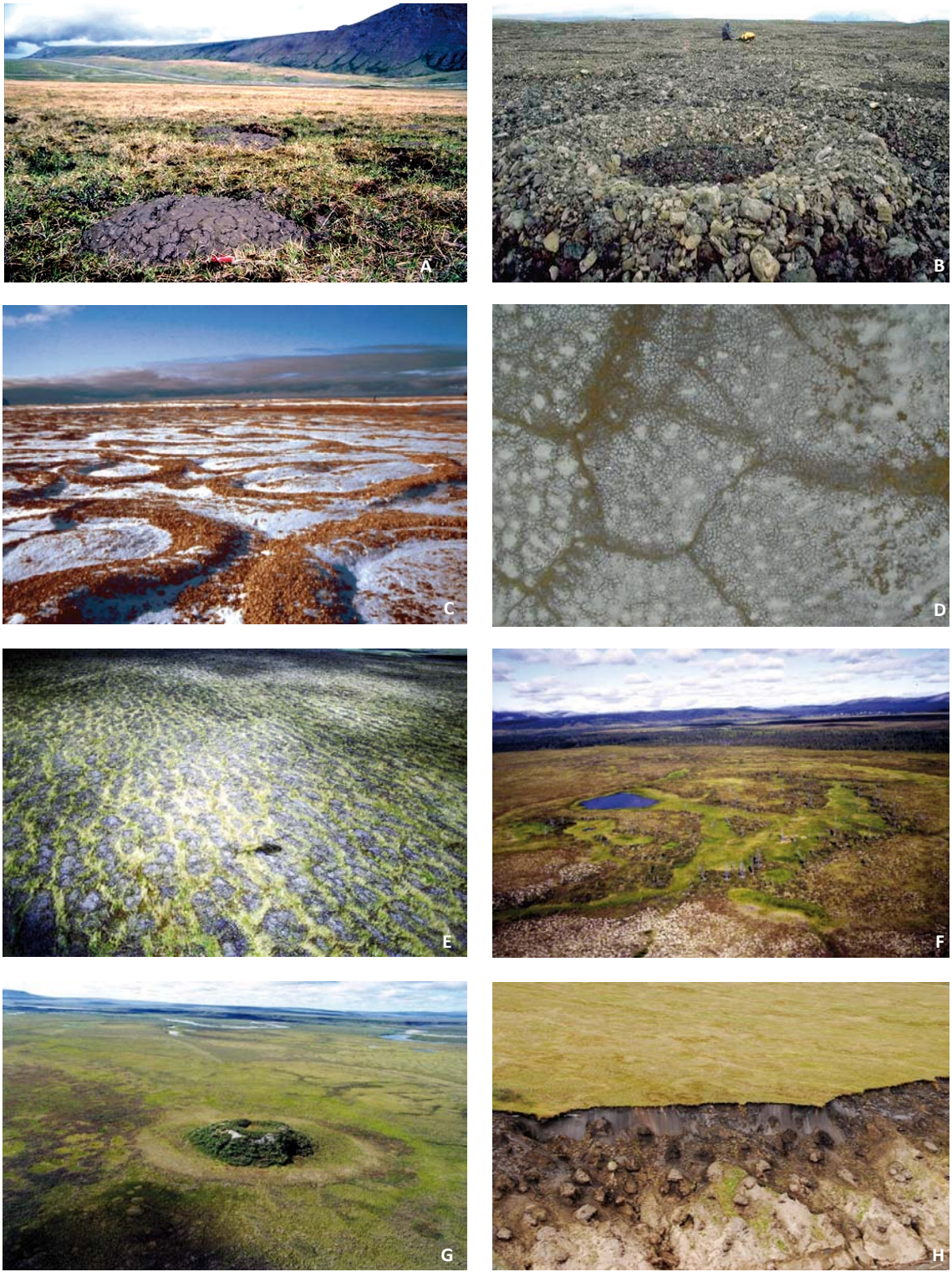

Figure 1: Examples of permafrost patterned ground photographed at various sites. The size of the patterns is increasing from meters (top row) to several hundreds of meters (bottom row). A: circles (Galbraith Lake, North Slope, Alaska); B, C: circles and polygons (Brøgger peninsula, Spitsbergen); D: circles and polygons (Howe Island, Alaska); E: circles and polygons; F: thermokarst lake; G: pingo (all Seward Peninsula, Alaska); H: polygons and ground ice, exposed from erosion (Lena Delta, Siberia).

It is clear that patterned ground activity varies over glacial cycle time scales and has the potential to provide feedback to climate cycles. While patterned ground features are a result of both past and current environmental conditions, observations of their phenomenology will also be direct indicators of changes over times scales from seasons to millennia (Figure 2).

Figure 2: Example of drastic landscape changes caused by thaw of permafrost (thermokarst) on Alaska's North Slope during August 2004. A: helicopter aerial picture (courtesy by L. Hinzman), B.-E. ground based pictures. It is not clear what caused the thaw and subsequent collapse of the surface, which was followed by retrogressive erosion of the stream. On a short term, the sediment and solute transport was significantly enhanced into nearby Toolik lake (~ 10 km north) affecting fish habitat (Bowden *et al.*, 2008). On a long term, the landscape surface and drainage characteristics changed.

Since these features are a function of current environmental conditions, the analysis of their phenomenology and the dynamic processes that form them can be used to deduce clues of past and future climate and environmental conditions (Romanovskii, 1996; Washburn, 1979b). For example, during cold climate periods in the past two million years, ice wedge networks formed at lower altitudes on most continents (Black, 1976). Today these are still visible as relic troughs and ridges from these thawed ice bodies. In landscapes underlain by permafrost, where the topographic gradient is low (approximately 5-10 % of the Earth's land surface) these landforms play a dominant role in determining surface morphology, drainage and patterns of vegetation (French, 1996).

About 25 % of the land surface area of the northern hemisphere is covered by permafrost. In agreement with currently observed climate warming, measurements and modelling show a general warming trend for the upper permafrost layers in many arctic regions. The decrease in thickness and reduction in the areal extent of permafrost in response to natural and anthropogenic variability will ultimately modify the character and function of arctic landscapes. Rowland *et al.* (2010) suggest that arctic landscapes are particularly sensitive to perturbations and respond rapidly. Examples of landscape responses include land subsidence due to thaw of frozen ground (Liu *et al.*, 2010; Overduin and Kane, 2006), increased coastal and river bank erosion at some sites in Alaska (Jones *et al.*, 2009), but not at others in Canada and Siberia (Lantuit and Pollard, 2008), shrinking and expansion of freshwater bodies and channel networks (Smith *et al*., 2005a; Toniolo *et al.*, 2009), increased hillslope soil erosion and landslides (eg., Gooseff *et al.*, 2009) as well as thermokarst processes (Jorgenson *et al.*, 2006).

Permafrost physical characteristics and linkage to the carbon cycle

In the past, large-scale modelling studies greatly overestimated the extent of near-surface permafrost reduction expected in 2100, revealing a broad misconception. For example, Lawrence and Slater (2005) overestimate the geographic extent by 60 to 90 %. These modelling results initiated a still ongoing discussion of the correct parameterization of permafrost in small and larger scale models (i.e. Lawrence *et al.*, 2008; Langer *et al.*, 2010a).

Spatially distributed modelling with more spatial detail by Romanovsky *et al.* (2008) predict that current warm permafrost (where warm is defined as having mean annual ground temperature (MAGT) currently between 0 and -2.5°C) will be thawing by 2100. If true, thawing will affect the extent of almost half of the current permafrost in the Northern Hemisphere. The ongoing discussion on the degradation of permafrost has now reached a wide scientific, public and political audience since consequences are expected locally (i.e. infrastructure) and regionally (i.e. water supply), and also globally due to green house gas (GHG) emissions. Trenberth (2010) highlights the need to include feedback mechanisms, such as GHG-emissions from reduced permafrost areas, in climate models for the next Intergovernmental Panel on Climate Change (IPCC) assessment. Changes in carbon cycling (for example mobilization of old, formerly protected soil carbon pools) or changes in surface energy partitioning (Chapin *et al.*, 2005) are expected to be nonlinear. According to this school of thought, when thresholds in a system are reached, subsequent, incremental changes can produce extreme effects. However, in these so called ‘tipping elements’ in the earth’s climate system, where a small change in the control parameters can have large consequences for some

system variable(s), permafrost is not yet included (Lenton *et al*., 2008). This is due to limitations in existing models (e.g., Lawrence and Slater, 2005) and process understanding (carbon stocks, cycling and feedbacks) which makes it highly uncertain if the permafrost's behaviour is non linear. Doomsday scenarios such as winter CH_4 emission (Mastepanov *et al.*, 2008), extensive thawing of permafrost carbon stocks accelerated by soil microbial processes (Khvorostyanov *et al.*, 2008) and bubbling of lakes (Walter *et al.*, 2006) have been popular in the media and clearly, scientific investigations are required to put these findings in perspective (Kerr, 2010).

Publications have emphasized the role of permafrost as a crucial factor affecting carbon availability within the global carbon budget. Thawing of permafrost has the potential to release large carbon reservoirs (e.g., Schuur *et al.*, 2008). However, the sensitivity of the carbon cycle of the Arctic of the 21st century is highly uncertain (McGuire *et al.*, 2009). This is due to our limited knowledge of the large Arctic area in general, as well as small scale variability, and the complexity of processes. Furthermore, non-standardised field methods and non-standardised upscaling methods (for example using using 1 or 3 m soil depth for carbon storage estimates) compromise comparability of field results between sites and among researchers studying the same sites. For example, two studies conducted in the same area, the Thule peninsula in Greenland, reported soil organic content that varied widely between 4.3 Tg (Burnham and Sletten, 2010) and 18.4 Tg (Tarnocai *et al.*, 2009). For the North American Arctic, Ping *et al.*, 2008 estimate the carbon storage to be 98.2 Pg. Burnham and Sletten (2010) calculate 12 Pg for the high Arctic. The results are limited datasets and wide discrepancies in estimated parameters. Still, the contributions from arctic permafrost areas are considerable when compared with global carbon estimates for the upper 1 meter of soil of 1,462 to 2,344 Pg (Batjes, 1996; Denman *et al.*, 2007). The estimates of the total permafrost carbon pool are variable due to sampling location and interpolation method: 495 Pg (only top meter of soil), 1024 Pg (upper three meters) and an additional 648 Pg for deeper carbon stored in Yedoma (Pleistocene formed, carbon-rich sediments) and alluvial deposits (Tarnocai *et al.*, 2009).

Ideally, feedback mechanisms could be incorporated into future computer models used to estimate climate change. However, this would require i) accurate estimates of state variables such as soil organic carbon, thermal and hydraulic conductivities and ii) upscaled data on these state variables both vertically and horizontally (Ciais, 2010), as well as iii) an understanding of the key physical processes in permafrost and iv) an understanding of the interaction and feedback mechanisms between permafrost and climate. As Wania *et al.* (2009a,b) state, a major uncertainty in models is the prediction of regional and local hydrological processes as a result of permafrost thaw. For

example, degradation of permafrost with subsequent formation of ponds and lakes (wetting of surface) may result in enhanced CH_4 production. On the other hand, the presence of an efficient drainage network may result in drier conditions and thus increased CO_2 fluxes as a consequence of permafrost decomposition (Wania *et al.*, 2009b).

Predicting the sensitivity of permafrost to climate warming is furthermore complicated by changes in complex interactions between the hydrology, soil thermal regimes, and vegetation, which can lead to both positive and negative feedbacks to permafrost. For example, the growth of shrubs on tundra can work to "preserve" permafrost by reducing the mean annual permafrost temperature by several degrees (i.e. Blok *et al.*, 2010). In a warming climate, enhanced shrub growth, such as observed in Alaska (Sturm *et al.*, 2001; Tape *et al.*, 2006) may counteract the effect of warming. Overall, changes in land cover such as vegetation type and distribution, or the areal extent of water bodies and drainage systems, will affect the vertical and horizontal fluxes of water, energy and matter. The hydrologic and thermal regimes are dynamically coupled and interact to such an extent that neither can be fully understood without considering the other. Clearly, simultaneous measurements of the surface energy balance are required (Chapin *et al.*, 2005; Hinzman *et al.*, 1996).

Implementing a potential feed-back mechanism by GHG-emission from warming permafrost in regional and global models requires a correct parameterization of a sufficient and critical set of thermal and hydrologic processes and parameters, such as snow and soil thermal properties. The surface wetness is determined by the hydrologic budget which depends on parameters such as precipitation (snow and rainfall), snowmelt, damming of snowmelt runoff by the snowpack, infiltration and storage in the substrate, evaporation, transpiration, and runoff (Woo, 1986). Furthermore, knowledge of the permafrost geomorphic landforms and their function in terms of water storage and pathways is required. Although these processes act on a local scale, they have effects on the regional surface energy and water balance, such as infilling of new thermokarst lakes observed in Central Yakutia (Boike *et al.*, 2010).

1.1.1. Introduction to the habilitation thesis

This thesis represents a summary of selected research results obtained during the period from 1998 to 2010. Field data was collected by me or I supervised the data collection during months of field

expeditions in Siberia and Spitsbergen. Additionally, I was a guest scientist in Alaska between 2000 and 2003, which permitted research at Alaskan sites and access to existing data. Since 2006, and the start of my association with the Helmholtz University Junior Research Group, I have had the opportunity to investigate research ideas that were originally born when the field sites were first instrumented.

The focus of this habilitation is on heat and water transport processes that take place at various scales and sites across the Arctic. The thesis includes field and modelling studies from three permafrost sites to study energy and water fluxes between (i) small-scale spatial features and their short-term (diurnal, seasonal, annual, wet/dry) variability and ii) features and processes at the larger scale, both spatially and temporally (Figure 3).

The organization of the chapters in this thesis mimics the theme of scale; small-scale processes, and processes that occur under short timeframes and locally, up to a watershed scale, are considered in Chapters 2 and 3. Thereafter, Chapters 4 and 5 consider methods and models of studying processes at large scales – regional areas and timeframes of decades or longer.

Specifically the following aspects are addressed:

1. Development of a quantitative process understanding by identification of key processes determining seasonal and annual energy and water balances and the factors that affect these processes at the three study sites. This includes:
   - winter energy balance, importance of snow cover formation and ablation (Chapter 2.1), annual surface energy budget (2.2); Spitsbergen
   - climatology, summer energy and water budget between dry and wet year (Chapter 2.3) and annually (Chapters 2.4 & 2.5); Siberia
   - climatology, measuring and spatial distributed modelling of water budget components (Chapter 2.6); Alaska
   - comparison of snow ablation processes at all three sites (Chapter 2.7)

2. Elucidation of the relationships between thermal and hydrologic processes and patterned ground. This includes processes that are affected by, or occur in patterned ground):
   - spatial, thermal, hydrologic and solute characteristics of a mud boil (Chapter 3.1); Spitsbergen

- quantifying ground thermal processes in a mud boil (Chapter 3.2); Spitsbergen
- importance of ice wedge polygonal network for hydrologic processes subsurface flow (Chapter 2.3.) and atmospheric heat fluxes (Chapter 2.4); Siberia
- influence of water tracks upon discharge (Chapter 2.6); Alaska

3. Development of tools and techniques for mapping and quantifying permafrost patterns using remote sensing:
   - application of kite aerial photography for surface classification (Chapter 3.1) and balloon/helicopter aerial photography for digital elevation model construction (Chapter 3.2)
   - geometrical functions for quantification of permafrost patterned ground (Chapter 3.3)

4. Elucidation of how patterned ground affects transport processes of heat and water on a very large scale:
   - modelling the effect of disappearance of high latitude surface waters during the 21st century (Chapter 4.1)

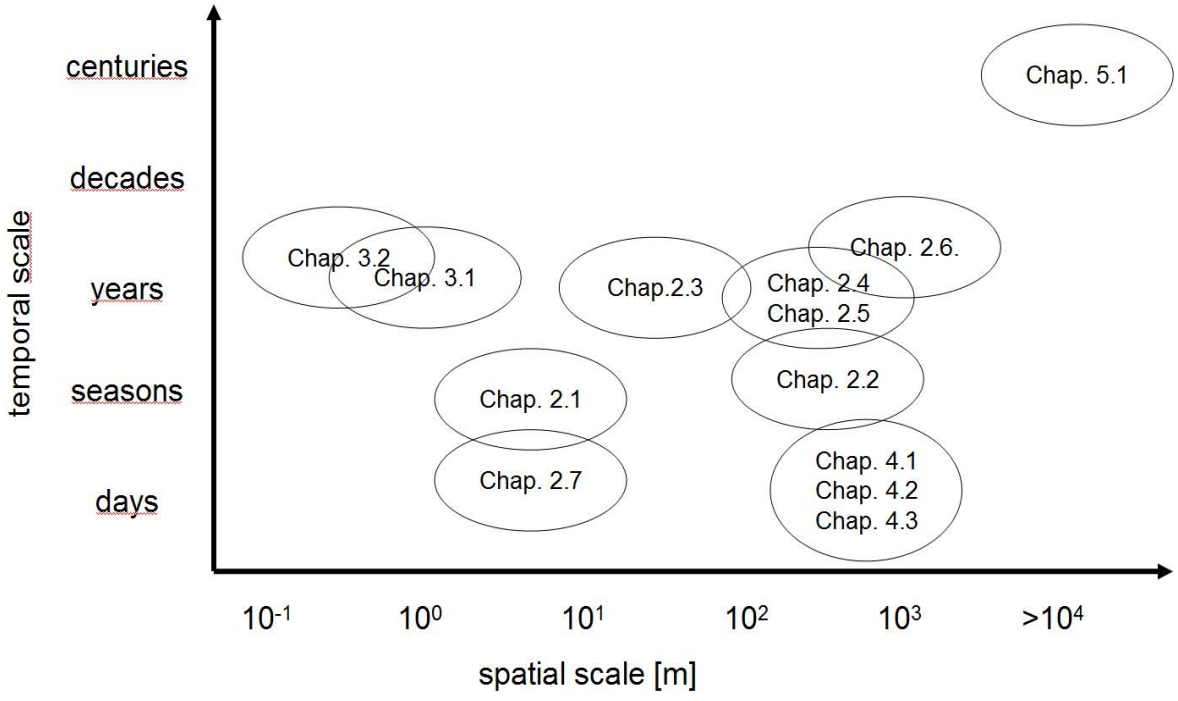

Figure 3: The range of temporal and spatial scales addressed in this thesis; the first publication (Boike *et al.*, 2003; Chapter 2.1) covers diurnal to seasonal time scales, and spatial scales of meters to tens of meters, whereas the last publication (Krinner and Boike, 2010, Chapter 5.1) considers time scales of decades to centuries and spatial scales of hundreds of meters to kilometres or larger.

Through this “step ladder approach” and checking if the model replicates the key processes characteristics at each scale, larger spatial and temporal domains are explored. The outcome from (1) to (4) is synthesized in the conclusion section with the overall goal for a unified view of key processes and parameters that needs to be considered for future earth system observation and modelling.

1.2. Synopsis

1.2.1. Description of the study sites (Siberia, Alaska and Spitsbergen)

Climate conditions and surface characteristics

All three sites are located in zones of continuous permafrost (Figure 4), but they span very different ecosystems across the pan Arctic. The Siberian site has the most continental climate (coldest winter air temperature and least precipitation), coldest and deepest permafrost, while Spitsbergen has a mild, maritime winter climate (due to the influence of the Atlantic current) and warmest and most shallow permafrost. The winter at the Alaskan site is colder than at the Spitsbergen site, but not as cold as in central Siberia. According to the CAVM Team classification (2003), three different bioclimatic and vegetation zones are covered: (i) sedge, moss, dwarf-shrub dominated wetland (Siberia), (ii) dry, patchy prostrate-shrub tundra (Spitsbergen) and (iii) moist graminoid, tussock-sedge, dwarf-shrub tundra. These sites represent *in-situ* laboratories for studying current and past processes over a range of typical arctic regions with different (thermal) histories and varying climate conditions. The similarities and differences in parameters such as climate, topography, parent material, geology and history) provide a unique opportunity to investigate the significance of these parameters on a range of spatial and temporal scales.

The Siberia site

The Lena Delta, located in Northern Yakutia, is one of the largest arctic deltas and Eurasian watersheds (2.430.000 km^2): about 30 km^3 of discharge drain every year into the arctic Ocean. Observations of substantial increases in the Lena River discharge have inspired a number of publications with controversial statements explaining the cause of the increases. These include, for example permafrost thaw (McClelland *et al*., 2004), and positive anomalies in late winter snow equivalent (Rawlins *et al.*, 2009a,b). While others (Shiklomanov *et al.*, 2007) have postulated that there is no agreement between cold season precipitation and maximum discharge.

Figure 4: Circum-polar permafrost distribution and classification in continuous, discontinuous, sporadic and isolated permafrost from Brown *et al.* (1997). The three arctic field sites in Siberia, Spitsbergen and Alaska are highlighted.

The Siberian study site is located at Samoylov, one of the 1500 islands composing the Lena Delta and has been instrumented since 1998. The island is located in one of the main river channels in the southern part of the delta (72°22'N, 126°28'E). Siberia was not glaciated during the Pleistocene. Continuous permafrost underlies the area to about 400 to 600 m below surface. This area has some of the most extreme climate conditions, displaying very cold air temperature and low precipitation records (Table 1). On the island, strong winds redistribute snow, resulting in bare surfaces on polygonal apices and snow-filled polygonal centers with up to 43 cm of snow. Strong winds lead to aeolian sedimentation of sands. Permafrost temperature is coldest in comparison to the other sites (mean annual top of permafrost temperature is about -9°C), with a large annual amplitude (Figure 5). The surface is characterized by low-centered polygonal patterned ground on peatish sand deposits of an ancient delta flood plain. The dominant types of patterned ground are (low-centered) ice wedge polygonal networks and thermokarst lakes (Figure 6).

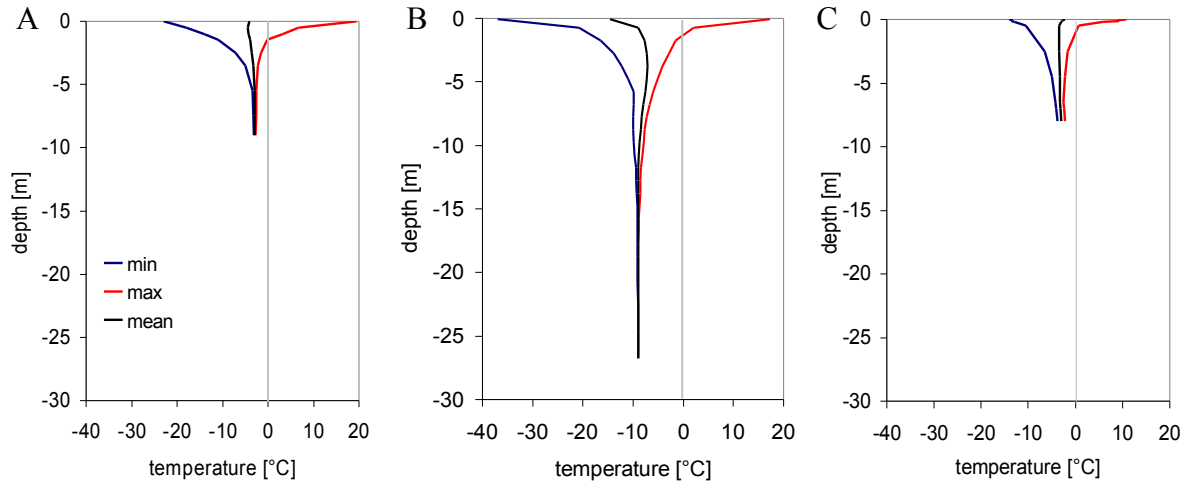

Figure 5: Mean, maximum, minimum permafrost temperatures recorded in boreholes at the Spitsbergen (A), Siberia (B) and Alaska (C) sites. The same depth and temperature scales are used to demonstrate the differences in warm (Spitsbergen) and cold (Siberia) permafrost. Different penetration depths are due to different thermal properties (diffusivity) and total water content. Analysis based on August 2009-August 2010 (Spitsbergen), August 2007- August 2008 (Siberia) and February 2006 - February 2007 (Alaska). Data for the Alaska site courtesy of L. Hinzman (Hinzman *et al.*, 2008).

The sandy material at the Siberian site is prone to deep infiltration, and the observed large thermal gradient promotes ice wedge growth though the refreeze of snow melt water. The micro-topography of the ice wedge formation leads to its further development by water transport from the apex towards the site of wedge growth.

The Spitsbergen site

In Europe, arctic permafrost exists in northern Scandinavia and in the non-glaciated areas of Greenland and Svalbard. The island of Svalbard was glaciated several times during Quaternary Period and is currently largely covered by ice sheets and glaciers. Since 1960, a significant warming of air temperatures has been detected, which is generally attributed to changes in circulation patterns (Hanssen-Bauer and Førland, 1998). Warmer air temperatures are also reflected in enhanced warming of permafrost as measured in boreholes (Isaksen *et al.*, 2001, 2007). Continuous permafrost in this region underlies coastal areas to depths of about 100 m and mountainous areas to depths greater than 500 m. The North Atlantic Current warms this area to an average air temperatures of about –13 and 5°C in January and July, respectively, and provides about 400 mm of precipitation annually, falling mostly as snow between September and May. Permafrost temperatures are warmest compared to the other two sites with a mean annual top of permafrost

temperature of about -2°C (Figure 5).

The Spitsbergen site is located on the Brøgger peninsula, in the Bayelva catchment, about 2 km from the village of Ny-Ålesund (78°55'N, 11°50'E). The site was chosen, because there is very little disturbance of the natural environment by the village. For example, the onset of snow melt in the village is about 2 weeks prior to snowmelt observed at the study site. The research site is bordered by inland glaciers (Brøggerbreen) and mountains and is about 1 km from the arctic Ocean (Figure 6). Sparse vegetation alternates with exposed soil and rock fields, and permafrost features, such as mud boils and sorted circles, are found in many parts of the study area.

The study site is located at about 25 m above mean sea level, on top of a small hill. The dominant patterned ground at the study site is non-sorted circles (Figure 6) which were formed after the last glacial period. The bare soil circle centres are about 1 m in diameter and are surrounded by vegetated borders consisting of a mixture of low vascular plants, mosses and lichens. The silty clay soil has a high mineral content, while the organic content is low, with volumetric organic fractions below 10 % (Chapter 3.1). Instrumentation started in 1998 and included automated weather and soil stations. Instrumentation has been augmented with micrometeorological stations (eddy covariance) and spatially distributed temperature sensors in soil and deeper permafrost.

The Alaska site

Imnavait Creek (68°37'N, 149°19'W) and Ivotuk (68°29'N, 155°44'W) are both located north of the Brooks Range on the North Slope of Alaska. The Imnavait Creek watershed is a small watershed at the headwaters of the Kuparuk River Basin (KRB), which flows northward into the arctic Ocean. The area was glaciated during the Pleistocene and is underlain by continuous permafrost, about 250 - 300 m deep (Osterkamp and Payne, 1981). Near-surface air temperatures have warmed by about 2°C over the past 20 years (Chapman and Walsh, 1993; Serreze *et al.*, 2000). In response to this and to recent increases in snow depth, significant increases in permafrost temperatures in the area have been reported: up to 1.5°C at a 20 m depth over a period of 15 years (Osterkamp, 2007; Stieglitz *et al.*, 2003; Hinzman *et al.*, 2005). Current mean annual air temperatures are about -7.4°C, with a range from -17°C in January to 9.4°C in July.

The mineral soils are wet, poorly-drained silt loams with a high organic content, containing many glacial erratic of various sizes. The soils are covered by a peaty layer. The vegetation is mostly tussock sedges and mosses, but there are also lichens and shrubs such as willows, alder and dwarf birch. “Water tracks”, shrubby corridors with a width of ~2 m and spacing between ~10-20 m, are a dominant patterned ground feature effectively routing surface water down slope (Figure 6). A

continuous record of meteorological, hydrological, and soil data from the Imnavait watershed site since 1985 is available online (http://ine.uaf.edu/werc/projects/NorthSlope/imnavait/imnavait.html). Imnavait Creek is a so- called beaded stream, meaning that the channel connects numerous small interspersed ponds. The ponds formed when massive ground ice melted due to some past thermal disturbance. These ponds are about 2 m deep and a few meters in length and width.

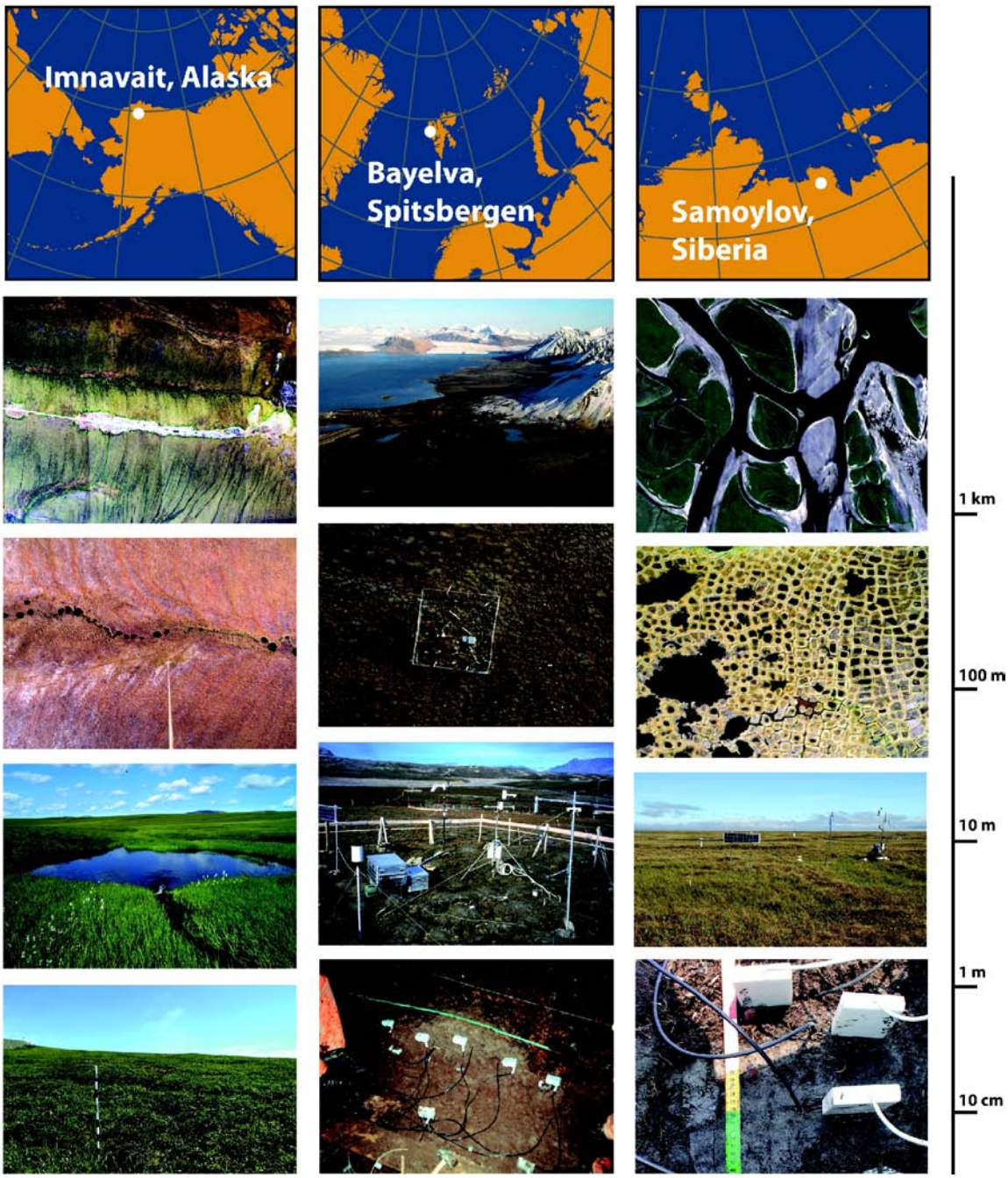

Figure 6: Pictures of the study sites demonstrating the scale from the watershed scale (top pictures) to the soil plot (bottom pictures). Imnavait catchment: A: aerial mosaic with water tracks (white areas are mineral surfaces and road construction areas). B: beaded stream, C: beaded stream pond, D: water track; Bayelva catchment: A: view from Schetelig mountain towards Ny- Ålesund, B: aerial view of fenced measuring site, C: fenced measuring plot, D: installed circle; Samoylov Island: A: aerial mosaic, B: network of low centred polygons, C: measurement site, D: installed soil profile in polygon. All nadir aerial images are obtained using balloon or drone aerial photography.

Overview of methods at the sites

Data has been collected since 1998 at the Siberia and Spitsbergen sites and since 1985 in Alaska using automated weather and soil stations. During the months of April to September, expeditions with durations of weeks up to several months were conducted to maintain equipment, install new instruments and perform additional field experiments, such as sampling of soil, snow and water, mapping and surveying of landcover and measuring hydrologic budget components. A summary of field and analytical methods is provided in Table 2.

Region	**Spitsbergen**	**Alaska**	**Siberia**
Study site name	Bayelva	Imnavait	Samoylov
Latitude	78°55'N	68°30'N	72°22'N
Longitude	11°50'E	149°15'W	126°28'E
Elevation [m]	25	900	10
Glacial history	Repeated glaciations during Quaternary	Glaciated during Pleistocene	Not glaciated
Permafrost thickness [m]	100	300	500
Total precipitation [mm]	400	340	250
% rainfall of total precip.	~25	~75	~75
Mean annual air temp. [°C]	-5.5	-7.4	-14.8
Mean January air temp. [°C]	-13	-17	-33.9
Mean July air temp. [°C]	5	9.4	11.2
Average summer thaw depth [cm]	110	52 **	49#
Mean annual top of permafrost temp. [°C]	-2.8	-3.4	-9.0
Microrelief/Patterned ground	Non sorted circles	Water tracks (tussocks, hummocks)	Ice wedge low-centered polygons
Vegetation classification (CAVM Team, 2003)	Prostrate-shrub tundras *tundra with patchy vegetation:* Prostrate shrubs < 5 cm tall (such as Dryas and Salix arctica), with graminoids forbs, lichens; dry	Graminoid tundra: Tussock-sedge, dwarf-shrub, moss tundra; dominated by tussock cottongrass, dwarf shrubs <40 cm; mosses are abundant; moist	Sedge, moss, dwarf-shrub wetland dominated by sedges, grasses, and mosses, but including dwarf shrubs < 40 cm tall; wetland
Soil type	Not determined	Histic Pergelic Cryaquepts	Typic Historthes, (center), Typic Aquiturbels (rim)
Soil material	Silty clay, interspersed stones	Silt loams, high organic content, covered by peaty layer; glacial erratics	Sandy loams and sands with interspersed sand layers, peat
Snow covered season	October-June	September-May	September-May
Range of end of winter snow	83-150	1-100	0-43

depth [cm]			
Pre melt bulk snow density [kg m^{-3}]	350	239	250 (excluding ice layers)
Bulk melt density [kg m^{-3}]	450	318	290
Snow characteristics	Basal ice layer and several internal ice layers; depth hoar	Depth hoar with several layers of blown snow over top	Several relict wind crusts with large amount of aeolian sediment, 2/3 of snow are depth hoar (grain size > 3 mm), recent snow on top

** Source: http://www.udel.edu/Geography/calm/data/north.html
# 150 point grid across on polygonal tundra (18 x 27.5 m) measured since 2002

Table 1: Climate, history and surface characteristics of the three arctic study sites. In the text, only the region names are used (Alaska, Spitsbergen, Siberia).

Automated ground stations refer to temperature and volumetric water content sensors (Time Domain Reflectometry; TDR) installed at a point in the ground, snow or water body. These instruments are employed for quantifying fluxes at a small scale (centimetres). In contrast to TDR-probes and temperature sensors in soil, atmospheric micrometeorological instruments average over a much larger area, depending on the choice of method and height of instruments. For example, stationary and mobile eddy covariance towers, installed at heights of 2-3 m integrate fluxes over a fetch area of about 200-300 m. The micrometeorological methods, including eddy covariance towers are presented and discussed in Chapter 2.

To estimate the thickness and thermal state of the seasonally freezing and thawing active layer, of snow and of the deeper permafrost, numerical methods including heat conduction methods (Chapter 2.2), and volume energy balance calculations (Chapter 2.1 and 2.3) are performed. The fluxes are balanced as atmospheric budgets together with measured radiation budgets and ground flux in various materials (snow, water, permafrost). In addition, hydrologic budget components including precipitation (rain), discharge and storage changes in lakes and ponds are measured directly (Chapter 2.3).

Subject	units	Field instrumentation	Method	Site	Chapter	Field data collection
Energy balance: Q_{net} -Q_h -Q_e -Q_g -Q_m= C	[W m^{-2}]			SP SP SIB SIB	2.1 2.2 2.3 2.4, 2.5	1998-2001 2008-2009 1999, 2003 2007-2008
Q_{net}	[W m^{-2}]	Radiation budget sensors	Radiation budget	SIB SP SP AK	2.3,2.4, 2.5 2.1 2.2 2.6	1998-2008 1998-2001 2008-2009 2001-2003
Q_e	[W m^{-2}]	Weather stations Eddy covariance stations	Priestley Taylor Eddy covariance Priestley Taylor	SIB SIB AK	2.3 2.4, 2.5 2.7	1998-2001 2007-2008 2001-2003
Q_h	[W m^{-2}]	Weather stations Eddy covariance stations	Remainder of energy balance Aerodynamic profile Eddy covariance	SIB SP SP	2.3 2.1 2.2	1999, 2003 1998-2001 2008-2009
Q_g (snow, permafrost, water bodies)	[W m^{-2}]	Temperature and water content profiles	Calorimetric/volumetric Calorimetric/volumetric Calorimetric/volumetric Conductive method Conductive method	SIB SIB SP SP AK	2.3 2.4, 2.5 2.1 2.2 2.7	1999,2003 2007-2008 1998-2001 2008-2009 2001-2003
Q_m	[W m^{-2}]	Snow depth and density	Change in field SWE/ snow heat flux (melt, refreeze) Temp. index model	AK AK SIB SP AK	2.6 2.7 2.7 2.7 2.6	2001-2003 2000 1999 1999 2001-2003
Water balance: P-ET-R= ΔStorage	[mm]	Direct water budget measurements; Field surveys	Spatial distributed hydrologic modelling	AK	2.6	2001-2003 2004, 2005
ET (= Q_e)	[mm]	Weather stations	Priestley Taylor	AK	2.6	2001-2003
P	[mm]	Rain gauge; Snow depth and density	Precipitation (rain) SWE (snow)	AK	2.6	2001-2003
R	[mm]	Discharge/stage	Discharge	AK	2.6	2001-2003
ΔStorage	[mm]	Soil moisture profiles; Water level	Total soil water storage changes; residual of water balance Spatial distributed hydrologic modelling	AK	2.6	2001-2003
ΔStorage	[mm]	Water level Dye tracer test	Storage Darcy's law	SIB	2.3	1999, 2003
Soil thermal processes	[-]	Temperature and water content profiles	Projection of temp. data using heat diffusion equation	SP	3.2 3.2	1998-2000
Soil thermal and geochemical processes	[-]	Temperature, water content and bulk soil electrical conductivity profiles (TDR); Soil water extracts	Soil water electrical conductivity modelling; Thermodynamic equilibrium modelling	SP	3.2	1999-2000
Snow thermal	[-]	Temperature and	Snow volume energy	SP	2.1, 2.7	1998-2001

processes		Water content profiles; snow physical profiles	Balance model	AK SIB	2.7 2.7	2000 1999
Land cover	[-]	Aerial photography (balloon, kite)	Supervised classification Geometric analysis	AK SIB SP	4.1 2.4 4.3	2001 2006-2008 2008
Digital elevation model	[-]	Aerial photography (balloon, drone)	Photogrammetric analysis	SIB SP	4.2 2.2	2007 2008

Table 2: Summary of field and analysis methods applied in this thesis. AK: Alaska, SIB: Siberia, SP: Spitsbergen. Note: The notation for energy and water balance components varies between individual chapters 2-5. Evapotranspiration in energy budget calculations is termed Q_e and in water budget models ET. Acronyms are defined in section 1.4.

1.2.2. Energy and water balance characteristics of the study sites (Siberia, Alaska and Spitsbergen)

A quantitative understanding of the processes underlying the thermal and hydraulic dynamics of permafrost soils is paramount to improving the parameterization of the soil-atmosphere interaction in climate models and especially if we wish to anticipate consequences of a changing atmospheric forces. In this section, the seasonal and annual energy and water balances of small-scale spatial features and their short-term (seasonal, annual, wet/dry) variability are analysed quantitatively.

1-dimensional thermal and hydrologic dynamics of a mud boil

Thermal dynamic of a mud boil is investigated using temperature and TDR probes installed in the centre and rim of a single mud boil at the Spitsbergen site (Figure 6 and Table 2). Detailed data profiles from the middle thermistor string are obtained from this instrumentation and are used for the analysis of the 1-dimensional thermal dynamics during the period September 1998 to October 2000. It is found that four periods could be distinguished, based on the analysis of temperature data (Chapter 3.2, Plate 2). During the *cold period (i)*, the snow cover regulates the thermal and vapour exchange between soil and atmosphere. If the snow cover is thick, cooling of the soil is reduced. Excess water, produced by cooling of the soil, evaporates at intermediate depths and vapour diffuses upwards towards colder layers of soil and possibly snow. When soil-surface temperatures increase at the end of winter, the soil's liquid water and vapour content increase, consuming heat. The soil warms as a result of vapour migration to deeper, slightly colder layers and heat release via condensation and freezing. The *warming period (ii)* includes the warming, ripening and melting of the snow pack. This temperature increase causes a downward flux of vapour into colder soil layers. Furthermore, episodic infiltration of water from snowmelt and subsequent refreezing causes rapid warming of the soil. The *thaw period (iii)* comprises the progression of a thaw front where large amounts of heat are consumed. In the thawed soil, heat is produced below ~ 0.4 m by condensing water originating from warmer layers above. The highest water contents are found at the base of the thawed soil. With the onset of autumn, and decreasing air temperatures, the soil cools to 0°C and freezing starts, initiating an *isothermal period or plateau (iv)*. During this last period, a frozen layer at the surface inhibits propagation of temperature fluctuations from the surface. As a result, temperatures stay close to 0°C and conductive heat fluxes are negligible.

Excellent agreement is observed between expected and measured temperatures for the cold period at the Spitsbergen site. This agreement confirms that (i) simple heat conduction is the dominating

heat transport process and (ii) the characteristic soil freezing characteristic (SFC) curve plays a crucial role in freezing/thawing processes and thus modelling of water and heat transport.

The soil freezing characteristic curve describes the relationship between the soil's temperature and (liquid) water content in freezing and frozen soils. In frozen soils water can remain unfrozen at temperatures well below the freezing point due to soil matric forces. The decrease of liquid water content with decreasing temperature is mainly explained by the phase change of water to ice. Two examples of experimentally determined SFC are shown for the Spitsbergen site (Chapter 3.2, Figure 1) and for the Siberia site (Chapter 2.5, Figure 3). At - 10°C, about 6 % remains unfrozen in the loamy clay at the Spitsbergen site in contrast to only 1 % sandy soils at the Siberia site demonstrating the effect of the soil matric forces.

Movement of water and vapour phase is expected to be small with decreasing temperatures. Although the total amount of water transferred via these more complicated processes is generally small, they may become important over longer timeframes. Soil heave, secondary ice lens growth and large scale phenomena, such as pingos, are at least in part due to migration of water and vapour in freezing and frozen soils and subsequent accumulation of the ice phase.

2-dimensional thermal and hydrologic dynamics of a mud boil

The same mud boil is studied using instruments installed in the centre and the rim of the mud boil underneath vegetation. The soil material at the Spitsbergen site generally consists of silty clay with interspersed stones. The silt content decreases from the top of the profile to the bottom, concomitant with an increase of clay content (Chapter 3.1, Figure 3). Only very small horizontal differences between liquid water content due to texture differences is observed.
With the onset of snowmelt in spring, warmer temperatures rapidly penetrate downwards, and liquid water content increases. The bare circle centre starts to thaw first, while the vegetated border remains frozen; this process continues resulting in a non-uniform thaw depth. In the autumn, the freezing front propagates from surface to depth, with progressive conversion of water into ice until the soil column is completely frozen in December.

In summary, the energy exchange at the surface and the soil physical properties create a non-uniform thermal dynamic system. The mud boil centre thaws to greater depths, freezes more quickly and is subject to larger amplitude cycles than the surrounding vegetated border. Thus, the silty clay of the centre is most prone to ice-lensing and heave resulting in the typical elevated circle

structure (Chapter 3.1, Figure 3). While no modelling or measurements of the mechanics were conducted, some general explanation is possible. Differential frost heave occurs due to the non-uniform penetration of the freezing front from the surface, and upward from the frost table. Moisture and vapour migration (Chapter 3.1) favour ice lens growth in surface layers and towards the permafrost table; the overall measured heave at this site is between 2-4 cm per year. The freezing-induced stress may displace the soil upward, either in fluid, plastic or frozen conditions. This would lead to a theoretical cycling period of the mud boil of 50…100 years (2 * 100 cm thaw depth /2…4 cm heave) thus potentially mixing the material.

Solute concentrations are measured to investigate whether chemical gradients could be the cause of the non-uniform freezing front. Vertical solute concentration gradients are found to be much larger than horizontal gradients with highest concentrations at the bottom of the profile. The depression of the freezing point due to solute exclusion is insignificant. Thus, variation in soil freezing points due to solute concentrations is not large enough to induce irregularities in the permafrost table that result in a bowl-shaped depression. The differences in surface cover and soil physical properties between the centre and rim affect the subsurface thermal regime in such a way that the non-sorted circle structure is maintained through differential frost heave.

2-dimensional water budget characteristics (watershed scale)

Low topographic environment-polygonal network (Siberia)

The water budget at the low polygonal tundra site in Siberia is investigated using measured energy and water budget components from 1999, 2003, 2007-2008 (Chapters 2.3-2.5; Table 2). At this site, vertical water fluxes dominate during the summer (>50 %) due to the low topographical gradient and the water availability in the polygonal ponds and lakes. About 20 % of the snow sublimates and evaporates in 2008 (12 mm), supplying 45 mm to the water budget. Thus only 20 % of the total annual precipitation input is supplied by snow, highlighting the importance of rainfall for the hydrologic budget.

Spatially distributed measurements of evapotranspiration (Chapter 2.4, Figure 1) suggest distinctly different surface energy balances over scales of ten meters due to the pattern of dry and wet areas of the tundra polygons. However, these differences only exist during conditions of high radiative energy input (Q_{net} >200 W m^{-2}), which only occur occasionally at this site due to frequently cloudy conditions (Chapter 2.4, Figure 3.7). Only during very contrasting years, such as during a very dry year (1999: 88 mm) or a very wet year (2003: 208 mm), do seasonal differences in the surface

energy balance become pronounced (Chapter 2.3). During a drier year, with less surface moisture in lakes and vegetation, the atmospheric fluxes are, in general, evenly portioned between evapotranspiration, sensible heat flux and ground heat flux. During a normal year, which is dependent on a minimum of precipitation (mean summer rainfalls: ~137 mm), the evapotranspiration amounts to at least 50 % of the net radiation, reducing the sensible heat transfer into the atmosphere and the ground heat flux. The latent heat flux is a factor of two higher than the sensible heat flux. The observed precipitation in 2007/2008 balances with the evapotranspiration. This indicates a regionally closed water cycle between the atmosphere and the tundra surface. However, at the Siberian site, the underestimation of the water budget calculated from P-ET alone and tracer experiments (Chapter 2.3; Figures 8 and 9) suggests that the study pond is connected with neighbouring ponds via subsurface flow through sandy soil layers with high hydraulic conductivity. In addition, after heavy rainfall events, water is drained and conveyed to streams via the existing polygonal ice wedge drainage network and newly formed thermo-erosional channels (Chapter 2.3, Figure 11). As a result, the water table returns to its original position within about 4 weeks, even after high precipitation events, such as observed in 2003 (Chapter 2.4, Figure 7). However, vertical fluxes are still dominant in the overall water budget. This fact is supported by direct measurements of the full water balance in 2008 where lateral runoff only accounts for about 10 % of the total budget, mostly fed by rain water (Abnizova *et al.*, 2010).

Hillslope dominated water track watershed (Alaska)

A 2-dimensional water budget for the hillslope-dominated watershed in Alaska, determined based on measured and modelled water balance components (Chapter 2.6), is quite different from that of the Siberian site. At the Alaskan site, the water balance is dominated by lateral fluxes (>50 %). During the years 2001-2003 runoff accounts for 54 %, 60 %, 67 %, and evapotranspiration for 48 %, 42 %, and 28 % of the water budget. For each year, the winter snow pack is a major source of water to the system. For the years of this study it accounts to 33–41 % of the total amount of water added. The modelled subsurface storage term is more or less balanced: only during a year with high summer precipitation input it is “enlarged”. The major processes of the water balance (precipitation, snowmelt, evapotranspiration, groundwater flow, and overland/channel flow) as well as some storage processes (snow accumulation and infiltration/percolation) are simulated using a spatially distributed, process-based hydrological model (TopoFlow). Climatic conditions vary greatly during the course of the year and between the three years and overall are well reproduced by the model. A digital elevation model (DEM) with a pixel size of 25 x 25 m is used; the simulated channel network (Chapter 2.6, Figure 2) reproduces the channel structure of water tracks that is visible in

aerial pictures. Including water tracks improves the simulation result when compared to the measured hydrograph (Chapter 2.6, Figure 11). The simulation indicates that the existence of water tracks accelerates runoff and leads to higher amplitudes in the hydrograph than without water tracks.

Annual energy and water fluxes

Results of the annual energy and water fluxes from the low polygonal tundra site are discussed for Siberia (Chapters 2.4 and 2.5) for the years 2007-2008 and for the Spitsbergen site from 1998-2001 (Chapter 2.1) and 2008-2009 (Chapter 2.2). The applied field and modelling methods are furthermore summarized in Table 2. A summary of the typical summer and winter energy balance for Spitsbergen and Siberia is given in Figure 7.

As measurements of the energy balance components are based on different methods which are subject to errors a residual in the energy balance (closure term: C) remains. Due to the larger magnitude of fluxes during the summer, C is larger as well. The accuracy and precision of the employed field instruments is described in detail in Chapters 2.2, 2.4, 2.5.

At both locations, the surface energy budget is determined largely by radiation: net short-wave radiation during summer (energy source) and net longwave radiation during the winter (energy sink). The net radiation essentially depends on the seasonality of the short-wave radiation budget, the presence or absence of the snow cover and the cloudiness. The first two factors mainly influence the radiation budget, reflecting the largest fraction of the incoming short-wave radiation in spring, and by increasing the incoming long-wave radiation.

Turbulent heat fluxes have their largest impact on the surface energy budget during summer, when they balance about 70 % of the net radiation. The latent heat flux is a factor of two higher than the sensible heat flux at the Siberia site, while at the Spitsbergen site, the sensible and latent heat flux are nearly equal (Figure 7). About 15 % of the net radiation is consumed by the seasonal thawing of the active layer in July and August at the Spitsbergen site, and up to 20 % (60 % for thaw of ice rich ground, 40 % for warming) at the Siberia site.

During the winter period the radiative energy fluxes are negative and all fluxes are significantly smaller, compared with those measured during summer except for the ground heat flux at the Siberian site. The latent heat fluxes used for sublimation are the smallest term in the energy balance

(Figure 7). The sensible heat flux is the second largest flux term, providing heat input for the surface, thus, together with the ground heat flux, balancing the large radiation sink at the Spitsbergen site (Figure 7). In contrast, the winter ground heat flux is about 3 times as large at the Siberian site. Here, the ground heat flux is a significant component in the surface energy balance, with relative contributions of up to 60 % during the winter. The high contribution of the ground heat flux to the surface energy balance at the Siberian site is due to the cold permafrost temperatures, the high ice content and large annual surface temperature amplitude, which is related to the climate conditions. The heat flux is increased by a factor of two in the refreezing thermokarst pond (Chapter 2.4, Figure 1; “Lake station”) thus demonstrating the overall importance of water bodies in the surface energy budget of the polygonal landscape. Inter-annual differences in the surface energy balance are related to differences in onset of snow accumulation and snow thickness. The annual surface energy budget is more sensitive to processes in winter, due to (i) the long winter period and (ii) high variability of snow and cloud cover. The later one is manifest, for example, in refreezing of soil and water bodies, which varies significantly in duration between years. Thus, the winter snow cover plays a dominant role controlling the thermal regime of the subsurface permafrost.

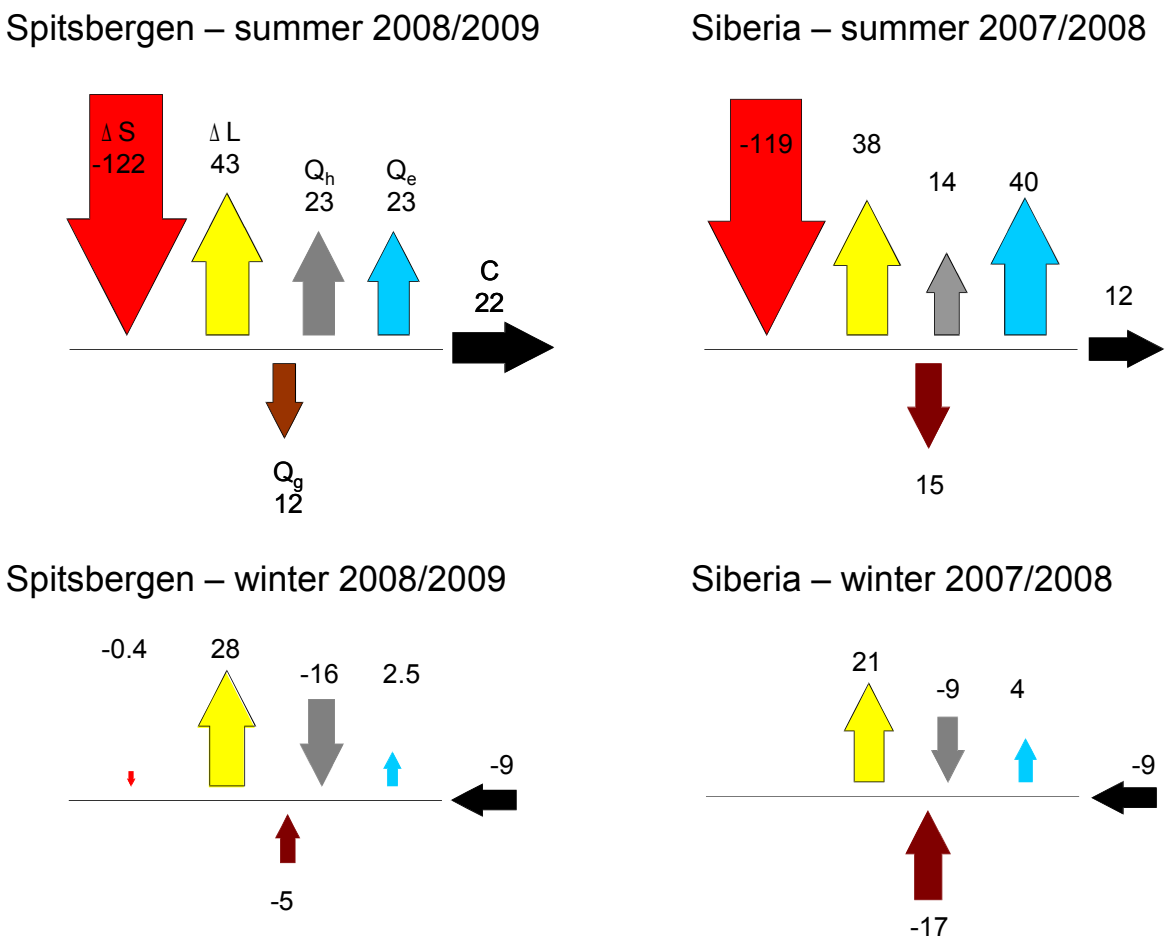

Figure 7: Comparison of typical mean summer (upper two figures) and winter (lower two figures) fluxes (W m^{-2}) for the Spitsbergen and Siberia sites. Fluxes are scaled to each other. ΔS net shortwave radiation, ΔL: net longwave radiation, Q_h: sensible heat flux; Q_e: latent heat flux; Q_g: ground heat flux; C: closure term (see Chapter 2.2, 2.4, 2.5 for methods).

Snow ablation, internal processes and melt

The physical properties of the snow cover, when it is established, its duration and its thickness, control the thermal regime of the subsurface permafrost. Thus, special emphasis is given to understanding the build up and ablation of the snow cover and its affect on the energy balance.

A volume energy balance model is applied for three sites (Samoylov, Siberia; Ivotuk, Alaska, Bayelva, Spitsbergen) for the duration of the spring snow ablation period to investigate larger scale differences due to climate (Chapter 2.7). It is noteworthy that almost 50 % of available energy, mostly provided by net radiation is consumed by sublimation and evaporation from melt water ponds in Siberia (Chapter 2.7, Figure 7). The loss of heat into the ground is the smallest component

in the balance, with a maximum (18 %) at the Siberian site and minimum (6 %) at the Alaska site. At the Spitsbergen site, the loss of heat into the ground ranges between 10 to 30 %: infiltration and refreeze of water is a source of up to 10 % of the energy. The differences in duration of snow ablation (several days at the Siberian, several weeks at the Alaska and several months at the Spitsbergen site) are related to differences in total snow water equivalent and energy source. The dominant energy source for snow melt at the Spitsbergen and Siberia sites is net radiation, while sensible heat and net radiation are the dominant sources at the Alaska site. At this site, dry and warm air descending from the Brooks mountain range provides sensible heat used for snow melt.

Classification of snow profiles in the field provides precious information about the past winter climate conditions during which the snow cover is formed. The snow profile on Spitsbergen shows several internal ice layers and a basal ice layer overlying the frozen soil, indicating winter melt and freeze conditions. In contrast, no melt takes place at the very cold site in Siberia. The snow here consists of very loose, large grained depth hoar in addition to hardened, sediment rich layers, suggestions a large thermal gradient and high winds with transport of aeolian material (Chapter 2.7, Figure 5).

Among the three sites, wintertime rainfall and warming events are unique for the Spitsbergen site. At this site, the snow-free period is only about 3 months, thus the snow cover and the timing of snow melt in spring essentially control the amount of short-wave radiation that is available for energy partitioning. The thick layer of snow greatly reduces the heat exchange between the permafrost soil and the atmosphere. Soil cooling is observed to be about twice as effective during a winter when the snow cover was half as thick. Also, year-to-year variation in thickness and duration of the snow cover can be large (for example, the number of snow-free days at the Spitsbergen site in 2000 is about half compared to 1999). This affects the total amount of energy transferred towards the surface and thus the permafrost's thermal regime.

The evolution, ablation of snow cover and its internal processes are studied in detail over several years (1998-2001). The applied volume energy balance model (Chapter 2.1) includes net radiation and turbulent heat fluxes (sensible and latent), heat flux supplied by rain and sensible and latent heat fluxes of the ground and snow. The calculation of the ground and snow's sensible and latent heat content is based on *in situ* measurements of temperature and volumetric moisture content (Chapter 2.1). Snow accumulation begins in October, but is interrupted by winter melt events, creating internal ice lenses and/or basal ice which can be widespread. Internal processes in the

snow, such as the formation of an internal ice lens or a basal ice layer (overlying the soil) is quantified using the volume energy model: infiltrating water in a cold snow pack creates internal ice lenses, while infiltration in warmer snow permits through-flow and refreezing at the surface of the cold soil, creating a basal ice layer which releases heat that warms the permafrost (Chapter 2.1, Figure 6). Furthermore, the energy balance model permits two separate ablation periods to be distinguished from one another: stage I, where the snow pack is homogenized and its height becomes reduced due to internal processes occurring in the snow. During stage II, the snow water equivalent (SWE) is reduced and meltwater is produced. Overall, the heat provided by winter rain on snow events' is of great importance for correct estimation of the ground's thermal budget (Boike *et al.*, 2010; Westermann, 2010). Furthermore, since these events can create widespread basal ice layers, they also have been discussed as important for ungulate survival (Putkonen and Roe, 2003).

In summary, differences between the sites in radiative, atmospheric fluxes and ground heat fluxes are relatively small during the summer. Evapotranspiration ranges between 1-2 mm d^{-1} for all the three studied sites during the snow free period. The summer water budget, however, varies significantly between the sites and depends largely on the precipitation input and timing. At all sites, patterned ground exerts a major influence on the heat and water budget. At the Spitsbergen site, small-scale differences in surface and subsurface heat budget induce and maintain small-scale differences such as greater thaw depths underneath mudboils. With a larger feature, such as polygonal pond in Siberia, the heat release during fall freeze back affects the surface temperature. At the watershed scale (Alaska, Siberia) the water storage and runoff is affected by topography and patterned ground features, such as water tracks and polygonal ponds and lakes. Understanding their dynamic as well as their phenomenological appearance on larger spatial and temporal scales is thus required.

1.2.3. Quantifying the patterns from air and space?

The small-scale processes investigated in previous chapters, such as water and vapour movement in permafrost soils, can take place over time scales of seasons up to millennia and form the characteristic patterned ground landscape. These patterns, as well as biophysical characteristics of the water/vegetation/snow surface (e.g. roughness, spectral characteristics) define the fluxes of energy and water horizontally and vertically, into the atmosphere and into the subsurface. Thus, mapping and classifying the structure and properties of the surface, which can vary greatly over scale, is of great importance for upscaling from local sites.

The use of kites, balloons, blimps, drones for aerial photography

Smaller-scale patterns on the order of meters to tens of meters are usually not recognizable on commercially available satellite images. Furthermore, identifying patterns from the ground (that are larger than what the eye can distinguish) is also difficult. For example, ice wedge patterns (Chapter 4.1, Figure 2) have a size of >30 m and thus are hard to identify on the ground. The use of airplanes and helicopters is expensive and often they are not fitted with the equipment required for taking pictures facing downward (nadir) which requires a camera hatch or a camera suspension system.

Chapter 4.1 discusses a method for obtaining images using conventional digital cameras. Cameras can either be triggered by an internal interval function (for example Nikon D200) or through an additional programmable data back (Olympus C2020). The cameras can be suspended from the aerial vehicle using a simple T-shaped pendulum suspension (made from a camera tripod; Chapter 4.1, Figure 1), or a more sophisticated apparatus (such as a self levelling platform," Picavet") or a universal joint suspension that allows rotation about the vertical and horizontal axes. The choice of aerial vehicle (kite, balloon, blimp or drone) depends on the weather conditions, and the size of area that needs to be covered. In no- or low-wind conditions (<3 m sec^{-1}), balloons and blimps work well. A remote-controlled drone can be used at wind speeds up to 8 m sec^{-1}. Various kites can be used in higher wind conditions, between 6-12 m sec^{-1}. The ground resolution of the image is calculated from reference marks on the ground (ground control points; GCPs). Aerial images are used for quantifying (i) vegetation (Chapter 4.1, Figure 5) (ii) geometry of small scale patterns (Chapter 4.3) and (ii) identifying wet and dry areas for micro-meteorological flux footprint calculations (Chapters 2.2 and 2.5) and (iv) for classification of surface characteristics for thermal infrared remote sensing (Langer *et al.*, 2010b) and barren ground surfaces on Spitsbergen

(Westermann *et al.*, 2010). An example of the application of high resolution classified images is shown in Figure 8 for the Siberia study site. Differences between wet and dry areas are quantified for the four eddy covariance foot print areas, showing a range between 52 to 79 % of dry area. The second eddy foot print has 71 % of dry surfaces compared to 60 % of the stationary reference site (Figure 8). Accordingly, the spatial differences are reflected in differences in turbulent fluxes. Simultaneous eddy covariance measurements at both locations indicate differences in sensible and latent heat fluxes in the order of 20 W m^{-2} (10-20 %) under conditions of high radiative forcing (Chapter 2.4, Figure 3.7). Mapping of land cover characteristics thus offers a potential for upscaling of energy and water fluxes at larger scales.

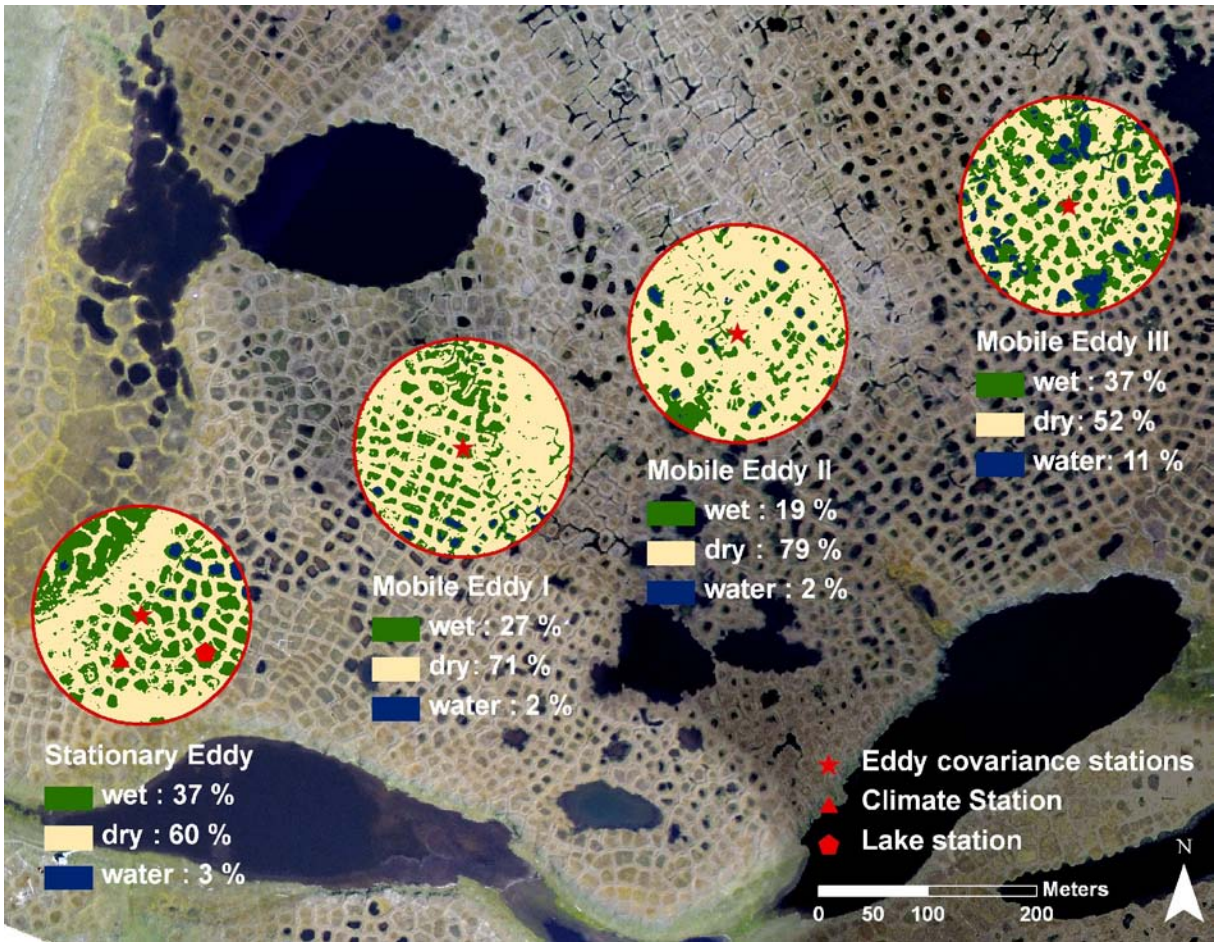

Figure 8: Aerial mosaic obtained from balloon aerial images in 2007 at the Siberian site (Island Samoylov). The quantification of areas is based on supervised classification and field mapping; water bodies are extracted via threshold (density slice) in the near infrared band and masked; the remaining areas are classified using a supervised maximum likelihood classifier. The stationary eddy covariance, climate and lake station remained at these locations, while a second eddy covariance station (mobile eddy) is moved across the transect (Chapter 2.4).

Application: construction of digital elevation models (DEM)

In areas with low topographic gradients it is difficult to obtain small scale digital elevation models that are required input for hydrologic modelling. For the Siberia site (the island Samoylov) the best available DEM is a topographic map (1:200 000) with a ground resolution between 0.5 to 1 km. The method presented here is suitable for obtaining higher resolution DEMs at remote sites. It requires distribution of GCPs that are clearly visible in images and knowledge of the coordinates (x, y, z). For this site, 20 GCPs with a spacing of about 500 m are laid out over an area of about 5 km² (Chapter 4.4, Figure 3) and their position is surveyed in the local coordinate system using a tachymeter. Using overlapping aerial photographs of a flying height between 600 and 800 m, position, orientation and intersection of the images are determined and combined in "bundle adjustment procedures", where the image orientation parameters and the ground coordinates of tie points are simultaneously calculated (Chapter 4.2). As a result, a DEM with a final ground resolution on the order of 10 m and a horizontal and vertical accuracy better than 1.0 m is created (Chapter 4.4, Figure 8). This DEM can be used as input for creation of stream network as input for hydrologic modelling (Chapter 2.6) or terrain georeferencing of thermal images for obtaining surface temperatures (Westermann *et al.*, 2010).

Application: Quantification of permafrost patterns

Permafrost patterns are useful indicators for identifying geomorphological and environmental conditions and their changes over time. Enhanced satellite observation programs (for example the commencement of Raid Eye, with a resolution of up to 5 m), provide frequently updated images. These images function as a comparative data base to detect and identify landscape changes.

The method introduced in this section is based on Minkowski numbers. It uses quantitative geometric descriptions to reduce complex spatial information to a limited number of relevant quantities that are easily comparable. This concept of geometric description was applied by Mecke (2000) in the field of statistical physics to quantify diverse structures such as porous media and patterns of dissipative systems. Using this approach (Chapter 4.3), patterned ground surfaces are quantitatively described using geometrical properties, specifically size, spatial distribution and topology of the 2-dimensional patterns.

The method is used to compare two kite aerial images obtained on an island off the Alaskan Coast, Howe Island (70°18'N, 147°59'W). The patterned ground observed in the first picture, H1, (Chapter 4.3, Figure 5) is multi-structured, i.e. it shows patterned ground on different scales, ice wedge polygons with sizes of tens of meters, non-sorted circles with sizes of meters and even smaller-scale non-sorted polygons (centimetre scale). The second aerial image, H_2 is largely dominated by non-

sorted circles (Chapter 4.3, Figure 5). The differences of the patterns are quantitatively described as differences in surface areas, length of interfaces of patterns and topology (connectivity of the pattern) using Minkowski numbers.

Thus, quantifying patterns through numbers and relating them to, for example, physical parameters (for example surface water fluxes) could be a subject for future investigation, as well as a method for quantifying changes.

1.2.4. Predictions on larger spatial and temporal scales

Wetlands, lakes and ponds are a typical feature of northern ecosystems and play an important role in the local and regional climate and hydrology by governing the heat and water fluxes as well as the carbon cycle. Even larger, global effects are reported. For example, the formation of thermokarst lakes and their methane emission is currently discussed as the main factor for high methane levels at about 12 kyr BP in ice cores from Greenland and Antarctica (Walter *et al.*, 2007; Petrenko *et al.*, 2008).

Lakes absorb and store heat in the spring and summer, and release heat during autumn and winter, thus playing a significant role in surface energy budgets. As discussed in Chapter 2.5, even a small pond with a volume of about 70 m^3 continuously supplies heat during refreezing, increases the surface temperature and consequently turbulent heat fluxes. Furthermore, larger-scale lake area fluctuations alter surface albedo and energy partitioning in the expanding and contracting lake area.

General circulation model and arctic water bodies

There are various scenarios regarding the extent of inland water surface (IWS) in the future. To assess the effect of a potential reduction of IWS on the energy and water cycles, a climate model sensitivity test for the end of the 20th and 21st century is carried out in Chapter 5.1 The sensitivity test considered all IWS on the ice-free continental areas between the arctic coastline and the southern limit of the taiga. The simulations are based on the SRES (IPCC Special report on emission scenarios), the A1B greenhouse gas concentration scenario using a general circulation model with 144x108x19 (longitude x latitude x vertical) grid points. At this resolution, lakes will not be represented explicitly, but the large-scale model parametrization is analysed by running

different sensitivity tests. The dependency of the simulated future boreal climate change to future IWS changes is evaluated by the following simulations: (i) a total disappearance of all IWS (ii) a 50 % reduction of future IWS extent and (iii) a fractional reduction of high latitude IWS as a function of the simulated reduction of the area of annual-mean subsurface temperatures. Scenario (iii) is based on the hypothesis and figures set forth by Smith *et al.* (2005a, 2007), and prescribes a 40 % IWS reduction in regions where the permafrost would eventually disappear under a climate of the end of the 21st century, together with a 10 % increase in the remaining permafrost areas.

Overall, this sensitivity test suggests that the direct climatic impact of expected future IWS changes will be moderate on large spatial scales, with fairly weak precipitation and circulation changes. Near-surface temperature appears to be more sensitive. The future mean annual warming in the continental regions of the high northern latitudes may be reduced by about 10 % by the effect of the warming based on the future extent of IWS. Seasonal characteristics of the future temperature changes may be more strongly affected, for example, an increase in the summer surface temperature. In the most likely simulation (iii) the future near-surface warming is reduced by up to 30 % regionally and seasonally. However, in summer, the future warming might be intensified due to the reduced cooling induced by the decreased IWS extent. The impact of these IWS changes on the simulated surface water balance (precipitation minus evapotranspiration; P-ET) do not contradict the expected changes of IWS: in the most northerly regions, where the scenario would suggest an increase of IWS, the simulated annual mean P-ET increases. Further south, there are no systematic changes of P-ET.

Overall, these estimates are still very crude, since it is not clear how and when permafrost degradation and lake drainages would occur. This would require landscape modelling, including thermal information from lakes as well as permafrost information (for example, the thermal state, thickness and ice content). Furthermore, discrepancy between these large-scale data sets and high resolution data sets on distribution and coverage of lakes shows an underestimation by a factor two to seven (Grosse *et al.*, 2008).

Since there is a large gap, in both spatial and temporal scale between these general circulation simulation results (Chapter 5.1) and results from the experimental field sites (Chapters 2.3-2.6), in the following another method for modelling past and potential future changes on the water and energy balance on an intermediate scale is introduced.

Introducing an intermediate scale between global and local scales- an example from Siberia

The following example from the Siberia site utilized the concept of scale to resolve uncertainties in a large-scale dataset. Good knowledge of site processes is available from measurements made at a centimeter scale (soil profile) and at a small watershed scale (~7 km^2). These are used as background information to interpret data for a grid cell of at least 2.5° latitude-longitude. This grid cell describes the (max) spatial resolution of long term reanalysis data such as ERA-40 or ERA Interim, a data set based on a combination of weather observations from land- and sea-based stations, including wind, temperature and humidity profiles from radio soundings, satellite observations of atmospheric water vapour and wind fields (Uppala *et al.*, 2006).

Figure 9 shows the modelled long term water budget (total precipitation minus evapotranspiration) since 1958 for the Siberian site using reanalysis data. Evapotranspiration is calculated using Thornthwaite (1948) which is tested and calibrated for several years using site eddy covariance data (Kattenstroth, 2009). The total amounts of water are generally small, the long term water budget is roughly balanced, tending towards slightly positive values (P > ET). Agreement exists between the water balance determined on aerial images, visualized qualitatively as "filling" status of the ponds and lakes, and modelled P-ET water balance. The years 1964 and 2007 represent normal (positive; P > ET) years, whereas the dry year (P < ET) in 1968 is atypical (Figure 9 B). The CORONA satellite image from 1968 indicates a dry tundra landscape as ponds disappear and thermokarst lakes shrink. This concurs with the modelled negative water balance, a consequence of reduced summer precipitation. These results demonstrate the need for an integrated field and model approach: the importance of a one summer drying event is put into perspective within longer time scales; higher than average precipitation rates only increase the water level of the tundra on a short time scale since the microtopography and drainage network of polygonal ground channels water into the stream network.

Seasonal CH_4 emission rates are determined by the wetness status of the tundra, (polygons, thermokarst lakes on a larger scale (Sachs *et al.*, 2010) and thus are mostly driven by precipitation and hydrologic channel networks which are site specific. Thus, observing hydrologic processes is one important key process necessary for future predictions of CH_4 emissions.

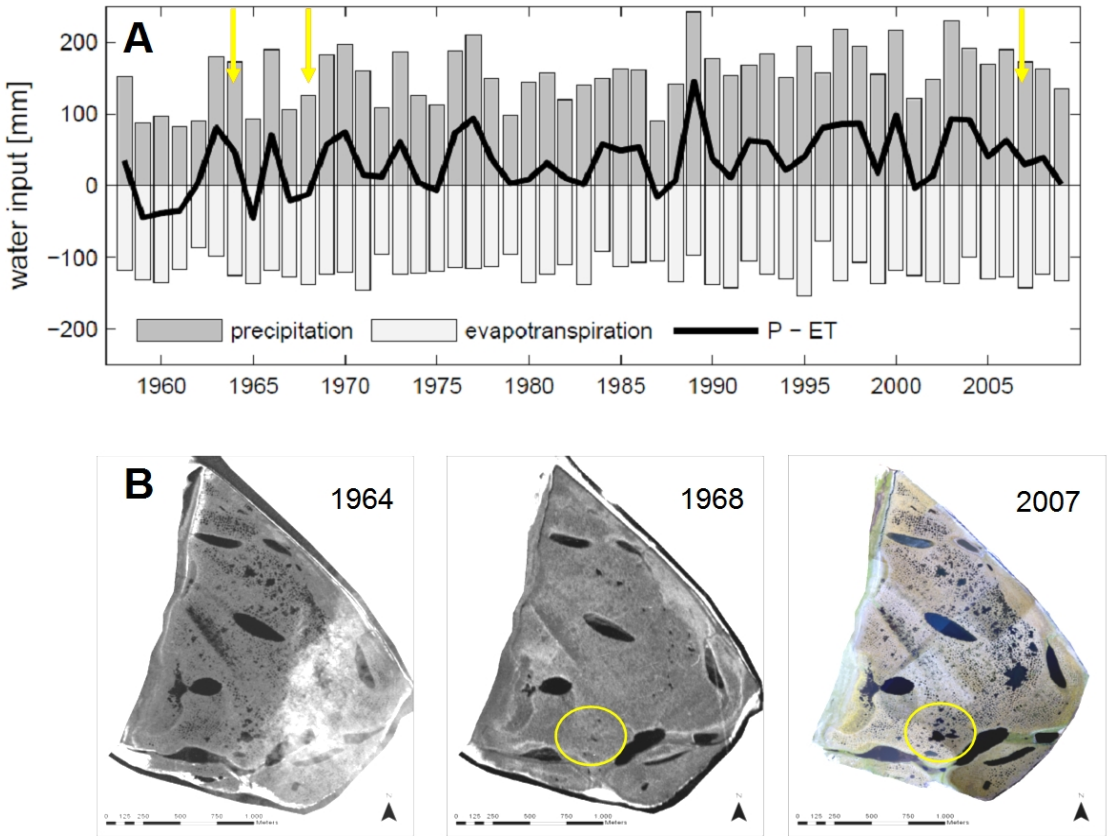

Figure 9: A. Annual long term water budget calculations (precipitation- evapotranspiration) from 1958 to 2009. Air temperature (2 m height) and total precipitation data are obtained from ERA-40 and ERA-interim data sets using 6 hourly data sets. The ERA–40 data are available on a Gaussian grid with spatial resolution of 2.5°×2.5°, while the resolution with 1.5°×1.5° is marginally better for ERA–interim. The data are interpolated between the four closest-lying grid cells for the Siberian site. Evapotranspiration is calculated using the Thornthwaite (1948) approach calibrated for this site using eddy covariance data (Kattenstroth, 2009). The years where high resolution CORONA data are available are marked with yellow arrows. B. CORONA high resolution images of the Siberian site (CORONA images from August 17, 1964 and September 29, 1968; aerial mosaic from balloon aerial photography August 2007). 1968 is the only recorded year on available satellite images where drying of ponds and shrinkage of lakes is observed (for example inside the yellow ring). ERA data provided by ECMWF (http://data-portal.ecmwf.int/data/).

1.2.5. Conclusions- the big picture

Climate change models must consider greenhouse gas emissions from arctic soils if they are to provide reasonable simulation results. Physical processes occurring in permafrost such as freeze and thaw, the resulting carbon fluxes and feedback mechanisms have a huge effect on climate and, in

particular, the emission of CH_4, which is a very efficient greenhouse gas. Thus, it is not possible to model climate change without considering permafrost. Yet only few climate models consider freeze thaw processes, and none of the models so far do not include physical processes occurring in permafrost on a subgrid scale (thermokarst) or carbon storage and fluxes.

In the Coupled Carbon-Climate Change Model Intercomparison Project (C_4MIP)2, most terrestrial biosphere models predict an enhanced carbon sink due to warming at high latitudes (i.e. Friedlingstein *et al.*, 2006). According to these models, longer growing seasons and enhanced productivity offset the heterotrophic respiration caused by the warming. However, these models do not include permafrost. Without a realistic reproduction of the current physical state of permafrost, and reproduction of surface energy, water and carbon balances, then large-scale climate assessments of green house gas emissions remain uncertain.

How does this habilitation thesis add to the big picture?

The following key aspects are synthesized from the results of this thesis:

1. The study of permafrost patterned ground is scientifically relevant because of the following: (i) patterned ground regulates the partitioning of atmospheric and ground fluxes on all studied scales- from small circles to large-scale wetlands and lakes dotting the arctic permafrost landscape, (ii) their phenomenology indirectly indicates their hydrologic characteristics (wetness status, dominance of vertical or horizontal fluxes), (iii) distinct changes in the landscape are caused by "extreme" precipitation events, for example "empty" ponds and polygons (dry), refilled thermokarst lakes in Central Yakutia, new drainage system following thermo erosion processes after intense summer rainfalls. Thus, observation of the permafrost patterned landscape and its changes in surface morphology have potential as indirect methods to detect wetness status, hydrologic characteristics and climate changes.
2. The water and energy balance of permafrost areas is most strongly affected by changes in the radiation and precipitation (rain and snow) budget. While the impacts are difficult to estimate on a global basis due to the complex interplay between local and larger-scale climate factors, local and regional observations and process understanding are mandatory for upscaling.
3. The subsurface heat flow in permafrost is associated with temperature change, as well as phase change of soil water. The temperature change in the frozen and unfrozen soil can be largely described by conductive heat transport, whereas the phase change of soil water can

be seen as a discrete heat sources or sinks at the thawing or freezing front. The magnitude of the seasonal heat exchange is strongly affected by site-specific subsurface properties, such as the thermal conductivity of the soil. The key factors affecting the ground heat flux are especially influenced by the amount of water in form of (i) ground ice and soil water, (ii) surface water bodies and (iii) snow water equivalent. Especially the high heat storage of water bodies plays an important role, influencing the local and regional climate.

Recommendation for a future research strategy

The primary goal, to understand permafrost and its role in the earth's climate system, including feed back mechanisms, requires new model developments and upscaling strategies.
One successful upscaling approach using a combination of climate reanalysis data and process understanding is presented in 1.2.5. Another approach has recently been applied to surface temperature monitoring using a thermal imaging camera and MODIS data (1 km^2) in Siberia and Spitsbergen (Langer *et al.*, 2010b; Westermann *et al.*, 2010). Hence,

i) field studies should be run at representative sites to systematically long term monitor key parameters and processes, thereby improving our understanding of permafrost dynamics at a range of scales
ii) development and incorporation of conceptual and numerical permafrost landscape models, including suitable upscaling methods from local to global scales
iii) utilisation of remote sensing products to test, validate and monitor i) and ii).

It is important to note that all strategies require field-based knowledge of the surface characteristics, key processes and monitoring data for a few key parameters. Obtaining funds for this is often impeded by political and technical limitations. Funds are often cut from budgets, since the merit of field studies is often first apparent after a longer time frame (Nisbet, 2007). However, the vision of a pan Arctic state-of-the-art network of "Arctic Observatories" in support of modeling efforts should be developed. By providing reliable data sets on the impact of climate change, such a showcase of international science collaboration could provide guidance for policy makers and international agencies in search for sustainable strategies for the Arctic.

I hope that this work is a further motivation for creating a pan Arctic network, brought forward by the scientific community.

1.2.6. Literature

Abnizova, A., Bornemann, N., Langer, M. and Boike, J. (2010): Linkage between seasonal hydrology and carbon flux dynamics in tundra ponds: Samoylov Island, Lena River Delta, Siberia, *European Geosciences Union General Assembly* 2010, May 2 – 7, Vienna, Austria.

Batjes, N. H. (1996): Total carbon and nitrogen in the soils of the world, *European Journal of Soil Science* 47, 2, 151-163.

Black, R. F. (1976): Periglacial features indicative of permafrost: Ice and soil wedges, *Quaternary Research* 6, 3-26.

Block, D., Heijmans, M. M. P. D., Schaepman-Strub, G., Kononov, A. V., Maximov, T. C. and Berendse, F. (2010): Shrub expansion may reduce summer permafrost thaw in Siberian tundra, *Global Change Biology* 16, 1296-1305.

Boike, J., Roth, K. and Ippisch, O. (2003): Seasonal snow cover on frozen ground: energy balance calculations of a permafrost site near Ny-Ålesund, Spitsbergen, *Journal of Geophysical Research (Atmosphere)* 108 (D2), 8163, 4/1-11.

Boike, J., Westermann, S., Piel, K. and Overduin, P. P. (2010): Warming of permafrost temperatures on Svalbard - what is the effect of the snow cover? *3rd European Conference on Permafrost*, June 13 - 17, 2010, Longyearbyen, Svalbard, Norway.

Bowden, W. B., Gooseff, N., Balser, A., Green, A., Peterson, B. J. and Bradford J. (2008): Sediment and nutrient delivery from thermokarst features in the foothills of the North Slope, Alaska: Potential impacts on headwater stream ecosystems, *Journal of Geophysical Research* 113, G02026.

Brown, J., Ferrians Jr., O. J., Heginbottom, J. A. and Melnikov, E. S. (eds.) (1997): Circum-arctic map of permafrost and ground-ice conditions. Washington, DC: U.S. Geological Survey in Cooperation with the Circum-Pacific Council for Energy and Mineral Resources, *Circum-Pacific Map Series* CP-45, scale 1:10000000, 1 sheet, 1997.

Burnham, J. H. and Sletten, R. S. (2010): Spatial distribution of soil organic carbon in northwest Greenland and underestimates of high arctic carbon stores, *Global Biogeochemical Cycles* 24, GB3012.

CAVM Team (2003): Circumpolar arctic vegetation map, Scale 1:7,500,000, Conservation of Arctic Flora and Fauna (CAFF), Map No. 1. U.S., Fish and Wildlife Service, Anchorage, Alaska.

Chapin III, F. S., Sturm, M., Serreze, M. C., McFadden, J. P., Key, J. R., Lloyd, A. H., McGurie, A. D., Rupp, T. S., Lynch, A. H., Schimel, J. P., Beringer, J., Chapman, W. L., Epstein, H. E., Euskirchen, E. S., Hinzman, L. D., Jia, G., Ping, C. -L., Tape, K. D., Thompson, C. D. C., Walker, D. A. and Welker, J. M. (2005): Role of land-surface changes in arctic summer warming, *Science* 310, 5748, 657–660.

Chapman, W. L. and Walsh, J. E. (1993): Recent variations of sea ice and air temperatures in high latitudes, *Bulletin of the American Meteorological Society* 74, 1, 33-47.

Ciais, P. (2010): Soil map digs under the tundra, *Nature* 467, 30-31.

Dennman, K. L., Brasseur, G., Chidthaisong, A., Ciais, P., Cox, P. M., Dickinson, R. E., Hauglustaine, D., Heinze, C., Holland, E., Jacob, D., Lohmann, U., Ramachandran, S., da Silva Dias, P. L., Wofsy, S. C. and Zhang, X. (2007): Couplings between changes in the climate

system and biogeochemistry, Climate Changes 2007: The Physical Science Basis. Contribution of Working Group I to the Fourth Assessment Report of the Intergovernmental Panel on Climate Changes. S. Solomon, D. Qin, M. Manning *et al*, Cambridge University Press, Cambridge, United Kingdom and New York, NY, USA, 499-587.

French, H. M. (1996): The periglacial environment, Third Edition, The University of Ottawa, John Wiley and Sons, Ltd., 458pp.

Friedlingstein, P., Cox, P., Betts, R., Bopp, L., von Bloh, W., Brokin, V., Cadule, P., Doney, S., Eby, M., Fung, I., Bala, G., John, J., Jones, C., Joose, F., Kato, T., Kawamiya, M., Knorr, W., Lindsay, K., Matthews, H. D., Raddatz, T., Rayner, P., Reick, C., Roechner, E., Schnitzler, K. -G., Schur, R., Strassmann, K.Weaver, A. J., Yoshikawa, C. and Zeng, N. (2006): Climate-carbon cycle feedback analysis: Results from the C4MIP-Model intercomparison, *Journal of Climate* 19, 3337-3353.

Gooseff, M. N., Balser, A., Bowden, W. B. and Jones, J. B. (2009): Effects of hillslope thermokarst in Northern Alaska, *Eos* 90 (4), 29-31.

Grosse, G., Romanovsky, V., Walter, K., Morgenstern, A., Lantuit, H. and Zimov, S. (2008): Distribution of thermokarst lakes and ponds at three Yedoma sites in Siberia, *Proceedings of the 9th International Conference on Permafrost*, University of Alaska, Fairbanks, USA, 551-556.

Hanssen-Bauer, I. and Førland, E. J. (1998): Long-term trends in precipitation and temperature in the Norwegian Arctic: Can they be explained by changes in atmospheric circulation patterns, *Climate Research* 10, 143-153.

Hinzman, L. D., Kane, D. L., Benson, C. S. and Everett, K. R. (1996): Energy balance and hydrological processes in an arctic watershed, Ecological Studies, Springer-Verlag Berlin Heidelberg, 120, 131-154.

Hinzman, L. D., Bettez, N. D., Bolton, W. R., Chapin, F. S., Dyurgerov, M. B., Fastie, C. L., Griffith; B., Hollister, R. D., Hope, A., Huntington, H. P., Jensen, A. M., Jia, G. J., Jorgenson, T., Kane, D. L., Klein, D. R., Kofinas, G., Lynch, A. H., Lloyd, A. H., McGurie, A. D., Nelson, F. E., Oechel, W. C., Osterkamp, T. E., Racine, C. H., Romanovsky, V. E., Stone, R. S., Stow, D. A., Sturm, M., Tweedie, C. E., Vourlitis, G. L., Walker, M. D., Walker, D. A., Webber, P. J., Welker, J. M., Winker, K. S. and Yoshikawa, K. (2005): Evidence and implications of recent climate change in Northern Alaska and other arctic regions, *Climatic Change* 72, 251-298.

Hinzman, L. D., Gieck, R. E. and Kane, D. L. (2008). Spatial and temporal variation of soil temperatures and arctic hydrology in the Kuparuk River Basin, Alaska (2008). Proceedings of the 9th International Conference on Permafrost, University of Alaska Fairbanks, June 29–July 3, 2008, 713-715.

Isaksen, K., Holmlund, P., Sollid, J. L. and Harris, C. (2001): Three deep alpine-permafrost boreholes in Svalbard and Scandinavia, *Permafrost and Periglacial Processes* 12, 13-25.

Isaksen, K., Benestad, R. E., Harris, C. and Sollid, J. L. (2007): Recent extreme near-surface permafrost temperatures on Svalbard in relation to future climate scenarios, *Geophysical Research Letters* 34, L17502.

Jones, B.M., Arp, C. D., Jorgenson, M. T., Hinkel, K. M., Schmutz, J. A. and Flint, P. L. (2009): Increase in the rate and uniformity of coastline erosion in arctic Alaska, *Geophysical Research Letters* 36, L03503.

Jorgenson, M. T., Shur, Y. L. and Pullman, E. R. (2006): Abrupt increase in permafrost degradation in arctic Alaska, *Geophysical Research Letters* 33, L02503.

Kane, D. I., Gieck, R. E. and Bowling, L. C. (2003): Impacts of surficial permafrost landforms on

surface hydrology, *Proceedings of the 8th International Conference on Permafrost*, Zürich, Switzerland, 21 – 25 July 2003, 507-511.

Kattenstroth, B. (2009): Long term climate, water balance and energy partitioning characteristics of a tundra site in the Lena River Delta, Siberia, Universität Potsdam, Diplomarbeit, 81pp.

Kerr R. A. (2010): `Arctic Armageddon´ needs more science, less hype, *Science* 329. 5992, 620-621.

Khvorostyanov, D. V., Ciais, P., Krinner, G. and Zimov, S. A. (2008): Vulnerability of east Siberia's frozen carbon stores to future warming, *Geophysical Research Letters* 35, L10703.

Krinner, G. and Boike, J. (2010): A study of a large-scale climatic effects of a possible disappearance of high-latitude inland water surface during the 21st century, *Boreal Environment Research* 15, 203-217.

Langer, M., Westermann, S. and Boike, J. (2010a): Spatial and temporal variation of summer surface temperature of wet polygonal tundra in Siberia - implications for MODIS LST based permafrost monitoring, *Remote Sensing of Environment* 114, 2059-2069.

Langer, M., Westermann, S., Piel, K. and Boike, J. (2010b): The surface energy balance of a polygonal tundra permafrost site at the Lena-River Delta, north Siberia - Part II: Winter, *The Cryosphere Discussions*. In review, 4, 1391-1413.

Lantuit, H. and Pollard, W. H. (2008): Fifty years of coastal erosion and retrogressive thaw slump activity on Herschel Island, southern Beaufort Sea, Yukon Territory, Canada, *Geomorphology* 95 (1/2), 84-102.

Lawrence, D. M. and Slater, A. G. (2005): A projection of severe near-surface permafrost degradation during the 21st century, *Geophysical Research Letters* 32, L24401.

Lawrence, D. M., Slater, A. G., Romanovsky, V. E. and Nicolsky, D. J. (2008): Sensitivity of a model projection of near-surface permafrost degradation to soil depth and representation of soil organic matter, *Journal of Geophysical Research* 113, F02011.

Lenton, T. M., Held, H., Kriegler, E., Hall, J. W., Lucht, W., Rahmstorf, S. and Schellnhuber, H. J. (2008): Tipping elements in the earth's climate system, *Proceedings of the National Academy of Science of the USA* 105 (6), 1786-1793.

Liu, L., Zhang, T. and Wahr, J. (2010): InSAR measurements of surface deformation over permafrost on the north slope of Alaska, *Journal of Geophysical Research* 115, F03023.

Mastepanov, M., C. Sigsgaard, Dlugokencky, E. J., Houweling, S., Ström, L., Tamstorf, M. P. and Christensen, T. (2008): Large tundra methane burst during onset of freezing, *Nature* 456, 628-631.

McClelland, J. W., Holmes, R. M. and Peterson B. J. (2004): Increasing river discharge in the Eurasian Arctic: Consideration of dams, permafrost thaw, and fires as potential agents of change, *Journal of Geophysical Research*, Vol. 109, D18102.

McGuire, A. D., Anderson, L. G., Christensen, T. R., Dallimore, S., Guo, L., Hayes, D. J., Heimann, M., Lorenson, T. D., Macdonald, R. W. and Roulet, N. (2009): Sensitivity of the carbon cycle in the Arctic to climate change, *Ecological Monographs* 79 (4), 523-555.

Mecke, K. R. (2000): Additivity, Convexity and Beyond: Applications of Minkowski functionals in statistical physics, K. R. Mecke and D. Stoyan L. N. P., Springer-Verlag Berlin Heidelberg, 111–184.

Niesbet, E. (2007): Earth monitoring: Cinderella science, *Nature* 450, 789-790.

Osterkamp, T. E. (2007): Causes of warming and thawing of permafrost in Alaska, *Eos Trans. AGU*, 88, 522-523.

Osterkamp, T. E. and Payne, M. W. (1981): Estimates of permafrost thickness from well logs in northern Alaska, *Cold Regions Science and Technology*. 5, 13-27.

Overduin, P. P. and Kane, D. L. (2006): Frost boils and soil ice content: Field observation, *Permafrost and Periglacial Processes* 17, 291-307.

Petrenko, V. V., Smith, A. M., Severinghaus, J. P., Brook, E. J., Lowe, D., Riedel, K., Brailsford, G., Hua, Q., Reeh, N., Schaefer, H., Weiss, R. F. and Etheridge, D. (2008): Measurements of carbon-14 of methane in Greenland ice: Investigating methane sources during the last glacial termination, *Eos* 89 (53).

Ping, C. L., Michaelson, G. J., Jorgenson, M. T., Kimble, J. M., Epstein, H., Romanovsky, V. E. and Walter, D. A. (2008): High stocks of soil organic carbon in the North America arctic region, *Nature Geoscience* 1, 615-619.

Putkonen, J. and Roe, G. (2003): Rain-On-Snow events impact soil temperatures and affect ungulate survival, *Geophysical Research Letters* 30, 1188.

Rawlins, M. A., Ye, H., Yang, D., Shiklomanov, A. and McDonald, K. C. (2009a): Divergence in seasonal hydrology across northern Eurasia: Emerging trends and water cycle linkages, *Journal of Geophysical Research* 114, D18119.

Rawlins, M. A., Serreze, M. C., Schroeder, R., Zhang, X. and McDonald, K. C. (2009b): Diagnosis of the record discharge of Arctic-draining Eurasian rivers in 2007, *Environmental Research Letters* 4, 045011, 7pp.

Repo, M. E., Susiluoto S., Lind, S. E., Jokinen, S., Elsakov, V., Biasi, C., Virtanen, T. and Martikainen, P. J. (2009): Large N_2O emissions from cryoturbated peat soil in tundra, *Nature Geoscience*, 2, 189–192.

Romanovskii, N. N. (1996): Periglacial processes as geoindicators in the cryolithozone, Rotterdam, Balkeman, 47-68.

Romanovsky, V. E., Kholodov, A. L., Marchenko, S. S., Oberman, N. G., Drozdov, D. S., Malkova, G. V., Moskalenko, N. G., Vasiliev, A. A., Sergeev, D. O., and Zheleznyak, M. N.: Thermal state and fate of permafrost in Russia: First results of IPY, In: *Proceedings of the 9th International Conference on Permafrost*, June 29-July 3, Fairbanks, Alaska, 2008, Vol. 2, 1511-1518.

Rouse, W. R., Oswald,C. J., Binyamin, J., Spence, C., Schertzer, W. M., Blanken, P. D., Bussières, N. and Duguay, C.R. (2005): The role of northern lakes in a regional energy balance**.** *Journal of Hydrometeorology*, 6 (3), 291–305.

Rowland, J. C., Jones, C. E., Altmann, G., Bryan, R., Crosby, B. T., Geernaert, G. L., Hinzman, L. D., Kane, D. L., Lawrence, D. M., Mancino, A., Marsh, P., McNamara, J. P., Romanovsky, V. E., Toniolo, H., Travis, B. J., Trochim, E. and Wilson, C. J. (2010): Arctic landscapes in transition: Responses to thawing permafrost, *Eos* 91, 26.

Sachs, T., Giebels, M., Boike, J. and Kutzbach, L. (2010): Environmental controls on CH_4 emission from polygonal tundra on the micro-site scale in the Lena River Delta, Siberia, *Global Change Biology,* 16 (11), 3096–3110.

Schuur, E. A. G., Bockheim, J. G., Canadell, J. G., Euskirchen, E. S., Field, C. B., Goryachkin, S. V., Hagemann, S., Kuhry, P., Lafleur, P. M., Lee, H., Mazhitova, G., Nelson, F. E., Rinke, A., Romanovsky, V. E., Shiklomanov, N., Tarnocai, C., Venevsky, S., Vogel, J. G. and Zimov, S. A. (2008): Vulnerability of permafrost carbon to climate change: implications for the Global

Carbon Cycle, *BioScience* 58 (8), 701-714.

Serreze, M. C., Walsh, J. E., Chapin, F. S., Osterkamp, T., Dyurgerov, M., Romansky, V., Oechel, W. C., Morison, J., Zhang, T. and Barry, R. G. (2000): Observational of recent change in the northern high-latitude environment, *Climatic Change* 46, 159-207.

Shiklomanov, A. I., Lammers, R. B., Rawlins, M. A., Smith, L. C. and Pavelsky, T. M. (2007): Temporal and spatial variations in maximum river discharge from a new Russian data set, *Journal of Geophysical Research* 112, G04S53.

Smith, L. C., Sheng, Y., McDonald, G.M. and Hinzman, L. D. (2005): Disappearing arctic lakes, *Science* 308 (5727), 1429.

Stieglitz, M, Shaman, J., McNamara, J., Engel, V., Shanley, J. and Kling, G. W. (2003): An approach to understanding hydrologic connectivity on the hillslope and the implications for nutrient transport, *Global Biogeochemical Cycles* 17, 1105, 15pp.

Sturm, M., Racine, C. and Tape, K. (2001): Increasing shrub abundance in the Arctic, *Nature* 411, 546.

Tape, K., Sturm, M. and Racine C. (2006): The evidence for shrub expansion in Northern Alaska and the Pan-Arctic, *Global Change Biology* 12, 686-702.

Tarnocai, C., Canadell, J. G., Schurr, E. A. G., Kuhry, P., Mazhitova, G. and Zimov, S. (2009): Soil organic carbon pools in the northern circumpolar permafrost region, *Global Biogeochemical Cycles* 23, GB2023, 11pp.

Toniolo, H., Kodial P., Hinzman, L. D. and Yoshikawa, K. (2009): Spatio-temporal evolution of a thermokarst in interiorAlaska, *Cold Regions Science and Technology* 56, 39-49.

Thornthwaite, C. (1948): An approach toward a rational classification of climate, *Geographical review*, 55-94.

Trenberth, K. (2010): More knowledge, less certainty, *Climate Change* 4, 20-21.

Uppala, S., Kallberg, P., Simmons, A., Andrae, U., Bechtold, V., Fiorino, M.,Gibson, J., Haseler, J., Hernandez, A. and Kelly, G. (2006): The ERA-40 re-analysis, *Quarterly Journal of the Royal Meteorological Society* 131 (612), 2961-3012.

Walter, K. M., Smith, L. C. and Chapin III, F. S. (2007): Methane bubbling from northern lakes: Present and future contributions to the global methane budget, *Philosophical Transactions of the Royal Society* A 15, 365 (1856), 1657-1676.

Walter, K. M., Zimov, S. A., Chanton, J. P., Verbyla, D. and Chapin III, F. S. (2006): Methane bubbling from Siberian thaw lakes as a positive feedback to climate warming, *Nature* 443, 71-75.

Wania, R., Ross, I. and Prentice, I. C. (2009a): Integrating peatlands and permafrost into a dynamic global vegetation model: 1. Evaluation and sensitivity of physical land surface processes, *Global Biogeochemical Cycles* 23, GB3014.

Wania, R., Ross, I. and Prentice, I. C. (2009b): Integrating peatlands and permafrost into a dynamic global vegetation model: 2. Evaluation and sensitivity of vegetation and carbon cycle processes, *Global Biogeochemical Cycles* 23, GB3015.

Washburn, A. L. (1979a): Geocryology - A survey of periglacial processes and environments, Londin, Edward Arnold, 406pp.

Washburn, A. L. (1979b): Permafrost features as of climatic changes, *Earth Science Review* 15, 327-402.

Westermann, S., Langer, M., Boike, J. (2010): Spatial and temporal variations of summer surface temperatures of high-arctic tundra on Svalbard- implications for MODIS LST based permafrost monitoring, *Remote Sensing of Environment*, in press.

Westermann, S. (2010): Permafrost's water and energy balance on the meso scale, Bayelva catchment Ny-Alesund, Svalbard. University of Heidelberg, Ph. D. Thesis, 172pp.

Woo, M.-K. (1986): Permafrost hydrology in North America, *Atmosphere-Ocean* 24(3), 201-234.

1.3. List of publications included in the thesis

Chapter 2

Boike, J., Roth, K. and Ippisch, O. (2003): Seasonal snow cover on frozen ground: energy balance calculations of a permafrost site near Ny-Ålesund, Spitsbergen, *Journal of Geophysical Research (Atmosphere)* 108 (D2), 8163, 4/1-11.

Westermann, S., Lüers, J., Langer, M., Piel, K. and **Boike, J**. (2009): The annual surface energy budget of a high-arctic permafrost site on Svalbard, Norway, *The Cryosphere* 3, 245-263.

Boike, J., Wille, C. and Abnizova, A. (2008): The meteorology, and energy and water balances of polygonal tundra in the Lena Delta, Siberia during wet and dry years, *Journal of Geophysical Research (Biogeosciences)* 113, G03025.

Langer, M., Westermann, S., Piel, K. and **Boike, J**. (2010): The surface energy balance of a polygonal tundra permafrost site at the Lena-River Delta, north Siberia- Part I: Spring to fall, *The Cryosphere Discussions*. In review, 4, 901-947.

Langer, M., Westermann, S., Piel, K. and **Boike, J.** (2010): The surface energy balance of a polygonal tundra permafrost site at the Lena-River Delta, north Siberia- Part II: Winter, *The Cryosphere Discussions*. In review, 4, 1391-1413.

Schramm, I., **Boike, J.**, Hinzman, L. and Bolton, R. W. (2007): Application of Topoflow, a spatial distributed hydrological model to the Imnavait Creek watershed, Alaska, *Journal of Geophysical Research (Biogeosciences)* 112, G04S46.

Boike, J., Hinzman, L., Overduin, P. P., Romanovsky, V., Ippisch, O. and Roth, K. (2003): A comparison of snow melt at three circumpolar sites: Spitsbergen, Siberia, Alaska, *Proceedings of the 8th International Conference on Permafrost*, 21-25 July 2003, Zürich, Switzerland (Phillips, M., Springman, S.M.,Arenson, L.U. (eds)), 79-84.

Chapter 3

Boike, J., Ippisch, O., Overduin, P. P., Hagedorn, B. and Roth, K. (2007): Water, heat and solute dynamics of a mud boil, Spitsbergen, *Geomorphology* 95, 61-73.

Roth, K. and **Boike, J.** (2001): Quantifying the thermal dynamics of a permafrost site near Ny-Ålesund, Svalbard, *Water Resources Research* 37 (12), 2901-2914.

Chapter 4

Boike, J. and Yoshikawa, K. (2003): Mapping of periglacial geomorphology using kite/balloon aerial photography, *Permafrost and Periglacial Processes* 14 (1), 81-85.

Scheritz, M., Dietrich, R., Scheller, S., Schneider, W. and **Boike, J.** (2008): High Resolution Digital Elevation Model of Polygonal Patterned Ground on Samoylov Island, Siberia, Using Small-Format Photography, *Proceedings of the 9th International Conference on Permafrost*, June 29 - July 3, 2008, University of Alaska, Fairbanks, USA, 1589-1594.

Roth, K., **Boike, J.** and Vogel, H. -J. (2005): Quantifying permafrost patterns using Minkowski Densities, *Permafrost and Periglacial Processes* 16 (3), 277-290.

Chapter 5

Krinner, G. and **Boike, J.** (2010): A study of the large-scale climatic effects of a possible disappearance of high-latitude inland water surfaces during the 21st century, *Boreal Environment Research* 15, 203-217.

1.4. List of acronyms

AK	Alaska
C	Energy balance closure term
CAVM	Circumpolar Arctic Vegetation Map
DEM	Digital elevation model
ECMWF	European Centre for Medium-Range Weather Forecasts
ET	Evapotranspiration
GCP	Ground control point
GHG	Green house gas
IPCC	Intergovernmental Panel on Climate Change
IWS	Inland water surface
KRB	Kuparuk River Basin
m	Meter
MAGT	Mean annual ground temperature
P	Precipitation
Pg	Peta gram [$1*10^{15}$ g]
Q_e	Latent heat flux/Evapotranspiration
Q_h	Sensible heat flux
Q_g	Ground heat flux
Q_m	Snow (melt) heat flux
Q_{net}	Net radiation
R	Runoff
sec	Seconds
SFC	Soil freezing characteristic
SIB	Siberia
SP	Spitsbergen
SWE	Snow water equivalent
TDR	Time domain reflectometry
W	Watt
ΔS	Net shortwave radiation
ΔL	Net longwave radiation

Chapter 2

Chapter 2.1

Boike, J., Roth, K., and Ippisch, O. (2003): Seasonal snow cover on frozen ground: Energy balance calculations of a permafrost site near Ny-Ålesund, Spitsbergen. *Journal of Geophysical Research (Atmosphere)* 108(D2), 8163, 4/1-11, doi: 10.1029/2001JD000939.

Seasonal snow cover on frozen ground: Energy balance calculations of a permafrost site near Ny-Ålesund, Spitsbergen

Julia Boike[1]
Alfred Wegener Institute for Polar and Marine Research, Potsdam, Germany

Kurt Roth and Olaf Ippisch
Institute of Environmental Physics, University of Heidelberg, Heidelberg, Germany

Received 11 June 2001; revised 3 May 2002; accepted 13 June 2002; published 10 January 2003.

[1] We apply an energy balance model to the snow cover for snowpack accumulation and ablation at a continuous permafrost site on Spitsbergen for the snow-covered periods from fall 1998 to winter 2000. The model includes net radiative, turbulent, ground, snow, and rain heat flux. The balance yields two distinct types of snow ablation: winter and spring ablation. Energy transferred by sensible heat and rain input reduces the snow cover during the winter, creating internal ice lenses and basal ice. The snowpack ablates during spring in two stages in both years. During the first stage, surface melt and subsequent internal freezing compact and reduce the snow cover, but no runoff is produced. This phase lasts more than twice as long as the second stage. During the second stage, which takes 14 days in both years, melt rates from the snowpack are represented well using the energy balance model. Ground heat fluxes are comparable during spring in both years, but the long persistence of the snow cover in 2000 delays the thawing of the ground. Due to the duration of the snow cover during spring snow melt of both years, the total energy supplied to the ground is significant, between 30 and 50% of the total energy supplied by net radiation. *INDEX TERMS:* 1823 Hydrology: Frozen ground; 1863 Hydrology: Snow and ice (1827); 1878 Hydrology: Water/energy interactions; 3307 Meteorology and Atmospheric Dynamics: Boundary layer processes; *KEYWORDS:* snow cover, snow melt, frozen ground, energy balance, Spitsbergen

Citation: Boike, J., K. Roth, and O. Ippisch, Seasonal snow cover on frozen ground: Energy balance calculations of a permafrost site near Ny-Ålesund, Spitsbergen, *J. Geophys. Res.*, *108*(D2), 8163, doi:10.1029/2001JD000939. 2003.

1. Introduction

[2] The formation (accumulation) and melting of a snowpack is an important feature in Arctic landscapes. The snow cover exercises considerable influence on the surface energy balance, since variations in snow cover change the surface albedo. Long-term measurements at Ny-Ålesund, Spitsbergen, show that the albedo remains above 80% until late May. After that, a rapid decrease in albedo occurs and snow usually disappears within two to four weeks [*Winther et al.*, 1999].

[3] According to *Dingman* [1994], the snow melt can be divided into a warming, ripening and output phase. During the first phase, the temperature of the snowpack is raised to isothermal conditions at the melting point. Additional energy input creates surface melt; water is retained in the snow up to the point where the liquid holding capacity is exceeded (ripening phase). This initiates the output phase, in which water flows out of the snowpack and the energy input is proportional to the produced meltwater. Most snow melt models with varying degrees of complexity are written to predict runoff during the last phase. The simplest model for the calculation of snow melt runoff is the temperature index model, in which a simple linear relation is obtained between air temperature and snow melt intensity. Many field studies have been undertaken in the Arctic to investigate snow melt processes on point or watershed scales using surface energy balance models [*Woo et al.*, 1983; *Young et al.*, 1997]. Some surface energy balance models neglect the snow and ground heat flux [*Harstveit*, 1984], while other models estimate the snow and soil heat content [e.g., *Kane et al.*, 1997; *Zhang et al.*, 1997]. Internal snowpack processes, such as meltwater percolating and refreezing and snow settling are included in numerical models such as CROCUS [*Brun et al.*, 1989] and SNTHERM [*Jordan*, 1991].

[4] The snow cover's physical properties, thickness, establishment and duration control the ground thermal regime. *Roth and Boike* [2001] found that a thicker layer of snow greatly reduced the heat exchange of the permafrost soil with the atmosphere. Soil cooling was about twice as pronounced during the winter of 2000 where the snow cover was about half as thick (about 0.4 m). *Zhang et al.* [1996]

[1]Now at Water and Environmental Research Center, University of Alaska, Fairbanks, Alaska, USA.

Copyright 2003 by the American Geophysical Union.
0148-0227/03/2001JD000939$09.00

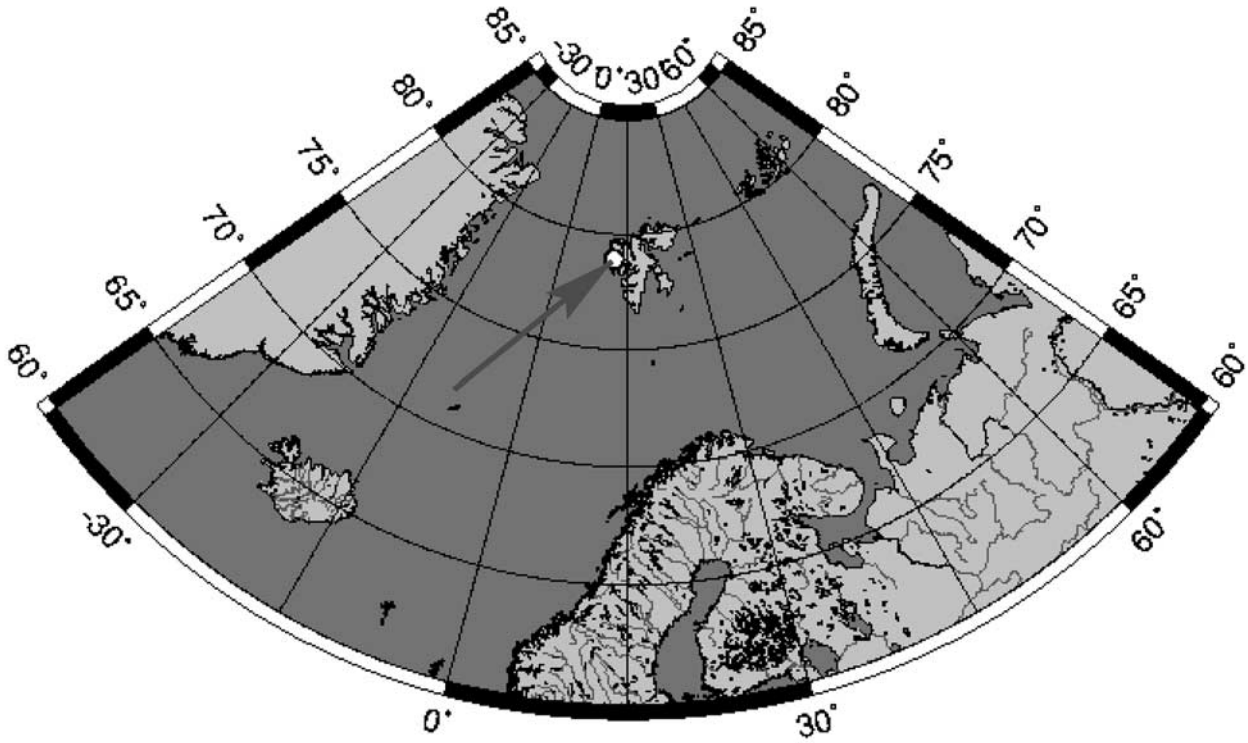

Figure 1. Geographical map showing the location of the study site in the high Arctic. The arrow indicates the area of the study site on west Spitsbergen.

showed that an increase of depth hoar, typically present at the base of the snowpack, can significantly increase ground temperatures and delay freeze back. *Sturm et al.* [2001] found recently that winter soil temperatures are substantially higher in Arctic shrubs where the snow cover is thicker due to trapping of snow. These areas also produced the highest CO_2 winter fluxes.

[5] The winter snow cover on Spitsbergen is unique for a high Arctic site since it contains internal ice lenses and basal ice. Our goal is to explore processes that govern the winter formation and ablation of the snow cover for the entire snow covered periods during the years 1999 and 2000. The melting of the snow cover and possible infiltration of snow meltwater and/or temperature induced vapor flux towards colder layers warmed the permafrost soil at this site down to depths of 0.9 m [*Roth and Boike*, 2001]. Thus our energy balance includes the ground heat flux. Energy balance components are quantitatively examined during the snow-covered period using highly resolved atmospheric and soil temperature and moisture data.

2. Site Description and Measured Data

[6] The Bayelva catchment is located about 3 km west from Ny-Ålesund, Spitsbergen at (78°55′N 11°50′E; Figure 1). Continuous permafrost in this region underlies coastal areas to depths of about 100 m and mountainous areas to depths greater than 500 m [*Liestøl*, 1977]. The North Atlantic Current warms this area to average air temperatures around 5 and −13°C in July and January, respectively, and provides about 400 mm annual precipitation falling mostly as snow between September and May [*Førland et al.*, 1997].

[7] Our study site is located some 30 m above mean sea level, on top of a small hill covered with unsorted circles. The bare soil circle centers range about 1 m in diameter and are surrounded by vegetated borders consisting of a mixture of low vascular plants, mosses and lichens. We instrumented one of these circles in August 1998 to automatically monitor hourly temperature and liquid water content [*Roth and Boike*, 2001]. A weather station measures hourly solar radiation, net radiation, air temperature, humidity, snow depth and rainfall within 5 m of the instrumented soil site. Net radiation, Q_n, was first measured using a Campbell Scientific Q 7 net radiometer, which was exchanged on 18 April 2000 (day 839) for an NR Lite net radiometer. All data are checked against the radiation balance measurements of the Koldewey research station, where instruments are maintained daily. Their field accuracy ranges between 10% (Q 7) and 20% (NR Lite). Further hourly data used from the Koldewey and Norsk Polar weather station include: atmospheric pressure, relative humidity (for days 257–839), wind speed (for days 686 to 839), rainfall (for days 257 to 578). Hourly rainfall data obtained from the Norwegian Meteorological Institute's automatic precipitation gauge were cross-checked with daily precipitation measurements collected from a manual gauge.

[8] Snow water content is measured using a vertically installed time domain reflectometry (TDR) probe. When the snow cover is less than the length of the snow TDR probe, l_0, the measured dielectric constant ϵ_m is corrected for the

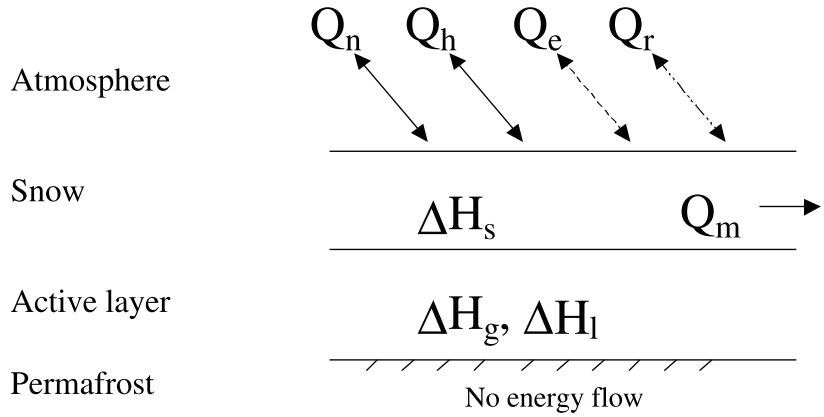

$$Q_n+Q_h+Q_e+Q_r = \Delta H_s+\Delta H_g+\Delta H_l+Q_m$$

Atmospheric fluxes are defined positive towards surface

'Storage' terms are defined positive when storage is increased

Figure 2. Schematic diagram of the volume energy balance model.

length of the probe exposed to air, l_a, to calculate the snow dielectric constant ϵ_s:

$$\epsilon_s = \left(\frac{l_0\sqrt{\epsilon_m} - l_a}{l_s}\right)^2, \quad (1)$$

where l_s is the snow depth. The length of the TDR probe is 0.5 m.

[9] The snow liquid water content θ_s is calculated following *Lundberg* [1997], applying an average snow density of 350 kg m^{-3}. Changing the snow density by 100 kg m^{-3} results in a absolute change in snow liquid water content of about 1%. Two temperature sensors are installed above the ground at 0.35 and 0.48 m height to record snow temperatures; between days 851 and 1035 the sensor at 0.35 m malfunctioned and after day 751 the sensor at 0.48 m failed completely. For these days, the air temperature is used as an approximation for snow temperature. Computed ground and snow heat flux data are smoothed using a cubic spline to eliminate high frequency changes in amplitude. Other snow physical characteristics (density, temperature, stratigraphy) were measured in snow pits during May and June of 1999 and 2000 (K. Sand, unpublished data, 2001) and on 20 April 2000 using standard methods.

[10] Hourly data collection started in September 1998. The data spans more than two years, from 14 September 1998 to 24 January 2001 (day 1120).

3. Model Description

[11] A simple volume energy balance of a snowpack may be formulated as:

$$Q_n + Q_h + Q_e + Q_r = \triangle H_g + \triangle H_l + \triangle H_s + Q_m\ , \quad (2)$$

where Q_n is the net radiation balance, Q_h and Q_e are turbulent fluxes of sensible and latent heat and Q_r is the heat flux supplied by rain (Figure 2). The terms on the right side of the equation describe the soil and snow's change in thermal energy. The rate of heat flow into soil and snow is calculated as change of the sensible and latent heat per unit time (hourly time steps).

[12] The thermal energy stored as sensible heat at time t in soil to a depth of 1.13 m, $H_g(t)$, and in the snowpack, $H_s(t)$, is estimated by the summation over the phases ice i and fluid w and soil matrix sm along the vertical axis of soil and snow z [*Boike et al.*, 1998]:

$$H_{g,s} = \sum_{\alpha\in i,w,sm} c_\alpha \rho_\alpha \int \theta_\alpha(z,t)T(z,t)dz\ , \quad (3)$$

where c_α is specific heat capacity, ρ_α mass density, θ_α volumetric content of phase α and T temperature. For calculation of snow heat content, the ice thermal capacity and density are set to $C_s = 2.11 \cdot 10^3$ J kg^{-1} K^{-1} and 350 kg m^{-3}, respectively.

[13] The term H_l is the latent heat of ground and is calculated as:

$$H_l = -L_f \rho_i \int \theta_i(z_g,t)dz\ , \quad (4)$$

where θ_i is the ice content estimated from TDR measurements of unfrozen water content and from soil water content before freeze-back. This implicitly assumes that no significant moisture redistribution takes place during winter. $L_f = 0.333 \cdot 10^6$ J kg^{-1} is the latent heat of fusion. Since our instruments extend below the depth of seasonally thawing and freezing ground, ground heat fluxes below 1.13 m are negligible within the context of this paper. The reference state for the energy storage calculations is liquid water at 0°C. The latent heat flux of the snowpack, Q_m, is the remainder in the balance. For $Q_m > 0$, melting is expected

while for $Q_m < 0$, freezing and recrystallization are expected. The estimated potential error in Q_m lies between ±15 and 25%.

[14] Atmospheric fluxes (defined here as Q_n, Q_h, Q_e and Q_r) towards the snowpack are defined as positive (energy gain), away from it as negative (energy loss). In contrast to simple surface energy balance equations applied for snow melt modeling at a point, this approach considers the changes of sensible and latent heat of ground and snow. Since the rain heat flux is generally small, this term is often ignored in snow melt studies [*Zhang et al.*, 1997], but we include it here since winter rain events are common at this site on Spitsbergen.

[15] Since accurate measurements of snow surface temperature, T_s at unsupervised, remote, Arctic sites are extremely difficult to obtain, they are often estimated using the air temperature T_a. Here T_s is estimated with the formula of *Woo et al.* [1999] using the average T_a of the past (t_{i-1}) and present (t_i) time step (hourly measurements):

$$T_s(t) = \frac{T_a(t_{i-1}) + T_a(t_i)}{2} \ , \tag{5}$$

for $T_a(t_i) < 0$. For $T_a(t_i) \geq 0$°C, $T_s = 0$°C.

[16] Turbulent heat fluxes Q_h and Q_e are governed by the complex exchange processes in the lower atmosphere. A common parameterization in snow melt models is the bulk aerodynamic formulae by *Price and Dunne* [1976]:

$$Q_h = \rho_a C_a D_{h(n,s,u)}(T_a - T_s) \ , \tag{6}$$

$$Q_e = \rho_a L_{(v,s)} D_{e(n,s,u)}(0.622/p)(e_a - e_s) \ , \tag{7}$$

where ρ_a and C_a are the density and specific heat of air, D_h and D_e are heat and vapor transfer coefficients for neutral (n), stable (s), unstable (u) conditions, T_a is the temperature at 2 m height, $L_{(v,s)}$ is the latent heat of vaporization or sublimation ($2.48 \cdot 10^6$ J kg^{-1} and $2.83 \cdot 10^6$ J kg^{-1}, respectively), p is atmospheric pressure, e_a is vapor pressure at 2 m height and e_s is ice saturated vapor pressure over a cold snowpack ($T_s < 0$°C) or water saturated vapor pressure over a melting snowpack ($T_s = 0$°C).

[17] The direction of Q_e and the surface temperature determine whether vapor condensates, sublimates or resublimates (phase change from vapor to ice). If Q_e is positive, i.e., directed towards the surface, and $T_s = 0$, the surface experiences condensation and L_v is applied; if $T_s < 0$°C, resublimation occurs and L_s is used. For negative heat fluxes, snow always sublimates independent of T_s and L_s is applied.

[18] The heat and vapor transfer coefficients D_h and D_e are assumed to equal that for momentum D_m. For neutral conditions they can be estimated as:

$$D_{h(n)} = D_{e(n)} = D_{m(n)} = \frac{u_{z_i} k^2}{(ln(z_i/z_0))^2} \ , \tag{8}$$

where k is the von Kármán constant (=0.41), u_{zi} is wind speed at instrument height z_i and z_0 is the roughness length, assumed to be constant at 0.16 mm over the measurement period.

[19] Following *Price and Dunne* [1976], the bulk Richardson number, R_i, is used to adjust for atmospheric conditions other than neutral:

$$R_i = \frac{g\Delta z_i(T_a - T_s)}{\left(u_{z_i}^2 T_a\right)} \ , \tag{9}$$

where the term Δz_i is the distance between instrument height and snow surface, T is absolute temperature (K) and g is the gravitational constant.

[20] If conditions are stable ($R_i > 0$), the stable transfer coefficient is:

$$D_{h(s)} = D_{h(n)}/(1 + 10R_i) \ , \tag{10}$$

and for unstable conditions:

$$D_{h(u)} = D_{h(n)}(1 - 10R_i) \ . \tag{11}$$

The bulk transfer equations and stability adjustment have successfully been applied in various settings in the Arctic [e.g., *Woo et al.*, 1999; *Hinzman et al.*, 1991; *Kane et al.*, 1997]. *Tarboton et al.* [1995] reported unreasonable correction factors during times of large temperature differences and low wind speeds and thus used neutral transfer coefficients only. At higher wind speeds, common at our site, a high temperature difference results only in small variations in the correction factor [*Braithwaite*, 1995].

[21] Assuming that the rain has the same temperature as the air, the heat flux supplied by rain is computed using rainfall rate and air temperature.

[22] The following assumptions were made for the snow melt computations: (1) When energy balance is positive, surplus energy is consumed by snow melt; (2) a snow cover with homogeneous density and thermal capacity is assumed at the onset of the snow melt computation; (3) heat transfer is assumed to be instantaneous.

[23] The rate of surface snow melt, M, is expressed as snow water equivalent (SWE) and is calculated from the energy balance equation as:

$$M = Q_m/\left(\rho_w L_f\right) \ , \tag{12}$$

where ρ_w is the density of water and from

$$M = \frac{\rho_s}{\rho_w}\frac{dz_s}{dt}, \tag{13}$$

where z_s is the thickness of the snowpack, t is time and ρ_s is the density of snow. Snow densities were measured daily in snow pits at a site nearby during premelt and melt period (K. Sand, unpublished data, 2001). Since density variations between sites are large, a range of snow densities is used for the calculation of surface melt in equation (13). The average vertical snow density between 19 May and 13 June 1999 ranged between 377 and 487 kg m^{-3} (average 455 kg m^{-3}) and from 9 May to 27 July 2000 between 350 and 478 kg m^{-3} (average 423 kg m^{-3}). Based on the average density field data, a snow density range between 350 and 500 kg m^{-3} is used for the calculation of surface melt from

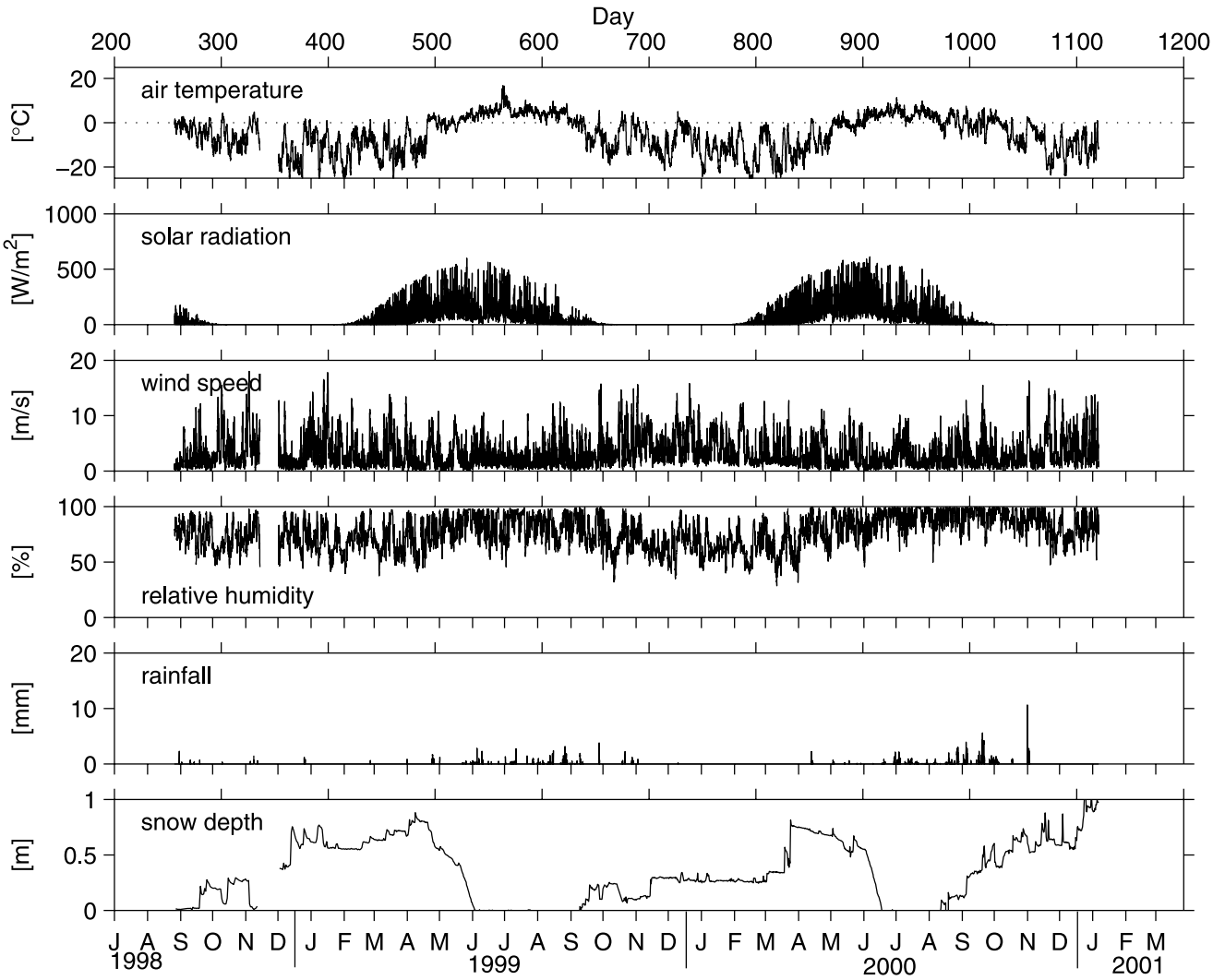

Figure 3. Measured meteorological variables (air temperature, solar radiation, wind speed, relative humidity, rainfall, snow depth).

equation (13). The calculated surface melt rates in equations (12) and (13) do not necessarily predict melt flowing out of the snowpack. As discussed earlier, the energy input and meltwater production are linearly related during the output phase only.

4. Results

4.1. Climate and Snow Cover

[24] The meteorological record from September 1998 to January 2001 is shown in Figure 3. Solar radiation turns positive around days 410 and 775 (14 February 1999 and 2000) and stays positive for about 260 days until about November 1st. Solar radiation input peaks during the snow melt season. Air temperatures typical of a mild, maritime winter show the influence of the Atlantic current in this high Arctic setting. Often, air temperatures above 0°C occur in combination with rainfall and higher wind speeds. Wind speed is highest during the winter periods, reaching averaged maximum values of 18 m s^{-1}. Relative humidity is lowest during the cold winter period, but reaches values between 90 and 100% during the snow melt period and during the summer. Rain falls regularly during the snow free periods. Furthermore, rain falls frequently on snow during the cold snow period (which interrupts the accumulation of snow) and during snow melt. Overall, the predominance of snow cover is obvious: From a total of 864 days, only 154 days are snow free. The snow cover is highly variable over time as a result of fresh snowfall, compaction and rain events. The first snow period lasts about 250 days and is shorter than the second snow period (about 290 days). Although the duration of the second snow period is longer, the thinner, 0.3 m snow cover persists longer compared to the first snow period. The third build up of snow starts around day 975 (2 September 2000) and its accumulation is very irregular. The greatest snow depth of more than 1 m is recorded on day 1108 (12 January 2001).

4.2. Energy Balance Components

[25] Throughout the winter Q_n remains negative when solar radiation input is zero (Figure 4). Even though solar radiation becomes positive in early spring, Q_n stays negative due to the high albedo of the snow cover. Following

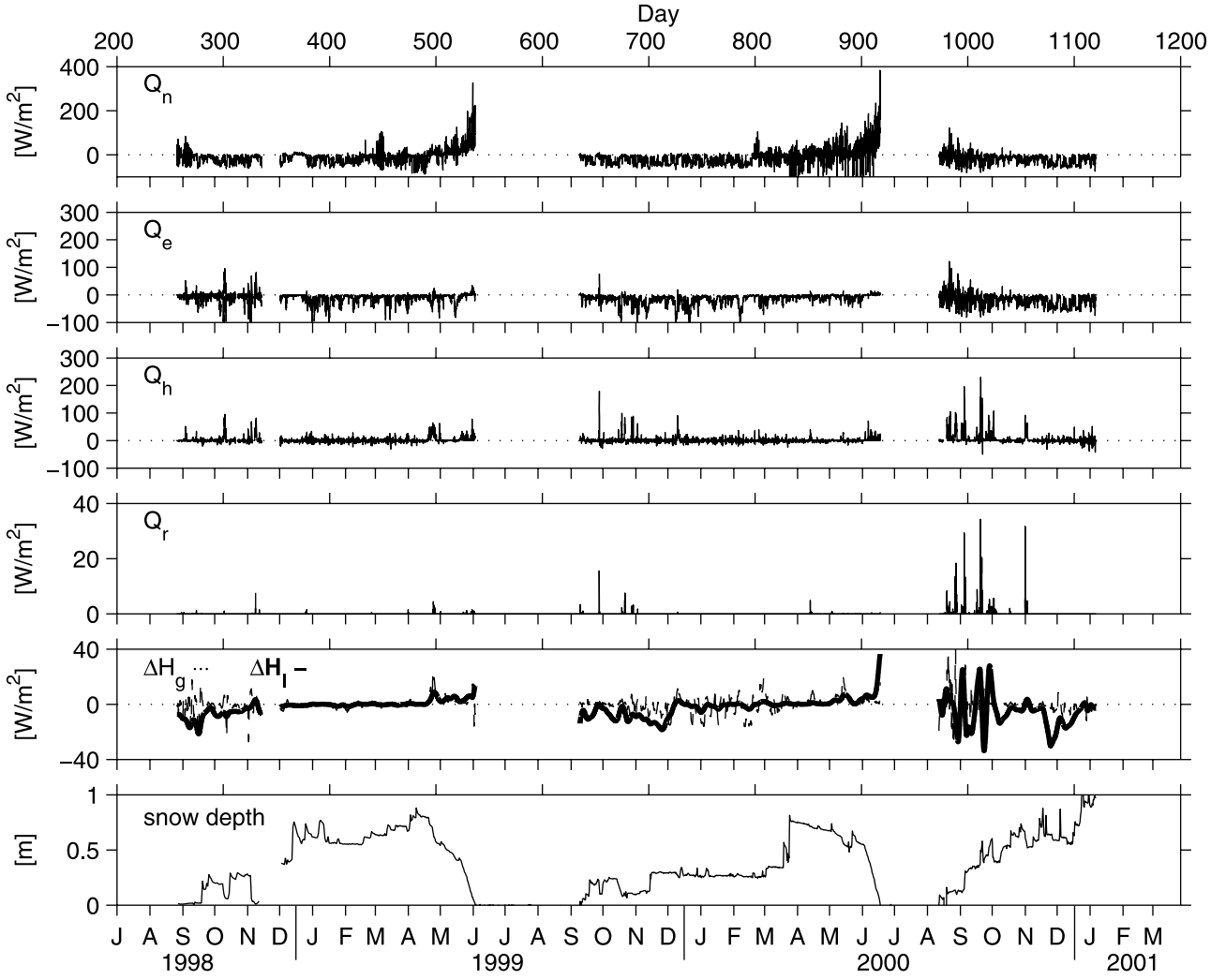

Figure 4. Measured net radiation (Q_n), estimated values of atmospheric sensible (Q_h) and latent (Q_e) and rain (Q_r) heat flux. The ground heat flux is partitioned into sensible (ΔH_g) and latent heat (ΔH_l) flux. Snow depth is shown again to visualize the snow covered periods from 1998 to 2000. No data are shown during snow free periods; data around day 350 are missing due to instrument failure.

ablation and change of snowpack physical properties during spring (day 490 and day 840), Q_n values increase towards positive values.

[26] Sensible heat fluxes, Q_h, away from the snow surface are generally small during the winter period. Positive Q_h fluxes are a significant heat input when the air temperature during the winter rises above 0°C. These events occur with rain events of low intensity throughout the snow-covered period. These rain events supply small amounts of Q_r, with maximum fluxes of about 35 W m^{-2}. Q_e fluxes are generally small and negative throughout the winter snow-covered period. Positive Q_e fluxes, such as those detected toward the end of the snow melt period, indicate condensation at the snow surface. This process is a potentially important energy source for melt, since the release of L_v is about 7.5 times larger than L_f. For this site, however, the contribution of Q_n and Q_h dominate the energy balance. Generally, Q_e fluxes compare well with those calculated during snow melt period by the aerodynamic profile method and bulk methods from snow models CROCUS and SNTHERM (A. Semadeni-Davies et al., manuscript in preparation, 2002).

[27] The heat flux of the ground (ΔH_g and ΔH_l) is a small term in the energy balance, ranging between ±40 W m^{-2}. More than half of the total ground heat flux is ΔH_l, thus an important energy term for the ground. During freeze back, ΔH_l is negative since energy is released from the ground into the snowpack due to the release of latent heat and vice versa, is consumed during spring warming. Total ground heat flux during freeze back is more negative during the second period (days 650–720) compared to the first snow-covered period (days 250–320) due to the thinner snow cover. The ground receives energy during the second snow-covered period (days 800–900; March to June 2000), while snow accumulates and with the start of positive net radiation. The latent heat of the refreezing snow cover is a possible source of energy, as is suggested by the drop in snow liquid water content (Figure 5). The larger fluctuations of ΔH_g during the onset of the third snow-covered period are connected to large energy inputs by Q_h, Q_e and Q_r,

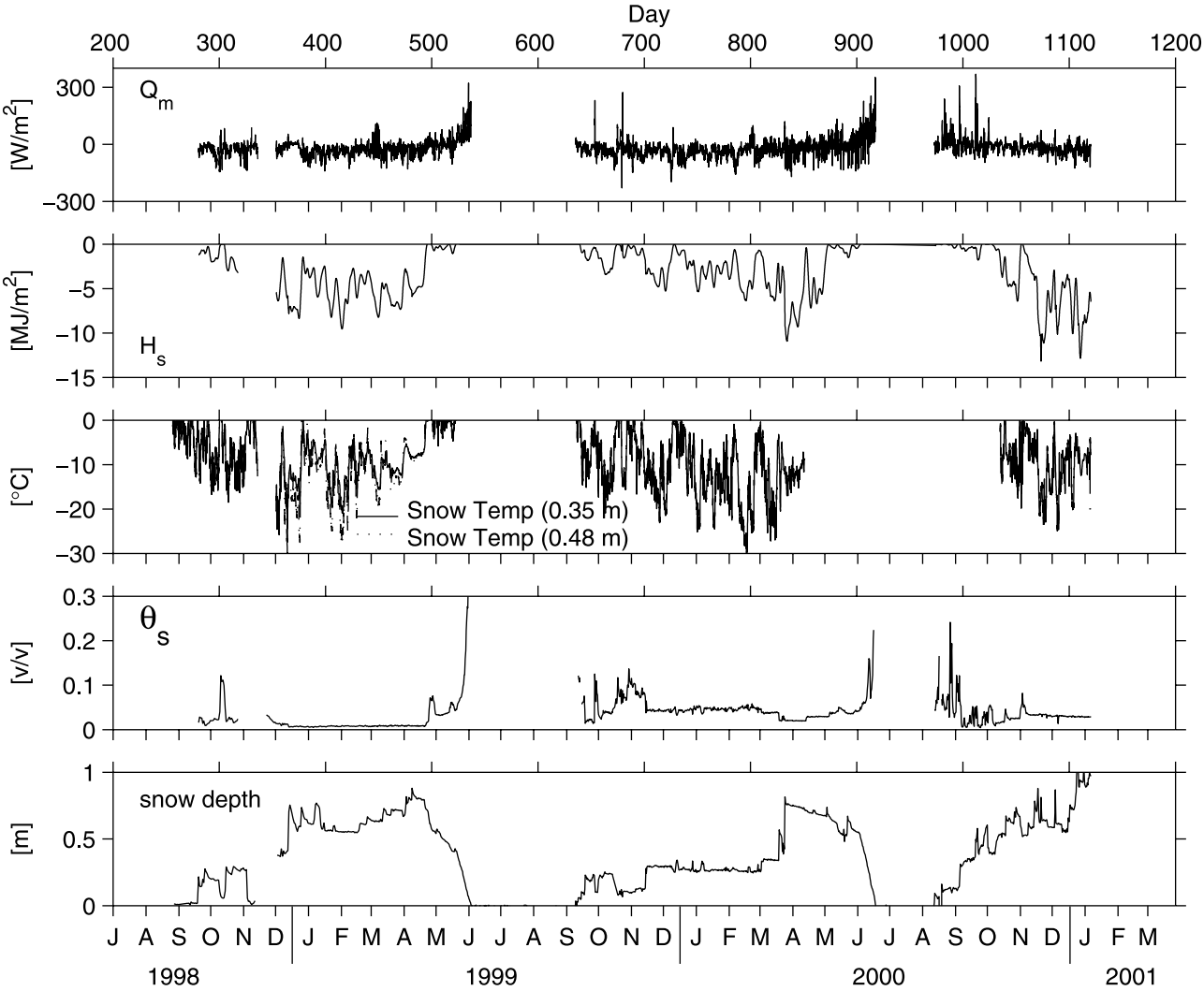

Figure 5. Melt energy Q_m, calculated from the energy balance equation (2), and snow physical properties: snow heat content (H_s), snow temperature, snow volumetric liquid water content (θ_s) and snow depth. The high snow liquid water content during the end of the 1999 snow melt (30%) is the result of slush snow and/or standing water conditions.

hence to repeated interruption of cooling and freezing of the ground.

4.3. Snow Internal Processes During Winter 1999/2000

[28] During the period of no solar radiation input, Q_m is supplied predominantly by Q_h and to a smaller extent by Q_r. In combination with a thinner snow cover, a positive Q_m causes a drastic decrease in snow cover (i.e., days 300, 330, 650, 680–700; Figure 5).

[29] Further insight into the relationship between snow cover physical characteristics and energy balance components may be gained from Figure 5. The snow sensible heat content, expressed in MJ m^{-2}, is quite variable due to fluctuations in temperature and snow thickness; with increasing snow depth or decreasing temperature, the negative heat content increases.

[30] Differences between positive melt events can be demonstrated by examining the Q_m events around days 301 (supplied by Q_h) and around 450 (supplied by Q_n). During the first event, sensible heat transfer is 95 W m^{-2}, yielding positive melt energy of about 70 W m^{-2}. In the second event, similar amounts of energy are supplied, ranging between 50 and 100 W m^{-2} over seven days. During the first event, the snow sensible heat content is high. Meltwater percolates through the snowpack (''through flow'') and infiltrates into the soil. This interpretation is supported by the measured increase of soil volumetric water content [*Roth and Boike*, 2001]. Refreezing of meltwater within or on top of the soil releases latent heat, warming the soil down to 0.5 m depth. Depending on the temperature regime and infiltration capacity of the ground, this process can create a basal ice layer.

[31] During the second event, energy is supplied to a cold, stratified snowpack. The snow is warmed rapidly (the probe at 0.48 cm height warms from about −17° to −5°C) and the temperature gradient reverses. The snow heat content increases, but it is still very low so that meltwater generated on the snow surface percolates and refreezes in the upper snowpack. The snow liquid water content does not show an increase in the lower 0.50 m of the snowpack,

suggesting a limited percolation and the creation of ice within the snowpack.

[32] Both of these snow stratigraphic characteristics, basal ice on the ground surface and snowpack ice structures, are identified in snow pits close to the site (Figure 6) and are characteristic for this area [*Gerland et al.*, 1999]. In both cases, percolating water and subsequent freezing act as an energy source.

[33] The snow temperature profile is further discussed using days 360 to 500 (December 1998 to May 1999), i.e., when probes are completely covered with snow. Snow temperature and air temperature differ by up to 20°C between days 460 and 500, a time when the snow cover depth increases to about 0.8 m. Freshly fallen snow effectively insulates the snowpack during this large air temperature change. The snow temperature at 0.35 m is dampened from the surface signal, and differs by up to 8°C from the air temperature.

4.4. Snow Melt in 1999 and 2000

[34] The start of surface snow melt computation in 1999 is determined as the point in time when snow depth begins a continuous decrease in spring. Air temperatures are below 0°C at the onset of snowpack ablation and remain close to 0°C during further progress of melt, probably stabilized by the snow cover. A warming event (supplied by Q_r and Q_h) in the beginning of May in 1999 (day 490), causes the snow temperature gradient to reverse (i.e., temperature at the upper probe became warmer than at the lower probe) and to become isothermal at 0°C. The snow liquid water content rises from 1 to 7.5% (Figure 5), i.e., meltwater percolates within the snowpack. As a result of the physical change of the snow (increase in effective snow grain size and hence decreased albedo), the optical properties of the snow cover change and Q_n increases. Cold air temperatures on the following days interrupt this process, and the meltwater refreezes again, as suggested by the drop in snow liquid water content. The observation that snow cover internal processes (involving percolating and refreezing meltwater) are responsible for reducing the snow height, but not the SWE, until day 523 (7 June 1999) is supported by: (1) the sensible heat content of snow turns zero after day 523 (Figure 5) (2) the snow liquid water content continuously increases after day 523 (Figure 5) (3) cumulative Q_m is negative up to day 523, i.e., refreezing is predicted (Q_m becomes positive on day 523; Figure 7a) (4) runoff is observed visually starting on day 523. Two stages of snowpack ablation can be defined (Figures 7b and 7c): when the snow heat content is still varying (diurnal variations), snow internal processes such as refreezing, physical changes (densification/settling) are at work. These processes result in a decreasing snow cover, not in SWE, and thus no runoff from the snowpack is produced. During the first stage of ablation, measured and modeled ablation rates do not agree since the cumulative sum of Q_m remains negative. When only positive Q_m values are used in the calculation (i.e., both the overnight refreezing of snow and internal processes are ignored), as in simple surface energy balance models, a closer fit between modeled and measured ablation data is obtained (Figure 7b). As discussed above, this does not reflect the physical processes of the snow cover. When the model is started on day 523, once the conditions for melt from the snowpack are met, the modeled and measured ablation rates agree reasonably well, assuming a snow density in the range of 350 kg m^{-3} to 500 kg m^{-3}. Slight changes in snow density and snowpack heterogeneity are expected to affect the SWE estimated from measured snow depths.

Figure 6. Snow pit dug close to the instrumented site in June 1998 showing internal ice lenses and basal ice. Snow was manually removed between the ice layers to underline the stratigraphy. Total snow depth was 0.55 m.

[35] The cumulative sum of energy balance components during snow ablation in 1999 is shown in Figure 7a. The dominant source of energy for melt is provided by Q_n (radiative melting). Q_h contributes about 30% of Q_n over the entire period, but 2/3 are generated during the first stage. Thus Q_h plays a minor role in the energy budget of the melt stage. Q_r and ΔH_s are the smallest terms and do not play an important role in the energy balance. Evaporation and sublimation use about 30% of Q_n, but since the latent heat involved is large, the ablation rate is low. This agrees with values from A. Semadeni-Davies et al. (manuscript in preparation, 2002), who found that 20 to 30% of Q_n was lost to evaporation during this period.

[36] The snow ablation calculations in 2000 are started on day 840 (19 April 2000). At this time, the snowpack is thermally stratified (−13.6°C on surface, −15.5°C at 0.10 m, decreasing to −9.6°C at 0.8 m depth), four major stratigraphic units are identified and densities range between 350 and 400 kg m^{-3}. Measured snow densities increase to

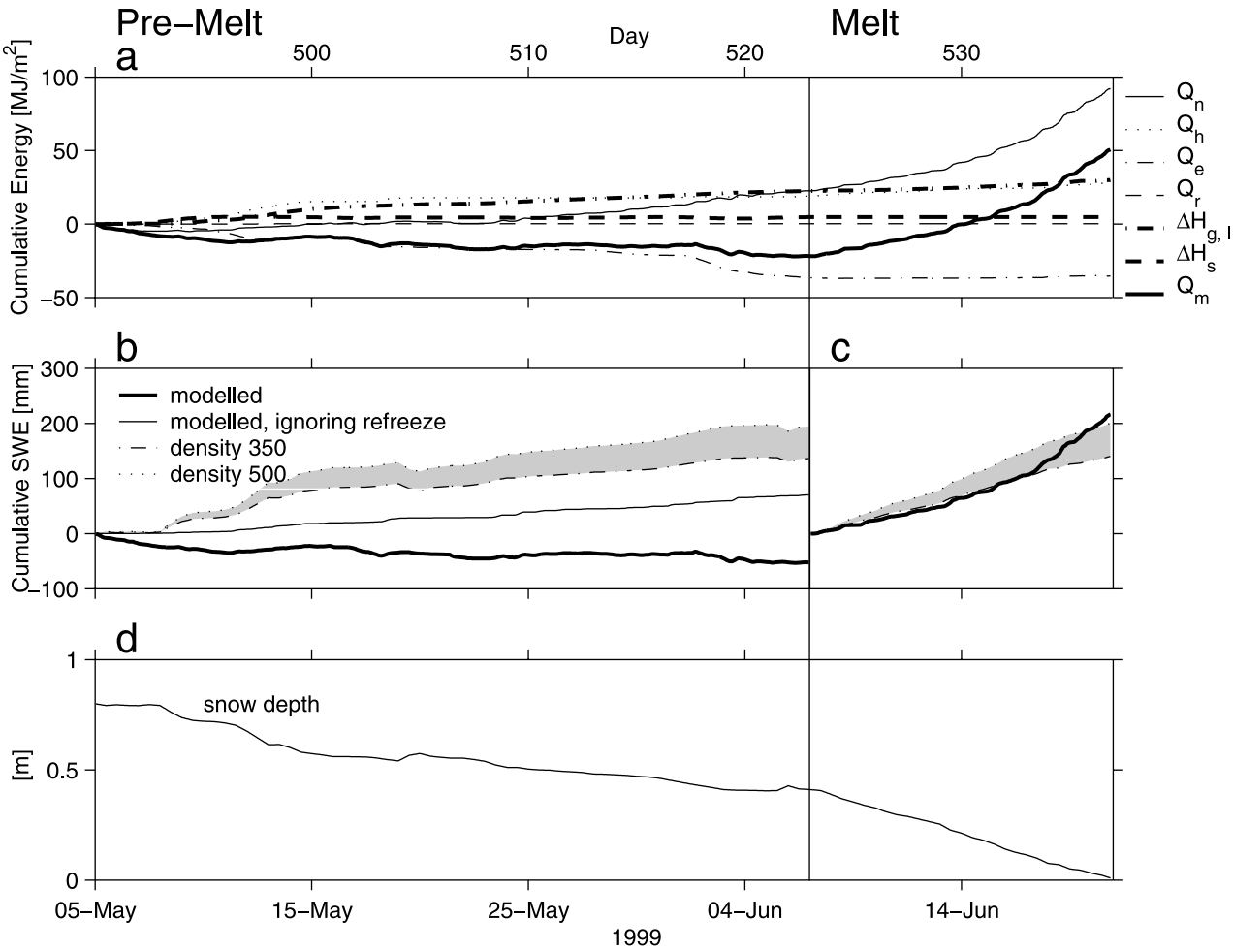

Figure 7. Cumulative energy balance components (a), melt rates expressed as cumulative snow water equivalents (b and c) and snow depth (d) for the premelt and melt period from 5 May to 21 June 1999 (days 504 to 537). Modeled melt rates, calculated using Q_m from the energy balance, are compared to melt rates obtained from snow depth measurements and a range (gray zone) of snow densities between 350 and 500 kg m^{-3}. Modeled ablation rates ignoring refreeze are calculated using positive Q_m values only.

an average value of about 445 kg m^{-3} toward the end of snow melt. Snow ablation in 2000 resembles that of 1999 in that two significant stages (premelt and melt) can be identified (Figures 8b and 8c). During the first stage, the cumulative sum of Q_m remains negative and snow internal processes compact the snow cover. Output of melt starts on day 903, again supported by field measurements of the snow liquid water content, which show a rapid and continuous increase after this day. As in 1999, Q_n increases concomitant with an increase of snow liquid water content; after fresh snow fall on day 890 (8 June 2000), Q_n drops. The model is started when Q_m values become and remain positive and a excellent fit of measured and modeled ablation rates is obtained (Figure 8c). Similar to 1999, ablation is driven by Q_n, Q_h increases during the second stage of ablation and Q_r and ΔH_s are the smallest terms.

4.5. Difference Between Snow Melt Processes of the Two Years

[37] A comparison of snow melt processes and energy balance components shows distinct differences between the two years. The ablation of snow starts later in 1999 (5 May) compared to 2000 (19 April) and takes half of the time to melt, about 47 days in 1999 and 78 days in 2000. The rate of snow melt during the second stage of ablation is higher in 2000, about 0.036 m/d compared to 0.028 m/d in 1999, with comparable melt energy inputs (using snow depth data). During both years ablation is initiated by Q_n, which remains the dominant energy source. The snow cover persists for a long time during the premelt stage of warming and ripening, 33 days in 1999 and 63 days in 2000, respectively. This is followed by a short melt stage (14 days in both years), in which meltwater is produced from the pack.

4.6. Snow Cover and Ground Heat Flux

[38] The thicker snow cover during the first winter reduces the heat exchange with the atmosphere [*Roth and Boike*, 2001]. Thus the ground heat content immediately before snow melt in 1999 (day 490) is -82 MJ m^{-2} whereas a thinner snow cover during the second winter results in a ground heat content just before snow melt (day 840) of -113 MJ m^{-2}.

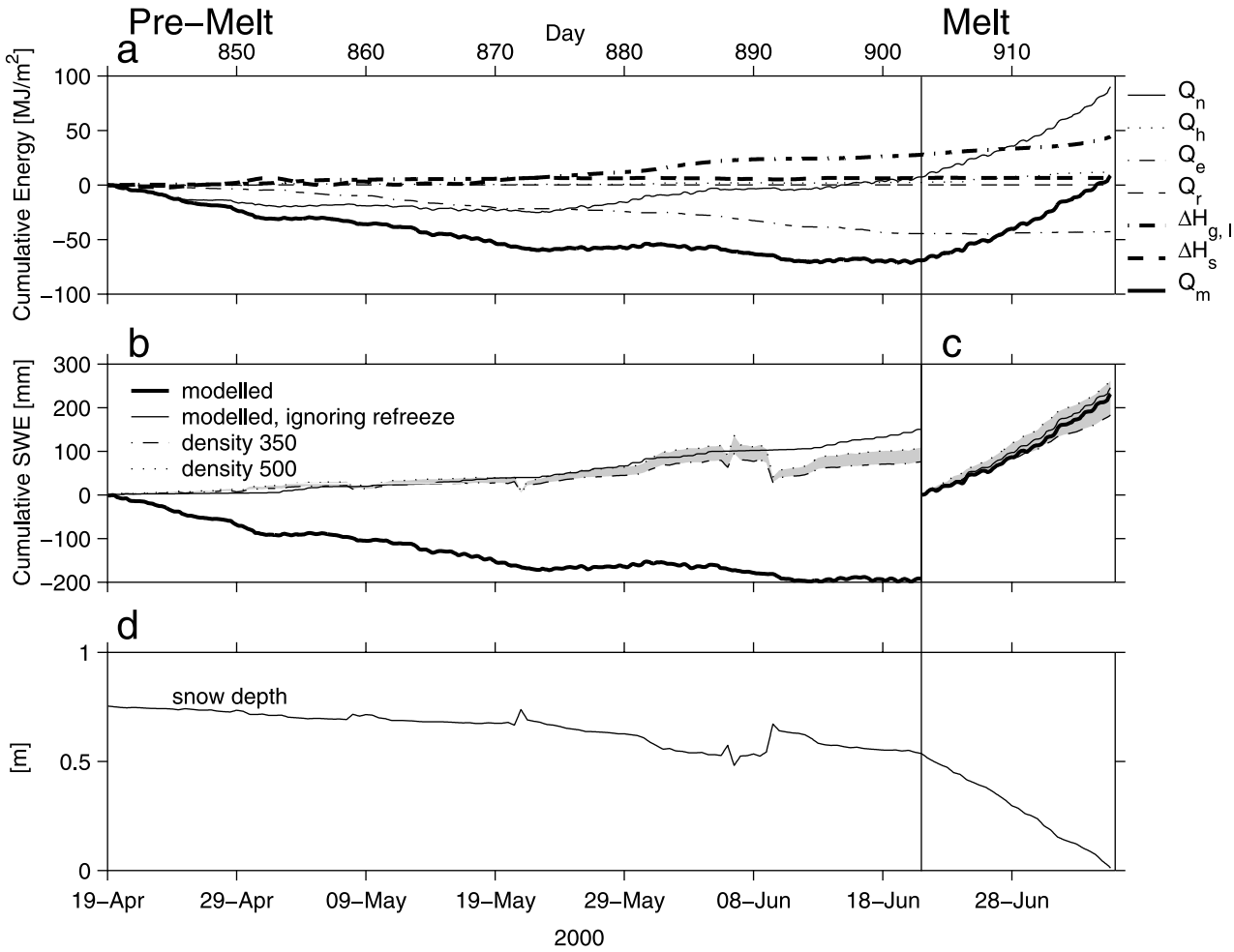

Figure 8. Cumulative energy balance components (a), melt rates expressed as cumulative snow water equivalents (b and c) and snow depth (d) for the premelt and melt period from 19 May to 6 July 2000 (days 870 to 918). Modeled melt rates, calculated using Q_m from the energy balance, are compared to melt rates obtained from snow depth measurements and a range (gray zone) of snow densities between 350 and 500 kg m^{-3}. Modeled ablation rates ignoring refreeze are calculated using positive Q_m values only.

[39] Due to the prolonged snow melt period in 2000, the total heat supplied to the ground is larger in 2000 than in 1999. The total amount of energy supplied to the ground during snow melt in 2000 (days 840 to 917) is about 44 MJ m^{-2} and in 1999 (days 490 to 537) 30 MJ m^{-2}. The average heat fluxes supplied during ablation are quite similar, about 6.3 W m^{-2} in 2000 and 7.5 W m^{-2} in 1999. During both years, the heat supplied to the ground during snow melt is a significant energy sink, using up to 50% of the total energy supplied by Q_n.

5. Conclusion

[40] The maritime climate of this high Arctic permafrost site makes it unique. Warm weather events during the winter interrupt the build up of the snow cover. Depending on the heat content of the snowpack, either internal ice lenses or basal ice are created. At other high Arctic settings (e.g., Canadian high Arctic), internal ice and basal ice layers are usually formed during spring melt [*Marsh and Woo*, 1984], and are thus not a biological barrier during the winter.

[41] Depending on the snow's physical properties, winter thaw events warm the soil through convective heat transfer, a process ignored when the soil thermal regime is modeled using conduction only. This supports the observation by *Putkonen* [1997], who found warming of the soil as a result of winter rain events in 1985/86. Furthermore, a snow cover of longer duration or increased thickness has a warming impact on the ground thermal regime, as the comparison between 1999 and 2000 shows. On the other hand, the long duration of the spring melt period results in a significant loss of heat to the ground.

[42] The energy balance model depicts two distinctly different stages of spring melt. During the first stage, surface melt infiltrates the snow which has a negative heat content. The snowpack's height is reduced by snow internal processes, such as water percolation, settling and compaction. During the second stage, the SWE decreases and meltwater production is modeled well using the energy balance model. Thus changes in snow height or simple temperature index models are not applicable for the prediction of runoff amounts and timing. At this site, melt

energies are predominantly supplied by radiation, which was also observed by *Harding and Lloyd* [1998] for the years 1995 and 1996.

[43] **Acknowledgments.** We gratefully acknowledge financial support by the Deutsche Forschungsgemeinschaft (Ro 1080/4-1&2), the European Union (LSF grant NP-98-5), and a research grant by the Deutsche Akademie der Naturforscher Leopoldina awarded to Julia Boike (BMBF-LPD 9901/8-11). Essential logistic support was provided by the German and the Norwegian Research Stations in Ny-Ålesund. Pier Paul Overduin was indispensable for the initial instrumentation of the site. Discussions were helpful with Annette Semadini-Davies, Larry Hinzman, Regine Hock, David Maréchal, Pier Paul Overduin and Kathy Young. Snow density data were collected by Knut Sand, David Maréchal and Oddbøjrn Bruland. Precipitation data from September 1998 to July 1999 were obtained from the Norwegian Meteorological Institute. Thanks to the anonymous reviewers who helped to improve the manuscript.

References

Boike, J., K. Roth, and P. P. Overduin, Thermal and hydrologic dynamics of the active layer at a continuous permafrost site (Taymyr Peninsula, Siberia), *Water Resour. Res.*, *34*, 355–363, 1998.

Braithwaite, R. J., Aerodynamic stability and turbulent sensible-heat flux over a melting ice surface, the Greenland ice sheet, *J. Glaciol.*, *41*, 562 – 572, 1995.

Brun, E., E. Martin, V. Simon, C. Gendre, and C. Coléou, An energy and mass model of snow cover suitable for operational avalanche forecasting, *J. Glaciol.*, *35*, 333–342, 1989.

Dingman, S. L., *Physical Hydrology*, 575 pp., Prentice-Hall, Old Tappan, N. J., 1994.

Førland, E. J., I. Hanssen-Bauer, and P. O. Nordli, Climate statistics and long term series of temperature and precipitation at Svalbard and Jan Mayen, *Rep. 21/97 KLIMA*, Norw. Meteorol. Inst., Oslo, 1997.

Gerland, S., J.-G. Winther, J. B. Ørbæk, G. E. Liston, N. A. Øritsland, A. Blanco, and B. Ivanov, Physical and optical properties of snow covering Arctic tundra on Svalbard, *Hydrol. Processes*, *13*, 2331–2343, 1999.

Harding, R. J., and C. R. Lloyd, Fluxes of energy and water from three high latitude tundra sites in Svalbard during the snowmelt and snow free periods, *Nord. Hydrol.*, *29*(4/5), 267–284, 1998.

Harstveit, K., Snowmelt modelling and energy exchange between the atmosphere and a melting snow cover, *Sci. Rep. 4*, 119 pp. Geophys. Inst., Univ. of Bergen, Norway, 1984.

Hinzman, L. D., D. L. Kane, and R. E. Gieck, Regional snow ablation in the Alaskan Arctic, in *Northern Hydrology: Selected Perspectives*, edited by T. D. Prowse and C. S. L. Ommaney, pp. 122–139, Nat. Hydrol. Res. Inst., Saskatoon, Sask., Canada, 1991.

Jordan, R., A one-dimensional temperature model for a snow cover: Technical documentation for SNTHERM89, *Spec. Rep. 91-16*, 49 pp., U.S. Army Cold Reg. Res. and Eng. Lab., Hanover, N.H., 1991.

Kane, D. L., R. E. Gieck, and L. E. Hinzman, Snowmelt modeling at small Alaskan Arctic watershed, *J. Hydrol. Eng.*, *2*, 204–210, 1997.

Liestøl, O., Pingos, springs, and permafrost in Spitsbergen, Årbok 1975, pp. 7–29, Norsk Polarinstit., Oslo, 1977.

Lundberg, A., Laboratory calibration of TDR-probes for snow wetness measurements, *Cold Reg. Sci. Technol.*, *25*, 197–205, 1997.

Marsh, P., and M. K. Woo, Wetting front advance and freezing of meltwater within a snow cover, 1, Observation in the Canadian Arctic, *Water Resour. Res.*, *20*, 1853–1864, 1984.

Price, A. J., and T. Dunne, Energy balance computations of snowmelt in a Subarctic area, *Water Resour. Res.*, *12*, 686–694, 1976.

Putkonen, J. K., Climatic control of the thermal regime of permafrost, northwest Spitsbergen, Ph.D. thesis, 121 pp., Univ. of Wash., Seattle, 1997.

Roth, K., and J. Boike, Quantifying the thermal dynamics of a permafrost site near Ny-Ålesund Svalbard, *Water Resour. Res.*, *37*, 2901–2914, 2001.

Sturm, M., J. P. McFadden, G. E. Liston, F. S. Chapin III, C. H. Racine, and J. Holmgren, Snow-shrub interactions in Arctic Tundra: A hypothesis with climatic implications, *J. Clim.*, *14*, 336–344, 2001.

Tarboton, D. G., D. G. Chowdhury, and T. H. Jackson, A spatially distributed energy balance snowmelt model, in *Biogeochemistry of Seasonally Snow-Covered Catchments, IAHS Publ. 228*, edited by K. A. Tonessen, M. W. Williams, and M. Tranter, pp. 141–155, Int. Assoc. Hydrol. Sci., Gentbrugge, Belgium, 1995.

Winther, J.-G., S. Gerland, J. B. Ørbæk, B. Ivanov, A. Blanco, and J. Boike, Spectral reflectance of melting snow in a high Arctic watershed on Svalbard: Some implications for optical satellite remote sensing studies, *Hydrol. Processes*, *13*, 2033–2049, 1999.

Woo, M. K., P. Marsh, and P. Steer, Basin water balance in a continuous permafrost environment, in *Proceedings of the Fourth International Conference on Permafrost*, pp. 1407–1411, Nat. Acad. Sci., Washington, D.C., 1983.

Woo, M. K., D. Yang, and K. L. Young, Representativeness of Arctic weather station data for the computation of snowmelt in a small area, *Hydrol. Processes*, *13*, 1859–1870, 1999.

Young, K. L., M. K. Woo, and S. A. Edlund, Influence of local topography, soil and vegetation on microclimate and hydrology at a high Arctic site, *Arct. Alp. Res.*, *29*, 270–284, 1997.

Zhang, T., T. E. Osterkamp, and K. Stamnes, Influence of the depth hoar layer of the seasonal snow cover on the ground thermal regime, *Water Resour. Res.*, *32*, 2075–2086, 1996.

Zhang, T., S. A. Bowling, and K. Stamnes, Impact of the atmosphere on surface radiative fluxes and snowmelt in the Arctic and Subarctic, *J. Geophys. Res.*, *102*, 4287–4302, 1997.

J. Boike, Water and Environmental Research Center, University of Alaska, Fairbanks, Fairbanks, AK 99775, USA. (ffjb2@aurora.uaf.edu)

O. Ippisch and K. Roth, Institute of Environmental Physics, University of Heidelberg, D-69120 Heidelberg, Germany. (kurt.roth@iup.uni-heidelberg.de; olaf.ippisch@iwr.uni-heidelberg.de)

Chapter 2.2

Westermann, S., Lüers, J., Langer, M., Piel, K., **Boike**, J. (2009): The annual surface energy budget of a high-arctic permafrost site on Svalbard, Norway, *The Cryosphere*, *3, 245-263.*

The Cryosphere, 3, 245–263, 2009
www.the-cryosphere.net/3/245/2009/
© Author(s) 2009. This work is distributed under
the Creative Commons Attribution 3.0 License.

The Cryosphere

The annual surface energy budget of a high-arctic permafrost site on Svalbard, Norway

S. Westermann[1], **J. Lüers**[2], **M. Langer**[1], **K. Piel**[1], **and J. Boike**[1]

[1]Alfred-Wegener-Institute for Polar and Marine Research, Telegrafenberg A43, 14473 Potsdam, Germany
[2]Department of Micrometeorology, University of Bayreuth, 95440 Bayreuth, Germany

Received: 11 August 2009 – Published in The Cryosphere Discuss.: 27 August 2009
Revised: 6 December 2009 – Accepted: 13 December 2009 – Published: 18 December 2009

Abstract. Independent measurements of radiation, sensible and latent heat fluxes and the ground heat flux are used to describe the annual cycle of the surface energy budget at a high-arctic permafrost site on Svalbard. During summer, the net short-wave radiation is the dominant energy source, while well developed turbulent processes and the heat flux in the ground lead to a cooling of the surface. About 15% of the net radiation is consumed by the seasonal thawing of the active layer in July and August. The Bowen ratio is found to vary between 0.25 and 2, depending on water content of the uppermost soil layer. During the polar night in winter, the net long-wave radiation is the dominant energy loss channel for the surface, which is mainly compensated by the sensible heat flux and, to a lesser extent, by the ground heat flux, which originates from the refreezing of the active layer. The average annual sensible heat flux of $-6.9\,\mathrm{Wm}^{-2}$ is composed of strong positive fluxes in July and August, while negative fluxes dominate during the rest of the year. With $6.8\,\mathrm{Wm}^{-2}$, the latent heat flux more or less compensates the sensible heat flux in the annual average. Strong evaporation occurs during the snow melt period and particularly during the snow-free period in summer and fall. When the ground is covered by snow, latent heat fluxes through sublimation of snow are recorded, but are insignificant for the average surface energy budget. The near-surface atmospheric stratification is found to be predominantly unstable to neutral, when the ground is snow-free, and stable to neutral for snow-covered ground. Due to long-lasting near-surface inversions in winter, an average temperature difference of approximately 3 K exists between the air temperature at 10 m height and the surface temperature of the snow.

Correspondence to: S. Westermann
(sebastian.westermann@awi.de)

As such comprehensive data sets are sparse for the Arctic, they are of great value to improve process understanding and support modeling efforts on the present-day and future arctic climate and permafrost conditions.

1 Introduction

In permafrost regions, the partitioning of energy at the surface is a crucial process, which strongly influences the heat flux into the ground and thus ultimately the thermal conditions of the permafrost. This surface energy budget depends on a number of factors, such as the available radiation, synoptic weather conditions, surface characteristics and soil moisture. Ground-based measurements, satellite data and results of climate modeling have revealed an ongoing warming trend in the Arctic (e.g. Serreze et al., 2000; Hansen et al., 2001; Comiso and Parkinson, 2004; Comiso et al., 2008; Overland et al., 2008). On Svalbard, a significant warming of air temperatures since 1960 has been detected, which is mainly attributed to changes in circulation patterns (Hanssen-Bauer and Førland, 1998). This is also reflected in permafrost temperatures, which display a significant warming (Isaksen et al., 2001, 2007). Climate models predict an accelerated future warming trend, with the largest warming occurring during winter (Førland and Hanssen-Bauer, 2003).

Such large-scale changes will be modulated by the locally determined conditions of the surface energy budget, which may result in an amplification as well as in a damping of the large-scale signal on the local scale. Moreover, a modification of the surface energy budget over large areas within the Arctic, e.g. triggered by a change in the vegetation, can even induce a feedback on the climate system (Chapin et al., 2005). Hereby, land-atmosphere exchange processes, i.e.

Published by Copernicus Publications on behalf of the European Geosciences Union.

turbulent fluxes of sensible and latent heat, play a dominant role, as they vary considerably depending on the surface cover (Chapin et al., 2000; Eugster et al., 2000).

The redistribution of energy at the surface is one of the driving forces for the global climate system. The basic contributions of the surface energy budget are the short- and long-wave radiation, the sensible and latent heat fluxes and the ground heat flux. The adequate representation of this surface forcing is one of the challenges in atmospheric circulation models, on which predictions on climate change are based. The models make use of mostly semi-empirical parameterizations of the different fluxes of the surface energy budget, which have usually been developed and validated for non-arctic regions (e.g. Viterbo and Beljaars, 1995). In the Arctic, the perennial snow cover and the annual snowmelt, which greatly modify the surface processes for a large part of the year, constitute additional challenges for modeling which have not yet been fully resolved (Douville et al., 1995; Slater et al., 1998). Another unresolved problem is the parameterization of the sensible and latent heat fluxes during stable atmospheric stratification conditions which frequently occur in the arctic winter (Zilitinkevich et al., 2002; Lüers and Bareiss, 2009a). The same problems occur in process-orientated permafrost models (Hoelzle et al., 2001), which in principle use the same parameterizations of the surface energy budget to evaluate the ground heat flux and the thermal conditions of the subjacent permafrost (Hinzman et al., 1995; Ling and Zhang, 2004).

Direct measurements of the surface energy budget in arctic regions are therefore indispensable to evaluate the performance of the employed flux parameterizations and surface parameter sets, especially if the study can provide the entire annual cycle and thus a complete picture including snow-associated processes. Great efforts have been initiated to study the annual cycle of the surface energy budget over arctic sea ice (Persson et al., 2002; Uttal et al., 2002), while comprehensive long-term studies are still missing for arctic land areas.

Under arctic conditions, particularly the quantification of sensible and latent heat fluxes still remains a challenging task (Lynch et al., 1999). The eddy covariance method has proven to be most suitable to directly measure sensible and latent heat fluxes (Foken, 2008b) and its potential has been demonstrated in a number of studies in the Arctic (McFadden et al., 1998; Oechel et al., 1998; Vourlitis and Oechel, 1999; McFadden et al., 2003). However, due to the difficult logistics and the extreme environmental conditions, few long-term eddy covariance studies of land-atmosphere exchange processes exist in arctic regions (Grachev et al., 2007; Stöckli et al., 2008). On Svalbard, they have been limited to short study periods during spring (Georgiadis et al., 2000), during the snow melt period (Harding and Lloyd, 1998; Lüers and Bareiss, 2009a) and during summer (Lloyd et al., 2001). In addition, the surface energy budget during the snow melt period has been investigated with techniques other than eddy covariance (Takeuchi et al., 1995; Nakabayashi et al., 1996; Boike et al., 2003a,b).

This study presents eddy covariance measurements of the sensible and latent heat flux at a high-arctic permafrost site on Svalbard, which were conducted over a full seasonal cycle from March 2008 to March 2009. The eddy covariance measurements are complemented by measurements of the radiative parts of the energy budget and the ground heat flux, so that a complete set of independent measurements of all contributions of the surface energy budget is accessible at a temporal resolution of one hour for an entire year. In this study, we focus on the annual and diurnal cycles of the surface energy budget. This not only allows to identify the driving parameters of the coupled permafrost-snow-atmosphere system, but also provides a basis for further investigations and modeling efforts, e.g. on the impact of small-scale variations of the surface cover on the local energy budget and the thermal conditions of the subjacent permafrost.

While the current study extends the sparse data set on the surface energy budget in the Arctic, we hope to encourage similar studies at other circumarctic locations, which would greatly improve the understanding of the climate of high-latitude ecosystems and its susceptibility to climate change.

2 Study site

2.1 Climatological conditions

Ny-Ålesund is situated at the Kongsfjorden in NW Svalbard (Fig. 1a). It has long been in the focus of a wide range of measurement campaigns and long-term monitoring programs, which have created an outstanding data basis, particularly with respect to climatological and atmospheric variables (e.g. Yamanouchi and Ørbaek, 1995; Beine et al., 2001; Winther et al., 2002). The area is strongly influenced by the North Atlantic Current, leading to a maritime climate with cool summer and comparatively mild winter temperatures. The average air temperature is around +5 °C in July and −13 °C in January, with an annual precipitation of around 400 mm (Førland et al., 1997). The short-wave radiation budget naturally follows the rhythm of polar night and day, but is strongly modulated by albedo changes due to the seasonality of the snow cover. The snow-free period can vary from 50 to 150 days, but the typical duration is around three months (Winther et al., 2002).

During summer, the west coast of Svalbard is predominantly influenced by moist atlantic air masses, which leads to a high percentage of cloudy days. In winter, it is under the influence of both moist atlantic and dry polar air masses, which are typically associated with comparatively warm air temperatures with overcast skies and cold air temperatures with clear skies, respectively (e.g. Førland et al., 1997). As a result of the exchange of the air masses during winter, the incoming long-wave radiation is found to vary over a wide

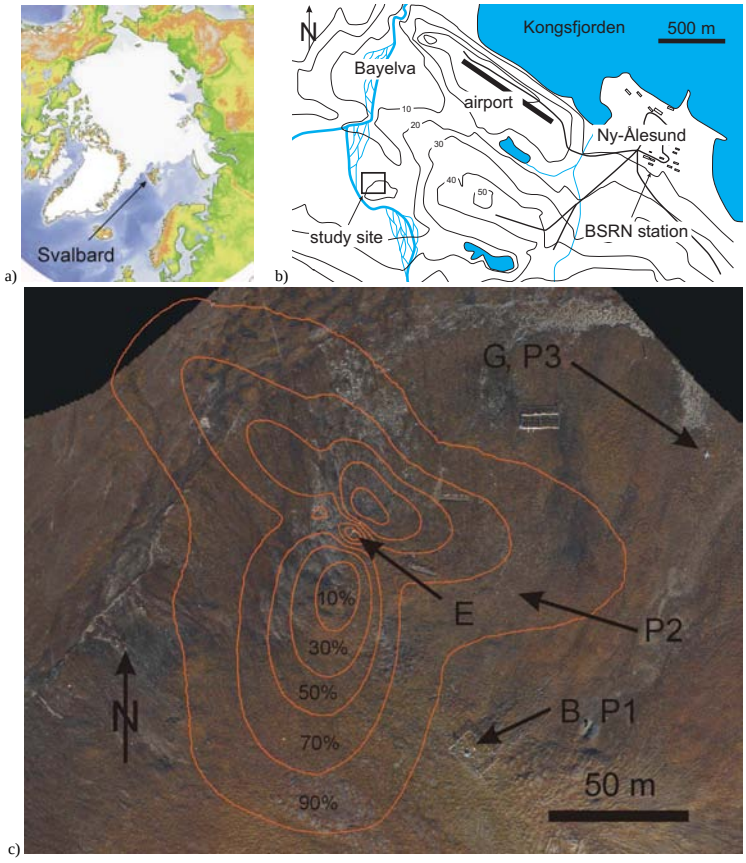

Fig. 1. (a) Map of the Arctic. **(b)** Location of the study site and the BSRN site; thick black lines: roads; contour lines in meters above sea level. **(c)** Orthorectified aerial photo with all installations (E: eddy covariance system; B: Bayelva climate station; G: gradient tower; P1, P2, P3: temperature profile measurements). The average footprint of the eddy covariance system from 1 July to 30 September 2008 is shown, with the percentages of the total flux originating within the respective contours.

range, while its range is much smaller during summer (Yamanouchi and Ørbaek, 1995).

Compared to the reference period 1961 to 1990, about 10% more precipitation was recorded during the study period, while the observed air temperature was on average 1.5 K warmer (eklima, 2009). Therefore, the study period integrates well in the warming trend found for the last decade (Førland and Hanssen-Bauer, 2003), and does not represent exceptionally warm conditions, which have been recorded previously (e.g. Isaksen et al., 2007). With less than half of the precipitation of the long-term average, the first half of the study period from March to August 2008 was drier, while considerably more precipitation was measured from September 2008 to March 2009. With almost 100 mm of precipitation each, the months of September and December 2008 stood out with more than twice of the long-term average. However, similar precipitation rates have been observed at a number of occasions in fall and early winter since 2000 (eklima, 2009), so that the second half of the study period must be considered "wet conditions" rather than an extreme exception. The Kongsfjorden, located 2 km NE of the study area (Fig. 1b), was free or almost free of sea ice during the entire study period, which has been the case since 2006 (Gerland and Renner, 2007; Cottier et al., 2007, own observations).

2.2 Site description

The measurements were performed in the Bayelva catchment on the NW slope of Leirhaugen hill at 78°55′ N, 11°50′ E (Fig. 1b), located approximately 2 km SW of the village of Ny-Ålesund. The observation site is situated in hilly tundra at the foot of two major glaciers at elevations of 15 m to 25 m above sea level and is characterized by sparse vegetation alternating with exposed soil and rock fields. On the top of Leirhaugen hill, the surface is covered with mud boils, a form of non-sorted circles. The soil at the study site features a high mineral content, while the organic content is low, with volumetric fractions below 10%. The soil texture ranges from clay to silty loam (Boike et al., 2008). The Bayelva climate and soil monitoring station has provided a long-term

record of climatological parameters and permafrost temperatures since 1998. At present, the permafrost at Leirhaugen hill is relatively warm, with a mean annual temperature around $-2\,^{\circ}$C at 1.5 m depth. The maximum active layer depth in 2008 was on the order of 1.5 m. Since the installation of the station, the average soil temperatures have increased significantly at the observation site (compare to Roth and Boike, 2001). The eddy covariance system is located at a slightly inclined slope ($<5^{\circ}$). The flow paths in the main wind directions are unobstructed by man-made artificial structures, so that we can assume an undisturbed footprint area. An aerial picture with all installations is shown in Fig. 1c.

3 Measurements

3.1 Definitions and constants

S_{in}: incoming short-wave radiation
S_{out}: outgoing short-wave radiation
ΔS: net short-wave radiation
L_{in}: incoming long-wave radiation
L_{out}: outgoing long-wave radiation
ΔL: net long-wave radiation
Q_h: sensible heat flux
Q_e: latent heat flux
Q_g: ground or snow heat flux
Q_{melt}: energy flux consumed by melt of snow
C: residual of the energy balance
$\Delta S+\Delta L+Q_h+Q_e+Q_g+Q_{\mathrm{melt}}+C=0$
u_*: friction velocity
z_0: aerodynamic roughness length
ξ =z/L: stability parameter (z: measurement height, L: Obukhov length)
T_{air}: air temperature
T_{surf}: surface temperature
ϵ: Kirchhoff emissivity
σ: Stefan-Boltzmann constant
c_p: specific heat capacity of air at constant pressure
ρ_{air}: density of air
d_h: thermal diffusivity
K_h: thermal conductivity
c_h: volumetric heat capacity
$c_{h,\mathrm{water}} = 4.2\,\mathrm{MJm^{-3}K^{-1}}$
$c_{h,\mathrm{ice}} = 1.9\,\mathrm{MJm^{-3}K^{-1}}$
$c_{h,\mathrm{mineral}} = 2.0\,\mathrm{MJm^{-3}K^{-1}}$
$c_{h,\mathrm{organic}} \approx c_{h,\mathrm{mineral}}$
$c_{h,\mathrm{air}} \approx 0.001\,\mathrm{MJm^{-3}K^{-1}}$
$\rho_{\mathrm{ice}} = 0.91\,\mathrm{gcm^{-3}}$: density of ice
$L_{\mathrm{sl}} = 0.33\,\mathrm{MJkg^{-1}}$: specific latent heat of fusion of water
$L_{\mathrm{lg}} = 2.5\,\mathrm{MJkg^{-1}}$: specific latent heat of vaporization of water

The surface is defined as the interface between the atmosphere and the soil or snow, respectively. We use the convention that fluxes, which transport energy away from the surface, are denoted positive and fluxes, which transport energy towards the surface, are denoted negative.

3.2 Radiation

The Bayelva climate station is located about 100 m from the eddy covariance site (Fig. 1c), where measurements of S_{in} with a Skye Pyranometer SP1110 and L_{out} with a Kipp & Zonen CG1 long-wave radiation sensor are performed. S_{out} and L_{in} are not measured at the Bayelva station (see below). Under the extreme conditions of the Arctic, reliable radiation measurements are a challenging task. Since it is not possible to maintain the sensors at the Bayelva station regularly, a reduced accuracy and frequent data gaps must be accepted. However, a maintained station of the Baseline Surface Radiation Network (BSRN) is located in the village of Ny-Ålesund, about 2 km from the study site (Fig. 1b), where incoming and outgoing short- and longwave radiation are measured according to WMO accuracy standards (Ohmura et al., 1998). The BSRN data set can not be entirely assigned to the study site due to differences in the surface cover and the timing of the snow melt between both sites. However, the incoming long-wave radiation L_{in} is used in this study, since it is mainly determined by the cloud cover and the atmospheric temperature and water vapor profile, which do not vary considerably between the two sites. Furthermore, the BSRN data are used as a reference to assess the quality of and, if necessary, to fill gaps in the Bayelva radiation data. In addition, the average surface albedo is inferred from measurements at the BSRN site to calculate S_{out}, except for the snow melt period. When the ground is covered by snow, systematic differences in the albedo of the undisturbed snow surfaces at the study and the BSRN site are not to be expected. When the ground is snow-free, the albedo at the two sites may be slightly different, though. In August 2008, the surface albedo was estimated at 40 points within and in the 300 m vicinity of the eddy footprint area (see Sect. 3.3, Fig. 1c) from single measurements of incoming and outgoing short-wave radiation under clear-sky conditions using a pyranometer. The resulting average albedo of 0.18 ± 0.05 compares well with the albedo of 0.15, which we infer from the time series of the BSRN station for the months of July and August. We use the latter value for our analysis, but assume an error of at least 5% on the net short-wave radiation, when the ground is snow-free. For the snow melt period, we assume an albedo estimate of 0.65, which is the average albedo at the BSRN station between 1 and 15 June 2008. In this period, the snow melt occurred at the BSRN station, associated with a decrease in albedo from the winter value 0.8 to 0.5, before it dropped sharply to the summer value.

The outgoing and incoming long-wave radiation L_{out} and L_{in} are linked to the surface temperature T_{surf} by

$$L_{\text{out}} = \epsilon \sigma T_{\text{surf}}^4 + (1-\epsilon) L_{\text{in}}. \quad (1)$$

The emissivity ϵ is set to 0.96 for snow-free and 0.99 for snow-covered surfaces in this study (e.g. Rees, 1993; Bussières, 2002).

3.3 Turbulent fluxes

The turbulent land-atmosphere exchange fluxes of sensible and latent heat are measured with the eddy covariance method. The employed system consists of a Campbell CSAT 3D sonic anemometer and a fast-responding open-path LiCor LI–7500 CO_2 and H_2O gas analyzer, which are sampled at 20 Hz using a CR3000 Campbell Scientific datalogger. From the sonic temperature T_s, the specific humidity q and the horizontal and vertical wind speed u and w measured at the eddy covariance system, the covariances $\overline{u'w'}$, $\overline{T_s'w'}$ and $\overline{q'w'}$ are calculated. They are then used to infer the momentum flux u_*^2 and the sensible and latent heat flux Q_h and Q_e as (e.g Foken, 2008b).

$$\begin{aligned} u_*^2 &= -\overline{u'w'} \\ Q_h &= c_p \rho_{\text{air}} \left(\overline{T_s'w'} - 0.51 T_{\text{air}} \overline{q'w'} \right) \\ Q_e &= L_{\text{lg}} \rho_{\text{air}} \overline{q'w'}. \end{aligned} \quad (2)$$

The evaluation is performed with the internationally standardized QA/QC software package "TK2" (Mauder and Foken, 2004; Mauder et al., 2008), which includes all "state-of-the-art" corrections and tests. For quality assessment of the flux measurements, we use the scheme of Foken et al. (2004) (see also Foken and Wichura, 1996), which is based on a steady-state and an integral turbulence characteristics test. However, the integral turbulence characteristics test is not well defined for intermittent turbulence and stable atmospheric conditions (Lüers and Bareiss, 2009a), which prevail during a large part of the study period. To achieve a consistent quality assessment, only the steady-state test is employed in this study. Hereby, the covariances $\overline{u'w'}$, $\overline{T_s'w'}$ and $\overline{q'w'}$ obtained for a 30-min interval are compared to the averages of the respective covariances calculated for 5-min subintervals. Stationary conditions can be assumed, if both results agree within 30%, while a graduation of the deviation is used to classify the quality of the fluxes (Foken, 2008b).

At the 30-min timescale, the sensible heat flux Q_h is considered in this study if both the quality flags for $\overline{u'w'}$ and $\overline{T_s'w'}$ feature a value of 6 or better, corresponding to flux measurements, which can be considered for long-term studies (Foken and Wichura, 1996). For the latent heat flux Q_e, the quality flags for $\overline{u'w'}$ and $\overline{q'w'}$ are used, respectively. Both for the sensible and the latent heat flux, approx. 15% of the values have been excluded due to the quality assessment. Furthermore, all flux values from wind sectors have been removed where the upwind tower structure could produce some flow distortions affecting the sonic anemometer (wind direction 15°–55°). However, this applies only to about 1.5% of the flux values, as the tower structure is placed away from the prevailing wind directions. The half-hourly values are averaged to obtain a data set with an hourly resolution.

From 2 October to 18 October 2008 and from 1 January to 6 February 2009, the raw data sampled at 20 Hz were not recorded by the datalogger due to instrument failure. In these cases, fluxes based on preliminary, uncorrected 30-min covariances calculated by the standard datalogger software are used. Hereby, an adequate post-processing can not be applied and a subsequent quality assessment is not possible. However, the obtained flux values are considered in this study, because the standard datalogger software can reproduce the magnitude of the average fluxes for times when the sophisticated evaluation and quality assessment scheme is available.

For the snow-free period, the aerodynamic roughness length z_0 is estimated to be 7 mm from the measured values of u_* and the horizontal wind speed during neutral atmospheric stratification conditions (e.g. Foken, 2008b). We then use the footprint model of Schmid (1994) to estimate the fetch area of the eddy covariance system. The average flux source area during the snow-free period from July to September 2008 is displayed in Fig. 1c. The main contributions originate from tundra areas in the prevailing wind directions from approx. 180°(wind from the glacier Austre Brøggerbreen), approx. 110°(wind from the inner Kongsfjorden) and from approx. 310°to 350°(wind from the outer Kongsfjorden).

To account for the changing height of the eddy covariance system due to accumulation or melting of snow, the snow depth at the eddy covariance site is recorded using an ultrasonic ranging sensor. From March to May 2008, the distance between the CSAT anemometer and the snow surface was around 1.0 m. In the course of the snow melt, it increased to 2.1 m, which was the measurement height of the CSAT during the snow-free time. From end of September 2008 onwards, the distance decreased again, but remained above 1.0 m until end of January 2009. Heavy snowfall led to a further decrease to around 0.5 m at the end of the study period. Paticularly flux data obtained at measurement heights below 1.0 m may bear a considerable uncertainty due to high-frequency losses (e.g. Moore, 1986) or drifting snow affecting the sonic anemometer (Lüers and Bareiss, 2009a). However, since the quality assessment still indicates a good overall data quality and the magnitude of the measured fluxes matches well with periods, where the measurement height was considerably above 1.0 m, the data are considered for this study.

3.4 Ground heat flux

In the context of the surface energy budget, we are interested in the heat flux through the interface between the atmosphere and the ground or snow, respectively. The latter is denoted snow heat flux in the following. Two different methods are

employed to calculate the ground or snow heat flux. The first method, which we refer to as the bulk method, was successfully applied at the study site by Boike et al. (2003b), where it is described in detail. It is based on differences in the absolute sensible and latent heat content of the soil and snow column, from which an average ground or snow heat flux for the considered time interval can be calculated. The water content of the soil and thus the latent heat content is compiled from a profile of seven Time Domain Reflectometry (TDR) measurements located next to a profile of temperature measurements (P1 in Fig. 1c), from which the sensible heat content is derived. No measurements exist for a potential non-zero water and thus latent heat content of the snow pack. Therefore, the snow is completely excluded from the evaluation during the snow melt period (see Sect. 3.5). The latent heat added to the snow pack by so-called "rain-on-snow"-events during winter (Putkonen and Roe, 2003) is estimated from precipitation records (see Sect. 3.6). This is justified, since no run-off occurs during these events and the entire amount of water refreezes subsequently. Using the specific latent heat of fusion, L_{sl}, the total heat input through rain-on-snow events can be calculated, which is then converted to an average flux.

The bulk method is well suited to deliver reliable average fluxes for longer periods, but has short-comings on the timescale of one hour due to the limited number of temperature and soil moisture sensors, which cannot resolve the temperature distribution in the uppermost soil column. Furthermore, the maximum active layer thickness was around 1.5 m during the study period, which is well below the deepest TDR sensor, located at 1.13 m. Therefore, the fluxes are biased, when the soil below the deepest TDR sensor thaws or freezes, which mainly affects the thaw period in August and September 2008 and the following refreezing period in October and November 2008.

The second method directly calculates the ground heat flux through the surface by solving the differential equation of conductive heat transport. It is referred to as the conduction method (see Appendix A). Although convective heat transport, e.g. through infiltrating rain water, is not accounted for, the assumption of a conductive heat transfer was shown to be adequate for the study area during winter (Roth and Boike, 2001), a site approx. 10 km from the study area (Putkonen, 1998) and for other permafrost areas (e.g. Romanovsky and Osterkamp, 1997). Periods, where a phase change of water occurs within the considered soil column, are excluded from the evaluation. To evaluate the thermal diffusivity d_h, the heat capacity c_h and the thermal conductivity K_h of the soil during the snow-free period, we use the shallow temperature profile P2 (Fig. 1c, Table 1).

The thermal diffusivity is fitted for different periods in July and August 2008, with values ranging from $d_h = 5.2\times10^{-7}\,\mathrm{m^2 s^{-1}}$ to $d_h = 6.5\times10^{-7}\,\mathrm{m^2 s^{-1}}$. For the fit, we exclude periods with measurement errors or strong rain events, which may induce non-conductive transport of heat. The found variability of d_h may at least partly originate from natural processes, e.g. through changing soil water content. For the evaluation of the ground heat fluxes in the snow-free period, we apply a constant value $d_h = (5.5\pm1.0)\times10^{-7}\,\mathrm{m^2 s^{-1}}$.

Table 1. Installations of the temperature profiles used to calculate the ground heat flux; z_{min}, z_{max}: minimum and maximum depths of the temperature sensors; Th: thermistor; TC: type T thermocouple; PT100: platinum resistance temperature sensor; TDR: measurement of soil water content using Time Domain Reflectometry.

profile	P1	P2	P3
z_{min}/ m	0.02	0.01	0.01
z_{max}/ m	1.55	0.25	0.30
soil	7 × PT100, 6 × TDR	1 × Th, 2 × TC	2 × Th, 1 × TC
snow	2 × PT100	3 × TC	3 × TC
installed	09/01/1998	07/07/2008	10/01/2008

In soil samples collected in the vicinity of the temperature profiles, the volumetric bulk (mineral and organic) content was determined to be between 45% and 65%, and the volumetric soil water content varied between 20% and 40%. Thus, the heat capacity of the soil can be estimated to $c_h = (2.3\pm0.5)\,\mathrm{MJ m^{-3}}$, which results in a thermal conductivity of $K_h = (1.3\pm0.4)\,\mathrm{W m^{-1} K^{-1}}$. The value is well within the range predicted by widely-used models such as the de-Vries-model (De Vries, 1952; Campbell et al., 1994) for such soils. With K_h known, the ground heat flux can be evaluated (see Appendix A). Note, that the considerable uncertainties on both d_h and c_h propagate to K_h, resulting in an uncertainty of more than 25% for the obtained ground heat flux.

During the winter 2008/2009, a profile of three temperature sensors (located at the soil surface and 0.15 m and 0.4 m above the surface) in the snow pack located next to P3 is used to fit the thermal diffusivity of the snow. This is possible from December 2008 onwards, as soon as the snow pack has reached the uppermost sensor. Initially, the array is contained in the young snow pack, but gets progressively buried with increasing snow height. The obtained values range from $d_h = 4.5\times10^{-7}\,\mathrm{m^2 s^{-1}}$ to $d_h = 7.0\times10^{-7}\,\mathrm{m^2 s^{-1}}$, with a tendency towards higher values of d_h at the end of the considered period for the then older snow. However, we have no measurements of the thermal diffusivity of the overlying, not instrumented snow pack. For the evaluation of the snow heat flux, we therefore choose a constant value of $d_h = (5.5\pm1.5)\times10^{-7}\,\mathrm{m^2 s^{-1}}$ and include the found variability of d_h as uncertainty. In March 2009, snow density profiles were gravimetrically measured in increments of 0.1 m at five sites in the eddy fetch area and in its vicinity. The average snow density was determined to $\rho_{snow} = (0.37\pm0.05)\,\mathrm{g cm^{-3}}$, which results in a heat

capacity $c_{h,\mathrm{snow}} = (0.75 \pm 0.1)\,\mathrm{MJm^{-3}K^{-1}}$ (using $c_{h,\mathrm{snow}} = c_{h,\mathrm{ice}} \times \rho_{\mathrm{snow}}/\rho_{\mathrm{ice}}$). Hence, the resulting snow conductivity is $K_h = (0.45 \pm 0.15)\,\mathrm{Wm^{-1}K^{-1}}$.

Since the temperature sensors are placed at fixed heights above the ground, it is only possible to infer the heat flux within the snow pack up to the height of the uppermost sensor, which is clearly different from the targeted heat flux through the snow surface. Therefore, the snow surface temperatures inferred from measurements of long-wave radiation (Eq. 1) at the Bayelva climate station, next to P1, are used as upper boundary condition, while temperatures at the snow-soil interface at P1 are used as lower boundary. The snow heat flux is then calculated (see Appendix A) for periods defined by snow heights that fall within classes of 0.1 m increments. The snow height is measured next to P1 with an ultrasonic ranging sensor. This method induces discontinuities in the flux at the boundary of each two periods, so the flux values have to be discarded at these boundaries. The obtained snow heat flux is associated with an error of approx. 30%, which mainly originates from the uncertainty in the thermal conductivity. It must be emphasized that the snow pack is treated as homogeneous in time and space, which does not reflect processes such as aging and densification of the snow. However, at least the snow density measurements indicate a homogeneous snow pack, both for each profile and among different locations.

When a rain-on-snow event occurs, the fluxes are discarded, until all measured temperatures in the snow decrease below $-0.5\,^{\circ}\mathrm{C}$ and refreezing processes can be excluded. This leads to the exclusion of in total seven days during the winter 2008/2009. Particularly the strong rain-on-snow events provoke a pronounced warming of the underlying soil column, which then slowly cools by means of conductive heat transport through the snow. Therefore, the conduction method accounts for at least some part of the heat input through rain-on-snow events, although the time directly after the rain-and-snow events is excluded.

3.5 Melt energy of the snow

During snow melt, the latent heat consumed by the melting snow Q_{melt} appears as an additional component in the surface energy budget. Between 25 May and 28 May 2008, before the onset of the snow melt, the snow water equivalent of the snow at the study site was estimated by seven snow density measurements and systematic snow depth measurements on a 20×20 square meter grid. With the specific latent heat of fusion, L_{sl}, the total energy required to melt the snow can be evaluated, which is then converted to an average flux for the snow melt period. A considerable uncertainty is induced by a basal ice layer underneath the snow, which has not been spatially surveyed.

3.6 Ancillary measurements

We use the detailed record of the Norwegian Meteorological Institute from the village of Ny-Ålesund (Fig. 1b) for data on precipitation, air pressure, relative humidity and cloud fraction (eklima, 2009). The air temperature at 2 m height above ground is measured at the Bayelva climate station. The precipitation is recorded at the study site with an unheated RM Young 52203 Tipping Bucket rain gauge, which can only measure precipitation in the form of rain and possibly slush. These data are used as a coarse estimate for the amount of liquid precipitation during the winter season, from which we obtain the energy input through rain-on-snow events (see Sect. 3.4).

From October 2008 to March 2009, measurements of the air temperature at 2 m and 10 m above ground, denoted $T_{\mathrm{air}}(2\,\mathrm{m})$ and $T_{\mathrm{air}}(10\,\mathrm{m})$, were performed approx. 150 m from the location of the eddy covariance system (Fig. 1c) to obtain additional data on the atmospheric stratification. With increasing snow height, the distances of the sensors to the snow surface decreased accordingly, with the lower temperature sensor being approximately at the same height above the surface as the eddy covariance system (see Sect. 3.3).

4 Results

The one year study period is divided into six segments, each of which feature distinct characteristics of the surface energy budget. The transition between different segments is mostly gradual, but the segmentation is closely orientated at "real" events, such as the onset or termination of the snow melt or the beginning of the polar night. The average fluxes for each of the segments are presented in Table 2.

4.1 Summer (1 July 2008–31 August 2008)

The summer period is characterized by a strong forcing by short-wave radiation and the absence of the seasonal snow cover. The net short-wave radiation ΔS is compensated by the net long-wave radiation, the sensible and latent heat flux, and the ground heat flux, which leads to the seasonal thawing of the active layer (Fig. 2, Table 2). Cloudy conditions are typical for the summer season (Table 2), which effectively reduces the incoming solar radiation. The difference in ΔS between cloud-covered and clear skies can exceed $150\,\mathrm{Wm^{-2}}$ in the daily average. On the other hand, the incoming long-wave radiation L_{in} increases during cloudy periods, with daily average differences of around $80\,\mathrm{Wm^{-2}}$. The absolute values of L_{in} range from $-230\,\mathrm{Wm^{-2}}$ to $-340\,\mathrm{Wm^{-2}}$, while the outgoing long-wave radiation L_{out} ranges from $300\,\mathrm{Wm^{-2}}$ to $400\,\mathrm{Wm^{-2}}$, corresponding to surface temperatures between $-5\,^{\circ}\mathrm{C}$ and $+17\,^{\circ}\mathrm{C}$ (Eq. 1).

A measure for the atmospheric stability is the dimensionless parameter $\xi = z/L$, which is obtained from the sonic anemometer (L Obukhov-length, z measurement height).

Table 2. Average values for air temperature T_{air}, precipitation P, air pressure p, relative humidity RH, cloud fraction cf. (see Sect. 3.6) and for the various contributions of the surface energy budget (see Sect. 3.1) for different segments of the study period. Values in parentheses are estimates or based on data records with frequent data gaps. The value for $Q_{g\,\mathrm{bulk}}$ during dark winter is composed of the flux due to the refreezing of the active layer, $-5.0\,\mathrm{Wm}^{-2}$, and a flux of $-1.8\,\mathrm{Wm}^{-2}$ due to rain-on-snow events.

	Summer	Fall	Dark winter	Light winter	Pre-melt	Snow melt	Total
	07/01/08	09/01/08	10/01/08	03/15/08	04/16/08	06/01/08	03/15/08
	–08/31/08	–09/31/08	–03/15/09	–04/15/08	–05/31/08	–06/30/08	–03/15/09
T_{air}/ °C	5.0	2.7	−10.1	−16.0	−5.6	2.0	−5.4
P/mm	32	99	278	12	11	8	440
p/hPa	1011	1008	1004	1017	1018	1014	1009
RH	82%	81%	73%	59%	71%	73%	74%
cf	6.4/ 8	6.9/ 8	5.5/ 8	3.6/ 8	5.7/ 8	5.5/ 8	5.6/ 8
S_{in}/ Wm^{-2}	−144	−33	−2.1	−73	−185	−261	−78
S_{out}/ Wm^{-2}	22	9	1.7	55	144	(170)	42
ΔS/ Wm^{-2}	−122	−24	−0.4	−18	−41	(−91)	−36
L_{in}/ Wm^{-2}	−303	−299	−234	−196	−255	−276	−254
L_{out}/ Wm^{-2}	346	318	262	237	288	319	286
ΔL/ Wm^{-2}	43	19	28	41	33	43	32
Q_h/ Wm^{-2}	22.5	(−7)	−16	−18	−8	−6	−6.9
Q_e/ Wm^{-2}	22.5	(9)	2.5	0.7	2.5	11	6.8
$\mathrm{Q}_{g\,bulk}$/ Wm^{-2}	(11)	–	(−5.0)−1.8	−3.1	3.0	13	∼0.5
$\mathrm{Q}_{g\,cond}$/ Wm^{-2}	12	(0.6)	−5.0	−5.9	–	–	
Q_{melt}/ Wm^{-2}	?	?	0	0	?	(27)	2.3
C/ Wm^{-2}	22	2	−9	0	10.5	3	1

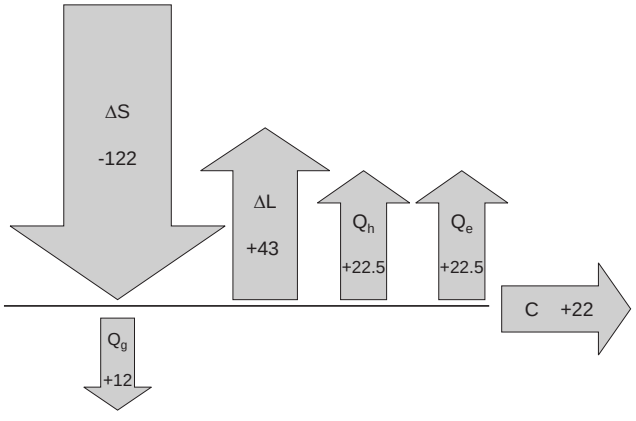

Fig. 2. Schematic diagram of the contributions of the surface energy budget for the summer period. The area of the arrows is proportional to the relative importance in the energy budget. Arrows pointing away from the surface indicate positive fluxes. The flux values are given in Wm^{-2}.

Positive values indicate stable, while negative values represent unstable atmospheric stratifications. During the polar day season, approx. until mid of August, the atmospheric stratification is either unstable or neutral. Later, the general situation can be characterized as neutral to weakly unstable atmospheric stratification during the day and stable atmospheric stratification during the night. The sensible, latent and ground heat fluxes are shown in Fig. 3. The average Bowen ratio is approximately one, but it shows strong variations, which are closely related to the soil water content of the surface layer (Figs. 3, 4). For a wide range of intermediate soil moisture conditions, it remains around one, but extremely wet or dry conditions lead to Bowen ratios of around 0.25 or 2, respectively (Fig. 4). The sensible and the latent heat flux display a strong diurnal amplitude, with peak fluxes between $60\,\mathrm{Wm}^{-2}$ and $120\,\mathrm{Wm}^{-2}$ associated with maxima of net radiation around midday. At the lowest sun angles, around midnight, the absolute values of both fluxes decrease to close to zero, but usually remain positive. The latent heat flux observed in July and August 2008 corresponds to a total evaporation of 48 mm, which is significantly more than the precipitation of 32 mm recorded during the same period. This can be related to the drying of the water-saturated tundra after snow melt. The average ground heat fluxes peaks at the beginning of the summer period, when the thaw front is close to the soil surface and a strong temperature gradient exists in the soil. Peak values are around $60\,\mathrm{Wm}^{-2}$, which is of comparable magnitude as the sensible and latent flux (Fig. 3). However, the storage effect of the soil is reflected in generally negative ground heat fluxes of up to $-30\,\mathrm{Wm}^{-2}$ during night times (i.e. times with low solar angle during polar day), so that the average ground heat flux is considerably less than the average sensible and latent heat flux (Fig. 2, Table 2).

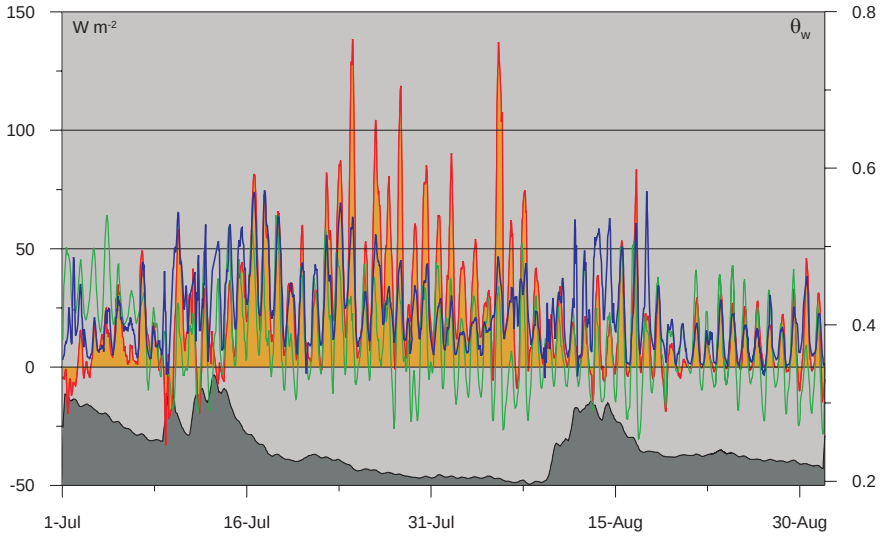

Fig. 3. Sensible (red), latent (blue) and ground heat fluxes (green) for the summer period from 1 July to 31 August 2008 (left axis). The soil water content θ_w measured with Time Domain Reflectometry at a depth of 0.1 m at the Bayelva climate station is shown below (right axis).

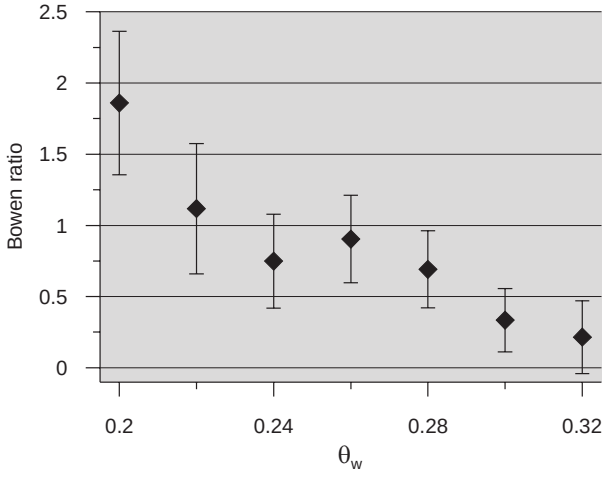

Fig. 4. Average daily Bowen ratio vs. volumetric soil water content θ_w in soil water content classes of widths of 0.02 for the summer period from 1 July to 31 August 2008 (see Fig. 3). The points are drawn at the center of each class, and the error bars represent the standard deviation of the Bowen ratio values within one class. Three days with negative average Q_h are discarded.

An energy balance closure term of 22 Wm^{-2} remains. This residual typically appears in energy budget studies (Foken, 2008a), possible reasons are discussed in Sect. 5.1.

4.2 Fall (1 September 2008–30 September 2008)

During fall, the net short-wave radiation strongly decreases due to the much lower solar angles, but a permanent snow cover has not yet formed and a sustained refreezing of the active layer has not started. September 2008 was characterized by a series of cyclones, which transported warm air masses from the south and led to strong precipitation. At Ny-Ålesund, 99 mm of precipitation were recorded, almost entirely as rain, which is more than twice of the usual September precipitation. The many rain events resulted in frequent data gaps and generally poor data quality regarding the eddy covariance measurements, but the general magnitude of the average fluxes should still be correctly reproduced.

The observed latent heat flux (Fig. 5, Table 2) corresponds to an evaporation of 9 mm during the fall period, so that the precipitation is not even roughly balanced by the evaporation. As a consequence, the water content of the soil is increased compared to the summer season, just before the soil starts to freeze. Most likely, this process still occurs, when the precipitation during September is not unusually high. Other than during summer, the sensible heat flux is on average negative, i.e. the advection of relatively warm air results in a warming of the surface. The average ground heat flux is still positive, corresponding to a transport of energy in the ground, which results in a further increase of the active layer depth.

In 2008, the perennial snow cover formed on 29 September, when the average incoming short-wave radiation at the Bayelva station had decreased to approx. $-12\,\mathrm{Wm}^{-2}$ (average data from 25 September to 5 October 2008).

4.3 Dark winter (1 October 2008–15 March 2009)

The short-wave radiation is essentially zero during this period (Fig. 6, Table 2), as it mostly falls within the polar night, which lasts from 25 October until 14 February at the

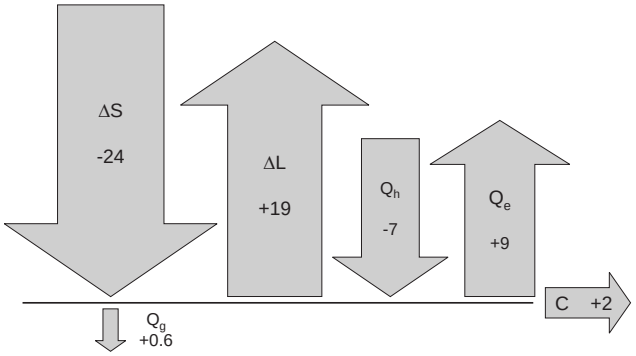

Fig. 5. Schematic diagram of the contributions of the surface energy budget for the fall period. Notation as in Fig. 2.

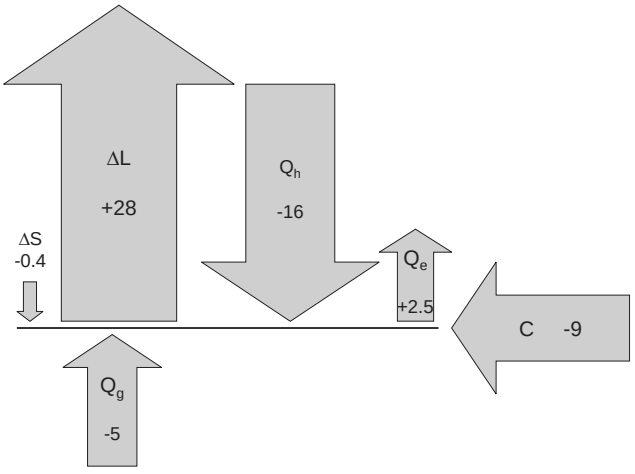

Fig. 6. Schematic diagram of the contributions of the surface energy budget for the dark winter period. Notation as in Fig. 2.

study site. The peak values of ΔS during midday at the very beginning and end of the dark winter period are around $-20\,\mathrm{Wm}^{-2}$. In the absence of short-wave radiation, the long-wave radiation becomes the main forcing of the system. Between October 2008 and March 2009, L_{in} ranges from $-140\,\mathrm{Wm}^{-2}$ to $-320\,\mathrm{Wm}^{-2}$, while L_{out} is between $190\,\mathrm{Wm}^{-2}$ and $320\,\mathrm{Wm}^{-2}$. For the entire period, the absolute value of L_{in} is found to be equal or smaller than L_{out}. With an average value of $28\,\mathrm{Wm}^{-2}$, the net long-wave radiation represents the dominant energy loss term during dark winter.

The net long-wave radiation is mainly compensated by a negative average sensible heat flux, corresponding to a warming of the surface and a cooling of the atmosphere. With an average of $-16\,\mathrm{Wm}^{-2}$, the sensible heat flux is a strong supply of energy to the snow surface. In addition, the snow heat flux compensates for about 20% of the energy loss by net long-wave radiation. The latent heat flux is found to be of minor importance in the overall surface energy budget during the dark winter period (Fig. 6, Table 2). A residual term of $-9\,\mathrm{Wm}^{-2}$ remains.

During the dark winter period, we estimate about 80 mm of rain, which fell to great parts during three rain-on-snow events in October 2008, January 2009 and February 2009. This corresponds to an average heat flux of $-1.8\,\mathrm{Wm}^{-2}$ (see Sect. 3.4) and is thus significant compared to the heat flux supplied by the refreezing active layer, which is about $-5\,\mathrm{Wm}^{-2}$ (bulk method for Q_g).

The incoming long-wave radiation is clearly the determining factor for the temperature of the snow surface and hence for the outgoing long-wave radiation (Fig. 7), but a significant influence of other factors, particularly of the wind speed, remains. At high wind speeds, atmospheric turbulence is mechanically induced. This facilitates the exchange of energy between the surface and the warmer atmosphere, so that the surface temperature is sustained at higher values (Fig. 7). The influence of the wind speed is clearly less pronounced for large values of L_{in} and high surface temperatures. A possible explanation is that the gradient between the air and the snow surface temperature is generally small in these cases, which prevents a strong exchange of energy independent of the formation of turbulence.

Throughout the entire dark winter period, strong sensible fluxes around $-30\,\mathrm{Wm}^{-2}$ to $-70\,\mathrm{Wm}^{-2}$ are associated with high wind speeds, which cause neutral or only weakly stable atmospheric stratifications, with a stability parameter $\xi = z/L$ close to zero. When wind speeds are low, a stable stratification and a strong near-surface temperature inversion can form, which significantly reduces the fluxes between surface and atmosphere. This is illustrated in Fig. 8, which shows surface temperature, wind speed, air temperature inversion between 9.3 m and 1.3 m height and the fluxes Q_h, Q_e and Q_g for a period with approximately constant L_{in} of around $-180\,\mathrm{Wm}^{-2}$. Initially, the wind speed is low and a stable atmospheric stratification or even an inversion layer close to the surface exists, which prevents a significant sensible heat flux. Thus, the surface temperature can not be sustained and starts to decrease to a minimum value of $-18\,^{\circ}\mathrm{C}$. This increases the temperature gradient across the snow pack and hence triggers a strong snow heat flux, which moderates the drop in surface temperature. Around 27 November, an increase in wind speed breaks up the stable stratification, and significant sensible heat fluxes of up to $-50\,\mathrm{Wm}^{-2}$ stabilize the surface temperature around $-15\,^{\circ}\mathrm{C}$. Decreasing wind speeds around 29 November again lead to a stable atmospheric stratification, with an associated drop in surface temperature to about $-23\,^{\circ}\mathrm{C}$.

Even during the polar night, considerable latent heat fluxes of up to $30\,\mathrm{Wm}^{-2}$ occur, mainly at high wind speeds and neutral atmospheric stratifications (see Fig. 8). These positive fluxes correspond to a cooling of the surface through sublimation of snow or, when present, evaporation of water. Particularly at stable stratifications, negative latent heat fluxes of up to $-5\,\mathrm{Wm}^{-2}$ are detected (Fig. 8). Hence, a limited

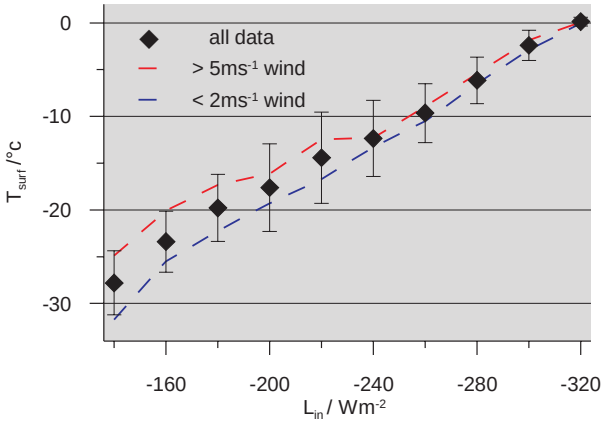

Fig. 7. Surface temperature T_{surf} vs. incoming long-wave radiation L_{in} during the dark winter period in classes of L_{in} of 20 Wm^{-2} width. The points are drawn at the center of each class, and the error bars represent the standard deviation of the surface temperature values within one class. The red and blue lines represent the average curves for situations with high and low wind speeds.

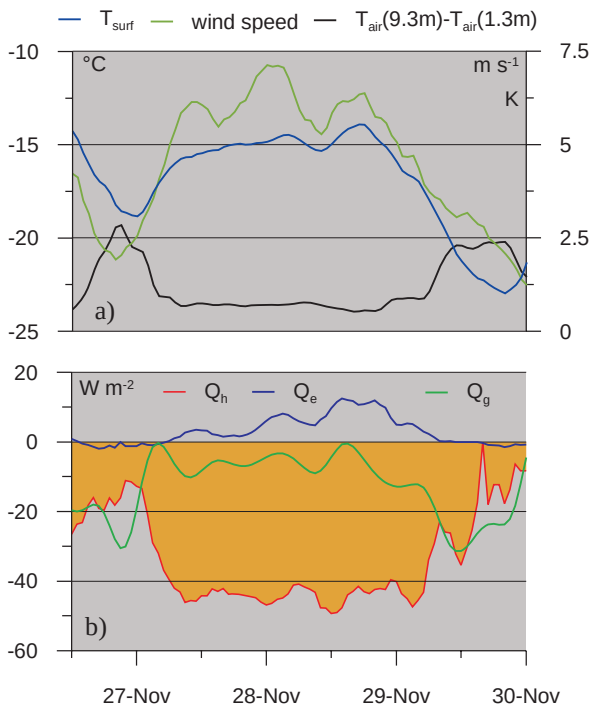

Fig. 8. (a) Surface temperature (left axis), wind speed (right axis), and temperature difference at the gradient tower (right axis) for a period in November 2008. The snow depth was 0.7 m at this time. **(b)** Sensible heat flux Q_h, latent heat flux Q_e and snow heat flux Q_g (conduction method) for the same period.

amount of condensation or resublimation occurs, but its contribution to the total energy budget is insignificant. The total net sublimation or evaporation during dark winter amounts to 30 kgm^{-2}, which corresponds to a snow column of almost 0.1 m at the recorded snow densities (see Sect. 3.4 and 3.5).

The snow heat flux is of great importance, particularly when a stable atmospheric stratification limits the sensible heat flux. Then, the snow heat flux becomes the dominant energy supply. The refreezing active layer provides a weak, but constant flux of energy, which is reflected in a negative average heat flux through the snow surface. Nevertheless, the storage effect of the snow and strong fluctuations of the surface temperature result in both positive and negative snow heat fluxes at the snow surface.

A strong stable atmospheric stratifications occurs frequently, but usually does not last longer than a few days. The stability parameter $\xi = z/L$ exceeds values of 0.5 in about 15% of the time, while values greater than 5 have only been recorded in about 1% of the time. During stable stratifications, the temperature inversion in the lowest 10 m of the atmosphere can be considerable, so that an average difference of +0.8 K could be calculated between the air temperatures at 10 m and 2 m height (Fig. 9). An even more pronounced temperature inversion is found between the surface temperature and the air temperature measured at different heights, i.e. T_{air}(2 m) and T_{air}(10 m), where temperature differences of more than 5 K are common (Fig. 9).

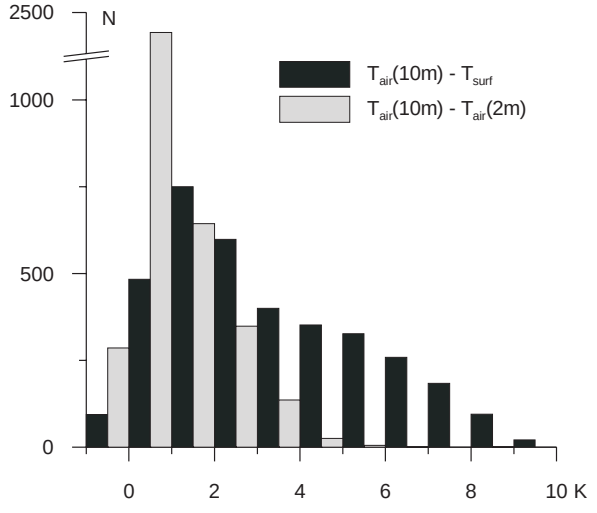

Fig. 9. Number of hourly values during the dark winter period N vs. temperature difference (in classes of 1 K) between air temperature at 10 m height and air temperature at 2 m height, and air temperature at 10 m height and surface temperature, respectively. Due to the snow accumulation, the heights decreased from 10 m to 8.8 m and 2.0 m to 0.8 m during the considered period.

4.4 Light winter (15 March 2008–15 April 2008)

The net short-wave radiation is rapidly increasing in light winter, although its role is still limited due to the high snow

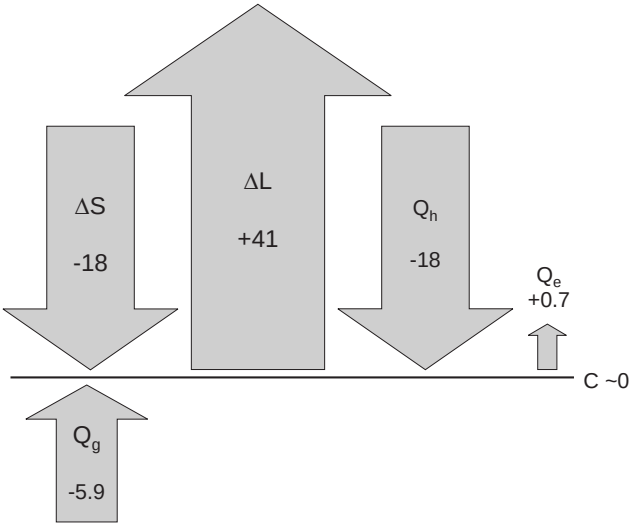

Fig. 10. Schematic diagram of the contributions of the surface energy budget for the light winter period. Notation as in Fig. 2.

albedo of about 0.8. Other than that, the surface energy budget very much resembles the dark winter period: the energy loss through the net long-wave radiation is compensated to equal parts by the sensible heat flux and the short-wave radiation (Fig. 10, Table 2). The snow heat flux still remains negative, corresponding to a further cooling of the underlying soil column. At the end of the light winter period, the lowest soil temperatures are reached, with about $-8\,^{\circ}\mathrm{C}$ at the soil surface and $-4\,^{\circ}\mathrm{C}$ at 1.5 m depth.

4.5 Pre-melt period (16 April 2008–31 May 2008)

From mid of April, the net short-wave radiation ΔS becomes the dominant energy supply, with an average of $-41\,\mathrm{Wm}^{-2}$ (Fig. 11, Table 2). The sensible heat flux provides an additional energy of $-8\,\mathrm{Wm}^{-2}$, while the net long-wave radiation ΔL is the main balancing factor, with an average of $33\,\mathrm{Wm}^{-2}$. The latent heat flux is positive, but remains insignificant with an average of $2.5\,\mathrm{Wm}^{-2}$. The snow and soil column start to gradually warm during the pre-melt period, which is reflected in a now positive average snow heat flux. A positive residual of around $10\,\mathrm{Wm}^{-2}$ remains, which largely builds up at the end of the pre-melt period. This indicates that melting of the snow already occurs, which is not accounted for in the surface energy budget during the pre-melt period. One snow melt event has indeed been observed on 30 May. Hereby, the temperature sensor at the snow-soil interface at P1 recorded a rapid temperature increase of 2 K within a few hours, which can only be explained by infiltrating melt water. In addition to this single strong melt event, it is possible that more snow melt occurs close to the surface without causing detectable melt water infiltration.

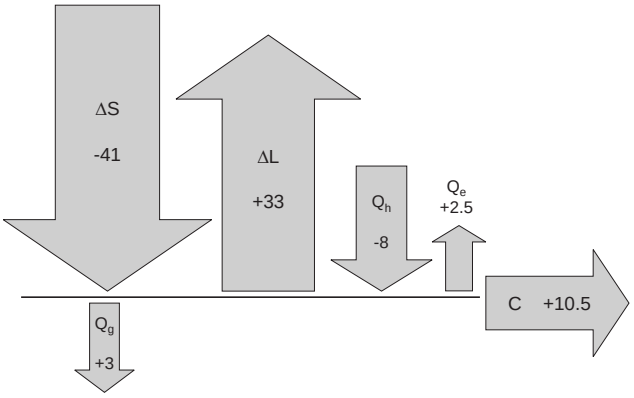

Fig. 11. Schematic diagram of the contributions of the surface energy budget for the pre-melt period. Notation as in Fig. 2.

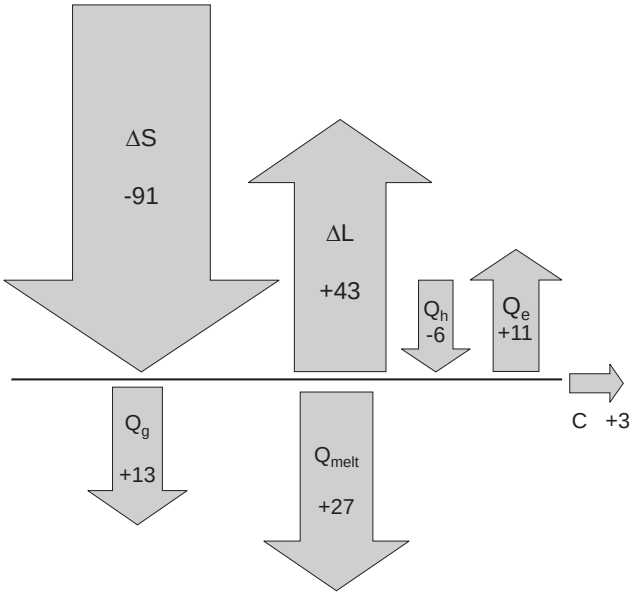

Fig. 12. Schematic diagram of the contributions of the surface energy budget for the snow melt period. Notation as in Fig. 2.

4.6 Snow melt (1 June 2008–30 June 2008)

The warming of the snow pack towards $0\,^{\circ}\mathrm{C}$ at the end of the pre-melt period is followed by the period of snow melt. Hereby, the energy consumed by the phase change of the melting snow appears as a dominant component in the energy budget (Fig. 12, Table 2). The average snow density before snow melt in 2008 was found to be $0.35\,\mathrm{gcm}^{-3}$, with an average snow depth of 0.6 m. Thus, the average latent heat stored in the snow pack amounts to $70\,\mathrm{MJm}^{-2}$, which yields an average energy consumption of $27\,\mathrm{Wm}^{-2}$ for the time between 1 June and 30 June, during which most of the snow melt occurred in 2008.

The net short-wave radiation ΔS increases considerably (Fig. 12, Table 2) despite of the still high albedo of the

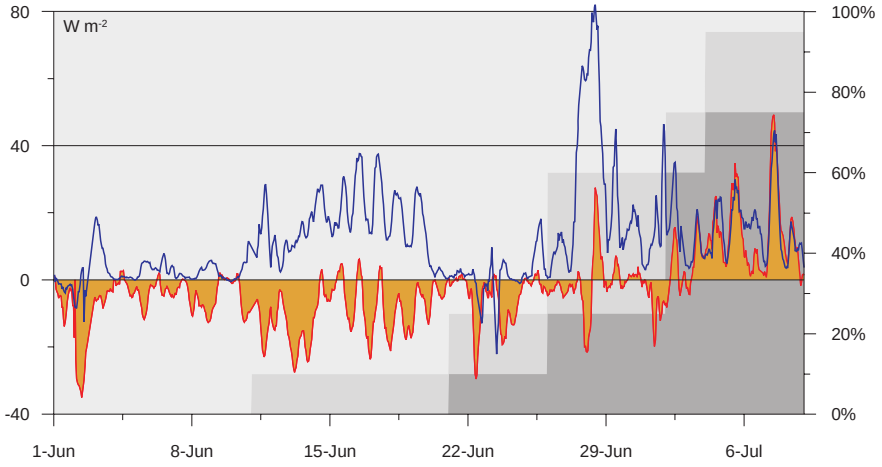

Fig. 13. Sensible (red) and latent heat flux (blue) for the snow melt and the beginning of the summer period (left axis). The light gray area represents the snow-covered and the dark gray area the snow-free fraction of the surface area around the eddy covariance system (right axis), which is taken to be approx. equal to the 90% source limit shown in Fig. 1c. The intermediate gray area indicates the uncertainty in area fraction between consecutive surveys.

snow. It is partly compensated by the net long-wave radiation ΔL, so that the average net radiation $\Delta S{+}\Delta L$ is around $-40\,\mathrm{Wm}^{-2}$. Until large snow-free patches appear, the air temperature is confined in a narrow range between $-1\,^{\circ}\mathrm{C}$ and $+5\,^{\circ}\mathrm{C}$ and the snow surface temperature remains close to $0\,^{\circ}\mathrm{C}$ due to the melt processes, so that the resulting temperature gradient is necessarily small. This yields weak sensible heat fluxes, with peak values around $-20\,\mathrm{Wm}^{-2}$ and an average of $-6\,\mathrm{Wm}^{-2}$. The positive latent heat flux, which causes a cooling of the surface, becomes more and more significant during the snow melt period, with an average of $11\,\mathrm{Wm}^{-2}$. Most likely, it is stimulated by the presence of water due to the melting snow.

During the snow melt period, the net radiation $\Delta S{+}\Delta L$ is a much stronger energy supply channel compared to the sensible heat flux (Fig. 12, Table 2). The snow melt can therefore be considered as almost entirely controlled by radiation, which confirms earlier studies during snow melt by Harding and Lloyd (1998) and Boike et al. (2003a) at the same location. Our study can also confirm the order of magnitude and sign of the fluxes of these previous studies.

During snow melt, infiltrating melt water and subsequent refreezing processes dominate the snow pack, which is more or less isothermal close to $0\,^{\circ}\mathrm{C}$. The underlying soil still shows colder temperatures, which results in a heat transport from the snow-soil interface into the soil. The energy consumed by this ground heat flux is provided by the cooling and refreezing of melt water at the snow-soil interface, but initially originates from the short-wave radiation. At $13\,\mathrm{Wm}^{-2}$ (estimated with the bulk method), this ground heat flux constitutes an important component of the surface energy budget. The large value can be explained by the fact that the temperatures in the upper soil column are within the freezing range of the soil (Roth and Boike, 2001), where a temperature change is associated with a change in latent heat content.

The sensible and latent heat fluxes during the snow melt period and the first eight days of the summer period, when snow patches were still present, are displayed in Fig. 13. As in winter, pronounced flux peaks such as the one around 15 June are associated with high wind speeds and neutral stratifications. Dewfall or white frost (negative latent heat flux), which has been found during snow melt in previous studies (Takeuchi et al., 1995; Boike et al., 2003b), occurs in few cases, but is insignificant as an energy source for snow melt. In 2008, the evolution of the snow-free areas around the eddy covariance system was monitored in intervals of two to ten days using aerial photography and systematic GPS-surveys. The results show that a patchwork of snow-covered and snow-free surfaces exists for several weeks due to the large spread in snow depth throughout the study area. Snow-free areas feature a completely different energy turnover compared to the snow patches. Accordingly, the sensible and latent heat fluxes must be seen as a mixture of both surface properties and their relevant percentages of the total footprint area. An example is the pronounced latent heat flux peak of about $80\,\mathrm{Wm}^{-2}$ on 28 June (Fig. 13), which is presumably triggered by a high percentage of wet snow-free patches with strong evaporation in the footprint at that time. Meanwhile, the sensible heat flux is still negative or only slightly positive with absolute values below $20\,\mathrm{Wm}^{-2}$, most likely because the remaining cold snow patches prevent a net exchange of sensible heat. The sensible heat flux keeps on alternating between negative and positive values for another couple of days, until it finally turns positive, after about three quarters of the area are free of snow (Fig. 13).

5 Discussion

5.1 Measurement errors and energy balance closure

For nearly all periods, a residual term of the surface energy budget remains, which is usually found in investigations of the surface energy budget (overview in Foken, 2008a). We can identify four levels of uncertainty in our study: a) measurement errors; b) uncertainties due to assumptions taken or parameters used; c) inconsistencies due to different measurement locations and/or footprint areas; d) systematic bias inherent in the measurement method.

a) For turbulent flux measurements with a similar eddy covariance system, Mauder et al. (2006) estimate relative uncertainties between 5 and 15% for data of the quality classes 1 to 6 (Foken and Wichura, 1996) which we use in our study. The BSRN radiation measurements have an accuracy of better than $10\,\mathrm{Wm}^{-2}$ (Ohmura et al., 1998). Unsupervised measurements under arctic conditions bear an additional potential for measurement errors due to e.g. snow-covered sensors or instrument malfunctions. The unmaintained radiation measurements are checked against the reference data set of the BSRN station, so that unreasonably large deviations are prevented. The soil temperature measurements from which the ground heat flux is inferred contain a few spikes and erroneous measurements, which are not considered in the evaluation. We conclude that random measurement errors and data gaps do not strongly influence the long-term averages presented in this study. Only in the fall period, data gaps of the turbulent fluxes occur frequently (see Sect. 4.2), so that a bias of the average fluxes is possible.

b) To evaluate the thermal conductivity, the soil and snow are idealized as a domain with constant thermal properties (in space and time) and purely conductive heat transfer is assumed (see Appendix A). In reality, the soil or snow properties can change, which is reflected in different values for the thermal diffusivity, if the fit is conducted for different periods (see Sect. 3.4). The range of obtained diffusivity values, in conjunction with the spread of soil or snow compositions determined in field measurements, is used to estimate the uncertainty of the thermal conductivity. Despite the resulting relative error of 25–30%, the absolute error of the ground or snow heat flux remains at least a factor of four smaller than the energy balance closure term due to the generally low magnitude of the fluxes. Another issue associated with the ground heat flux is the storage effect of the thin soil layer above the uppermost sensor, which is not accounted for in the calculation of Q_g. However, the day and night-time contributions of this effect cancel, so it is insignificant on the considered timescales.

c) Point measurements from different locations are considered as well as eddy covariance measurements, which integrate over an extended footprint area (Amiro, 1998; Schmid, 2002) with considerable small-scale heterogeneity of the surface cover (Fig. 1c). As the study focuses on average fluxes, only a sustained difference between the average flux of the eddy footprint area and the flux at the point measurement site is of importance. Firstly, this may be the case for the albedo, mainly for the snow melt, summer and fall period. From 40 point measurements (see Sect. 3.2), we estimate the spread in summer albedo throughout the study area and thus the albedo uncertainty to about 0.05. For the snow melt period, the albedo value is estimated from the BSRN station, where the albedo decreases from 0.8 to 0.5 during the course of the snow melt. An additional uncertainty arises, as a small fraction of snow-free surfaces with much lower albedo contributes to the eddy footprint area at the end of the snow melt period (Fig. 13), so that a maximum albedo uncertainty of 0.1 appears realistic during snow melt. The potential bias in net short-wave radiation may thus be as large as $8\,\mathrm{Wm}^{-2}$ for the summer and $25\,\mathrm{Wm}^{-2}$ for the snow melt period, while it is presumably negligible for the other periods

   In addition to albedo variations, the average surface temperature could vary due to differences in soil moisture and surface properties, which would affect both L_{out} and Q_g. A sustained difference of 1 K would lead to a bias of L_{out} on the order of $5\,\mathrm{Wm}^{-2}$, so the spatial variability of surface temperatures deserves attention in future studies (Langer et al., 2009). An uncertainty in the ground heat flux is not only induced by variations of the surface temperature, but also by spatial variations of the soil properties, which most likely occur throughout the study area. However, the good agreement between the fluxes inferred with different methods from the locations P1 and P3 during the summer period gives us confidence in the accuracy of Q_g, within the liberal error estimates of about 25–30% (see above).

d) A basal ice layer present in parts of the study area has not been included in the survey of snow water equivalent prior to snow melt (see Sect. 3.5). An average ice layer thickness of 5 cm corresponds to an additional flux of $5\,\mathrm{Wm}^{-2}$, so the true value of Q_{melt} during the snow melt period is most likely higher than $27\,\mathrm{Wm}^{-2}$ (Table 2). Furthermore, there may be a contribution of Q_{melt} in the pre-melt period (see Sect. 4.5).

   Large eddy or secondary circulation patterns, advection and free convection events (Lüers and Bareiss, 2009a) are known to lead to a systematic underestimation of the true sensible and latent heat fluxes with the eddy covariance method (Inagaki et al., 1996). Flux losses exceeding 25% have been estimated for both the sensible and latent heat flux (Foken, 2008a), which could explain a large part of

the closure term in our study. At least in the summer and dark winter period where the closure terms are largest (we do not consider the pre-melt period as the contribution of snow melt is unclear), the signs of the dominant turbulent flux terms and the closure term match, so that the energy balance could indeed be closed by increasing the magnitude of the turbulent fluxes (Foken, 2008a). The wider area around the study site is dominated by mountains, glaciers and the open water body of the Kongsfjorden, so large temperature contrasts and extremely inhomogeneous surface heating exist over distances of a few kilometres, which most likely create advective circulation patterns. We cannot provide an independent estimate of the magnitude of the flux bias caused by these features, which could only be examined by area-averaging flux measurements, e.g. using scintillometers (Meijninger et al., 2006), or Large Eddy Simulation (LES) studies of the entire boundary layer dynamics (Beare et al., 2006).

We conclude that the magnitude of the observed closure terms is still in range of the closure terms found in a number of carefully designed field experiments (overview in Foken, 2008a), despite the measurement uncertainties under arctic conditions. Therefore, it seems reasonable that the true magnitude and relative importance of the terms of the surface energy budget do not differ substantially from the results given in this study.

5.2 The annual energy budget

The presented data set allows an estimate for the annual net budget for each of the components of the energy budget (see Table 2). With an average value of $-35\,\mathrm{Wm}^{-2}$, the net short-wave radiation is the dominant source of energy. It is almost compensated by the net long-wave radiation, with an annual average of $32\,\mathrm{Wm}^{-2}$. The latent heat flux is usually positive, and the annual average of $6.8\,\mathrm{Wm}^{-2}$ is almost exclusively a result of strong fluxes during snow melt, summer and fall. The value corresponds to a water loss of approx. 85 mm, so that about 20% of the precipitation of the study period evaporates or sublimates. While insignificant for the overall energy budget, positive average latent heat fluxes are detected during the polar night, which was not found at similar latitudes on arctic sea ice by the SHEBA study (Persson et al., 2002). The average sensible heat flux is negative with a value of $-6.9\,\mathrm{Wm}^{-2}$, but shows a strong seasonal dependence. While the study site is actually a strong heat source for the atmosphere during the two months of summer ($Q_h = 22.5\,\mathrm{Wm}^{-2}$), it is a heat sink for the rest of the year, with an average of $Q_h = -13\,\mathrm{Wm}^{-2}$. During winter, the nearby ice-free sea is most likely an important heat source for the near-surface atmosphere, which might increase the air temperatures at the study site and thus fuel the relatively strong sensible heat transfer to the snow surface. The average ground heat flux is close to zero, as should be the case for equilibrium or near-equilibrium conditions of the permafrost. A strong warming of the permafrost at the study site has not occurred over the course of the considered year.

During winter, the system is entirely forced by long-wave radiation, while a strong short-wave forcing dominates the system during summer. The timing of the albedo change induced by the snow melt is a key point for the annual surface energy budget, since the snow at the study site usually disappears between end of May and beginning of July (Winther et al., 2002), when the incoming short-wave radiation reaches its annual maximum with daily averages of about $-200\,\mathrm{Wm}^{-2}$. In contrast, the timing of the albedo change due to the formation of the snow cover in fall is of little importance, as the daily average for incoming short-wave radiation is already low during September, when the permanent snow cover usually forms (Winther et al., 2002).

Given the present data set, an earlier termination of the snow melt, e.g. by end of May instead of end of June, would not only lead to an increase of the net short-wave radiation in the annual budget, but also to an enhanced flux of latent heat. In case of the sensible heat flux, the ratio between summer conditions with atmospheric warming and winter conditions with atmospheric cooling would be shifted, resulting in a smaller, but presumably still negative net sensible heat flux.

5.3 Implications for permafrost

At the study site, the seasonal thaw of the active layer after snow melt is driven by short-wave radiation. About 15% of the total net radiation during the summer season is consumed by the ground heat flux, which compares well to the value found by Harding and Lloyd (1998). However, a pronounced warming of the soil towards 0 °C already occurs during snow melt. This leads to a significant increase in unfrozen water and thus latent heat content according to the freezing characteristics of the soil. The overall magnitude of the occurring heat flux in the ground is in good agreement with the findings of Boike et al. (2003b). The energy is mainly supplied by short-wave radiation, but is mediated through conduction in the snow pack or percolating and refreezing melt water. The increase in latent heat content of the soil during snow melt facilitates a more rapid thawing of the ground, after the snow has melted.

In September, when the incoming short-wave radiation is much lower than in the summer season, a further increase in active layer depth has been recorded in 2008. Hereby, the additional energy input by the sensible heat flux due to the influx of warm air masses most likely plays a significant role.

During winter, the most important factor for the permafrost is the incoming long-wave radiation, as it determines the general magnitude of the surface temperature (Fig. 7), which in turn finally governs the energy loss of the ground. Since the incoming long-wave radiation is mainly determined by synoptical weather patterns and thus air mass distribution and cloud properties (Yamanouchi and Ørbaek,

1995), the permafrost is mainly susceptible to changes in these large-scale systems. For the on Svalbard anomalously warm winter of 2005/2006, which was characterized by a sustained influx of relatively warm air masses, Isaksen et al. (2007) detected a thermal response of the permafrost to depths of 15 m. The influx of warm southerly air masses can culminate in rain-on-snow events, which lead to a long-lasting warming of the snow pack and thus the near-surface permafrost. Putkonen and Roe (2003) showed, that few strong rain-on-snow events can confine the temperature at the bottom of the snow to around 0 °C for most of the winter.

During winter, the strong near-surface temperature inversion is a striking feature, which clearly limits the use of air temperatures as surrogate for the temperature of the snow surface (Lüers and Bareiss, 2009b). In the present study, the average temperature difference between the air temperature at 10 m height and the surface temperature was measured to be more than 3 K for the dark winter period. It should be carefully checked, whether this strong near-surface inversion is accounted for by models, which calculate the surface temperature based on a closed surface energy budget (e.g. Hinzman et al., 1995; Hoelzle et al., 2001).

6 Summary and outlook

In this study, we have documented the annual cycle of the surface energy budget at a high-arctic permafrost site for the example of the year 2008/2009:

1. During polar night conditions in winter, the long-wave radiation, the sensible heat flux and the heat input from the refreezing active layer have been identified as the main components of the surface energy budget. The incoming long-wave radiation is the determining factor for the surface temperature of the snow, but a significant influence particularly of the sensible heat flux remains.

2. During the snow-free period of the polar day season, the system is governed by the short-wave radiation, while turbulent fluxes and the long-wave radiation are the main balancing factors in the surface energy budget.

3. A more "winter-like" surface energy budget is found during the first half of the polar day season due to the the long-lasting snow cover with its high albedo, which effectively limits the role of the short-wave radiation. The albedo change induced by the snow melt is therefore of critical importance for the annual surface energy budget, as it marks the transition point between two fundamentally different regimes.

Due to its central role in the annual cycle, the correct representation of the snow melt must be considered crucial for both monitoring and modeling schemes in permafrost areas. During arctic winter and especially polar night conditions, the parameterization of the relevant processes of energy exchange between surface and atmosphere remains one of the major deficiencies in current models. A number of studies have suggested improved parameterizations for the sensible heat flux under stable conditions (e.g. Grachev et al., 2007), which have to be incorporated in existing process-based permafrost models, so that they can be successfully applied over a full seasonal cycle. Further studies will focus on the validation and improvement of such models by exploiting the hourly resolution of the current data set.

The study is performed at a site on Svalbard where a significant warming trend is expected in the near future, so it can be considered a baseline study to assess future shifts in the surface energy budget. It must be emphasized that an ongoing monitoring of radiation, land-atmosphere exchange processes and ground heat fluxes is indispensable to gain a better understanding of future changes and their impact on permafrost. This should include the winter season, where the most pronounced future warming is projected to occur (Førland and Hanssen-Bauer, 2003). Major improvements to the accuracy could be achieved by: 1) a detailed footprint analysis of the eddy covariance measurements in conjunction with spatially resolved measurements of the surface radiation and the ground heat flux; 2) area-averaging measurements of sensible and latent heat fluxes with large aperture and microwave scintillometers; and 3) the application of Large Eddy Simulations (LES) for a better understanding of the vertical structure of the arctic troposphere and the meso-scale large eddy or secondary circulation patterns in the wider Kongsfjorden area. Such studies may also allow to assess the impact of larger-scale factors, such as synoptic weather patterns, precipitation or sea ice conditions, on the surface energy budget of the study site.

In its exclusive use of measured rather than modeled values, the presented data set is unique for arctic land areas. Such comprehensive observations of soil, snow and atmospheric quantities, which could serve as a test data set to validate and support modeling efforts, are sparse for the Arctic. While Eugster et al. (2000) have compiled a data basis on the summer surface energy budget for a range of arctic tundra and boreal ecosystems, similar efforts covering the entire annual cycle have not yet been accomplished. Such a compilation would be of fundamental value in order to improve the understanding of physical processes involved in the surface energy budget and permafrost-snow-atmosphere interactions on arctic land areas.

Appendix A

Calculation of ground heat fluxes

To calculate the ground heat flux

$$j_z(z,t) = -K_h(z,t)\frac{\partial}{\partial z}T(z,t) \quad \text{(A1)}$$

from temperature profile measurements, the first step is to evaluate the thermal conductivity K_h of the soil or snow. For this purpose, we select three time series of temperature measurements in a profile, $T_{\mathrm{meas}}(z_1,t)$, $T_{\mathrm{meas}}(z_2,t)$ and $T_{\mathrm{meas}}(z_3, t)$ with $z_1<z_2<z_3$. We then assume a conductive 1-D-heat transport without phase change of water according to Fourier's law

$$\frac{\partial}{\partial t}(c_h(z,t)T(z,t)) + \frac{\partial}{\partial z} j_z(z,t) = 0 \quad \text{(A2)}$$

where c_h denotes the heat capacity of the soil or snow, respectively. If heat capacity c_h and thermal conductivity K_h are constant, Eq. (A2) simplifies to

$$\frac{\partial}{\partial t}T(z,t) - d_h \frac{\partial^2}{\partial z^2}T(z,t) = 0 \quad \text{(A3)}$$

where $d_h = K_h/c_h$ denotes the thermal diffusivity of the soil or snow. To solve Eq. (A3) numerically, we assume Dirichlet boundary conditions given by the time series $T_{\mathrm{meas}}(z_1,t)$ and $T_{\mathrm{meas}}(z_3, t)$ of two outer temperature sensors in the profile. The initial condition is chosen as a linear interpolation between the first two data points of the boundary conditions. In this case, the exact choice of the initial condition is not critical, since the solution converges to a value independent of the initial condition after few time steps. The numerical solution of Eq. (A3) is performed with the partial differential equation solver of MATLAB, yielding the modeled times series of temperatures for a given d_h, $T_{d_h}(z_2,t)$, for all values of z_2 with $z_1<z_2<z_3$.

With $T_{\mathrm{meas}}(z_2,t)$, we can perform a least-square fit for d_h by minimizing the RMS error between $T_{\mathrm{meas}}(z_2,t)$ and $T_{d_h}(z_2,t)$. Note that this method relies on rapid temperature changes which induce a time lag of the surface temperature signal in deeper soil layers characteristic for a certain d_h. In the summer period, when a strong diurnal temperature signal exists, the method generally works at the study site for depths of $z_1 \approx 0.01$ m, $z_2 \approx 0.15$ m and $z_3 \approx 0.30$ m below the surface.

The same procedure is used by Putkonen (1998), and the basic idea of obtaining soil properties from a time series of temperature measurements is extended by Nicolsky et al. (2007) and Nicolsky et al. (2009).

When the heat capacity c_h of the soil is estimated from soil samples, the thermal conductivity K_h can be evaluated. The heat flux $j_{z_1}(t)$ through the upper boundary can then be calculated using

$$j_{z_1} = -K(z_1,t)\frac{\partial}{\partial z}T(z,t)|_{z=z_1}. \quad \text{(A4)}$$

Note that the required derivative of the temperature can be easily evaluated since the numerical solution of Eq. (A3) delivers the full temperature field between z_1 and z_3.

Acknowledgements. We are grateful to M. Maturilli for providing us with the data of the BSRN station. We thank M. Schumacher, R. Vockenroth, E. Larmanou, M. Sieber and A. le Tressoler from the AWIPEV base in Ny-Ålesund for the ongoing support of our permafrost research, which contributed greatly to the success of this work. We are thankful to the Department of Micrometeorology of the University of Bayreuth headed by Foken for the advice and for the use of the eddy-covariance post-processing software. We thank two anonymous referees who gave valuable suggestions for improvement of the manuscript. We gratefully acknowledge financial support by the Helmholtz Association through a grant (VH-NG 203) awarded to Julia Boike.

Edited by: S. Gruber

References

Amiro, B.: Footprint climatologies for evapotranspiration in a boreal catchment, Agr. Forest Meteorol., 90, 195–201, 1998.

Beare, R., MacVean, M., Holtslag, A., Cuxart, J., Esau, I., Golaz, J., Jimenez, M., Khairoutdinov, M., Kosovic, B., Lewellen, D., et al.: An intercomparison of large-eddy simulations of the stable boundary layer, Bound.-Lay. Meteorol., 118, 247–272, 2006.

Beine, H., Argentini, S., Maurizi, A., Mastrantonio, G., and Viola, A.: The local wind field at Ny-Ålesund and the Zeppelin mountain at Svalbard, Meteorol. Atmos. Phys., 78, 107–113, 2001.

Boike, J., Hinzman, L., Overduin, P., Romanovsky, V., Ippisch, O., and Roth, K.: A comparison of snow melt at three circumpolar sites: Spitsbergen, Siberia, Alaska, in: Proceedings of the 8th International Conference on Permafrost, Zürich, Switzerland,21–25, 2003a.

Boike, J., Roth, K., and Ippisch, O.: Seasonal snow cover on frozen ground: Energy balance calculations of a permafrost site near Ny-Ålesund, Spitsbergen, J. Geophys. Res.-Atmos., 108, 8163–8173, 2003b.

Boike, J., Ippisch, O., Overduin, P., Hagedorn, B., and Roth, K.: Water, heat and solute dynamics of a mud boil, Spitsbergen, Geomorphology, 95, 61–73, 2008.

Bussières, N.: Thermal features of the Mackenzie Basin from NOAA AVHRR observations for summer 1994, Atmos.-Ocean, 40, 233–244, 2002.

Campbell, G., Jungbauer Jr, J., Bidlake, W., and Hungerford, R.: Predicting the effect of temperature on soil thermal conductivity, Soil Sci., 158, 307–313, 1994.

Chapin, F., Eugster, W., McFadden, J., Lynch, A., and Walker, D.: Summer differences among arctic ecosystems in regional climate forcing, J. Climate, 13, 2002–2010, 2000.

Chapin, F., Sturm, M., Serreze, M., McFadden, J., Key, J., Lloyd, A., McGuire, A., Rupp, T., Lynch, A., Schimel, J., et al.: Role of land-surface changes in Arctic summer warming, Science, 310, 657–660, 2005.

Comiso, J. and Parkinson, C.: Satellite-observed changes in the Arctic, Physics Today, 57, 38–44, 2004.

Comiso, J., Parkinson, C., Gersten, R., and Stock, L.: Accelerated decline in the Arctic sea ice cover, Geophys. Res. Lett., 35, L01703, doi:10.1029/2007GL031972, 2008.

Cottier, F., Nilsen, F., Inall, M., Gerland, S., Tverberg, V., and Svendsen, H.: Wintertime warming of an Arctic shelf in response

to large-scale atmospheric circulation, Geophys. Res. Lett., 34, L10607, doi:10.1029/2007GL029948, 2007.

De Vries, D.: The thermal conductivity of soil, Mededelingen van de Landbouwhogeschool te Wageningen, 52, 1–73, 1952.

Douville, H., Royer, J., and Mahfouf, J.: A new snow parameterization for the Meteo-France climate model, Clim. Dynam., 12, 21–35, 1995.

eklima: Free access to weather- and climate data from Norwegian Meteorological Institute from historical data to real time observations, online available at: http://www.eklima.no, 2009.

Eugster, W., Rouse, W., Pielke Sr, R., McFadden, J., Baldocchi, D., Kittel, T., Chapin, F., Liston, G., Vidale, P., Vaganov, E., and Chambers, S.: Land–atmosphere energy exchange in Arctic tundra and boreal forest: available data and feedbacks to climate, Glob. Change Biol., 6, 84–115, 2000.

Foken, T.: The energy balance closure problem – An overview, Ecol. Appl., 18, 1351–1367, 2008a.

Foken, T.: Micrometeorology, Springer, Berlin Heidelberg, Germany, 2008b.

Foken, T. and Wichura, B.: Tools for quality assessment of surface-based flux measurements, Agr. Forest Meteorol., 78, 83–105, 1996.

Foken, T., Göckede, M., Mauder, M., Mahrt, L., Amiro, B., and Munger, J.: Post-field data quality control, in: Handbook of Micrometeorology: A guide for surface flux measurement and analysis, Kluwer, 2004.

Førland, E. and Hanssen-Bauer, I.: Past and future climate variations in the Norwegian Arctic: overview and novel analyses, Polar Res., 22, 113–124, 2003.

Førland, E., Hanssen-Bauer, I., and Nordli, P.: Climate statistics and longterm series of temperatures and precipitation at Svalbard and Jan Mayen, Det Norske Meteorologiske Institutt Klima Report 21/97, 1997.

Georgiadis, T., Bonafè, U., Calzolari, F., Nardino, M., Orsini, A., Pirazzini, R., Ravegnani, F., Sozzi, R., Trivellone, G., Argentini, S., et al.: Study of the surface energy balance at Ny-Ålesund, Svalbard, in: Conference Proceedings-Italian Physical Society, vol. 69, pp. 163–174, Editrice Compositori; 1999, 2000.

Gerland, S. and Renner, A.: Sea-ice mass-balance monitoring in an Arctic fjord, Ann. Glaciol., 46, 435–442, 2007.

Grachev, A., Andreas, E., Fairall, C., Guest, P., and Persson, P.: SHEBA flux–profile relationships in the stable atmospheric boundary layer, Bound.-Lay. Meteorol., 124, 315–333, 2007.

Hansen, J., Ruedy, R., Sato, M., Imhoff, M., Lawrence, W., Easterling, D., Peterson, T., and Karl, T.: A closer look at United States and global surface temperature change, J. Geophys. Res.-Atmos., 106, 23947–23963, 2001.

Hanssen-Bauer, I. and Førland, E.: Long-term trends in precipitation and temperature in the Norwegian Arctic: can they be explained by changes in atmospheric circulation patterns?, Climate Res., 10, 143–153, 1998.

Harding, R. and Lloyd, C.: Fluxes of water and energy from three high latitude tundra sites in Svalbard, Nordic Hydrol., 29, 267–284, 1998.

Hinzman, L., Goering, D., and Kane, D.: A distributed thermal model for calculating soil temperature profiles and depth of thaw in permafrost regions, J. Geophys. Res.-Atmos., 103, 28975–28991, 1995.

Hoelzle, M., Mittaz, C., Etzelmueller, B., and Haeberli, W.: Surface energy fluxes and distribution models of permafrost in European mountain areas: an overview of current developments, Permafrost and Periglacial Processes, 12, 53–68, 2001.

Inagaki, A., Letzel, M., Raasch, S., and Kanda, M.: Impact of surface heterogeneity on energy balance: A study using LES, J. Meteorol. Soc. Jpn, 84, 187–198, 1996.

Isaksen, K., Holmlund, P., Sollid, J., and Harris, C.: Three deep alpine-permafrost boreholes in Svalbard and Scandinavia, Permafrost and Periglacial Processes, 12, 13–25, 2001.

Isaksen, K., Sollid, J., Holmlund, P., and Harris, C.: Recent warming of mountain permafrost in Svalbard and Scandinavia, J. Geophys. Rese.-Earth Surf., 112, F02S04, doi:10.1029/2006JF000522, 2007.

Langer, M., Westermann, S., and Boike, J.: Spatial and temporal variations of summer surface temperatures of wet polygonal tundra in Siberia - implications for MODIS LST based permafrost monitoring, Remote Sens. Environ., submitted, 2009.

Ling, F. and Zhang, T.: A numerical model for surface energy balance and thermal regime of the active layer and permafrost containing unfrozen water, Cold Reg. Sci. Technol., 38, 1–15, 2004.

Lloyd, C., Harding, R., Friborg, T., and Aurela, M.: Surface fluxes of heat and water vapour from sites in the European Arctic, Theor. Appl. Climatol., 70, 19–33, 2001.

Lüers, J. and Bareiss, J.: Direct near surface measurements of sensible heat fluxes in the arctic tundra applying eddy-covariance and laser scintillometry - The Arctic Turbulence Experiment 2006 on Svalbard (ARCTEX-2006), Theor. Appl. Climatol., submitted, 2009a.

Lüers, J. and Bareiss, J.: The effect of misleading surface temperature estimations on the sensible heat fluxes at a high Arctic site – the Arctic turbulence experiment 2006 on Svalbard (ARCTEX-2006), Atmos. Chem. Phys. Discuss., 9, 16913–16939, 2009b.

Lynch, A., Chapin, F., Hinzman, L., Wu, W., Lilly, E., Vourlitis, G., and Kim, E.: Surface energy balance on the arctic tundra: Measurements and models, J. Climate, 12, 2585–2606, 1999.

Mauder, M. and Foken, T.: Documentation and instruction manual of the eddy covariance software package TK2, Univ. of Bayreuth, Dept. of Mikrometeorology, 2004.

Mauder, M., Liebthal, C., Göckede, M., Leps, J., Beyrich, F., and Foken, T.: Processing and quality control of flux data during LITFASS-2003, Bound.-Lay. Meteorol., 123, 67–88, 2006.

Mauder, M., Foken, T., Clement, R., Elbers, J. A., Eugster, W., Grünwald, T., Heusinkveld, B., and Kolle, O.: Quality control of CarboEurope flux data – Part 2: Inter-comparison of eddy-covariance software, Biogeosciences, 5, 451–462, 2008, http://www.biogeosciences.net/5/451/2008/.

McFadden, J., Chapin, F., and Hollinger, D.: Subgrid-scale variability in the surface energy balance of arctic tundra, J. Geophys. Res.-Atmos., 103, 28947-28961, 1998.

McFadden, J., Eugster, W., and Chapin, F.: A regional study of the controls on water vapor and CO_2 exchange in arctic tundra, Ecology, 84, 2762–2776, 2003.

Meijninger, W. M. L., Lüdi, A., Beyrich, F., Kohsiek, W., and DeBruin, H. A. R.: Scintillometer-based turbulent surface fluxes of sensible and latent heat over a heterogeneous land surface: a contribution to LITFASS-2003, Bound.-Lay. Meteorol., 121, 89-110, 2006.

Moore, C.: Frequency response corrections for eddy correlation systems, Bound.-Lay. Meteorol., 37, 17–35, 1986.

Nakabayashi, H., Kodama, Y., Takeuchi, Y., Ozeki, T., and Ishikawa, N.: Characteristics of heat balance during the snowmelt season in Ny-Ålesund, Spitsbergen Island, Memoirs of National Institute of Polar Research, Special issue, 51, 255–266, 1996.

Nicolsky, D. J., Romanovsky, V. E., and Tipenko, G. S.: Using in-situ temperature measurements to estimate saturated soil thermal properties by solving a sequence of optimization problems, The Cryosphere, 1, 41–58, 2007, http://www.the-cryosphere-discuss.net/1/41/2007/.

Nicolsky, D., Romanovsky, V., and Panteleev, G.: Estimation of soil thermal properties using in-situ temperature measurements in the active layer and permafrost, Cold Reg. Sci. Technol., 55, 120–129, 2009.

Oechel, W., Vourlitis, G., Brooks, S., Crawford, T., and Dumas, E.: Intercomparison among chamber, tower, and aircraft net CO_2 and energy fluxes measured during the Arctic System Science Land-Atmosphere-Ice Interactions (ARCSS-LAII) Flux Study, J. Geophys. Res.-Atmos., 103, 28993-29003, 1998.

Ohmura, A., Gilgen, H., Hegner, H., Müller, G., Wild, M., Dutton, E., Forgan, B., Fröhlich, C., Philipona, R., Heimo, A., et al.: Baseline Surface Radiation Network (BSRN/WCRP): New precision radiometry for climate research, B. Am. Meteorol. Soc., 79, 2115–2136, 1998.

Overland, J., Wang, M., and Salo, S.: The recent Arctic warm period, Tellus A, 60, 589–597, 2008.

Persson, P., Fairall, C., Andreas, E., Guest, P., and Perovich, D.: Measurements near the Atmospheric Surface Flux Group tower at SHEBA: Near-surface conditions and surface energy budget, J. Geophys. Res.-Oceans, 107, 8045, doi:10.1029/2000JC000705, 2002.

Putkonen, J.: Soil thermal properties and heat transfer processes near Ny-Ålesund, northwestern Spitsbergen, Svalbard, Polar Res., 17, 165–179, 1998.

Putkonen, J. and Roe, G.: Rain-on-snow events impact soil temperatures and affect ungulate survival, Geophys. Res. Lett., 30, 1188, doi:10.1029/2002GL016326, 2003.

Rees, W.: Infrared emissivities of arctic land cover types, Int. J. Remote Sens., 14, 1013–1017, 1993.

Romanovsky, V. and Osterkamp, T.: Thawing of the active layer on the coastal plain of the Alaskan Arctic, Permafrost and Periglacial Processes, 8, 1–22, 1997.

Roth, K. and Boike, J.: Quantifying the thermal dynamics of a permafrost site near Ny-Ålesund, Svalbard, Water Resour. Res., 37, 2901–2914, 2001.

Schmid, H.: Source areas for scalars and scalar fluxes, Bound.-Lay. Meteorol., 67, 293–318, 1994.

Schmid, H.: Footprint modeling for vegetation atmosphere exchange studies: A review and perspective, Agr. Forest Meteorol., 113, 159–183, 2002.

Serreze, M., Walsh, J., Chapin, F., Osterkamp, T., Dyurgerov, M., Romanovsky, V., Oechel, W., Morison, J., Zhang, T., and Barry, R.: Observational evidence of recent change in the northern high-latitude environment, Climatic Change, 46, 159–207, 2000.

Slater, A., Pitman, A., and Desborough, C.: The validation of a snow parameterization designed for use in general circulation models, Int. J. Climatol., 18, 595–617, 1998.

Stöckli, R., Lawrence, D., Niu, G., Oleson, K., Thornton, P., Yang, Z., Bonan, G., Denning, A., and Running, S.: Use of FLUXNET in the Community Land Model development, J. Geophys. Res.-Biogeosciences, 113, G01025, doi:10.1029/2007JG000562, 2008.

Takeuchi, Y., Kodoma, Y., and Nakabayashi, H.: Characteristics of evaporation from snow and tundra surface in Spitsbergen in the snowmelt season 1993, in: Proceedings of the NIPR Symposium on Polar Meteorology and Glaciology, vol. 9, 54–65, 1995.

Uttal, T., Curry, J., Mcphee, M., Perovich, D., Moritz, R., Maslanik, J., Guest, P., Stern, H., Moore, J., Turenne, R., et al.: Surface heat budget of the Arctic Ocean, B. Am. Meteorol. Soc., 83, 255–275, 2002.

Viterbo, P. and Beljaars, A.: An improved land surface parameterization scheme in the ECMWF model and its validation, J. Climate, 8, 2716–2748, 1995.

Vourlitis, G. and Oechel, W.: Eddy covariance measurements of CO_2 and energy fluxes of an Alaskan tussock tundra ecosystem, Ecology, 80, 686–701, 1999.

Winther, J., Godtliebsen, F., Gerland, S., and Isachsen, P.: Surface albedo in Ny-Ålesund, Svalbard: variability and trends during 1981–1997, Global Planet. Change, 32, 127–139, 2002.

Yamanouchi, T. and Ørbaek, J.: Comparative study of the surface radiation budget at Ny-Ålesund, Svalbard and Syowa Station, Antarctica, 1987, in: Proceedings of the NIPR Symposium on Polar Meteorolgy and Glacialogy, National Institute of Polar Research, Japan, 118–132, 1995.

Zilitinkevich, S., Perov, V., and King, J.: Near-surface turbulent fluxes in stable stratification: Calculation techniques for use in general-circulation models, Q. J. Roy. Meteorol. Soc., 128, 1571–1587, 2002.

Chapter 2.3

Boike, J., Wille, C., and Abnizova, A. (2008): Climatology and summer energy and water balances of polygonal tundra in the Lena Delta, Siberia during wet and dry years. *Journal of Geophysical Research* 113, G03025, doi:10.1029/2007JG000540.

JOURNAL OF GEOPHYSICAL RESEARCH, VOL. 113, G03025, doi:10.1029/2007JG000540, 2008

Click Here for Full Article

Climatology and summer energy and water balance of polygonal tundra in the Lena River Delta, Siberia

Julia Boike,[1] Christian Wille,[1,3] and Anna Abnizova[2]

Received 30 June 2007; revised 6 February 2008; accepted 19 March 2008; published 21 August 2008.

[1] Meteorological and soil temperature and moisture data for the period 1998–2005 are presented from a long term monitoring station in the central Lena River Delta at 72°N, 126°E. The investigation site, Samoylov Island, is situated in the zone of continuous permafrost and is characterized by wet polygonal tundra. The summer energy and water balance of the tundra was analyzed for the dry year 1999 and the wet year 2003. The summer water balance of the tundra was found to be mainly controlled by precipitation. The partitioning of the available energy was controlled by precipitation via the soil moisture regime, and by the synoptic weather conditions via radiation and the advection of maritime cold or continental warm air masses. In 2003, regular high precipitation resulted in a constant recharge of polygonal ponds. Of the available energy, 61% were partitioned into latent heat flux and 17% into ground heat flux; hence, the tundra behaved like a typical wetland. In 1999, low precipitation resulted in a loss of polygonal pond waters and a drying of upper soil layers. This led to lower latent heat flux (31% of available energy), higher ground heat flux (29%), and a considerably higher soil thaw depth compared to 2003. Surface and subsurface water flow had a significant influence on the tundra water balance. In 2003, the formation of new surface flow channels through thermo-erosion was observed, which is expected to have a strong and lasting influence on the hydrologic system of the tundra.

Citation: Boike, J., C. Wille, and A. Abnizova (2008), Climatology and summer energy and water balance of polygonal tundra in the Lena River Delta, Siberia, *J. Geophys. Res.*, *113*, G03025, doi:10.1029/2007JG000540.

1. Introduction

[2] The prediction of the response of land surface water and energy fluxes to environmental change is a major challenge for experimentalists and climate modelers alike. Several studies documented potential changes in the Arctic hydrologic system. These include lake drainage through thawing permafrost [*Smith et al.*, 2005; *Yoshikawa and Hinzman*, 2003] and changes in Siberian river runoff [*Yang et al.*, 2002; *Berezovskaya et al.*, 2004, 2005]. Quantifying the coupled surface energy and water balance is a prerequisite to understand the causes of changes in these systems. Measurements of the fluxes between the terrestrial and atmospheric systems are difficult to obtain. *Eugster et al.* [2000] state that one of the most important uncertainties for assessment of susceptibility and vulnerability of the boreal and Arctic are the difficulties in measuring surface fluxes. Some of the experimental problems include the remoteness of Arctic sites and extreme weather conditions which can prohibit the use of precise flux measurements techniques such as the eddy covariance technique, and the great variety of measurement and analysis techniques used by different studies [e.g., *Eugster et al.*, 2000; *Lynch et al.*, 1999].

[3] According to *Vörösmarty et al.* [2001], the understanding of the seasonal and spatial variability of the pan Arctic water balance is one major open question. However, it is recognized that wet tundra environments represent a major contribution to land-atmosphere exchanges of water, energy, carbon and greenhouse gases [*Chapin et al.*, 2000]. The tundra environments are underlain by continuous permafrost which creates an impermeable layer and, together with low topographic gradients, results in numerous ponds and lakes (wetland). The drainage network is restricted downward by frozen ground, and evapotranspiration is a major mechanism of water loss. Several studies have been carried out recently to characterize the morphology and understand the developmental factors of small, patchy wetlands in the Canadian High Arctic [e.g., *Woo and Young*, 2003; *Young and Woo*, 2000]. The existence of wetlands requires a positive water balance associated with precipitation and evapotranspiration regimes and interactions between surface and groundwater flows [*Woo and Young*, 2006]. In the Alaskan Arctic close to Prudhoe Bay, evapotranspiration exceeds precipitation during the thaw period, leading to a general drying of the watershed [*Mendez et al.*, 1998]. In the study of extensive wetland in a low gradient Putuligayuk River watershed in northern Alaska, *Bowling et al.* [2003] identified meltwater as the primary source of the

[1]Periglacial Section, Alfred Wegener Institute for Polar and Marine Research, Potsdam, Germany.
[2]Department of Geography, York University, Toronto, Ontario, Canada.
[3]Now at Institute of Botany and Landscape Ecology, University of Greifswald, Greifswald, Germany.

Copyright 2008 by the American Geophysical Union.
0148-0227/08/2007JG000540$09.00

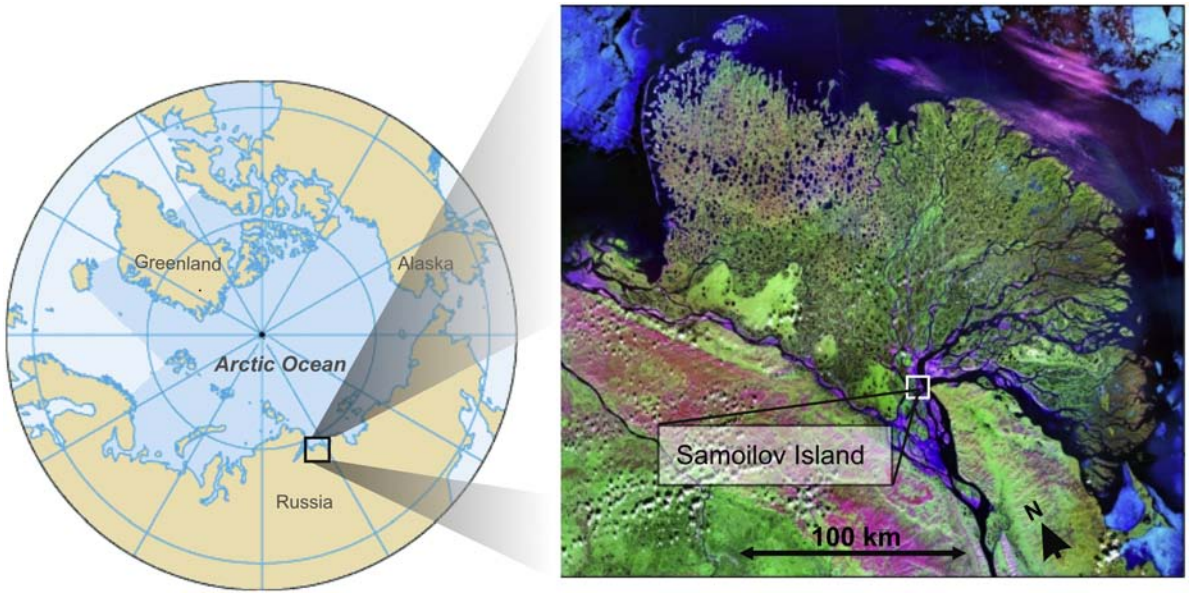

Figure 1. Circumpolar map showing the Lena River Delta in Siberia. The location of the investigation area within the delta is marked by a white square. The closest settlement is Tiksi, about 110 km southeast of the site. Satellite image provided by Statens Kartverk, UNEP/GRID-Arendal and Landsat, 2000.

wetland's water budget. In contrast to these well researched sites in the North American Arctic, there is a complete lack of long-term energy balance data from Siberia and a poor representation in the rest of the circumpolar boreal and Arctic zones [*Eugster et al.*, 2000].

[4] This paper's research site is located in the Lena River Delta, which is the largest river delta in northern Asia and one of the richest areas in the Arctic for both species diversity and breeding densities of migratory birds [*Gilg et al.*, 2000]. The delta channels one of the largest fluvial contributions of water to the Laptev Sea [*Yang et al.*, 2002; *Spielhagen et al.*, 2005]. The goals of this paper are to (1) characterize the site's climatology for the years 1998–2005, and (2) quantify and discuss the coupled energy and water balance for a dry (1999) and a wet summer (2003) at a polygonal tundra site. Thus the study aims to display differences and similarities in the response of the energy and water balance to climate variability.

2. Study Site

2.1. Geography

[5] The investigation site is located on Samoylov Island (72°22′N, 126°30′E, Figure 1), one of the 1500 islands within the Lena River Delta, in one of the main river channels approximately 120 km south of the Arctic Ocean. The Lena Delta is located in the zone of continuous permafrost with permafrost depths ranging from 500–600 m [*Zhang et al.*, 1999; *National Snow and Ice Data Center* (*NSIDC*), 2003]. The western part of the island (3.4 km^2) represents a modern floodplain with an elevation of 1 to 5 m a.s.l., which is flooded annually in spring. The eastern part of the island (4.1 km^2), where instruments were set up, is composed of sediments of the Late-Holocene river terrace [*Schwamborn et al.*, 2002] and is characterized by wet polygonal tundra. Its elevation ranges from 10 to 16 m a.s.l., and only small parts of it are flooded during the annual spring flood. The macrorelief of the eastern part of Samoylov Island is level with slope gradients <0.2%. The only abrupt changes in elevation, of up to 2.5 m, are associated with the shorelines of the larger lakes.

[6] The surface of the terrace is structured by a microrelief with elevation differences of up to 0.5 m over a few meters distance, which is caused by the genesis of low-centered ice wedge polygons (Figure 2). In the depressed polygon centers, drainage is strongly impeded due to the underlying permafrost, and water-saturated soils or small ponds occur. In contrast, the elevated polygon rims are characterized by a moderately moist water regime. The typical soil types are *Typic Historthels* in the polygon centers and *Glacic* or *Typic Aquiturbels* at the polygon rims, respectively [*United State Department of Agriculture* (*USDA*), 1998]. The polygon centers have a water level near the soil surface and a silty sand soil texture with anaerobic accumulation of organic matter. The soils of polygon rims are characterized by a silty and loamy sand texture with low organic matter content due to oxic conditions and low water levels [*Wagner et al.*, 2005]. Measured laboratory soil porosities range between 0.52 and 0.68 [*Kutzbach*, 2006]. The vegetation in the polygon centers and rims is composed of a moss and lichen strata of about 5 cm thickness and a vascular plants strata of 20–30 cm height [*Kutzbach et al.*, 2004]. The prevailing vascular plant is the hydrophilic sedge *Carex aquatilis*, which is generally dominant in the polygon centers (25%) and found to a lesser extent on polygon rims (8%). Apart from *C. aquatilis*, the vegetation of polygonal centers includes the mosses *Limprichtia revolvens* and *Meesia longeseta*. The polygon rims are dominated by mesophytic dwarf shrubs *Dryas octopetala* and the mosses *Hylocomnium splendens* and *Timmia austriaca* [*Kutzbach et al.*, 2004]. More detailed information on soil types and vegetation of the polygonal tundra

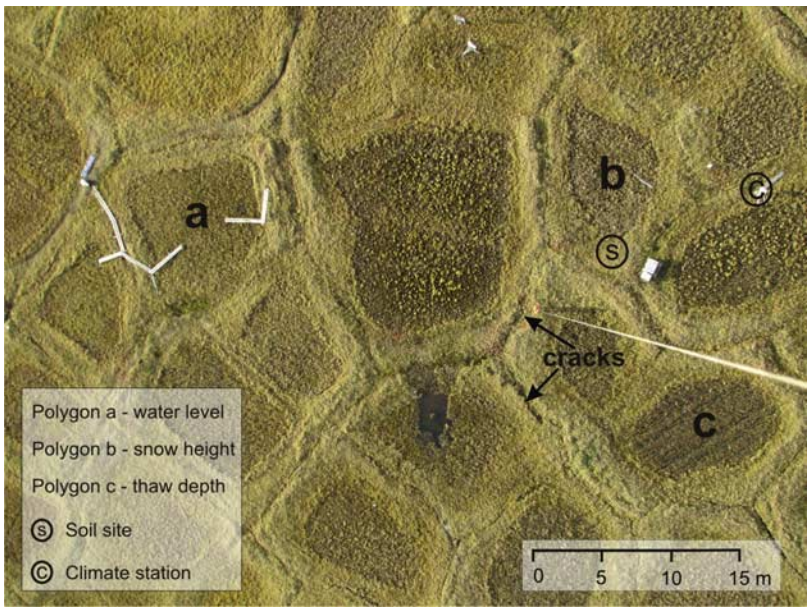

Figure 2. Aerial picture of experimental sites on the polygonal tundra on Samoylov, taken in August 2006. The ice wedge polygonal network is clearly visible. The low center polygons are usually water filled, while the surrounding elevated rims appear drier. Note that the rims above the ice wedges are divided by surficial cracks.

on Samoylov Island is given by *Pfeiffer et al.* [2002], *Fiedler et al.* [2004], and *Kutzbach et al.* [2004].

2.2. Climate Characteristics

[7] The Lena Delta region has a dry continental Arctic climate, characterized by very low temperatures and low precipitation. The mean annual air temperatures and total rainfall for the years 1961–1999 measured by the meteorological station Tiksi, 110 km south-east of Samoylov, are −13.6°C and 319 mm, respectively [*ROSHYDROMET*, 2006]. Polar day lasts from 7 May to 7 August and polar night from 15 November to 28 January. The snowmelt typically starts at around the beginning of June and the growing season lasts from the middle of June to the middle of September. About 45% of the precipitation falls as rain during the growing season. During spring, summer and autumn, the weather at Samoylov Island is characterized by the rapid change between the advection of arctic cold and moist air masses from the north and continental warm and dry air masses from the south. The mean annual temperature at the top of the permafrost is −10.1°C, which is extremely cold compared to other Arctic sites. Colder permafrost is only encountered on the Taymyr Peninsula to the North-West of the Lena River Delta and on the Canadian Arctic Archipelago [*Natural Resources Canada*, 1995; *Kotlyakov and Khromova*, 2002]. In comparison, the top of permafrost temperature on Svalbard is much higher, about −3°C [*Boike et al.*, 2003b].

3. Methods

3.1. Experimental Setup

[8] A soil profile located at a polygonal rim site was instrumented in August 1998 for the monitoring of soil temperature and soil water content. Soil temperatures were recorded using thermistors (107, Campbell Scientific Ltd., UK). The thermistors were calibrated at 0°C so that the absolute error was less than 0.02 K over the temperature range ±30°C. Liquid water content was calculated from time domain reflectometry measurements (Tektronix 1502, TDR100, CR10X, Campbell Scientific Ltd., UK) using the semiempirical mixing model of *Roth et al.* [1990]. The accuracy of the measurement of volumetric water content by TDR is estimated to be between 2 to 5% volumetric water content (VWC), while the precision is better than 0.5% VWC [*Boike and Roth*, 1997].

[9] A meteorological station was set up within 10 m of the instrumented soil site. The variables measured were air temperature and relative humidity at heights of 0.5 and 2.0 m above the ground (MP103A, Rotronic AG, Switzerland), wind speed and direction (05103, R.M. Young Company, USA), snow depth (SR50, Campbell Scientific Inc., USA), and rainfall (52203, R.M. Young Company, USA). Net radiation was measured initially using a Q7 net radiometer (REBS, USA), which was replaced by an NR-Lite net radiometer (Kipp & Zonen B.V., Netherlands) in August 2000. Both sensors were installed during the period August 2001 to August 2002 for comparison. A linear fit of net radiation readings showed that, compared to the NR-Lite sensor, the Q7 overestimated negative net radiation and underestimated positive net radiation by typically 7% and 8%, respectively. Hourly data collection of soil and climate data began in August 1998. Because of technical problems, several gaps in the data exist, most notably during May 2000 to March 2001, and January to July 2003. The soil instruments were replaced by new sensors during the summer of 2002. During this process, soil and climate stations were moved to a new neighboring site, approximately 30 m northeast from the first site (site s, Figure 2).

[10] Water level was measured in 5 wells reinforced by perforated PVC pipes which were located in a polygon near

the climate station (polygon a, Figure 2, *Wagner et al.* [2003]). The change of (surface and subsurface) water storage ΔS_{meas} was calculated as the relative change of water level in mm. The depth of the thawed active layer was determined from soil temperature profile measurements.

3.2. Energy Balance Calculation

[11] A simple volume energy balance of the seasonally thawing and freezing soil may be formulated as (adapted from *Boike et al.*, 2003a):

$$Q_n + Q_h + Q_e + Q_r = Q_g \quad (1)$$

where Q_n is the net radiation, Q_h and Q_e are turbulent fluxes of sensible and latent heat, Q_r is the heat flux supplied by rain, and Q_g is the ground heat flux. The atmospheric fluxes on the left side of the equation are defined as positive when they are directed toward the soil surface (energy gain). The net radiation Q_n is measured by a net radiometer, Q_r is calculated using rainfall rate and the difference between air and soil temperature at 6 cm depth, and Q_e, and Q_g are estimated as described below. The turbulent sensible heat flux Q_h is calculated as the remainder in the balance. Assuming an error of Q_g and Q_n of ±15%, the error of Q_e and Q_h by error propagation was estimated to be about ±21%.

[12] The latent heat flux Q_e was calculated using the model developed by *Priestley and Taylor* [1972], which has been successfully applied in various settings in the Arctic [*Mendez et al.*, 1998; *Rouse*, 1990; *Marsh et al.*, 1981; *Woo and Marsh*, 1990]:

$$Q_e = \frac{\alpha_{PT}\Delta VP(T)(Q_n - Q_g)}{\Delta VP(T) + \gamma} \quad (2)$$

[13] Here $\Delta VP(T)$ is the slope of the saturation vapor pressure-temperature curve, γ is psychrometric constant, and α_{PT} is a parameter expressing the ratio of actual to equilibrium evapotranspiration. The value of α_{PT} for our study site was derived empirically by application of the Bowen Ratio - energy balance method (BREB) to 1999 and 2003 data sets to approximate the ratio of actual to equilibrium evapotranspiration [*Eichinger et al.*, 1996]. To estimate the relative humidity at the soil surface the relation between water potential and relative humidity was used [*Campbell*, 1985; *Stewart and Broadbridge*, 1999]. Estimation of water potential using volumetric soil moisture relationship was performed following *Hinzman et al.* [1998]. The average estimated value of α_{PT} in 2003 was 1.26, which is a value generally accepted for saturated surfaces [e.g., *Rouse et al.*, 1977; *Stewart and Rouse*, 1977; *Bello and Smith*, 1990]. A lower mean α_{PT} value of 0.8 was derived for the period with available soil moisture in 1999. The same value of the α_{PT} was found by *Friedrich* [2001] at this location in an energy and water balance study in 1999. Similar values for α_{PT} were estimated for a well-drained upland lichen-heath tundra near Churchill, Manitoba (*Eaton et al.* [2001]: $\alpha_{PT} = 0.81$), and for dry upland regions characterized by sedge tussocks, mosses, and lichens (*Rouse and Stewart* [1972]: $\alpha_{PT} = 0.95$; *Stewart and Rouse*, [1976]: $\alpha_{PT} = 1.0$).

[14] The ground heat flux Q_g was calculated as change of soil sensible energy H_{gs} and soil latent energy H_{gl} per unit time using hourly time steps, $Q_g = \Delta(H_{gs} + H_{gl})$. The thermal energy stored as sensible heat at time t in the soil to a depth of 0.7 m (late summer season thaw depth and also maximum depth of TDR measurements) was estimated by summing the thermal energy of the soil components ice, *i,* liquid water, *w,* and soil matrix, *sm,* in the soil profile [*Boike et al.*, 1998]:

$$H_{gs} = \sum_{\alpha \in i,w,sm} c_\alpha \rho_\alpha \int \theta_\alpha(z,t) T(z,t) dz \quad (3)$$

where c_α, is the specific heat capacity, ρ_α is the mass density, and θ_α, is the volumetric content of phase α, and T is the temperature. The latent heat energy of the soil was calculated as:

$$H_{gl} = -L_f \rho_i \int \theta_i(z,t)\, dz \quad (4)$$

where $L_f = 0.333 * 10^6$ J kg^{-1} is the latent heat of fusion, ρ_i is the ice mass density, and θ_i is the volumetric ice content, which is estimated from TDR measurements of soil water content directly before the freeze-back of soils [*Boike et al.*, 1998]. This implicitly assumes that no significant lateral moisture redistribution takes place during winter. The reference state for the energy storage calculations is liquid water at 0°C.

[15] Due to technical problems in 1999, the soil volumetric water content necessary for calculation of H_{gl} is not available for the whole summer. Therefore the ground heat flux was calculated from temperature difference at depths *z,* using the thermal conduction equation [*Incropera and Dewitt*, 1996]:

$$Q_g = -\lambda \frac{\Delta T}{\Delta z}. \quad (5)$$

[16] A constant soil thermal conductivity of $\lambda = 0.4$ W m^{-1} K^{-1} was applied. This value was obtained by linear best fit ($R^2 = 0.95$) of Q_g data from heat flux plate measurements and the thermal gradient calculated from temperature sensors located at 6 and 9 cm depth in 1998 [*Friedrich*, 2001]. The same value of λ was found using the thermal gradient and modeled $\Delta(H_{gs} + H_{gl})$ data when soil water content measurements were available in 1999. A comparable value for the effective thermal conductivity of surface organic soils of 0.3 W m^{-1} K^{-1} was found by *Hinzman et al.* [1991] in the study of hydrologic and thermal properties of soil in the Alaskan Arctic. A comparison of hourly estimates of heat fluxes using equations (3) and (4) and equation (5) for the period with available soil water content data in 1999 showed a good agreement between the two methods when the empirically derived

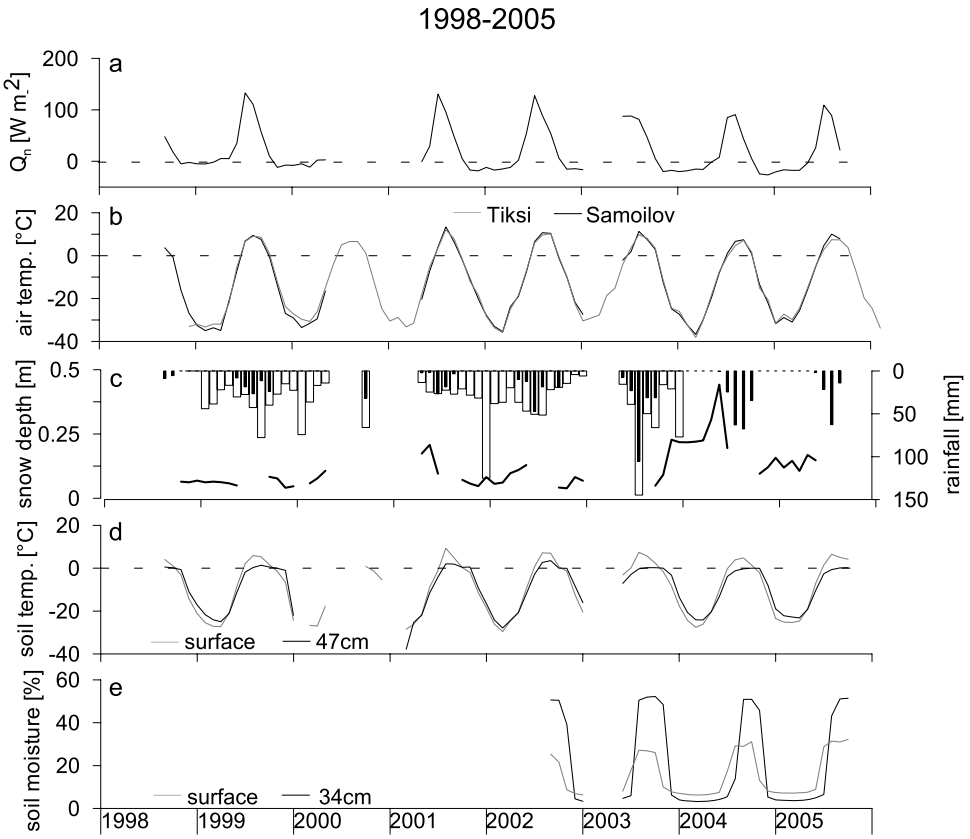

Figure 3. Monthly average meteorological and soil data from the monitoring station on Samoylov Island. (a) Net radiation; (b) air temperature for Samoylov (black) and Tiksi (grey); (c) snow depth and daily totals of rainfall for Samoylov (black filled bars) and Tiksi (non filled bars); (d) soil temperature at 47 cm depth and close to the surface (9 cm depth until July 2002, 6 cm depth thereafter); and (e) soil volumetric water content at 34 cm depth and surface.

value of λ was applied (R^2 = 0.85 for 14–17 May; R^2 = 0.79 for 14–15 August).

3.3. Water Balance Calculation

[17] The change of (surface and subsurface) water storage ΔS can be expressed as

$$P - ET - R = \Delta S \tag{6}$$

where P is precipitation, ET is evapotranspiration when water is lost to the atmosphere (negative ET) or condensation when water is gained from the atmosphere (positive ET), and R is lateral surface and subsurface water flow. If lateral water flow R is neglected, the water storage can be estimated as:

$$P - ET = \Delta S_{est}. \tag{7}$$

No snowfall occurred during the summer periods of 1999 and 2003, thus accumulation or melt of snow is not included in the water balance.

4. Results

4.1. Climatology 1998–2005

[18] Monthly average air temperatures during summer showed large variation between the years 1998–2005 (Figure 3b). July and August were the warmest months; but the monthly average varied between 6.6°C (July 2004) and 13.4°C (July 2001). The coldest period was typically January–February with monthly averages of about −35°C. The monthly average net radiation was typically highest during June, decreased strongly during July–September, and was negative from October (Figure 3a). It was continuously negative for 5 months during the winters 1998–1999 and 1999–2000, for 6 months during the winter of 2001–2002, and for 7 months during the winters 2003–2004 and 2004–2005. During the summers of 2003 and 2004, the net radiation was considerably lower (~20%) than during the years 1999–2002, which was caused by a prevalence of cloudy weather conditions in 2003, and a late snowmelt in 2004.

[19] Snow started to accumulate in September in most years (Figure 3c). The pattern of snow accumulation was very variable, as was the depth of the snow cover. During the winter 1998–1999, the maximum monthly average snow depth was recorded in December (7 cm), during the winter 2003–2004 it was recorded in May (44 cm). The snow usually melted within 7–10 d; in years with thin snow cover the snow was gone by the end of May or first days of June (1999, 2002, 2003), otherwise at about the middle of June (2001, 2004, 2005). Redistribution of snow by wind and the polygonal microtopography resulted in a spatially highly variable depth of the snow cover. For instance in the

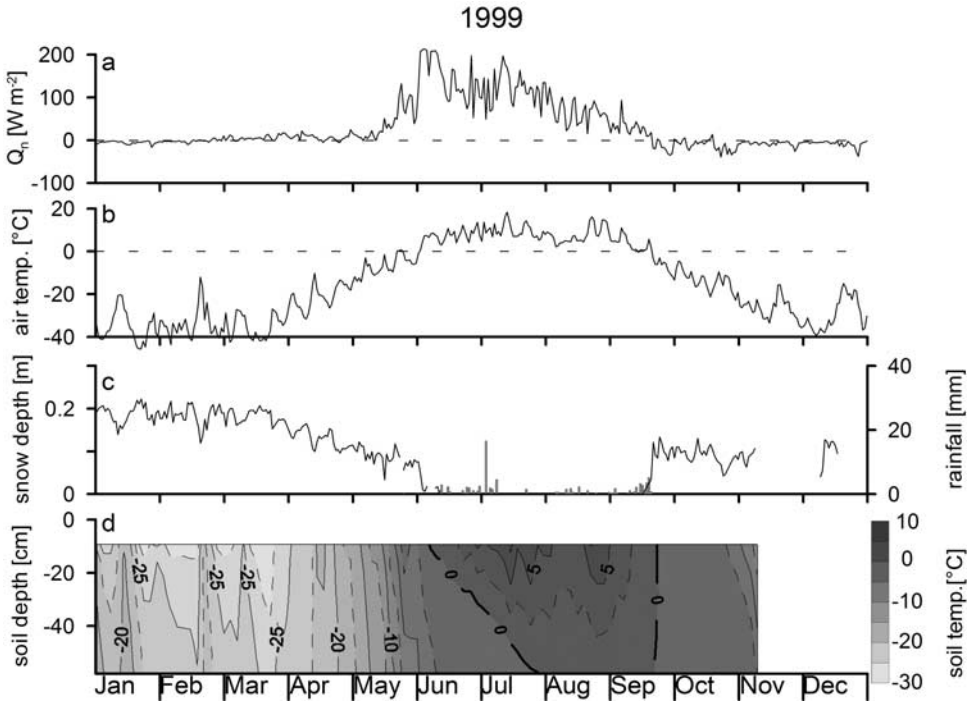

Figure 4. Daily average meteorological and soil data for 1999. (a) Net radiation, (b) air temperature at 2 m height, (c) snow depth and daily sums of rainfall (bar graph), and (d) soil temperature.

spring of 2004, snow depth varied between 40–50 cm in the polygon centers and 0–10 cm on the rims.

[20] Rainfall usually occurred between the middle of May and the middle of September, depending on the length of the frost period and the synoptic weather situation (Figure 3c). The total amount of rainfall measured varied between 72 and 88 mm in 2001 and 1999, and 193 and 208 mm in 2004 and 2003, respectively (mean 137 mm).

[21] Average monthly soil temperatures were generally low (Figure 3d). The maximum monthly temperature of the uppermost soil layer did not exceed 10°C; the maximum of 9.4°C was recorded in July 2001. The amplitude of seasonal surface temperature variations was 40 K (+10 to −30°C). Soil moisture in the thawed active layer for the years 2002–2005 showed only small differences between years (Figure 3e). In the organic surface layer, the average monthly water content reached about 20–30%, indicating that it was not saturated. This is expected since the elevated rim permits micro topographically controlled drainage of water. At a depth of 34 cm, the water content stayed close to 50% after thawing, which means that the sandy silt soil was always saturated. During winter, the liquid water content of the frozen soils was below 8%.

4.2. Meteorological and Soil Conditions 1999

[22] In the spring of 1999, the snow cover was thin with a depth of 20 cm in the polygon centers. The snow water equivalent before melt was about 40 mm. Snow thaw started around 25 May and lasted for about 10 d (Figure 4c). Before snowmelt, the snow exclusively sublimated, consuming about 50% of the available energy, and exposing the polygonal ridges [*Boike et al.*, 2003b]. Consequently, the net radiation reached large positive values already during snowmelt; it was on average 63 W m^{-2} during the second half of May (Figure 4a). After snowmelt, net radiation increased strongly; it averaged to 145, 121, and 67 W m^{-2} in June, July, and August, respectively. The monthly average air temperature was 6.7, 9.7, and 7.8°C during June, July, and August, respectively (Figure 4b). There were only short warm periods which were associated with the advection of warm air from the south (14, 23 July, 23, 29 August); however, the first half of August was characterized by a pronounced cold period. The total rainfall for 1999 was 88 mm; for the period June–August it was 56 mm with highest intensity of about 3 mm h^{-1} on 4 July (Figure 4c).

[23] The soil thaw started at the beginning of June and progressed rapidly; the upper 9 cm of the soil profile were thawed by 10 June, the layer at 15 cm depth was thawed on 16 June (Figure 4d). On 24 July, the thaw front passed the lowest temperature sensor at 58 cm depth. From the increase of thaw depth during June and July, and the typical length of the soil thaw period (until early September), the maximum thaw depth was estimated to be at least 70 cm. The soil water content at 9 cm depth was 25% directly after thaw on 10 June, and 26% on 22 August. The water content at and below 15 cm depth (down to 0.47 cm) ranged from 42 to 49%, which indicates that the soil layers were close to saturation (data not shown). The freezing of the soil started during the second half of September and the ground remained isothermal (zero curtain) until mid October. The freezing front moved from the ground surface to the bottom of the active layer, and by 4 November the active layer was completely frozen.

4.3. Summer Energy and Water Balance 1999

[24] During June and July, the energy input of Q_n was 17–18 MJ m^{-2} d^{-1} on clear days and about 4 MJ m^{-2} d^{-1} on cloudy and rainy days such as 28 June and 4 July

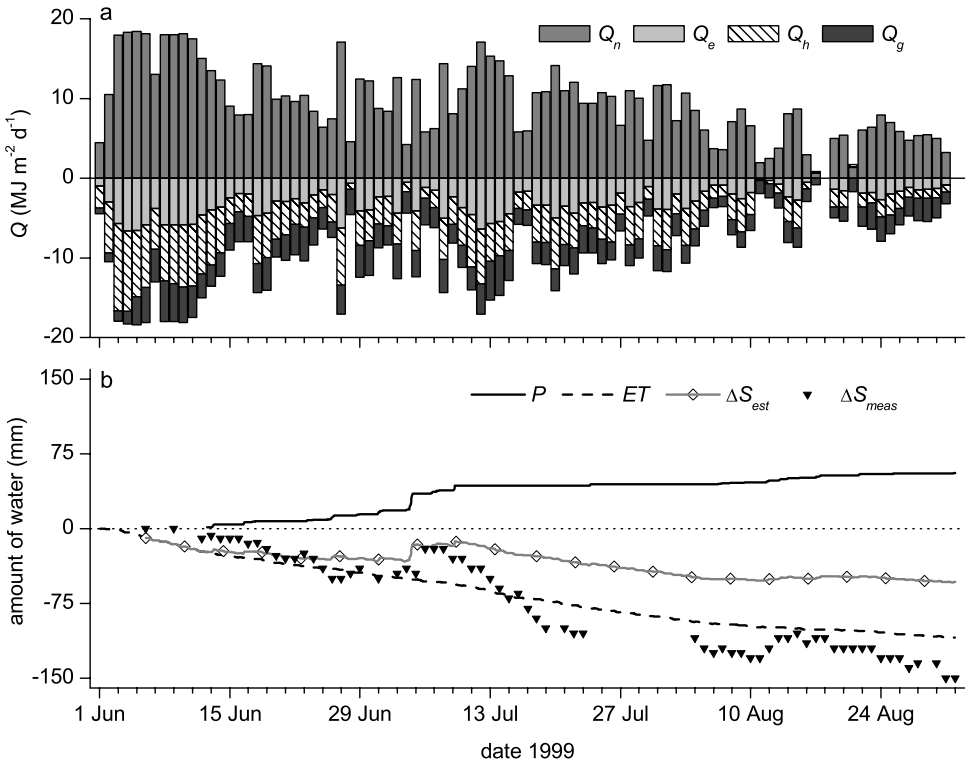

Figure 5. Energy and water balance components during the period 1 June to 31 August 1999. (a) Daily sums of energy balance components Q_n, Q_e, Q_h, and Q_g; (b) cumulative water balance components ΔS_{est} (equation (7)), and ΔS_{meas}.

(Figure 5a). The average energy input through Q_n was 12.5 MJ m^{-2} d^{-1} during June (1–13 June: 15.5 MJ m^{-2} d^{-1}), 10.3 MJ m^{-2} d^{-1} during July (14–31 July: 10.1 MJ m^{-2} d^{-1}), and 5.7 MJ m^{-2} d^{-1} during August. The energy input through rain Q_r was negligible on most days, the maximum value of 0.17 MJ m^{-2} d^{-1} was observed on 4 July (4% of Q_n). Q_h was the largest energy sink during June and July, consuming 43% (1–13 June: 48%) and 39% (14–31 July: 39%) of Q_n, respectively, and the second largest sink during August (35% of Q_n). Q_g was the smallest energy sink in June and July, consuming 26% (1–13 June: 20%) and 29% (14–31 July: 28%) of Q_n, respectively. However, during August, Q_g consumed 37% of Q_n and was the largest energy sink. Between 28 and 33% of Q_n went into Q_e, thus making it the second largest energy sink during June and July, and the smallest energy sink in August. Cumulative sums of all energy balance components over the complete summer period are given in Table 1.

[25] Over the course of the period June–August, the measured water storage ΔS_{meas} showed a generally decreasing trend; it was only markedly interrupted by the precipitation events on 4 July and 11–15 August (Figure 5b). Changes of ΔS_{est} and ΔS_{meas} were comparable until 8 July; afterward ΔS_{meas} decreased much faster than ΔS_{est}. Until 20 July, a difference of +70 mm built up between ΔS_{est} and ΔS_{meas}. After 20 July, the changes of ΔS_{meas} and ΔS_{est} were again similar; the difference between the two increased only slowly to +97 mm until 31 August (Table 2).

4.4. Meteorological and Soil Conditions 2003

[26] In 2003, due to technical problems there exist no data before 10 May and during the period 15 June to 12 July. The snow thaw started before 10 May and the snow was largely gone by 15 May (Figure 6c). However, due to cloudy weather conditions, the daily average net radiation seldom reached values >100 W m^{-2} until the middle of June; the average during the first half of June was 84 W m^{-2} (Figure 6a). Net radiation was also frequently low during July and August; the average values were 79 and 49 W m^{-2} for the period 14–31 July and during August, respectively. The average air temperature was 1.7, 11.2,

Table 1. Cumulative Energy Budget Components in 1999 and 2003[a]

	Q_n, MJ m^{-2}	Q_e, MJ m^{-2} (%)	Q_h, MJ m^{-2} (%)	Q_g, MJ m^{-2} (%)	Q_r, MJ m^{-2} (%)
1999	+866	−268	−345	−254	+0.58
1 Jun to 31 Aug		31	40	29	<0.1
1999	+353	−108	−131	−114	+0.05
14 Jul to 31 Aug		31	37	32	0.0
2003	+257	−158	−57	−52/+9	+0.36
14 Jul to 31 Aug		61	22	20/3	0.1

[a]Values are given as totals and in percent of Q_n.

Table 2. Water Balance Components for 1999 and 2003

	P, mm	ET, mm	ΔS_{est}, mm	ΔS_{meas}, mm
1999				
1 Jun to 31 Aug	+56	−109	−53	−150
1999				
14 Jul to 31 Aug	+13	−44	−31	−90
2003				
14 Jul to 31 Aug	+135	−63	+72	−10

and 7.7 C during 1–13 June, 14–31 July, and August, respectively (Figure 6b). Daily average air temperatures in the middle of July and at the beginning of August were frequently greater than 15°C (Figure 6b). These pronounced warm periods were separated by a cold period at the end of July which was accompanied by heavy rainfall (94 mm). During this event, large rainfall intensities between 6 and 7.7 mm h^{-1} were observed on 22 and 24 July. The total amount of rainfall during the period 14 July to 22 October was 168 mm (Figure 6c). The soil thaw started at the beginning of June, and the surface at 5 cm depth thawed between 7 and 12 June (Figure 6e). The progression of the thaw front was slower compared to 1999; on 24 July 2003 the thaw depth was between 37 and 47 cm (1999: 58 cm). Thus the thaw depth was at least 10 cm smaller in 2003 compared to 1999. Soil freeze back (zero curtain effect) started from the top of the profile on 30 September. The late freeze back is due to advection of warm continental air from the south that led to unusually warm air temperatures at the beginning and during the second half of September. Freeze back was completed by 11 November, when the layer at 50 cm depth froze. At the beginning of July, the soil was water-saturated only below a depth of 12 cm (Figure 6d). During the large rainfall at the end of July, also the surface layer became saturated. However, after a few days the water content decreased and then remained about 20% below saturation until the freeze back of soils. The profile below this layer was saturated throughout the summer. The differences in soil moisture below 20 cm depth indicate soil texture differences. Of note is the steep step increase in soil moisture in thawed and frozen soil in July and August during and after the two rainfall events indicating the infiltration of water into frozen soil.

4.5. Summer Energy and Water Balance 2003

[27] The daily energy input through Q_n was on average 7.2, 7.0, and 4.3 MJ m^{-2} d^{-1} during 1–13 June, 14–31 July, and August, respectively. On the cloudy and rainy days 24 and 27 July, total Q_n was less than 0.5 MJ m^{-2} d^{-1} (Figure 7a). During these days, Q_r was significant; it was an energy source of 10% of Q_n on the relatively warm 24 July (mean air temperature +7.9°C), whereas it was an energy sink of 19% of Q_n on the relatively cold 27 July (+3.3°C). Q_e was the largest energy sink on most days. The percentage of Q_n

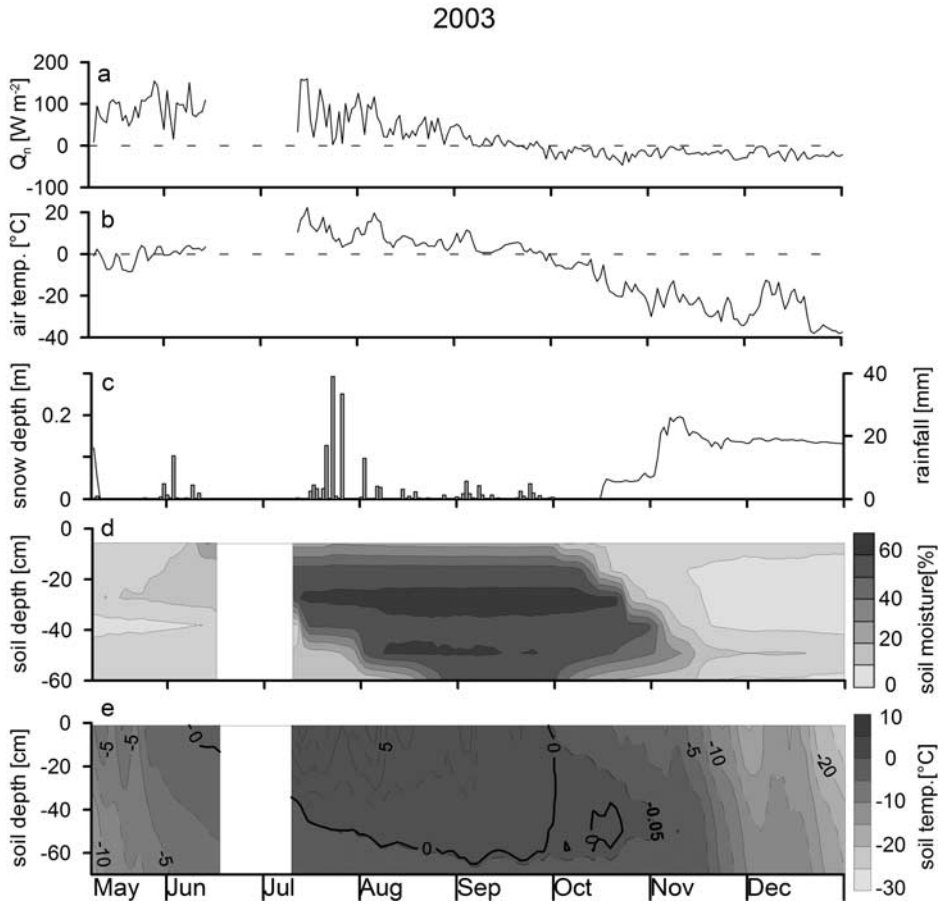

Figure 6. Daily average meteorological and soil data for 2003. (a) Net radiation, (b) air temperature at 2 m height, (c) snow depth and daily sums of rainfall (bar graph), (d) soil temperature, and (e) soil moisture. Because of technical problems there are no data before 10 May and during the period 15 June to 12 July.

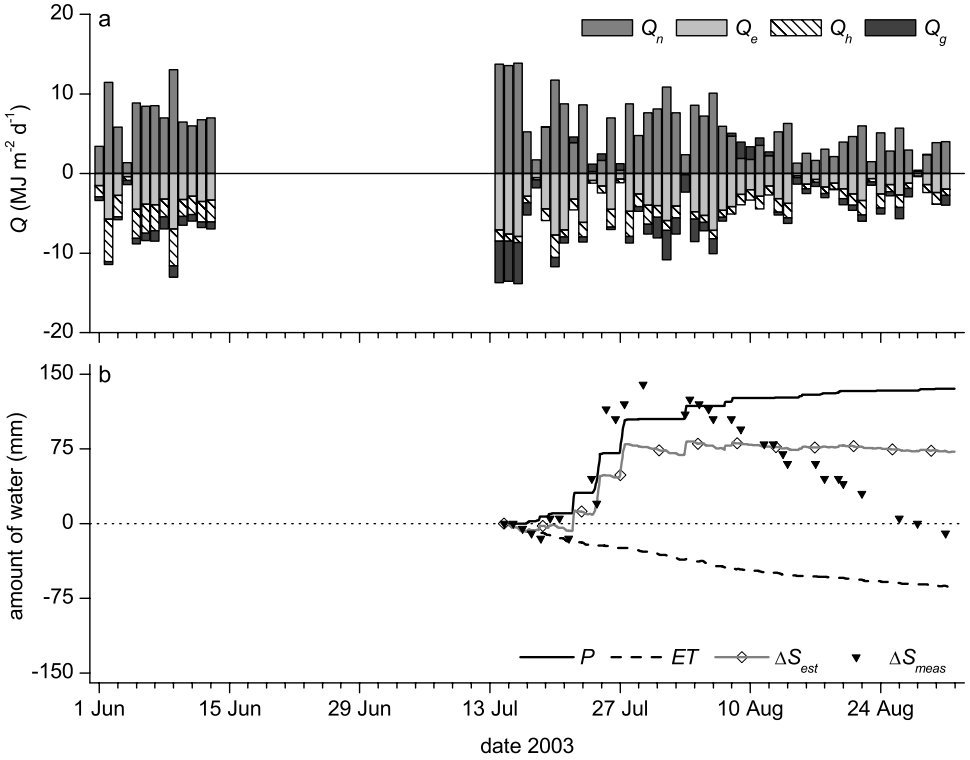

Figure 7. Energy and water balance components in 2003. (a) Daily sums of energy balance components Q_n, Q_e, Q_h, and Q_g for the periods 1–13 June and 14 July to 31 August; (b) cumulative water balance components for the period 14 July to 31 August ΔS_{est} (equation (7)), and ΔS_{meas}.

which went into Q_e was 49% during 1–13 June, 62% during 14–31 July, and 61% during August. Q_h was the second largest energy sink; 39, 20, and 24% of Q_n went into Q_h during 1–13 June, 14–31 July, and August, respectively. Q_g consumed 12% of Q_n during 1–13 June, 18% during 14–31 July, and 15% during August, and was the smallest energy sink. During cold and cloudy days, e.g., 22–27 July and 8–12 August, the ground was a source of energy and returned about one seventh of the gross Q_g to the atmosphere. Of the remaining energy, 98% went into the change of soil latent heat, i.e., the thaw of the ice rich permafrost soil.

[28] The water storage in 2003 was characterized by the repeated strong rain events at the end of July (Figure 7b). However, ΔS_{meas} and ΔS_{est} reacted markedly different: During the period 21–29 July ΔS_{meas} increased by 155 mm, whereas ΔS_{est} increased by only 70 mm. Also after the rain events, ΔS_{meas} and ΔS_{est} behaved differently: Until 31 August, ΔS_{meas} decreased continuously by roughly 5 mm d^{-1} while ΔS_{est} decreased by only 5 mm, because ET and R nearly balanced. Thus the difference between ΔS_{est} and ΔS_{meas} changed from −63 mm on 29 July to +82 mm on 31 August (Table 2).

4.6. Comparison of Water Balance 1999 and 2003

[29] For quantitative analyses of the water balance, ΔS_{est} and ΔS_{meas} were plotted against each other for several periods with low precipitation (Figure 8). As indicated by the slope of the linear regressions, in 1999 measured storage decreased 4 and 7 times faster than estimated storage, whereas in 2003, measured storage decreased about 20 times faster. This indicates that ΔS_{est}, which is based on P-ET and excludes lateral surface and subsurface flows, does not describe the water balance of the polygonal tundra adequately. In 2003 during and after strong rain events, surface runoff and channel formation was observed. In 1999, no visible surface flow into or out of ponds was observed because the water level position was already below the soil surface in the polygon center.

4.7. Subsurface Flow Experiment

[30] A dye tracer experiment was undertaken in August 2006 to evaluate the flow of water between polygons through the polygonal rim (Figure 9). On 21 August 10 L of water dyed with a blue tracer (5 mg L^{-1} Vitasyn Blue AE85, Hoechst AG, Germany) were poured in a pit (45 cm × 15 cm wide) which had been dug to the thaw depth of 30 cm. The pit was located at the outermost edge of the polygonal rim separating polygon A and B (Figures 9a and 9b). The location for the experiment was chosen at a rim that was not divided by a crack since only subsurface flow (and not surface flow inside the crack) was the scope of this study. The difference in water level between Polygons A and B was 5 cm. It was hypothesized that subsurface water flowed between these two polygons. On 30 August further pits were dug to visualize the subsurface pathways of the tracer dye. Within 9 d, blue water had moved 1.3 m toward polygon B within a 3–5 cm layer of fine to medium sand. This sand layer was bounded by lower hydraulic conductivity layers (sandy silt) above and below (Figure 9c). Using Darcy's law [*Freeze and Cherry*, 1979] and a hydraulic conductivity of 1.30×10^{-4} m s^{-1} for a 5 cm sand layer (estimated from the

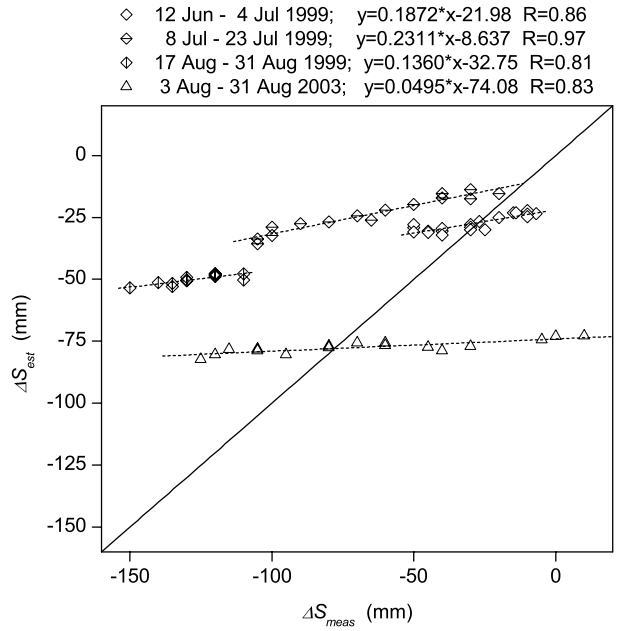

Figure 8. Estimated storage (cumulative *P-ET*) versus measured storage during periods with low precipitation in 1999 and 2003. For 2003 data the sign was reversed for better illustration. The dashed lines are linear fits of the data, the solid line is the function y = x.

tracer experiment), a distance of 4 m between polygons (width of polygon rim), an estimated polygon pond surface area of 100 m^2, and a time 60 d (July–August), the total water transported via groundwater flow would result in a water level decrease of 42 mm in polygon A. This values lies in the same order of magnitude of difference between estimated and measured storage change in 1999 (59 mm).

4.8. Seasonal Drivers of Energy Balance

[31] The relationship of energy partitioning and air temperature was illustrated by comparison of the ratio of Q_e, Q_h, Q_g, and Q_n for different air temperature ranges (Figure 10). In both years 1999 and 2003, Q_e/Q_n increased and Q_h/Q_n decreased with increasing air temperature. However, the sensitivity of Q_e/Q_n to air temperature was more pronounced during the wet year 2003 compared to the dry year 1999: Qe/Qn increased by 21% in 2003 and by only 7% in 1999 between the temperature classes <0°C and >15°C, With an increase of 34% between temperature classes <0°C and >15°C during both years, the sensitivity of Q_h/Q_n to air temperature was greater than that of Q_e/Q_n, but did not depend on the moisture regime.

5. Discussion

5.1. Summer Energy Balance 1999 and 2003

[32] The total Q_n during June to August 1999 of 868 MJ m^{-2} is very similar to the value of 854 MJ m^{-2} reported by *Ohmura* [1982] for a tundra site at Barrow, Alaska (71°N), and the values of 700–800 MJ m^{-2} reported by *Lloyd et al.* [2001] from Zackenberg, Greenland (74°N) and Skalluvaara,

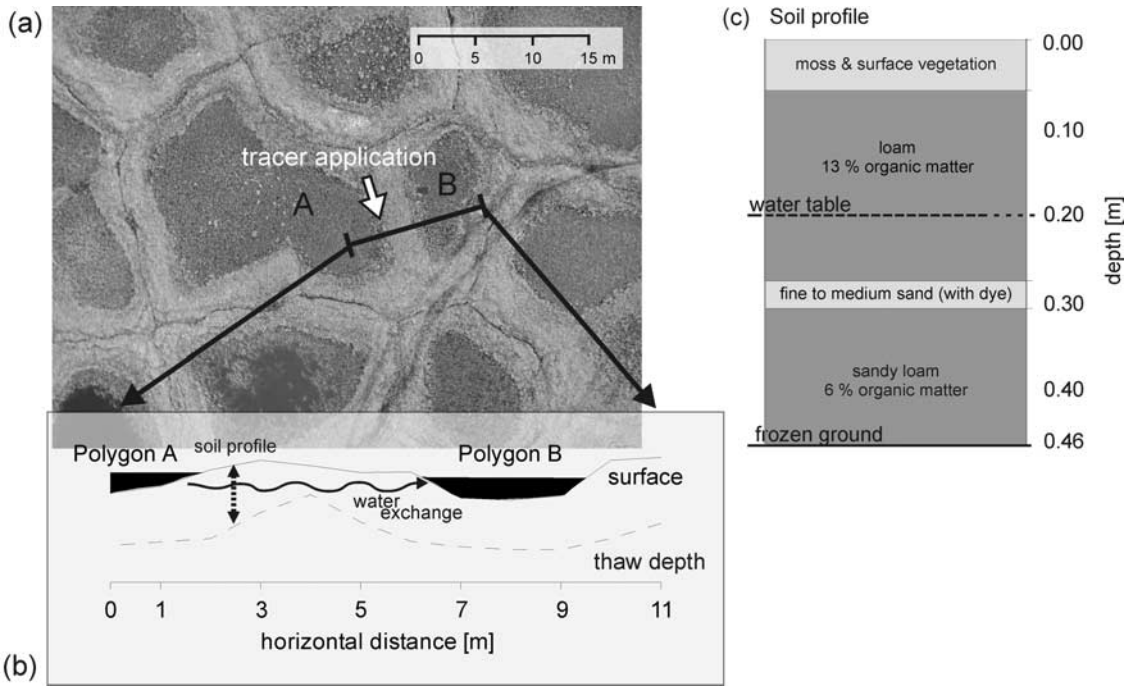

Figure 9. Scheme of subsurface flow tracer experiment in August 2006. (a) Aerial picture of experimental site, (b) cross section A-B, the width of the polygonal wall was about 4 m and the thaw depth at the soil profile where the dye tracer was applied was 46 cm, and (c) typical soil profile along A-B at the end of the experiment. The dye was exclusively found in a continuous sand layer, approximately 3 cm thick.

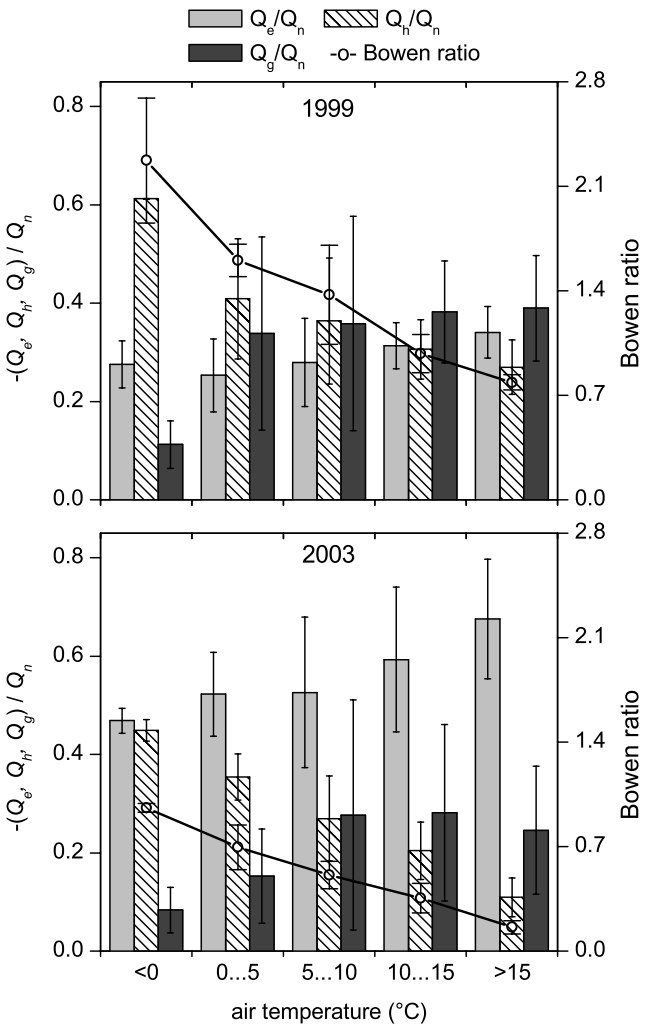

Figure 10. Bowen ratio and ratios of energy fluxes Q_e, Q_h, Q_g, and net radiation Q_n based on daily sums of fluxes as displayed in Figures 5 and 7. The data were grouped into five bins according to mean daily air temperature and averaged within each bin. The error bars are standard deviations within the bins. During days with positive Q_g in 2003, Q_g/Q_n was disregarded and $Q_e/(Q_n + Q_g)$ and $Q_h/(Q_n + Q_g)$ was used.

Finland (70°N) for the period 9 June to 29 August. However, Q_n differed greatly between the years 1999 and 2003. During the period 14 July to 31 August, the available energy was 24% lower in 2003 compared to 1999. This was due to the predominance of cloudy weather in 2003, which is exemplified by the cloudy and rainy period at the end of July when Q_n was reduced to less than 10% of the monthly average.

[33] The fraction of 29% of Q_n that was partitioned into Q_g in 1999 was large compared to values of Q_g/Q_n of 10–16% reported from North American [*Ohmura*, 1982; *Vourlitis and Oechel*, 1997; *Harazono et al.*, 1998] and European Arctic sites [*Harding and Lloyd*, 1998; *Soegaard et al.*, 2001]. In general, the Q_g/Q_n ratio is low for wetlands due to the high soil moisture content and a high evapotranspiration [*Jacobsen and Hansen*, 1999]. The high soil heat flux at our site in 1999 is explained by the generally dry soil conditions which, compared to wet tundra soils, led to lower soil hydraulic conductivity and thus less evaporation [*Boike et al.*, 1998] and hence an overall shift of the energy partitioning toward Q_g. This is supported by the increase of the value of Q_g/Q_n from 26% in June to 37% in August 1999, which concurs with a falling water table and further drying of the upper soil layers. On the other hand, the Q_g/Q_n value of 17% found in 2003 is closer to the results of the studies cited above, albeit at the upper end of the range given there. This could be explained by the low permafrost temperature in our study region, which leads to a strong temperature gradient in the thawed soil layer and promotes a generally high ground heat flux during summer [*Boike et al.*, 2003b].

[34] The fractions of Q_n that were partitioned into Q_e (61%) and Q_h (22%) in 2003 are comparable to values found by other arctic wetland studies. Values of Q_e/Q_n and Q_h/Q_n reported are 57% and 29% for a flooded sedge tundra at the North Slope of Alaska [*Harazono et al.*, 1998], 39% and 27% for an Arctic fen at northeast Greenland [*Soegaard et al.*, 2001], 64% and 28% for two Canadian sub-Arctic tundra sites [*Eaton et al.*, 2001], and 51% and 34% for a sub-Arctic elevated mire in Northern Finland [*Lloyd et al.*, 2001]. The mean Bowen ratio, β, for the measurement periods 2003 was 0.36. Thus in 2003 the tundra behaved like a typical wetland in terms of the energy partitioning. In 1999, the energy partitioning was drastically different compared to 2003. The fractions of Q_n that were partitioned into Q_e and Q_h were 31% and 40%, respectively, and the mean Bowen ratio was 1.29. The smaller value of Q_e/Q_n was caused by the drying of the upper soil and the moss layer. It is thought that a substantial part of 50–85% of tundra *ET* is evaporation from the moss layer [*Miller et al.*, 1980; *Vourlitis and Oechel*, 1999; *Grant et al.*, 2003]. Mosses lack stomatal control, but their resistance to water loss was shown to increase exponentially as tissue water decreases [*Oechel and Sveinbjörnsson*, 1978; *McFadden et al.*, 2003].

[35] During both years, the Bowen ratio was largest in June (1999: 1.39; 2003: 0.81), was lowest in July (1.19/0.32), and rose again slightly in August (1.24/0.40). A similar pattern was observed at Arctic and boreal wetlands in Europe, North America, and Greenland [e.g., *Lafleur et al.*, 1997; *Lloyd et al.*, 2001]. It can be explained by the phenological development of vascular plants in the tundra canopy and their contribution to the total tundra *ET* and hence Q_e. The fact that the seasonal change of the Bowen ratio was observed during both years 1999 and 2003 suggests that despite the dry conditions and the low water level in 1999, vascular plants were not limited by water availability. This is supported by the typical root horizon depth of 11–26 cm in polygon centers and 0–15 cm at polygon rims [*Kutzbach et al.*, 2004], and the soil moisture measurements which showed that soils were close to water saturation at all times at and below depths of 15 cm.

5.2. Seasonal Drivers of Energy Balance

[36] Net radiation was the dominant energy source, as visualized in Figures 5a and 7a. However, the large variations in daily Bowen ratio indicate that the turbulent fluxes of energy are driven not by net radiation alone. *Harazono et*

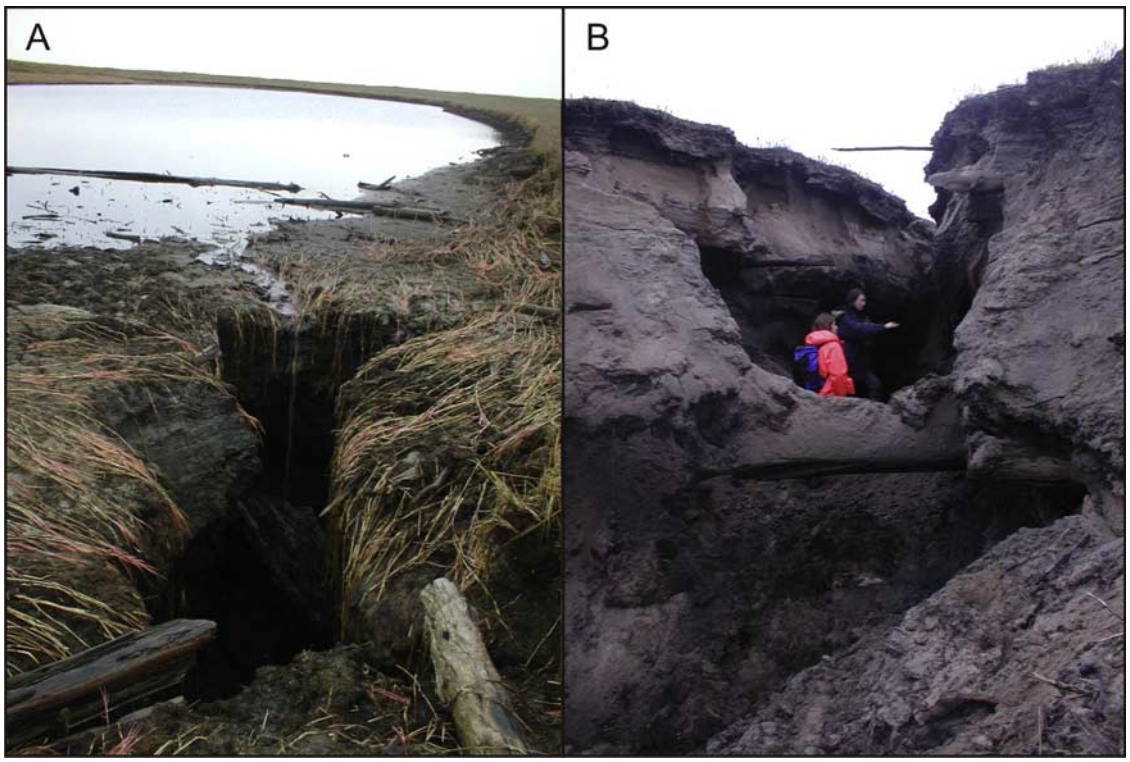

Figure 11. Thermoerosion features at the polygonal tundra of Samoylov Island, initiated by strong rainfall events in summer 2003. (A) A large lake is drained by one outflow. The log at the front right has a length of about 1 m. (B) Drainage channel outflow at the cliff of the river terrace that builds up the Eastern part of Samoylov Island [from *Kutzbach*, 2006].

al. [1998] related observed fluctuations of Bowen ratio at a wet sedge tundra at the North Slope, Alaska to air temperature variations connected to synoptical weather patterns, namely the change between onshore winds from the Arctic Ocean and offshore winds from the continental hinterland. This finding is thought to apply also to our study site. During periods of advection of continental warm and dry air masses (e.g., 14–16 July 2003), Q_g/Q_n was greatly increased (37%) and Q_h/Q_n was very low (7%). On the other hand, during periods of advection of maritime cold air (e.g., 24–27 July 2003), the soil turned into a significant source of heat (25% of Q_n), and Q_h increased greatly (42%).

[37] The strong decline of Q_h/Q_n with increase in air temperatures (Figure 10) is the result of the reduction in surface to air temperature gradients and demonstrates the importance of air temperature as a driver of Q_h. The ratio Q_g/Q_n increased initially with increasing temperature but shows no further increase in the temperature range above 10°C during both years 1999 and 2003. This could be explained by the increased thaw depth, which reduces the temperature gradient and thus leads to a reduction of Q_g. All the above findings are in agreement with the results by *Harazono et al.* [1998], who compared the relationship of energy partitioning and air temperature of a wet sedge tundra and a dry tussock tundra at the North Slope of Alaska during one growing season.

[38] In summary, the air temperature has a significant influence on the energy partitioning of the tundra. Because of the location of the study site at the border between continental and maritime arctic air masses, the synoptical weather patterns are of major importance for the energy balance of the tundra.

5.3. Comparison of Water Balance 1999 and 2003

[39] The evaluation of the water balance of the polygonal pond demonstrated the response of water balance components to climatic variability between two study seasons. In 2003, high precipitation inputs resulted in the recharge of polygonal ponds. Similarly, *Woo and Guan* [2006] found that arctic ponds can be recharged to snowmelt levels by sizable rain events. *Bowling et al.* [2003] showed that late summer precipitation may result in runoff from upland tundra areas to partially recharge pond storage. On the other hand, low amounts of precipitation in 1999 resulted in a total loss of pond surface waters. This underlines the importance of the frequency and duration of precipitation events in the water budget of polygonal ponds during the postsnowmelt season. *Kane and Carlson* [1973] concluded from their studies that direct precipitation was the major hydrologic input to an arctic lake in the Low Arctic.

[40] Evapotranspiration led to a steady pond storage decline in both study seasons. Even during the dry year of 1999 evaporation continued during the whole summer, despite the fact that water levels fell well below the soil surface in the depressed polygon centers. This is explained by the large depth of 34 cm of the rooting zone in the polygonal centers [*Kutzbach et al.*, 2004], which guaranteed the availability of water for plant uptake. According to *Lafleur et al.* [2005], the rooting depth of vascular plants represents a critical limit of water table depth, below which

evapotranspiration is limited to some degree by water supply.

[41] However, water balance calculations based on *P-ET* did not describe the water balance of the polygonal tundra adequately (Figures 5 and 7). The storage loss in 1999 must have been due to subsurface outflow of water. The trace experiment conducted in August 2006 suggests a possible connection of the pond with neighboring ponds via subsurface flow through sandy soil layers with high hydraulic conductivity. The occurrence of sand layers is widespread as found in detailed cross sections of low centered polygons on Samoylov Island [*Pfeiffer et al.*, 2002]. The occurrence of thin sandy layers with higher hydraulic conductivity compared to the prevalent loam or silt layers could also explain the varying speed of the storage loss in 1999. *Woo and Guan* [2006] found during a post snowmeltwater balance study of tundra ponds that, in addition to vertical fluxes, change in the pond storage was driven by low magnitude lateral flow exchanges with neighboring ponds. The importance of lateral fluxes for the seasonal water balance of a northern boreal fen during a dry year was also shown by *Lafleur et al.* [1997], who observed that the fen drained gradually throughout the summer in response to evaporation and lateral outflow. Furthermore, a subsurface hydrologic connections enable the transport of nutrients which could be an important factor for sustaining this wetland ecosystem.

[42] In 2003, high soil moisture conditions and a high water table together with a shallow active layer contributed to surface connectivity of the pond with the surrounding catchment during and after rain events. Field observations during the 2003 rain event included runoff across polygon rims and the development and widening of old and new hydrologic channels due to thermo-erosion (Figure 11). This surface runoff was the reason for the much larger decrease of ΔS_{meas} compared to ΔS_{est} as illustrated in Figure 8. Similarly, during the strong rain events in 2003, ΔS_{meas} increased much stronger than ΔS_{est} which suggests the inflow of water. *Woo and Guan* [2006] observed at their polygonal tundra pond research site in the Canadian Arctic that, during high and prolonged rain events, surface connectivity between the ponds was established through lateral surface flow, which recharged the ponds. They also suggest that cracks may act as natural channels for pond drainage. The formation of new channels as observed at our study site in 2003 was important for the regulation of surface runoff during extensive rain events, and may have a strong and lasting effect on the hydrologic connectivity within this tundra system.

[43] For both years, water balance calculations based solely on *P-ET* calculations underestimated the water budget of this polygonal tundra due to omission of surface and subsurface flows.

6. Conclusion

[44] The summer water balance of the studied wetland tundra was found to be mainly controlled by precipitation. Furthermore, the partitioning of the available energy was controlled by precipitation via the moisture regime of the tundra soils. The two years showed very different regimes in terms of the energy partitioning and it's relation to air temperature. During the dry year, the available energy was largely evenly partitioned between Q_e, Q_h, and Q_g for all air temperatures >0°C. During the wet year, the flux partitioning was highly dependent on air temperature: Q_e increased strongly with air temperature and drastically reduced the energy available for Q_h and Q_g. Hence with increasing air temperature and abundant moisture supply as predicted by global climate scenarios [*IPCC*, 2001], evaporation could increase strongly, thus reducing the sensible and ground heat flux.

[45] The formation of new surface flow channels through thermo-erosion and the drainage is expected to have a strong and lasting influence on the hydrologic system of the tundra. Subsurface flow is important in the tundra water budget, which is shown by gross underestimation of the water budget calculated from *P-ET* alone. These processes are not well understood and require further experimental and modeling studies. Improving our understanding of land atmosphere exchange processes will allow evaluating the degree of sensitivity of heat and water budget components to climate change in these northern permafrost landscapes.

Notation

Q_n	net radiation balance
Q_h	turbulent fluxes of sensible heat
Q_e	turbulent fluxes of latent heat
Q_r	heat flux supplied by rain
Q_g	ground heat flux
H_{gl}	thermal energy stored as latent heat in the soil
H_{gs}	thermal energy stored as sensible heat in the soil
α_{PT}	empirical parameter expressing actual to equilibrium evapotranspiration
α	phase (ice, *i*, liquid water, *w*, soil matrix, *sm*)
c_α	specific heat capacity
ρ_α	mass density
θ_α	volumetric content of phase α
T	temperature
z	depth
λ	soil thermal conductivity
P	precipitation
ET	evapotranspiration
S	surface storage
R	surface discharge
γ	psychrometric constant

[46] **Acknowledgments.** We thank the following for their assistance in the field and for data discussion and analyses: Bob Bolton, Lars Kutzbach, Sina Muster, Imke Schramm, Günter Stoof and Paul Overduin. Thanks to the logistical and financial support of the Russian-German research station on Samoylov that made this study possible. We also thank the anonymous reviewers whose comments greatly helped to improve the manuscript.

References

Bello, R., and J. D. Smith (1990), The effect of weather variability on the energy balance of a lake in the Hudson Bay Lowlands, Canada, *Arct. Alp. Res.*, *22*(1), 98–107.

Berezovskaya, S., D. Yang, and D. Kane (2004), Compatibility analysis of precipitation and runoff trends over the large Siberian watersheds, *Geophys. Res. Lett.*, *31*, L21502, doi:10.1029/2004GL021277.

Berezovskaya, S., D. Yang, and L. Hinzman (2005), Long-term annual water balance analysis of the Lena river, *Global Planet. Change*, *48*, 84–95.

Boike, J., and K. Roth (1997), Time domain reflectometry as a field method for measuring water content and soil water electrical conductivity at a continuous permafrost site, *Permafrost Perigl. Process.*, *8*, 359–370.

Boike, J., K. Roth, and P. P. Overduin (1998), Thermal and hydrologic dynamics of the active layer at a continuous permafrost site (Taymyr Peninsula, Siberia), *Water Resour. Res.*, *34*, 355–363.

Boike, J., K. Roth, and O. Ippisch (2003a), Seasonal snow cover on frozen ground: Energy balance calculations of a permafrost site near Ny-Ålesund, Spitsbergen, *J. Geophys. Res.*, *108*(D2), 8163, doi:10.1029/2001JD000939.

Boike, J., L. D. Hinzman, P. P. Overduin, V. Romanovsky, O. Ippisch, and K. Roth (2003b), A comparison of snow melt at three circumpolar sites: Spitsbergen, Siberia, Alaska, in *Permafrost: Proceedings of the 8th International Conference on Permafrost 2003*, edited by L. U. Arenson, M. Phillips, and S. M. Springman, pp. 79–84, Balkema Publishers, Netherlands.

Bowling, L. C., D. L. Kane, R. E. Gieck, L. D. Hinzman, and D. P. Lettenmaier (2003), The role of surface storage in a low-gradient arctic watershed, *Water Resour. Res.*, *39*(4), 1087, doi:10.1029/2002WR001466.

Campbell, G. S. (Ed.) (1985), *Soil Physics With BASIC: Transport Models for Soil-Plant Systems*, 150 pp., Elsevier, New York.

Chapin, F. S., III, et al. (2000), Arctic and boreal ecosystems of western North America as components of the climate system, *Global Change Biol.*, *6*, 211–223.

Eaton, A. K., W. R. Rouse, P. M. Lafleur, P. Marsh, and P. D. Blanken (2001), Surface energy balance of the western and central Canadian subarctic: Variations in the energy balance among five major terrain types, *J. Clim.*, *14*, 3692–3703.

Eichinger, W., M. B. Parlange, and H. Stricher (1996), On the concept of equilibrium evaporation and the value of Priestley-Taylor coefficient, *Water Resour. Res.*, *32*, 161–164.

Eugster, W., et al. (2000), Land-atmosphere energy exchange in Arctic tundra and boreal forest: Available data and feedbacks to climate, *Global Change Biol.*, *6*(Suppl. 1), 84–115.

Fiedler, S., D. Wagner, L. Kutzbach, and E.-M. Pfeiffer (2004), Element redistribution along hydraulic and redox gradients of low-centered polygons, Lena Delta, Northern Siberia, *Soil Sci. Soc. Am. J.*, *68*, 1002–1011.

Freeze, R. A., and J. A. Cherry (1979), *Groundwater*, 604 pp., Prentice-Hall, Englewood Cliffs, N. J.

Friedrich, K. (2001), Energie-und Wasserhaushalt eines Tundrenstandortes im Lena-Delta, Diploma thesis, 74 pp., Tech. Univ. Dresden, Inst. for Hydrol. and Meteorol., Dresden, Germany.

Gilg, O., R. Sané, D. V. Solovieva, V. I. Pozdnyakov, B. Sabard, D. Tsanos, C. Zöckler, E. G. Lappo, E. E. Syroechkovski Jr., and G. Eichhorn (2000), Birds and mammals of the Lena Delta nature reserve, Siberia, *Arctic*, *53*(2), 118–133.

Grant, R. F., W. C. Oechel, and C.-L. Ping (2003), Modelling carbon balances of coastal tundra under changing climate, *Global Change Biol.*, *9*(1), 16–36, doi:10.1046/j.1365-2486.2003.00549.x.

Harazono, Y., M. Yoshimoto, M. Mano, G. L. Vourlites, and W. C. Oechel (1998), Characteristics of energy and water budgets over wet sedge and tussock tundra ecosystems at North Slope in Alaska, *Hydrol. Proc.*, *12*, 2163–2183.

Harding, R. J., and C. R. Lloyd (1998), Fluxes of water and energy from three high latitude tundra sites in Svalbard, *Nord. Hydrol.*, *29*(4/5), 267–284.

Hinzman, L. D., D. L. Kane, R. E. Giek, and K. Everett (1991), Hydrologic and thermal properties of the active layer in the Alaskan Arctic, *Cold Reg. Sci. Technol.*, *19*, 95–110.

Hinzman, L. D., D. J. Goering, and D. L. Kane (1998), A distributed thermal model for calculating soil temperature profiles and depth of thaw in permafrost regions, *J. Geophys. Res.*, *102*, 28,975–28,911.

Incropera, F. P., and D. P. Dewitt (1996), *Fundamentals of Heat and Mass Transfer*, John Wiley, New York.

IPCC (2001), Climate Change 2001: Impacts, Adaptation, and Vulnerability, in *Contribution of Working Group II to the Third Assessment Report of the Intergovernmental Panel on Climate Change*, Cambridge Univ. Press, Cambridge, U.K.

Jacobsen, A., and B. U. Hansen (1999), Estimation of soil heat flux/net radiation ratio based on spectral vegetation indexes in high-latitude Arctic areas, *Int. J. Remote Sens.*, *20*(2), 445–461.

Kane, D. L., and R. E. Carlson (1973), Hydrology of the central arctic river basins of Alaska, *Report, IWR-41*, 51 pp., Inst. of Water Resour., Univ. of Alaska, Alaska.

Kotlyakov, V., and T. Khromova (2002), Permafrost, Snow and Ice, in *Land Resources of Russia* [CD-ROM], edited by V. Stolbovoi and I. McCallum, Int. Inst. of Appl. Syst. Analysis and the Russian Academy of Science, Laxenburg, Austria.

Kutzbach, L. (2006), The Exchange of Energy, Water and Carbon Dioxide between Wet Arctic Tundra and the Atmosphere at the Lena River Delta, Northern Siberia, in *Reports on Polar and Marine Research 541*, 157 pp., Alfred Wegener Institute, Bremerhaven, Germany.

Kutzbach, L., D. Wagner, and E.-M. Pfeiffer (2004), Effect of microrelief and vegetation on methane emission from wet polygonal tundra, Lena Delta, Northern Siberia, *Biogeochemistry*, *69*, 341–362.

Lafleur, P. M., J. H. McCaughey, D. W. Joiner, P. A. Bartlett, and D. E. Jelinski (1997), Seasonal trends in energy, water, and carbon dioxide fluxes at a northern boreal wetland, *J. Geophys. Res.*, *102*, 29,009–29,020.

Lafleur, P. M., R. A. Hember, W. A. Stuart, and N. T. Roulet (2005), Annual and seasonal variability in Evapotranspiration and water table at a shrub-covered bog in southern Ontario, Canada, *Hydrol. Process.*, *19*(18), 3533–3550.

Lloyd, C. R., R. J. Harding, T. Friborg, and M. Aurela (2001), Surface fluxes of heat and water vapour from sites in the European Arctic, *Theor. Appl. Climatol.*, *70*, 19–33.

Lynch, A. H., F. S. Chapin III, L. D. Hinzman, W. Wu, E. Lilly, G. Vourlitis, and E. Kim (1999), Surface energy balance on the Arctic tundra: Measurements and models, *J. Clim.*, *12*, 2585–2606.

Marsh, P., W. R. Rouse, and M. Woo (1981), Evaporation at a High Arctic site, *J. Appl. Meteorol.*, *20*, 713–716.

McFadden, J. P., and W. Eugster (2003), A regional study of the controls on water vapour and CO2 exchange in arctic tundra, *Ecology*, *84*(10), 2762–2776.

Mendez, J., L. D. Hinzman, and D. L. Kane (1998), Evapotranspiration from a wetland complex on the Arctic coastal plain of Alaska, *Nord. Hydrol.*, *29*, 303–330.

Miller, P. C., P. J. Webber, W. C. Oechel, and L. L. Tieszen (1980), Biophysical processes and primary production, in *An Arctic Ecosystem: The Coastal Tundra at Barrow, Alaska*, edited by Brown et al.,Van Nostrand Reinhold, Stroudsburg, Pa.

Natural Resources Canada (1995), Map Canada - Permafrost, in *The National Atlas of Canada*, 5th ed., (Available at http://atlas.gc.ca/), Geol. Surv. of Canada, Natural Resources Canada, Ottawa, Canada.

NSIDC, National Snow and Ice Data Center (2003), *Circumpolar Active-Layer Permafrost System (CAPS)* [CD-ROM], Univ. of Colorado, Boulder, Colo.

Oechel, W. C., and B. Sveinbjörnsson (1978), Primary production processes in arctic bryophytes at Barrow, Alaska, in *Vegetation of Production Ecology of an Alaskan Arctic Tundra. Ecological Studies*, vol. 29, edited by L. L. Tieszen, Springer, New York.

Ohmura, A. (1982), Climate and energy balance on the Arctic tundra, *J. Climatol.*, *2*, 65–84.

Pfeiffer, E.-M., D. Wagner, S. Kobabe, L. Kutzbach, A. Kurchatova, G. Stoof, and C. Wille (2002), Modern processes in permafrost-affected soils, in *Reports on Polar Research*, *426*, Alfred Wegener Institute, Bremerhaven, Germany.

Priestley, C. H. B., and R. J. Taylor (1972), On the assessment of surface heat flux and evaporation using large-scale parameters, *Mon. Weather Rev.*, *100*, 81–92.

ROSHYDROMET (2006), Weather Information for Tiksi, (Available at http://www.worldweather.org/107/c01040.htm), Russian Federal Service for Hydrometeorology and Environmental Monitoring, Moscow.

Roth, K., R. Schulin, H. Flühler, and W. Attinger (1990), Calibration of time domain reflectometry for water content measurement using a composite dielectric approach, *Water Resour. Res.*, *26*, 2267–2273.

Rouse, W. R. (1990), The regional energy balance, *Northern Hydrol., NHRI Sci. Rep.*, *1*, 187–206.

Rouse, W. R., and R. B. Stewart (1972), A simple model for determining the evaporation from high latitude upland sites, *J. Appl. Meteorol.*, *11*, 1063–1070.

Rouse, W. R., P. F. Mills, and R. B. Stewart (1977), Evaporation in high latitudes, *Water Resour. Res.*, *13*, 909–914.

Schwamborn, G., V. Rachold, and M. N. Grigoriev (2002), Late quaternary sedimentation history of the Lena Delta, *Quat. Int.*, *89*, 119–134.

Smith, L. C., Y. Sheng, G. M. MacDonald, and L. D. Hinzman (2005), Disappearing Arctic lakes, *Science*, *308*(5727), 1429, doi:10.1126/science.1108142.

Soegaard, H., B. Hasholt, T. Friborg, and C. Nordstroem (2001), Surface energy- and water balance in a High-Arctic environment in NE Greenland, *Theor. Appl. Climatol.*, *70*, 35–51.

Spielhagen, R. F., H. Erlenkeuser, and C. Siegert (2005), History of freshwater runoff across the Laptev Sea (Arctic) during the last deglaciation, *Global Planet. Change*, *48*(1–3), 187–207, doi:10.1016/j.gloplacha.2004.12.013.

Stewart, J. M., and P. Broadbridge (1999), Calculation of humidity during evaporation from soil, *Adv. Water Resour.*, *22*(5), 495–505.

Stewart, R. B., and W. R. Rouse (1976), Simple models for calculating evaporation from dry and wet tundra surfaces, *Arct. Antarct. Alp. Res.*, *8*(3), 263–274.

Stewart, R. B., and W. R. Rouse (1977), Substantiation of the Priestley and Taylor parameter $\alpha = 1.26$ for potential evaporation in high latitudes, *J. Appl. Meteorol.*, *16*(6), 649–650.

USDA, United States Department of Agriculture, Natural Resources Conservation Service (1998), *Keys to Soil Taxonomy*, 8th ed., Soil Survey Staff, Washington, D. C.

Vörösmarty, C. J., L. D. Hinzman, B. J. Peterson, D. H. Bromwich, L. C. Hamilton, J. Morison, V. E. Romanovsky, M. Sturm, and R. S. Webb (2001), The hydrologic cycle and its role in arctic and global environmental change: A rationale and strategy for synthesis study, in *Arctic Research Consortium of the U.S.*, 84 pp., Arctic Research Consortium of the U.S., Fairbanks, Alaska.

Vourlitis, G. L., and W. C. Oechel (1997), Landscape-scale CO_2, H_2O vapour and energy flux of moist-wet coastal tundra ecosystems over two growing seasons, *J. Ecol.*, *85*, 575–590.

Vourlitis, G. L., and W. C. Oechel (1999), Eddy covariance measurements of net CO_2 and energy fluxes of an Alaskan Tussock tundra ecosystem, *Ecology*, *80*(2), 686–701.

Wagner, D., S. Kobabe, E.-M. Pfeiffer, and H.-W. Hubberten (2003), Microbial controls on methane fluxes from a polygonal tundra of the Lena Delta, Siberia, *Permafrost Perigl. Process.*, *14*, 173–185, doi:10.1002/ppp.443.

Wagner, D., A. Lipski, A. Embacher, and A. Gattinger (2005), Methane fluxes in extreme permafrost habitats of the Lena Delta: Effects of microbial community structure and organic matter quality, *Environ. Microbiol.*, *7*, 1582–1592.

Woo, M. K., and X. J. Guan (2006), Hydrological connectivity and seasonal storage change of tundra ponds in a polar oasis environment, Canadian High Arctic, *Permafrost Perigl. Process.*, *17*, 309–323.

Woo, M. K., and P. Marsh (1990), Response of soil moisture change to hydrological processes in a continuous permafrost environment, *Nord. Hydrol.*, *21*, 235–252.

Woo, M. K., and K. L. Young (2003), Hydrogeomorphology of patchy wetlands in the High Arctic, polar desert environment, *Wetlands*, *23*(2), 291–309.

Woo, M. K., and K. L. Young (2006), High Arctic wetlands: Their occurrence, hydrological characteristics and sustainability, *J. Hydrol.*, *320*(3–4), 432–450.

Yang, D., D. Kane, L. Hinzman, X. Zhang, T. Zhang, and H. Ye (2002), Siberian Lena River hydrologic regime and recent change, *J. Geophys. Res.*, *107*(D23), 46–94, 4694, doi:10.1029/2002JD002542.

Yoshikawa, K., and L. D. Hinzman (2003), Shrinking thermokarst ponds and groundwater dynamics in discontinuous permafrost near Council, Alaska, *Permafrost Perigl. Process.*, *14*, 151–160, doi:10.1002/ppp.451.

Young, K. L., and M. K. Woo (2000), Hydrological response of a patchy High Arctic wetland, *Nord. Hydrol.*, *31*(4/5), 317–338.

Zhang, T., R. G. Barry, K. Knowldes, J. A. Heginbottom, and J. Brown (1999), Statistics and characteristics of permafrost and ground-ice distribution in the northern hemisphere, *Polar Geogr.*, *23*(2), 132–154.

A. Abnizova, Department of Geography, York University, 4700 Keele Street, Toronto, Ontario, Canada M3J 1P3.

J. Boike, Periglacial Section, Alfred Wegener Institute for Polar and Marine Research, Telegrafenberg A43, 14473 Potsdam, Germany. (jboike@awi-potsdam.de)

C. Wille, Institute of Botany and Landscape Ecology, University of Greifswald, Grimmer Strasse 88, 17487 Greifswald, Germany.

Chapter 2.4

M.Langer, S. Westermann,S.Muster, K.Piel ans J. Boike (2010): Permafrost and surface energy balance of a polygonal tundra site in northern Siberia – Part 1: Spring to fall, *The Cryoshere Discussions*, 4, 901-947,2010

The Cryosphere Discuss., 4, 901–947, 2010
www.the-cryosphere-discuss.net/4/901/2010/
doi:10.5194/tcd-4-901-2010
© Author(s) 2010. CC Attribution 3.0 License.

The Cryosphere Discussions

This discussion paper is/has been under review for the journal The Cryosphere (TC).
Please refer to the corresponding final paper in TC if available.

Permafrost and surface energy balance of a polygonal tundra site in northern Siberia – Part 1: Spring to fall

M. Langer, S. Westermann, S. Muster, K. Piel, and J. Boike

Alfred-Wegener-Institute for Polar and Marine Research, Telegrafenberg A43, 14473 Potsdam, Germany

Received: 17 June 2010 – Accepted: 23 June 2010 – Published: 12 July 2010

Correspondence to: M. Langer (moritz.langer@awi.de)

Published by Copernicus Publications on behalf of the European Geosciences Union.

Abstract

Permafrost thawing is essentially determined by the surface energy balance, which potentially triggers the activation of a massive carbon source, if previously frozen organic soils are exposed to microbial decomposition. In this article, we present the first part of a comprehensive annual surface energy balance study performed at a polygonal tundra landscape in northeast Siberia, realized between spring 2007 and winter 2009. This part of the study focuses on the half year period from April to September 2007–2008, during which the surface energy balance is obtained from independent measurements of the radiation budget, the turbulent heat fluxes and the ground heat flux at several sites. The short-wave radiation is the dominant factor in the surface energy balance during the entire observation period. About 50% of the available net radiation is consumed by latent heat flux, while the sensible and the ground heat flux are both on the order of 20 to 30%. The ground heat flux is mainly consumed by active layer thawing, where 60% of soil energy storage are attributed to. The remainder is used for soil warming down to a depth of 15 m. The controlling factors for the surface energy partitioning are in particular the snow cover, the cloud cover and the soil temperature gradient. Significant surface temperature differences of the heterogeneous landscape indicate spatial variabilities of sensible and latent heat fluxes, which are verified by measurements at different locations. However, differences in the partition between sensible and latent heat flux for the different sites only exist during conditions of high radiative forcing, which only occur occasionally.

1 Introduction

The thermal state of permafrost and its susceptibility towards degradation is fundamentally determined by the surface energy balance. Recent studies revealed that essential climate changes take place in the Arctic and are expected to proceed in the future (Overpeck et al., 1997; Hansen et al., 2001; Comiso, 2006; Overland et al., 2008).

There is observational evidence that energy and water exchange processes in the arctic landscapes are already substantially affected, which also involves the thermal state of permafrost (Serreze et al., 2000; Hinzman et al., 2005). Permafrost, which occupies about 25% of the land area of the Northern Hemisphere (Brown et al., 1997), is considered an important factor in the complex feedback mechanisms of the climate system due to its massive carbon storage capabilities (Christensen and Cox, 1995; Callaghan et al., 2004; McGuire et al., 2006). Zimov et al. (2006) estimated that about 970 Gt of carbon are stored in permafrost soils worldwide, which is about twice the amount of the actual atmospheric carbon concentration. Until now it is unclear whether permafrost regions will turn into massive sources of greenhouse gases, such as methane and carbon dioxide, as the frozen soils begin to thaw (Hobbie et al., 2000; Davidson and Janssens, 2006). This raises the question about the amount of stored organic material that will be exposed to microbial decomposition according to permafrost degradation and progressing thaw depths under a warming climate. Recent measurements at wet tundra landscapes demonstrate the importance of the freeze and thaw dynamics for methane emission, which are related in a non-linear manner (Christensen et al., 2003; Sachs et al., 2008; Mastepanov et al., 2008). For this purpose, efforts have been initiated to incorporate permafrost and the annual freeze and thaw dynamics in global climate models (e.g. Stendel and Christensen, 2002; Lawrence and Slater, 2005; Nicolsky et al., 2007; Lawrence et al., 2008). However, the energy exchange processes at the soil-atmosphere interface strongly depend on the landscape characteristics, such as surface moisture, vegetation cover, snow cover and soil properties. These characteristics are incorporated in climate models as parameterizations of e.g. surface roughness, resistance to evaporation and thermal properties of soil or snow. The representation of permafrost in climate models therefore essentially depends on the parameterization that is used to describe the surface energy balance. To support and validate modeling, it is desirable to obtain process studies, which deliver important information about the landscape specific energy balance characteristics and their determining factors. Long-term energy balance studies are especially important in arctic regions, where the

surface energy budget is characterized by an extreme seasonality and meteorological measurements are sparse (Westermann et al., 2009).

This study presents the annual energy balance of a wet tundra landscape in northern Siberia from spring 2007 until winter 2009. The study has been performed at a site dominated by polygonal tundra, which is a typical arctic landscape. Based on standard meteorological measurements Boike et al. (2008) contrasts the energy and water balances of a wet and a dry summer at the study site. In this study, we extend this previous work over the entire annual cycle by using independent measurements of all components of the surface energy balance. Furthermore, we investigate the impact of the considerable surface heterogeneity of the wet tundra landscape on the regional energy balance. The results of this study are presented in two parts: Part I comprises the period from April to September, which is characterized by increasing soil temperatures at the study site. Part II focuses on the winter period from October to March, which represents the period of soil cooling (Langer et al., 2010b).

The aim of the study is (i) to evaluate the annual surface energy balance at the study site, (ii) to determine the controlling and limiting factors in the energy partitioning and the transport processes, (iii) to evaluate the seasonal and inter-annual variability and (iv) to elucidate the impact of surface heterogeneities on the energy balance at the landscape scale.

2 Study site

The study site is located on Samoylov Island (72°22′ N; 126°30′ E) at the upper part of the Lena River Delta (Fig. 1). It is characterized by a wet tundra landscape typical of northern Siberia. Samoylov Island covers an area of about 4.5 km^2 with an elevated eastern terrace and a lower western flood plain. The region features a typical arctic-continental climate with a mean annual air temperature (MAAT) of about −13 °C and a total annual precipitation around 250 mm (Boike et al., 2008). The ice break-up of the Lena River and the snow melt usually start at beginning of June. The snow-free period

lasts until the end of September, during which maximum air temperatures of about 20 °C are reached. The regional climate and the synoptic conditions are influenced by both the Siberian High and the Polar Low pressure system. During the summer period, intermediate cyclone activity with low intensity are typically observed, while cyclones with high intensity, but short lifetime are more frequently found in winter (Zhang et al., 2004). However, the strong Siberian High strongly affects the Lena Delta region during the winter months and causes air temperatures to fall frequently below −45 °C. The study site is in the zone of continuous permafrost, with permafrost depths reaching 500 to 600 m in the wider area around the study site (Grigoriev, 1960). The soil temperatures are very low: in the depth of the zero annual amplitude (approximately 15 m), the soil temperatures are about −10 °C. The maximum thaw depths during summer range from 0.40 to 0.50 m. The permafrost landscape features characteristic polygonal surface structures, which are typical for the wet tundra landscapes. These patterns are 50 to 100 m^2 large and usually consist of dry elevated rims and depressed centers, which are filled with water-saturated peat soils or shallow ponds. The vegetation at the wet centers is dominated by hydrophilic sedges and mosses, while the elevated dry rims are dominated by mesophytic dwarf shrubs, forbs and mosses. For a more detailed description of the vegetation and landscape characteristics, refer to Are and Reimnitz (2000), Kutzbach et al. (2004), Kutzbach et al. (2007), Boike et al. (2008) and Sachs et al. (2008).

3 Methods

The energy balance equation is written as

$$Q_{\mathrm{net}} = Q_{\mathrm{H}} + Q_{\mathrm{E}} + Q_{\mathrm{G}} + \left[Q_{\mathrm{melt}}\right] + C, \quad (1)$$

where Q_{net} denotes the net radiation, Q_{H} the atmospheric sensible heat flux, Q_{E} the atmospheric latent heat flux, Q_{G} the ground heat flux, Q_{melt} is the energy flux consumed by the snow melt, which can be inferred from to the energy required to thaw the snow

pack, E_{melt}, and the duration of the melt period. As independent field measurements of the components are subject to errors, a residual of the energy balance or closure term C can remain. The measurement setup and the expected margins of error are described in detail in the following paragraphs.

3.1 The Radiation balance

The net radiation budget is the most essential term in the surface energy balance and can be written as

$$Q_{\mathrm{net}} = Q_{\mathrm{S}\downarrow} - Q_{\mathrm{S}\uparrow} + Q_{\mathrm{L}\downarrow} - Q_{\mathrm{L}\uparrow}, \quad (2)$$

where $Q_{\mathrm{S}\downarrow}$ and $Q_{\mathrm{S}\uparrow}$ are the incoming and outgoing short-wave components and $Q_{\mathrm{L}\downarrow}$ and $Q_{\mathrm{L}\uparrow}$ the incoming and outgoing long-wave components, respectively. Using the surface albedo α and Stefan-Boltzmann law, the radiation balance can also be rewritten as

$$Q_{\mathrm{net}} = Q_{\mathrm{S}\downarrow}(1 - \alpha) + \epsilon Q_{\mathrm{L}\downarrow} - \epsilon\sigma T_{\mathrm{surf}}^4, \quad (3)$$

where ϵ is the surface emissivity, T_{surf} the surface temperature and σ is the Stefan-Boltzmann constant. In the present study, a variety of sensors is used to determine the radiation components. The net radiation Q_{net} is measured with the NR-Lite (Kipp & Zonen, The Netherlands) net radiation sensors mounted in 1.5 m height. Additional net radiation measurements (CNR1, Kipp & Zonen, The Netherlands) with higher accuracy are available during mid summer 2007 and for the entire observation period of 2008. The CNR1 four component sensor separately measures all radiation balance components. The sensor is located in the vicinity of the eddy-covariance station and is mounted on a 2 m mast (Fig. 1). Further net radiation measurements with an NR-Lite sensor are conducted at a thermokarst pond, which is approximately 0.8 m deep. These additional measurements are performed to investigate differences in the radiation balance between the tundra surface and shallow water bodies, which are a frequent landscape element (Fig. 1). The evaluation of the accuracy of the employed

net radiation sensors is difficult, since World Meteorological Organization (WMO) quality standards are not available for net radiation sensors. Studies comparing the employed sensors with high-accuracy single component sensors (Brotzge and Duchon, 2000; Kohsiek et al., 2007) suggest a relative measurement accuracy of about 20% for the NR-Lite and about 10% for the CNR1 sensor. A sensor comparison under field conditions shows that daily averages of the NR-Lite sensor are about 5 to 10 Wm^{-2} lower compared to the values obtained by the four component sensor. This bias is in most cases within the assumed error margins, but becomes significant under conditions of low net radiation. In addition to the net radiation sensors, measurements of the upwelling thermal radiation (CG1, Kipp & Zonen, The Netherlands) are available at the standard climate tower (Fig. 1), while spatial differences are measured with distributed infrared surface temperature sensors (IRTS-P, Apogee Instruments, USA). The infrared sensors are mounted on small tripods about 0.8 m above the surface and are directed on different tundra soils. According to instrument specifications, the IRTS-P sensors deliver surface temperatures with an accuracy of about 0.5 °C, from which we infer the upwelling thermal radiation following Stefan-Boltzmann law (compare Eq. 3). We assume emissivities ϵ of 0.98 for wet and 0.96 for dry tundra surfaces (Langer et al., 2010a). In order to obtain a more differentiated picture of the short-wave radiation balance, spatially distributed albedo measurements are conducted with a mobile short-wave radiation sensor (SP1110, Skye Instruments, USA). The albedo measurements are conduced during solar noon under clear-sky conditions to obtain a maximum accuracy.

3.2 Turbulent heat fluxes

The turbulent fluxes of momentum, u_*^2, sensible heat, Q_H and latent heat, Q_E, are determined with the eddy covariance method. The applied eddy covariance system consists of a Campbell C-SAT 3D sonic anemometer and open path LICOR LI-7500 CO_2 and H_2O gas analyzer mounted on a 2.4 m mast. The data are sampled at a rate of 20 Hz using a Campbell CR3000 data logger. Sonic anemometer measurements

are conducted during the entire observation period, while the gas analyzer is operated only during the field campaigns, when a reliable power supply and regular maintenance can be accomplished. The eddy-covariance method is based on high-frequency measurements of the sonic temperature T_s, the specific humidity q, the horizontal and vertical wind speed components u and w. Using Reynolds decomposition, the turbulent flux components can be evaluated from the covariances $\overline{u'w'}$, $\overline{T_s'w'}$ and $\overline{q'w'}$ of the fluctuations u', w', T_s' and q' around the average values of the above quantities as

$$u_*^2 = \overline{u'w'}, \tag{4}$$

$$Q_{HB} = \rho_{air}\, c_p\, \overline{T_s'w'}, \tag{5}$$

$$Q_H = \rho_{air}\, c_p\, \overline{T'w'} = \rho_{air}\, c_p\, (\overline{T_s'w'} - 0.51\,\overline{T}\,\overline{q'w'}), \tag{6}$$

$$Q_E = \rho_{air}\, L_{lg}\, \overline{q'w'}, \tag{7}$$

where Q_{HB} denotes the buoyancy flux, c_p the specific heat capacity of air at constant pressure and L_{lg} the specific latent heat of vaporization of water. Note that in the case of measurements over a frozen (snow) surface, L_{lg} must be replaced by the latent heat of sublimation L_{sg}. The buoyancy flux Q_{HB} differs from the true sensible heat flux Q_H due to the difference between the measured sonic and the real air temperature T_s=T (1+0.51q). Hence, the covariance $\overline{T'w'}$ must be corrected according to Eq. 6, if measurements of the specific humidity q are available (Schotanus et al., 1983). As the LICOR gas analyzer is not operated continuously (see above), this correction cannot be applied during parts of the spring and summer period in 2007. The error induced by interpreting the buoyancy flux as sensible heat flux can be estimated using the Bowen ratio, Q_H/Q_E. For Bowen ratios of approximately 0.5 and average air temperatures of $\overline{T}\approx$300 K, the offset is on the order of 15%, which constitutes an additional error during the respective periods. The turbulent fluxes are calculated for 30 min intervals with the internationally standardized "QA/QC" software package "TK2" (Mauder and Foken,

2004; Mauder et al., 2007), which includes all "state-of-the-art" corrections and tests. The quality assessment follows the scheme of Foken et al. (2004), which is based on tests for stationarity of the turbulence and the integral turbulence characteristic (ITC). In this study, the latter is not applied, since the quality criterion of the integral turbulence characteristic is not well defined in arctic region, where stable atmospheric stratification and intermittent turbulence are common (Lüers and Bareiss, 2009). The stationarity criterion is considered to be sufficiently fulfilled (quality flags 1 and 2), if the average covariance inferred from 5 minute subintervals do not deviate more than 30% from the covariance value over the entire 30 min interval (Foken et al., 2004). A graduation of the deviation is used as a quality measure, expressed with quality flags between 1 and 9. In this study, we accept sensible heat fluxes, if both the quality flags of $\overline{u'w'}$ and $\overline{T_s'w'}$ feature quality values of 6 or better. For the latent heat fluxes Q_E, we use the quality flags of $\overline{u'w'}$ and $\overline{q'w'}$, respectively. This quality standard is recommended for long-term observations (Foken and Wichura, 1996). In other field experiments, this quality level is found to be associated with a relative measurement accuracy of about 15% (Mauder et al., 2006), which we assume as the general accuracy of the obtained turbulent heat fluxes. The quality assessment causes a data reduction of about 3% for the sensible and about 4% for the latent heat fluxes. A further data reduction of about 14% originates from the exclusion of the wind sector between 263° to 277°, which is considered to be the lee area of the measurement setup. In order to obtain the magnitude of the latent heat fluxes, when measurements of the LICOR gas analyzer are not available, we use a model approach based on the parametrization of turbulent fluxes introduced by Høgstrøm (1988). The required parameters, such as roughness lengths and surface resistance to evaporation, are determined by model optimization to available measurements. A detailed description of the used model is given in Appendix D. An overview of the available dataset is given in Table 2, where the modeled latent heat fluxes are marked.

Large-scale differences in the distribution of wet and dry tundra patches as well as shallow ponds potentially create differences in the turbulent heat fluxes on the

landscape scale. It is therefore unclear whether the turbulent heat fluxes obtained at a single location are representative on the landscape scale. The impact of such surface heterogeneities on the turbulent heat flux characteristics is evaluated by a second eddy covariance system during the summer of 2008. The second system is identical to the first one and is used as a mobile station, which is moved in a weekly interval along a 1 km east-west transect across the study site (Fig. 1) while the first system provides simultaneous measurements at the reference location. The flux source area of each half-hour value is determined with the footprint model of Schmid (1994). For the footprint calculations, we assume a constant roughness length $z_0=10^{-3}$ m, which we directly infer from the turbulence measurements under neutral atmospheric stratification (Foken, 2008). This value is consistent with typical roughness lengths reported for short grassland (Oke, 1987; Foken, 2008). The fractions of wet and dry tundra areas as well as polygonal ponds for eddy footprint areas are derived from aerial photographs using supervised classification based on field mapping. The locations of the stationary and the mobile eddy system feature differences in average surface soil moisture according to differences in the polygonal structures. The blending height l_b can be approximated by $l_b \approx L_x/200$ (Garratt, 1994), where L_x is the horizontal scale of heterogeneity. With an approximate size of 20 m of the polygonal surface elements, the measurement height of 2.4 m is well above the blending height, so that the obtained flux values can be considered a spatial average of the footprint areas.

3.3 Ground heat flux

The ground heat flux is essential for permafrost, since it determines the annual active layer dynamics as well as the long-term thermal stability of the permanently frozen ground. In this study we apply two different methods to determine the ground heat flux on different time scales.

3.3.1 Calorimetric method

The calorimetric method is used to evaluate the average ground heat flux over longer periods (Appendix B). The method is based on soil temperature and moisture measurements and calculates the average ground heat flux from changes in the sensible and latent heat content of a soil column. The method has been successfully applied in several permafrost regions and is described e.g. by Boike et al. (1998) and Westermann et al. (2009). We use a measurement setup consisting of an active layer temperature and moisture profile to a depth of 0.5 m, which features 5 thermistors (107-L, Campbell Scientific, USA) and 5 Time-Domain-Reflectometry (TDR) soil moisture probes (CS610-L, Campbell Scientific, USA). The calorimetric methods requires temperature measurements to a depth, where no temperature changes occur in the considered time interval (Appendix B). The temperature profile to the depth of zero annual amplitude (15m) are measured in a 26 m bore-hole with a temperature chain featuring 24 thermistors (XR-420, RBR Ltd., Canada).

3.3.2 Conductive method

The conductive method is primarily used to evaluated the diurnal course of the ground heat flux through the upper most ground surface Westermann et al. (2009). Depending on the surface conditions, the ground surface is either defined as the soil or the snow surface. This method directly calculates the heat flux through the soil surface by solving the differential equation of conductive heat transport (Appendix C), which involves the determination of the thermal conductivity of the soil using shallow temperature profile measurements. As the conductive method is not feasible during periods, when a phase change of water occurs, we exclude the transition periods in spring and fall from such calculations. The employed temperature profiles are installed between the surface and about 30 cm depth in different soil substrates, and consist of at least three thermocouples or thermistors with accuracies better than 0.2 K. The instrumented soil substrates are classified as dry, wet and saturated peat soils (Table 1). The sensors

of each profile are placed in soil layers considered to be homogeneous in composition according to visual examination. Furthermore, we assume constant thermal properties over the considered time intervals (Appendix C), which is a good assumption for wet and saturated soils.

During early spring, the heat flux through the snow cover can be calculated using a similar approach. The determination of the snow thermal properties is based on measurements of the snow density and of temperature profiles in the snow conducted in spring 2008. The boundary conditions for the heat flux calculations are obtained from a infrared surface temperature sensor and a thermistor located at the soil-snow interface. Snow heat fluxes are calculated for periods of constant snow depth, which is measured with a ultrasonic ranging sensor (SR50, Campbell Scientific, USA) located next to the measurement setup. The obtained snow heat fluxes must be considered a rough approximation, since the assumption of constant thermal snow properties may be violated in reality (e.g. Sturm et al., 1997; Zhang, 2005).

3.3.3 Soil and snow parameters

Both methods of ground heat flux calculations require knowledge about the thermal properties of soil or snow (compare Appendix B, C). The heat capacity is an essential parameter, which we infer from soil component analyses of soil samples taken during the field campaigns and in situ water content measurements. We assume an error of 10% on each soil fraction, such as water content, ice content and solid soil matrix. A bulk heat capacity of $2.3 \pm 0.3\,\mathrm{MJ\,m^{-3}\,K^{-1}}$ is used for the solid soil fraction. The obtained soil properties and the associated heat capacities are depicted in Table 1. It is evident, that large uncertainties in heat capacity occur at the dry peat soils, since already small variations in the soil composition induce errors of about 60%. As a consequence, we do not evaluate soil heat fluxes at dry locations. The conductive method allows to determine further soil properties, such as the thermal diffusivity and the heat conductivity (Appendix C), which are displayed in Table 1. For wet tundra soils, the obtained diffusivity values show variations in the range of 20%, which results

in a combined error of about 30% for the heat conductivity. A similar error range is calculated for the snow heat conductivity, which we infer from snow density and snow temperature profile measurements using the conductive method (see Appendix C). For simplicity, we assume an error of 30% as appropriate for all ground heat flux calculations, which is about 10% larger than the errors assumed for the other energy balance components.

3.4 Ancillary measurements

Measurements of air temperature and relative humidity (MP-100, Rotronic, Switzerland) are performed at the standard climate tower in the vicinity of the eddy covariance system (Fig. 1). The snow melt during spring is evaluated based on ultrasonic ranging sensors (SR50, Campbell Scientific, USA) located at the standard climate station and the polygonal pond. In addition, we approximate the evolution of snow free areas during the ablation period by automatic daily photographs of the measurement site. The latent heat content of the snow cover E_{melt} is inferred from spatially distributed measurements of the snow-water equivalent immediately before the onset of snow melt in 2008. With an almost identical snow depth, a similar snow-water equivalent is assumed for 2007.

4 Results

4.1 Seasonal energy balance characteristics

The time span considered in this study ranges from April until September of the years 2007 and 2008. For the description of the seasonal energy balance characteristics, we separate the observation period into three subsections according to the specific seasonal climate conditions. The segmentation of the observation period follows broad synoptic changes, such as the presence of snow, the general air temperature evolution and the occurrence of frost events. While the resulting segmentation is unequally

spaced, we provide an equally spaced overview over the seasonal energy balance in Fig. 5. In the following paragraphs, we also examine inter-annual differences in the surface energy balance.

4.1.1 Spring (1 April–31 Mai)

During the spring period, the daily average air temperatures increase strongly from −16 °C to 6 °C in 2007 and from −25 °C to 2 °C in 2008, with notable differences between both years. The increasing temperatures are accompanied by steadily increasing short-wave radiation after the end of the polar night and the shrinking snow cover towards the end of the period. According to the ultrasonic snow depth sensor, the early spring snow depths are in the range from 0.30 and 0.35 m in both years. These point values are confirmed by spatially distributed snow water equivalent measurements in 2008, which yield an average snow depth of about 0.30 m with an average snow density of 190 kg m^{-3}. The onset and course of the snow melt are almost identical for both years. While the snow melt starts in the mid of May shortly after the beginning of the polar day, it typically does not occur in a single event, but is interrupted by declining air temperatures and subsequent snowfall. The first snow melt event last only a few days (10–19 May 2007/10–14 May 2008), during which the elevated polygonal rims become partly snow-free (Fig. 2). The subsequent snow fall delivers only a few centimeters of additional snow cover, which disappear quickly in the second and final melt event (22–30 May 2007/21–29 May 2008). In the following, we refer to the period before the onset of melting as the pre-melt period, while the subsequent time is denoted the snow melt period. The average radiation budget is positive during the entire spring period and of similar magnitude in both years (Fig. 5). Before the onset of snow melt, the diurnal cycle of the net radiation ranges from −40 to 50 Wm^{-2}, but increases significantly after the snow cover has disappeared. This rapid change in the radiation budget is related to the drastic change of the surface albedo, which is about 0.8 before and 0.2 after snow melt. This change in the surface characteristics is reflected in all energy balance components, which we depict in Fig. 2. The turbulent sensible heat flux ranges

from −30 to 20 W m^{-2} during the pre-melt period and basically follows the course of the surface radiation budget. About two days before the onset of snow melt, persistent negative sensible heat fluxes are observed, which appear to be partly decoupled from the net radiation (Fig. 2). The snow surface temperature approaches 0 °C around noon. This relation indicates that both the turbulent sensible heat fluxes as well as the incoming short-wave radiation contribute to the snow melt. As soon as snow free areas are present, the sensible heat flux rapidly exceeds values of 40 W m^{-2}. After the snow cover has disappeared entirely at the end of May, the sensible heat flux reaches peak values of 90 W m^{-2}. A similar evolution is observed for the latent heat flux, which is between 0 and 10 W m^{-2} before the onset of snow melt and quickly increases to values of 50 W m^{-2} during the first snow melt event. After the final melt period, the latent heat flux exceeds values of 100 W m^{-2} and features an average value of 35 W m^{-2} during the last ten spring days of 2008. This average heat flux corresponds to 30 MJ m^{-2} or to 12 mm of evaporated water, respectively. As the snow water equivalent of 2008 amounts to approximately 57 mm, about 20% of the snow cover sublimate or evaporate during the last spring days. Hence, the snow cover effectively supplies 45 mm to the summer time water budget, which constitutes about 20% of the precipitable water of the entire observation period. Considering similar snow heights and the identical course of the ablation process, a similar magnitude of snow cover contribution to the water balance can be assumed in 2007.

The atmospheric stratification is reflected in the stability parameter ζ, which is essentially zero during neutral conditions, larger than zero for stable and smaller than zero for unstable atmospheric stratifications. During the pre-melt period, the atmospheric stratification changes frequently between stable and unstable conditions (Fig. 2). At this time, neutral stratifications occur occasionally in conjunction with wind speeds larger than 2 m s^{-1}. With the onset of snow melt, the wind speed is generally high and the atmospheric stratification becomes essentially neutral (Fig. 2). The average ground heat flux during the spring period is remarkably positive and dominated by storage of sensible heat in both years (Table 2), which is associated with a steady warming of the

deeply frozen soil. A closer look at the evolution of the ground heat storage (Fig. 3) reveals a faster soil warming in early spring 2007. This difference in the evolution of the ground heat budget compared to 2008 is related to significantly warmer air and snow surface temperatures, but relatively cold soil temperatures in early spring 2007 (Table 2). In both years, the amplitude of the ground heat flux through the snow cover typically ranges from −20 and 20 W m^{-2} during the pre-melt period and is thus in the range of the turbulent sensible heat fluxes.

4.1.2 Summer (1 June–31 August)

The summer period is characterized by a strong short-wave radiative forcing, a snow-free surface, day time temperatures well above the freezing point and the thawing of the active layer (Fig. 5, Table 2). Polar day conditions last until 7 August, featuring high values of incoming short-wave radiation. Daily averages of incoming short-wave radiation frequently exceed values of 300 W m^{-2} under clear-sky conditions and can be as low as 20 W m^{-2} under overcast situations, which occur frequently. The reduced solar radiation during cloudy conditions is partly compensated by the thermal sky radiation, which is then significantly increased. The daily average of incoming long-wave radiation typically ranges from 280 W m^{-2} for clear-sky and 380 W m^{-2} for cloudy situations. The daily average of emitted long-wave radiation varies between 330 W m^{-2} and 420 W m^{-2}, which corresponds to average surface temperatures of 3 and 20 °C. Consequently, the net long-wave losses frequently exceed 100 W m^{-2} during clear-sky conditions, while they are almost zero during overcast situations. The average summer net radiation of 2007 is slightly higher compared to 2008 (Fig. 5), which is most likely caused by differences in cloudiness. This is also confirmed by the precipitation rates, which are doubled during the early summer period of 2008.

In both years, unstable stratifications (ζ<0) occur frequently during the day, but usually do not last longer than 12 h. The nights are dominated by neutral stratifications ($\zeta \approx 0$), while stable atmospheric conditions (ζ>0) are only observed occasionally under calm conditions and highly negative values of the net radiation. The turbulent heat

fluxes constitute dominant components in the summer time energy balance. About 20 to 30% of the available radiative energy is consumed by turbulent sensible heat flux, while evapotranspiration amounts to about 40 to 50% (Fig. 5, Table 2). The turbulent heat fluxes show a strong diurnal cycle and frequently exceed values of 130 W m^{-2} for the sensible and 150 W m^{-2} for the latent heat flux during the day. During the night, significant negative sensible heat fluxes on the order of −20 W m^{-2} are observed, while negative latent heat fluxes (dew fall) occur only occasionally. Such events are then associated with a highly negative net radiation and low surfaces temperatures, as they occur at the end of the summer section. We depict an exemplary period during late summer 2008 in Fig. 4, which illustrates the typical diurnal cycle of the heat flux components forced by the incoming solar radiation. The wind speed appears to be associated with a diurnal pattern (Fig. 4), which indicates enhanced turbulent heat exchange during the day and lowered turbulence during the night. A dependence of the wind direction on the day time is not detected. For both years, the average Bowen ratio Q_H/Q_E is essentially below zero and indicates high rates of evapotranspiration. The amount of evaporated water is about 70 mm in 2007 and about 100 mm in 2008, which is about the same as the precipitation measured in the concerned sub-periods (Table 2).

When comparing the turbulent heat fluxes for the two years, it must be emphasized that the average flux values depicted in Table 2 are based on different sub-periods and are not directly comparable. For the inter-annual comparison, we make use of modeled latent heat flux values. The gap-filled energy balance with equally spaced averaging intervals is illustrated in Fig. 5. Inter-annual differences in the turbulent heat fluxes occur during the early and mid summer period, when the net radiation budget of 2008 is also affected by clouds. The reduced radiation budget results in generally decreased sensible heat fluxes, while the latent heat fluxes appear to be slightly increased during early summer 2008. In both years, the ground heat flux is a remarkable term in the summertime energy balance, which consumes about 20 to 25% of the available radiation budget. The ground heat flux is characterized by active layer thawing, which makes up 60% of the entire ground heat flux (Fig. 3). The remaining fraction

is stored as sensible heat in the deeper soil. With a high soil water content of about 70%, a maximum thaw depth of only 0.40 m is reached during the summer period. The shallow thaw depth causes strong soil temperature gradients in the active layer, which enhance the ground heat flux. The ground heat flux shows a strong diurnal cycle and frequently exceeds values of 50 W m^{-2} during the day (Fig. 4), while negative ground heat fluxes are observed only occasionally during clear-sky nights.

4.1.3 Fall (1 September–30 September)

We denote a short transition period as fall segment, which in both years is characterized by steadily decreasing air and surface temperatures, the onset of freezing and occasional snow fall, while a continuous snow cover does not form yet. In both years, the fall period starts with air and surface temperatures well above the freezing point and ends with temperatures around 0 °C. Only occasional freezing events are observed during the fall period 2007, while sustained freezing already occurs in 2008. The inter-annual difference in the temperature evolution is reflected in the average air and surface temperatures, as well as in the ground heat fluxes (Table 2). In 2008, the entire active layer already approaches temperatures of 0 °C at 17 September, but warms again for one week, before the soil temperatures finally reach the zero-curtain around 25 September. In contrast, the soil temperature in 2007 never enters the zero-curtain during the fall period. Hence, the average ground heat flux in 2007 only indicates positive sensible heat storage (Table 2), which is caused by the delayed warming of soil in a depth of 1 to 10 m, which in 2008 is almost equal to the released latent heat from the initial freezing (Table 2). The average radiation budget is significantly reduced, but still positive in both years and features a distinct diurnal cycle with daytime values on the order of 100 W m^{-2}. A negative net radiation on the order of −50 W m^{-2} is frequently observed during the nights in 2008, which occurs only sporadically in 2007. Contrary to the summer segment, the reduced radiative losses during the nights and the significantly higher amount of precipitation indicate an increased cloudiness in fall 2007 (Table 2). The average atmospheric sensible heat flux is directed towards the surface in

both years, but is more negative in 2008. This corresponds to the pronounced negative night time temperature gradients (T_{surf}–T_{air}) in 2008. Despite the reduced net radiation, the latent heat fluxes still play a dominant role in the surface energy balance (Fig. 5). Almost 50% of the net short-wave radiation is consumed by evapotranspiration, which corresponds to the amount of precipitation during the fall section. The atmospheric stratification in both years is dominated by neutral conditions, corresponding to high wind speeds. However, occasional events of stable stratification occur during calm nights, when the radiation budget becomes highly negative and strong temperature gradients in the atmospheric boundary layer arise. In accordance with the described inter-annual differences in the energy balance evolution, such events are observed more frequently in 2008. In both years, the energy balance closure term C is relatively high (Table 2). This high closure term can be partly explained by an underestimation of the net radiation: a comparison of the NR-Lite and the four component sensor during fall 2008 reveals an offset of 6 W m^{-2}, which is substantial considering the generally low radiation budget.

4.2 Spatial energy balance variability

The polygonal tundra features pronounced micro-scale heterogeneity, regarding the surface moisture and vegetation cover. The elevated polygonal rims are typically covered with dry mosses, while the lowered centers are filled with wet peat soils or shallow ponds. Considering these surface heterogeneities, spatial differences in the energy balance are likely to occur. Spatially distributed albedo measurements yield typical values in the range of 0.2 for dry and 0.15 for wet tundra surfaces. The latter value is consistent with the average albedo of 0.14 obtained from measurements of the four component radiation sensor, which is directed towards a wet tundra spot. During local noon and clear-sky conditions, the typical surface temperature differences between dry and wet locations are on the order of 5 to 10 °C, which indicates increased radiative losses at the dry and warm surfaces. During the nights and during overcast periods, the spatial differences in the surface temperature and thus the radiation budget largely

vanish. However, sustained differences in the net radiation budget exist between the tundra soil and the polygonal pond (Fig. 6). During the pre-melt period, the net radiation at the polygonal pond is constantly 5 to 10 W m^{-2} lower compared to the tundra surface. After the melt period, the measurements show a significantly higher net radiation at the water body on the order of 20 to 30 W m^{-2}, which gradually diminish in the course of the summer season (Fig. 6).

Spatial differences in the turbulent heat fluxes are examined for an exemplary situation at the second location of the mobile eddy system. According to the footprint analysis, the second mobile eddy station features a 20% higher fraction of dry surface area than the reference location (Fig. 1). The simultaneous measurements at both location indicates that moderate spatial differences on the order of 20 W m^{-2} (10–20%) can be expected for the sensible and latent heat fluxes under conditions of high radiative forcing (Q_{net} > 200 W m^{-2}) (Fig. 7), which occur only sporadically during the summer period (Fig. 7). During the fall period, when the radiation balance is further reduced, almost no spatial differences in sensible and latent heat fluxes are measured along the transect.

5 Discussion

5.1 Data quality

The quality of the energy balance measurements can be evaluated according to the energy balance ratio (Wilson et al., 2002)

$$\mathrm{EBR} = \frac{Q_H + Q_E}{Q_{net} - Q_G}, \tag{8}$$

which in the case of a closed energy balance (C=0) is unity. The EBR distribution contains information about the characteristics of the errors of the energy balance measurements, such as the presence of systematic and random errors. Since the EBR is highly

sensitive to measurement errors during situations of low heat fluxes, we only consider measurements conducted during conditions of $Q_{net} \leq -30\,W\,m^{-2}$ and $Q_{net} \geq 30\,W\,m^{-2}$. The normalized EBR distribution of the entire data set roughly resembles a normal distribution featuring a mean value of 0.86, a standard deviation of 0.34, and a slightly positive skewness of 0.47 (Fig. 8). If only random measurement errors would be involved, the expected EBR distribution should be more similar to the normal distribution displayed in Fig. 8. This distribution is calculated assuming a relative error of 15% for Q_H+Q_E (see Sect. 3.2) and 20% for $Q_{net}-Q_G$ (see Sect. 3.1), which results in a standard deviation of 0.25. The measured EBR distribution suggests that the energy balance is systematically not closed by about 15%, which is potentially caused by a negative bias of the turbulent heat fluxes or a positive bias of the term $Q_{net}-Q_G$. The latter is not likely since the employed net radiation sensor (NR-Lite) slightly underestimates the radiation budget (compare Sect. 3.1), while the ground heat flux would have to be unrealistically small to cause a positive bias of $Q_{net}-Q_G$. The shape and width of the measured EBR distribution is similar to the normal distribution, which suggests that the assumed error margins of the energy balance components are realistic.

5.2 Controlling factors in the energy balance

Three factors can be identified that essentially determine the energy balance characteristics at the investigated wet tundra landscape. The determining factors are (i) the snow cover, (ii) the presence or absence of a cloud cover and (iii) the thermal state of the permafrost.

(i) Although the snow cover is only shallow at the study site, it has strong implications for the surface energy balance. Firstly, the albedo of the snow cover is about a factor of four higher than the albedo of the snow-free tundra surface. Secondly, the thermal conductivity of snow is about a factor of two lower than the thermal conductivity of frozen peat. The second point is of particular importance during winter, when the low thermal conductivity of the snow cover impedes the release of

energy from the ground and leads to a reduced ground heat flux (see Langer et al., 2010b). During spring, however, the soil has already cooled out, so that the lower thermal conductivity of the snow is of minor importance for the ground heat budget and the surface energy balance (Goodrich, 1982). In contrast, the high albedo of the snow has a strong impact on the surface energy budget during the spring period, when the incoming short-wave radiation already features high values. At the study site, the snow cover effectively reduces the net short-wave radiation until the beginning of the polar day period. The melting of the snow cover with the associated change in surface albedo triggers a sudden change from a winter to a summer surface energy balance, so that the timing of snow melt is a critical point in the annual course of the surface energy balance. In both investigated years, the timing of the snow melt is almost identical. Iijima et al. (2007) point out that snow cover disappearance in eastern Siberia is strongly related to the attenuation of the Siberian-High with subsequent advection of warm and moist air masses from the west. According to the distinct contribution of sensible atmospheric heat flux to the snow melt, our measurements indicate the presence of warm air masses. However, we identify the short-wave radiation as the dominant factor in the snow melt process. We emphasize that the correct representation of the snow melt must be considered crucial in permafrost modeling. It is therefore highly desirable to gather a better understanding of the triggering processes of the snow melt and their representation in models.

(ii) The large-scale advection of warm air is usually related to increased cloudiness, which essentially alters the surface radiation budget and the prevailing surface and air temperature conditions. During the spring period, our results indicate that the observed inter-annual differences in the ground temperatures are caused by different air temperatures, which are presumably related to the general synoptic conditions. During the summer months, the net radiation is essentially reduced for cloud-covered skies, which leads to an effective surface cooling. During the summer months, the cloud cover has an impact on the turbulent heat fluxes, while

the ground heat budget is only marginally affected. Since the average surface temperature is not drastically reduced by the increased cloud cover the active layer thawing is only slightly affected. During the fall period, the contrary effect of a cloud cover is observed, as clouds reduce the long-wave radiative losses, which in turn leads to increased surface temperatures. The impact of clouds on the ground heat budget is observed to be largest during the fall season, when increased cloudiness significantly delays the refreezing process in 2007, while the average air temperatures are similar. This ambiguous influence of the cloud cover on the surface radiation budget in the Arctic is confirmed in several studies (Curry et al., 1996; Intrieri et al., 2002; Shupe and Intrieri, 2004).

(iii) During the entire observation period, the ground heat flux is an essential component in the surface energy balance. About 20% of the net radiation is stored as latent and sensible heat in the ground, which is in the upper range of typical values reported for other arctic permafrost regions (Boike et al., 1998; Lynch et al., 1999; Eugster et al., 2000; Westermann et al., 2009). The high contribution of the ground heat flux to the surface energy balance is clearly caused by the cold permafrost temperatures, the shallow active layer depth and the large annual surface temperature amplitude, which is related to the continental climate conditions. Due to the low permafrost temperatures, the sensible heat storage makes up about 50% of the entire ground heat flux. This clearly limits the value of the widely used Stefan equation, that evaluates the active layer dynamics by assuming the ground heat flux to be entirely used for thawing. As the contribution of the ground heat flux to the surface energy balance is significant even in the summer months, an adequate representation of the soil domain in global climate models seems mandatory, if the land-atmosphere exchange processes in permafrost regions are to be modeled correctly. This issue is of particular importance, as permafrost areas with continental climate, where a significant contribution of the ground heat flux can be expected, occupy vast areas in the Arctic. The improvement of modeling results by employing more realistic parameterizations of the soil processes

has been outlined in a number of studies (e.g Peters-Lidard et al., 1998; Cox et al., 1999; Viterbo et al., 1999; Pitman, 2003). In the second part of this study (Langer et al., 2010b), the representation of the soil and particularly of soil freezing processes in models is discussed in more detail.

5.3 Spatial differences of the surface energy balance

In this study, spatial differences in the surface energy balance are observed for (i) the radiation budget and (ii) the turbulent fluxes.

(i) With albedo differences between wet and dry areas on the order of 0.05, the net short-wave radiation can be on average by up to $7\,W\,m^{-2}$ higher at wet compared to dry areas, while the differences can exceed $25\,W\,m^{-2}$ for high radiative forcing during midday. This difference is further contrasted by the higher surface temperatures of dry surfaces, which can be about 5 K warmer than wet surfaces during conditions of high radiative forcing. It is therefore conceivable, that the net radiation balance at wet and dry locations can deviate up to $50\,W\,m^{-2}$ from each other. This difference is partly attenuated during the night, when the wet surfaces are warmer and the short-wave forcing is nonexistent or negligible. Moreover, due to the rare occurrence of high values of net radiation we assume that the average differences in net radiation between wet and dry areas does not exceed $10\,W\,m^{-2}$. More pronounced spatial differences in the radiation balance are measured between the tundra and water bodies. The net radiation of the investigated pond is slightly lower in frozen conditions during spring, but significantly higher during the summer months. Albedo differences during spring are not likely, since all surfaces are covered by snow, so that the measured differences in the radiation budget are most likely explained by increased surface temperatures at the frozen pond during spring. During the summer period, almost similar average surface temperatures are observed for the water body and the tundra surface (see Langer et al., 2010b). Hence, the differences in net radiation are most likely explained by a lower albedo

of the water body. The pond investigated in this study indicates that small shallow water bodies can have a significant influence on the radiation budget in polygonal tundra landscapes, as they are frequent landscape elements. While the impact of larger water bodies on the arctic climate conditions has been investigated (Krinner, 2003; Rouse et al., 2005; Krinner and Boike, 2010), such small water bodies have not received similar attention. It is thus highly desirable to evaluate the impact of small water bodies on the larger-scale surface energy balance, particularly since such micro-scale landscape structures usually remain undetected in remote sensing applications and are neglected in model approaches. In the second part of this study (Langer et al., 2010b), the winter aspect of the surface energy balance of small ponds is addressed in more detail.

(ii) Micro-scale differences of the turbulent fluxes are verified by the mobile eddy covariance system. The measurements reveal differences in sensible and latent heat fluxes according to variations in the fractions of dry and wet surfaces in the footprint areas (Fig. 4). The observed spatial variations are caused by the small scale surface temperature differences between wet and dry areas. As the temperature difference between wet and dry surfaces depends on the net radiation budget, significant differences in the turbulent fluxes are limited to clear-sky situations, which only occur occasionally during the summer period. Since the long-term averages of the turbulent heat fluxes are almost equal for the stationary and the mobile eddy covariance system, we conclude that the presented sensible and latent heat fluxes are representative on the landscape scale.

6 Conclusions

In this study we present a comprehensive surface energy balance study of at wet polygonal tundra landscape from April to September (2007–2008) considering seasonal and spatial variations. This comprehensive study improves the understanding of the energy exchange processes at soil-atmosphere interface of a typical permafrost landscape. The obtained results can be of great value for the improvement and development of permafrost model schemes, as they are intended to be incorporated in climate models. In particular the following conclusions can be drawn from the obtained results:

– The spring, summer and fall energy balance is dominated by the net radiation. Critical factors for the surface radiation budget are in particular the snow cover and clouds. The timing of snow melt in spring essentially controls the amount of short-wave radiation that is available for energy partitioning. The relevance of the snow cover for the surface radiation budget is further intensified by the presence of almost polar day conditions. The cloud cover has its greatest impact on the ground heat budget during fall, when radiative losses are largely reduced and the refreezing of the tundra is significantly delayed.

– The surface energy balance is essentially affected by the ground heat flux, which is of similar magnitude as the sensible heat flux. The significant ground heat flux is induced by strong temperature gradients in the shallow active layer and in the permafrost body, which are the result of both continental climate and high soil water and ice content.

– The larger scale surface energy balance is significantly affected by the occurrence of small water bodies, which essentially increase the surface radiation budget and the ground heat storage of the tundra landscape during the summer time.

Appendix A

Definitions and constants

Q_{net} – net radiation
$Q_{S\downarrow}$ – incoming short-wave radiation
$Q_{S\uparrow}$ – outgoing short-wave radiation
ΔQ_S – net short-wave radiation
$Q_{L\downarrow}$ – incoming long-wave radiation
$Q_{L\uparrow}$ – outgoing long-wave radiation
ΔQ_L – net long-wave radiation
Q_{HB} – buoyancy flux
Q_H – sensible heat flux
Q_E – latent heat flux
Q_G – ground or snow heat flux
E_{melt} – latent heat content of the snow pack
Q_{melt} – energy flux through melting of the snow pack
C – residual of the energy balance
u – horizontal wind speed
w – vertical wind speed
T_{air} – air temperature
T_s – sonic air temperature
T_v – virtual temperature
q – specific humidity
u_* – friction velocity
z_0 – aerodynamic roughness length
$\zeta = z/L_*$ – stability parameter (z: measurement height, L_*: Obukhov length)
$\kappa = 0.4$ – von Kármán constant
R_H – relative humidity
T_{surf} – surface temperature
α – surface albedo
ϵ – surface emissivity
σ – Stefan-Boltzmann constant

c_p – specific heat capacity of air at constant pressure
ρ_{air} – density of air
$\rho_w = 1.0\,\mathrm{g\,cm^{-3}}$ – density of water
$\rho_{ice} = 0.91\,\mathrm{g\,cm^{-3}}$ – density of ice
$L_{sl} = 0.33\,\mathrm{MJ\,kg^{-1}}$ – specific latent heat of fusion of water
$L_{lg} = 2.5\,\mathrm{MJ\,kg^{-1}}$ – specific latent heat of vaporization of water
$L_{sg} = 2.8\,\mathrm{MJ\,kg^{-1}}$ – specific latent heat of sublimation of ice
D_h – thermal diffusivity
K_h – thermal conductivity
C_h – volumetric heat capacity
$C_{h,w} = 4.2\,\mathrm{MJ\,m^{-3}\,K^{-1}}$ – volumetric heat capacity of water
$C_{h,i} = 1.9\,\mathrm{MJ\,m^{-3}\,K^{-1}}$ – volumetric heat capacity of ice
$C_{h,a} \approx 0.001\,\mathrm{MJ\,m^{-3}\,K^{-1}}$ – volumetric heat capacity of air
$C_{h,s} \approx 2.3\,\mathrm{MJ\,m^{-3}\,K^{-1}}$ – volumetric heat capacity of the solid soil matrix
A bulk heat capacity $C_{h,s}$ is used for the solid matrix, since typical values of organic and mineral soils do not differ more than 20% from each other (compare Sect. 3.3.3)

Appendix B

The calorimetric method

The change of the sensible heat content of a soil volume with area A and depth z with uniform temperature and a constant heat capacity is given by

$$E(t_2) - E(t_1) = A\, z\, C_h\, (T(t_2) - T(t_1)), \tag{B1}$$

where $T(t_1)$ and $T(t_2)$ are the temperatures at times t_1 and t_2. In the case of a temperature dependence of the heat capacity and non-uniform temperature distribution in depth $C_h(T(t,z))$, Eq. B1 must be rewritten to

$$E(t_2) - E(t_1) = A \int_0^z \int_{T(t_1,z')}^{T(t_2,z')} C_h(T')\, dT'\, dz'. \tag{B2}$$

The temperature dependence of C_h is caused by the phase change of water and is calculated as

$$C_h(T) = \theta(T)\, C_{h,w} + (\theta_{max} - \theta(T))C_{h,i} + (1 - P_{dry})C_{h,s}, \quad \text{(B3)}$$

where P_{dry} is the porosity of the soil, θ_{max} is the maximum unfrozen water content, and $\theta(T)$ is the temperature-dependent liquid water content, which is referred to as "freeze characteristic". The volumetric fraction of the solid matrix and thus the porosity is determined from soil samples and the volumetric water and ice content is obtained from in situ TDR-measurements (see Boike et al., 2003, for details). To account for the release or consumption of energy through freezing and thawing, Eq. B2 is extended to

$$E(t_2) - E(t_1) = A \int_0^z \rho_w L_{sl}[\theta(T(t_2,z')) - \theta(T(t_1,z'))]\, dz' + A \int_0^z \int_{T(t_1,z')}^{T(t_2,z')} C_h(T')\, dT'\, dz'. \quad \text{(B4)}$$

This method of ground heat flux determination requires knowledge about the soil-specific freeze characteristics or direct measurements of the soil water content. The employed soil temperature measurements must extend to a depth of constant temperatures during the considered measurement period. If such a deep temperature profile is not available, the heat flux below the measurement depth can be obtained by solving the heat transfer equation at the lower boundary (Eq. C3, see below).

Appendix C

The conductive method

The conductive method makes use of the heat transfer equation to determine the ground heat flux. Firstly, the thermal conductivity of the soil or snow must be evaluated. This procedure requires a time series of soil temperatures measured in a profile at three depths, $T_m(z_1,t)$, $T_m(z_2,t)$ and $T_m(z_3,t)$ with $z_1<z_2<z_3$. The one-dimensional heat transfer equation is written as

$$C_h(t,z)\frac{\partial T(t,z)}{\partial t} = \frac{\partial}{\partial z}K_h(t,z)\frac{\partial T(t,z)}{\partial z} \quad \text{(C1)}$$

where $T(t,z)$ denotes the soil or snow temperature at time t and depth z. Assuming constant heat capacities and thermal conductivities $K_h(t,z)$ in space and time, the one-dimensional heat transfer equation is simplified to

$$\frac{\partial T(z,t)}{\partial t} = D_h \frac{\partial^2 T(z,t)}{\partial z^2} \quad \text{(C2)}$$

where $D_h = K_h/C_h$ denotes the thermal diffusivity. The solution of Eq. C2) is obtained by the partial differential equation solver incorporated in MATLAB. The required boundary conditions are given by the outer sensors of the temperature profile, $T_m(z_1,t)$ and $T_m(z_3,t)$. The initial conditions are inferred from linear interpolation between all the three sensors at $t=0$, which is not critical to the solution, since it becomes independent of the initial temperature state after a few time steps in the shallow soil layer. The numerical solver delivers the temperature distribution of the considered spatial domain, including $T(t,z_2)$, so that the thermal diffusivity D_h can be evaluated by minimizing the least mean square error to the measured temperatures at depth z_2, $T_m(t,z_2)$. We use time series of several days for the determination of the thermal diffusivity of different surface substrates (see Table 1). Note that this procedure assumes homogeneous substrate composition in the considered soil or snow layer, which may not be the case in nature. The heat flux through the upper boundary can be evaluated by

$$Q_G(t) = D_h C_h \left.\frac{\partial T(z,t)}{\partial z}\right|_{z=z_1}. \quad \text{(C3)}$$

The conductive methods has been applied by Westermann et al. (2009), while similar concepts are explored by Nicolsky et al. (2009).

Appendix D

Modeling of latent heat fluxes

This model approach is used when eddy covariance measurements of the latent heat flux are not available. The model is based on eddy-covariance measurements of wind speed and sonic temperature and uses ancillary measurements of relative humidity and surface temperature.

The model is based on commonly used parameterizations of the atmospheric transport mechanisms (Foken, 2008), which we shortly describe in the following. According to Monin-Obukhov similarity theory, the latent heat flux can be related to the difference between specific humidity at measurement height $\overline{q}(z_m)$ and roughness length $\overline{q}(z_0)$ by

$$\overline{q'w'} = (\overline{q}(z_m) - \overline{q}(z_0))\,\kappa\,u_* \left[\ln\frac{z_m}{z_0} - \Psi_W\left(\frac{z_m}{L_*}, \frac{z_0}{L_*}\right)\right]^{-1} \tag{D1}$$

with

$$\Psi_W\left(\frac{z_m}{L_*}, \frac{z_0}{L_*}\right) = \int_{z_0}^{z_m} \frac{1 - \varphi_W(z'/L_*)}{z'} dz', \tag{D2}$$

where κ denotes the von Kármán constant (0.4), u_* the friction velocity and $\varphi(z/L_*)$ is a universal function (see below). The quotient z/L_* denotes the stability parameter ζ, where L_* is the Obukhov length L_* defined in Eq. D6. Using Eq. D1 and rewriting the turbulent transport terms as atmospheric resistance r_a, the latent heat flux Q_E can be evaluated by

$$Q_E = -\frac{\rho_{air}\,L_{lg}}{r_a + r_s}\left(\overline{q}(z_m) - \overline{q}(z_0)\right), \tag{D3}$$

with

$$r_a := (\kappa u_*)^{-1}\left[\ln\frac{z_m}{z_0} - \Psi_W\left(\frac{z_m}{L_*}, \frac{z_0}{L_*}\right)\right], \tag{D4}$$

where ρ_{air} is the density of air, L_{lg} the latent heat of vaporization of water and r_s the surface resistance to evapotranspiration (Garratt, 1994). For calculation over the snow surface L_{lg} must be replaced by the latent heat of sublimation L_{sg}. The specific humidity at the surface $q(z_0)$ is inferred from to the surface temperature T_{surf} using the Magnus formula that delivers the water vapor pressure over a water surface or an ice surface, respectively. During the summer month, the surface is not entirely saturated, and a surface resistance is required to account for the reduced availability of water. We use measured time series of the latent heat flux to fit the surface resistance of summer and fall. We assume the surface resistance to be constant in time. The roughness length z_0 can be inferred from measurements of u_*^2 under neutral atmospheric conditions (Foken, 2008). Note that we assume the aerodynamic roughness length to be the

roughness length of water vapor. The fitting procedure yields a surface resistance of about $50\,s\,m^{-1}$ with a roughness length determined to be 10^{-3} m during the summer period. When the ground is snow-covered, the surface resistance is set to zero, while the roughness is determined to 5×10^{-4} m. The universal universal function Ψ_W is chosen according to Høgstrøm (1988) as

$$\varphi_W(\zeta) = \begin{cases} 0.95\,(1 - 11.6\,\zeta)^{-1/4} & \text{for } \zeta \le 0 \\ 0.95 + 7.8\,\zeta & \text{for } \zeta > 0 \end{cases} \tag{D5}$$

The Obukhov length L_*, which is required for the stability parameter ζ is directly obtained from eddy-covariance measurements using

$$L_* = -\frac{u_*^3 \overline{T}_v}{\kappa\,g\,(\overline{T_v'w'})}, \tag{D6}$$

where g is the gravitational acceleration and T_v the virtual temperature. Note that the virtual temperature T_v is substituted by the sonic temperature T_s (Foken, 2008).

Acknowledgements. We are thankful to the Department of Micro-Meteorology of the University of Bayreuth headed by Thomas Foken for providing the eddy-covariance post-processing software. We are also thankful to Claudia Fiencke and Tina Sanders from the Institute of Soil Science of the University of Hamburg for the soil component analyses. We gratefully acknowledge financial support by the Helmholtz Association through a grant (VH-NG 203) awarded to Julia Boike.

References

Are, F. and Reimnitz, E.: An overview of the Lena River Delta setting: geology, tectonics, geomorphology, and hydrology, J. Coast. Res., 16, 1083–1093, 2000. 905

Boike, J., Roth, K., and Overduin, P.: Thermal and hydrologic dynamics of the active layer at a continuous permafrost site (Taymyr Peninsula, Siberia), Water Resour. Res., 34, 355–363, 1998. 911, 923

Boike, J., Roth, K., and Ippisch, O.: Seasonal snow cover on frozen ground: Energy balance calculations of a permafrost site near Ny-Alesund, Spitsbergen, J. Geophys. Res.-Atmos., 108, 8163–8173, 2003. 929

Boike, J., Wille, C., and Abnizova, A.: Climatology and summer energy and water balance of polygonal tundra in the Lena River Delta, Siberia, J. Geophys. Res.-Biogeo., 113, G03025, doi:10.1029/2007JG000540, 2008. 904, 905

Brotzge, J. and Duchon, C.: A field comparison among a domeless net radiometer, two four-component net radiometers, and a domed net radiometer, J. Atmos. Ocean. Tech., 17, 12, 1569–1582, 2000. 907

Brown, J., Ferrians Jr., O., Heginbottom, J., and Melnikov, E.: Circum-Arctic map of permafrost and ground-ice conditions, US Geological Survey Circum-Pacific Map, 1997. 903, 940

Callaghan, T., Björn, L., Chernov, Y., Chapin, T., Christensen, T., Huntley, B., Ims, R., Johansson, M., Jolly, D., Jonasson, S., et al.: Effects of changes in climate on landscape and regional processes, and feedbacks to the climate system, AMBIO, 33, 459–468, 2004. 903

Christensen, T. and Cox, P.: Response of methane emission from Arctic tundra to climatic change: Results from a model simulation, Tellus B, 47, 301–309, 1995. 903

Christensen, T., Ekberg, A., Ström, L., Mastepanov, M., Panikov, N., Öquist, M., Svensson, B., Nykänen, H., Martikainen, P., and Oskarsson, H.: Factors controlling large scale variations in methane emissions from wetlands, Geophys. Res. Lett., 30, 1414, doi:10.1029/2002GL016848, 2003. 903

Comiso, J.: Arctic warming signals from satellite observations, Weather, 61, 2006. 902

Cox, P., Betts, R., Bunton, C., Essery, R., Rowntree, P., and Smith, J.: The impact of new land surface physics on the GCM simulation of climate and climate sensitivity, Clim. Dynam., 15, 183–203, 1999. 924

Curry, J., Rossow, W., Randall, D., and Schramm, J.: Overview of Arctic cloud and radiation characteristics, J. Climate, 9, 1731–1764, 1996. 923

Davidson, E. and Janssens, I.: Temperature sensitivity of soil carbon decomposition and feedbacks to climate change, Nature, 440, 165–173, 2006. 903

Eugster, W., Rouse, W., Pielke Sr., R., McFadden, J., Baldocchi, D., Kittel, T., Chapin, F., Liston, G., Vidale, P., Vaganov, E., and Chambers, S.: Land-atmosphere energy exchange in Arctic tundra and boreal forest: available data and feedbacks to climate, Global Change Biol., 6, 84–115, 2000. 923

Foken, T.: Micrometeorology, Springer, 2008. 910, 931, 932

Foken, T. and Wichura, B.: Tools for quality assessment of surface-based flux measurements, Agr. Forest Meteorol., 78, 83–105, 1996. 909

Foken, T., Göckede, M., Mauder, M., Mahrt, L., Amiro, B., and Munger, J.: Post-field data quality control, in: Handbook of Micrometeorology: A Guide for Surface Flux Measurement and Analysis, Kluwer, 2004. 909

Garratt, J.: The atmospheric boundary layer, Cambridge Univ. Pr., 1994. 910, 931

Goodrich, L.: The influence of snow cover on the ground thermal regime, Can. Geotech. J., 19, 421–432, 1982. 922

Grigoriev, N.: The temperature of permafrost in the Lena delta basin – deposit conditions and properties of the permafrost in Yakutia, Yakutsk, chap. 2, 97–101 pp., 1960. 905

Hansen, J., Ruedy, R., Sato, M., Imhoff, M., Lawrence, W., Easterling, D., Peterson, T., and Karl, T.: A closer look at United States and global surface temperature change, J. Geophys. Res.-Atmos., 106, 23947–23963, 2001. 902

Hinzman, L., Bettez, N., Bolton, W., Chapin, F., Dyurgerov, M., Fastie, C., Griffith, B., Hollister, R., Hope, A., Huntington, H., et al.: Evidence and implications of recent climate change in northern Alaska and other arctic regions, Climatic Change, 72, 251–298, 2005. 903

Hobbie, S., Schimel, J., Trumbore, S., and Randerson, J.: Controls over carbon storage and turnover in high-latitude soils, Global Change Biol., 6, 196–210, 2000. 903

Høgstrøm, U.: Non-dimensional wind and temperature profiles in the atmospheric surface layer: A re-evaluation, Bound.-Lay. Meteorol., 42, 55–78, 1988. 909, 932

Iijima, Y., Masuda, K., and Ohata, T.: Snow disappearance in Eastern Siberia and its relationship to atmospheric influences, Int. J. Climatol., 27, 169–178, 2007. 922

Intrieri, J., Shupe, M., Uttal, T., and McCarty, B.: An annual cycle of Arctic cloud characteristics observed by radar and lidar at SHEBA, J. Geophys. Res.-Oceans, 107, 8030, doi:10.1029/2000JC000423, 2002. 923

Kohsiek, W., Liebethal, C., Foken, T., Vogt, R., Oncley, S., Bernhofer, C., and Debruin, H.: The Energy Balance Experiment EBEX-2000, Part III: Behaviour and quality of the radiation measurements, Bound.-Lay. Meteorol., 123, 55–75, 2007. 907

Krinner, G.: Impact of lakes and wetlands on boreal climate, J. Geophys. Res.-Atmos., 108, 4520, doi:10.1029/2002JD002597, 2003. 925

Krinner, G. and Boike, J.: A study of the large-scale climatic effects of a possible disappearance of high-latitude inland water surfaces during the 21st century, Boreal Environ. Res., 15, 203–217, 2010. 925

Kutzbach, L., Wagner, D., and Pfeiffer, E.: Effect of microrelief and vegetation on methane emission from wet polygonal tundra, Lena Delta, Northern Siberia, Biogeochemistry, 69, 341–362, 2004. 905

Kutzbach, L., Wille, C., and Pfeiffer, E.-M.: The exchange of carbon dioxide between wet arctic tundra and the atmosphere at the Lena River Delta, Northern Siberia, Biogeosciences, 4, 869–890, doi:10.5194/bg-4-869-2007, 2007. 905

Langer, M., Westermann, S., and Boike, J.: Spatial and temporal variations of summer surface temperatures of wet polygonal tundra in Siberia - implications for MODIS LST based permafrost monitoring, Remote Sens. Environ., 114, 2059–2069, 2010a. 907

Langer, M., Westermann, S., Muster, S., Piel, K., and Boike, J.: Permafrost and surface energy balance of a polygonal tundra site in northern Siberia – Part II: Winter, in preparation, 2010b. 904, 922, 924, 925

Lawrence, D. and Slater, A.: A projection of severe near-surface permafrost degradation during the 21st century, Geophys. Res. Lett., 32, L24401, doi:10.1029/2005GL025080, 2005. 903

Lawrence, D., Slater, A., Romanovsky, V., and Nicolsky, D.: Sensitivity of a model projection of near-surface permafrost degradation to soil column depth and representation of soil organic matter, J. Geophys. Res, 113, F02011, doi:10.1029/2007JF000883, 2008. 903

Lüers, J. and Bareiss, J.: Direct near surface measurements of sensible heat fluxes in the arctic tundra applying eddy-covariance and laser scintillometry – The Arctic Turbulence Experiment 2006 on Svalbard (ARCTEX-2006), submitted to Theor. Appl. Climatol., 2009. 909

Lynch, A., Chapin, F., Hinzman, L., Wu, W., Lilly, E., Vourlitis, G., and Kim, E.: Surface energy balance on the arctic tundra: Measurements and models, J. Climate, 12, 2585–2606, 1999. 923

Mastepanov, M., Sigsgaard, C., Dlugokencky, E., Houweling, S., Ström, L., Tamstorf, M., and Christensen, T.: Large tundra methane burst during onset of freezing, Nature, 456, 628–630, 2008. 903

Mauder, M. and Foken, T.: Documentation and instruction manual of the eddy covariance software package TK2, Univ. of Bayreuth, Dept. of Mikrometeorology, 2004. 908

Mauder, M., Liebethal, C., Göckede, M., Leps, J., Beyrich, F., and Foken, T.: Processing and quality control of flux data during LITFASS-2003, Bound.-Lay. Meteorol., 121, 67–88, 2006. 909

Mauder, M., Foken, T., Clement, R., Elbers, J. A., Eugster, W., Grünwald, T., Heusinkveld, B., and Kolle, O.: Quality control of CarboEurope flux data - Part 2: Inter-comparison of

eddy-covariance software, Biogeosciences, 5, 451–462, doi:10.5194/bg-5-451-2008, 2008. 909

McGuire, A., Chapin, F., Walsh, J., and Wirth, C.: Integrated Regional Changes in Arctic Climate Feedbacks: Implications for the Global Climate System, Ann. Rev. Env. Resour., 31, 61–91, 2006. 903

Nicolsky, D., Romanovsky, V., Alexeev, V., and Lawrence, D.: Improved modeling of permafrost dynamics in a GCM land-surface scheme, Geophys. Res. Lett., 34, L08501, doi:10.1029/2007GL029525, 2007. 903

Nicolsky, D., Romanovsky, V., and Panteleev, G.: Estimation of soil thermal properties using in-situ temperature measurements in the active layer and permafrost, Cold Reg. Sci. Technol., 55, 120–129, 2009. 930

Oke, T.: Boundary layer climates, Methuen, 1987. 910

Overland, J., Wang, M., and Salo, S.: The recent Arctic warm period, Tellus A, 60, 589–597, 2008. 902

Overpeck, J., Hughen, K., Hardy, D., Bradley, R., Case, R., Douglas, M., Finney, B., Gajewski, K., Jacoby, G., Jennings, A., et al.: Arctic environmental change of the last four centuries, Science, 278, 1251, doi:10.1126/science.278.5341.1251, 1997. 902

Peters-Lidard, C., Blackburn, E., Liang, X., and Wood, E.: The effect of soil thermal conductivity parameterization on surface energy fluxes and temperatures, J. Atmos. Sci., 55, 1209–1224, 1998. 924

Pitman, A.: The evolution of, and revolution in, land surface schemes designed for climate models, Int. J. Climatol., 23, 479–510, 2003. 924

Rouse, W., Oswald, C., Binyamin, J., Spence, C., Schertzer, W., Blanken, P., Bussières, N., and Duguay, C.: The role of northern lakes in a regional energy balance, J. Hydrometeorol., 6, 291–305, 2005. 925

Sachs, T., Wille, C., Boike, J., and Kutzbach, L.: Environmental controls on ecosystem-scale CH_4 emission from polygonal tundra in the Lena River Delta, Siberia, J. Geophys. Res.-Biogeo., 113, G00A03, doi:10.1029/2007JG000505, 2008. 903, 905

Schmid, H.: Source areas for scalars and scalar fluxes, Bound.-Lay. Meteorol., 67, 293–318, 1994. 910, 940

Schotanus, P., Nieuwstadt, F., and Bruin, H.: Temperature measurement with a sonic anemometer and its application to heat and moisture fluxes, Bound.-Lay. Meteorol., 26, 81–93, 1983. 908

Serreze, M., Walsh, J., Chapin, F., Osterkamp, T., Dyurgerov, M., Romanovsky, V., Oechel, W., Morison, J., Zhang, T., and Barry, R.: Observational evidence of recent change in the northern high-latitude environment, Climatic Change, 46, 159–207, 2000. 903

Shupe, M. and Intrieri, J.: Cloud radiative forcing of the Arctic surface: The influence of cloud properties, surface albedo, and solar zenith angle, J. Climate, 17, 616–628, 2004. 923

Stendel, M. and Christensen, J.: Impact of global warming on permafrost conditions in a coupled GCM, Geophys. Res. Lett., 29, 1632, doi:10.1029/2001GL014345, 2002. 903

Sturm, M., Holmgren, J., König, M., and Morris, K.: The thermal conductivity of seasonal snow, J. Glaciol., 43, 26–41, 1997. 912

USGS: The Lena River Delta, US Geological Survey: Digital Image, http://eros.usgs.gov/imagegallery/collection.php?type=earth_as_art#26, last access: 8 June 2010, 2000. 940

Viterbo, P., Beljaars, A., Mahfouf, J., and Teixeira, J.: The representation of soil moisture freezing and its impact on the stable boundary layer, Q. J. Roy. Meteor. Soc., 125, 2401–2426, 1999. 924

Westermann, S., Lüers, J., Langer, M., Piel, K., and Boike, J.: The annual surface energy budget of a high-arctic permafrost site on Svalbard, Norway, The Cryosphere, 3, 245–263, doi:10.5194/tc-3-245-2009, 2009. 904, 911, 923, 930

Wilson, K., Goldstein, A., Falge, E., Aubinet, M., Baldocchi, D., Berbigier, P., Bernhofer, C., Ceulemans, R., Dolman, H., Field, C., et al.: Energy balance closure at FLUXNET sites, Agr. Forest Meteorol., 113, 223–243, 2002. 920

Zhang, T.: Influence of the seasonal snow cover on the ground thermal regime: An overview, Rev. Geophys., 43, 1–23, 2005. 912

Zhang, T., Barry, R., Knowles, K., Heginbottom, J., and Brown, J.: Statistics and characteristics of permafrost and ground-ice distribution in the Northern Hemisphere, Polar Geogr., 31, 47–68, 2008.

Zhang, X., Walsh, J., Zhang, J., Bhatt, U., and Ikeda, M.: Climatology and interannual variability of Arctic cyclone activity: 1948–2002, J. Climate, 17, 12, 2300–2317, 2004. 905

Zimov, S., Schuur, E., and Chapin III, F.: Permafrost and the global carbon budget, Science, 312, 1612–1613, 2006. 903

Zhang, T., Barry, R., Knowles, K., Heginbottom, J., and Brown, J.: Statistics and characteristics of permafrost and ground-ice distribution in the Northern Hemisphere, Polar Geogr., 31, 47–68, 2008.

Table 1. Used soil and snow parameters for ground heat flux calculations. Values of porosity P_{dry} and water content θ_w are inferred from soil sample analysis and in situ soil water content measurements. The heat capacities are calculated by weighting $C_{h,w}$ and $C_{h,s}$ according to water content and porosity. The thermal diffusivities D_h are determined with the conductive method (see Sect. 3.3.2), from which we obtain the thermal conductivities K_h in conjunction with the assumed heat capacity. Errors are calculated using Gaussian error propagation.

Substrate	P_{dry}	θ_w	C_h [MJ m^{-3} K^{-1}]	D_h [m^2 s^{-1}]	K_h [W m^{-1} K^{-1}]
dry peat	0.8±0.1	0.1±0.1	0.9±0.5	0.16±0.01	0.14±0.08
wet peat	0.8±0.1	0.7 ±0.1	3.4 ±0.5	0.19±0.04	0.6±0.17
saturated peat	0.8±0.1	0.8±0.1	3.8±0.2	0.19±0.02	0.72±0.08
snow	ρ_{snow}=190±10 kg m^{-3}		0.40±0.04	0.54±0.04	0.22±0.03

Table 2. Average heat fluxes and essential climate parameters. Values are in Wm^{-2}, if not indicated differently. Turbulent heat flux values marked in bold are affected by minor data gaps, due to quality or lee sector data exclusion. Radiation values measured with the NR-Lite sensor are marked with [1], and values obtained with the four component sensor (CNR1) are indicated with [2]. Modeled values of latent heat flux are indicated with [3]. The springtime precipitation is replaced by the snow water equivalent (SWE).

	Spring		Summer		Fall	
	2007	2008	2007	2008	2007	2008
	28 Apr–31 May	22 Apr–31 May	12 Jul–23 Aug	7 Jun–8 Jul 29 Jul–30 Aug	1 Sep–30 Sep	1 Sep–30 Sep
Q_{net}	44[1]	27[2]	81[2]	104[2]	7[1]	11[2] 5[1]
ΔQ_S	–	61	119	145	–	–
ΔQ_L	-	-34	−38	−41	–	–
Q_H	**8.7**	**1.3**	14	22	−1.5	−4.4
Q_E	**12**[3]	**9.7**	40	44	**15**[3]	**19**
$Q_{G,\ net}$	18	14	15	20	6	0.5
$Q_{G,\ sensible}$	17	13	5	9	6	4
$Q_{G,\ latent}$	1	1	10	11	0	−3.5
E_{melt} [MJ m^{-2}]	19	19	–	–	–	–
C	**−1.7**	**−3**	12	18	**−12.5**	**−10.1**
T_{surf} [° C]	−3.8	−6.9	10.5	9.2	3	1.2
T_{air} [° C]	−4.7	−6.9	9.2	8.2	2.6	1.6
R_H [%]	84	84	84	84	88	87
P [mm]	SWE: 60	SWE: 57	58	100	49	21

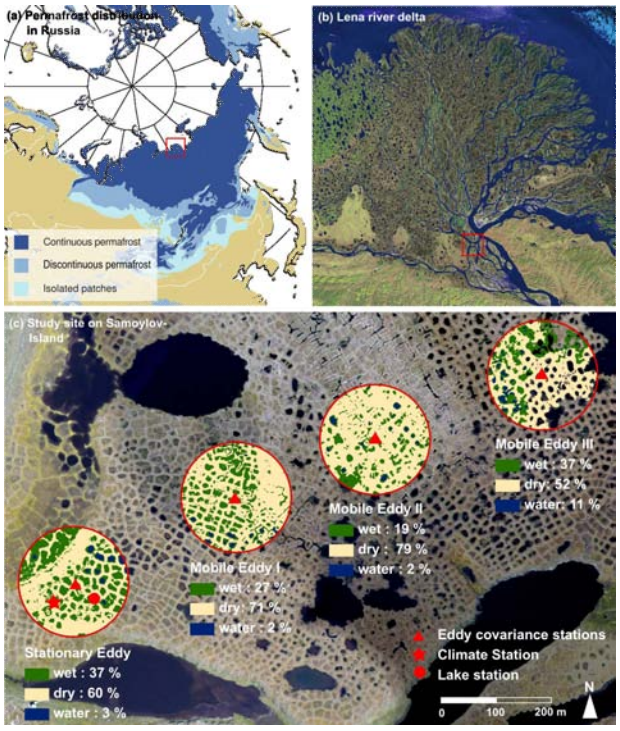

Fig. 1. **(a)** Permafrost distribution in Siberia (Brown et al., 1997); the location of the Lena River delta is marked in red. **(b)** Satellite image of the Lena River delta obtained from the Landsat Thematic Mapper (USGS, 2000); the location of Samoylov Island is marked in red. **(c)** High-resolution aerial image of the study site on Samoylov Island, where the considerable small-scale heterogeneity of the surface cover is visible. The locations of all installations are marked, the approximate footprint areas of the eddy covariance systems are indicated in red. The fractions of wet, dry and water surfaces in the concerning foot print areas are calculated using the foot print model of Schmid (1994).

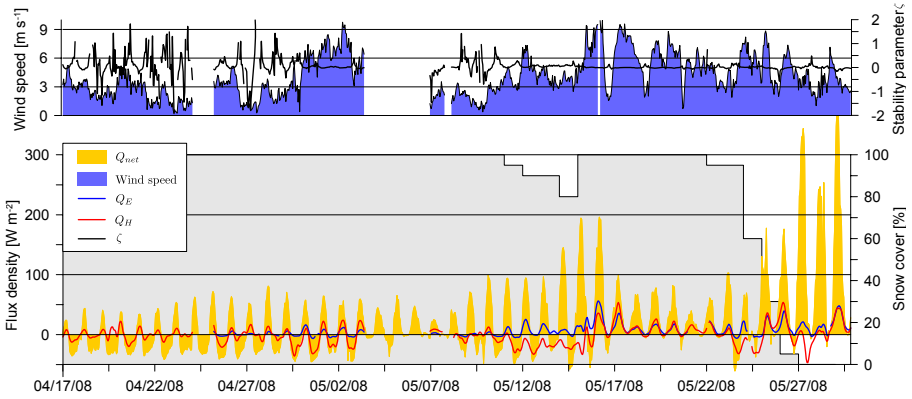

Fig. 2. Net radiation, sensible heat flux, latent heat flux, wind speed, atmospheric stability parameter $\zeta = z/L_*$ and approximate fraction of the snow-covered area (in gray) during spring 2008. The energy balance is strongly related to the evolution of the snow melt. The wind speed is significantly increased during the melt period and the atmospheric stratification is essentially neutral. Varying atmospheric conditions are observed in the pre-melt period.

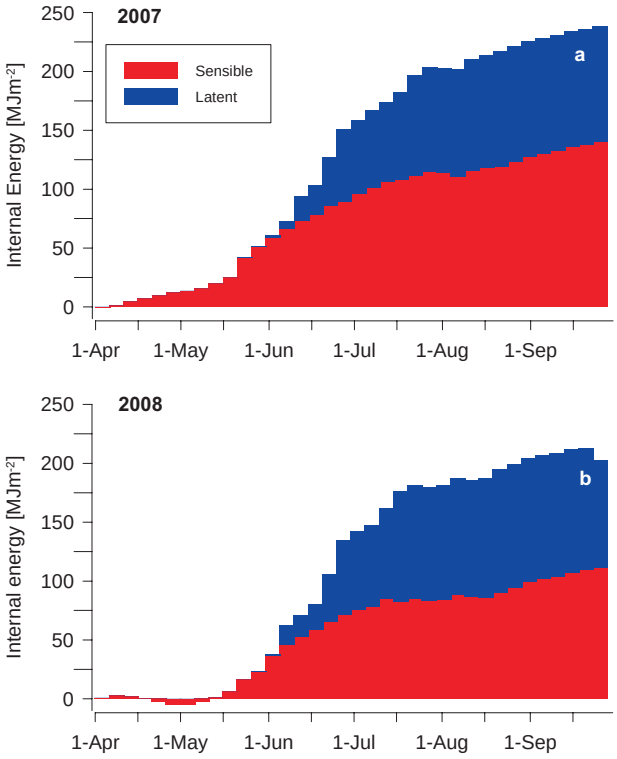

Fig. 3. Internal energy of the soil over the entire observation period in **(a)** 2007 and **(b)** 2008. The soil temperatures of 2007 are colder in spring and the air temperatures are warmer, which explains the increased heat storage at the beginning of the period. Towards the end, the soil temperatures are almost equal.

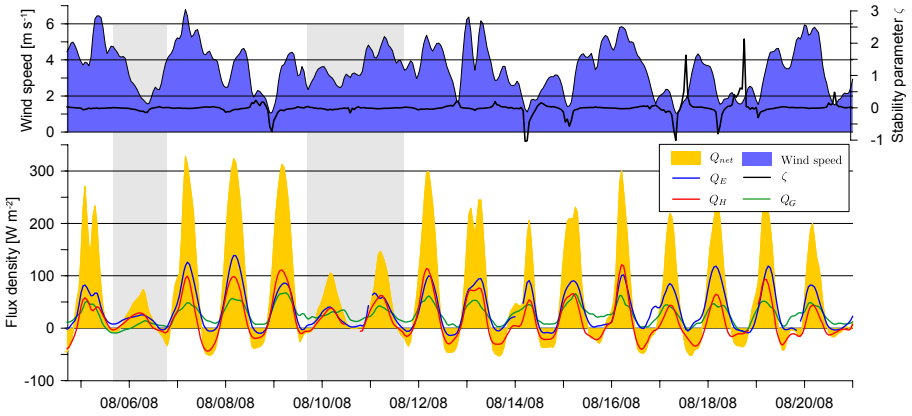

Fig. 4. Exemplary heat fluxes, wind speed and stability parameter during late summer 2008, overcast periods are marked in gray.

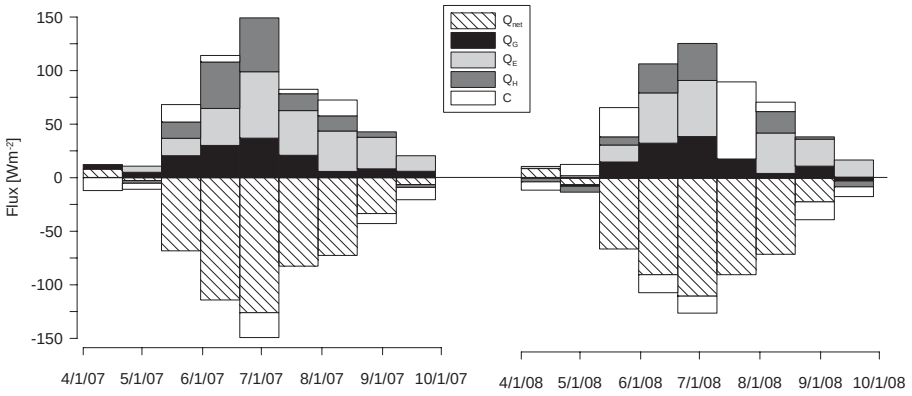

Fig. 5. The energy balance of 2007 and 2008. Heat fluxes are averaged over 20 days and data gaps in the latent heat fluxes are filled by modeled values. Averages are discarded if the data density is less than 60%.

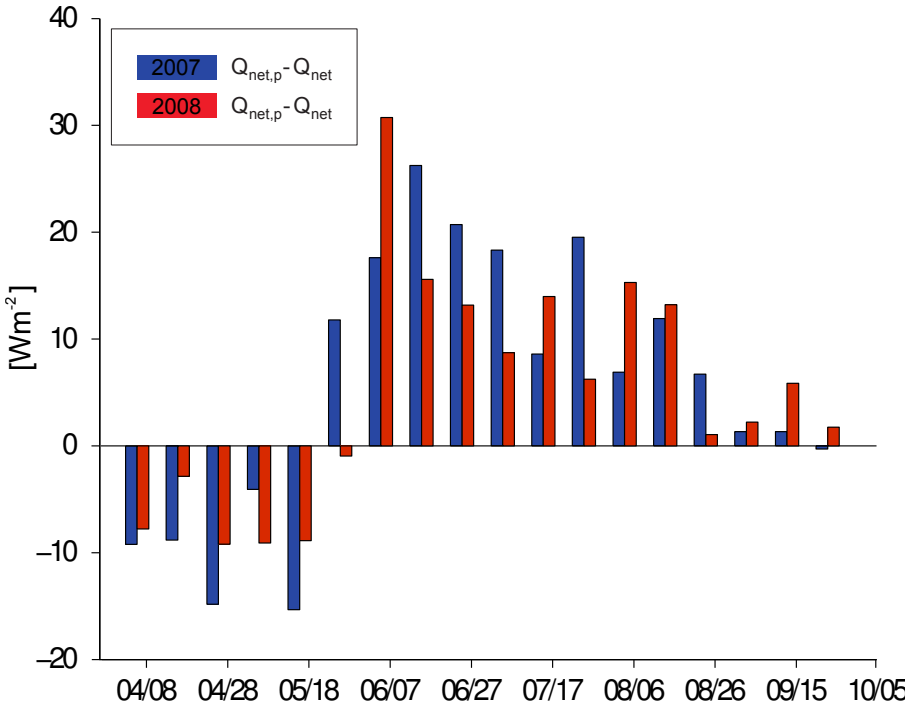

Fig. 6. Differences in the net radiation budget between the pond and the tundra surface during both observation periods in 2007 and 2008.

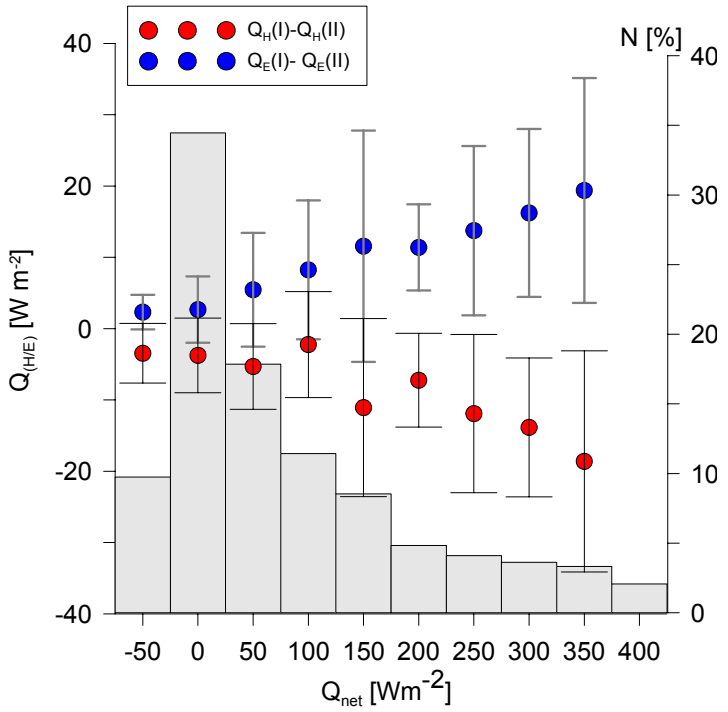

Fig. 7. The differences of the turbulent heat fluxes between the reference station $Q_{H/E}$(I) and the mobile station $Q_{H/E}$(II) at the second location of the mobile eddy system. The flux source area of the second Eddy-Covariance system features a 20% higher fraction of dry surface area. The spatial heat flux differences are directly related to the net radiative forcing. The histogram depicts the distribution of net radiation values during the entire summer period.

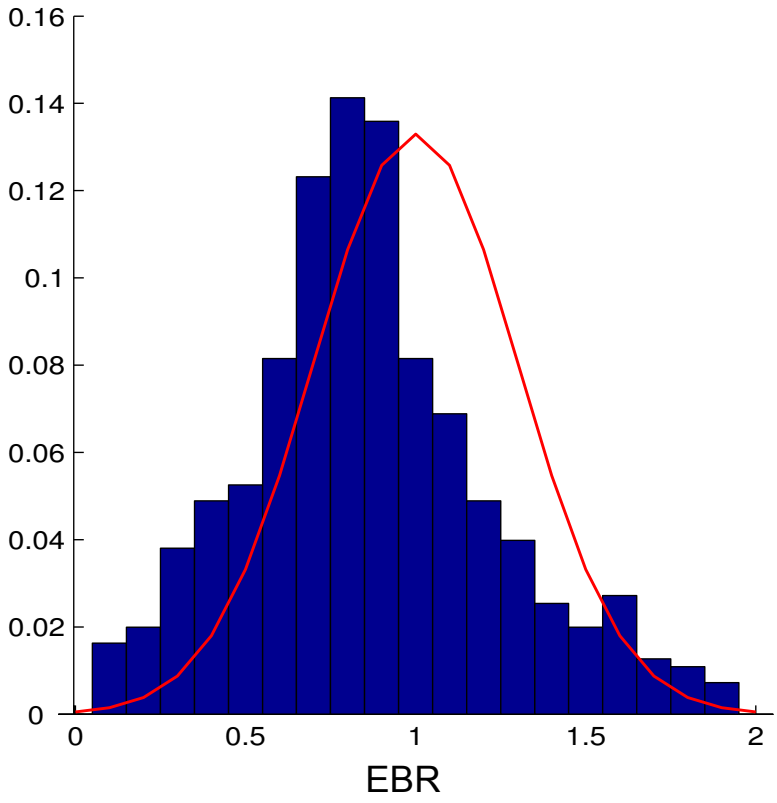

Fig. 8. The Energy balance ration EBR=$(Q_H+Q_E)/(Q_{net}-Q_G)$ measured during the summer period. The red line depicts the normal distribution, which would be expected for a closed surface energy balance with random errors.

947

Chapter 2.5

M.Langer, S. Westermann,S.Muster, K.Piel ans J. Boike (2010): Permafrost and surface energy balance of a polygonal tundra site in northern Siberia – Part 2: Winter, *The Cryoshere Discussions*, 4, 1391-1431,2010

The Cryosphere Discuss., 4, 1391–1431, 2010
www.the-cryosphere-discuss.net/4/1391/2010/
doi:10.5194/tcd-4-1391-2010
© Author(s) 2010. CC Attribution 3.0 License.

The Cryosphere Discussions

This discussion paper is/has been under review for the journal The Cryosphere (TC).
Please refer to the corresponding final paper in TC if available.

Permafrost and surface energy balance of a polygonal tundra site in Northern Siberia – Part 2: Winter

M. Langer, S. Westermann, S. Muster, K. Piel, and J. Boike

Alfred-Wegener-Institute for Polar and Marine Research, Telegrafenberg A43, 14473 Potsdam, Germany

Received: 5 August 2010 – Accepted: 12 August 2010 – Published: 25 August 2010

Correspondence to: M. Langer (moritz.langer@awi.de)

Published by Copernicus Publications on behalf of the European Geosciences Union.

Abstract

Permafrost is largely determined by the surface energy balance. Its vulnerability to degradation due to climate warming depends on complex soil-atmosphere interactions. This article is the second part of a comprehensive surface energy balance study at a polygonal tundra site in Northern Siberia. It comprises two consecutive winter periods from October 2007 to May 2008 and from October 2008 to January 2009. The surface energy balance is obtained by independent measurements of the radiation budget, the sensible heat flux and the ground heat flux, whereas the latent heat flux is inferred from measurements of the atmospheric turbulence characteristics and a model approach. The measurements reveal that the long-wave radiation is the dominant factor in the surface energy balance. The radiative losses are balanced to about 60% by the ground heat flux and almost 40% by the sensible heat fluxes, whereas the contribution of the latent heat flux is found to be relatively small. The main controlling factors of the surface energy budget are the snow cover, the cloudiness and the soil temperature gradient. Significant spatial differences in the surface energy balance are observed between the tundra soils and a small pond. The heat flux released from the subsurface heat storage is by a factor of two increased at the freezing pond during the entire winter period, whereas differences in the radiation budget are only observed at the end of winter. Inter-annual differences in the surface energy balance are related to differences in snow depth, which substantially affect the temperature evolution at the investigated pond. The obtained results demonstrate the importance of the ground heat flux for the soil-atmosphere energy exchange and reveal high spatial and temporal variabilities in the subsurface heat budget during winter.

1 Introduction

Numerous studies based on climate models revealed that the large-scale atmospheric conditions are greatly impacted by the heat and moisture turnover at the

surface-atmosphere interface (e.g. Viterbo et al., 1999; Delire et al., 2002; Pitman, 2003; Rinke et al., 2008). Recent studies also showed that the most pronounced arctic warming occurs during the winter and early spring period (Moritz et al., 2002; Johannessen et al., 2004). According to model predictions, it is expected that the significant arctic warming during the last decades (e.g. Overpeck et al., 1997; Comiso, 2003; Hinzman et al., 2005; Tape et al., 2006; Turner et al., 2007; Overland et al., 2008) is accelerated due to positive feedback mechanisms, such as a shrinking sea-ice cover and increased cloudiness (e.g. Holland and Bitz, 2003; Kaplan et al., 2003; Vavrus, 2004).

The winter time surface energy balance of the Arctic constitutes an essential factor in the regional climate system, since it affects the atmospheric heat budget due to sensible, latent and radiative energy exchange with the surface over a long-lasting period. Hence, for the evaluation and the development of large-scale model parameterizations, energy balance studies are an indispensable tool. In the Arctic, only few comprehensive energy balance studies exist within this large geographical area, especially for the winter period. The importance of the winter surface energy balance on the thermal state of the permafrost has been most recently demonstrated by Westermann et al. (2009) for a site on Svalbard: here, the snow surface temperature is largely controlled by the long-wave radiation balance, which in conjunction with the evolution of the snow cover and more complex processes, such as wintertime rain events, determines the thermal regime of the ground. Osterkamp (2005) reported that the winter and spring warming essentially affects the heat budget of permafrost soils.

Energy balance studies give insight into the processes, which are relevant for both the permafrost and the atmospheric heat budget. This is especially important for the development of new model schemes, which aim to incorporate permafrost due to its high carbon stock and its potential feedback to climate change. Recent effort in global permafrost modeling has already been initiated (e.g. Stendel and Christensen, 2002; Lawrence and Slater, 2005; Nicolsky et al., 2007; Lawrence et al., 2008). However, the accuracy of these models depend on the realistic representation of the

ground-atmosphere energy exchange processes, which are determined by parameterizations of the local surface and subsurface properties (e.g. roughness length, soil heat conductivity, snow cover characteristics).

This study is the second part of a comprehensive investigation on the annual surface energy balance at a wet tundra site in Northern Siberia. The results of the first part of this study (Langer et al., 2010) revealed that the sensitivity of the permafrost heat budget towards variations in radiation balance and turbulent heat fluxes is highest at the beginning and end of the summer thaw cycle. Furthermore, the permafrost heat budget appears to be less sensitive to surface energy balance variations during the high summer period. In this second paper, we focus on the surface energy balance during the winter periods from 1 October 2007, until 30 March 2008, and 1 October 2008, until 30 January 2009. We aim to achieve (i) the identification of the controlling and limiting factors of the surface energy balance , (ii) the evaluation of the seasonal and inter-annual variability of the energy balance components and (iii) the detection and evaluation of spatial differences of the surface energy balance by spatially distributed measurements. The results are discussed with respect to larger-scale modeling of the arctic boundary layer and the permafrost.

2 Study site

The study site is located at the southern part of the Lena River Delta on Samoylov Island (72°22′ N; 126°30′ E) (Fig. 1). The regional climate is arctic-continental with a mean annual air temperature (MAAT) of about −13 °C, a pronounced annual temperature amplitude of about 60 °C and a total annual precipitation around 250 mm (Boike et al., 2008). Snow fall and soil refreezing begins towards the end of September. The winter period is characterized by the polar night, which lasts from mid of November until end of January. The climate and synoptic conditions during the winter are largely determined by the Siberian High, which causes air temperatures to fall frequently below −45 °C. The high pressure system is often disturbed by the influx of cyclones with high

intensity and short lifetime (Zhang et al., 2004). The continental climate conditions are also reflected in the thermal regime of the soil, which is characterized by continuous permafrost reaching depths of 500–600 m (Grigoriev, 1960). At the depth of the zero annual amplitude (≈15 m) the soil temperature is about −10 °C. During the summer months, the maximum thaw depth ranges from 0.4–0.5 m. The tundra surface is highly fractionated due to polygonal structures, which are typically 50–100 m^2 large. The rims of these polygons are elevated by about 0.2 to 0.5 m compared to the centers, which consist of water-saturated peat soils or constitute ponds, which frequently occur at the study site. During the winter period, the tundra soils are covered by a shallow snow layer, which typically features depths of less than 0.5 m at the depressed centers and only a few centimeters at the elevated rims.

3 Methods

For the evaluation of the surface energy balance and the quantification of spatial variabilities at the study site we distinguish between two basic landscape features during the winter period: the snow covered tundra soils and freezing or frozen water bodies. The surface energy balance of the snow covered tundra soils (referred to as tundra site) is measured as a spatial average including polygonal centers and rims (compare Sect. 2). Components of the energy balance (net radiation, subsurface heat flux) of water bodies are exemplified at a polygonal pond (referred to as pond site). The energy balance equation for the tundra site is written as

$$Q_{\mathrm{net}} = Q_{\mathrm{H}} + Q_{\mathrm{E}} + Q_{\mathrm{G}} + C \quad (1)$$

where Q_{net} is the net radiation, Q_{H} the turbulent sensible heat flux, Q_{E} the turbulent latent heat flux, Q_{G} the subsurface (ground or snow) heat flux and C is the residual of the energy balance, which accounts for inaccuracies of measurement. The pond, at which the net radiation $Q_{\mathrm{net,p}}$ and the subsurface heat flux $Q_{\mathrm{G,p}}$ are measured, features a depth of about 0.8 m and a water volume of about 150 m^3. The basic concepts

of the measurements and the data analysis applied in the present study are already described in the first part of this study (Langer et al., 2010). The applied methods are re-summarized briefly, while new methods and additional measurements are described in more detail in the following sections.

3.1 Radiation balance

The net radiation at the tundra Q_{net} and pond sites $Q_{\mathrm{net,p}}$ are measured with net radiations sensors (NR-Lite, Kipp and Zonen, The Netherlands). The net radiation sensor at the tundra site is not available in the second winter period (2008–2009), but we apply a four-component radiation sensor (CNR1, Kipp and Zonen, The Netherlands) to calculate the net radiation. The outgoing thermal radiation at the tundra site is measured separately by a long-wave radiation sensor in winter 2007–2008 (CG1, Kipp and Zonen, The Netherlands) and calculated from infrared surface temperature sensors (IRTS-P, Apogee Instruments, USA) in winter 2008–2009 using Stefan-Boltzmann law (compare Langer et al., 2010). For this calculation, we assume the surface emissivity of the snow cover to be 0.98 according to commonly used values (Rees, 1993).

3.2 Turbulent heat fluxes

Measurements of the sensible heat flux Q_{H} are only available for the tundra site. The flux sources area at the location of the eddy covariance system is characterized to about 95% by tundra soils, according to a foot print analyses (Langer et al., 2010). The eddy covariance setup is reduced to the 3-D sonic anemometer (C-SAT, Campbell Scientific, USA) during the observation period from 1 October to 30 March. The reduced measurement setup only permits the detection of the momentum flux u_*^2 and the buoyancy flux Q_{HB}, which in principle must be corrected according to the flux of water vapor to obtain the true sensible heat flux Q_{H} (Schotanus et al., 1983). Due to the extremely cold air temperatures, we assume the flux of water vapor to be very small during winter, so that the difference between the buoyancy and sensible heat flux is small. Hence,

we accept the buoyancy flux to be a good approximation of the real sensible heat flux during the winter period. According to a quality check and the exclusion of the lee wind sector (263° to 277°), about 18% of the flux measurements must be discarded. From the stability parameter ζ, the atmospheric stratification can be inferred, with $\zeta \approx 0$ for a well mixed or neutrally stratified atmosphere, $\zeta > 0$ for stable and $\zeta < 0$ for unstable atmospheric stratifications.

The latent heat flux Q_E at the tundra site is modeled by an approach similar to the one used in the first part of this study (Langer et al., 2010). The model uses the often applied parametrization introduced by Høgstrøm (1988) and is based on available eddy-covariance measurements of the momentum flux u_*^2 and the buoyancy flux Q_{HB}, from which a turbulent transport coefficient can be inferred (compare Langer et al., 2010). In addition, the model requires measurements of relative humidity and surface temperature for calculating the near-surface gradient of the specific humidity. During winter 2007–2008, we rely on measurements of relative humidity from the standard climate station in the vicinity of the eddy covariance system. During winter 2008–2009, the relative humidity is estimated to be in the range of (70 ± 5)% according to the measurements of the previous year.

3.3 Subsurface heat fluxes

Subsurfaces heat fluxes are calculated for a tundra site (Q_G) and a thermokarst pond ($Q_{G,p}$). The subsurface heat flux is the heat flux across the surface, which depending on the applied measurement method is defined as the soil, the snow, or the lake ice surface. For the heat flux calculations, we apply the calorimetric and the conductive method (compare Langer et al., 2010).

3.3.1 The calorimetric method

The calorimetric method calculates the ground heat flux based on changes in the internal energy of a soil column using measurements of the soil temperature and liquid

water content θ_w. This method is used for evaluating averages of the ground heat flux over periods longer than a few days. Due to the measurements of temperature and liquid water content, it is possible to distinguish sensible and latent heat storage, which we express as energy fluxes $Q_{G,sensible}$ and $Q_{G,latent}$. Note, that the heat storage in the shallow snow layer becomes negligible for long-term averages, so that temperature profiles in the snow pack are not required. During winter 2007–2008, soil temperatures are available from a 26 m borehole and a thermistor profile in the active layer (CA I) (Fig. 2). The liquid water content θ_w is measured in the active layer by Time-Domain-Reflectometry (TDR) probes (compare Langer et al., 2010). Since the deep borehole and the TDR probes are not available during winter 2008–2009 (CA II), we rely on a shallow borehole of 4 m depth and a parametrization of the liquid water content in dependence of the soil temperature. This so-called freezing characteristic is inferred by fitting a polynomial function to measurements of water content and temperature of the previous year (Fig. 3). Since the calorimetric method requires measurements down to a depth of zero temperature change in the concerned averaging period, heat fluxes below 4 m are required. We therefore calculate the heat flux through the lower boundary of the temperature profile by using the conductive method (compare Langer et al., 2010). Soil heat capacities, thermal diffusivity and heat conductivity of frozen tundra soils are evaluated similar to the summer time values (Table 6).

3.3.2 The conductive method

The conductive method calculates the heat flux across a layer by solving the differential equation of conductive heat transport (compare Langer et al., 2010). In addition, the conductive method involves the determination of the thermal diffusivity of snow or soil, which are presented in Table 6. The conductive method is applied for both calculations of the subsurface heat flux at (a) the tundra site and (b) the thermokarst pond.

(a) For the tundra site, this method is applied for calculating heat fluxes with hourly resolution. These high resolution heat fluxes are only obtained at polygonal

centers, where snow cover measurements are available. Two different sets of measurements (CO I and CO II) are used to calculate the heat flux across the snow cover with the conductive method (Fig. 2). Firstly, snow temperature measurements at three depths with known relative distance are employed. This method is similar to the conductive heat flux calculation used for the uppermost soil layer in the first part of this study (compare Langer et al., 2010) and involves the determination of the thermal diffusivity of the snow cover. The required snow temperature profile measurements are available during winter 2008–2009. The used measurement setup (CO I) consists of an array of temperature sensors (thermocouple) fixed on very thin (4 mm) carbon rods of different length, which are placed vertically about 3 cm apart from each other (Fig. 2). The height difference between the temperature sensors is 5 cm. Secondly, when the snow temperature profile is not available during the winter 2007–2008, the snow heat flux is calculated using the surface temperature of the snow cover, the temperature at the snow-soil interface, the snow depth and the thermal diffusivity and conductivity of the snow cover (CO II). The snow surface temperature is measured by an infrared sensor, the temperature at the snow-soil interface is measured by a thermistor close to the surface and the required snow depth is obtained by an ultrasonic ranging sensor (Fig. 2). We further assume a similar thermal diffusivity of the snow cover, as calculated from the temperature profile measurements of the following year. The obtained snow heat fluxes must be considered a rough approximation, since the assumption of constant thermal snow properties may be violated in reality (e.g. Sturm et al., 1997; Zhang, 2005).

(b) For the pond site the conductive method is used to calculate long-term averages of the heat flux through the ice layer $Q_{G,p}$. The employed temperature profile (CO III) consists of four temperature sensors which are fixed on a mast located in the middle of the water body, where the water depth is approximately 0.8 m (Fig. 2). In the course of the winter, the temperature sensors freeze in the ice of the pond. From the temperature profile, we can calculate the heat flux trough the

ice layer, as soon as it approaches a thickness of 24 cm, which then contains the two uppermost temperature sensors of the profile. We use the conductive method described in Langer et al. (2010) to evaluate the heat flux through the ice cover surface with the known thermal diffusivity and conductivity of ice. The employed values are depicted in Table 6.

3.4 Snow cover measurements

We use different methods for the detection of the snow depth. The snow depth is measured with an ultrasonic ranging sensors (SR50, Campbell Scientific, USA) located at the tundra site and at the pond site. During winter 2008–2009, the ultrasonic sensor is not available at the tundra site. Therefore, we infer the snow depth from the snow temperature profile described in Sect. 3.3 using the method of Lewkowicz (2008), who determines the snow depth from a significant temperature decoupling between buried and unburied sensors. The temperature profile provides a vertical resolution of 5 cm. In addition, we use the AMSR-E 5-Day L3 snow water equivalent (SWE) product (Kelly et al., 2004) to obtain a complementary snow cover information in addition to our point measurements. The satellite product is based on passive microwave detection and features a spatial resolution of 25 km. A detailed technical description of the product and the retrieval algorithm is given by Pulliainen and Hallikainen (2001). For tundra surfaces, the accuracy of the SWE product is expected to be in the range of 10%, since the shallow vegetation only marginally affects the snow cover signal (Foster et al., 2005). We selected the closest pixel to the study site, which must be understood as an averages value over a large variety of surface structures.

Moreover, SWE field measurements are conducted during April 2008 and 2009. From these measurements, we calculate the snow heat capacity, which is used for the heat flux calculations. The obtained values are presented in Table 6. The field measurements of the snow density ρ_{snow} are further used for the conversion of the AMSR-E dataset from SWE to snow depths.

4 Results

In the following, we describe the winter surface energy balance. We divide the observation period into three sections, according to the availability of sunlight. During the first and the last winter sections short wave radiation is still or again present, whereas the middle period is characterized by the absence of sunlight due to polar night conditions.

4.1 Early winter (1 October–30 November)

The first winter period lasts from the beginning of October until the end of November, immediately before the beginning of the polar night. The surface energy balance is characterized by a strongly negative radiation budget on the order of $-20\,\mathrm{W\,m^{-2}}$, which is about $25\,\mathrm{W\,m^{-2}}$ less compared to the preceding fall season (compare Langer et al., 2010). The short-wave radiation budget is very small ($\approx 2\,\mathrm{W\,m^{-2}}$) due to the high albedo of the snow cover. The negative radiation budget is largely balanced by the ground heat flux Q_G (-10 to $-20\,\mathrm{W\,m^{-2}}$), whereas the sensible heat flux Q_H shows only a marginal contribution of about $-5\,\mathrm{W\,m^{-2}}$, which is only slightly more negative than during the fall season. The modeled latent heat flux Q_E is still significantly positive ($\approx 10\,\mathrm{W\,m^{-2}}$), which agrees with the high values measured in the previous fall period. Similar to the fall period, the energy balance residual C is considerable, which indicates that some heat flux is not detected.

The general weather conditions are characterized by rapidly declining air temperatures, decreasing sun angles, snow accumulation and the freezing of soil and water bodies. In both years, the air temperatures rapidly fall from about 0 °C at the beginning to −20 °C at the end of the period. The build-up of a continuous snow cover starts in both winters at the beginning of October. However, we observe significant differences in the evolution of the snow cover at the tundra site. In 2007, the snow cover reaches a depth of about 0.15 m shortly after the first snow fall and remains almost constant until the end of the period. In 2008, the snow cover accumulation is much slower and ends up with a snow depth of about 0.1 m (Fig. 4). An even greater inter-annual variability

the snow depth is observed at the pond site, which in 2007 is covered by about 0.2 m of snow shortly after the first snow fall, whereas in 2008 almost no snow cover is measured until the end of this winter period (Fig. 4). The observed inter-annual differences in snow cover accumulation agree with the satellite observations (AMSR-E) (Fig. 4).

The net radiation budget of the first winter period is dominated by the long-wave radiation ΔQ_L, which in 2008 is about fifteen times larger than the net short-wave radiation (Table 6, Fig. 5). The incoming long-wave radiation steadily decreases from about $300\,\mathrm{W\,m^{-2}}$ to $180\,\mathrm{W\,m^{-2}}$. This general trend is overlain by rapid variations in the range of 60–70 $\mathrm{W\,m^{-2}}$, which are most likely associated with changes in cloudiness. In frequent situations, the outgoing and the incoming long-wave radiation are in quasi-balance ($Q_{net} \approx 0$), which is most likely caused by a dense cloud cover. The outgoing long-wave radiation follows the general trend of its incoming counterpart and decreases from about $315\,\mathrm{W\,m^{-2}}$ to $200\,\mathrm{W\,m^{-2}}$, which corresponds to a surface temperature cooling from 0 to −24 °C. The surface temperature of 2008 appears to be slightly increased compared to 2007 (Table 6), which on average amounts to an increased radiative loss on the order of $5\,\mathrm{W\,m^{-2}}$ in 2008. The surface temperature follows to a large extent the short-term fluctuations of the incoming long-wave radiation. The observed fluctuations are on the order of 10 °C. The negative net radiation is partly balanced by the sensible heat flux Q_H, which is negative in both years. In both years, the average values of the sensible heat fluxes are small compared to the ground heat fluxes, but show strong short-term variations on the order of $30\,\mathrm{W\,m^{-2}}$. The observed fluctuations in the sensible heat fluxes largely follow the stepwise variations of the net radiation. Slightly positive sensible heat fluxes, that drag heat from the surface to the atmosphere, are observed occasionally. These events are strictly correlated to high values of downwelling thermal radiation and positive temperature gradients between the surface and the near-surface air temperature. High absolute values of the sensible heat flux are almost always associated with high wind speeds and strong turbulent exchange. The atmospheric stratification is mostly neutral ($\zeta \approx 0$), while stable stratification ($\zeta > 0$) only occur occasionally under clear-sky and calm conditions. Such stable stratifications are

characterized by a very high snow heat flux, which compensates for the reduced sensible heat flux under stable conditions. The largest fraction of the negative radiation budget is balanced by the ground heat flux Q_G, which is predominately supplied by latent heat of freezing (Table 6). In the inter-annual comparison, the ground heat flux of 2008 is significantly larger than in 2007. This difference corresponds to the lower surface temperatures, the faster snow cover build-up and the slightly increased sensible heat flux of 2007 (Table 6). The observed inter-annual differences in the soil heat fluxes agree with the fact, that the active layer is completely frozen by the end of the early winter period in 2008, but not in 2007.

The most pronounced inter-annual differences in the ground heat budget are observed at the polygonal pond. According to the temperature profile measurements, we can estimate the ice cover thickness to be about 30 cm at the end of the early winter period in 2007. In 2008, the temperature measurements indicate that the water body is completely frozen down to a depth of 85 cm. Assuming an ice density of about 920 kg m^{-3}, this amount of ice corresponds to an average heat flux $Q_{G,p}$ of about -12 W m^{-2} in 2007 and about -34 W m^{-2} in 2008. Note, that these heat fluxes are only estimated according to the amount of frozen water, which does not contain the temperature change of the water body and the ground underneath. Hence, the true ground heat flux at the pond must be even larger. However, in the 2007, the estimated heat flux value at the freezing pond is in a good agreement with the net radiation $Q_{net,p}$, which we measure directly at the surface of the water body (Table 6). It is evident, that such an energy balance agreement is not given in 2008, were the pond heat flux releases about 10 W m^{-2} more than is lost by radiation. Hence, additional heat transport, such as a positive sensible heat flux, may be involved at the pond surface.

4.2 Polar winter (1 December–30 January)

The polar winter section features a highly negative net radiation budget in the range of -20 to -25 W m^{-2}. Due to polar night conditions, the radiation balance is only

determined by thermal radiation. The largest fraction of the radiative loss is balanced by the ground heat flux Q_G, which is on the order of about -15 W m^{-2}. Compared to early winter, the sensible heat flux Q_H decreases and is now on the order of -10 W m^{-2}. The latent heat flux Q_E is significantly lowered and features a value of only 4 W m^{-2}.

The polar winter section is characterized by the absence of solar radiation during which the air temperatures reach their annual minimum of about -44 °C in winter 2007–2008 and -42 °C in winter 2008–2009. During winter 2007–2008, the snow cover remains almost constant featuring a depth of about 15 cm at the tundra surface and about 20 cm at the polygonal pond. A slightly different evolution of the snow cover is found for 2008–2009, when the snow depth remains between 10 and 15 cm at the tundra surface, whereas almost no snow cover is detected at the pond. For the winter 2007–2008, freezing continues from early winter into the polar night period. While the remaining unfrozen soil layer is already frozen after a few days, the pond remains partially unfrozen until the end of this section (Fig. 4). This delayed freezing process in 2007–2008 significantly influences the temperature at the bottom of the water body, which is about 15 °C warmer compared to the following year (Fig. 4).

The energy balance of the polar winter section is entirely governed by the long-wave budget ΔQ_L, which is significantly negative (Table 6). In both years, the incoming long-wave radiation shows frequent fluctuations according to changes between overcast and clear-sky conditions. The measured radiation values vary between 140 and 240 W m^{-2}. Conditions of constant incoming radiation typically last between two and three days. The surface temperatures and thus the outgoing thermal radiation show a strong variability in the range of -15 °C to -45 °C in both years, which corresponds to emitted radiative fluxes of about -150 and -250 W m^{-2}. The negative radiation budget is partly balanced by a slightly increased sensible heat flux compared to early winter (Table 6, Fig. 5). The largest fraction of the net radiation is balanced by the ground heat flux Q_G, which is mainly supplied by the release of sensible heat $Q_{G,sensible}$ (Table 6) that originates to about 85% from the first four meters of the soil column. Recalling the inter-annual difference in the ground heat fluxes during the early winter section, the

differences are now reversed. The ground heat flux of 2007 is now higher compared to 2008, which corresponds to a warmer soil in 2007 and therefore to a steeper soil temperature gradient.

An exemplary situation during the transition from the early winter to the polar night in 2007–2008 is depicted in Fig. 6. The example shows the typical stepwise pattern of the long-wave radiation budget, most likely caused by the influence of clouds. These large-scale variations are followed by the course of the sensible heat flux and the ground heat flux, which usually balances the largest fraction of the radiative losses. The turbulent heat flux becomes large ($Q_H \approx -30\,W\,m^{-2}$) under clear-sky and windy conditions (wind speed $\approx 8\,m\,s^{-1}$), as they occur around 23 November and 4 December. The negative radiation budget is then primarily balanced by the sensible heat flux, which leads to a subsequent surface warming that essentially reduces the snow temperature gradient and thus the ground heat flux (compare Fig. 6). On rare occasions, the net radiation is found to be positive, which can only be associated with the influx of warm air mass that are warmer than the surface and lead to slightly positive sensible heat fluxes (Fig. 6). During one of these situations, we can observe the development of a slightly unstable stratification ($\zeta < 0$) around 25 November (Fig. 6). This situation is due to a precedent long-lasting period of calm conditions featuring stable stratifications and high radiative losses, which most likely cool the atmosphere. The sudden influx of warm air, which is indicated by the rapidly increasing net radiation to positive values heats up the surface. This consequently leads to a positive near-surface temperature gradient and the short-time development of unstable conditions. The unstable stratification breaks down as the net radiation falls back to negative values (Fig. 6).

The largest inter-annual differences in the ground heat budget are again observed at the investigated pond (Table 6), which in 2007–2008 is finally frozen by the end of the polar winter. Similar to the ground heat flux Q_G, the pond heat fluxes $Q_{G,p}$ is now higher in 2007–2008 than in 2008–2009. We also observe that in both years the released energy at the pond $Q_{G,p}$ is larger than the radiative losses $Q_{net,p}$, which indicates that amplified turbulent sensible heat fluxes might occur at the surface of the

frozen water body similar to the early winter period. Compared to the ground heat flux at the tundra surface Q_G, the pond heat flux is higher by a factor of about two.

4.3 Late winter (1 February–30 March)

The energy balance of the late winter section is still characterized by negative net radiation Q_{net} of about $-15\,W\,m^{-2}$, which is still significantly lower compared to the following spring period, described in the first part of this study. This is due to the fact that the net radiation budget steeply increases during this and the following period. The ground heat flux Q_G features about $-5\,W\,m^{-2}$ and looses its dominant role in balancing the radiation budget. The largest fraction of radiative losses is now balanced by a further increased sensible heat flux Q_H, which is on the order of $-10\,W\,m^{-2}$. The modeled latent heat flux Q_E remains small at about $3\,W\,m^{-2}$.

The synoptic conditions are determined by the end of the polar night and increasing air temperatures from about −35 to −5 °C. The snow depth in 2008 slightly increases of about 5–10 cm and reaches its annual maximum of 25–30 cm.

The average net radiation budget is still negative and reaches values as low as $-40\,W\,m^{-2}$, while positive fluxes can exceed $20\,W\,m^{-2}$ (Fig. 7). Positive net radiation values frequently occur within a pronounced diurnal cycle towards the end of this period. The upwelling long-wave radiation ranges from 160 and $300\,W\,m^{-2}$, which corresponds to surface temperatures of −40 and −3 °C. The sensible heat flux is significantly more negative compared to the polar winter period and balances about 70% of the negative radiation budget, while the ground heat flux looses its dominant role. This corresponds to the evolution of a strong temperature gradient in the atmospheric boundary layer, which frequently exceeds values of −3 °C with an average gradient of about −1 °C (Table 6). The sensible heat flux features a diurnal cycle towards the end of the later winter period and ranges from $-40\,W\,m^{-2}$ to $5\,W\,m^{-2}$ (Fig. 7). Positive sensible heat fluxes are usually observed during local noon, when the net radiation is positive due to high values of incoming solar radiation. The atmospheric stratification is essentially neutral during the first half of the late winter section, which corresponds

to high wind speeds (Fig. 7). Within the course of the late winter period, the stability parameter ζ indicates frequent changes between stable and unstable stratifications (Fig. 7). The ground heat flux is essentially supplied by sensible heat from the deep soil layers. About 85% of the released heat originates from soil cooling down to a depth of 7 m. A more detailed look at the ground heat flux reveals more frequent positive heat fluxes towards the end of the period, which are usually associated with strongly negative sensible heat fluxes (Fig. 7). This indicates that at the end of the entire winter period the initial warming of the ground is mainly supplied by sensible heat fluxes from the atmosphere. These observations are in good agreement with heat fluxes measured in the following spring period, which are described in the first part of this study.

Significant spatial differences of the energy balance are still observed between the polygonal pond and the tundra site. The ground heat flux at the polygonal pond $Q_{G,p}$ is significantly increased compared to the tundra ground heat flux Q_G, which corresponds to the more negative radiation budget at the pond $Q_{net,p}$ (Table 6). This indicates that the polygonal pond most likely features slightly higher surface temperatures. If we assume the surface albedo at the snow covered tundra to be similar to the snow-covered pond, the surface at the pond would be about 1 °C warmer, according to the increased ground heat flux.

4.4 Controlling factors of surface temperature

The surface temperature T_{surf} is a direct result of the surface energy balance. It is therefore worthwhile to give an insight into its determining factors. We can see in Fig. 8, that the surface temperature variations are primarily determined by the incoming thermal radiation, while other factors, such as wind speed only have a secondary impact. Figure 8 also shows that the impact of wind on the surface temperature is highest during low values of incoming long-wave radiation. This relation is explained by the fact, that the surface cools down strongest under clear-sky conditions when the turbulent heat transport from the atmosphere to the surface is limited by the absence of wind. This describes the typical situation of a near-surface temperature inversion under a stable

atmospheric stratification ($\zeta>0$), which leads to pronounced surface cooling. However, such conditions are observed only occasionally, since wind-induced turbulent mixing dominates during the polar night (Fig. 8), so that the formation of stable stratifications ($\zeta>0$) is essentially limited.

5 Discussion

5.1 The winter time energy balance

According to our measurements, the surface energy balance during winter is predominately characterized by (i) the long-wave radiation budget, (ii) the ground heat flux and (iii) to a minor extent by the atmospheric sensible heat flux. The latent heat flux is found to be small in proportion to the other heat fluxes.

(i) The radiation budget of the considered winter period is largely determined by the long-wave radiation, as it mostly falls within the polar night, while the high albedo of the snow cover limits the role of the short-wave radiation at the beginning and the end of the period (Table 6). The net long-wave radiation fluctuates strongly between almost zero and highly negative values of up to $-50\,W\,m^{-2}$. The fluctuations are largely caused by fast changes of the incoming long-wave radiation, which most likely can be attributed to the presence or absence of a cloud cover (Curry et al., 1993; Shupe and Intrieri, 2004). The incoming long-wave radiation is the determining factor for the surface temperature, as it sets the general range within which the surface temperature can adjust depending on the other components of the energy balance (Fig. 8).

(ii) The ground heat flux is of outstanding importance for the surface energy balance during the winter periods, since it is the main balancing factor of the radiative losses. It originates from both the refreezing of the active layer and the cooling of the soil, with both contributing about 60% to the energy balance. Hereby the

refreezing of the active layer strongly dominates until about the beginning of December. Afterwards the ground heat flux is entirely supplied by soil cooling up to a depth of 15 m. Strong inter-annual differences in the subsurface heat flux are observed particularly during the early winter section (Table 6), with reduced heat fluxes and a delayed refreezing in 2007. This is most likely due to the faster snow cover build up in this year (Fig. 4), related to the low thermal conductivity by a factor of four to eight lower than the thermal conductivity of frozen peat (Table 6). Consequently, the release of heat occurs over a longer period in 2007, while it is more concentrated at the beginning of the winter in 2008. Moreover, profound spatial differences in the subsurface heat fluxes are observed between the tundra soils and the shallow water bodies at which the released heat flux is almost a factor of two higher.

(iii) While the interplay between the net radiation, the ground heat flux and the sensible heat flux can be complex (Fig. 6), the magnitude of the average sensible heat flux is significantly smaller than the ground heat flux. The highest values of sensible heat fluxes are observed at the end of the winter season. During the entire winter period the observed average sensible heat flux of about $-8\,\mathrm{W\,m^{-2}}$ amounts to a cooling of an air column of 1000 m height by about 30 °C over a period of 6 months. This matches the order of magnitude of the observed near-surface temperature cooling, which is also on the order of 30 °C (compare Table 6). In addition, the well mixed boundary layer with predominantely neutral stratifications suggests a prominent role of the sensible heat flux for the cooling of the near surface atmosphere. It must be emphasized, that the contribution of the wintertime sensible heat flux to the surface energy balance is by a factor of two smaller than values reported for arctic-oceanic conditions on Svalbard (Westermann et al., 2009), but of similar magnitude as values reported from measurements on sea-ice at the Arctic Ocean (Persson et al., 2002).

5.2 Seasonal differences of the surface energy balance

The surface energy balance at the study site is characterized by a strong seasonality, featuring a distinctly different partitioning of the energy balance within the annual cycle. The seasonal differences in the surface energy balance are caused by factors such as the availability of solar radiation, the surface characteristics and the atmospheric conditions. The differences of these controlling mechanisms are exemplified based on the energy balances during summer and polar winter (Fig. 9).

The radiation budget during the summer season is largely determined by the incoming shortwave radiation, which is further intensified by the polar day conditions. Conversely, the radiation budget during the winter is mainly controlled by thermal radiation facilitated by the high reflectance of the snow cover and the low or not available short wave radiation. In both periods, the surface radiation budget is strongly altered by clouds. Our observations reveal, that the net radiation is attenuated during the summer season by the presence of clouds, while the radiative losses are reduced during winter.

During the summer season, the largest fraction of the net radiation (40–50%) is consumed by the latent heat flux, whereas similar fractions of about 20% are attributed to the sensible and the ground heat flux (Fig. 9). This partitioning of the energy balance is presumably determined by the high soil moisture content at the study site, which controls both the latent heat flux and the ground heat flux. The high soil moisture content at the study site is facilitated by the shallow active layer depth, which also affects the soil temperature gradient and hence the ground heat flux. Consequently, the surface energy balance during the summer time is, to a certain degree, directly affected by the permafrost conditions, in particular by its thermal state and the soil water/ice content. The observed magnitude to the energy balance components corresponds well with values observed at other wet tundra landscapes of similar latitude (Eugster et al., 2000). However, the magnitude of the summer time ground heat flux is at the upper edge of the reported values.

During the winter period the radiative forcing is negative and significantly smaller than during summer (Fig. 9). The main part of the surface energy loss is attributed to the thermal radiation and 20% are consumed by the latent heat flux, which constitutes the smallest component in the winter energy balance. Despite of the reduced radiative forcing, the ground heat flux is of similar magnitude as during the summer period. In the presented case, the ground heat flux supplies about 60% to the entire energy loss, whereas only 40% are balanced by the sensible heat flux. The exceptional high contribution of the ground heat flux to the surface energy balance is related to the strong soil temperature gradient, as a result of the continental climate conditions and facilitated by the shallow snow cover. Compared to the ground heat flux, the sensible heat flux appears to be depleted corresponding to the low air temperature gradient near the surface (Table 6).

5.3 Implications for permafrost modeling

With respect for permafrost modeling four major implications can be drawn from our results:

1. The ground heat flux at the study site is of remarkable magnitude, especially during the long-lasting arctic winter. In contrast to lower latitudes and less continental climates, the ground heat flux essentially characterizes the surface energy budget and affects the atmospheric conditions near the surface. This suggests a certain impact on the atmospheric processes in climate models. It has been demonstrated in several experiments that the soil parameterization affect the performance of climate models (Pitman, 2003; Rinke et al., 2008; Lawrence and Slater, 2008). The representation of the boundary layer dynamics in weather and climate models was essentially improved by incorporating soil freezing (Viterbo et al., 1999; Cox et al., 1999). In the Arctic, inaccuracies of weather forecast models in the near surface air temperature are found to be related to the parametrization of the ground heat flux (Beesley et al., 2000).

2. The surface energy balance and hence permafrost is very sensitivity to the snow cover, especially the timing of snow accumulation and melt, the snow depth and the albedo. Our measurements reveal, that the thermal isolation of the snow cover results in a positive temperature difference of about 4 °C between the average soil and surface temperature. This effect is described in detail in a theoretical study by Goodrich (1982). Due to the high albedo, the surface energy balance during late winter and spring is largely determined by sensible heat flux despite high values of incoming short-wave radiation. Numerous studies demonstrated the impact of the snow cover on the atmospheric conditions ranging from the local scale (meters to kilometers) (e.g. Neumann and Marsh, 1998; Pohl et al., 2006; Bewley et al., 2010) to global effect (e.g. Walland and Simmonds, 1996; Cook et al., 2008).

3. The permafrost at the study site is mainly controlled by the net radiation, which in turn can be strongly altered by clouds, especially during winter. This suggests that the thermal state of permafrost is affected by large scale atmospheric circulation processes such as cyclone activity and the annual dynamics of the Siberian High. The initial warming in spring is mainly forced by sensible heat flux, which additionally suggests a certain contribution of air mass advection to the permafrost heat budget. The impact of atmospheric circulation patterns on the energy balance of the Arctic has been outlined in numerous studies (e.g. Curry et al., 1993; Serreze et al., 2000; Petrone and Rouse, 2000).

4. Our measurements reveal high spatial and temporal variabilities of refreezing. Differences in completion of freeze back between water bodies and soil can amount up to several months and the duration of refreezing in different years can vary up to 3 months. This indicates that the time available for microbial decomposition features a significant spatial and inter-annual variability, which in turn may affect the green house gas emissions especially of small ponds. The importance of high-arctic water bodies for the atmospheric methane budget has been demonstrated by Walter et al. (2006, 2007). These findings have strong implications

for model schemes as introduced by Khvorostyanov et al. (2008), which aim to include biochemical processes in permafrost regions on larger scales.

6 Summary and conclusions

Based on the results of the first and the second part of this study, we conclude with an overview of the main characteristics of the annual surface energy balance.

During the entire annual cycle, the surface energy budget is determined by the radiation balance. The net radiation essentially depends on the seasonality of the short-wave radiation budget, the presence or absence of the snow cover and the cloudiness. The snow cover has its greatest impact over 4 months from the end of the polar night until snow melt, when the high snow albedo significantly reduces the net short-wave radiation. Clouds are generally found to reduce the net radiation by about 50% during the snow-free season, while they almost prevent radiative losses during winter.

The turbulent heat fluxes have their largest impact on the surface energy budget during the snow-free period, when they balance about 70% of the net radiation. The latent heat flux is a factor of two higher than the sensible heat flux, so that the average Bowen ratio yields 0.5. During the summer months, the latent heat flux is largely in balance with the observed precipitation rates, which suggests a regionally closed water cycle between the atmosphere and the tundra surface. During the winter period, the latent heat flux is relatively small and so is sublimation at the snow cover. The sensible heat flux reaches its largest relative contribution to the surface energy balance during the late winter period, when it balances almost 70% of the radiative losses. This indicates that warming after the winter period is influenced by the influx of warm air. Furthermore, it is worthwhile to note that the lower atmosphere is well mixed during a major part of the winter season and stable stratifications are very rare.

The ground heat flux is a significant component in the surface energy balance, with relative contributions of about 20% during summer and 60% during polar winter. During the summer months about 60% of the ground heat flux is consumed by active layer

thawing, whereas 40% are used for the warming of the soil. The refreezing period, which can last from the end of September until the beginning of December, is mainly controlled by the radiation balance. At that time, clouds and the snow cover have their most persistent impact on the ground thermal regime as they significantly influence the duration of the refreezing period. The rare occurrence of atmospheric inversions near the surface during winter is partly attributed to the considerable ground heat flux. The already high heat storage capacity of the tundra can be further increased by the presence of water bodies, which can be remarkable even for small water bodies, such as ponds.

We conclude that the realistic simulation of the surface energy balance in climate models is mandatory with regard to large scale permafrost predictions. This issue involved the reproduction highly variable features such as cloudiness, snow cover and the thermal soil properties. Furthermore, there are indications that a more accurate representation of the thermal dynamics of permafrost could aid to improve the modeling of the atmospheric boundary layer in the Arctic.

Acknowledgements. We are thankful to the Department of Micro-Meteorology of the University of Bayreuth headed by Thomas Foken for providing the eddy-covariance post-processing software. We especially acknowledge the help of Günther Stoof for the support of our field work especially during the spring expeditions. We gratefully acknowledge financial support by the Helmholtz Association through a grant (VH-NG 203) awarded to Julia Boike.

References

Beesley, J., Bretherton, C., Jakob, C., Andreas, E., Intrieri, J., and Uttal, T.: A comparison of cloud and boundary layer variables in the ECMWF forecast model with observations at surface heat budget of the Arctic Ocean(SHEBA) ice camp, J. Geophys. Res., 105, 12337–12349, 2000. 1411

Bewley, D., Essery, R., Pomeroy, J., and Ménard, C.: Measurements and modelling of snowmelt and turbulent heat fluxes over shrub tundra, Hydrol. Earth Syst. Sci., 14, 1331–1340, doi:10.5194/hess-14-1331-2010, 2010. 1412

Boike, J., Wille, C., and Abnizova, A.: Climatology and summer energy and water balance of polygonal tundra in the Lena River Delta, Siberia, J. Geophys. Res.-Biogeo., 113, G03025, doi:10.1029/2007JG000540, 2008. 1394
Comiso, J.: Warming trends in the Arctic from clear sky satellite observations, J. Climate, 16, 3498–3510, 2003. 1393
Cook, B., Bonan, G., Levis, S., and Epstein, H.: The thermoinsulation effect of snow cover within a climate model, Clim. Dynam., 31, 107–124, 2008. 1412
Cox, P., Betts, R., Bunton, C., Essery, R., Rowntree, P., and Smith, J.: The impact of new land surface physics on the GCM simulation of climate and climate sensitivity, Clim. Dynam., 15, 183–203, 1999. 1411
Curry, J., Schramm, J., and Ebert, E.: Impact of clouds on the surface radiation balance of the Arctic Ocean, Meteorol. Atmos. Phys., 51, 197–217, 1993. 1408, 1412
Delire, C., Levis, S., Bonan, G., Foley, J., Coe, M., and Vavrus, S.: Comparison of the climate simulated by the CCM3 coupled to two different land-surface models, Clim. Dynam., 19, 657–669, 2002. 1393
ESA: The Lena River Delta, http://earth.eo.esa.int/cgi-bin/satimgsql.pl?show_url=1471&startframe=0, last access: 21 July 2010, 2006. 1423
Eugster, W., Rouse, W., Pielke Sr., R., McFadden, J., Baldocchi, D., Kittel, T., Chapin, F., Liston, G., Vidale, P., Vaganov, E., and Chambers, S.: Land–atmosphere energy exchange in Arctic tundra and boreal forest: available data and feedbacks to climate, Global Change Biol., 6, 84–115, 2000. 1410
Foster, J., Sun, C., Walker, J., Kelly, R., Chang, A., Dong, J., and Powell, H.: Quantifying the uncertainty in passive microwave snow water equivalent observations, Remote Sens. Environ., 94, 187–203, 2005. 1400
Goodrich, L.: The influence of snow cover on the ground thermal regime, Can. Geotech. J., 19, 421–432, 1982. 1412
Grigoriev, N.: The temperature of permafrost in the Lena Delta Basin – deposit conditions and properties of the permafrost in Yakutia, chap. 2, Yakutsk, 97–101, 1960. 1395
Hinzman, L., Bettez, N., Bolton, W., Chapin, F., Dyurgerov, M., Fastie, C., Griffith, B., Hollister, R., Hope, A., Huntington, H., et al.: Evidence and implications of recent climate change in Northern Alaska and other arctic regions, Climatic Change, 72, 251–298, 2005. 1393
Høgstrøm, U.: Non-dimensional wind and temperature profiles in the atmospheric surface layer: a re-evaluation, Bound.-Lay. Meteorol., 42, 55–78, 1988. 1397

Holland, M. and Bitz, C.: Polar amplification of climate change in coupled models, Clim. Dynam., 21, 221–232, 2003. 1393
Johannessen, O., Bengtsson, L., Miles, M., Kuzmina, S., Semenov, V., Alekseev, G., Nagurnyi, A., Zakharov, V., Bobylev, L., Pettersson, L., et al.: Arctic climate change: observed and modelled temperature and sea-ice variability, Tellus A, 56, 328–341, 2004. 1393
Kaplan, J., Bigelow, N., Prentice, I., Harrison, S., Bartlein, P., Christensen, T., Cramer, W., Matveyeva, N., McGuire, A., Murray, D., et al.: Climate change and Arctic ecosystems: 2. Modeling, paleodata-model comparisons, and future projections, J. Geophys. Res., 108, 8171, doi:10.1029/2002JD002559, 2003. 1393
Kelly, R., Chang, A., Foster, J., and Tedesco, M.: AMSR-E/Aqua 5-day 3 Global Snow Water Equivalent EASE-Grids V002, National Snow and Ice Data Center, Boulder, Colorado, USA, digital media, (data used from 2007–2009), 2004. 1400
Khvorostyanov, D., Krinner, G., Ciais, P., Heimann, M., and Zimov, S.: Vulnerability of permafrost carbon to global warming, Part I: model description and role of heat generated by organic matter decomposition, Tellus B, 60, 250–264, 2008. 1413
Langer, M., Westermann, S., Muster, S., Piel, K., and Boike, J.: Permafrost and surface energy balance of a polygonal tundra site in northern Siberia - Part 1: Spring to fall, The Cryosphere Discuss., 4, 901–947, doi:10.5194/tcd-4-901-2010, 2010. 1394, 1396, 1397, 1398, 1399, 1400, 1401, 1431
Lawrence, D. and Slater, A.: A projection of severe near-surface permafrost degradation during the 21st century, Geophys. Res. Lett., 32, L24401, doi:10.1029/2005GL025080, 2005. 1393
Lawrence, D. and Slater, A.: Incorporating organic soil into a global climate model, Clim. Dynam., 30, 145–160, 2008. 1411
Lawrence, D., Slater, A., Romanovsky, V., and Nicolsky, D.: Sensitivity of a model projection of near-surface permafrost degradation to soil column depth and representation of soil organic matter, J. Geophys. Res., 113, F02011, doi:10.1029/2007JF000883, 2008. 1393
Lewkowicz, A.: Evaluation of miniature temperature-loggers to monitor snowpack evolution at mountain permafrost sites, Northwestern Canada, Permafrost Periglac., 19, 323–331, 2008. 1400
Moritz, R., Bitz, C., and Steig, E.: Dynamics of recent climate change in the Arctic, Science, 297, 1497–1502, doi: 10.1126/science.1076522, 2002. 1393
Neumann, N. and Marsh, P.: Local advection of sensible heat in the snowmelt landscape of Arctic tundra, Hydrol. Process., 12, 1547–1560, 1998. 1412

Nicolsky, D., Romanovsky, V., Alexeev, V., and Lawrence, D.: Improved modeling of permafrost dynamics in a GCM land-surface scheme, Geophys. Res. Lett., 34, L08501, doi:10.1029/2007GL029525, 2007. 1393

Osterkamp, T.: The recent warming of permafrost in Alaska, Global Planet. Change, 49, 187–202, 2005. 1393

Overland, J., Wang, M., and Salo, S.: The recent Arctic warm period, Tellus A, 60, 589–597, 2008. 1393

Overpeck, J., Hughen, K., Hardy, D., Bradley, R., Case, R., Douglas, M., Finney, B., Gajewski, K., Jacoby, G., Jennings, A., et al.: Arctic environmental change of the last four centuries, Science, 278, 1251–1256, doi:10.1126/science.278.5341.1251, 1997. 1393

Persson, P., Fairall, C., Andreas, E., Guest, P., and Perovich, D.: Measurements near the atmospheric surface flux group tower at SHEBA: near-surface conditions and surface energy budget, J. Geophys. Res.-Oceans, 107(C10), 8045 pp., doi:10.1029/2000JC000705, 2002. 1409

Petrone, R. and Rouse, W.: Synoptic controls on the surface energy and water budgets in sub-arctic regions of Canada, Int. J. Climatol., 20, 1149–1165, 2000. 1412

Pitman, A.: The evolution of, and revolution in, land surface schemes designed for climate models, Int. J. Climatol., 23, 479–510, 2003. 1393, 1411

Pohl, S., Marsh, P., and Liston, G.: Spatial-temporal variability in turbulent fluxes during spring snowmelt, Arct. Antarct. Alp. Res., 38, 136–146, 2006. 1412

Pulliainen, J. and Hallikainen, M.: Retrieval of regional snow water equivalent from space-borne passive microwave observations, Remote Sens. Environ., 75, 76–85, 2001. 1400

Rees, W.: Infrared emissivity of Arctic winter snow, Int. J. Remote Sens., 14, 3069–3073, 1993. 1396

Rinke, A., Kuhry, P., and Dethloff, K.: Importance of a soil organic layer for Arctic climate: a sensitivity study with an Arctic RCM, Geophys. Res. Lett., 35, L13709, doi:10.1029/2008GL034052 , 2008. 1393, 1411

Schotanus, P., Nieuwstadt, F., and Bruin, H.: Temperature measurement with a sonic anemometer and its application to heat and moisture fluxes, Bound.-Lay. Meteorol., 26, 81–93, 1983. 1396

Serreze, M., Walsh, J., Chapin, F., Osterkamp, T., Dyurgerov, M., Romanovsky, V., Oechel, W., Morison, J., Zhang, T., and Barry, R.: Observational evidence of recent change in the northern high-latitude environment, Climatic Change, 46, 159–207, 2000. 1412

Shupe, M. and Intrieri, J.: Cloud radiative forcing of the Arctic surface: the influence of cloud properties, surface albedo, and solar zenith angle, J. Climate, 17, 616–628, 2004. 1408

Stendel, M. and Christensen, J.: Impact of global warming on permafrost conditions in a coupled GCM, Geophys. Res. Lett., 29, 1632, doi:10.1029/2001GL014345, 2002. 1393

Sturm, M., Holmgren, J., König, M., and Morris, K.: The thermal conductivity of seasonal snow, J. Glaciol., 43, 26–41, 1997. 1399

Tape, K., Sturm, M., and Racine, C.: The evidence for shrub expansion in Northern Alaska and the Pan-Arctic, Global Change Biol., 12, 686–702, 2006. 1393

Turner, J., Overland, J., and Walsh, J.: An Arctic and Antarctic perspective on recent climate change, Int. J. Climatol., 27, 277–293, 2007. 1393

Vavrus, S.: The impact of cloud feedbacks on Arctic climate under greenhouse forcing, J. Climate, 17, 603–615, 2004. 1393

Viterbo, P., Beljaars, A., Mahfouf, J., and Teixeira, J.: The representation of soil moisture freezing and its impact on the stable boundary layer, Q. J. Roy. Meteor. Soc., 125, 2401–2426, 1999. 1393, 1411

Walland, D. and Simmonds, I.: Sub-grid-scale topography and the simulation of Northern Hemisphere snow cover, Int. J. Climatol., 16, 961–982, 1996. 1412

Walter, K., Zimov, S., Chanton, J., Verbyla, D., and Chapin, F.: Methane bubbling from Siberian thaw lakes as a positive feedback to climate warming, Nature, 443, 71–75, 2006. 1412

Walter, K., Edwards, M., Grosse, G., Zimov, S., and Chapin III, F.: Thermokarst lakes as a source of atmospheric CH_4 during the last deglaciation, Science, 318, 633, 633–636, doi:10.1126/science.1142924, 2007. 1412

Westermann, S., Lüers, J., Langer, M., Piel, K., and Boike, J.: The annual surface energy budget of a high-arctic permafrost site on Svalbard, Norway, The Cryosphere, 3, 245–263, doi:10.5194/tc-3-245-2009, 2009. 1393, 1409

Zhang, T.: Influence of the seasonal snow cover on the ground thermal regime: an overview, Rev. Geophys., 43, RG4002, doi:10.1029/2004RG000157, 2005. 1399

Zhang, X., Walsh, J., Zhang, J., Bhatt, U., and Ikeda, M.: Climatology and interannual variability of Arctic cyclone activity: 1948–2002, J. Climate, 17(12), 2300–2317, 2004. 1395

Table 1. Definitions and constants.

Q_{net}	net radiation
ΔQ_S	net short-wave radiation
ΔQ_L	net long-wave radiation
$Q_{L\downarrow}$	incoming long-wave radiation
Q_{HB}	buoyancy flux
Q_H	sensible heat flux
Q_E	latent heat flux
Q_G	ground or snow heat flux
$Q_{G,sensible}$	sensible ground heat flux
$Q_{G,latent}$	latent ground heat flux
$Q_{net,p}$	net radiation at the pond
$Q_{G,p}$	heat flux released from pond
C	residual of the energy balance
u_*	friction velocity
$\zeta = z/L_*$	stability parameter (z: measurement height, L_* Obukhov length)
T_{air}	air temperature
T_{surf}	surface temperature
R_H	relative humidity
θ_w	volumetric liquid water content
$\theta_{w,min}$	minimum liquid water content (frozen)
$\theta_{w,max}$	maximum liquid water content (thawed)
θ_i	volumetric ice content
P_{dry}	porosity
c_p	specific heat capacity of air at constant pressure
ρ_{air}	density of air
$\rho_{ice} = 0.91\,g\,cm^{-3}$	density of ice
$\rho_{snow} = 0.19\,g\,cm^{-3}$	density of snow

Table 1. Continued.

D_h	thermal diffusivity
K_h	thermal conductivity
C_h	volumetric heat capacity
$C_{h,i} = 1.9\,MJ\,m^{-3}\,K^{-1}$	volumetric heat capacity of ice
$C_{h,s} \approx 2.3\,MJ\,m^{-3}\,K^{-1}$	volumetric heat capacity of the solid soil matrix

Table 2. Used soil parameters for ground heat flux calculations during the winter period. Values of porosity P_{dry} and volumetric ice content θ_i are estimated based on soil sample analysis and in situ soil water content measurements during summer. The heat capacities are calculated by weighting $C_{h,i}$ and $C_{h,s}$ according to the assumed ice content and porosity. The thermal diffusivities D_h are determined by using the conductive method described in the first part of this study, from which we evaluate the thermal conductivity values K_h with the estimated heat capacity. Errors are calculated using Gaussian error propagation.

Substrate	P_{dry}	θ_i	C_h (MJ m^{-3} K^{-1})	D_h (m^2 s^{-1})	K_h (W m^{-1} K^{-1})
Frozen dry peat	0.8±0.1	0.1±0.1	0.7±0.3	0.68±0.19	0.46±0.25
Frozen wet peat	0.8±0.1	0.7±0.1	1.8±0.3	0.54±0.09	0.95±0.23
Frozen saturated peat	0.8±0.1	0.8±0.1	2.0±0.05	0.96±0.09	1.92±0.19
Snow	ρ_{snow}=190±10 (kg m^{-3})		0.40±0.04	0.54±0.04	0.22±0.03
Ice	ρ_{ice}=920 (kg m^{-3})		1.9	1.2	2.3

Table 3. Average heat fluxes and essential climate parameters. According to the available dataset, sub-periods are required during the late winter section. Values are in W m^{-2}, if not indicated differently. Turbulent heat flux values marked in bold are affected by minor data gaps due to quality assessment or the exclusion of lee wind sectors. Radiation values measured with the NR-Lite sensor are marked with $^{\ominus}$, and values obtained with the four component sensor (CNR1) are indicated with $^{\oplus}$. Modeled values of latent heat flux are indicated with ‡.

	Early winter		Polar winter		Late winter	
	2007	2008	2007–2008	2008–2009	2008	2009
	1 Oct–30 Nov	1 Oct–30 Nov	1 Dec–30 Jan	1 Dec–30 Jan	27 Feb–30 Mar	1 Feb–30 Mar
Q_{net}	−17$^{\ominus}$	−21$^{\oplus}$	−21$^{\ominus}$	−25$^{\oplus}$	−14.7$^{\ominus}$	–
ΔQ_S	–	1.5	0	0	–	–
ΔQ_L	–	−22	−21	−25	–	–
Q_H	**−6**	**−5**	**−9**	–	**−10.3**	–
Q_E	**9**‡	**13**‡	**4**‡	–	**3**‡	–
Q_G	−11	−20	−17	−14	−5.4	−10.4
$Q_{G,sensible}$	3	−3	−14	−14	−5.4	−10.4
$Q_{G,latent}$	−14	−17	−3	0	0	–
C	−9	−9	−1	–	2	–
$Q_{net,p}$	−18	−23	−22	−25	−20	−21.5
$Q_{G,p}$	−12†	−34†	−32	−28	−12.6	−22.3
T_{surf} (°C)	−16	−15	−29.9	−29.7	−25.9	−35.5
T_{air} (°C)	−16.1	−14.8	−29.7	−29.5	−24.8	−34.7
R_H (%)	81	–	70	–	75	–
Snow depth (m)	0.09	0.05	0.11	0.15	0.18	–

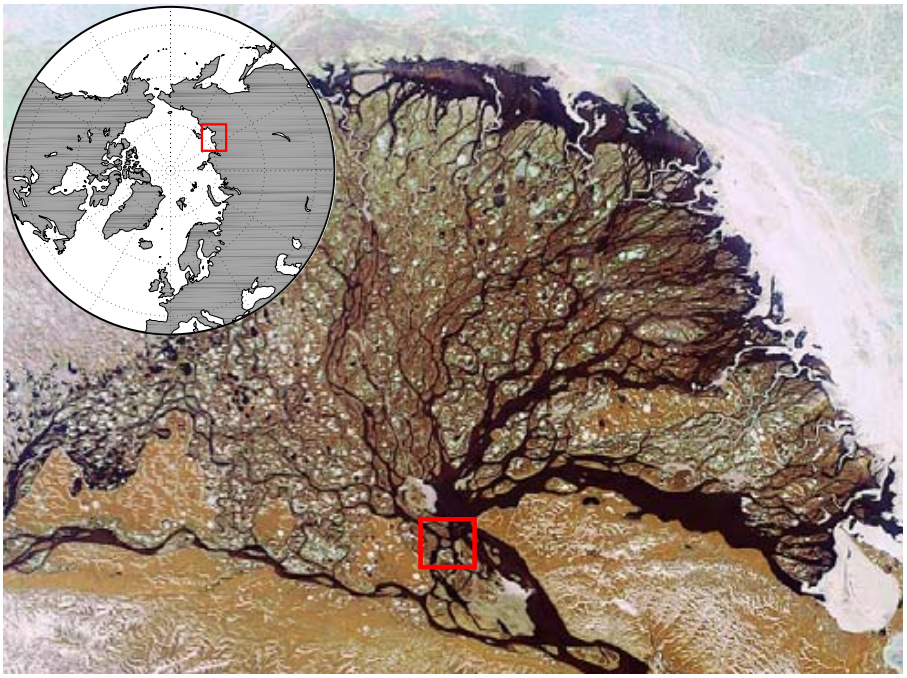

Fig. 1. The location of the study site in the Lena River Delta on a Envisat (MERIS) image acquired on 15 June 2006 (ESA, 2000). The Lena Delta covers an area of approximately 30 000 km^2.

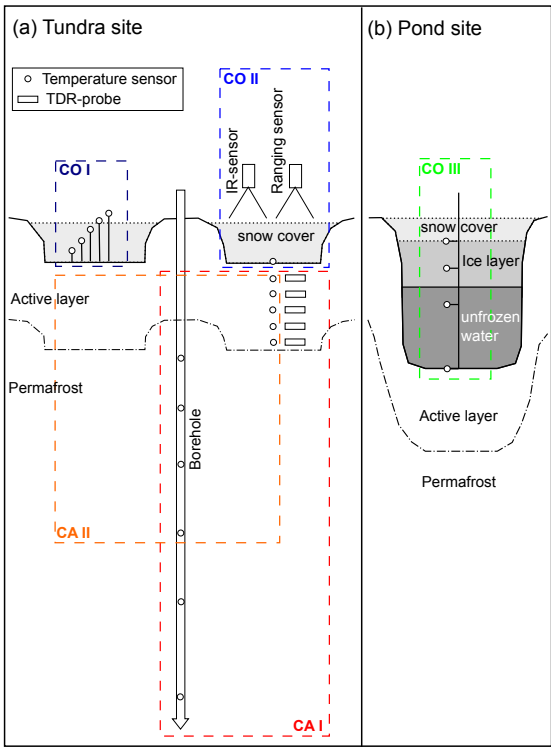

Fig. 2. Scheme of the different measurement setups used for the evaluation of subsurface heat flux. **(a)** Cross-section of the tundra soil indicating polygonal rims and centers. **(b)** Cross-section of the polygonal pond during the stage of freezing. Note that, the depicted scheme is not to scale.

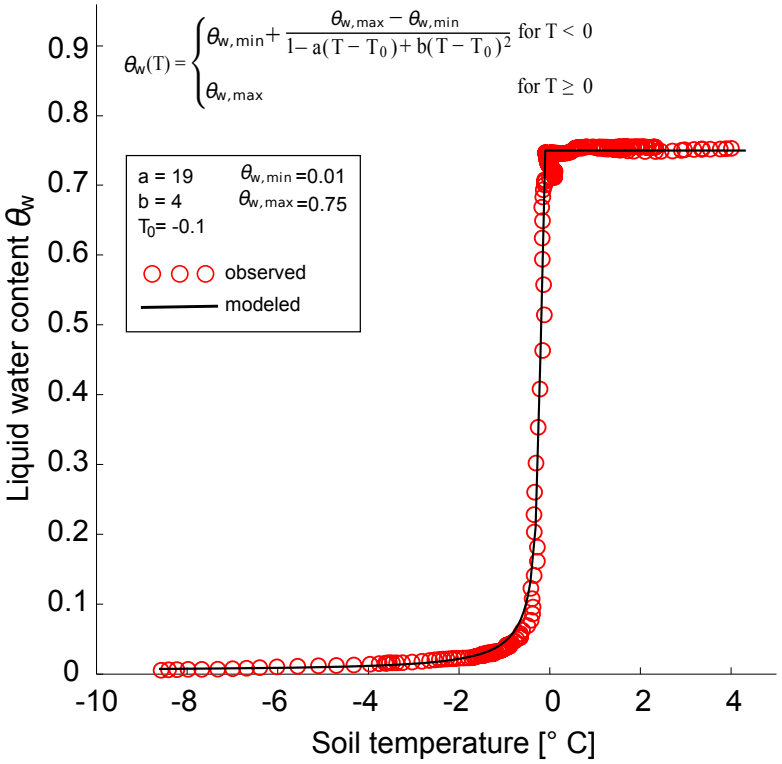

Fig. 3. The freezing characteristic of the soil at the study site, which parameterizes the soil water content θ_w in dependence to the soil temperature. The used polynomial function and the fitted parameters are depicted in the figure.

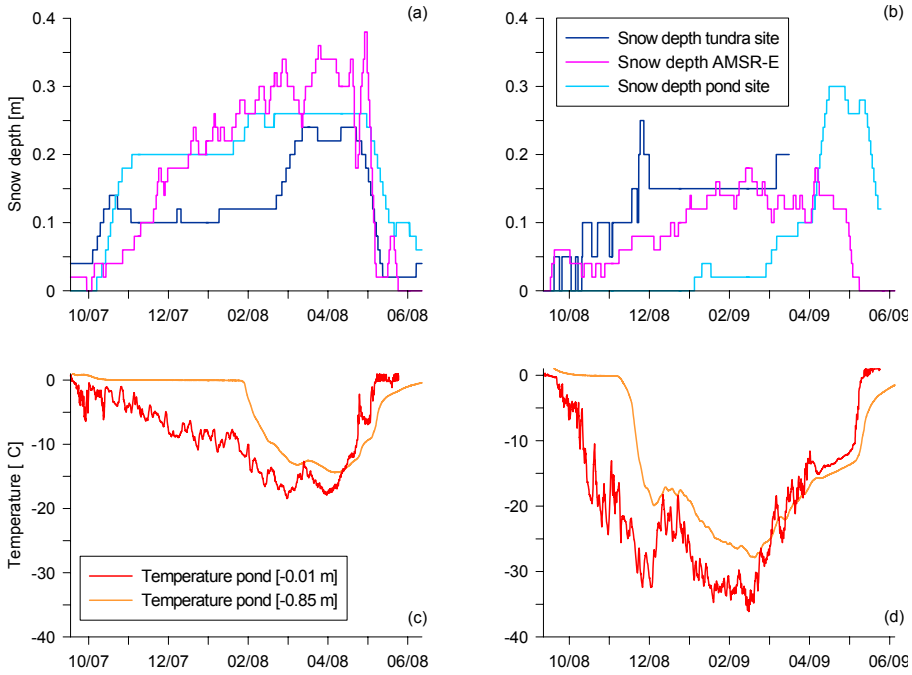

Fig. 4. The diagrams at the top show the evolution of the snow depth measured at the tundra site (polygonal center) and the pond site during the winter periods of **(a)** 2007 and **(b)** 2008. Moreover, we depict the snow depth inferred from the AMSR-E snow-water equivalent product using a snow density of 190 kg m^{-3} for both periods. The diagrams at the bottom depict the temperatures observed at the surface and the top of sediment of the investigated polygonal pond for the winter periods of **(c)** 2007 and **(d)** 2008.

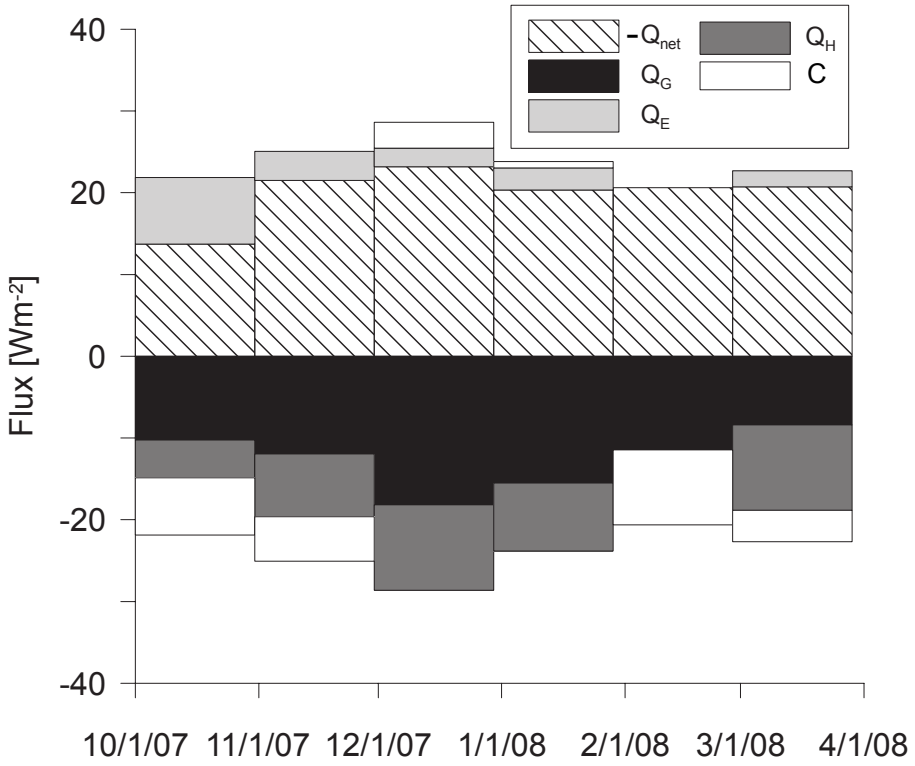

Fig. 5. Monthly averages of energy balance components for the winter 2007/2008. Note that the net radiation Q_{net} is depicted with opposite sign.

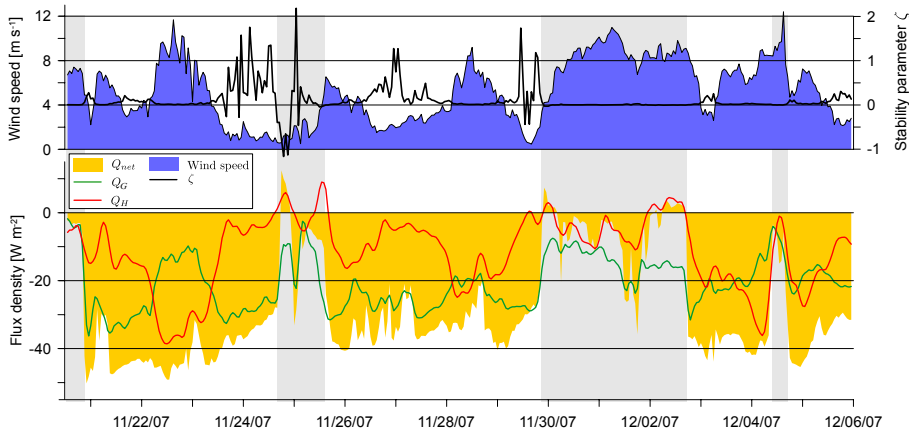

Fig. 6. Exemplary measurements of Q_{net}, Q_H and Q_G during the transition from early to polar winter in 2007 (lower graph). Presumably overcast conditions are shaded. Measurements of the wind speed and the stability parameter ζ are depicted in the upper graph.

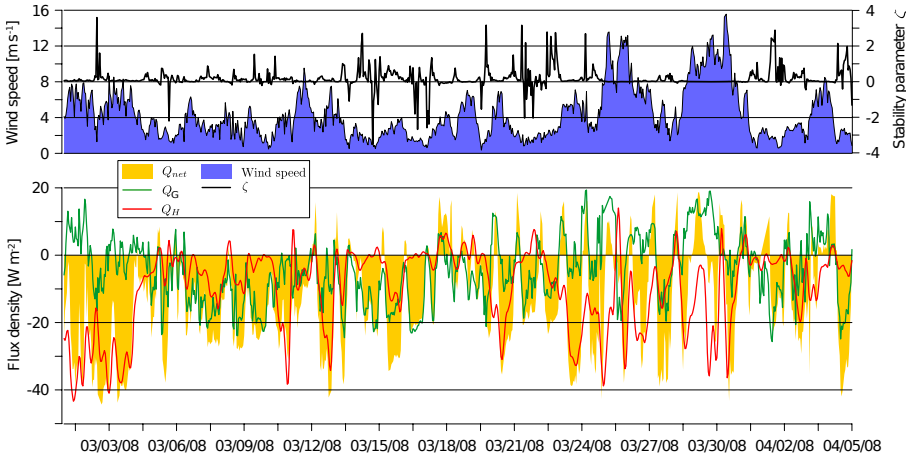

Fig. 7. Measurements of Q_{net}, Q_H and Q_G during the late winter in 2008 (lower graph). The wind speed and the stability parameter ζ are depicted in the upper graph.

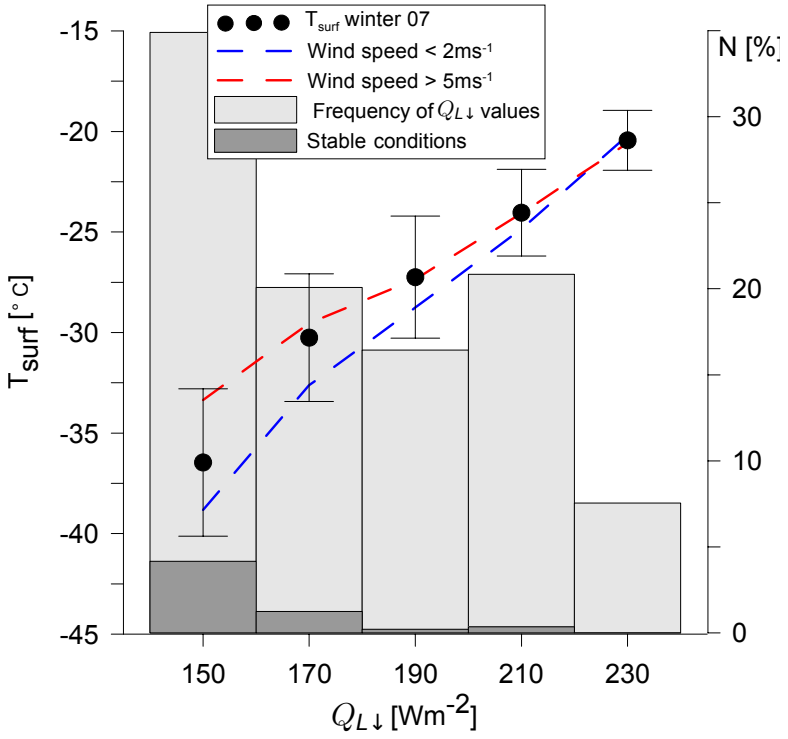

Fig. 8. The surface temperature T_{surf} in dependence to the incoming long-wave radiation $Q_{L\downarrow}$ and different wind speeds. The first histogram (light grey) indicates the frequency of observations that feature the displayed classes of incoming long-wave radiation. The second histogram (dark grey) shows the occurrence of stable atmospheric stratification under the different $Q_{L\downarrow}$ conditions.

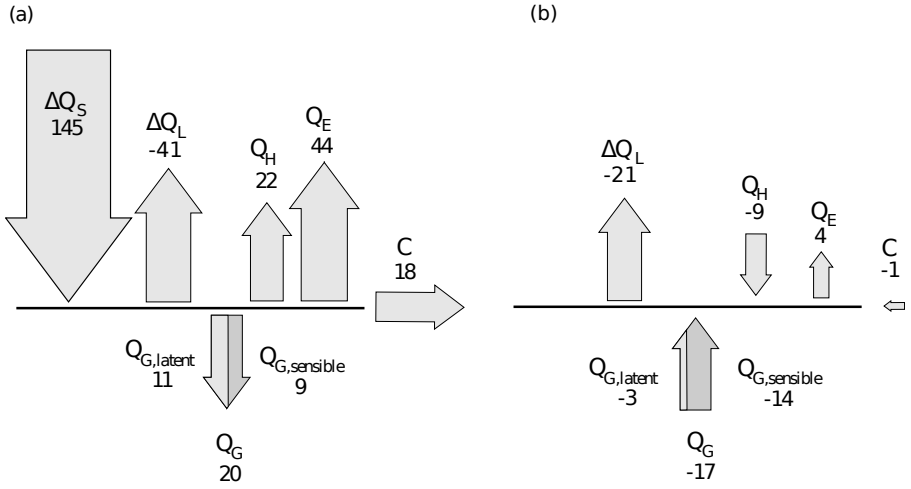

Fig. 9. The partitioning of the surface energy balance during **(a)** the summer period from 7 June–30 August 2008 (compare Langer et al., 2010) and **(b)** the winter period from 1 December 2007–30 January 2008 (Table 6). The areas of the arrows are scaled according to the heat flux values. The subsurface hat flux at the tundra site Q_G is separated according to the energy storage of sensible $Q_{G,sensible}$ and latent heat $Q_{G,latent}$.

Chapter 2.6

Schramm, I., **Boike**, J., Hinzman, L., and Bolton, R. W. (2007): Application of Topoflow, a spatial distributed hydrological model to the Imnavait Creek watershed, Alaska. *Journal of geophysical research (Biogeosciences)* 112, G04S46, 7doi:10.1029/2006JG000326.

JOURNAL OF GEOPHYSICAL RESEARCH, VOL. 112, G04S46, doi:10.1029/2006JG000326, 2007

Click Here for Full Article

Application of TopoFlow, a spatially distributed hydrological model, to the Imnavait Creek watershed, Alaska

Imke Schramm,[1] Julia Boike,[1] W. Robert Bolton,[2] and Larry D. Hinzman[3]

Received 26 September 2006; revised 11 January 2007; accepted 6 April 2007; published 7 December 2007.

[1] This study presents the application of the hydrological model TopoFlow to the Imnavait Creek watershed, Alaska, United States. It summarizes the hydrologically important processes in this arctic basin, and focuses on the modeling of the hydrological processes in 2001. The model is evaluated for its capability to reproduce the different components of the hydrological cycle. Model simulations are done for different climate change scenarios to evaluate the impacts on the hydrology. Imnavait Creek ($\sim$2 km^2) is underlain by continuous permafrost, and two features characterize the channel network: The stream is beaded, and numerous water tracks are distributed along the hillslopes. These facts, together with the constraint of the subsurface system to the shallow active layer, strongly influence the runoff response to rain or snowmelt. Climatic conditions vary greatly during the course of the year, providing a good testing of model capabilities. Simulation results indicate that the model performs quantitatively well. The different components of the water cycle are represented in the model, with refinements possible in the small-scale, short-term reproduction of storage-related processes, such as the beaded stream system, the spatial variability of the active layer depth, and the complex soil moisture distribution. The simulation of snow melt discharge could be improved by incorporating an algorithm for the snow-damming process.

Citation: Schramm, I., J. Boike, W. R. Bolton, and L. D. Hinzman (2007), Application of TopoFlow, a spatially distributed hydrological model, to the Imnavait Creek watershed, Alaska, *J. Geophys. Res.*, *112*, G04S46, doi:10.1029/2006JG000326.

1. Introduction

1.1. Hydrology of the Arctic

[2] The presence of permafrost is the primary factor distinguishing arctic from temperate watersheds. Permafrost underlies approximately 24% of the exposed land area in the Northern Hemisphere, making it a significant proportion of the land mass [*Romanovsky et al.*, 2002]. The permafrost condition is a crucial component in its influence on many of the hydrologic processes in the arctic and subarctic environments. The presence of permafrost significantly alters surface and subsurface water fluxes, as well as vegetative functions [*Walsh et al.*, 2005]. Permafrost dominates microclimatology and the thermal regime, including evapotranspiration [*Hinzman et al.*, 1996, 2006]. Permafrost controls water storage processes and the energy and water balances [*Boike et al.*, 1998; *Bowling et al.*, 2003].

[3] *Hinzman et al.* [2005] point out that the primary control on hydrological processes is dictated by the presence or absence of permafrost, but is also influenced by the thickness of the active layer, the thin layer of soil overlying permafrost that thaws in the summer. The active layer in the arctic varies from several tens of centimeters to 1 or 2 m in depth. It is of pivotal importance, as most hydrological and biogeochemical processes occur in this zone [*Kane et al.*, 1991a; *Walsh et al.*, 2005]. The conditions for plant growth, gas fluxes, groundwater flow regimes, and soil formation are all limited and to some extent determined by the active layer [*Boike et al.*, 1998]. The permafrost beneath the active layer limits the amount of soil water percolation and subsurface storage of water [*Vörösmarty et al.*, 2001]. Whereas nonpermafrost soils allow a deep groundwater system, the subsurface movement of water in permafrost-affected soils is largely confined to the shallow active layer. Therefore lateral flow is more important than in nonpermafrost soils [*Slaughter and Kane*, 1979]. These characteristics have a large impact on the runoff response. Permafrost generally accelerates the initiation of runoff [*McNamara et al.*, 1998]. As the water movement through the near-surface soils is relatively fast, the runoff response to precipitation is characterized by a rapid rise to peak flow and a rapid decline following peak flow [*Dingman*, 1973]. In addition, response times are shortened because vegetation in these areas tends to be sparse [*Church*, 1974]. While permafrost-dominated watersheds generally have a larger contributing area and a higher specific discharge, the specific base flow is lower compared to nonpermafrost regions [*McNamara et al.*, 1998].

[4] The annual thawing and freezing of the active layer are the driving forces for many surficial processes, such as

[1]Alfred Wegener Institute for Marine and Polar Research, Potsdam, Germany.
[2]Water and Environmental Research Center, University of Alaska, Fairbanks, Fairbanks, Alaska, USA.
[3]International Arctic Research Center, University of Alaska, Fairbanks, Fairbanks, Alaska, USA.

Copyright 2007 by the American Geophysical Union.
0148-0227/07/2006JG000326$09.00

cryoturbation. These perennial processes also have a control on the hydraulic properties of the soil, specifically the storage capacity and hydraulic conductivity [*Hinzman et al.*, 1991]. The variation of hydraulic properties results in runoff patterns which change throughout the thaw season. To understand hydrologic dynamics of the arctic, it is conducive to study the seasonal change in soil moisture in the active layer. An overview over the seasonal active layer characteristics is given in section 2.

1.2. Arctic Hydrology in a Changing Climate

[5] Air temperature, snow cover, and vegetation, all of which are affected by climate change, affect the temperature of the frozen ground and the depth of seasonal thawing. In interior Alaska, United States, the warmer climate has led to shrinking permafrost coverage and an increased active layer depth [*Osterkamp and Romanovsky*, 1999].

[6] General circulation models predict that the effects of anthropogenic greenhouse warming will be amplified in the northern high latitudes due to feedbacks in which variations in snow and sea ice extent, the stability of the lower troposphere, and thawing of permafrost play key roles [*Serreze et al.*, 2000]. Over the next 100 a the observed changes are projected to continue and their rate to increase, with permafrost degradation estimated to occur over 10–20% of the present permafrost area, and the southern limit of permafrost expected to shift northward by several hundred kilometers [*ACIA*, 2004].

[7] A progressive increase in the depth of seasonal thawing could be a relatively short-term reaction to climate change in permafrost regions, since it does not involve any lags associated with the thermal inertia of the climate/permafrost system [*Walsh et al.*, 2005]. There is a general consensus among models that seasonal thaw depths are likely to increase by more than 50% in the northernmost permafrost locations [*Walsh et al.*, 2005]. It appears that first-order impacts to the arctic, expected with a warming climate, result from a longer thawing/summer period combined with increased precipitation [*McCarthy et al.*, 2001]. The longer snow-free season and greater winter insulation produce secondary impacts that could cause deeper thaw of the active layer or greater melt of permanently frozen ice in glaciers and permafrost, increased biological activity, and changes in vegetative communities. Tertiary impacts arise as animals, people, and industry respond to the changing ecosystem.

[8] It is crucial to study the impacts of a changing climate on arctic water balances, as many processes are directly or indirectly influenced by components of the hydrological cycle, e.g., soil moisture, runoff, and evapotranspiration. However, the question if the arctic tundra will get wetter or drier is not a simple one as all the components interact with each other. In the Siberian arctic, for example, there is evidence of decreasing lake abundance despite increases in precipitation [*Smith et al.*, 2005].

[9] Changes to the water balance of northern wetlands are especially important because most wetlands in permafrost regions are peatlands, which may absorb or emit carbon depending on the depth of the water table [*ACIA*, 2004; *Walsh et al.*, 2005]. In this way, hydrologic changes will have global implications. Other important feedbacks to global warming are the albedo feedback and the weakening of the thermohaline circulation caused by increased freshwater flux into the Arctic Ocean.

1.3. Objective

[10] The study presented here is an application of the TopoFlow model, described in detail by *Bolton* [2006]. Our objective is to evaluate its capability of representing arctic hydrological processes. First, the hydrologically important processes of Imnavait Creek are described. The study then focuses on comparing the physical hydrology, measured and observed in the field, with model results. The model is executed and evaluated for its capability to reproduce the different components of the hydrological cycle.

2. Site Description

[11] The Imnavait Creek watershed is a small headwater basin of approximately 2 km^2, located in the northern foothills of the Brooks Range (68°30′N, 149°15′W), 250 km south of the Arctic Ocean (Figure 1). The Imnavait Creek flows parallel to the Kuparuk River for 12 km before it joins the Kuparuk River that drains into the Arctic Ocean. The elevation in this area ranges from 880 m at the outlet to 960 m at the southern headwaters. The area is underlain by continuous permafrost, and the topography consists of low rolling piedmont hills. Imnavait Creek has been intensively studied since 1985 by the Water and Environmental Research Center (WERC) at the University of Alaska, Fairbanks. This research is documented in, e.g., *Hinzman et al.* [1991, 1996], *Walker et al.* [1989], *Kane et al.* [1989, 1990, 1991b], and *McNamara* [1997].

[12] If not otherwise specified, all data reported in this section are documented by *Hinzman et al.* [1996]. In the Imnavait Creek watershed the mean annual temperature averages −7.4°C. In January (July) the average air temperature is −17°C (9.4°C). The annual precipitation averages 340 mm, two-thirds of which falls during the summer months of June, July, and August. Most rainfall is light (82% <1 mm/h) and appears evenly distributed over the catchment. Because of the influence of wind and topography, snow distribution and snow pack volumes in the Imnavait watershed are extremely variable both in time (year to year) and space (within the watershed), ranging from a few centimeters on windswept ridgetops to more than 1 m in the valley bottom. Winter snow accumulation generally starts around mid-September. A 20-a record shows that the annual snow water equivalent (SWE) in Imnavait Creek varies from 69 to 185 mm [*Berezovskaya et al.*, 2005]. Snowmelt is initiated between 1 and 27 May and is completed within 6–22 d. This reveals a considerable range in timing of snowmelt initiation. The vegetation is mostly water-tolerant plants such as tussock sedges and mosses [*Walker et al.*, 1989]. Generally, with a relatively impervious barrier so close to the surface, wet conditions exist in the active layer near the surface. This provides the conditions suitable for substantial evapotranspiration during the summer thawing months [*Kane et al.*, 1989].

[13] Imnavait Creek is a north draining, first-order stream. The stream is beaded, meaning that the channel connects numerous interspersed small ponds. These ponds are on the order of 2 m deep and a few meters in length and width [*Kane et al.*, 2000]; see Figure 1.

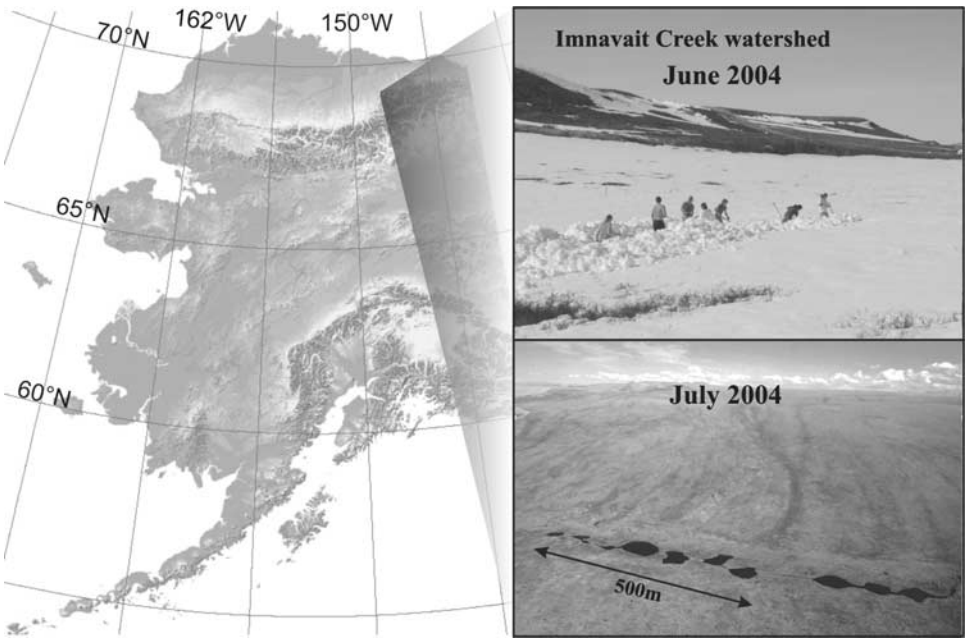

Figure 1. Map of Alaska, United States, with the location of the study area Imnavait Creek.

[14] The headwaters of the creek are found in a nearly level string bog, or strangmoor, with many poorly defined and interconnecting waterways [*Oswood et al.*, 1989]. Along the hillslopes, small drainage channels, or water tracks, carry water off of the slopes down to the valley bottom. The water tracks can be described as shrubby corridors with a width of ~2 m and spaced at ~10–20 m along the hillslope. The water tracks contain a system of interconnected deepenings, or small channels of ~5–10 cm width, which are partly directed parallel to the hillslope. Here the water flow follows microtopographic features, such as tussocks and hummocks [*Quinton et al.*, 2000]. Although quite obvious in aerial photographs, most of these water tracks are difficult to detect on the ground, as they are not incised [*Hastings et al.*, 1989; *McNamara*, 1997]. The water tracks generally take the most direct route down the slope but do not connect directly with the stream in the valley bottom. As the slope flattens out in the valley bottom, water moving down the water tracks disperses into numerous poorly defined channels and slowly makes its way over to the creek. Water moves downslope in these water tracks more rapidly than by subsurface means [*Kane et al.*, 1989].

[15] Runoff leaving the basin is usually confined to a period of 4 months, beginning during the snowmelt period in late May until freeze-up in September. Spring runoff is usually the dominant hydrological event of the year [*Kane and Hinzman*, 1988], typically producing the annual peak flow, and about 50% of the total annual runoff volume. Stream flow almost ceases after extended periods of low precipitation, whereas intense summer rainfall events produce substantial stream flow. Whether runoff is produced from rainfall events during the summer is strongly related to rain intensity and duration and antecedent soil moisture conditions [*Kane et al.*, 1989]. Furthermore, the runoff response depends on the snow cover (see section 5.2), the state of the active layer, and mechanisms related to the channel network: In a beaded stream system, small ponds act as reservoirs and can store water intermediately. This mechanism will, depending on the water level of each pond, result in a delayed hydrograph signal. Furthermore, the state of the active layer plays a pivotal role in altering runoff response. The maximum depth of thaw ranges from 25 to 100 cm, severely limiting the ability of the active layer to store large quantities of groundwater. The rate of thaw is dependent upon a number of factors, such as soil properties, soil moisture and ice content, and the distribution and duration of the snow cover. As a result, the depth of the active layer and thus the soil moisture is highly variable both in space and time [*Woo and Steer*, 1983; *Woo*, 1986]. Because of the excessive water supply from snowmelt, the water table in flatter areas rises above the ground surface to generate surface flow. Spring is therefore the time when the extent of surface flow is typically at a maximum. As summer progresses, the soil moisture content is reduced by an increasing depth of thaw and a continued evapotranspiration. This leads to a rapid depletion of the overall soil moisture content, and a nonsaturated zone develops. Occasional heavy rainstorms, however, can revive surface flow [*Woo and Steer*, 1983], and late summer and early fall rainstorms provide a recharge of soil moisture.

3. Models

3.1. Previous Studies

[16] At present, climate models do not represent the soil layers at high enough resolution to achieve the soil output needed to assess changes in permafrost distribution and active layer characteristics. The need for additional detail is particularly great for areas with thin or discontinuous permafrost [*Walsh et al.*, 2005]. Furthermore, the majority of land surface models have been primarily designed for lower latitudes and as such are not capable of realistically simulating the physical processes operating in the extreme

climate of the arctic. However, increasing efforts have been made to adequately model arctic environments over the last 2 decades. Several modeling studies with varying focuses have been applied to the Imnavait Creek watershed, where field data from multiple-year studies are available.

[17] *Hinzman and Kane* [1992] studied the potential hydrological response during a period of global warming using the HBV model. The original version of this model was developed in 1975 by the Swedish Meteorological and Hydrological Institute as a conceptual runoff model and modified for cold regions use by *Bergström* [1976]. It can be described as a reservoir-type model with routines for snowmelt, soil moisture accounting, control of surface and subsurface hillslope runoff response, and a transformation function to handle stream routing. The model input data are observations of air temperature, precipitation, and estimates of evapotranspiration. Model outputs are snowmelt runoff and the entire summer runoff response. Despite of the good congruence of measured and simulated hydrographs the authors report several shortcomings: First, the lack of physically based routines queries its capability of evaluating future changes. Second, the prediction capability could be improved by incorporating the redistribution of snow by winds and the retardation of runoff by snow damming [*Hinzman and Kane*, 1992].

[18] Another model was applied to the same study area by *Stieglitz et al.* [1999]. The simple land surface model TOPMODEL was used to explore the dynamics of the hydrologic cycle operating in arctic tundra regions. The model accounts for the topographic control of surface hydrology, ground thermal processes, and snow physics. This approach relies only on the statistics of the topography rather than its details. This has the advantage of being computationally inexpensive and compatible with the large spatial scales of today's climate models. However, the authors report several deficiencies, such as that the model performance in temperate watersheds is superior to that for arctic watersheds. This is attributed to the neglect of snow heterogeneity, which poses a real obstacle toward application on an arctic-wide basis. Furthermore, the representation of a seasonally changing connectivity of waterways (e.g. the beaded stream system) is seen to be difficult on a statistical base. As such, TOPMODEL is capable of simulating the overall balances, but shortcomings exist in the hydrograph simulation and soil moisture heterogeneity with high temporal resolution.

[19] A third modeling study with an application to Imnavait Creek is presented by *Zhang et al.* [2000]. Here a process-based, spatially distributed hydrological model is developed to quantitatively simulate the energy and mass transfer processes and their interactions within arctic regions (Arctic Hydrological and Thermal Model (ARHYTHM)). The model is the first of this kind for areas of continuous permafrost and consists of two parts: the delineation of the watershed drainage network and the simulation of hydrological processes. The last include energy-related processes such as snowmelt, ground thawing, and evapotranspiration. The model simulates the dynamic interactions of each of these processes and can predict spatially distributed snowmelt, soil moisture, and evapotranspiration over a watershed as well as discharge in any specified channels. Results from the application of this model demonstrate that spatially distributed models have the potential for improving our understanding of hydrology for certain settings. Nevertheless, the authors point out that an algorithm for snow damming, the usage of a higher resolution, and a better data collection network could improve the model results. Furthermore, the use of triangular elements makes it difficult to compare simulation results with other (e.g., remotely sensed) data sets.

[20] From former studies it becomes evident that topography plays a crucial role in the development of soil moisture heterogeneity. The fact that the impacts of this heterogeneity on surface water and energy fluxes are critical and perhaps overwhelming [*Stieglitz et al.*, 1999] leads to the conclusion that the representation of topographic features in a model cannot be neglected. Furthermore, there exist problems in the current models to handle the rapidly changing thermal (permafrost versus nonpermafrost and active layer development) and hydraulic (hydraulic conductivity and storage capacity) conditions typical of the (sub)arctic regime [*Bolton et al.*, 2000].

3.2. TopoFlow

[21] TopoFlow is a spatially distributed, process-based hydrological model, primarily designed for arctic and subarctic watersheds. TopoFlow is primarily based upon the merger of the ARHYTHM model [*Hinzman et al.*, 1995] and a D8-based rainfall-runoff model. Structurally, the most significant differences between the ARHYTHM and TopoFlow models are the incorporation of rectangular elements and flow routing using the D8 method. In the D8 method, horizontal water fluxes occur from one element to one of the eight adjacent elements in the direction of the steepest slope [*O'Callaghan and Mark*, 1984]. The model domain is defined by a rectangular, regular network DEM that encompasses the catchment area. Each TopoFlow element has dimensions of the DEM pixel (x and y directions) with up to ten user-specified layers of variable thickness in the z direction. On the basis of the conservation of mass principal, TopoFlow simulates major processes of the water balance (precipitation, snowmelt, evapotranspiration, groundwater flow, and overland/channel flow) as well as some storage processes (snow accumulation and infiltration/percolation). Most of these hydrologic processes are formulated in the exact manner as the ARHYTHM model and are well documented by *Zhang et al.* [2000]. Yet important improvements have been made in the process simulation component of the model. These improvements include expansion of the methods available to simulate the infiltration and channel flow processes, the ability to handle a variety of input variable formats, and a user-friendly interface. A detailed description of the model structure and the additional methods incorporated into TopoFlow can be found in the work of *Bolton* [2006].

[22] The development of soil moisture heterogeneity and its correct reproduction in models is crucial for the evaluation of its impacts on surface water and energy fluxes [*Boike et al.*, 1998]. TopoFlow addresses these issues through (1) its spatial distribution that explicitly models the movement of water from element to element; (2) by the implementation of physical routines that are unique in cold regions; (3) by providing user-friendly preprocessing tools that aid in handling the spatial variability, such as the

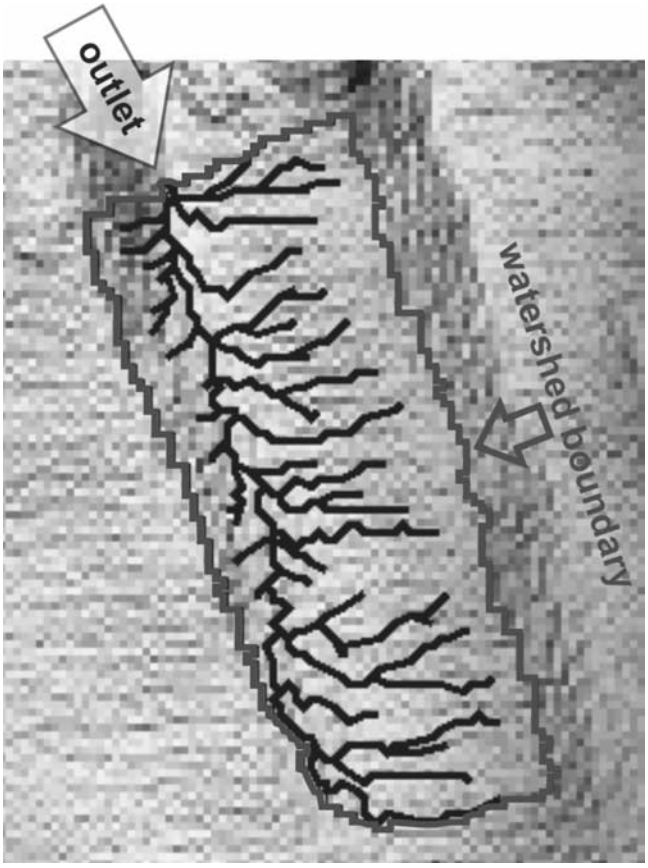

Figure 2. Digital Elevation Model of the Imnavait Creek watershed, its channel network, and watershed boundaries.

distribution of permafrost versus nonpermafrost, the active layer depth, and the snow pack distribution; and (4) by providing a flexible structure that allows the user deal with different data types or the lack of measured parameters.

[23] The hydrological simulation is initiated some hours prior to snowmelt with the end of winter snow pack distribution used as input. TopoFlow supports the degree day and the energy balance method for snowmelt. For evapotranspiration, two methods are provided to account for different availability of input data: the physically based energy balance and the semiempirical Priestley-Taylor approach. TopoFlow allows the spatial distribution of important parameters, such as meteorological variables or coefficients, soil moisture content, soil parameters, and snow pack distribution.

[24] At the time of this study an instantaneous infiltration method was available, and the three different flow processes (channel flow, overland flow, and subsurface flow in the shallow active layer) were incorporated into the model with Darcy's law and Manning's equation [*Schramm*, 2005]. Further improvements of the infiltration and percolation process, such as the finite difference solution of the Richards equation, Green-Ampt, and Smith-Parlange, have recently been incorporated [*Bolton*, 2006] (TopoFlow Web site, http://instaar.colorado.edu/topoflow/).

[25] The active layer starts thawing after snowmelt, continues to thaw during the summer, and reaches its maximum thickness in autumn. Therefore the soil depth in Darcy's equation potentially changes with each time step. Soil moisture capacities for each soil layer also change, because they are related to the soil depth. As the hydraulic conductivity is different for the frozen and the unfrozen soil, flow rates in the frozen layers differ significantly from those in the unfrozen soil. The thawing of the active layer is currently incorporated by a simple square root of time function [*Hinzman et al.*, 1990].

[26] For the overland and channel flow, Manning's formula is used, where the roughness parameter, the shape of the cross section, and the channel width can be specified by the user for each stream order.

4. Model Application

4.1. Digital Elevation Model (DEM)

[27] A DEM with a pixel size of 25 $\times$ 25 m is used in this study. In order to create the input files necessary for TopoFlow simulations, the hydrological software package RiverTools is used in this study. RiverTools defines computationally the watershed area that contributes to a user-specified element. In this study a watershed area of 1.9 km^2 was calculated. This is in good agreement with the manual delineation of 2.2 km^2, taking into account that the headwaters are complex topographically, i.e., a very flat area, and therefore the southern watershed boundary is difficult to determine visually and/or by way of calculation. Figure 2 depicts the DEM of the Imnavait Creek watershed, its channel network, and watershed boundaries.

[28] The DEM is used in RiverTools to generate several files that are needed to extract information for a river network. The flow grid indicates the direction in which water would flow away from the corresponding pixel in the DEM. Here RiverTools provides special algorithms to determine the flow direction in flat areas that are common in the arctic tundra. Furthermore, a RiverTools treefile is derived from the flow grid. This vector-formatted file stores data for the basin such as contributing area and relief. These attributes are stored for every element in a given basin.

[29] In order to differentiate where channel flow and overland flow processes occur, the simulated channel network is compared to the physical system. Elements with a stream order of less than 3 are considered to be overland flow, and those $\geq$3 are locations where channel flow is present. Considering the water tracks (described in section 2) to be channels, the simulated river network compares well with the channel structure that is visible in aerial pictures. Finally, grids of upstream areas, downstream slopes, and Horton-Strahler order are produced with RiverTools for further use with TopoFlow.

4.2. Input Data

[30] Various research projects on the North Slope of Alaska have, since the mid 1980s, resulted in the establishment of several unmanned meteorological and research sites on a north–south transect located along the Dalton Highway. The measurement program is maintained by WERC, and data are available on the WERC Web site (http://www.uaf.edu/water). In the Imnavait Creek basin there are four main sites where data collection takes place: Imnavait basin (68°36′N, 149°18′W, 937 m); Imnavait ridge (68°37′N, 149°19′W, 880 m); Imnavait valley (68°37′N,

Table 1. Soil Parameters of Imnavait Creek Used as Model Input[a]

Soil Layer Depth, cm	Porosity, %	Hydraulic Conductivity, 10^4 m/s
0–10	0.88	1.50
10–20	0.63	0.35
20–30	0.50	0.35
30–40	0.48	0.10
40–permafrost table	0.40	0.10

[a]Data based on *Hinzman et al.* [1991].

149°19′W, 876 m); and Imnavait flume station (68°37′N, 149°19′W, 881 m). Compared with other arctic research basins an immense amount of data has been collected in the Imnavait Creek watershed. Most of the major processes have been monitored continuously since 1985 [*Kane et al.*, 2004].

[31] Measurements collected from 2001 to 2003 are used in this study. Soil data from former studies complete the data collection. Sensors for air temperature, air pressure, wind speed, wind direction, relative humidity, radiation, soil temperature, and precipitation measure automatically. Except for the radiation measurements (March to September) the recording takes place throughout the year. All meteorological data used in this study are conducted at the Imnavait basin site. Liquid precipitation is measured using a tipping bucket rain gage equipped with a windshield. The threshold sensitivity of the tipping basket is 1 mm of rain, and the undercatch is estimated to be 5% (D. L. Kane, personal communication, 2007). The precipitation data used in this study have not been corrected to consider the undercatch. Stream discharge is estimated from stage data using a stage-discharge relationship. Discharge is measured from the beginning of the snowmelt until freeze-up. In July 2004, measurements were carried out at Imnavait Creek to obtain values for Manning's roughness parameter used in the modeling. These measurements were taken at two locations close to the flume station with both sections being several meters in length. An average value of 0.01 s/m$^{1/3}$ was determined, but is likely to be underestimated due to measurement restrictions [*Schramm*, 2005].

[32] The shallow soils consist of a layer of about 10 cm of organic material over 5–10 cm of partially decomposed organic matter mixed with silt which overlays the glacial till. Generally, there is a thicker organic layer in the valley bottom (~50 cm) than on the ridges (~10 cm). The soil parameters used in this study are based on a representative profile measured by *Hinzman et al.* [1991].

[33] Values for the annual active layer depth are based on Circumpolar Active Layer Monitoring (CALM) measurements (http://www.geography.uc.edu/~kenhinke/CALM/sites.html). The depth is measured each summer at the latest possible date prior to the annual freeze-up. The instrument used is a metal rod that is pushed vertically into the soil to the depth at which ice-bonded soil provides firm resistance. This determines the maximum depth of thaw (MDT). For Imnavait Creek, approximately 120 measurements are taken and averaged each year.

[34] The position of the water table used in this study is interpolated from measurements of volumetric soil moisture content made using time domain reflectometry sensors at seven depths within the soil profile at three sites located on the west facing slope of the watershed [*Overduin*, 2005].

[35] The SWE is measured late each spring just prior to snowmelt. To provide SWE data, snow depths are combined with pit studies to measure snow density, temperature, and hardness profile [*Reynolds and Tenhunen*, 1996]. The measurements are conducted along a valley transect, approximately in the middle of the basin. Each reported value is an average of at least 10 measurements [*Kane et al.*, 2001].

4.3. Calibration/Parameterization

[36] To simulate snowmelt, two methods are used to compare their ability to reproduce the snow pack ablation: the degree day method (model generated) and the energy balance method (calculated separately, as this method was not available at the time of this study). Concerning the degree day method, two parameters mainly determine the simulated snowmelt: the melt factor C_0 and the threshold value of the air temperature T_0. In this study a value of 2.3 mm/d °C for C_0, is found to produce the best results. T_0 is set to −1.2°C. When using the energy balance method for snowmelt (and later evapotranspiration), the average surface roughness length z_0 needs to be evaluated. In this study a constant value of 0.0013 m (0.02 m) for surface roughness length is used for the simulation of the melt period (evapotranspiration during summer). These values were determined by *Hinzman et al.* [1993]. Standard values are used for latent heat of fusion (3.34 10^6 J/kg), latent heat of vaporization (2.48 10^6 J/kg), water density (1000 kg/m^3), specific heat of air (1005.7 J/kg °C), density of air (1.2614 kg/m^3), and heat capacity of snow (2090 J/kg °C).

[37] Two methods are used in this study to calculate the amounts of water lost by evapotranspiration: the Priestley-Taylor method (model generated) and the energy balance method (calculated separately as this method was not available at the time of this study). For the Priestley-Taylor method the parameter α_{PT}, an empirical parameter, relates actual to equilibrium evaporation [*Priestley and Taylor*, 1972; *Rouse et al.*, 1977; *Mendez et al.*, 1998; *Kane et al.*, 1990]. In this study its calibration is based on the best alignment with the results obtained by the energy balance method, as this approach is physically based. Thus the best α_{PT} is determined to be 0.95. This value is used as an average for the entire watershed. For the thermal heat conductivity a value of 0.45 W/m °C was used that was determined through field measurements [*Hinzman et al.*, 1991].

[38] For the energy balance method, evapotranspiration is calculated as described by *Zhang et al.* [2000]. When this study was conducted, the energy balance methods (snow melt and evapotranspiration) were not incorporated into the model yet, and thus no spatially distributed variables could be used. This would have been possible for the degree day method and the Priestley-Taylor method, but was not done since the aim was to compare these methods to the results of the energy balance approach.

[39] The assignment of soil parameters to the horizontal soil layers (see Table 1) is based on studies by *Hinzman et al.* [1991] and the application of ARHYTHM to the same study site by *Zhang et al.* [2000]. When this study was conducted, a physically based representation of the active layer thawing process was not yet available. Instead, input files with changing hydraulic conductivities are used to

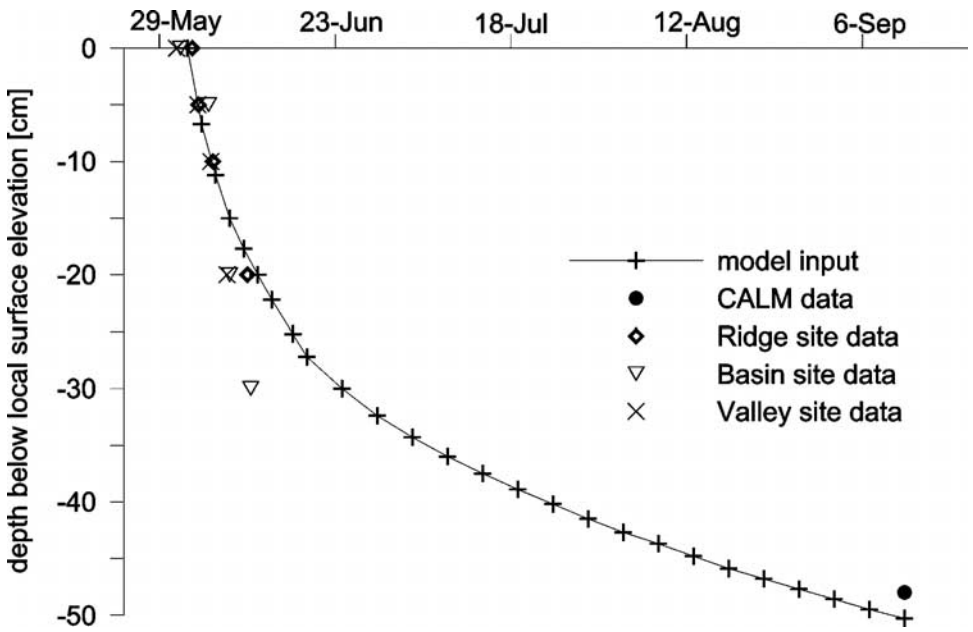

Figure 3. Thaw depth of the active layer 2001 used as a model input (α_{TD} = 0.068 during snow melt period 25 May to 14 June; α_{TD} = 0.032 during summer period 15 June to 13 September), determined from soil temperature measurements at the ridge, basin, and valley sites and from Circumpolar Active Layer Monitoring (CALM) grid measurements (average value).

account for the thawing of the soil. The soil is divided into layers of 10 cm, down to the maximum depth of thaw (MDT). During the course of the summer the thawing of the soil progresses and hydraulic conductivities are gradually (layer by layer) changed from frozen to unfrozen. The gradient controlling how the thaw depth evolves with time is determined by the α_{TD} value. The α_{TD} value is calibrated such that (1) during the initial thawing the input files match soil temperature recordings, and (2) at the end of the season the MDT matches the CALM grid measurements. Figure 3 shows the evolution of a gradually thawing active layer when used as a model input for 2001 and corresponding values obtained from measurements.

[40] When this study was conducted, the model did not allow the use of spatially distributed hydraulic conductivities and the thawing of the soil representing conductivities at the same time. In the case of a whole summer runoff simulation the thawing of the soil is an important factor and cannot be neglected. Thus the simulations are done on spatially homogeneous soil parameters.

[41] In this model, overland flow occurs when the water table rises above the surface. It is assumed that all of the water from precipitation or snowmelt is instantaneously infiltrated, meaning that the percolation time from the surface to the water table is neglected. The water content in each element may change with each time step, and the total storage capacity of each element may also increase or decrease as the active layer thaws.

[42] The crucial factor in determining overland and channel flow is the roughness parameter in Manning's equation [*Zhang et al.*, 2000]. In this study the coefficient is subjected to calibration within the range of values obtained from field measurements and literature [*Maidment*, 1992; *Emmett*, 1970]. For channel flow the channel bed width must be specified as well. Table 2 contains the corresponding values for each stream channel order.

5. Results

5.1. Water Balances 2001–2003

[43] The years 2001 to 2003 differ considerably in terms of hydrological and meteorological components. For the water balances (Figure 4), measured data are used for the rain, snow, and discharge components. Evapotranspiration is calculated with the energy balance method. The storage equals the residual term of the input (rain and snow) minus the output (discharge and evapotranspiration). Thus the storage term also includes the sum of errors caused by measurement uncertainties.

[44] In 2001 to 2003 the mean annual precipitation amounts to 337 mm, 520 mm, and 479 mm, respectively. Runoff accounts for 54%, 60%, and 67% of the water budget. The total amount of evapotranspiration is 48%, 42%, and 28% of the water budget. In each year the winter snow pack is a major source that adds water to the system. For the years of this study it accounts to 33–41% of the total amount of water added. A remarkable snow fall of 126 mm occurred in August 2002. The storage term,

Table 2. Overland and Channel Flow Parameters Used as Model Input[a]

	Manning's Roughness Parameter, $s/m^{1/3}$	Channel Bed Width, cm
Overland flow	0.30	-
Water tracks	0.15	5
Stream order 2	0.10	15
Stream order 1	0.07	40

[a]Data determined by field measurements and calibration.

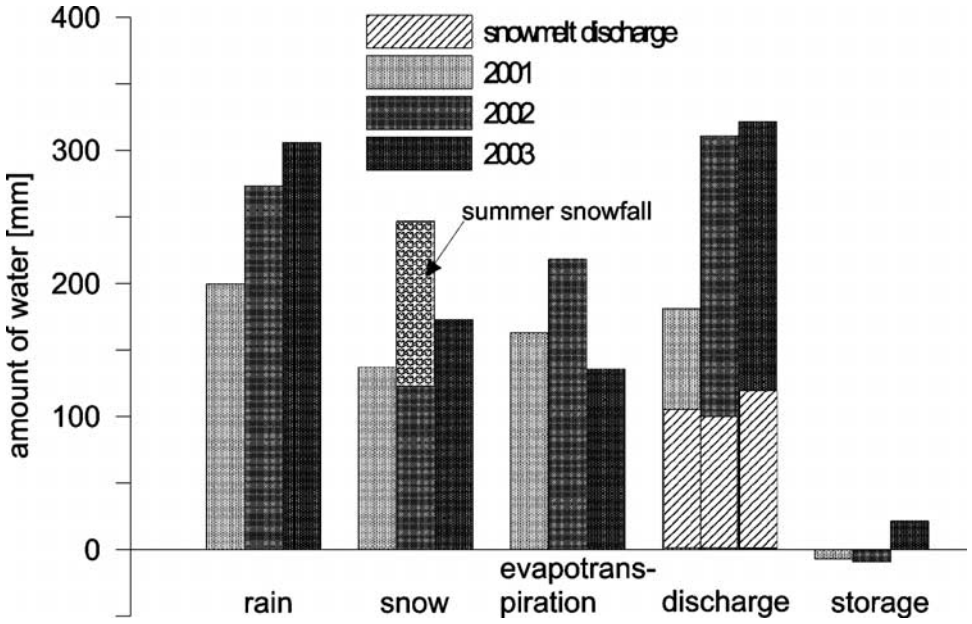

Figure 4. Water balance components for 2001–2003. Rain, snow, and discharge are based on measured data. Evapotranspiration is calculated using the energy balance method.

calculated as the residual term, shows little differences from year to year. Whereas in 2001 and 2002 the change in storage is slightly negative, there is a gain of 21 mm at the end of 2003.

[45] In the Imnavait watershed, 2001 represents an average year in most hydrologic components, whereas 2002 and 2003 show special characteristics that differ from mean values. 2003 is a wet year with continuously high precipitation, little evapotranspiration, high discharge, and a gain in soil moisture. Conversely, 2002 is characterized by the unusual summer snow fall and a high amount of evapotranspiration.

[46] Figure 5 shows the measured cumulative discharges of all years from the beginning of snowmelt until freeze-up, revealing distinct differences each year. The early onset of snowmelt in 2002 causes a considerably earlier start of discharge. Whereas in 2001 and 2003 the melt discharge is the highest discharge of the year, the peak discharge in 2002 originates from a snow/rain event in late summer.

[47] The influence of the antecedent soil moisture conditions on the runoff signal has been stated in section 2. This role is evident in each year of this study. For example, in 2002 the highest storm event of 9.3 mm/h recorded at 21 July results in a barely noticeable rise in runoff, after a

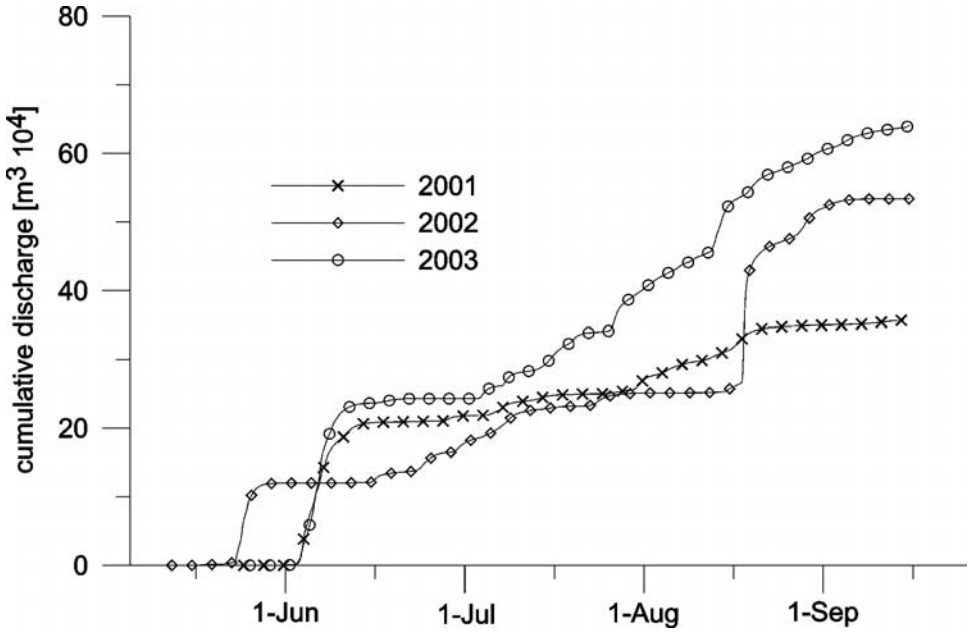

Figure 5. Measured cumulative discharges at Imnavait Flume station 2001–2003.

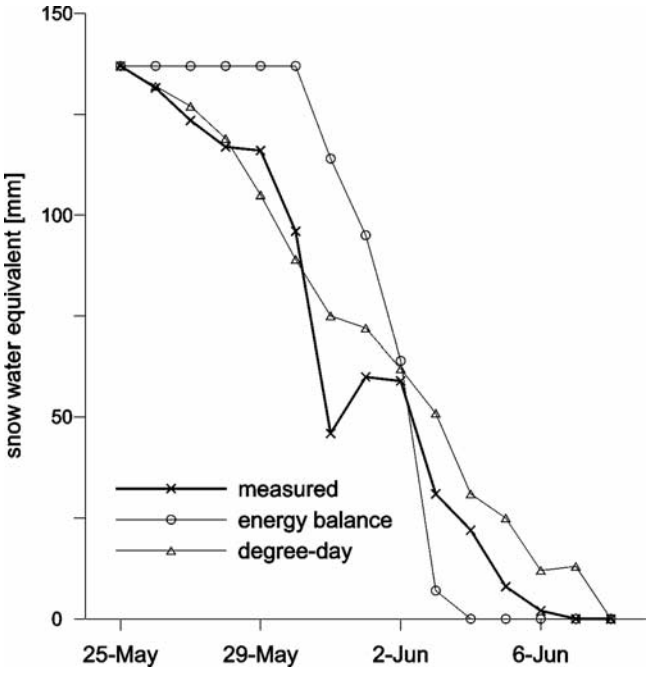

Figure 6. Measured and simulated snow ablation 2001.

7-h delay. Instead, a following rain event of 7 mm/h the next day generates a rise in discharge that exceeds the previous one by 3 times in peak and total amount. Also, the highest discharge on record with about 3.7 m^3/s is generated by a precipitation of 6 mm/h about 5 h earlier. In the first case a dry period of 7 d preceded the heavy rain event, whereas in the last two cases, precipitation was recorded previously.

[48] The discharge recorded at the end of the summer season 2003 shows an interesting feature not uncommon in arctic environments: At the time where the last peak occurs, freeze-up has already started, and surface temperatures show negative values for approximately 6 d. In addition, the last rain event that could have generated runoff is recorded 7 d prior to the peak in discharge. An explanation (R. E. Gieck, personal communication, 2004) for the occurring runoff could be that frazil ice and snow in the channel had blocked the outflow of one of the ponds upstream. When the ice dam broke, a small flood surge passed through the flume.

5.2. Modeling Results

5.2.1. Snowmelt

[49] In 2001 the snow pack ablated within 13 d. The initial SWE is obtained from snow survey measurements done prior to ablation. An average value is used for the entire watershed.

[50] Two methods, the degree day method (SM-DD) and the energy balance approach (SM-EB), are used to determine the snow pack ablation. SM-DD is used in the model simulation, whereas SM-EB is calculated separately. Figure 6 shows the simulated and the measured ablation curves for 2001. SM-DD achieves a better congruence than the energy balance method. Using the energy balance method, the onset of melt is delayed by 5 d, but completed earlier than measured. In the degree day method, the onset of snowmelt coincides exactly with the real onset, but the end of snowmelt is delayed.

[51] The discrepancy in congruence of the simulation and the recording could partly be due to the fact that field measurements are made daily in the morning, whereas both melt algorithms operate at hourly time steps. In addition, the pronounced spatial variability of the snow pack was stated previously, and other studies emphasize that the consideration of snow cover heterogeneity over complex arctic terrain provides a better representation of the end-of-winter snow water equivalent and an improved simulation of the timing and amount of water discharge due to snowmelt.

5.2.2. Discharge

[52] Measured versus simulated hydrographs for the year 2001, and the corresponding cumulative discharges, are depicted in Figure 7. It should be noted that because of the model configuration the simulation is split into snowmelt and summer period. The initial water table at the beginning of the summer simulation is set to the simulated height of the water table at the end of the snowmelt period.

[53] The diurnal fluctuations during the melt period, reflecting the influence of daily snowmelt cycles, are obvious in both, measured and simulated hydrographs. The onset of simulated discharge after snow melt occurs 7 d earlier than the measured one. Whereas this difference to the measured hydrograph is obvious, the total volume of melt discharge is very close to reality. The deviation in onset occurs because an algorithm for snow damming has not been incorporated into the model. Snow, redistributed by wind, accumulates in water tracks and valley bottoms, where melt water collects. The water seeps through the snow until it reaches a degree of saturation where both snow and melt water start to move, cutting a channel through the snow pack. *Kane et al.* [1989] found from measurements in the Imnavait watershed that the reduction of the snow water equivalent reaches up to 80% before stream runoff starts.

[54] Another explanation for the discrepancy between modeled and measured hydrograph could be the spatial variability of the snow pack. In this study an average value for initial SWE is used as an input, whereas in reality the variability of snow distribution with topography is pronounced [*Kane et al.*, 1991b; *Hinzman et al.*, 1996].

[55] During the summer runoff period the predicted cumulative discharge agrees well with the measured discharge volume. The simulated hydrograph caused by summer storm events shows some deviation from the recordings. For most rain events the simulated discharge leads measured data. Measured peak discharges are usually lower and have a longer recession time. The Nash-Sutcliffe coefficient for a weekly average is 0.64. An explanation for this discrepancy could be the beaded stream system, where small ponds act as reservoirs and store water intermediately, resulting in an attenuated hydrograph signal.

[56] Results indicate that the model performs well in the quantitative reproduction of the streamflow processes, but could be refined further in the timing of small-scale, short-term processes (see section 5.3).

5.2.3. Evapotranspiration

[57] Cumulative evapotranspiration and daily evapotranspiration rates for 2001 are shown in Figure 8. Evapotranspiration is only determined during the summer season. Priestley-Taylor (ET-PT) values are calculated by the

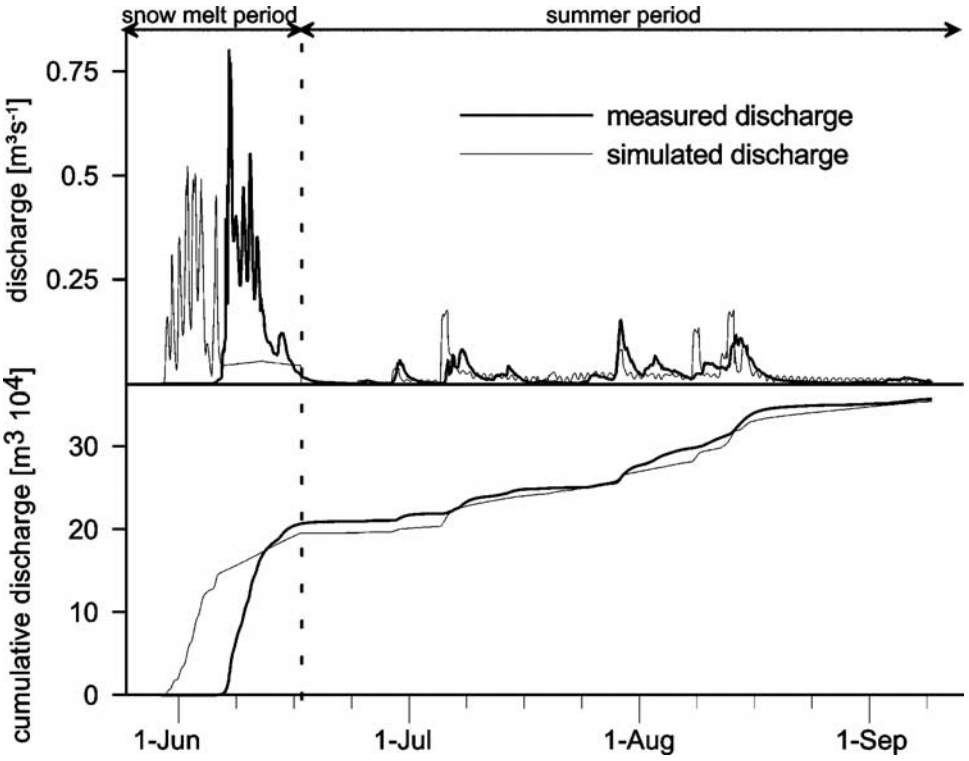

Figure 7. Measured and simulated discharge 2001.

model, whereas energy balance (ET-EB) calculations are done externally.

[58] In the total amount, ET-PT agrees well with the results of ET-EB. Figure 8 also illustrates the differences between ET-PT and ET-EB. Whereas fluctuations are pronounced in ET-EB, and fluxes are occasionally directed downward, ET-PT shows a steady rise without major fluctuations. This is due to the fact that both methods differ in the representation of the ventilation term, including the deficit in saturation and the wind component. ET-EB obtains this term from measurements, whereas in ET-PT this term is replaced by a constant. The ET-EB calculation shows the highest flux rates in early summer when both energy and water are relatively abundant.

5.2.4. Water Table

[59] Simulation results are compared with the measured water table height during summer 2003 at a water track site within the watershed (Figure 9). The year 2003 was chosen for this simulation, because measurements were available only for this period. Qualitatively, the simulation shows the

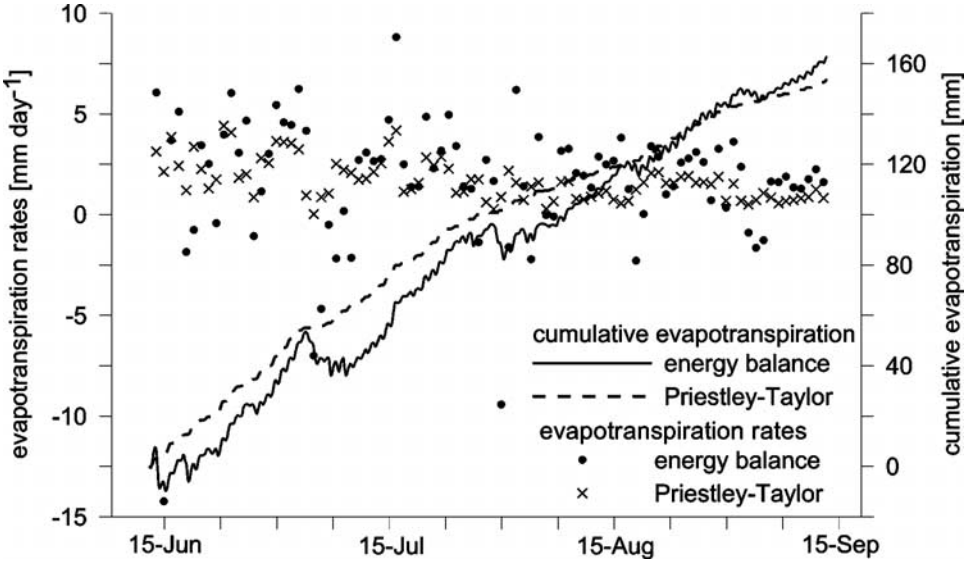

Figure 8. Cumulative hourly evapotranspiration 2001 and daily evapotranspiration rates 2001. The $\alpha_{PT} = 0.95$ in the Priestley-Taylor calculation.

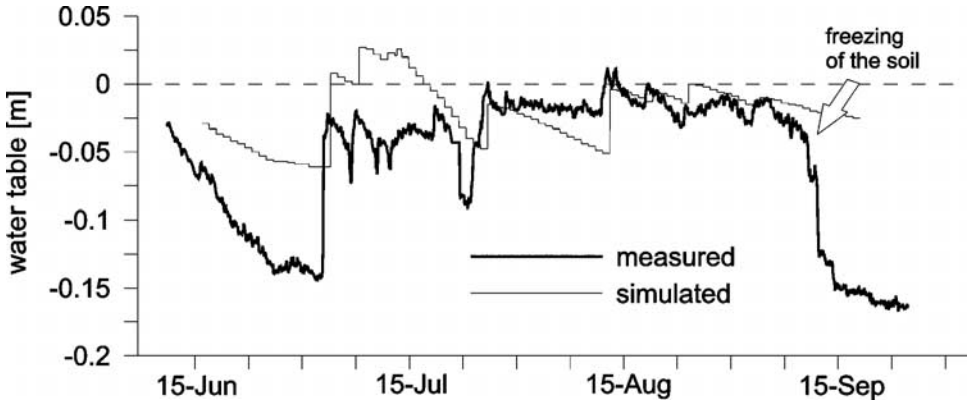

Figure 9. Comparison of simulated and measured water tables during the summer 2003 at a water track. Unit is water table (meters) relative to the local surface elevation. Refreezing of the soil results in the rapid decline of the measured water table in September.

same trends as the measurement. The sudden rises in the simulated water table are due to the instantaneous infiltration routine, where water percolation through the soil is neglected. The rapid decline in measured water table in September is caused by freezing of the soil. This process is not considered in the model simulations.

5.3. Model Sensitivity Toward Change in Parameters

[60] Figure 10a gives evidence of the influence of the MDT on total discharge. The importance of MDT is twofold: First, MDT has (in the current state of TopoFlow) to be given as input and thus underlies the uncertainties of measurements. For example, *Boike et al.* [1998] found that ground thaw depths determined using the probe method deviated considerably from the thaw depths determined by soil temperatures during the period when the active layer was dry. This is explained by a greater case of penetration of the frost probe when the active layer is saturated. Second, a simulation with increased MDT can reveal the runoff response to an increased melting of ground ice. In this study an increased MDT of 70 cm (compared to the normal case of 50 cm) is used in the summer simulation 2001.

[61] Figure 10b gives evidence of the importance of the initial water table height. It should be noted that only the

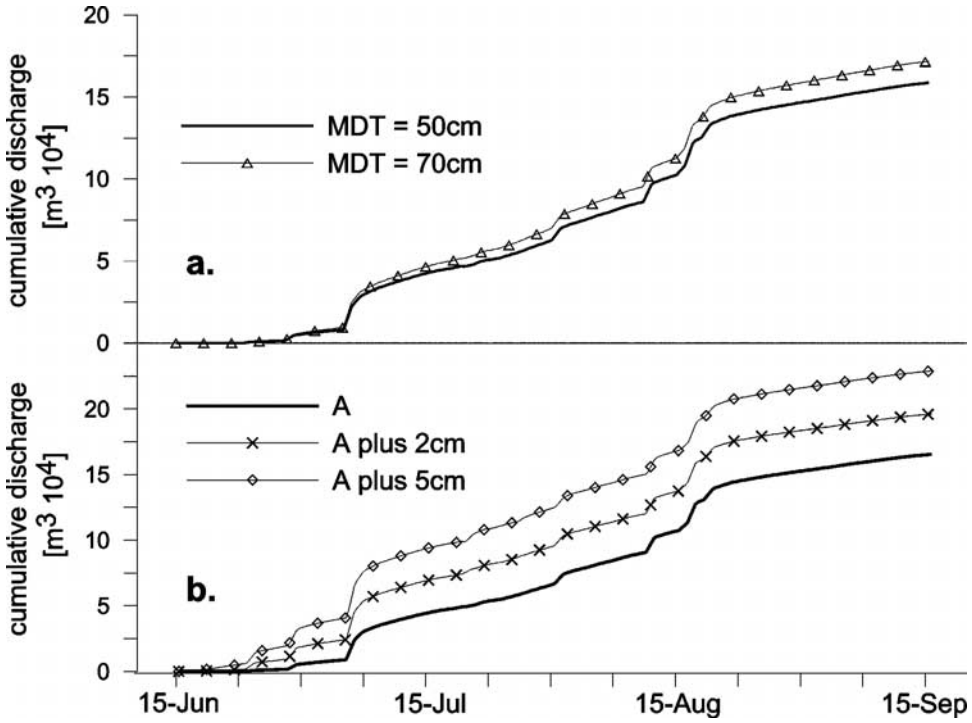

Figure 10. (a) Simulated discharge 2001 using different active layer depths. Maximum depth of thaw (MDT) is 50 cm in the normal 2001 simulation and was lowered to 70 cm for sensitivity studies. (b) Simulated discharge 2001 using different initial water table heights. Case A represents the normal water table height of the 2001 simulation. In the other simulations the water table height was raised by 2 cm and 5 cm, respectively.

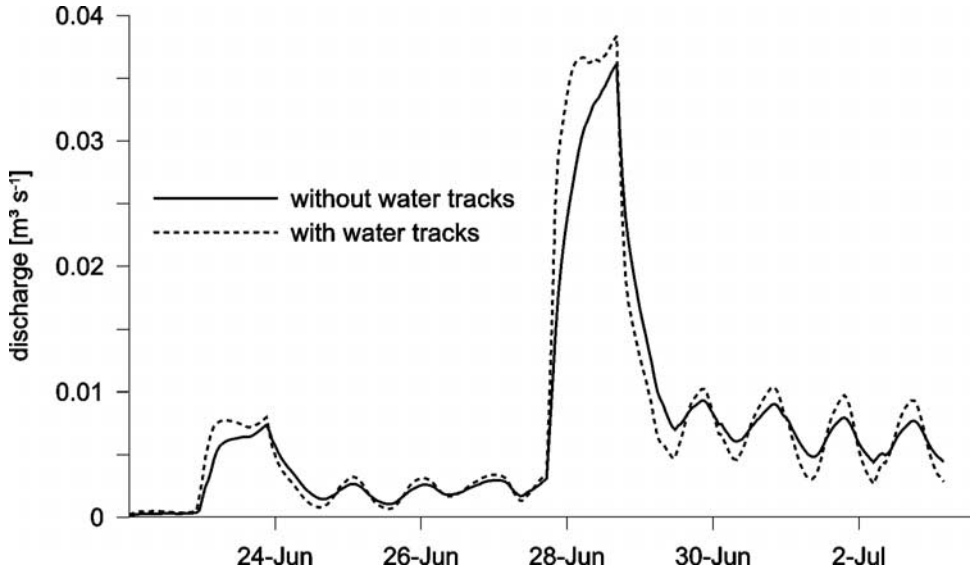

Figure 11. Simulated discharge 2001 illustrating the influence of water tracks. Solid line shows the normal 2001 simulation. Dashed line represents the discharge in a simulation where the water tracks were leveled to the adjacent surface elevation.

initial state of the water table height is given as an input, whereas its further evolution is calculated by the model. Here a small increase of 2 cm (5 cm), compared to the normal water table height (case A) causes an increase of 19% (38%) in the total amount of discharge. On the one hand, the influence of the antecedent soil water content on total discharge is characteristic for arctic watersheds where subsurface processes are limited to the shallow active layer. On the other hand, one should be aware of this sensitivity when calibrating the model.

[62] Figure 11 shows simulated hydrographs where the effect of water tracks (described in section 2) on the hydrograph is tested. The first simulation is based on the channel network depicted in Figure 2, whereas in the second simulation the water tracks are leveled to the adjacent surface elevation. The simulation indicates that the existence of water tracks accelerates runoff and leads to higher amplitudes in the hydrograph than would be present without them. Including water tracks improves the simulation result when compared to the measured hydrograph [*Schramm*, 2005]. Concerning the impact of soil parameters on subsurface flow, model studies reveal that the MDT has the highest influence, followed by the porosity and the hydraulic conductivity [*Schramm*, 2005].

5.4. Sensitivity of the Hydrological System Toward Changes in Climate Conditions

[63] As arctic temperatures and precipitation increase, there remains uncertainty on how the additional input of freshwater will be partitioned into streamflow and evapotranspiration. The interactions are further complicated by a contribution of melted ground ice to base flow when increasing temperatures deepen the active layer during summer. An open question is whether a change in climate will lead to a drying of the soil or to wetter conditions.

[64] Global and regional climate models predict different changes for the future climate state of the arctic depending on the warming scenario as well as on model performance. Regardless of the unanswered question, which scenario is the most likely one, changes on the hydrology can be investigated by presuming various conditions and using those as an input to model simulations. This was done in this study for different climate change scenarios (see Table 3) that include a change in three parameters: (1) the summer temperature, (2) the summer precipitation, and (3) the maximum depth of thaw.

[65] 2001 is used as the reference year, i.e., all changes of the above-mentioned parameters are relative to the observed climate conditions in 2001. Thus changes in the output, such as simulated runoff and evapotranspiration, can be compared to the 2001 simulation based on the real data set. Simulations were executed only for the summer season, lasting from 15 June until 13 September. The change in precipitation was distributed equally over the summer season, sustaining the range between minimum and maximum precipitation rates. For simplification the assumption of a 10 cm (20 cm) deepening of MDT by a 2°C warming was based on a study by *Kane et al.* [1991a]. The authors determine that a gradual but steady warming of 2°C would lead to a deepening of 10 cm (20 cm) after 20 a (45 a).

[66] Results indicate that a warming of 2°C without additional precipitation results in a higher R/P and ET/P ratio [*Schramm*, 2005]. Here the increase in runoff is

Table 3. Climate Change Scenarios A, C, and E and Their Changes in Mean Summer Temperature, Precipitation, and Maximum Depth of Thaw, Relative to the Observed Conditions in 2001

Scenario	A 10	A 20	C 10	C 20	E 10	E 20
Temperature, °C	+2	+2	+2	+2	+2	+2
Precipitation, %	-	-	+8	+8	−10	−10
Maximum depth of thaw, cm	58	68	58	68	58	68
Change in storage compared to 2001, mm	−7.8	−10.7	−3.5	−6.2	−7.9	−10.8

generated by a contribution of ground ice melted due to a deeper thaw depth. Runoff is significantly higher in the scenarios where an increase of precipitation is superimposed over the warming. The opposite accounts for the scenarios where precipitation input is decreased. All scenarios indicate an increased loss in storage compared to the reference amount in 2001, ranging from −3.5 to −10.8 mm. This indicates that the enhanced evapotranspiration overwhelms the increase in precipitation and results in a drying of the soil.

6. Conclusions

[67] This study presented the application of the hydrological model TopoFlow to Imnavait Creek, Alaska. Results indicate that the model is an excellent tool for simulating the overall water and energy balances of an arctic watershed. The model performs quantitatively well, with measured and simulated discharges being in a good agreement. The different components of the water cycle, i.e., evapotranspiration, snow melt, infiltration, and runoff, are well represented in the model, revealing that the model is able to handle the seasonal change in meteorological conditions. Some refinements are possible in the qualitative reproduction of some subprocesses: The onset of simulated snowmelt discharge occurs distinctly earlier than the measured discharge (7 d). This difference is in part due to the process of snow damming, which is not understood well enough to be incorporated into the model. Furthermore, the simulated summer hydrograph shows deviations from the recordings: Simulated discharge often leads site data; measured peak discharges are usually lower and have a longer recession time. This reveals that the model could be further refined in the small-scale, short-term reproduction of storage-related processes. Those can be attributed to the following facts: (1) The channel grid used in the simulation does not consider the ponds of the beaded stream system; (2) the spatial variability of the active layer depth is not represented in the simulation; and (3) the instantaneous infiltration used in the modeling simplifies the complex soil moisture distribution on short-term scales. Finally, simulation results could possibly be improved by spatially distributing several input variables (now possible in the model), such as snow depth, α_{PT} of the Priestley-Taylor method, the meteorological variables, and the soil parameters during the thawing season.

[68] Sensitivity studies reveal that the model is highly sensitive to the initial height of the water table that is given as an input to start the simulation. Even though this sensitivity is realistic, it requires calibration which naturally includes a source of error, as measurements are usually not available in full detail.

[69] While various studies present projected climate changes in the arctic, there remains uncertainty of how these changes will impact the hydrological cycle, resulting in enhanced or diminished runoff and soil moisture. This in turn is likely to affect the biogeochemistry and/or ecology of these systems (e.g., via changes in heat and water fluxes, vegetation cover, etc.). It is possible and desirable to couple TopoFlow with other models, and the authors encourage this development. This study shows that TopoFlow is a powerful tool for answering the question of how climate change will affect the sensitive wetlands of arctic tundra.

Notation

C_0	degree day melt factor, mm/d °C.
ET/P	evapotranspiration to precipitation ratio, no units.
R/P	runoff to precipitation ratio, no units.
T_0	temperature of snow for isothermal conditions, °C.
α_{PT}	alpha parameter controlling the thaw depth, no units.
α_{TD}	alpha parameter for the Priestley-Taylor equation, no units.
z_0	surface roughness length, m.

[70] **Acknowledgments.** We gratefully acknowledge financial support by the U.S. National Science Foundation Arctic System Science program (OPP-0229705). Special thanks are due to Robert Gieck, Pier Paul Overduin, and Peter Prokein for their support in the preparation and interpretation of field data. The two anonymous reviewers are thanked for their constructive comments that helped improve this paper.

References

ACIA (2004), *Impacts of a Warming Arctic: Arctic Climate Impact Assessment*, 1042 pp., Cambridge Univ. Press, New York.

Berezovskaya, S., D. L. Kane, and L. D. Hinzman (2005), Snowmelt hydrology of a headwater arctic basin revisited, *Eos Trans. AGU*, *85*(47), Fall Meet. Suppl., Abstract C41A-0195.

Bergström, S. (1976), Development and application of a conceptual runoff model for Scandinaian catchments, *SMHI Rep. RHO-7*, Swed. Meteorol. and Hydrol. Instit., Norrköping, Sweden.

Boike, J., K. Roth, and P. P. Overduin (1998), Thermal and hydrologic dynamics of the active layer at a continuous permafrost site, *Water Resour. Res.*, *34*(3), 355–363.

Bolton, W. R. (2006), Dynamic modeling of the hydrologic processes in areas of discontinuous permafrost, Ph.D. thesis, 163 pp., Univ. of Alaska Fairbanks, Fairbanks, Alaska.

Bolton, W. R., D. L. Hinzman, and K. Yoshikawa (2000), Stream flow studies in a watershed underlain by discontinuous permafrost, in *Water Resources in Extreme Environments*, edited by D. L. Kane, pp. 31–36, Am. Water Resour. Assoc. Proc., Anchorage, Alaska.

Bowling, L. C., D. L. Kane, R. E. Gieck, L. D. Hinzman, and D. P. Lettenmaier (2003), The role of surface storage in a low-gradient arctic watershed, *Water Resour. Res.*, *39*(4), 1087, doi:10.1029/2002WR001466.

Church, M. (1974), Hydrology and permafrost with reference to northern North America, in *Permafrost Hydrology, Proceedings Workshop Seminar*, pp. 7–20, Can. Natl. Comm., Int. Hydrol. Decade, Environ. Canada, Ottawa, Ont., Canada.

Dingman, L. S. (1973), Effects of permafrost on stream characteristics in the discontinuous permafrost zone of central Alaska, in *Permafrost, North American Contribution to the Second International Conference, Washington D. C.*, pp. 447–453, Natl. Acad. of Sci., Washington, D. C.

Emmett, W. W. (1970), The hydraulics of overland flow on hillslopes, *U. S. Geol. Surv. Prof. Pap., 662-A*, 68 pp.

Hastings, S. J., S. A. Luchessa, W. C. Oechel, and J. D. Tenhunen (1989), Standing biomass and production in water drainages of the foothills of the Philip Smith Mountains, Alaska, *Holarct. Ecol.*, *12*, 304–311.

Hinzman, L. D., and D. L. Kane (1992), Potential response of an arctic watershed during a period of global warming, *J. Geophys. Res.*, *97*, 2811–2820.

Hinzman, L. D., J. D. Fox, and D. L. Kane (1990), Soil freezing in a subarctic deciduous forest, in *International Frozen Soil Symposium, 21–22 March 1990, Spokane, Washington*, edited by K. R. Cooley, *CRREL Spec. Rep. 90-1*, pp. 21–30, U.S. Army Cold. Reg. Res. and Eng. Lab., Hanover, N. H.

Hinzman, L. D., D. L. Kane, R. E. Gieck, and K. R. Everett (1991), Hydrologic and thermal properties of the active layer in the Alaskan arctic, *Cold Reg. Sci. Technol.*, *19*, 95–110.

Hinzman, L. D., D. Wendler, R. E. Gieck, and D. L. Kane (1993), Snowmelt at a small Alaskan arctic watershed: 1. Energy related processes, in *Proceedings of the 9th International Northern Research Basins Symposium/Workshop Canada 1992*, edited by T. D. Prowse, C. S. Ommanney, and K. Ulmer, vol. 1, *NHRI Symp. 10*, pp. 171–226, Natl. Hydrol. Res. Inst., Saskatoon, Saskatchewan, Canada.

Hinzman, L. D., D. L. Kane, and Z. Zhang (1995), A spatially distributed hydrologic model for arctic regions, *International GEWEX Workshop on Cold-Season/Region Hydrometeorology, Summary Report and Proceedings, 22–26 May 1995, Banff, Alberta, Canada*, *Int. GEWEX Proj. Off. Publ. Ser. 15*, pp. 236–239, Washington, D. C.

Hinzman, L. D., D. L. Kane, C. S. Benson, and K. R. Everett (1996), Energy balance and hydrological processes in an arctic watershed, in *Landscape Function and Disturbance in Arctic Tundra*, *Ecol. Stud.*, vol. 120, edited by J. F. Reynolds and J. D. Tenhunen, pp. 131–154, Springer, Berlin.

Hinzman, L. D., et al. (2005), Evidence and Implications of recent climate change in northern Alaska and other arctic regions, *Clim. Change*, *72*, 251–298.

Hinzman, L. D., R. W. Bolton, K. Petrone, J. Jones, and P. Adams (2006), Watershed hydrology and chemistry in the Alaskan boreal forest: The central role of permafrost, in *Alaska's Changing Boreal Forest*, edited by F. S. Chapin III et al., pp. 269–284, Oxford Univ. Press, New York.

Kane, D. L., and L. D. Hinzman (1988), Permafrost hydrology of a small arctic watershed, in *Fifth International Conference on Permafrost*, edited by K. Senneset et al., pp. 590–595, Tapir Publ., Trondheim, Norway.

Kane, D. L., L. D. Hinzman, C. S. Benson, and K. R. Everett (1989), Hydrology of Imnavait Creek, an arctic watershed, *Holarct. Ecol.*, *12*, 262–269.

Kane, D. L., R. E. Gieck, and L. D. Hinzman (1990), Evapotranspiration from a small Alaskan arctic watershed, *Nordic Hydrol.*, *21*, 253–272.

Kane, D. L., L. D. Hinzman, and J. Zarling (1991a), Thermal response of the active layer in a permafrost environment to climatic warming, *Cold Reg. Sci. Technol.*, *19*(2), 111–122.

Kane, D. L., L. D. Hinzman, C. S. Benson, and G. E. Liston (1991b), Snow hydrology of a headwater arctic basin: 1. Physical measurements and process studies, *Water Resour. Res.*, *27*(6), 1099–1109.

Kane, D. L., L. D. Hinzman, J. P. McNamara, Z. Zhang, and C. S. Benson (2000), An overview of a nested watershed study in arctic Alaska, *Nord. Hydrol.*, *31*(4/5), 245–266.

Kane, D. L., K. M. Hinkel, D. J. Goering, L. D. Hinzman, and S. I. Outcalt (2001), Non-conductive heat transfer associated with frozen soils, *Global Planet. Change*, *29*(3–4), 275–292.

Kane, D. L., R. E. Gieck, D. C. Kitover, L. D. Hinzman, J. P. McNamara, and D. Yang (2004), Hydrologic cycle on the North Slope of Alaska, in *Northern Research Basins Water Balance*, *IAHS Publ.*, *290*, 224–236.

Maidment, D. R. (Ed.) (1992), *Handbook of Hydrology*, 1400 pp., McGraw-Hill, New York.

McCarthy, J. J., O. Canziani, N. A. Leary, D. J. Dokken, and K. S. White (Eds.) (2001), *Climate Change 2001: Impacts, Adaptation, and Vulnerability*, 1032 pp., Cambridge Univ. Press., New York.

McNamara, J. P. (1997), A nested watershed study in the Kuparuk River basin, arctic Alaska: Streamflow, scaling, and drainage basin structure, Ph.D. diss., Univ. of Alaska, Fairbanks.

McNamara, J. P., D. L. Kane, and L. D. Hinzman (1998), An analysis of streamflow hydrology in the Kuparuk River basin, arctic Alaska: A nested watershed approach, *J. Hydrol.*, *206*, 39–57.

Mendez, J., L. D. Hinzman, and D. L. Kane (1998), Evapotranspiration from a wetland complex on the arctic coastal plain of Alaska, *Nord. Hydrol.*, *29*(4/5), 303–330.

O'Callaghan, J., and D. Mark (1984), The extraction of drainage networks from digital elevation data, *Comput. Vision Graphics Image Process.*, *28*(3), 323–344.

Osterkamp, T. E., and V. Romanovsky (1999), Evidence for warming and thawing of discontinuous permafrost in Alaska, *Permafrost Periglacial Processes*, *10*, 17–37.

Oswood, M. W., K. R. Everett, and D. M. Schell (1989), Some physical and chemical characteristics of an arctic beaded stream, *Holarct. Ecol.*, *12*, 290–295.

Overduin, P. P. (2005), The physical dynamics of patterned ground in the northern foothills of the Brooks Range, Alaska, Ph.D. thesis, 182 pp., Univ. of Alaska, Fairbanks, Fairbanks, Alaska.

Priestley, C. H. B., and R. J. Taylor (1972), On the assessment of surface heat flux and evaporation using large-scale parameters, *Mon. Weather Rev.*, *100*, 81–92.

Quinton, W. L., D. M. Gray, and P. Marsh (2000), Subsurface drainage from hummock-covered hillslopes in the arctic-tundra, *J. Hydrol.*, *237*(1–2), 113–125.

Reynolds, J., , and J. D. Tenhunen (Eds.) (1996), *Landscape Function and Disturbance in Arctic Tundra*, *Ecol. Stud.*, vol. 120, edited by J. F. Reynolds and J. D. Tenhunen, 437 pp., Springer, Berlin.

Romanovsky, V., M. Burgess, S. Smith, K. Yoshikawa, and J. J. Brown (2002), Permafrost temperature records: Indicators of climate change, *EOS Trans. AGU*, *83*(50), 589–594.

Rouse, W. R., P. F. Mills, and R. B. Stewart (1977), Evaporation in high latitudes, *Water Resour. Res.*, *13*(6), 909–914.

Schramm, I. (2005), Hydrologic modeling of an arctic watershed, Alaska, M. S. thesis, 108 pp., Univ. of Potsdam, Germany.

Serreze, M. C., J. E. Walsh, F. S. Chapin III, T. Osterkamp, M. Dyurgerov, V. Romanovsky, W. C. Oechel, J. Morison, T. Zhang, and R. G. Barry (2000), Observational evidence of recent change in the northern high-latitude environment, *Clim. Change*, *46*, 159–207.

Slaughter, C. W., and D. L. Kane (1979), Hydrologic role of shallow organic soils in cold climates, paper presented at the Canadian Hydrology Symposium, Natl. Res. Counc. of Can., Ottawa, Canada.

Smith, L. C., Y. Sheng, G. M. McDonald, and L. D. Hinzman (2005), Disappearing arctic lakes, *Science*, *308*(5727), 1429.

Stieglitz, M., J. Hobbie, A. Giblin, and G. Kling (1999), Hydrologic modeling of an arctic tundra watershed: Toward pan-arctic predictions, *J. Geophys. Res.*, *104*, 507–518.

Vörösmarty, C. J., L. D. Hinzman, B. J. Peterson, D. H. Bromwich, L. C. Hamilton, J. Morison, V. E. Romanovsky, M. Sturm, and R. S. Webb (2001), *The Hydrologic Cycle and Its Role in the Arctic and Global Environmental Change: A Rationale and Strategy for Synthesis Study*, 84 pp., Arct. Res. Consortium of the U. S., Fairbanks, Alaska.

Walker, D. A., E. Binnian, B. M. Evans, N. D. Lederer, E. Nordstrand, and G. W. Petersen (1989), Terrain, vegetation and landscape evolution of the R4D research site, Brooks Range Foothills, Alaska, *Holarct. Ecol.*, *12*, 261–283.

Walsh, J. E., et al. (2005), Cryosphere and hydrology, in *Arctic Climate Impact Assessment*, chapter 6, pp. 181–242, Cambridge Univ. Press, London.

Woo, M. (1986), Permafrost hydrology in North America, *Atmos. Ocean*, *24*(3), 210–234.

Woo, M., and P. Steer (1983), Slope hydrology as influenced by thawing of the active layer, Resolute N.W.T., *Can. J. Earth Sci.*, *20*(6), 978–986.

Zhang, Z., D. L. Kane, and L. D. Hinzman (2000), Development and application of a spatially-distributed arctic hydrological and thermal process model (ARHYTHM), *Hydrol. Processes*, *14*, 1017–1044.

J. Boike and I. Schramm, Alfred Wegener Institute for Marine and Polar Research, Research Unit Potsdam, Telegrafenberg A43, 14473 Potsdam, Germany. (jboike@awi-potsdam.de)

W. R. Bolton, Water and Environmental Research Center, P.O. Box 755860, University of Alaska, Fairbanks, AK 99775-5860, USA.

L. D. Hinzman, International Arctic Research Center, P.O. Box 757340, University of Alaska, Fairbanks, AK 99775-7340, USA.

Chapter 2.7

Boike, J., Hinzman, L. D., Overduin, P.P., Romanovsky, V., Ippisch, O., and Roth, K. (2003): A comparison of snow melt at three circumpolar sites: Spitsbergen, Siberia, Alaska. *8th International Conference on Permafrost, Zuerich, Switzerland*, 79-84.

A comparison of snow melt at three circumpolar sites: Spitsbergen, Siberia, Alaska

J. Boike
(1) Alfred Wegener Institute for Polar and Marine Research, Potsdam, German; currently at (2)

L.D. Hinzman & P.P. Overduin
(2) Water and Environmental Research Center, University of Alaska, Fairbanks, Alaska, USA

V. Romanovsky
(3) Geophysical Institute, University of Alaska, Fairbanks, Alaska, USA

O. Ippisch & K. Roth
(4) Institute for Environmental Physics, University of Heidelberg, Heidelberg, Germany

ABSTRACT: Spring snow ablation is modelled at three patterned ground sites in Spitsbergen, Siberia and Alaska for 1999 and 2000 using a volume energy balance model. The sites on Spitsbergen and Alaska have a thick snow cover, while the Siberia snow pack is thin and spatially heterogeneous. The main components of the energy balance are atmospheric fluxes (radiative, turbulent), but their percentage differs significantly between sites. On Spitsbergen and Siberia ablation energy is mostly provided by net radiation, on Alaska by sensible heat and net radiation. Almost 50 % of available energy is lost by sublimation in Siberia. The loss of heat into the ground is the smallest component in the balance. The physical properties of snow, soil and surface vegetation determine the ground heat flux resulting in a maximum loss of 18% at the Siberia and minimum of 6 % at the Alaskan site.

1 INTRODUCTION

Snow has an important role in formation of patterned ground. For example, snow melt water infiltration into cracks creates polygonal patterned ground. Snow differs spatially over patterned ground in thickness and physical properties. This has two important consequences: (i) ground heat transfer varies spatially and (ii) snow melt varies spatially and temporally.

By comparing surface energy balance components, the control mechanism at the local scale (such as surface characteristics) are examined relative to the larger scale factors (such as climate). We compare the energy balance at three patterned ground sites during snowmelt seasons of 1999 and 2000: Ny-Ålesund (Spitsbergen), the Lena River Delta, (Siberia) and Ivotuk (Alaska). Continuous permafrost underlies all these sites, but they have different climates.

2 METHODS

A volume energy balance model between snow surface and permafrost table is applied to calculate turbulent heat fluxes, heat flux by rain and heat flux of the ground and snow (Boike et al. 2002):

$$Q_n+Q_h+Q_e+Q_r = \Delta H_g+\Delta H_l+\Delta H_s+Q_m$$

where Q_n is the net radiation balance, Q_h and Q_e are turbulent fluxes of sensible and latent heat, Q_r is the heat flux supplied by rain, ΔH_g and ΔH_s are the changes of sensible heat in the soil and the snow, respectively, and ΔH_l is the change in latent heat of the ground. The latent heat of the snow pack, Q_m, is the remainder in the balance. For $Q_m > 0$, melting is expected while for $Q_m < 0$, freezing and recrystallization are expected. Atmospheric fluxes (defined here as Q_n, Q_h, Q_e and Q_r) towards the snow pack are defined as positive (energy gain), away from it as negative. Net radiation is measured at all sites using Q7 or NR LITE net radiometers. The bulk aerodynamic method is used for the calculation of atmospheric sensible and latent heat fluxes using hourly measurements of air temperature, humidity, wind speed and snow depth. The heat flux by rain is computed using rainfall rate and air temperature. Ground and snow heat fluxes are calculated as hourly changes of the soil's and snow's sensible and latent heat using hourly temperature and volumetric liquid water content data. Ground heat flux below the instrumented soil volume is ignored because the temperature gradient at the permafrost table is very close to zero. Snow heat flux is only calculated for the Spitsbergen site since automatic snow temperature and liquid water content data are available. Details on the method and the calculations are provided in Boike et al. (2002) and Kane et al. (1997). Surface roughness z_o is used as a tuning parameter at the Ivotuk and Spitsbergen site since no wind profile measurements are available. At the Spitsbergen site,

turbulent heat fluxes agree well with fluxes calculated from the aerodynamic profile method utilizing two level measurements at a nearby site (Semandeni-Davies et al. 2002). For the Siberia site z_o is calculated using detailed topographic survey data from 1999 following the method of Lettau (1969). Calculated roughness lengths are 0.0001 m for the Spitsbergen site, 0.001 m for Alaska and 0.01 m for Siberia. These roughness lengths are well-documented over snow and support the distinct surface characteristics: the polygonal ridges and troughs at the Siberian site increase z_o, while a very smooth snow surface and a large fetch lower z_o at the Spitsbergen site.

3 STUDY SITES

IVOTUK is located on the North Slope in Alaska, on the central southern coastal plains north of the Brooks Range (68°29'N, 155°44'W). Mean air temperatures recorded at the site in 1999 are –26 and 11 °C for January and July. Mid-winter melt events are quite rare and usually only warm the near surface snow. The study site is located on typical arctic tussock tundra terrain with 0-1% slope and poor drainage. The loamy soil has been characterized as 'Ruptic-Histic Aquiturbel' (organic ruptured by frost heave, reducing conditions, cryoturbation). The upper 30 cm are peat and peat muck. Permafrost was encountered at about 68 cm depth.

Figure 1. Tussock tundra terrain at the study site at Ivotuk, Alaska. The Brooks Range is visible in the background.

The BAYELVA catchment is located about 3 km from Ny-Ålesund, Spitsbergen (78°55'N, 11°E). Continuous permafrost in this region underlies coastal areas to depths of about 100 m and mountainous areas to depths greater than 500 m. The North Atlantic Current warms this area to average air temperatures around –13 and 5 °C in January and July and provides about 400 mm annual precipitation falling mostly as snow between September and May. Our study site is located at about 25 m above mean sea level, on top of a small hill covered with unsorted circles. Soil instruments are installed in the bare inner part of one circle, consisting of silty clay with interspersed stones.

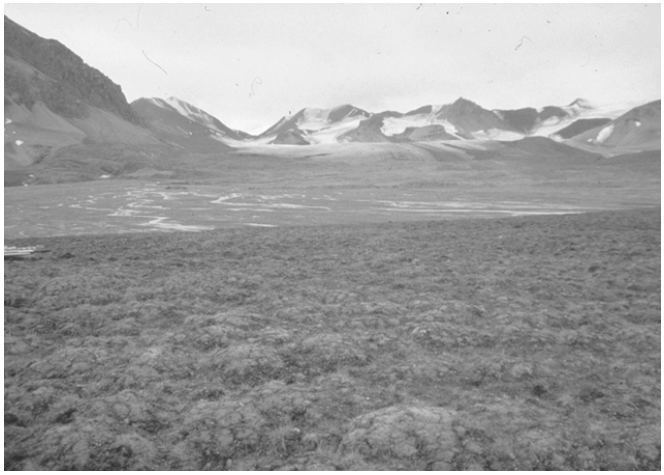

Figure 2. The Bayelva study site on Spitsbergen. The site is covered with unsorted circles ~1m in diameter. Bayelva river and Brøggerbreen glacier are in the background.

SAMOILOV is one of the 1500 islands of the Lena Delta, located in one of the main river channels in the southern part of the delta (72.°N, 126.°E). Continuous permafrost underlies the area to about 400 to 600 m. This area has the most extreme climate (coldest air temperature and lowest precipitation). Mean air temperatures recorded at Tiksi are –33.3 and 7.0 °C for January and July. Yearly total precipitation is around 125 mm, but winter snowfall is low (< 40 mm). Strong winds lead to aeolian sedimentation of sands. The climate station is situated on polygonal patterned ground (low-centered polygon) on peatish sand deposits of an ancient delta flood plain. Soil instruments are installed within the polygon's apex.

Figure 3. Polygonal patterned ground at the study site on the island Samoilov in the Lena River Delta, Siberia.

4 RESULTS

4.1 *Comparison of measured and modelled changes in snow water equivalent (SWE)*

Dingman (1994) divides the snow ablation period into warming, ripening and output phases. Melt wa-

ter flowing out of the snow pack is only created during the output phase; during the warming and ripening stage the snow densifies and compacts due to surface melt and snow internal processes. Boike et al. (2002) showed for the Spitsbergen site that the energy balance model is capable of distinguishing these two periods. When Q_m values become positive, the pre-melt period (warming and ripening of snow) is completed and runoff (output) starts. Measured and modelled ablation rates are in good agreement for the melt period for the examined years of 1999 and 2000 (Boike et al. 2002). A good agreement between measured and modelled snow ablation rates is also found for the melt period for the Alaska site starting on May 31, 2000 (Figure 4). Pre melt snow bulk density is about 250 kg m^{-3} increasing to about 350 kg m^{-3} towards June 4 (M. Sturm, pers. communication). Thus, a density of 350 kg m^3 is used for snow water equivalent calculation during the melt period.

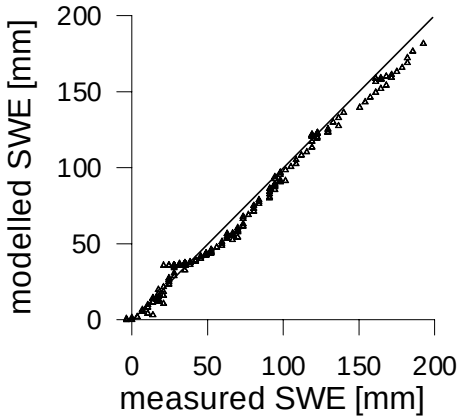

Figure 4. Comparison between measured and modelled cumulative changes in SWE for the melt period for the Alaska site at Ivotuk. Measured SWE was calculated using the decrease of snow height measured by the snow sensor and an average measured snow density of 350 kg m^{-3}. Modelled melt rates are calculated using Q_m from the energy balance.

At the Siberian site, a very heterogeneous snow cover, redistribution of snow due to high wind speeds and few manual measurements of snow depth (the automated snow sensor did not produce reliable measurements due to the very thin snow cover) make the comparison between modelled and measured SWE rates difficult. Measured decrease of SWE in the field at various sites agrees reasonably well with modelled results. The energy balance model calculates a total of 86 mm snow ablation from May 11 to 25, 1999. During the pre-melt (until May 18) 8 mm snow sublimates while minimum and maximum decrease in measured field SWE are 6 and 26 mm using an average measured snow density of 290 kg m^{-3}. Snow profiles and field data support the observation that sublimation is the dominant process during the pre-melt period. During the melt period, a total of 61, 81 and 90 mm SWE ablate at the stakes located at 2, 2.50 and 4 m along the transect (distance to apex), which are similar to the 78 mm SWE obtained from model estimates.

4.2 *Comparison of snow thermal properties before melt*

Mid winter warming events, and possibly rain, promote formation of internal ice lenses or basal ice in the snowpack on Spitsbergen, depending on thermal state of snow (Boike et al. 2002). A typical pre-melt snow profile is shown in Figure 5. Snow densities increase to an average of 450 kg m^{-3} towards the melt period. In Siberia, a 24 cm depth hoar layer, with a windslab 17 cm above the ground surface, and 8 cm of overlying snow comprise the snow profile. A surface crust and hardened layers within the snow profile contain a large amount of aeolian sediments and indicate high wind speeds (Figure 5). Large depth hoar crystals with grain sizes larger than 3 mm are the result of steep temperature gradients between soil and air and their associated vapor pressure gradients. In addition, the long grass tundra vegetation promoted depth hoar formation by preserving a loose, aerated layer at the snow cover base.

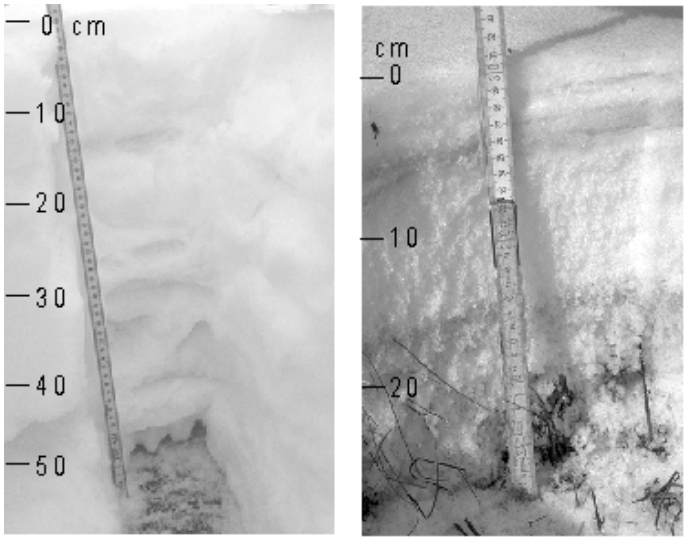

Figure 5. Contrasting pre-melt snow profiles in 1998 on Spitsbergen (left) and in 1999 in Siberia (right); the latter is taken within the polygon's snow filled center. The snow profile on Spitsbergen has a higher density, several internal ice layers and a basal ice layer. The snow on Siberia consists mainly of very loose, large grained depth hoar. Visible are also two hardened, sediment rich layers.

The Ivotuk profile consists (May 11, 2000) of a large depth hoar layer of 38 cm overlain by a further 32 cm of mixed snow types. Thin ice layers and glaze crusts are present in this mixed layer.

4.3 *Snow melt, Spitsbergen 1999*

The process of snow ablation for the years 1999 and 2000 has been examined in detail in Boike et al. (2002). In 1999, snow ablation takes 47 days:

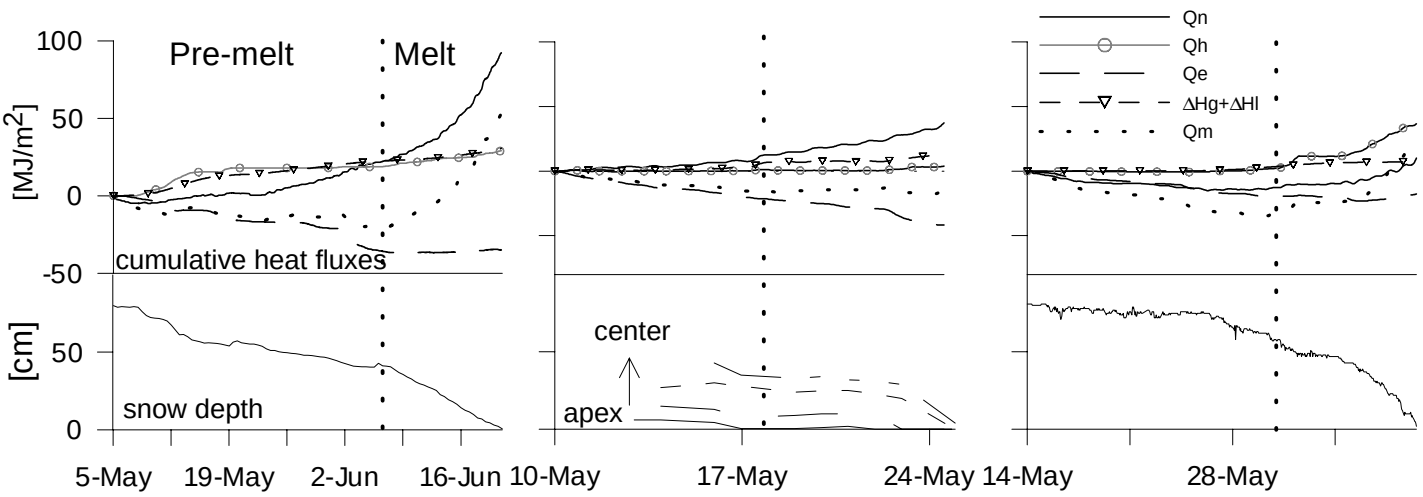

Figure 6. Cumulative sum of heat fluxes and snow depth for the three study sites during the snow ablation periods in 1999 and 2000. The ablation period is divided into pre-melt and melt periods when Q_m values become positive. The sensible and latent heat of the snow pack is only calculated for the Spitsbergen site. Q_r and ΔHs are negligible and not shown here.

surface melt and snow internal processes (ripening) reduce the snow pack thickness (but not SWE) from May 5 until June 7, after which output is produced within 14 days. Rain on snow events occur frequently, but do not contribute substantial energy. The cumulative sum of energy balance components during snow ablation in 1999 is shown in Figure 6. The dominant source of energy for melt is provided by Q_n. Evaporation and sublimation use about 30 % of Q_n. Q_r and ΔH_s are insignificant. Due to the long ablation period, $\Delta H_g + \Delta H_l$ are a significant energy sink, using 30 % of total energy supplied by Q_n. The snow melt at this site in 2000 is similar and thus is not discussed here.

4.4 *Snow melt, Siberia 1999*

The polygon pattern results in a highly variable microtopography and snow depth. The snow cover on the polygon's apexes ranges between 0 and 10 cm, while the center has a snow filling of up to 60 cm. Figure 6 shows the cumulative energy fluxes and ablation of snow at several positions along a transect extending from the polygon's apex to the center.

Throughout the winter and during the pre-melt period, snow exclusively sublimates (sublimation possible due to high wind speeds) exposing the polygon ridges. The air temperature remains far below 0 °C (Boike & Becker, 2000), wind speeds can average a maximum up to 15 m s $^{-1}$, increasing the turbulent losses through latent heat.

One warming event on May 17 melts the upper 5 cm of the snow, but snow temperatures are still far below freezing, –13 °C at the bottom of the snow. Infiltration of surface melt and subsequent densification is indicated by an increase of snow density (from 250 to 290 kg m^{-3}) and homogenization of snow layers. Melt starts around May 18 when Q_m becomes positive with Q_n providing the major source.

4.5 *Snow melt Alaska 2000*

During the 17-day pre-melt period (May 14-30, 2000) the snow cover decreases about 28 cm, caused by compaction due to surface melt (event with a positive air temperature on May 16) and snow internal processes. Continuous surface melting starts on May 26, suggested by positive air temperatures and a steep increase in snow temperatures (Hinzman & Peltier, 2001). Starting on May 31, Q_m values increase, indicating a ripe snowpack. This is corroborated by snow temperatures: isothermal conditions around 0 °C within the snow pack permit free percolation of melt water to the ground (Hinzman & Peltier, 2001). A period of cold sub zero air temperatures between June 1 to 4 interrupts the snow melt (Q_m plateau). This plateau of no SWE change is depicted by the model. After this, a pronounced increase in air temperature and net radiation concomitant with a drop in air humidity produces steadily increasing Q_m. The energy for warming and ripening of the snow is derived from Q_n and Q_h. During the first 6 days of the melt phase, the main energy source is provided by Q_h, but with progress of melt, Q_n becomes more important. As winds cross the Brooks Range to the south of the site, the air becomes drier as it rises and warmer as it descends, thus providing energy for Q_h.

5 COMPARISON OF ENERGY BALANCE COMPONENTS

The percentage of energy balance components for the three sites is presented in Figure 7. Source pies

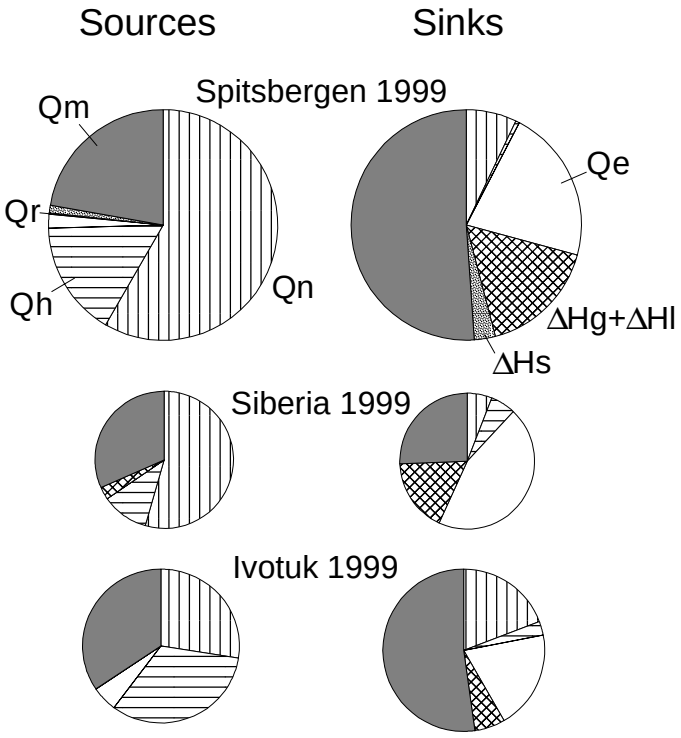

Figure 7. Percentage of energy balance components during the snow ablation periods for the three sites. The size of the pies is relative to the total amounts of energy transferred.

represent the total cumulative positive energy fluxes provided by the energy balance components, whereas sink pies represent negative totals. Pie size is proportional to the total amount of heat transferred and reflects the duration of the total ablation period: 47 days and 50 GJ m^{-2} at the Spitsbergen site, 27 days and 34 GJ m^{-2} at Alaska and 15 days and 28 GJ m^{-2} in Siberia. There are significant differences between the energy distributions. Melt energy at the Spitsbergen and Siberia sites is largely provided by Q_n, while almost half of the melt energy at the Alaska site comes from Q_h. Q_e is a small source for melt via condensation at the Spitsbergen and Alaska site. $\Delta H_g+\Delta H_l$ are a small source of heat at the Siberia site, through the infiltration and subsequent freezing of snow melt water at this apex site. The energy transferred into warming and ripening during the pre-melt period is largest at Spitsbergen and Alaska due to a thick snow cover in both locations. Biggest difference in the sinks of the energy balance of the three sites is the dominance of sublimation as energy sink in Siberia and differences in ground heat flux. The former is a result of high wind speed in Siberia. At Ivotuk the ground heat flux is lowest (6%) due to low thermal gradient across the snow pack and the insulating properties of the snow and upper soil horizons. A 38 cm thick depth hoar layer and deep snow profile (70 cm) plus a thick moss layer insulate the soil better at this site. The ground heat flux at the Spitsbergen and Siberian site is similar, 17% and 18% respectively. At the Siberian site, this is the result of a large thermal gradient and a very thin or absent snow cover on the polygonal ridges. In contrast, the snow cover at the Spitsbergen site is thick (~80 cm), but depth hoar- if present- is limited to a few centimeters. In addition, the lack of an insulating organic surface layer permits heat transfer across the mineral soil-snow interface.

6 OUTLOOK

Our energy balance method shows differences between microclimate and soil material effects on heat and mass transfer to the soil during the snow melt period. Climate affects the snowmelt period primarily via differences in snow pack and by whether atmospheric radiative or turbulent fluxes prevail in determining melt energy. Spitsbergen and Siberia, both located close to the sea, experience radiative melting. Local phenomena, such as the orographic influence of the Brooks Range in Alaska, increase the percentage of sensible heat flux.

The sandy material at the Siberia site is prone to deep infiltration, and the observed large thermal gradient promotes ice wedge growth though the refreeze of snow melt water. The micro-topography of the ice wedge form leads to its further development by moving water within the apex towards the site of wedge growth.

Further work will concentrate on factors and quantification of patterned ground formation throughout the year.

REFERENCES

Boike, J., Roth, K. and Ippisch, O. 2002. Seasonal snow cover on frozen ground: energy balance calculations of a permafrost site near Ny-Ålesund, Spitsbergen. *J. of Geophysical Research- Atmosphere*, accepted.

Boike, J. and Becker, H. 2000. Thermal and hydrologic dynamics of the active layer. In Rachold & Gregoriev. Reports on Polar Research: Russian-German Cooperative System Laptev Sea 2000 (354), 25-28.

Dingman, S.L. 1994. *Physical Hydrology*, Prentice Hall, New Jersey.

Hinzman, L.D. and B. Peltier. 2001. North American Arctic Snowmelt Season, Spring 2000 http://www.uaf.edu/water/projects/Snowmelt2000/CD/CDBrowser.htm.

Kane, D.L., R.E. Gieck, and L.D. Hinzman. 1997. Snowmelt modeling at small Alaskan arctic watershed. ASCE Journal of Hydrologic Engineering. 2(4), 204-210.

Lettau, H. 1969. Note on aerodynamic roughness-parameter estimation on the basis of roughness element description. *J. of applied Meteorology* 8: 828-832.

Semandeni-Davies, A., Maréchal, D., Bruland, O., Kodama, Y., Sand, K. 2002. Latent heat flux estimation over a melting Arctic snow cover, Svalbard. *Arctic and Alpine Research*, submitted.

We gratefully acknowledge financial support from the Deutsche Forschungsgemeinschaft, the European Union and a research grant awarded to Julia Boike by the Deutsche Akademie der Naturforscher Leopoldina. Essential logistic

support was provided by the German and the Norwegian Research Stations in Ny-Ålesund and U.S. National Science Foundation Arctic System Science Program (Grant Number OPP-9818066).

Chapter 3

Chapter 3.1

Boike, J., Ippisch, O., Overduin, P. P., Hagedorn, B. and Roth, K. (2007): Water, heat and solute dynamics of a mud boil, Spitsbergen, *Geomorphology* 95, 61-73.

Available online at www.sciencedirect.com
ScienceDirect
Geomorphology 95 (2008) 61–73
GEOMORPHOLOGY
www.elsevier.com/locate/geomorph

Water, heat and solute dynamics of a mud boil, Spitsbergen

Julia Boike [a,*], Olaf Ippisch [b,1], Pier Paul Overduin [c,2], Birgit Hagedorn [d,3], Kurt Roth [e,4]

[a] Alfred Wegener Institute for Polar and Marine Research, Telegrafenberg A43, 14473 Potsdam, Germany
[b] Interdisciplinary Center for Scientific Computing, INF368, University of Heidelberg, 69120 Heidelberg, Germany
[c] Water and Environment Research Center, University of Alaska Fairbanks, Fairbanks, AK 99775-5860, USA
[d] Quaternary Research Center, University of Washington, Box 351360, Seattle, WA 98195, USA
[e] Institute of Environmental Physics, INF 229, University of Heidelberg, 69120 Heidelberg, Germany

Received 17 May 2005; received in revised form 28 October 2005; accepted 9 July 2006
Available online 10 May 2007

Abstract

Mud boils, a form of non-sorted circles, cover the ground surface in many periglacial landscapes. The vegetation-covered trough acts as an effective buffer to the downward movement of water and chemicals, while the bare center experiences larger fluxes of heat and mass. Since dissolved ions affect the electric conductivity of the soil solution, measurements of the bulk soil electric conductivity offer potential for estimating solute concentration. Since 1998, bulk soil electric conductivity has been measured automatically and hourly using 32 time domain reflectometry probes over an approximately 1 m diameter mud boil close to Ny Ålesund, Spitsbergen. Soil water electric conductivity was calculated from bulk soil electric conductivity using volumetric soil water content and a calibration parameter. The seasonal and spatial behaviour of water, temperature and solute concentration within two profiles of this mud boil were analyzed. Concentrations of estimated soil water electric conductivity were highest during the summer period when the active layer was thawed. Thermodynamic equilibrium modelling of the soil solution during freezing suggests that precipitation of dissolved species leads to the observed decrease in electric conductivity. There is a pronounced vertical solute concentration gradient in both profiles, while there is little evidence for horizontal solute concentration gradients beneath the mudboil.
© 2007 Elsevier B.V. All rights reserved.

Keywords: Permafrost; Freezing; Geophysical methods; Electric conductivity; Solute dynamics; Patterned ground

1. Introduction

Analysis of the phenomenology and dynamic processes of patterned ground yields information on past and present climate and environmental conditions (Washburn, 1979; Romanovskii, 1996). The objective of this study is to characterize (seasonally and spatially) the water and solute dynamics of this heterogeneous system using soil solution sampling, high temporal resolution measurements of bulk soil electric conductivity and

* Corresponding author. Tel.: +49 331 288 2119; fax: +49 331 288 2137.
E-mail addresses: jboike@awi-potsdam.de (J. Boike), olaf.ippisch@iwr.uni-heidelberg.de (O. Ippisch), fsppo@uaf.edu (P.P. Overduin), hagedorn@u.washington.edu (B. Hagedorn), kurt.roth@iup.uni-heidelberg.de (K. Roth).
[1] Fax: +49 6221 54 4404.
[2] Tel.: +1 907 474 2758; fax: +1 907 474 7979.
[3] Fax: +1 206 543 0489.
[4] Fax: +49 6221 54 6405.

0169-555X/$ - see front matter © 2007 Elsevier B.V. All rights reserved.
doi:10.1016/j.geomorph.2006.07.033

thermodynamic equilibrium modelling of solution chemistry. This, in turn, adds insight to the mechanical dynamic of the mud boil, and to the discussions on the origin and formation of these periglacial features.

Furthermore, these findings contribute directly to the European Science Foundation project on 'Sedimentary Source-to-Sink-fluxes in Cold Environments'. An understanding of climate processes and their control on mass transfer processes, such as subsurface behaviour of solutes in a mudboil, aids in the understanding of mass export of cold drainage baisins.

2. Theories of mud boil formation

Mud boils are symmetric surface features in periglacial environments that have puzzled and fascinated researchers since at least 1900. Early observations and theories of the origin of patterned ground were the beginning of exciting research. Washburn (1956) summarized and discussed postulations of 19 separate mechanisms of formation for non-sorted circles in particular. These ideas are still central in today's discussions of patterned ground formation.

Mud boils (also known as frost boils, frost scars, mud circles and mud hummocks), classified as non-sorted circles, are found in areas where the ground is subject to seasonal freezing and thawing. They are characterized by a bare, usually doming round mineral soil center, surrounded by vegetation. Some of the mechanisms postulated for their formation are: the sorting of soil materials based on grain size; convection cell like cryoturbation; diapir formation or upwellings of lower soil horizons under pressure (Washburn, 1956). A review of the main mechanisms involved in cryoturbations was presented by Van Vliet-Lanoë (1991) based upon field measurements and micromorphological data. She concluded that "differential frost heaving appears to be the main mechanism of cryoturbation" (pp. 123) and that the presence of organics enhances differential frost heaving. Kessler et al. (2001) modelled sorted circle formation (with barren finer grained circle centers surrounded by stones) from two layers distinct in particle size using a purely mechanical model. The freezing front pushed soil to more compressible soil regions, accumulating in soil plugs that reach to the surface. During thawing, consolidation occurred vertically. The circle was maintained at the surface by the circulation of the stone and fine material domains, upward in the circle center and downward at the edges. Walker et al. (2004) presented horizontal soil profiles across a mud boil. Nutrient concentrations (available potassium, phosphor, nitrogen) and water content declined from the margins toward the center, a trend which they attributed to more 'mechanical' activity towards the center of the boil.

2.1. Study site

The Bayelva catchment is located about 3 km from Ny-Ålesund, Spitsbergen (78°55′N, 11°E) in the forefield of the Brøggerbreen glacier (Fig. 1A, B). In this region, continuous permafrost underlies coastal areas to depths of about 100 m and mountainous areas to depths greater than 500 m. The North Atlantic Current warms this area to mean monthly air temperatures around −13 °C in January and 5 °C in July, respectively and provides about 400 mm annual precipitation mostly as snow between September and May. Our study site is located at about 25 m above mean sea level, on top of a small hill covered with unsorted circles (Fig. 1C). It is not clear if the mud boils on this hill are currently being degraded (for example, by gelifluction) or maintained by active cryoturbation. Vegetation encroaching from the sides into the mud boil's center – though the centers are still doming – is an indicator for slow mass displacement and semi-active behaviour. While other patterned ground phenomena (such as sorted circles and stripes) are found in the vicinity of the hill, these mud boils are only present on Leirhaugen hill. The mud boils were or are formed under local conditions favourable for mud boil formation after the last glacial period.

Leirhaugen hill is mainly composed of rock, but partly covered by a mixture of sediments: glacial till, finer glacio-fluvial sediments and clay formed by the last glacial advance (Tolgensbakk, personal communication). The gray color of the sediments suggests that the material was deposited by the Kongsfjorden glacier and not the adjacent Brøggerbreen glacier, which deposits redder material. Marine sedimentation could also have contributed since the hill is located below the marine limit (about 38 m).

3. Methods

We instrumented one of these non-sorted circles (Fig. 1D) in August 1998 to automatically monitor hourly temperature and volumetric liquid water content (θ). Altogether 32 time domain reflectometry (TDR) probes and 32 temperature probes were installed over the 1×1 m profile. The position of the TDR probes is shown in Fig. 2. The TDR and temperature data set considered in this study is limited to 1999, the year in which suction lysimeter data were collected. During installation, soil samples were taken for the analysis of physical parameters. The texture and composition of 25

samples were determined using standard methods. Wet soil was passed through a sieve with 63 µm size to measure sand content. After destruction of organics and limestone, silt and clay were separated by sedimentation

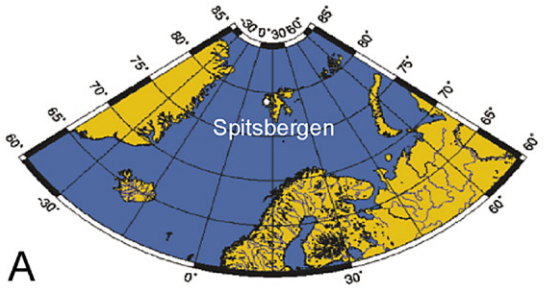

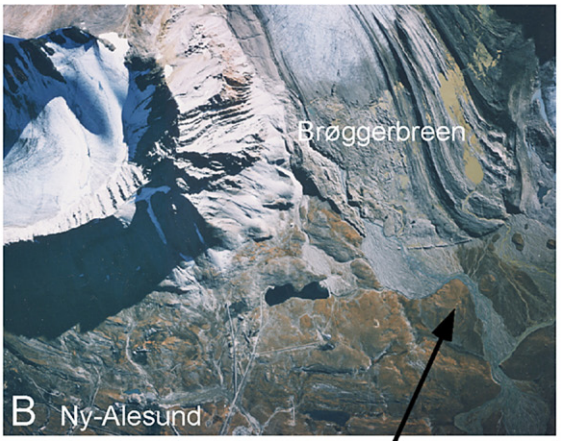

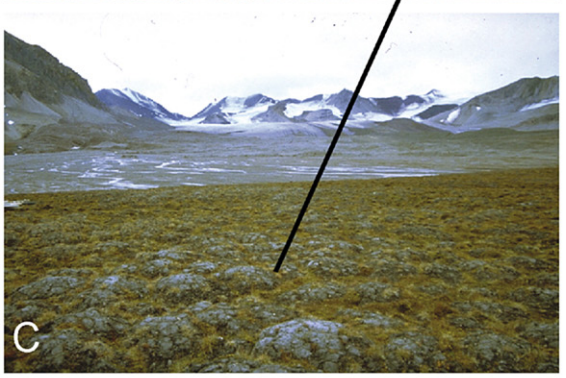

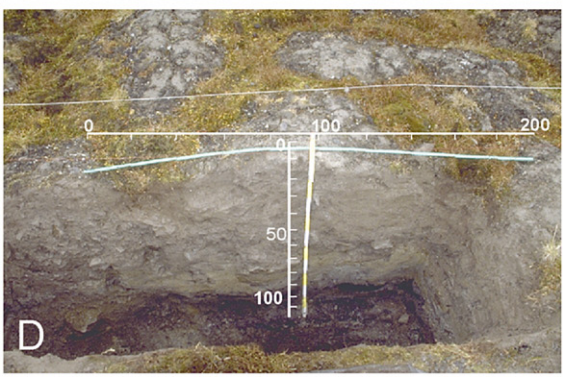

Fig. 1. The location of Spitsbergen (A) and aerial picture (1:15000) of the area around Ny-Ålesund (B). The study site (arrow) is located on Leirhaugen hill close to end moraines of the Brøggerbreen glacier. Parts of the road network of Ny-Ålesund can be seen in the lower left part of the picture. The Bayelva study site (C) is located in a field covered with non-sorted circles. The excavated mud boil is shown in D. The bare soil circle centers range about 1 m in diameter and are surrounded by vegetated borders consisting of a mixture of low vascular plants, mosses and lichens.

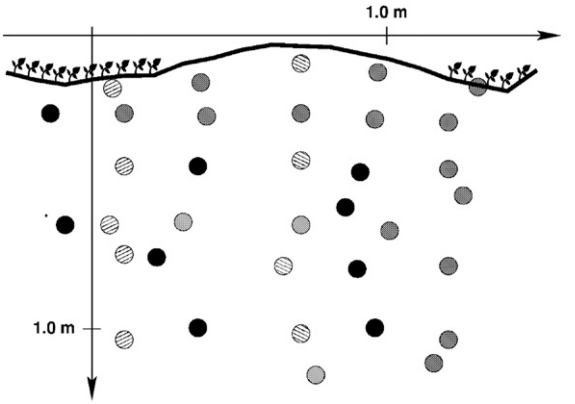

Fig. 2. Position of TDR probes (grey and hatched circles) installed in the mud boil. Temperature probes are installed adjacent to TDR probes. For the analysis, the left profile under vegetation and the profile underneath the center of the mud are used (hatched circles). In addition, nine suction lysimeters (black circles) are installed close to TDR probes (see also Table 1).

in Atterberg cylinders. Soil temperatures were recorded using thermistors calibrated at 0 °C with a precision of 2.4×10^{-4} °C at 0 °C and an absolute error less than ±0.02 °C over the temperature range ±30 °C. Volumetric liquid water content was calculated from TDR measurements with an accuracy of 0.02 to 0.005 and a precision better than 0.005. Soil water was sampled in 1999 using Prenart® suction cups (5 cm long, pore size 2 µm; Gravquick, Denmark) cups that were installed in 1998 at different depths close to TDR probes. Soil water was analyzed in the field for pH, electric conductivity and alkalinity. The remaining sample water was filtered and stored at 4 °C in pre-cleaned HDPE bottles until laboratory analysis took place. Cation concentrations were analyzed with ICP-OES (Optima 3000 XL, Perkin Elemer) and anion concentrations were measured with ion chromatograph (Dionex 320).

3.1. TDR and bulk electric conductivity

Data on spatial and temporal distribution of water and solutes in frozen and unfrozen soils are essential for energy and mass transport models. A fast method to measure the volumetric water content *in situ* is TDR.

TDR has become a reliable and widely used technique to measure the water content in frozen and unfrozen soils (for example, Topp et al., 1980; Patterson and Smith, 1980; Roth et al., 1990). The TDR technique for measuring the volumetric water content is based on the large disparity in the relative dielectric permittivities of water and the other soil constituents. The bulk relative dielectric permittivity of the soil determines the velocity with which an electromagnetic wave travels through the soil, so that measurement of the travel time for a known distance allows determination of the material's permittivity. We use a physically-based dielectric mixing model to compute the composite dielectric number of a multiphase mixture using the relative dielectric permittivities and volume fractions of its constituents (Roth et al., 1990).

TDR can also be used to measure the impedance of the bulk soil Z (Ω), which is related to the bulk soil electric conductivity as a function of time. The bulk soil electric conductivity is in turn related to the concentration of ionic solutes (Reluy et al., 2004) and hence TDR is suited for *in situ* detection of well-dissociating solutes. The impedance can be determined from the attenuation of an electromagnetic wave traveling along the probe after all multiple

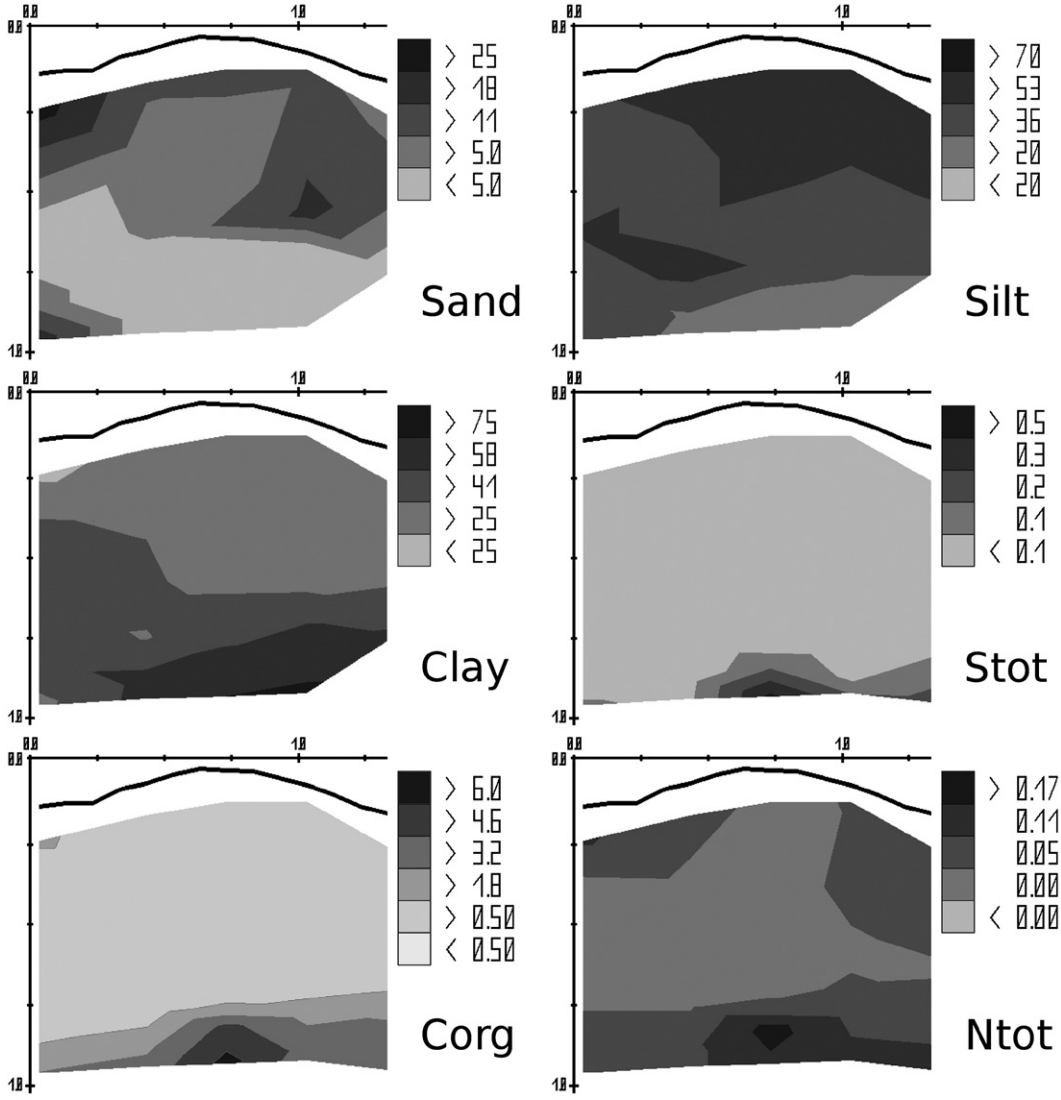

Fig. 3. 2-D distribution of sand, silt, clay and total carbon, nitrogen, sulphur of the mud boil in % weight. Linear interpolation is used between 25 sampling points.

reflections have ceased and the signal reaches a stable level. Usually it is assumed that the impedance is related to the bulk soil electric conductivity by:

$$\sigma_b^{25} = \frac{K_P}{Z - Z_{cable}} f_T \quad (1)$$

where σ_b^{25} [S m^{-1}] is the soil bulk electric conductivity corrected to 25 °C, K_p [m^{-1}] is the geometric cell constant of the TDR probe, Z_{cable} [Ω] accounts for the total resistance of cables, connectors and cable tester and f_T [−] is a temperature factor defined as:

$$f_T = 1 + \alpha(T - 25) \quad (2)$$

where T [°C] is the soil temperature and $\alpha = 0.019$ °C^{-1} is the temperature coefficient (Heimovaara et al., 1995). We calibrated our TDR probes in a range of solutions with known electric conductivities, following the method of Heimovaara et al. (1995). As there was no longer a linear relation between measured impedance and the inverse of the conductivity for high concentrations, we modified Eq. (2) to:

$$\sigma_b^{25} = \left(\frac{1}{Z - Z_{cable}} - B\right) K_p f_T \quad (3)$$

where B is an additional fitting parameter. B, K_p and Z_{cable} were determined by non-linear least squares fitting.

3.2. Calculation of soil solution electric conductivity σ_w

The relationship between bulk electric conductivity and the electric conductivity of the liquid phase depends on the conductivity of the solid phase and the geometry of the phases, which is related to soil structure and air, ice and water contents. There are several empirical models, partly with some theoretical justification. Boike and Roth (1997) compared the descriptive power of three models for a permafrost site in Siberia by a comparison of the conductivity measured in water extracted from suction cups with the conductivity predicted from TDR measurements. For the coarse textured soils studied they found the best agreement with a simple regression model:

$$\sigma_b = A\theta\sigma_w \quad (4)$$

where σ_w [S m^{-1}] is the electric conductivity of the soil solution, θ [−] is the volumetric liquid water content of the soil and A [−] is a fitting parameter. For three different mineral soils the parameter A varied between 0.7 and 4.8. Best results were obtained with probe specific calibrations. Furthermore, they suggested that A did not change from frozen to unfrozen soils and that this model may be applied to calculate σ_w for frozen conditions as well. To our knowledge, the only other model predicting σ_w from TDR-determined σ_b in frozen soils was introduced by van Loon et al. (1991; also reviewed in Boike and Roth, 1997). This model has been applied for the study of solute dynamics in Swedish field soils (Lundin and Johnsson, 1994) and in frozen lab columns (Stähli and Stadler, 1997) without prior calibration to soil solution electric conductivity. As the model by van Loon et al. (1991) did not predict solution electric conductivity as well as the regression model for permafrost soils in Siberia (Boike and Roth, 1997) we did not consider this model further in this study.

4. Results

Soil composition data from the 25 samples taken from the profile is presented in Fig. 3. The soil material generally consists of silty clay with some larger stones. The silt content decreases from over 50% at the top of the profile to less than 30% at the bottom, concomitant with an increase of clay content to over 50% (Fig. 3). Concentrations of organic carbon, total nitrogen and total sulphur are highest at the bottom of the profile, peaking below the mud boil center. Of note are especially high concentrations of organic carbon (>6%

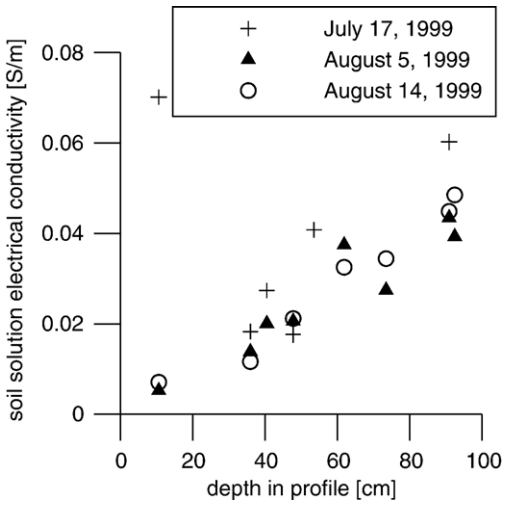

Fig. 4. Soil water electric conductivity obtained from suction lysimeter water at three different times over depth.

weight) at the bottom of the profile. Nitrogen is also elevated below the vegetated trough of the profile.

4.1. Determination of σw

The bulk electric conductivity of the soil is generally considered to be the sum of the conductive contributions of the liquid phase and the soil matrix surface

$$\sigma_b = \sigma_w + \sigma_s \quad (5)$$

The matrix surface contribution is generally assumed to be low relative to that of the soil solution, and is often neglected (Boike and Roth, 1997). The texture of the soil in this study site is finer and has far more clay than the coarse textured soils studied by Boike and Roth (1997). Since the clay content is high, the conductivity of the solid phase may no longer be negligible and it is not clear if these findings are also valid for this site. To verify this and to calibrate the measurement of σ_w we used the measured electric conductivity of water extracted on three dates (July 17, August 5 and 14, 1999) from suction cups installed at nine positions near the TDR probes (Fig. 4). The electric conductivity of the extracted water increased with increasing profile depth, thus the rise of bulk electric conductivity cannot be attributed solely to the increase in finer soil particles.

Suction lysimeter data were used to calibrate the model (Eq. (4)). The calculated mean A factors for the regression model are given in Table 1. Calculated A values lie within the same range as the ones calculated by Boike and Roth (1997). Fig. 5 shows a comparison of σ_w measured in soil water and the corresponding σ_w calculated from TDR measurements. Altogether we can see a good linear relation with some outliers. The two water samples with high concentrations were collected during the first sampling and have different ion composition, as will be explained later in the Discussion section. A closer examination of the values for individual probes shows a narrow range of conductivities covered by the limited amount of samples taken, so that within the accuracy of the measurements they represent one data point for each probe. This makes verification of the model difficult. However, we assume that there are monotone relations between σ_w and σ_b and θ and σ_b. Therefore the qualitative behaviour of σ_w derived from the TDR measurements is expected to be correct even if absolute errors are introduced by disregarding the conductivity of the solid phase.

Table 1
Mean calculated A factors for the linear regression model

Suction lysimeter	Suction lysimeter location depth [cm]	A factor	No. of water samples	pH
B1	91	1.1	4	Neutral, pH=7.1
B2	93	1.0	3	Acidic, pH=4.1
B3	62	2.4	4	Alkaline, pH=7.8
B4	74	2.8	2	Neutral, pH=7.1
B5	48	4.0	5	Alkaline, pH=7.9
B6	54	1.6	3	Alkaline, pH=8.1
B7	36	4.7	6	Alkaline, pH=7.5
B8	41	3.8	4	Alkaline, pH=8.0
B9	10	4.0	3	Neutral, pH=6.7

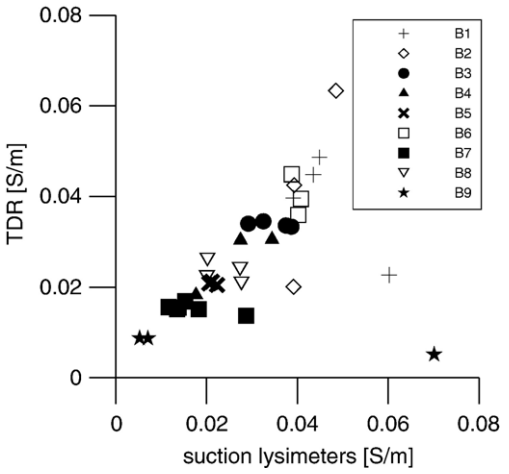

Fig. 5. Soil water electric conductivity obtained from suction lysimeters (names of suction lysimeters in legend) compared to values calculated from bulk electric conductivity (TDR probes) using model (4).

4.2. Temperature, volumetric water content and soil solution electric conductivity dynamics

For the following analysis, we chose two profiles: one located below the vegetated left trough and the other one below the center of the mud boil (Fig. 2). Fig. 6 shows rainfall and snow depth, soil temperature, soil volumetric water content and σ_w at 4 different depths below the vegetated trough. As expected, the probe closest to the surface (0.06 m) shows higher temperatures and daily temperature fluctuations compared to the lower probes. The temperature signal is attenuated with depth. In May, the snow liquid water content increases considerably, a process also enhanced by rain on snow events (Boike et al., 2003), and infiltration of water rapidly warms the soil at all depths. This is reflected in Fig. 6 by the dramatic increase in the volumetric water content of the soil at successive depths. The liquid water content mirrors most clearly the advance of the thaw front. The phase change ice/water starts during snow ablation and is much enhanced after the snow has ablated. The soil temperature

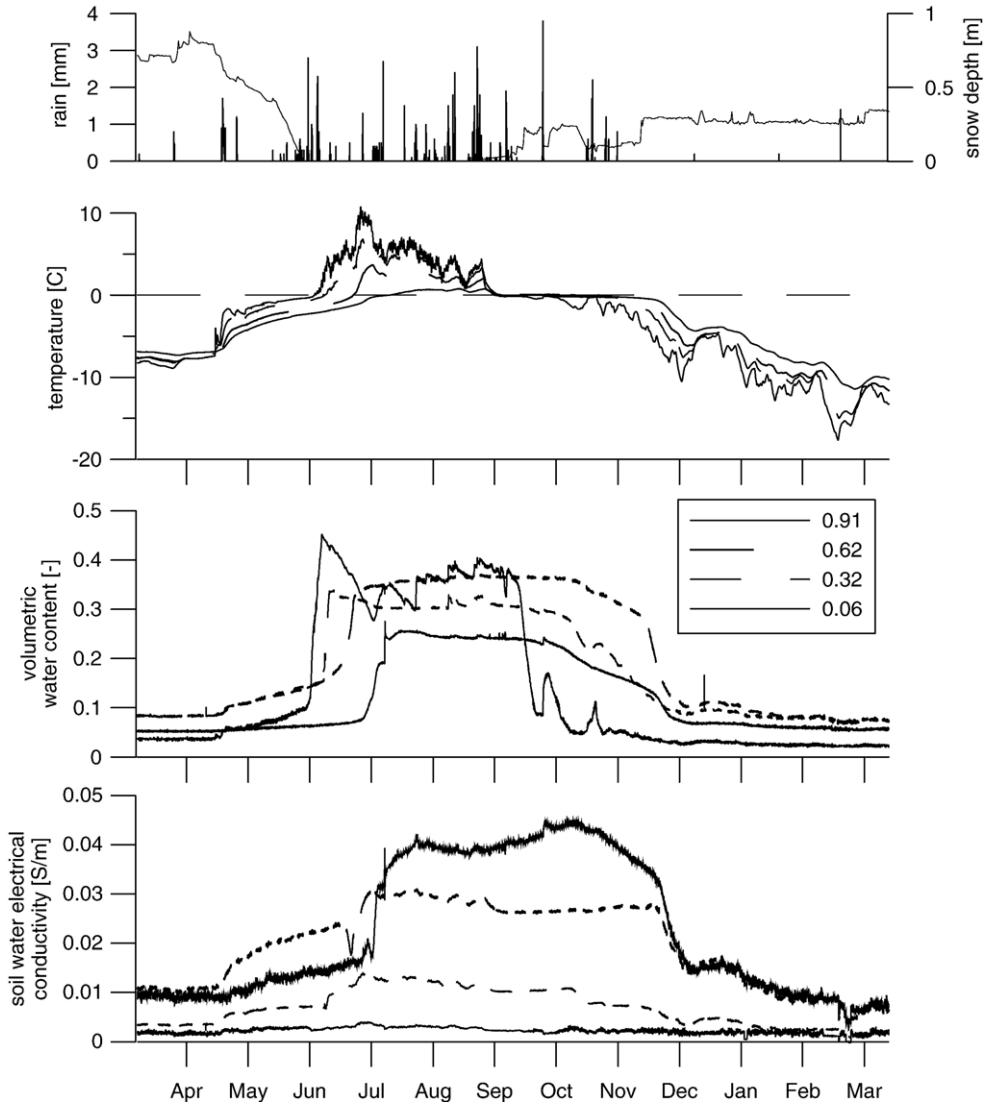

Fig. 6. Rainfall and snow depth, soil temperatures, soil water content and soil water electric conductivity from April 1999 to April 2000 at four depths for a profile underneath the vegetated cover.

sensor at 0.91 m depth passes 0 °C around the end of July. However, low volumetric water contents (~0.25) that remain constant over the summer indicate that the soil is not completely thawed. The temperature sensor at 1.22 m depth (not shown in diagram) indicates that the soil never thaws at this depth. During the summer, volumetric water content remains constant at 0.62 m depth, indicating the perched water table above the frozen ground. Once freezing starts in September, soil temperatures at all depths drop to below zero and phase change from water to ice is initiated ("zero curtain effect"). The phase change is completed by mid-November, after which the soil profile cools. The volumetric liquid water content in these frozen soils during winter ranges between 4 and 9% and is lowest at the surface due to desiccation (vapour migration out of the soil, see Roth and Boike, 2001).

The general seasonal behaviour of σ_w below the organic (except for the probe nearest to the surface at 0.06 m) can be summarized as follows: increase of σ_w during thawing, highest concentrations during the summer and decrease during the fall phase change. However, during the spring thaw, the behaviour of σ_w is different for each soil depth. At intermediate depth (0.32 m), σ_w increases during thaw, but continues to increase even after the soil is completely thawed, indicating either transport of solutes to this area or local and continued increases in the concentration of charged solutes. At 0.62 m depth, a pronounced drop in conductivity occurs

during thaw at about 15% liquid water content, which indicates that dilution of the soil water has occurred, probably via downward migration of meltwater with lower concentrations of dissolved ionic species. In addition, this is the soil depth with the highest σ_w in the frozen soil. Since this is the soil depth that remains thawed longest in the fall (Boike et al., 2003), migration of excluded ions would take place towards this depth. This is also suggested by a small increase of θ and σ_w in December after closure of the zero curtain.

Throughout the whole summer σ_w is relatively stable, with small increases of σ_w occurring at the three intermediate depths simultaneously with an increase of θ after a series of rain events during the latter half of August. However, there is also a peak in σ_w measured with the deepest probe at the end of July, which is not connected to a corresponding increase of water content. Only the surface probe shows an increase in θ at this time, caused by a minor rain event. As the same peak can be recognized at the deepest probe below the mud boil center, it is unlikely to be an artefact and either an *in situ* increase in solute concentration, for example by dissolution of salts, or lateral inflow must have occurred. Generally in the thawed organic profile, soil water conductivity increases with depth and the highest concentrations occur at the bottom of the profile (0.91 m).

In the barren soil below the center of the boil the fluctuations of temperature, water content (Fig. 7) and σ_w

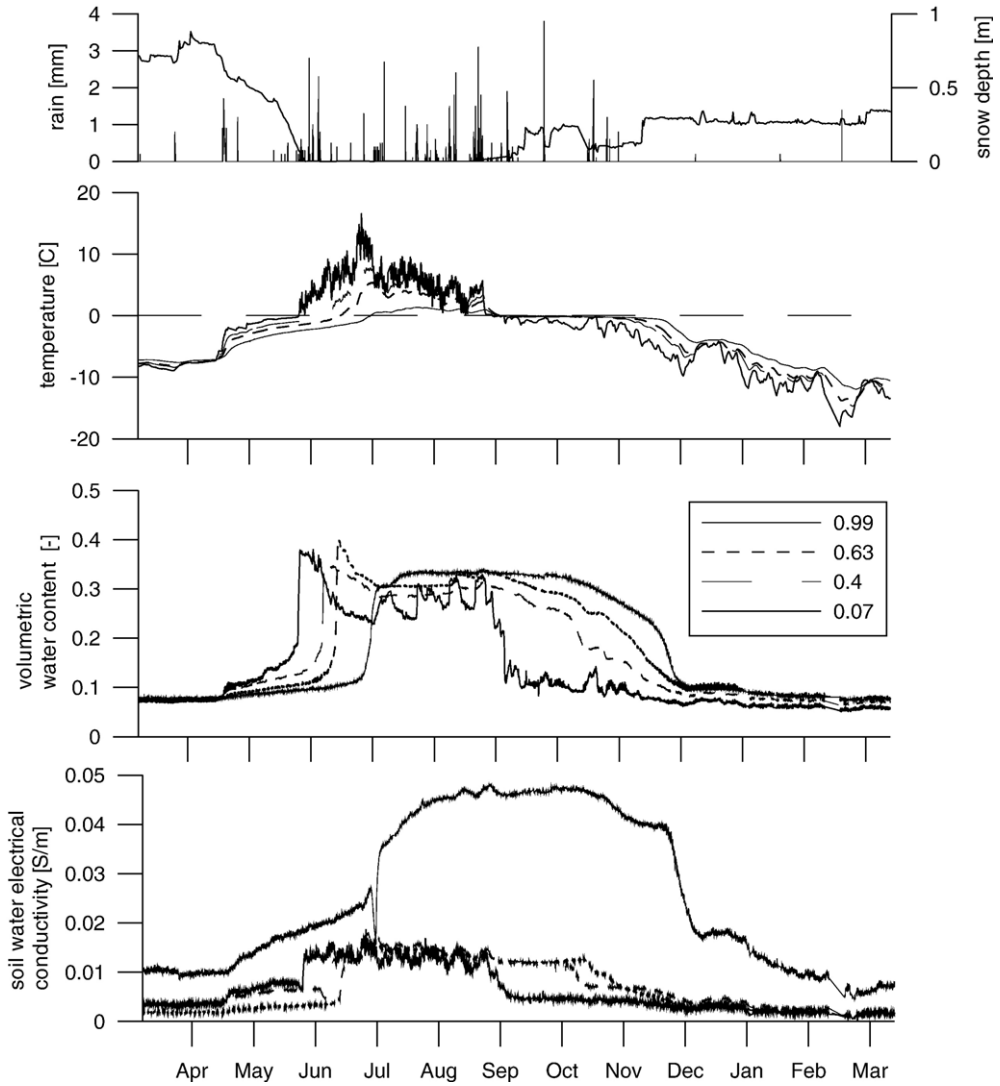

Fig. 7. Rainfall and snow depth, soil temperatures, soil water content and soil water electric conductivity from April 1999 to April 2000 for profile underneath mud. $A=3.8$ in Eq. (4) was used for TDR probe at 0.07 m under mud.

near the surface are generally higher than below the vegetation covered trough. Due to the lack of vegetation, the profile thaws earlier. In mid-July, the thaw front passes the probe at 0.99 m depth. Over the course of the summer, the center of the mud boil thaws to greater depth compared to the vegetated trough. The water content of the soil surface layer shows greater fluctuations in response to wetting by rainfall and subsequent drying since these processes are not buffered by vegetation. The σ_w values increase with depth in a fashion similar to the profile under the vegetated trough, with highest values of σ_w at the bottom of the boil and, σ_w values are generally higher at the bottom of the mud profile. Decreases in σ_w from the beginning of June (0.07 m) until the middle of July (0.99 m) in the mineral profile indicate the dilution of the soil solution by downward migration of meltwater. As observed for the organic profile, these decreases in soil solution electric conductivity are associated with thawing, but occur before the liquid water content increases.

Soil waters from deep suction lysimeters B1 and B2, and from shallower lysimeters B5 and B6, were analyzed for cation and anion concentrations. Based on lysimeters B6 and B5 (about 60 cm), the most concentrated species are HCO_3^- and Mg^{2+} followed by $Ca^{2+} > Si_{aq} > SO_4^{-2} > Cl^- > K^+ > NO_3^-$. Ionic concentrations at B6, beneath the center of the mud boil are generally higher than at B5, beneath the vegetated trough, with exception of NO_3^- and Si_{aq}. The deeper soil solutions (around 100 cm) are closer to the permafrost table and were most concentrated in SO_4^{2-}, followed by $Mg^{2+} > Ca^{2+} > HCO_3^- > Si_{aq} = K^+ = Cl^-$. The first samples collected from B2 in July 1999 show very low pHs of 4, higher Fe_{aq} (20–40 $\mu g\,L^{-1}$) and very high Al_{aq} (1–2 $mg\,L^{-1}$) concentration compared to later samples. A possible inorganic mechanism leading to such a low pH in natural water is dissolution of pyrite. Two possible overall redox reactions are given below (Langmuir, 1997, pp. 458):

$$FeS_2 + 7/2O_2 + H_2O \rightarrow Fe^{2+} + 2SO_4^{2-} + 2H^+ \quad (6)$$

$$FeS_2 + 14Fe^{3+} + 8H_2O \rightarrow 15Fe^{2+} + 2SO_4^{2-} + 16H^+ \quad (7)$$

This reaction needs electron acceptors that can either be provided by oxygen or by an abundance of Fe^{3+}. Although this reaction would explain both high sulphate concentrations and low pH, more details (e.g. redox potential) are required to reveal if oxidation and dissolution of pyrite is the reason for the low pH values. During excavation of this and another soil pit coal fragments were found and exploratory excavations for coal are located nearby. The low pH, occurrence of coal and enrichment in Fe all support dissolution of pyrite as a common cause. The low pH enhances chemical weathering and therefore contributes to the overall increase in solute concentration at depth.

The rapid decrease in σ_w when soils freeze (Figs. 6 and 7) is counter-intuitive, since an increase in concentration due to the exclusion of ions during freezing is expected. A first approach to model the change in solute composition and concentration of soil water at subfreezing temperatures can be performed with the geochemical equilibrium model FREZCHEM62 (Marion and Grant, 1994). This program is written to model changes in chemistry during stepwise freezing of a water solution and considers either continuous contact between solution and precipitated phase or fractional removal of precipitated phase from solution. It does not incorporate soil physical factors like mineral, organic or colloid surfaces that most likely contribute to changes in water chemistry. However, it allows estimation of the chemical development of a solution during freezing. Results of the modelling with FREZCHEM of solutions B1 and B6 collected at 1 and 0.6 m depth is shown in Fig. 8. Liquid water content rapidly decreases below subfreezing temperatures and at −5 °C only 0.006% of the total water content present before freezing is still unfrozen. During freezing salts of different composition precipitate from solution in the sequence: $CaSO_4 \cdot 2H_2O$, $MgCO_3$, $CaMg(CO_3)_2$, K_2SO_4, and $Na_2SO_4 \cdot 10H_2O$. The precipitation of these salts causes the changes in molar elemental ratios displayed in Fig. 8. The most striking difference between the soil solution with high SO_4^{2-} concentration (B1, B2) and high HCO_3^- concentration (B6) is in the change of Na/Cl ratios. While in the B1 soil solution the Na/Cl ratio constantly increases, it decreases in B6 due to the formation of KCl at −10 °C. Compared to TDR measurements, the calculated liquid water content based on water chemistry is much lower, a difference amounting to up to 9% by volume. An important part of liquid water in frozen soils exists as thin water films on particle surfaces (Ugolini and Anderson, 1973), and such water–surface interactions are not considered in FREZCHEM. If surface-bound water is not in contact with the solute-rich solution excluded from the forming ice, then the predicted precipitation of salts due to freezing would hold. Measurements of σ_w depend on a direct current pathway between electrodes (in this case, TDR sensor wave guides), so that isolated pockets of high concentration will not contribute to the measured bulk electric conductivity of the soil. Surface bound water, however, contributes to the measurement of σ_b (Guy–Chapman double layer theory).

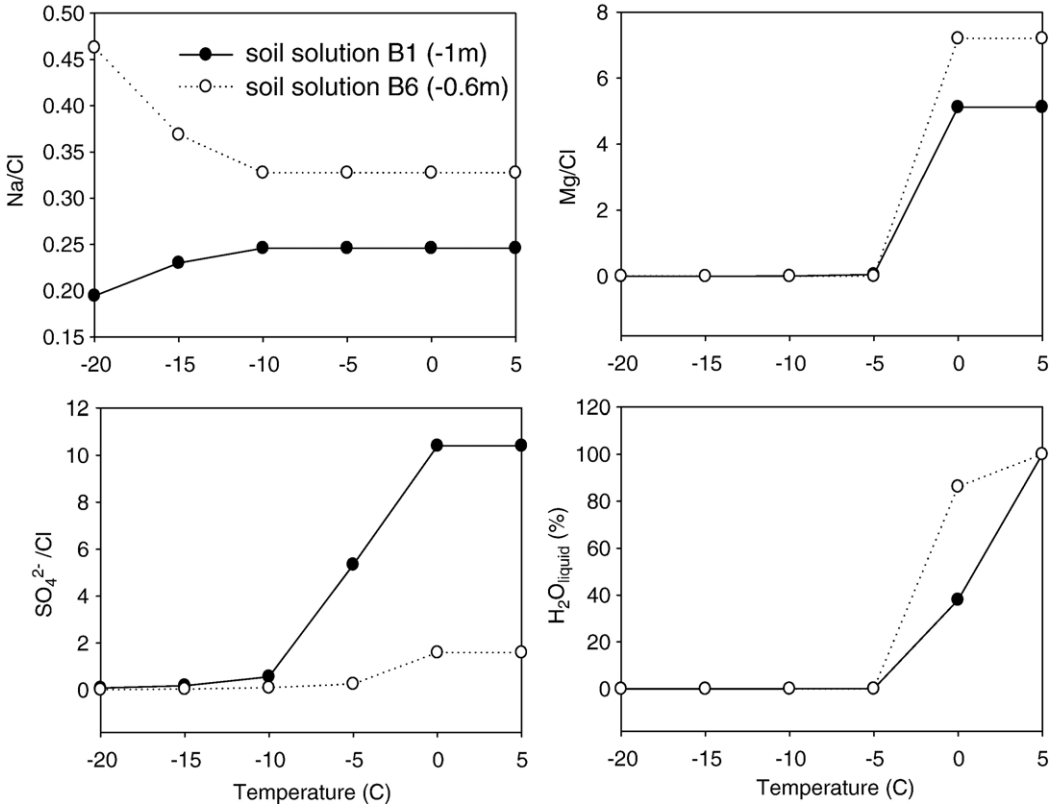

Fig. 8. Molar element ratios and liquid water concentration (%) modelled with FREZCHEM62 between +5 and −20 °C. The soil solutions are taken from suction cups B6 and B1. Changes in element ratios indicate formation of solid salt precipitates that remove specific elements from solution. Liquid water content refers to percent of liquid water of total amount of water that was present before freezing. At −20 °C liquid water content is less than one per mille.

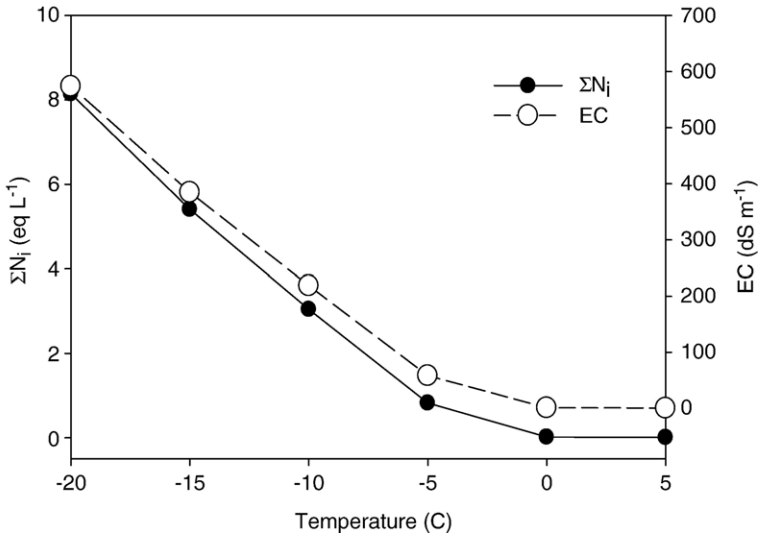

Fig. 9. Calculated total ion concentration in eq L^{-1} in remaining solution during freezing. EC is calculated from Eq. (8) using total ion activity (eq/L^{-1}) ($\sum a_i = \sum N_i \gamma_i$ where γ_i is the activity coefficient provided by FREZCHEM62) instead of ion concentration N_i.

To compare the modelled solution with measured conductivity, the electric conductivity is calculated following the approach of Reluy et al. (2004) relating electric conductivity (EC) to the equivalent concentration of ions in solution ($\sum N$). The relation between EC and $\sum N$ is given by:

$$EC = 10^{-6} u' F \sum_{i} N_i \tag{8}$$

where F is Faraday's constant ($Cmol^{-1}$), and u' is the concentration-weighted mean equivalent mobility:

$$u' = \frac{\sum_{i} N_i u_i}{\sum_{i} N_i} \tag{9}$$

where u_i is the limiting equivalent ionic mobility of ion i [mS cm^2 mol eq^{-1} C]. For calculation we used values of u_i from Reluy et al. (2004). Instead of normalities, N_i, we used the activities calculated with FREZCHEM for each ion and ion pair. The results of this calculation are shown in Fig. 9, indicating that the solution electric conductivity increases with increasing solute concentration from around 0.05 S m^{-1} to 60 S m^{-1}. The total concentration of ions in the remaining unfrozen solution increases by a factor of ~1000, whereas without precipitation of salts the concentration would increase by a factor of ~17000 at the final water content. Modelled changes to soil solution, in the absence of mineral–soil solution interactions, lead to a predicted increase in soil water electric conductivity of three orders of magnitude with freezing. The water electric conductivities in the thawed soil estimated for the solution analyzed here are of the same order of magnitude as those predicted by this model (e.g. for a measured solution electric conductivity of 0.038 S m^{-1}, we predict an electric conductivity of 0.050 S m^{-1}).

If the contribution of the clay particle surface conductivity to σ_b is significant, the isolation of clay particles by ice layers could be another reason for the reduction of σ_b. In that case σ_w in frozen soil might be underestimated by the values calculated from bulk electric conductivity measured with the TDR probes.

5. Discussion

5.1. Observed changes in soil water electric conductivity with time

Estimated soil water electric conductivity responds to freezing, thawing and summer rainfall events. Using the model of Boike and Roth (1997), we show that the largest annual increase and decrease are associated with thawing and freezing, respectively, of the soil. During thaw, for both soils under the boil and the vegetated trough, soil water electric conductivity at all depths decreases by up to 30% before the increase associated with thawing occurs. The thaw increase occurs simultaneously with the increase in liquid water content associated with the phase change of ice to water. We suggest that the initial decrease in electric conductivity indicates that the infiltration and refreezing of snow meltwater has diluted the available soil solution.

5.2. Increase in solute concentration with depth

Our data show that soil solutes within the mud boil are stratified horizontally throughout the year and that this stratification, with highest concentrations at the bottom of the profile, is dominant over any vertical stratification (organic versus mud). Lundin and Johnsson (1994) also find that σ_w increased with depth and percentage of fines in Swedish agricultural soils. Alekseev et al. (2003) and Kokelj and Burn (2003) also find the highest concentrations in the soil profile at the boundary between seasonally thawed soil and permafrost. Alekseev et al. (2003) conclude that permafrost landscapes in general accumulate solutes at the upper boundary of the permafrost, which acts as a geochemical barrier.

In addition to this depth stratification, we observe a slight increase in soil electric conductivity beneath the center of the mud boil. Depressions, as in our case the bowl-shaped region beneath the mud boil, have even higher concentrations of solutes. These subtle variations in concentration might be the initiator of irregularities in the permafrost table due to the depression of the freezing point and thus, the precursor of certain patterned ground, such as these non-sorted circles. Once a bowl-shaped depression of the permafrost table exists, cell-like circulation pattern within the active layer can be initiated (i.e. the equilibrium model after Mackay, 1980). However, Fig. 8 shows that the depression of the freezing point by solute exclusion from a freezing solution with the chemistry of extracted soil water is only sufficient to maintain less than 0.1 mL of water in the liquid state per liter of soil solution below −10 °C, implying that the effect of solute exclusion on the permafrost table depth are minimal compared to those of differences in surface cover and overlying soil thermal properties. Differential frost heave is more likely responsible for the formation of the mud boils as also stated by Van Vliet-Lanoë (1991). Walker et al. (2004, pp. 178) postulated that frost boils typical of coastal

areas pump solutes to the surface as a result of relatively high evaporation rates and that the salts thus deposited inhibit vegetation growth. In contrast to these findings, our data suggest that net accumulation of solutes occurs at the base of the active layer, with little difference between mud boil and adjacent vegetated regions. In both profiles, the highest values of σ_w occur at depth, whereas the lowest values are found in the upper coarser horizon.

The increase with depth probably results from one or both of two general processes. First, seasonal freezing may lead to a cumulative downward migration of solutes as a result of solute exclusion from the freezing soil water. This downward migration is ultimately limited by the presence of the permafrost table, which provides a natural boundary to downward percolation. Secondly, the fraction of finer material increases with depth at this site providing a higher surface area susceptible for chemical weathering.

5.3. Comparison to thermodynamically modelled freezing

The high temporal resolution of soil water electric conductivity data derived from TDR measurements permits qualitative identification of processes such as dilution (melting of pure ice) or concentration in frozen soil during snow ablation and water migration in the thawed soil. These are in congruence with the observed hydrologic and thermal dynamic. However, the absolute concentration values during the frozen period are much lower than expected if exclusion of solutes from the freezing soil solution occurs, despite the fact that thermodynamically modelled freezing indicates that several salts precipitate from soil solution during freezing. The time difference between the increase in water content and soil water electric conductivity during thawing might indicate kinetic delay of re-dissolution of these salt crystals. Furthermore, some of the precipitates, like carbonates and Ca-sulfates, may not re-dissolve completely. The higher amount of particulate inorganic carbon found at depth of mud boil may be a direct result of precipitation of fine carbonates combined with mechanical movement of fines to the bottom of the mud boil. The contribution of solute movement is unlikely since it would be against the concentration gradient.

The calculation of electric conductivity from salt concentration and salt composition strongly depends on ion mobility. However, values used for u_i have been determined for temperate solutions. Subfreezing temperatures and changes in the viscosity of water may decrease ion mobility and electric conductivity. Further experimental investigations are needed to determine mobilities of single ions and ion pairs at temperature below 0 °C. Furthermore, water bound to clay particle and ice surfaces may have lower solute concentrations than regions containing solutes excluded from freezing pore water, leading to lower overall measured salt concentration per unit volume of soil. Ostroumov et al. (2001) found that liquid drops on the surface of the forming ice were probably responsible for solute transport in frozen deposits close to the freezing front. The implication is that excluded solutes are restricted to small, unconnected domains within the soil that would not contribute to measured bulk soil electric conductivity.

5.4. Implications for cryoturbation

Walker et al. (2004) hypothesize that particles and dissolved organic material are carried downward at the margins of frost boils by soil movement and leaching, whereas organics accumulate in the thawed zone of the frost boil. At the center of the mud boil, upward migration of organics occurs. The high concentrations (>6%) of organic carbon in our mud boil (Fig. 2) support their hypothesis. The differences in thermal and hydrologic regime, thaw depth, and total nitrogen, organic carbon and total sulfur concentrations between mud and vegetated trough profiles create a physically different environment. This, in turn, affects the vegetation and possibly governs the mechanical forces that create the mud boils. Cryoturbation is the most effective process in moving organics and (weathered) minerals upwards from the bottom of the active layer, thus counteracting the downward fluxes. Cryoturbation is likely to change with a changing climate. On Svalbard, mean annual ground surface temperature currently increases at a rate of ~0.4 °C per decade (Isaksen et al., 2001).

6. Conclusion

The influence of mud boils on solute migration is small compared to the influence of the seasonal freeze–thaw cycle in the presence of permafrost. The soil solution electric conductivity increases with depth beneath a mud boil, irrespective of lateral position, but seasonal changes in conductivity between frozen and thawed soil are up to 5 times greater. TDR-determined bulk electric conductivity is a useful tool, since it permits high temporal resolution measurement of changes in soil electric conductivity, and thus a means of investigating solute dynamics. The deviation between TDR determined and thermodynamically modelled changes in soil solution chemistry identifies two future research goals: (i) a new model accounting for changes in phase geometry during freezing

and (ii) including the effects of soil surface physics in thermodynamic models of freezing.

Acknowledgements

We gratefully acknowledge financial support from the Deutsche Forschungsgemeinschaft (DFG), the European Union and a research grant awarded to Julia Boike by the Deutsche Akademie der Naturforscher Leopoldina. Essential logistic and technical support was provided by the German and the Norwegian Research Stations in Ny-Ålesund and by Christian Wille and Molo Stoof. Thanks to Antje Eulenburg for analyzing the water samples. Discussions with Hugh French during the 2nd Workshop Shifting Lands – New Insights Into Periglacial Geomorphology in France – motivated this contribution.

References

Alekseev, A., Alekseeva, T., Ostroumov, V., Siegert, C., Gradusov, B., 2003. Mineral transformation in permafrost-affected soils, North Kolyma Lowland, Russia. Soil Sci. Soc. Am. J. 67 (2), 596–605.

Boike, J., Roth, K., 1997. Time domain reflectometry as a field method for measuring water content and soil water electrical conductivity at a continuous permafrost site. Permafr. Periglac. Process. 8 (4), 359–370.

Boike, J., Roth, K., Ippisch, O., 2003. Seasonal snow cover on frozen ground: energy balance calculations of a permafrost site near Ny-Ålesund, Spitsbergen. Geophys. Res. 108 (D2), 8163. doi:10.1029/2001JD000939.

Heimovaara, T.J., Focke, A.G., Bouten, W., Verstraten, J.M., 1995. Assessing temporal variations in soil water composition with time domain reflectometry. Soil Sci. Soc. Am. J. 59, 689–698.

Isaksen, K., Holmlund, P., Sollid, J.L., Harris, C., 2001. Three deep alpine permafrost boreholes in Svalbard and Scandinavia. Permafr. Periglac. Process. 12, 13–25.

Kessler, M.A., Murray, A.B., Werner, B.T., Hallet, B., 2001. A model for sorted circles as self-organized patterns. J. Geophys. Res. 106 (B7), 13,287–13,306.

Kokelj, S.V., Burn, C.R., 2003. Ground ice and soluble cations in near-surface permafrost, Inuvik, Northwest Territories, Canada. Permafr. Periglac. Process. 14, 275–289.

Langmuir, D., 1997. Aqueous Environmental Geochemistry. Prentice-Hall, Upper Saddle River, New Jersey. 600 pp.

Lundin, L.-C., Johnsson, H., 1994. Ion dynamics of a freezing soil monitored in-situ by time domain reflectometry. Water Resour. Res. 30 (12), 3471–3478.

Mackay, J.R., 1980. The origin of hummocks, western Arctic coast. Can. J. Earth Sci. 17 (8), 966–1006.

Marion, G.M., Grant, S.A., 1994. FREZCHEM: A chemical-thermodynamic model for aqueous solutions at subzero temperatures. Hanover, NH, Cold Regions Research and Engineering Laboratory, U.S. Army Corps of Engineers.

Ostroumov, V., Hoover, R., Ostroumova, N., Van Vliet-Lanoe, B., Siegert, C., Sorokovikov, V., 2001. Redistribution of soluble components during ice segregation in freezing ground. Cold Reg. Sci. Technol. 32, 175–182.

Patterson, D.E., Smith, M.W., 1980. The use of time domain reflectometry for the measurement of unfrozen water content in frozen soils. Cold Reg. Sci. Technol. 3, 205–210.

Reluy, F.V., de Bécares, J.M., Hernandéz, R.D., Díaz, J.S., 2004. Development of an equation to relate electric conductivity to soil and water salinity in a Mediterranean agricultural environment. Aust. J. Soil Res. 42, 381–388.

Romanovskii, N.N., 1996. Periglacialial processes as geoindicators in the cryolithozone. In: Berger, A.R., Iams, W.J. (Eds.), Geoindicators: Assessing Rapid Environmental Changes in Earth Systems. Rotterdam, Balkema. 47–68 pp.

Roth, K., Boike, J., 2001. Quantifying the thermal dynamics of a permafrost site near Ny-Ålesund, Svalbard. Water Resour. Res. 37 (12), 2901–2914. doi:10.1029/2000WR000163.

Roth, K., Schulin, R., Flühler, H., Attinger, W., 1990. Calibration of time domain reflectometry for water content measurement using a composite dielectric approach. Water Resour. Res. 26 (10), 2267–2273.

Stähli, M., Stadler, D., 1997. Measurement of water and solute dynamics in freezing soil columns with time domain reflectometry. J. Hydrol. 195, 352–369.

Topp, G.C., Davis, J.L., Annan, A.P., 1980. Electromagnetic determination of soil water content: measurements in coaxial transmission lines. Water Resour. Res. 3 (16), 574–582.

Ugolini, F.C., Anderson, D.M., 1973. Ionic migration and weathering in frozen Antarctic soil. Soil Sci. 115, 461–470.

van Loon, W.K.P., Perfect, P.H., Groenevelt, P.H., Kay, B.D., 1991. Application of dispersion theory to time domain reflectometry in soils. Transp. Porous Media 6, 391–406.

Van Vliet-Lanoë, B., 1991. Differential frost heave, load casting and convection: converging mechanism; a discussion of the origin of cryoturbations. Permafr. Periglac. Process. 2, 123–139.

Walker, D.A., Epstein, H.E., Gould, W.A., Kelley, A.M., Kade, A.N., Knudson, J.A., Krantz, W.B., Michaelson, G., Peterson, R.A., Ping, C.-L., Raynolds, M.K., Romanovsky, V.E., Shur, Y., 2004. Frost-boil ecosystems: complex interactions between landforms, soils, vegetation and climate. Permafr. Periglac. Process. 15, 171–188.

Washburn, A.L., 1956. Classification of patterned ground and review of suggested origins. Bull. Geol. Soc. Am. 67, 823–866.

Washburn, A., 1979. Geocryology — a survey of periglacial processes and environments. Edward Arnold, London. 406 pp.

Chapter 3.2

Roth, K. and **Boike, J.** (2001): Quantifying the thermal dynamics of a permafrost site near Ny-Ålesund, Svalbard, *Water Resources Research* 37 (12), 2901-2914.

WATER RESOURCES RESEARCH, VOL. 37, NO. 12, PAGES 2901–2914, DECEMBER 2001

Quantifying the thermal dynamics of a permafrost site near Ny-Ålesund, Svalbard

Kurt Roth

Institute of Environmental Physics, University of Heidelberg, Heidelberg, Germany

Julia Boike[1]

Alfred-Wegener-Institute for Polar and Marine Research, Potsdam, Germany

Abstract. The dynamics of permafrost soils is manifest in the soil temperature which can be measured with high accuracy and high temporal resolution. Using continuous data over a period of 778 days from a mineral hummock field at the Bayelva site, Svalbard, we deduce and quantify the processes which constitute the dynamics. In particular, conductive heat flux, generation of heat from phase transitions, and migration of water vapor are analyzed. Support for the interpretation of the data comes from high-resolution time domain reflectometry measurements of the liquid water content.

1. Introduction

Permafrost underlies about one fifth of global land areas [*French*, 1996] and hence constitutes an important terrestrial system. Models indicate that high-latitude regions are affected most strongly by a change of the climate, and warming has actually been reported in several studies [*Overpeck et al*., 1997; *Huang et al*., 2000; *Serreze et al*., 2000]. Quantitative understanding of the processes underlying the thermal and hydraulic dynamics of permafrost soils is thus paramount to anticipate consequences of a changing atmospheric forcing as well as to improve the parameterization of the soil-atmosphere interaction in climate models.

The major stages for the seasonal thermal dynamics of the active layer at a permafrost site are a winter cold period when the soil is completely frozen, a warming period when snow melts and possibly infiltrates into the still frozen soil, a downward moving thaw front during the summer thaw period, and an isothermal plateau during the fall freeze back.

Conduction is widely accepted to be the dominant mechanism of heat transfer in soils. Other nonconductive heat transfer mechanisms associated with the convection of water, either in the liquid or in the vapor phase, are possible with appropriate gradients. The significance of conductive and convective heat transfer for the thermal dynamic of permafrost and active layer has been discussed in numerous, and often controversial, publications. Conduction is assumed to be the dominant heat transfer process during the winter cold period, although the possibility of convection in frozen soil has been reported in field and lab experiments [*Parmuzina*, 1978; *Chen and Chamberlain*, 1988]. When the snow cover becomes isothermal and snowmelt starts during the warming period, the soil rapidly warms at all depths, presumably because of the infiltration and refreezing of snowmelt water and of migrating vapor into the frozen soil. Most studies agree that nonconductive heat transfer processes must be responsible for the rapid warming of the soil [*Putkonen*, 1998; *Hinkel and Outcalt*, 1994]. Conversion of latent heat is thought to be most important during the summer when moisture evaporates from the surface and the active layer thaws. Evaporation consumes 25–50% of the total incoming energy at a Siberian study site [*Boike et al*., 1998] and 30–65% in northern Alaska [*Kane et al*., 1990]. According to *Outcalt et al*. [1998], evaporative cooling at the surface of the active layer was responsible for the deviation between observed and modeled soil temperatures of the active layer and upper permafrost. Thawing of the active layer is another important sink for thermal energy. It consumes up to 40% of the total net radiation at the Siberian site of *Boike et al*. [1998]. Generally, a high percentage of the total heat flux into the ground (between 70 and 100%) is converted into latent heat [*Rouse*, 1984; *Boike et al*., 1998].

Besides conduction of heat, transport of thermal energy by convection of water, either in the liquid or vapor phase, has been discussed. *Hinkel et al*. [1993] identified infiltration of summer precipitation as an effective method to transfer heat to the base of the active layer, especially in drained, organic soils. Pore water convection during the summer thaw period, driven by the density inversion of water, has been proposed as the initiator for the formation of sorted circles [*Krantz*, 1990; *Ray et al*., 1983], but *Hallet* [1990] argued that this process is unlikely and that it has not been observed in finer-grained sediments typically found in patterned ground. *Putkonen* [1998] calculated a Peclet number much smaller than 1 for this site and concluded that advection of heat due to water motion is negligible.

When net radiation decreases during the fall, the soil is cooled to a practically isothermal condition, the so-called zero curtain at 0°C. The large amount of latent heat which must be removed from the profile through an almost isothermal soil stabilizes soil temperatures at 0°C for a prolonged time. *Hinkel and Outcalt* [1993, 1994] suggested that internal distillation driven by osmotic gradients transfer heat across this isothermal zone. In contrast, *Romanovsky and Osterkamp* [2000] accurately predicted soil temperatures during the freeze back using a conductive heat exchange model by including effects of unfrozen water and therefore excluding moisture migrating as a

[1]On leave at Water and Environmental Research Center, University of Alaska, Fairbanks, Alaska, USA.

Copyright 2001 by the American Geophysical Union.

Paper number 2000WR000163.
0043-1397/01/2000WR000163$09.00

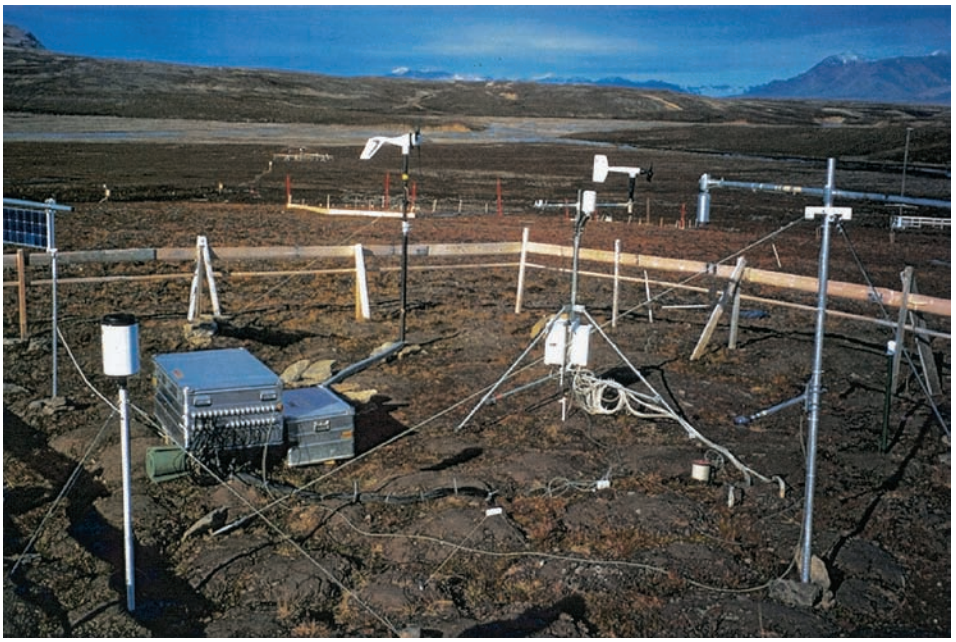

Plate 1. View of the experimental site with Bayelva river in the background. Instruments visible are, from left to right, solar power panel, rain gauge, boxes with electronics and batteries, wind generator, weather station, snow height sensor, and net radiation sensor.

transport mechanism. *Putkonen* [1998] estimated that the maximal possible vapor and latent heat flux under given soil thermal properties was >2 orders of magnitude smaller than conductive heat transport, hence being insignificant. The eventual progress of the frost front is governed by the spatial heterogeneity of the soil [*Boike et al*., 1998].

Experimental identification and quantification of heat transfer processes in permafrost soils is hampered by the lack of accurate methods for measuring relevant state variables of the system, for example the phase density of ice or water vapor, and even more so by the lack of sufficiently accurate instruments for measuring fluxes of thermal energy and of water. We are thus left with deducing process hypotheses based on the internal consistency of incomplete data sets. This situation is not alleviated significantly by numerical simulations which still suffer from incomplete representation of physical processes, such as the separation of the water phase upon freezing of the porous medium, and by typically inaccurate parameterizations of material properties, such as the conductivity for liquid water and vapor. As a consequence, detailed case studies are required to gain the type of knowledge prerequisite for assessing the impact of a changing atmospheric forcing on permafrost soils as well as the ensuing feedback on the atmosphere.

Apart from the relevance outlined so far, the dynamics of permafrost soils is of inherent scientific interest because it encompasses highly nonlinear and strongly coupled processes which lead to a complex phenomenology. Understanding such a system quantitatively will not only improve conceptualizations of terrestrial permafrost and its role in a dynamic environment, it is also pertinent to discussions about the environments of other planets, for example, to recent questions about water on Mars [*Costard*, 1988; *Zuber et al*., 1998].

In this paper we demonstrate an approach for exploring the thermal dynamics of a continuous permafrost site using a time series of soil temperature. Our goals are (1) to examine the soil thermal processes using bulk thermal properties and (2) to quantitatively examine soil heat transfer processes through the annual cycles using high-resolution soil temperature and moisture data.

2. Site Description and Measured Data

The Bayelva catchment is located ~3 km west of Ny-Ålesund, Svalbard, at (78°55′N, 11°50′E). Continuous permafrost in this region underlies coastal areas to depths of ~100 m and mountainous areas to depths >500 m [*Liestøl*, 1977]. The North Atlantic Current warms this area to an average air temperature ~5°C in July and −13°C in January, and it provides ~400 mm of annual precipitation that mostly falls as snow between September and May [*Førland et al*., 1997].

Our study site is located some 30 m above mean sea level, on top of a small hill covered with unsorted circles (Plate 1). The bare inner part of the soil circle is ~1 m in diameter and is surrounded by vegetated borders consisting of a mixture of low vascular plants, mosses, and lichens. We instrumented one of these circles in August 1998 to automatically monitor hourly temperature and half-daily liquid water content. Soil temperatures are recorded using thermistors calibrated at 0°C with a precision of 0.00024°C at 0°C and an absolute error less than ±0.02°C over the temperature range ±30°C. Liquid water content is calculated from time domain reflectometry (TDR) measurements using the semiempirical mixing model of *Roth et al*. [1990] which was augmented by including ice as the fourth phase. The accuracy of the measurement of volumetric water content by TDR is estimated to be between 0.02 and 0.05, while its precision is better than 0.005. A weather station measuring solar radiation, net radiation, air temperature, snow depth, and rainfall stands within 5 m of the instrumented soil site. Field accuracy of the net radiation measurements is estimated to range between 10 and 20% of the measured value.

During installation, soil samples were taken for the analysis of physical properties. The soil consists of silty clay with inter-

spersed stones. Clay content by weight increases from 20% near the surface to 80% at 0.8 m depth with a corresponding decrease of silt and sand content. The average soil bulk density obtained from six samples is 1.70×10^3 kg m^{-3} with porosity ranging from 0.36 to 0.5.

In this paper we are using data from temperature sensors and TDR probes installed in the circle's center at depths 0.065, 0.245, 0.405, 0.625, 0.765, 0.995, 1.125, and 1.250 m below the surface (Plate 2). Hourly data collection started in September 1998. The data spans over 2 years, from September 14, 1998 (day 257), to October 31, 2000 (day 1035), which results in measured values for ~18,500 points in time. In order to reduce the amount of data we used the linear hat filter

$$\bar{f}(t_k) := \sum_{i=-n}^{n} w(i)\, f(t_{k+i}) \Bigg/ \sum_{i=-n}^{n} w(i) \quad w(i) := 1 - |i/n|, \qquad (1)$$

where f is the quantity to be averaged, w is the weight function, and $\bar{f}$ is the averaged value. For our data we chose $n = 12$, which results in a temporal resolution of 12 hours. We remark that the final results are not affected by the order of filtering and analysis, which will be described in section 4, since both are linear. We thus applied the filter prior to the analysis.

Through both winters, the snow cover built up in two stages, first to a height of ~0.3 m then to ~0.7 m. They differ significantly in the duration of these two stages, however. During the first winter, the thin snow cover lasted some 50 days, and the thick one lasted for some 130 days. During the second winter, the lengths of the periods were reversed: almost 190 days for the thin and only 70 days for the thick cover. Since average air temperature and net radiation during both winters were comparable, the thinner snow cover caused a considerably stronger cooling of the soil. The minimum soil temperatures at 0.5 m depth were below −15°C.

During the first year, days 264–619, the average net radiative input was +13.4 W m^{-2}, while during the second year, days 620–986, it was −2.4 W m^{-2}. Mean air temperatures were comparable for these periods: −4.4°C and −5.6°C, respectively. Together with the longer duration of the snow-free ground in the first summer this atmospheric forcing led to a deeper and prolonged thawing of the active layer.

Soil temperatures exhibit the characteristic behavior of the freeze-thaw cycle that has already been described for other sites, for example, by *Boike et al.* [1998]. The active layer thaws gradually during the summer, at this study site to depths between 0.9 and 1.1 m. Freeze back occurs in succinctly different steps. First, temperatures drop to 0°C throughout the thawed zone, around days 628 and 990, respectively, at this site, which is often referred to as the zero curtain [*Outcalt et al.*, 1990]. This phenomenon practically eliminates conductive heat transfer because of the vanishing thermal gradient. In the second step a wide, almost isothermal plateau with temperatures between 0 and −2°C develops, which becomes slowly eroded from above as well as from below. The isothermal regime ends at a cold front that encroaches from the surface at a speed that is comparable to that of the thawing front in summer. This front is most prominent at the onset of the second winter between days 690 and 720. Afterward, temperatures drop rapidly.

As expected, liquid water content is highest near the bottom of the thawed zone where the frozen soil and the ice form an impermeable layer. Water contents during the second summer are much higher than during the first one because of significantly higher precipitation. Looking at the transition from the thawed to the frozen state, we notice that passing the 0°C line does not appear to noticeably affect the liquid water content. Instead, it decreases very slowly across the isothermal subfreezing plateau and only drops to small values with the passing of the winter's cold front. Liquid water exists in this profile even with temperatures below −15°C. This has also been reported for other sites [e.g., *Farouki*, 1981; *Romanovsky and Osterkamp*, 2000].

3. Theory

Conservation of thermal energy in a one-dimensional system may be formulated as

$$\frac{\partial}{\partial t}\left[c_h T\right] + \frac{\partial}{\partial z} j_h = r_h, \qquad (2)$$

where c_h is heat capacity, T is temperature, z is depth, j_h is heat flux, and r_h is the rate of heat production. For purely conductive transport of heat, to which we will restrict our analysis, the flux is described by Fourier's law

$$j_h = -k_h \frac{\partial}{\partial z} T, \qquad (3)$$

where k_h is the bulk thermal conductivity. For the most simple case of a stationary homogeneous soil these equations may be combined to obtain the diffusion equation

$$\frac{\partial}{\partial t} T - d_h \frac{\partial^2}{\partial z^2} T = \frac{r_h}{c_h}, \qquad (4)$$

where

$$d_h = \frac{k_h}{c_h} \qquad (5)$$

is the thermal diffusivity. Analytical solutions of (4) are available for a wide range of flow geometries and boundary conditions [*Carslaw and Jaeger*, 1990; *Crank*, 1975].

The diffusion equation (4) is based on the tacit assumption that the medium considered is a single-phase system, such as a solid, which is described in the continuum limit. The values of the material properties c_h and d_h may then be calculated from first principles. For the case of a multiphase system like a permafrost soil, (4) is only retrieved after averaging over a sufficiently large region [e.g., *Hassanizadeh and Gray*, 1979], and the material properties become dependent on the volume fractions of the constituting phases as well as on their geometry. The heat capacity is obtained easily by summing the contributions of the phases, i.e.,

$$c_h = \sum_k \theta_k \rho_k c_{h_k}, \qquad (6)$$

where θ_k, ρ_k, and c_{h_k} are volume fraction, mass density, and heat capacity per unit mass, respectively, of phase k. In contrast, the thermal diffusivity d_h depends on the geometry of the phases in a complicated way. It is often parameterized using the model of *Philip and de Vries* [1957].

In this work we assume the structure of the soil to be such that averaging the pore-scale processes will, indeed, produce a diffusion equation for the dynamics of heat transport, and we will consider the material properties c_h and d_h as bulk properties.

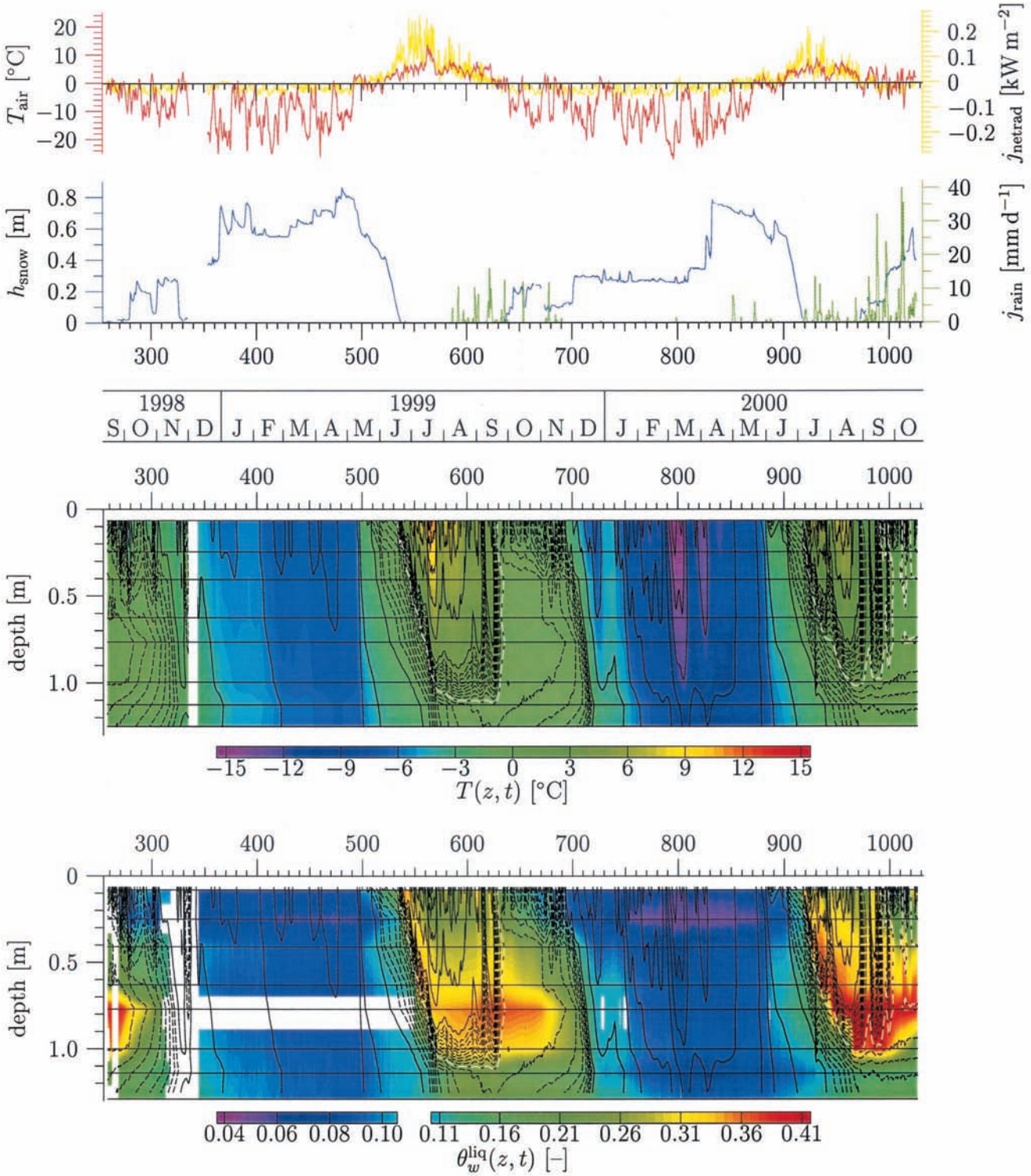

Plate 2. (top) Measured meteorological variables, (middle) soil temperature $T(z, t)$, and (bottom) volumetric water content $\theta_w^{liq}(z, t)$ after averaging over ± 12 hours with the linear hat filter (1). Rainfall data are only available after day 578. Contour lines of soil temperature are drawn with increments of 2°C (solid line) and 0.2°C (dashed line), respectively, around 0°C (black-and-white-dashed lines). These lines are repeated in the plots of θ_w^{liq} and all subsequent contour plots to facilitate cross-referencing. Time is given in Julian days starting January 1, 1998, as well as by month and year. Open areas indicate missing data, and horizontal black lines indicate the positions of the probes.

For the case of negligible heat production, $r_h = 0$, the solution of (4) in a semi-infinite medium with initial temperature $T = 0$ and surface temperature $T(0, t)$ is given by the convolution integral (see *Carslaw and Jaeger* [1990, chapter II, section 2.5] or *Jury and Roth* [1990, equation (2.51)])

$$T(z, t) = \int_0^t T(0, \tau) f_T(t - \tau, z)\, d\tau \tag{7}$$

with the kernel (transfer function)

$$f_T(t, z) = \frac{z}{2[\pi d_h t^3]^{1/2}} \exp\left(-\frac{z^2}{4 d_h t}\right). \tag{8}$$

Under the premises of a medium with uniform thermal properties and of a purely conductive heat transport with negligible heat production, (8) allows us to project temperatures measured at the soil surface to any depth.

Obviously, the thermal dynamics of permafrost soils cannot be understood from conductive heat transport alone. Further dominating processes are the transitions of water between the solid, liquid, and vapor phase and the convective transport of heat either in the liquid or in the vapor phase. In (2) all the heat-producing processes are lumped into r_h. To quantify them from temperature measurements, we integrate (2) over the small element $[z_i, z_{i+1}] \times [t^j, t^{j+1}]$, which will eventually be determined by the spatial and temporal discretization of the data. Assuming c_h and d_h are constant, we obtain with (3) and (5)

$$\int_{t^j}^{t^{j+1}} \int_{z_i}^{z_{i+1}} r_h(z, t)\, dz\, dt = c_h \left[\int_{z_i}^{z_{i+1}} T(z, t^{j+1}) - T(z, t^j)\, dz - d_h \int_{t^j}^{t^{j+1}} T'(z_{i+1}, t) - T'(z_i, t)\, dt \right], \tag{9}$$

where T' denotes the derivative of T with respect to z. This integral may be evaluated approximately from measured temperature data using the trapezoidal rule for integration and central finite differences for the derivative. It represents the heat produced in the depth interval $[z_i, z_{i+1}]$ during the time interval $[t^j, t^{j+1}]$. We notice that c_h and d_h affect the estimated heat production rate in different ways in that c_h is a multiplication factor, while d_h determines the relative weights of temperature changes and heat fluxes. Uncertainties in the value of c_h thus only translate into an uncertain magnitude of $r_h(z, t)$, while uncertainties of d_h may change its entire form.

4. Analysis

In this section we first look at the soil freezing characteristic, which is of utmost importance for understanding the dynamics of freezing soils. Then, postulating uniform thermal properties for the soil, we estimate values for the constant parameters c_h and d_h. The value for c_h is obtained from (6), the one for d_h is obtained from fitting projections of measured surface temperatures to temperatures measured at the corresponding depths. We verify a posteriori that the assumption of uniform thermal properties is justified for this site. Finally, the estimated values are used together with the high-resolution temperature measurements to calculate the rate of heat production. Relating the heat production to corresponding changes in liquid water content and, in turn, comparing them with the high-resolution TDR data allows for an independent verification.

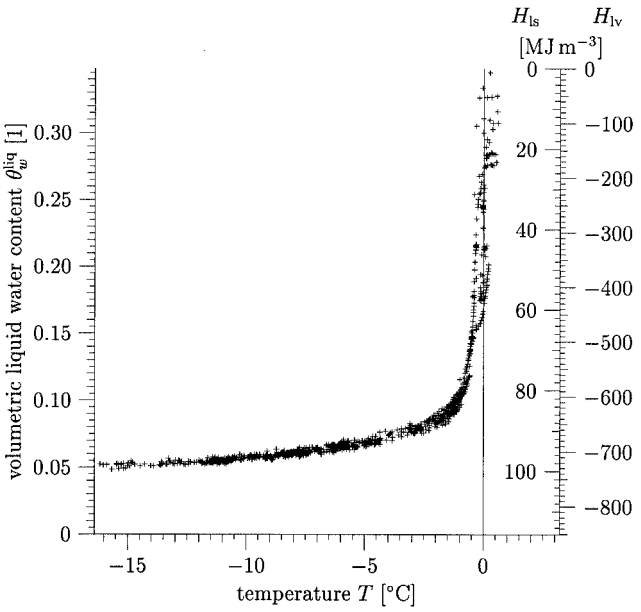

Figure 1. Empirical soil freezing characteristic obtained from plotting measured values of liquid water content versus temperature for the probes at 0.245 m depth. The axes on the right indicate the latent heat associated with the change of θ_w^{liq} if the excess water freezes (H_{sl}) or if it evaporates (H_{sv}). Notice that the origin of these axes is irrelevant, only differences matter.

4.1. Soil Freezing Characteristic

In a pure liquid, phase change occurs at a well-defined temperature. In contrast, a mixture of soil and water typically shows a rather smooth transition which is described by the soil freezing characteristic $\theta_w^{liq}(T)$ [*Yershov*, 1998]. Figure 1 shows the empirical soil freezing characteristic for the Bayelva site at a 0.245-m depth. For temperatures below −0.5°C, $\theta_w^{liq}(T)$ is a rather well-defined function, and, as a consequence, liquid water content may be expressed in terms of temperature. For T between −0.5 and 0°C, θ_w^{liq} does not only depend on T but also on the total water content. This may be understood as resulting from thermodynamic nonequilibrium which becomes stronger with increasing liquid water content because it takes more time to move the correspondingly larger amounts of latent heat. The data at other depths exhibit the same qualitative behavior with small vertical offsets.

It is worth noting that the measurements indicate a volume fraction of ~0.05 for liquid water at −15°C, which is comparable to the accuracy of the data. However, we recall the high clay content at this site and the fact that such high unfrozen water contents are generally encountered in fine-textured soils [*Farouki*, 1981] as well as in other porous materials [*Morishige and Kawano*, 1999]. In any case, for the present analysis a constant offset of the measurements, as it would most probably arise from using an inaccurate mixing model for inverting the TDR data, is immaterial since only differences of water contents are used.

4.2. Bulk Thermal Properties

On the basis of measured soil properties we estimate volume fractions $\{\theta_s, \theta_w, \theta_i\} = \{0.6, 0.05, 0.3\}$ for a frozen soil. Together with densities $\{\rho_s, \rho_w, \rho_i\} = \{2.65, 1.0, 0.91\} \times 10^3$ kg m^{-3} and specific heat capacities $\{c_{h_s}, c_{h_w}, c_{h_i}\} =$

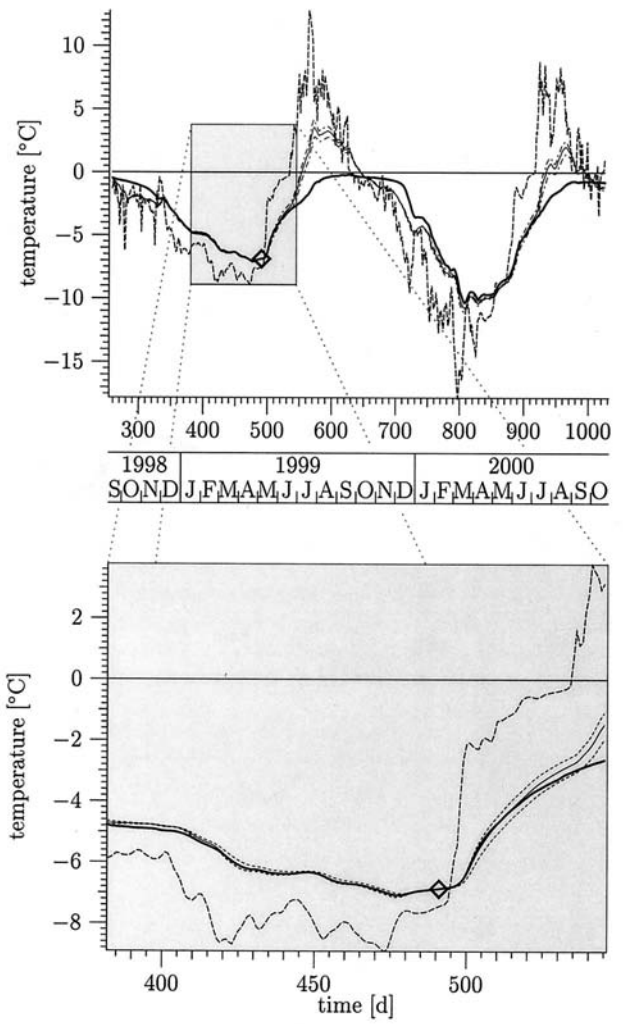

Figure 2. Measured temperatures at depths of 0.065 m (dashed line) and 1.25 m (thick solid line) together with projections of 0.065 m temperature to 1.25 m depth (thin solid line) using (7) and (8) with $d_h = 8 \times 10^{-7}$ m^2 s^{-1}. The dashed-dotted lines are projections with d_h changed by ±20%. Projected temperatures are matched to a measurement at the time indicated by the diamond. The top graph shows the entire data set; the bottom graph is the enlarged section outlined in the top graph.

$\{0.733, 4.22, 2.11\} \times 10^3$ J kg^{-1} K^{-1} we obtain with (6) the estimate $c_h^{\text{frozen}} = 2.0 \times 10^6$ J m^{-3} K^{-1} for the bulk volumetric heat capacity of the frozen soil. For the thawed soil with $\{\theta_s, \theta_w, \theta_i\} = \{0.6, 0.3, 0.0\}$ we similarly obtain $c_h^{\text{thawed}} = 2.4 \times 10^6$ J m^{-3} K^{-1}. In these calculations, we neglected the contribution of soil air because of its very low mass density. Hereinafter we will use the average value $c_h = (2.2 \pm 0.2) \times 10^6$ J m^{-3} K^{-1}.

As shown by (7) and (8), for pure heat conduction the temperature at depth z depends only on the temperature history of the soil surface and on the thermal diffusivity d_h. To estimate d_h, we choose a time interval during which nonconductive processes are presumably negligible. The surface soil temperature is approximated by the values measured by the topmost probe at a depth of 0.065 m. (Notice that because of snow cover and boundary effects this is a much better choice than the air temperature recorded at a 2-m height at the weather station.) The value of d_h is then adjusted such that the temperature projected to a depth of 1.25 m, the location of the deepest probe, is in optimal agreement with the actual measurements (Figure 2). To do this, we can adjust two parameters: the thermal diffusivity d_h and a constant temperature shift. The constant shift accounts for the initial condition that is different from $T = 0$°C and for nonconductive processes in the time between $t = 0$, the start of the measurements, and the time when the profile was completely frozen. We chose a time with a sufficiently low temperature as a matching point (diamond in Figure 4). As is apparent from the graph, the value of the essential free parameter d_h is not sensitive to the choice of this point as long as the temperature is sufficiently low. It could have been chosen anywhere between $t = 400$ days and $t = 500$ days. Setting $d_h = 8 \times 10^{-7}$ m^2 s^{-1} gives an excellent agreement for the time interval where temperatures are significantly below 0°C and most of the soil water is frozen. This compares favorably with values calculated by *Yershov* [1998, p. 284] which for frozen silty clay loess are in the range 5.5×10^{-7}–8×10^{-7} m^2 s^{-1}.

Obviously, this method cannot be used to project temperatures across a thawing or freezing front. Consequently, values calculated for the thawed period deviate considerably from the measurements. It is interesting, however, that the same projection without any further adjustments is able to describe reasonably well the temperatures for the following frozen period, as is shown in the top graph of Figure 4.

Estimating d_h for the nonfrozen soil is impaired (1) by the short time intervals and shallow depths where the soil is actually thawed and (2) by the heat consumed by evaporation from the soil surface. However, at least for short periods, the value $d_h = 8 \times 10^{-7}$ m^2 s^{-1} again leads to excellent agreement between projected and measured temperatures. This is illustrated in Plate 3, which displays the difference between measured and projected temperatures for the entire soil profile during periods where heat conduction is the dominating process. Apparently, effective heat conduction at this site may be described by a constant thermal diffusivity, at least for periods and regions without strong phase transitions. This gives a posteriori justification to our initial assumption of a uniform medium. Although we cannot say anything about bulk thermal parameters when the transitions between phases dominate the thermal regime, we presume that the value of d_h is not affected significantly. Thus we will hereinafter use $d_h = 8 \times 10^{-7}$ m^2 s^{-1} and roughly estimate its uncertainty from Figure 4 as 20%.

Figure 3 shows the kernel (8) for $d_h = 8 \times 10^{-7}$ m^2 s^{-1}. It illustrates that fluctuations of the surface temperature can travel rapidly through the soil: The maximum value of f_T at 0.6 m depth is reached after <1 day, and at 1.2 m it is reached after merely 3.5 days. On the other hand, the time over which the surface forcing is integrated increases rapidly with depth, as is apparent from the very long tail.

4.3. Conductive Heat Flux

The mean value theorem applied to (3) for the conductive heat flux through some depth $z_{i+1/2}$ with $z_i < z_{i+1/2} < z_{i+1}$ yields

$$j_h(t, z_{i+1/2}) = -k_h \frac{T(t, z_{i+1}) - T(t, z_i)}{z_{i+1} - z_i}. \qquad (10)$$

Choosing $z_{i+1/2} = [z_i + z_{i+1}]/2$, this becomes the traditional finite difference approximation (Plate 4). The value of

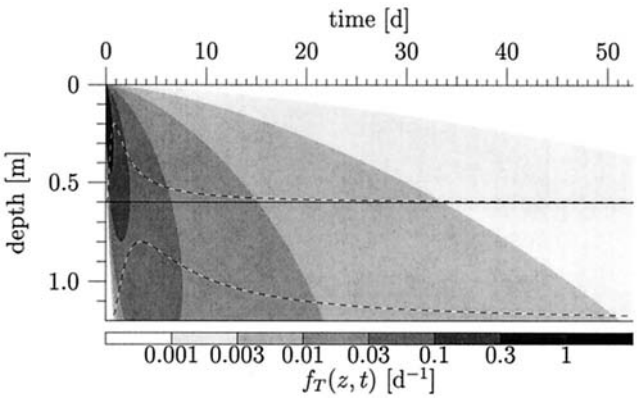

Figure 3. Transfer function $f_T(z, t)$, the normalized response of soil temperature to a narrow impulse perturbation at the surface, defined in (8) for $d_h = 8 \times 10^{-7}$ m^2 s^{-1}. The two dashed lines represent cuts of $f_T(z, t)$ for depths of 0.6 and 1.2 m.

$k_h = c_h d_h$ is obtained from the estimates of c_h and d_h as 1.7 W m^{-1} K^{-1} with a relative error of 30%. This again compares favorably with the results of *Yershov* [1998], who gives values of 1.2–1.6 W m^{-1} K^{-1} for a frozen silty clay loess. Compared with the uncertainty of k_h, the errors of the temperature measurements and their locations are negligible. We notice that the uncertainty of k_h affects the magnitude of the estimate of j_h but not its form. In contrast, the choice $z_{i+1/2} = [z_i + z_{i+1}]/2$ does not affect the magnitude, but it leads to a local distortion of the form in that the position where (10) applies in reality shifts between z_i and z_{i+1} depending on the magnitude and direction of j_h.

4.4. Production of Latent Heat

We define the mean production of latent heat in the element $[z_i, z_{i+1}] \times [t^j, t^{j+1}]$, where z_i and z_{i+1} are the depths of adjacent temperature probes and t^j and t^{j+1} are successive measurement times, by

$$\bar{r}^j_{h_i} = \frac{1}{[t^{j+1} - t^j][z_{i+1} - z_i]} \int_{t^j}^{t^{j+1}} \int_{z_i}^{z_{i+1}} r_h(z, t)\, dz\, dt. \qquad (11)$$

The integral is estimated using (9) with the spatial derivative T' approximated by finite differences. The value of $\bar{r}^j_{h_i}$ is assigned to the center of the element. Estimating $\bar{r}_h$ for the depth interval $[z_i, z_{i+1}]$ thus requires temperature measurements at the four depths of z_{i-1}, z_i, z_{i+1}, and z_{i+2}. Plate 5 shows $\bar{r}_h$ for two choices of the parameters c_h and d_h, namely for the upper and lower limits of their respective uncertainty band. To facilitate the later discussion, $\bar{r}_h$ is also expressed as the equivalent rate $\bar{r}_w$ of water undergoing phase change, which we define as

$$\bar{r}^{\alpha\beta}_w := \frac{\bar{r}_h}{L_{\alpha\beta}}, \qquad (12)$$

where $L_{\alpha\beta}$ is the enthalpy of the transition from phase α to phase β. Values used are $L_{sl} = 0.333$ MJ kg^{-1}, $L_{lv} = 2.45$ MJ kg^{-1}, and $L_{sv} = 2.78$ MJ kg^{-1}, where s, l, and v stands for solid, liquid, and vapor, respectively.

4.5. Importance of Latent Heat and Conduction

We consider stationary solutions of (2) in a uniform soil layer with constant r_h for the case where the boundaries are maintained at the same constant temperature. With the layer extending between $-\ell/2$ and $+\ell/2$, where ℓ is a characteristic length, we obtain $j_h(z) = r_h z$, where we have set the integration constant to 0. For a stationary situation the heat flux thus varies proportionally to r_h in each uniform layer. On this basis we define the dimensionless number $R := r_h \ell / j_h$. We recognize that R is the ratio between the change of heat flux over the distance ℓ resulting from r_h and the total conductive heat flux. Hence we use R as a measure for the relative contributions of latent heat and conductive flux to the thermal dynamics. Plate 6 shows the estimate

$$R^j_i := \frac{\bar{r}^j_{h_i} \ell}{\bar{j}^j_{h_i}}, \qquad (13)$$

where $\bar{r}_h$ is defined in (11); ℓ is taken from Figure 8 as 0.4 m, the typical width of the layer where latent heat is consumed in the cold period; and $\bar{j}^j_{h_i}$ is the average heat flux over the time interval $[t^j, t^{j+1}]$.

5. Discussion

The thermal and the hydraulic dynamics of a permafrost soil's active layer are strongly coupled and run through characteristically different stages during the annual freeze-thaw cycle. The aim of the following discussion is (1) to decipher and to quantify the contributing processes from temperature measurements and (2) to corroborate the findings with measurements of the liquid water content.

At this site we may distinguish four periods in the phenomenology of the thermal dynamics: (1) the "cold period" between the cold front and the transition to positive (incoming) heat fluxes, which approximately coincides with the onset of snow melt, (2) the "warming period" between the transition to positive heat fluxes and the thawing front, (3) the "thawed period" between the thawing front and the zero curtain, and (4) the "isothermal plateau" between the zero curtain and the cold front. Each has its characteristic dynamics which has already been described by others in a qualitative manner [e.g., *Hinkel and Outcalt*, 1994, 1995; *Putkonen*, 1998]. In sections 5.1–5.5 we consider these periods individually and quantify the relevant processes. As the basis we use Plate 2 for measured temperatures and liquid water contents, Plate 4 for the conductive heat flux and for the thermal gradient which is proportional to the flux, and Plate 5 for the production of heat.

5.1. Cold Period

The two cold periods covered by the data are roughly between days 340 and 500 and between days 700 and 880. During much of the first cold period the ground was covered by a thick layer of snow, which greatly reduced the heat exchange with the atmosphere. Thus cooling of the soil profile was rather moderate despite low air temperatures. Conductive heat fluxes in the measuring region during this period ranged between 0 and -6 W m^{-2} with a mean of -2.6 W m^{-2}. During most of the second cold period, snow cover was thin, and cooling of the soil profile was hence quite strong with heat fluxes exceeding -20 W m^{-2} at an average of -5.5 W m^{-2}.

As a consequence of the soil freezing characteristic, cooling of the profile requires the reduction of the liquid water content. The excess water may either freeze, or it may evaporate and migrate toward cooler regions where it condenses or freezes out. Freezing of liquid water releases latent heat and

hence counteracts cooling, whereas evaporation consumes latent heat and furthers cooling. The relative weight of the two processes depends on thermal diffusivity, the effective diffusion coefficient of water vapor, and the temperature gradient.

Looking at $\bar{r}_h$, we find strong consumption of heat at intermediate depths between 0.5 and 1 m and production above and below this zone. This is more pronounced in the second, colder period. Apparently, evaporation of excess water dominates at intermediate depths. The vapor diffuses toward the cooler layers above, supposedly also into the snow cover, where the latent heat is deposited. Inspection of the data shows that between days 340 and 480, θ_w^{liq} decreased by $\sim$0.03, corresponding to 30 kg m^{-3}. To evaporate this mass, some 73 MJ of heat are required per cubic meter of soil. For the 140 days this leads to an average power density of some -6 W m^{-3}. For the second period, θ_w^{liq} decreased by $\sim$0.04 between days 720 and 810, which leads to an average power density during this time interval of about -13 W m^{-3}. These numbers agree reasonably well with the calculations shown in Plate 5. The analysis was corroborated qualitatively by observations during a spring field trip which revealed a thick layer of depth hoar, large, beautiful snow crystals, at the bottom of the snow. This is interpreted as an indication of vapor migration into the snow. Direct measurements of vapor flux out of the ground have been reported for other sites [e.g., *Santeford*, 1978; *Woo*, 1982].

While we can at least estimate an upper limit for the amount of water evaporating from depths between 0.5 and 1 m from the TDR measurements and thereby corroborate the calculation of $\bar{r}_h$, this is not possible for the amount of condensing and freezing water vapor since it does not manifest itself in a change of the liquid water content. Still, we may estimate a lower bound for the amount of water transferred to the depth interval of 0.32–0.45 m between days 700 and 800 from $\bar{r}_h$. Inspection of the data yields $\bar{r}_h = 4.7 \pm 1.6$ W m^{-3} for this interval, where the uncertainty stems from the parameters c_h and d_h. This corresponds to the freezing of 15 ± 5 kg of water per cubic meter of soil during these 100 days.

The nature of the heat production at depths below 1 m during the cold period is less obvious. We interpret this as resulting from freezing or condensing water in the absence of appreciable vapor migration and hence of negligible evaporation. We suggest one reason for this is that during the thawed period, liquid water content at this site is maximal at depths between 0.8 and 1 m. Compared with the shallower depths with lower water contents, this region may thus be expected to become less permeable for water vapor upon freezing. Support for this interpretation comes again from field observations. During the instrumentation of the site, a massive ice-rich layer without apparent pores was actually identified below $\sim$1 m. Accumulation of ice at the base of the active layer, i.e., at the top of permafrost, has been quantified and reported from field and laboratory experiments by others [e.g., *Yershov*, 1998; *Solomatin and Xu*, 1994].

As would be expected, the production of heat, which depends strongly on migration and condensation of water vapor, is modulated by fluctuations of the surface temperature. We noticed earlier that such fluctuations can penetrate the entire soil profile in a rather short time. Prolonged warmer periods, for instance, between days 430 and 440 or between days 805 and 815, reduce or even invert the thermal gradient and thus reduce the condensation rate. This is reflected in a strong decrease of the heat consumption in the source regions of water vapor at intermediate depth and in a corresponding reduction of heat production in the drain regions above, as becomes particularly evident at later times of the cold period.

With temperatures still very low but rising after days 470 and 825, respectively, the processes discussed so far are reversed. From the surface, a temperature increase is forced, which releases frozen water according to the soil freezing characteristic and also increases the vapor content of the soil air. Melting and evaporation consumes heat, which counteracts the temperature increase. This heat is transported by the water vapor to deeper layers which are slightly cooler. Condensation and freezing, again in accordance with the soil freezing characteristic, releases this heat and warms the layers. As a consequence of this feedback, a uniform temperature profile develops, and the soil becomes warmer as a whole. The conductive heat flux, which is quite variable and changes its sign several times with depth, corroborates our interpretation. Apparently, this process reaches only down to $\sim$1 m as is indicated by $\bar{r}_h$ and by inspection of the temperature data, which show the warming of the profile below 1 m to lag behind that of the layers above. The less permeable soil layer suggested above would also explain this result.

We notice that our findings of the dynamics of the frozen active layer contrasts those of other sites for which it was stipulated that upon closing of the zero curtain, internal distillation and water advection cease for the rest of the winter [*Hinkel and Outcalt*, 1994; *Romanovsky and Osterkamp*, 2000].

5.2. Warming Period

With average daily air temperatures above 0°C after days 498 and 872, respectively, the conductive heat flux turned positive throughout the observed soil profile. It remained rather weak during the warming period, however, with a mean of 4.4 W m^{-2} at an average net radiation of 16.5 W m^{-2} for the interval between days 500 and 530. The corresponding numbers for the interval between days 880 and 915 are 5.7 W m^{-2} for the average conductive heat flux and 26.6 W m^{-2} for the average net radiation. The large difference between these fluxes reflects the heat consumed by the melting of the snow cover.

The onset of the first warming period is characterized by a rapid increase of the air temperature from -14°C to $+1$°C within 48 hours. The topmost temperature probe responded with an increase from -7°C to -3°C within 5 days. According to the soil freezing characteristic, this warming increases θ_w^{liq} by $\sim$0.015, which is confirmed by the TDR measurements, and consumes $\sim$5 MJ m^{-3} soil corresponding to $\bar{r}_h \approx -11$ W m^{-3}. However, instead of a consumption we find a release with $\bar{r}_h$ of the order of $+20$ W m^{-3} down to a depth of 0.9 m. This is explained by the dynamics of the snow cover. Temperature measurements, which are not reported here, show that it warmed between days 491 and 495 and was isothermal between days 495 and 500. This may even have generated some meltwater that could rapidly infiltrate the soil through cracks. In any case, the greatly increased temperature enforced a downward vapor flux toward the colder layers. While we cannot estimate the relative weight of these two processes, we can calculate the mass of water required for each of them to reproduce the observation that $\bar{r}_h$ is some 30 W m^{-3} larger than expected without movement of water. For the 5-day period between days 498 and 503 the freezing of some 38 kg of water per cubic meter of soil would be required if infiltrating meltwater was the only cause. Conversely, if we assume only vapor movement, some 4.5 kg m^{-3} would suffice. This corresponds to

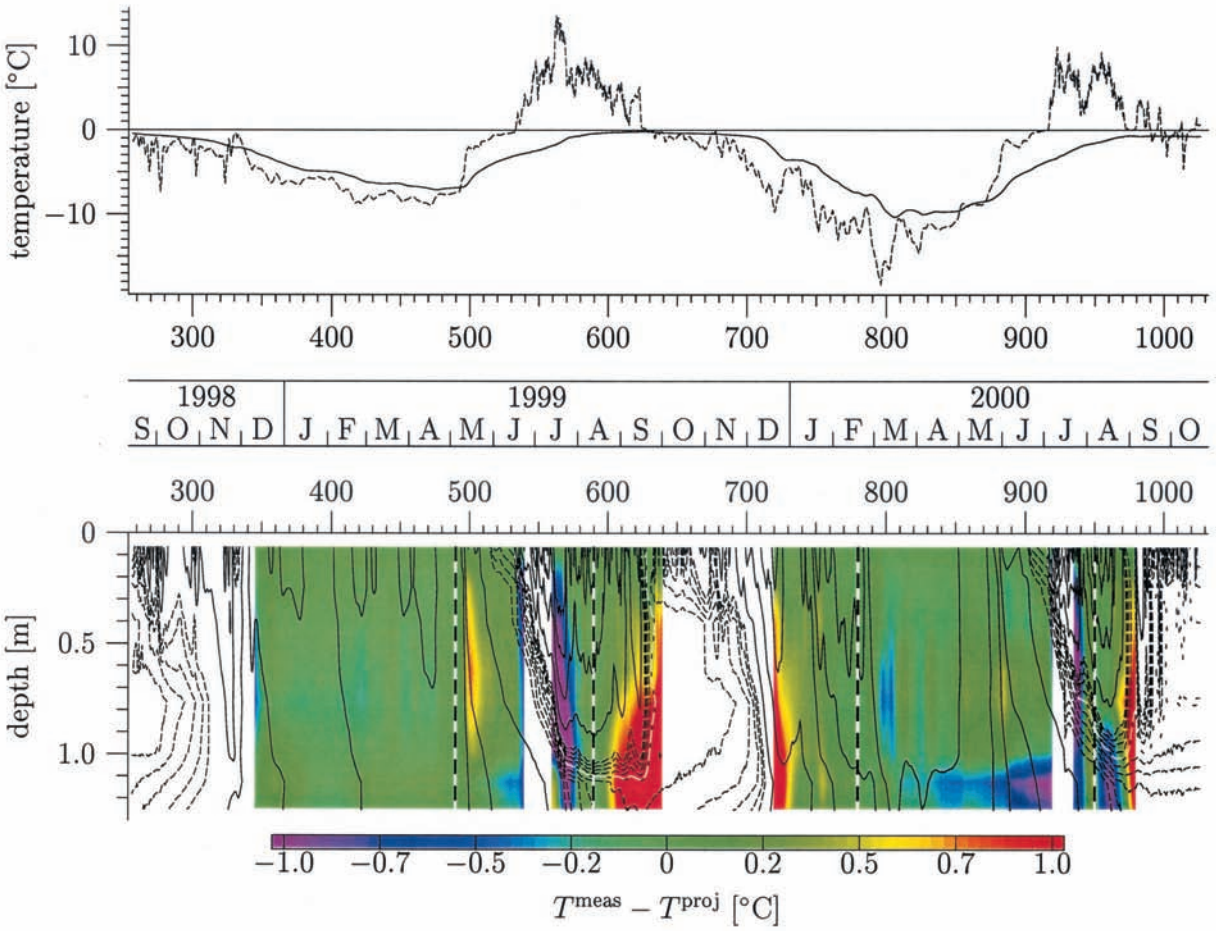

Plate 3. Difference between measured and projected temperatures for periods with dominating heat conduction. Projection is from a depth of 0.065 m using (7) and (8) with $d_h = 8 \times 10^{-7}$ m^2 s^{-1}. Along the vertical patterned lines, measured and projected temperatures were matched. Open areas indicate time intervals where projection is not permissible because of a strong influence of phase transitions. Measured temperatures in the shallowest probe at 0.065 m (dashed line) and of the deepest probe at 1.25 m (solid line) are shown in the top frame.

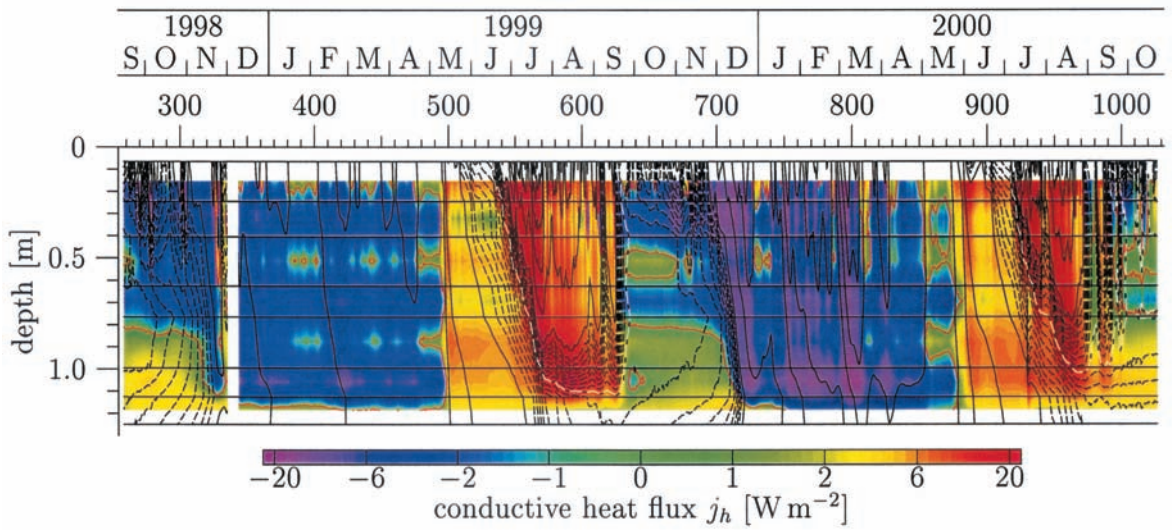

Plate 4. Conductive heat flux estimated from the centered finite difference approximation of (3). Black contour lines are for temperature and the red contour is $j_h = 0$. Horizontal lines indicate the depths for which j_h was estimated, and open areas correspond to missing data. Notice the logarithmic scale.

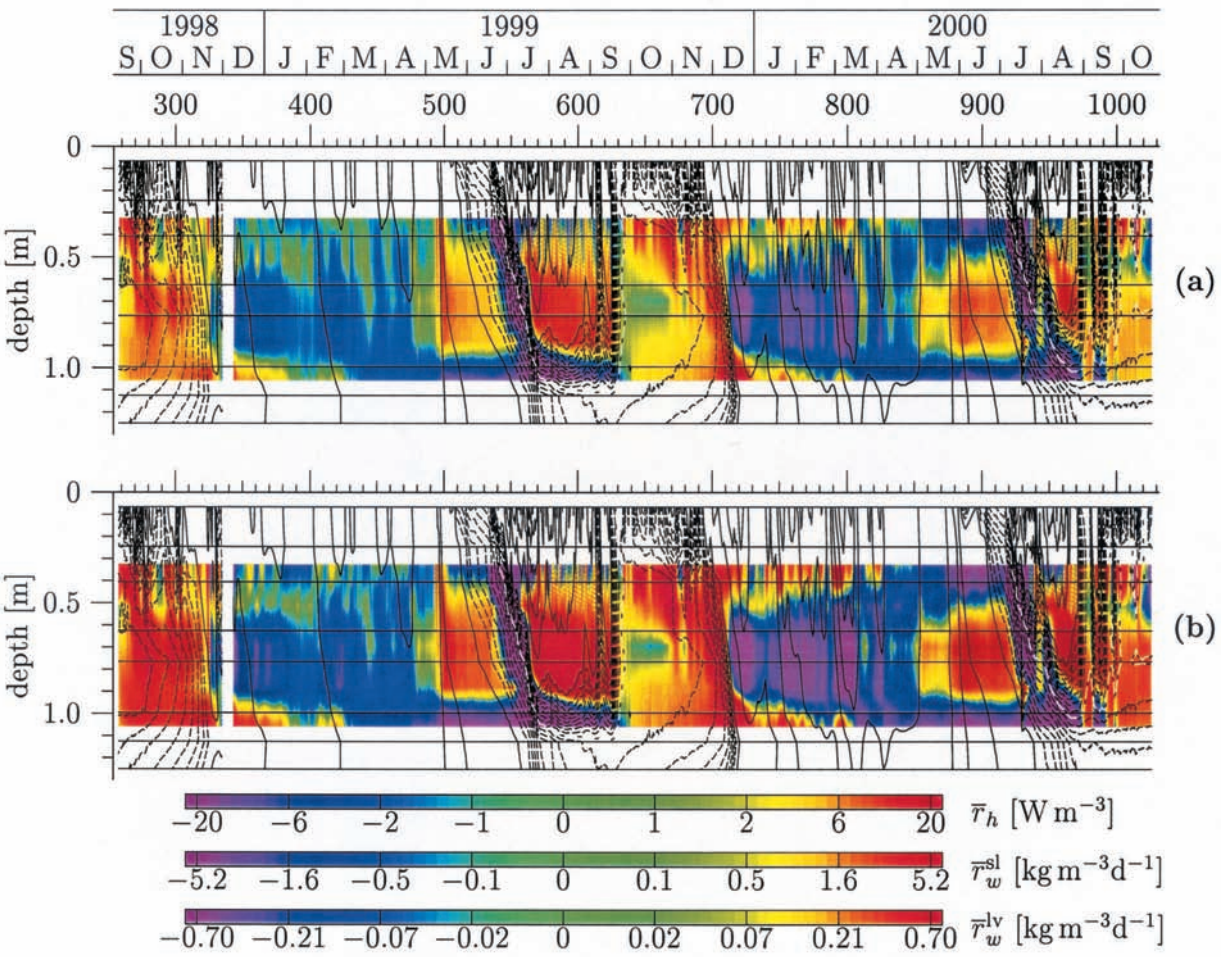

Plate 5. Production of latent heat estimated from (9) for (a) lower and (b) upper bounds of c_h and d_h. Horizontal black lines indicate the depth of temperature probes. As an aid for interpretation, color bars are given for $\bar{r}_h$ as well as for equivalent rates of water in a solid to liquid ($\bar{r}_w^{sl}$) and a liquid to vapor ($\bar{r}_w^{lv}$) phase change.

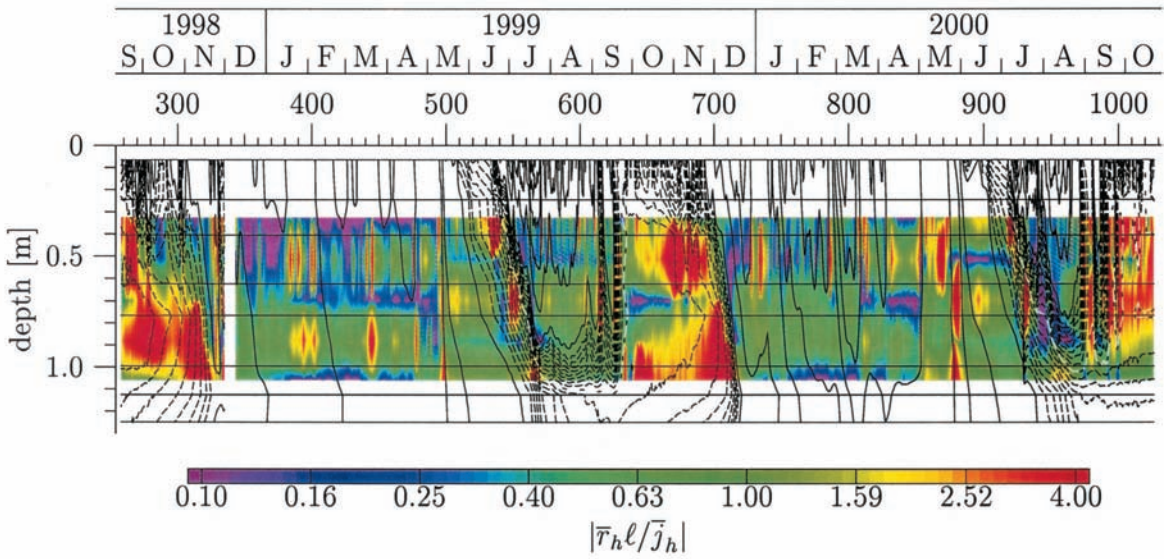

Plate 6. Dimensionless ratio between contributions to thermal dynamics originating from production of latent heat and from heat conduction.

an increase of the volumetric ice content by ~0.042 and 0.005, respectively. Both extremes could easily be generated by the melting snow cover. We comment that infiltrating snowmelt water has been observed in many field studies and that the corresponding warming of soil down to greater depths has been attributed to refreezing meltwater [e.g., *Thunholm et al*., 1989; *Woo and Marsh*, 1990; *Marsh and Woo*, 1993]. *Hinkel and Outcalt* [1994] also postulate that rapid warming of soil is caused by meltwater and downward migration of vapor.

By day 505, average daily air temperature returned to ~0°C for some 25 days, presumably stabilized by the thawing of the snow cover. The concurrent warming of the soil thus reduced the thermal gradient and with it the vapor flux. The advancing thawing front finally pushed the source region for the water vapor deeper into the soil with the drain region bounded by the less permeable layer at 0.9 m depth.

Below 0.9 m the heat consumed by the melting of water required by the soil freezing characteristic is not compensated by condensing vapor. Inspection of the data shows that during the period between days 500 and 550, θ_w^{liq} increases by 0.025, which leads to the estimate $\bar{r}_h \approx 2$ W m^{-3}. The average value calculated for this time interval and for $z > 1$ m is 2.5 ± 1.1 W m^{-3}, which is in excellent agreement with the measurements.

The dynamics during the second warming period is qualitatively identical to the first one and is not discussed any further here.

5.3. Thawed Period

The thawing front which starts this period is a macroscopic phase boundary between the partly frozen and the completely thawed soil. We distinguish it from the microscopic phase boundaries, which exist in the partly frozen zone, because the latent heat associated with the transition $T \rightleftharpoons T - \Delta T$ is much larger for $T = 0$°C than for subzero temperatures (Figure 1). As a consequence, the macroscopic phase boundary stabilizes the temperature against much larger heat fluxes, and thereby behaves more like a classical sharp phase boundary, than is the case for its microscopic counterpart.

As expected, we find the highest heat consumption rates in the rather narrow thawing front. Inspection of the data yields for the first thawing front, which we define as the region with $-0.6 < T$ [°C] < 0 between days 530 and 570, an average power density of -40 ± 13 W m^{-3}. The corresponding value for the second thawing front between days 910 and 960 is -32 ± 10 W m^{-3}. The consumption of heat in the thawing front reflects the net effect of three processes: (1) the thawing of the remaining frozen water, (2) the evaporation of water vapor which migrates to layers below the thawing front, and (3) the condensation of water vapor migrating downward from the warmer, already thawed soil above. The first two processes consume heat, whereas the third one produces heat. From the data available here it is not possible to reliably calculate the amounts of water involved in each of the processes.

We now consider the situation at depths greater than ~1 m. As already suggested in section 5.1, the migration of water vapor at these depths is severely impeded. On the basis of this premise we calculate the change of θ_w^{liq} from $\bar{r}_h$. Inspection of the data yields for the period between days 570 and 620 an average power density of -7.7 ± 2.5 W m^{-3}. Using (12), we calculate from this an increase of 0.10 ± 0.03 for θ_w^{liq} during this time. The TDR measurements actually show an increase of 0.10.

Turning to the actually thawed region, we find a strong production of heat for depths below ~0.4 m. The only process to generate it is the condensation of water vapor that originated at shallower, warmer depths and migrated toward the colder layers. The data give 18 ± 5.5 kg m^{-2} for the amount of water that is transferred in this process. The measurements of θ_w^{liq} support this interpretation if we make the reasonable assumption that after condensation the water flowed to the base of the thawed zone, where it accumulated. This downward migration of moisture is also supported by the TDR data.

We notice that during the thawed period a large portion of the net radiation, 25–70%, is consumed for evaporating water from the soil surface [*Ohmura*, 1982; *Rouse et al*., 1977; *Boike et al*., 1998]. This loss of water from the surface layer is compensated by rainfall and by the capillary rise of liquid water from greater depths. Inspection of the TDR data reveals that at our site the source region for the capillary rise reaches to a depth of only ~0.3 m. In a shallow zone we thus find water fluxes to be strongly transient, upward and downward, driven by atmospheric forcing. At greater depths, water flux is always downward: vapor migration toward lower temperatures and liquid migration in the gravity field.

The two thawed periods covered by the data are qualitatively similar. Quantitative differences resulted from the weather patterns, for instance, when a cold episode in the second period interrupted and delayed the thawing front for a few days. We notice that, again, as during the cold period, fluctuations of the air temperature rapidly propagate through the completely thawed zone and are stopped only by the thawing front which constitutes a macroscopic phase boundary. Temperatures in the thawed zone thus follow the air temperatures as described by (7).

With air temperatures decreasing, the thawed zone cools and eventually reaches 0°C. Freezing sets in and the dynamics becomes controlled by other processes.

5.4. Isothermal Plateau

The closing of the zero curtain may be interpreted as the rapid movement of the macroscopic phase boundary from the bottom of the completely thawed region to the soil surface. Compared with the reverse movement, i.e., the penetration of the thawing front, this is a fast phenomenon because only a small fraction of the water is involved in the associated phase change. With further cooling of the soil surface the macroscopic phase boundary advances into the soil as a cold front.

The macroscopic phase boundary prevents temperature fluctuations from the surface to reach greater depths. As a consequence, temperatures stay near 0°C, and conductive heat fluxes are very small. For instance, the average of j_h in the region where $-0.2 < T$ [°C] < 0 is only -0.6 W m^{-2}. While conductive processes are thus practically negligible, the production of heat from the freezing of water is not. For the interval between the depths of 0.31 and 1.03 m and the temperatures $-0.2° < T < 0°$ (°C), inspection of the data shows a decrease of the liquid water by 48 kg m^{-2} and for temperatures $-2° < T < -0.2°$ (°C) a decrease by 124 kg m^{-2}. Calculating the same quantities from $\bar{r}_h$, we obtain 24 ± 7 and 126 ± 38 kg m^{-2}, respectively. The significant difference for the first interval may be easily explained by water vapor that leaves the considered region. Indeed, after the discussion in section 5.3 we expect that part of the heat produced by freezing is immediately consumed by evaporating water. This vapor migrates toward colder zones where the heat is released again.

As Plate 5 shows, between days 630 and 670 a large part of the cold front is beyond the region where we can calculate $\bar{r}_h$, and we expect a significant loss of water vapor. Taking this into account, we find excellent agreement between measurements and calculations.

5.5. Why Does This Analysis Work?

The discussions in sections 5.1–5.4 emphasized the importance of latent heat production in all four periods. At first this appears to contradict the finding that temperatures at greater depths can be projected from measured surface temperatures assuming pure heat conduction (Plate 3). In order to resolve this we consider a homogeneous soil at $T < 0°C$ and negligible movement of water.

We calculate the effective heat capacity from the energy δE required to change the temperature of a unit volume by an infinitesimal value δT. This is

$$\delta E(T) = \delta T\left[c_h + \frac{d\theta_w^{\mathrm{liq}}(T)}{dT}\,\rho_w L_{sl}\right], \tag{14}$$

where the first term in brackets comes from the energy required for changing the temperature of the material, with c_h being the heat capacity defined in (6), and the second term comes from the energy consumed in the phase change. We neglect the small amount of energy associated with the corresponding change of the vapor content. The effective heat capacity thus becomes

$$c_h^{\mathrm{eff}}(T) := \frac{\delta E(T)}{\delta T} = c_h + \frac{d\theta_w^{\mathrm{liq}}(T)}{dT}\,\rho_w L_{sl}. \tag{15}$$

In the next step we calculate the production rate of latent heat associated with the rate of change of temperature. Using the chain rule of differentiation on the soil freezing characteristic, which we write as $\theta_w^{\mathrm{liq}}(T(z, t))$, we obtain

$$r_h = \frac{d\theta_w^{\mathrm{liq}}(T)}{dT}\,\frac{\partial T}{\partial t}\,\rho_w L_{sl}. \tag{16}$$

We now formulate the dynamics of the effective heat conduction in analogy to (2) as

$$\frac{\partial}{\partial t}\left[c_h^{\mathrm{eff}}(T)T\right] + \frac{\partial}{\partial z} j_h = r_h, \tag{17}$$

we insert (15) and (16) and obtain, after some transformations using the product rule on $c_h^{\mathrm{eff}}(T)T$ and, again, the chain rule,

$$\frac{\partial}{\partial t}\left[c_h^{\mathrm{eff}}(T)T\right] + \frac{\partial}{\partial z} j_h - r_h$$

$$= c_h \frac{\partial}{\partial t} T\left[1 + T\,\frac{\rho_w L_{sl}}{c_h}\,\frac{d^2\theta_w^{\mathrm{liq}}(T)}{dT^2}\right] + \frac{\partial}{\partial z} j_h = 0. \tag{18}$$

The second term in the brackets results from the rate of change along the soil freezing characteristic with time. As can be seen from Figure 1, for sufficiently low temperatures the curvature of $\theta_w^{\mathrm{liq}}(T)$ becomes very small. For our site the second term can actually be shown to be much smaller than 1 below about −2°C. Neglecting it, we recover

$$\frac{\partial}{\partial t}\left[c_h T\right] + \frac{\partial}{\partial z} j_h = 0, \tag{19}$$

which is the basis of (7) and (8). We thus find that for a homogeneous soil at sufficiently low temperatures and with negligible water fluxes, (19) gives an approximately correct description of the thermal dynamics even when production of latent heat is significant. This explains the success of the projections (7) and (8).

Finally, the apparent homogeneity with respect to effective thermal processes warrants some comments since, after all, this site is a classic example of patterned ground. We recall that the profile analyzed here is at the center of a mineral hummock and is thus much more uniform than one at the fringe where rather thick pockets of organic material are encountered. The very fine texture of the material adds to the homogeneity since total water content is roughly constant. Thermal capacity thus does not vary much over the year and through the profile, which may be seen from a short sensitivity analysis of (6). The case is not so simple with effective thermal diffusivity, as was mentioned in section 4.2. Avoiding speculations on its spatial and temporal variability, which are notoriously difficult to verify anyway, we base the assumption of a constant value of d_h on the success of projecting surface temperatures to deeper layers (Figure 2 and Plate 3). For cold periods the extent of agreement between measured and projected temperatures at all depths leaves little room for a possible variation of d_h. This is also true for the thawed periods, although to a lesser degree because the duration of the time series is much shorter. For periods with very strong phase changes the constant value of d_h is but a suggestion which we currently cannot check. This uncertainty obviously also extends to production rates of heat that are calculated using the constant value of d_h.

6. Summary and Conclusions

The thermal and hydraulic dynamics of a permafrost site was monitored over a period of 778 days in a depth interval between 0.06 and 1.25 m. We found it useful to separate the observed phenomenology into four sections: the cold period, the warming period, the thawed period, and the isothermal plateau.

We found that at this site, bulk thermal properties, in particular, heat capacity and thermal diffusivity, do not vary strongly, neither in time nor with depth. Also, the soil freezing characteristic was found to be invariant through the two freeze-thaw cycles observed so far.

We showed theoretically, in (14)–(19), that the effective thermal dynamics including phase transitions may be approximated by pure heat conduction, with the thermal properties assigned their bulk values, if (1) the mass movement of water is negligible and (2) temperatures are such that the curvature of the soil freezing characteristic is sufficiently small. The validity of this approximation was demonstrated by the successful prediction of the temperature in the entire soil profile from projections of measured near-surface temperatures. We concluded from this that the thermal properties at this site are approximately constant. Obviously, such a projection yields grossly wrong results when a macroscopic phase boundary lies between the measuring depth and the projection depth. We found, however, that reasonable prediction is possible even across time intervals during which such a boundary existed. In particular, temperatures fitted at some time during the first winter could be projected, using the forcing at the surface, to the next winter without any further adjustments.

Measurements of the soil temperature, together with the

constant bulk thermal parameters determined previously, enabled us to calculate conductive heat fluxes and heat production rates with high precision and high temporal resolution. From these calculations we could deduce and quantify the details of the thermal and hydraulic dynamics at this site. Independent quantitative verification was possible through measured liquid water contents. We remark that a crucial prerequisite for our analysis is a profile of calibrated temperature sensors with a high accuracy since unbiased estimates of spatial derivatives up to order 2 are required. Once such a measurement chain is established, it provides a very sensitive instrument for reliably detecting heat fluxes and releases of latent heat in the active layer of a permafrost soil.

We found that the production of latent heat and the associated migration of water vapor is an important agent in the thermal dynamics at this site for all four periods and that it is the dominating process in the isothermal plateau since heat conduction is practically negligible there. We further deduced from the measurements that practically unimpeded vapor migration is possible down to some 0.9 m. Below that depth, vapor migration was found to be severely restricted by a massive ice-rich layer. Although the amounts of water involved in the migration of latent heat were generally rather small, the large value of the enthalpy of evaporation, which is larger than that of melting by a factor of 7.4, makes vapor an efficient means for the transport of thermal energy.

Acknowledgments. We gratefully acknowledge financial support by the Deutsche Forschungsgemeinschaft (Ro 1080/4-1&2), the European Union (LSF grant NP-98-5), and a research grant awarded to Julia Boike (BMBF-LPD 9901/8-11) by the Deutsche Akademie der Naturforscher Leopoldina. Essential logistic support was provided by the German and the Norwegian Research Stations in Ny-Ålesund. Pier Paul Overduin and Olaf Ippisch were indispensable for the initial instrumentation of the site and for creating and maintaining the database. We gratefully acknowledge the constructive and very helpful comments of two anonymous reviewers.

References

Boike, J., K. Roth, and P. P. Overduin, Thermal and hydrologic dynamics of the active layer at a continuous permafrost site (Taymyr Peninsula, Siberia), *Water Resour. Res*., *34*, 355–363, 1998.

Carslaw, H. S., and J. C. Jaeger, *Conduction of Heat in Solids*, 2nd ed., Oxford Univ. Press, New York, 1990.

Chen, G., and E. J. Chamberlain, Observations of moisture migration in frozen soils during thawing, in *Fifth International Conference on Permafrost*, vol. 1, edited by K. Senneset, pp. 308–312, Tapir, Trondheim, Norway, 1988.

Costard, F., Mars: The periglacial planet, *Astronomie*, *102*, 80–90, 1988.

Crank, J., *The Mathematics of Diffusion*, 2nd ed., Oxford Univ. Press, New York, 1975.

Farouki, O. T., Thermal properties of soils, *Monogr. 81-1*, U.S. Army Cold Reg. Res. and Eng. Lab., Hanover, New Hampshire, 1981.

Førland, E. J., I. Hanssen-Bauer, and P. O. Nordli, Climate statistics and longterm series of temperature and precipitation at Svalbard and Jan Mayen, *Rep. 21/97 KLIMA*, Norwegian Meteorol. Inst., Oslo, 1997.

French, H. M., *The Periglacial Environment*, 2nd ed., Addison-Wesley-Longman, Reading, Mass., 1996.

Hallet, B., Self-organization in freezing soils: From microscopic ice lenses to patterned ground, *Can. J. Phys*., *68*, 842–852, 1990.

Hassanizadeh, S. M., and W. G. Gray, General conservation equations for multi-phase systems, 2, Mass, momenta, energy and entropy equations, *Adv. Water Res*., *2*, 191–203, 1979.

Hinkel, K. M., and S. I. Outcalt, Detection of nonconductive heat transport in soils using spectral analysis, *Water Resour. Res*., *29*, 1017–1023, 1993.

Hinkel, K. M., and S. I. Outcalt, Identification of heat-transfer processes during soil cooling, freezing, and thaw in Central Alaska, *Permafrost Periglacial Processes*, *5*, 217–235, 1994.

Hinkel, K. M., and S. I. Outcalt, Detection of heat-mass transfer regime transitions in the active layer using fractal geometric parameters, *Cold Reg. Sci. Technol*., *23*, 293–304, 1995.

Hinkel, K. M., S. I. Outcalt, and F. E. Nelson, Near-surface summer heat-transfer regimes at adjacent permafrost and non-permafrost sites in Central Alaska, in *Proceedings of the Sixth International Conference on Permafrost*, pp. 261–266, South China Univ. of Technol. Press, Beijing, 1993.

Huang, S., H. N. Pollack, and P.-Y. Shen, Temperature trends over the past five centuries reconstructed from borehole temperatures, *Nature*, *403*, 756–758, 2000.

Jury, W. A., and K. Roth, *Transfer Functions and Solute Movement Through Soils: Theory and Applications*, Birkhäuser Boston, Cambridge, Mass., 1990.

Kane, D. L., R. E. Gieck, and L. D. Hinzman, Evapotranspiration from a small Alaskan arctic watershed, *Nordic Hydrol*., *21*, 253–272, 1990.

Krantz, W. B., Self-organization manifest as patterned ground in recurrently frozen soils, *Earth Sci. Rev*., *29*, 117–130, 1990.

Liestøl, O., Pingos, springs and permafrost in Spitsbergen, Årbok 1975, Norsk Polarinstitutt, Tromsø, Norway, 1977.

Marsh, P., and M.-K. Woo, Infiltration of meltwater into frozen soils in a continuous permafrost environment, in *Proceedings of the Sixth International Conference on Permafrost*, pp. 443–448, South China Univ. of Technol. Press, Beijing, 1993.

Morishige, K., and K. Kawano, Freezing and melting of water in a single cylindrical pore: The pore-size dependence of freezing and melting behavior, *J. Chem. Phys*., *110*, 4867–4872, 1999.

Ohmura, A., Climate and energy balance on the arctic tundra, *J. Climate*, *2*, 65–84, 1982.

Outcalt, S. I., F. E. Nelson, and K. M. Hinkel, The zero-curtain effect: Heat and mass transfer across an isothermal region in freezing soil, *Water Resour. Res*., *26*, 1509–1516, 1990.

Outcalt, S. I., K. M. Hinkel, F. E. Nelson, and L. L. Miller, Estimating the magnitude of coupled-flow effects in the active layer and upper permafrost, Barrow, Alaska U.S.A., in *Proceedings of Seventh International Conference on Permafrost*, pp. 869–873, Centre d'Études Nordiques, Quebec, Canada, 1998.

Overpeck, J., et al., Arctic environmental change of the last four centuries, *Science*, *278*, 1251–1256, 1997.

Parmuzina, O. Y., Cryogenic texture and some characteristics of ice formation in the active layer (in Russian), in *Problems of Cryolithology*, edited by A. I. Popov, vol. 7, pp. 131–152, Moscow Univ. Press, Moscow, 1978. (English translation *Polar Geogr. Geol*., 131–152, 1980.)

Philip, J. R., and D. A. de Vries, Moisture movement in porous materials under temperature gradients, *Eos Trans. AGU*, *38*, 222–232, 1957.

Putkonen, J., Soil thermal properties and heat transfer processes near Ny-Ålesund, northwestern Spitsbergen, Svalbard, *Polar Res*., *17*, 165–179, 1998.

Ray, R. J., W. B. Krantz, T. N. Caine, and R. D. Gunn, A model for sorted patterned-ground regularity, *J. Glaciol*., *29*, 317–337, 1983.

Romanovsky, V. E., and T. E. Osterkamp, Effects of unfrozen water on heat and mass transport processes in the active layer and permafrost, *Permafrost Periglacial Processes*, *11*, 219–239, 2000.

Roth, K., R. Schulin, H. Flühler, and W. Attinger, Calibration of time domain reflectometry for water content measurement using a composite dielectric approach, *Water Resour. Res*., *26*, 2267–2273, 1990.

Rouse, W. R., Microclimate of arctic tree line, 2, Soil microclimate of tundra and forest, *Water Resour. Res*., *20*, 67–73, 1984.

Rouse, W. R., P. F. Mills, and R. B. Stewart, Evaporation in high latitudes, *Water Resour. Res*., *13*, 909–914, 1977.

Santeford, H. S., Snow soil interaction in interior Alaska, in *Modeling of Snow Cover Runoff*, edited by S. C. Colbeck and M. Ray, pp. 311–318, Cold Reg. Res. and Eng. Lab., Hanover, New Hampshire, 1978.

Serreze, M. C., J. E. Walsh, F. S. Chapin, T. Osterkamp, M. Dyurgerov, V. Romanovsky, W. C. Oechel, J. Morison, T. Zhang, and R. G. Barry, Observational evidence of recent change in the northern high-latitude environment, *Clim. Change*, *46*, 159–207, 2000.

Solomatin, V. I., and X. Xu, Water migration and ice segregation in

the transition zone between thawed and frozen soil, *Permafrost Periglacial Processes*, *5*, 185–190, 1994.
Thunholm, B., L.-C. Lundin, and S. Lindell, Infiltration into a frozen heavy clay soil, *Nordic Hydrol*., *20*, 153–166, 1989.
Woo, M.-K., Upward flux of vapor from frozen materials in the high Arctic, *Cold Reg. Sci. Technol*., *5*, 269–274, 1982.
Woo, M.-K., and P. Marsh, Response of soil moisture change to hydrological processes in a continuous permafrost environment, *Nordic Hydrol*., *21*, 235–252, 1990.
Yershov, E. D., *General Geocryology*, Cambridge Univ. Press, New York, 1998.
Zuber, M. T., et al., Observations of the north polar region of Mars from the Mars orbiter laser altimeter, *Science*, *282*, 2053–2060, 1998.

J. Boike, Water and Environmental Research Center, University of Alaska Fairbanks, P.O. Box 755860, Fairbanks, AK 99775. (ffjb2@uaf.edu)
K. Roth, Institute of Environmental Physics, University of Heidelberg, D-69120 Heidelberg, Germany. (kurt.roth@iup.uni-heidelberg.de)

(Received December 22, 2000; accepted May 9, 2001.)

Chapter 4

Chapter 4.1

Boike, J. and Yoshikawa, K. (2003): Mapping of periglacial geomorphology using kite/balloon aerial photography. *Permafrost and Periglacial Processes* 14(1), 81-85, doi: 10.1002/ppp.437.

PERMAFROST AND PERIGLACIAL PROCESSES
Permafrost Periglac. Process. **14**: 81–85 (2003)
Published online in Wiley InterScience (www.interscience.wiley.com). DOI: 10.1002/ppp.437

Short Communication

Mapping of Periglacial Geomorphology using Kite/Balloon Aerial Photography

Julia Boike and Kenji Yoshikawa*

Water and Environmental Research Center, Institute for Northern Engineering, University of Alaska, Fairbanks, USA

ABSTRACT

Kite and balloon aerial photography is introduced as a remote-sensing method for periglacial features and vegetation. High-resolution aerial pictures obtained by this method from Alaskan study sites are used for geometric analysis of ice-wedge networks, quantification of patterned ground, and mapping of water and vegetation. High-resolution aerial photographs could be an important data set for monitoring changes in permafrost pattern, periglacial processes and vegetation over time and space. Copyright © 2003 John Wiley & Sons, Ltd.

KEY WORDS: kite/balloon aerial photography; periglacial geomorphology; mapping patterned ground

INTRODUCTION

Kite and balloon aerial photography (KAP/BAP) is a well-known remote sensing method and has been used for scientific surveys, meteorological observations and military surveillance for centuries. With new, light-weight cameras, this method of obtaining remotely- sensed pictures is a lower cost alternative compared to pictures taken from airplanes or helicopters. KAP has been successfully used for mapping old forest on Axel-Heiberg Island (Bigas, 1997), and stereo observations of Antarctic penguins (Becot, 1998). Our interest is the mapping of snow, ice and periglacial landforms, typically of remote areas in the Arctic, where use of helicopters or planes is expensive and logistically cumbersome. We employed heavy duty weather balloons filled with helium (which is readily available) around Fairbanks and Ny-Ålesund, Svalbard. KAP was tested at Ellesworth Mountain, Antarctica; Svalbard, western Greenland and northern Japan; and at various sites in Alaska. In the following, we demonstrate the use of kite and BAP with examples from Alaskan study sites.

* Correspondence to: Dr J. Boike, Water and Environmental Research Center, Institute for Northern Engineering, University of Alaska, Fairbanks, 306 Tanana Drive, 99775-5860, USA. E-mail: ffjb2@uaf.edu

Copyright © 2003 John Wiley & Sons, Ltd.

EQUIPMENT

Platform

The basic equipment consists of a kite, line and spool, camera suspension and camera. Payload typically totals about 0.5 to 2 kg. The wind condition determines the size of the kite. Large rigid kites are flown in lighter wind conditions and soft parafoil kites in stronger winds. The kite line should be attached to a firm site and only be handled with gloves. If attached to the waist (for example by a harness), walking and thus choosing the desired location is possible. During the strongest winds (>12m/s), the kite system needs a ground anchor with a figure eight ring, to allow for the retrieval of the kite.

Depending on the application and budget size, there is a wide range of kites, suspensions and cameras available. We tested a variety of equipment with these main concerns in mind: i) weight and bulk

Received 20 November 2002
Revised 10 December 2002
Accepted 12 December 2002

size; ii) easy handling, especially in cold weather conditions; and iii) stability.

Our favourite kites are the rigid delta kite for light to moderate winds and the parafoil kite for moderate (>6 m/s) to strong winds (Figure 1A, B). The latter has no rigid parts and can be stuffed into a small sack.

BAP is easier to operate than kite-borne, and the camera can generally be positioned, both laterally and in terms of altitude, more easily than with a kite. This setup can be handled by one person, but it requires an environment with little or no wind. Transporting balloon helium to remote areas is difficult, and the helium itself is expensive.

Shutter Control

There are a number of ways in which the pictures can be taken. Radio-controlled exposure enables taking pictures of the desired location, but we found the extra equipment and handling more cumbersome compared to preset interval exposure functions. Some cameras have a built-in interval function (such as 35 mm Braun *trend*, digital Ricoh RDC-6000) or the possibility for a programmable data back (such as MF19 data back for Nikon F501). An option for digital cameras is a remote control accessory (such as DigiSnap), a small light-weight module that enables the external control of the camera via the serial port which provides an interval function.

Image Media

We experimented with various films (Fuji Color negative film, Kodak Ektachrome Professional, Infrared EIR Film, high speed infrared and Tri-X—i.e., black/white) with different bandwidth filters (ultraviolet, visible, infrared transparent or block). Our favourite camera is the Olympus C2020 (digital), triggered by the DigiSnap 2000 module. Benefits of this camera include its bright lens, small lens distortion, standard communication protocol, small size and robustness, suitability for filter attachment, and wide range CCD sensibility (ca. 300–1200 nm). Generally, the benefits of digital cameras are (1) images obtained immediately that can be evaluated and retaken on the spot, (2) wider wavelength sensibility than film, (3) cost performance, and (4) no waste of film. The image quality has become very close to conventional film; however, minimum target size and distance (elevation) should be adjusted. For example, set on maximum resolution the Olympus C2020 records a 1600 × 1200 pixel image. For recognition of a pattern, such as a 1 metre ice-wedge-trough depression, a minimum of 20 pixels is required, thus limiting the camera height to about 52 m:

$$H = L * \rho/(\rho_{min} * 2\tan(\theta/2))$$

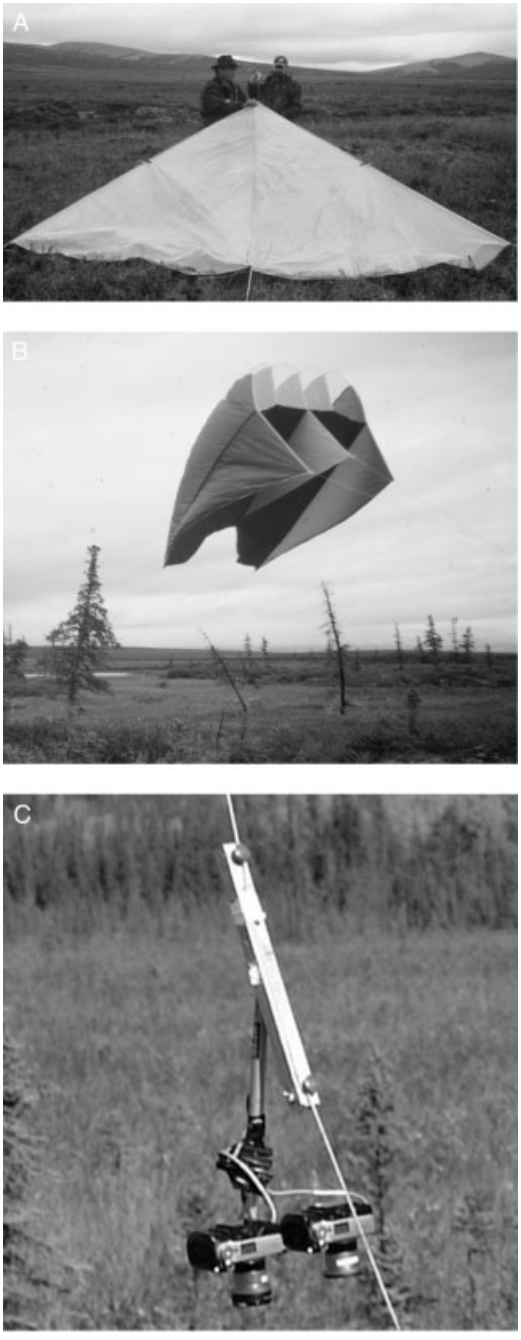

Figure 1 (A) Delta kite, (B) Parafoil kite and (C) T-suspension attached with balloon.

Copyright © 2003 John Wiley & Sons, Ltd.

where: H: camera height (m); L: recognition for threshold (m; 1 m in this example); ρ: camera resolution (pixel; 1200 in this example); ρ_{min}: minimum of required resolution (20 pixels for this study); and θ: camera lens angle (60 in this example)

With flying altitude and lens setting, the optimal subject size can be chosen. Increasing altitude decreases the overall contrast and brightness due to the increase of atmospheric backscatter.

Mount and Stabilization

Usually, a self-leveling apparatus, Picavet, helps to dampen the effects of vibrations and sudden movements of the kite or balloon. Another possibility is a universal joint suspension that allows rotation around the vertical and horizontal axes. Both suspensions can be built from materials available at hardware stores. Improved camera stabilization can also be attained by attaching two or three additional lines to the camera suspension (a triple system would enable controlled pictures). However, based on our field experience, handling with several lines—even with several people—is difficult. Furthermore, sudden line movement is still possible and/or the system can move altogether. We found the use of a simple T-shaped pendulum suspension (made from a camera tripod), directly attached to the kit line (Figure 1C), easiest and most effective to use. Simultaneous photographs of the same area with different band pass filters can be taken using a double or triple camera suspension. Two (or three) Olympus cameras mounted on a 22 cm long bar 10 cm apart, pointing in the same direction, are triggered simultaneously using one DigiSnap (Figure 1C). The bar can either be attached directly to the kite line or via a suspension.

EXAMPLES OF APPLICATIONS

Location of Ice-Wedge Polygons and Geometric Analysis of Polygonal Ground, Goldstream Creek, Fairbanks

Figure 2 shows the Goldstream Creek area near Fairbanks. We needed an aerial picture of this area for locating ice wedges for sampling (the ice-wedge depressions were not visible at ground surface) and for geometric analysis of the polygonal network. For the transformation of the original image into an orthonormal picture, a correction is carried out based on aspect ratio and Universal Transverse Mereator projection. Correction is applied using northing and easting transects of defined lengths (as shown in Figure 2) or several ground control points (GCP). The geometric analysis of the polygonal network rendered an average span of ice-wedge cracking of 17 m (standard deviation 2.9 m) and an aspect ratio of 1.5 (standard deviation 0.2).

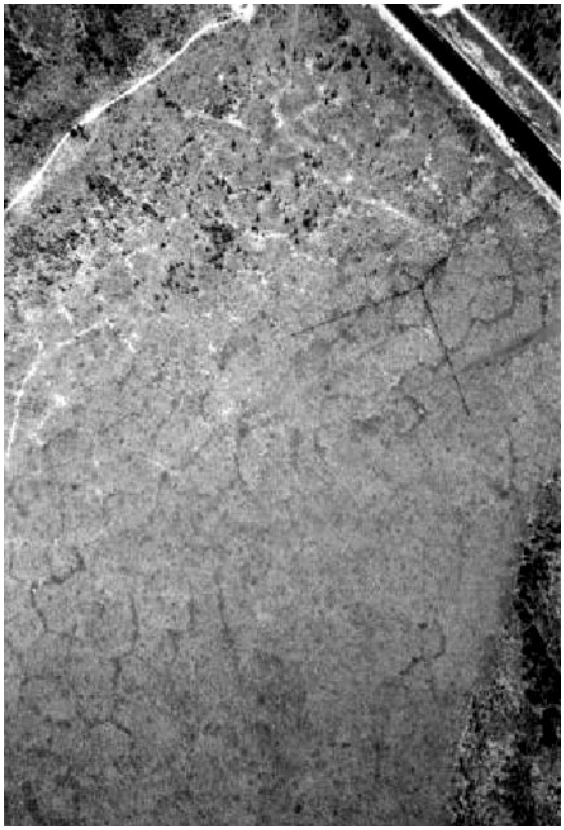

Figure 2 The Goldstream valley site in Fairbanks, Alaska, 2001. The picture was taken in November 2001 using balloon aerial photography with a Nikon camera and Fuji Color negative film (ASA 400). The marked angle on the ground in the right picture is 60 × 60 m to the north and west. Original red, green, blue colours are converted to a grey-scale image.

Quantification of Patterned Ground, Howe Island, Alaska

Aerial pictures made with KAP on Howe Island (located off the Alaskan Arctic coast northeast of the Prudhoe Bay oil fields) were taken for the quantitative analysis of permafrost patterned ground. The patterned ground forms present on the island are flat-centred polygons, non-sorted circles and small non-sorted polygons (Figure 3). Using Minkowski numbers (Mecke, 2000), it was shown that two adjacent sites had distinctly different

Copyright © 2003 John Wiley & Sons, Ltd.

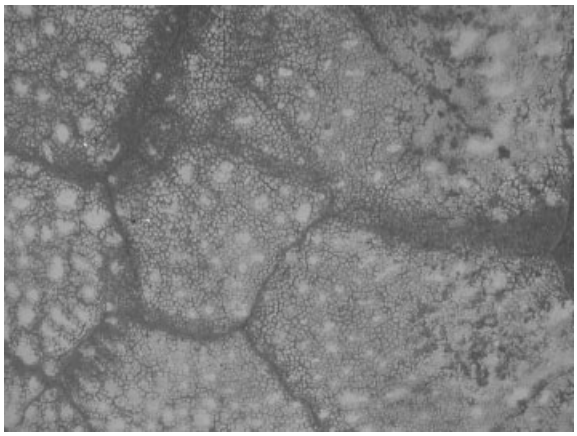

Figure 3 Kite aerial photograph using Olympus C2020 of Howe Island, August 2002. Polygonal ground, non-sorted circles, and small non-sorted polygons can be distinguished. The resolution, calculated using two white paper plates (diameter 26 cm) as ground control markers, is 38 mm per pixel.

characteristics, namely single-scale and multi-scale organization. The analysis of high resolution aerial photographs thus provides information about changes in permafrost patterns and periglacial processes over time and space.

Vegetation Mapping, Goldstream Creek, Fairbanks

We experimented with filters at the Goldstream polygonal site in Fairbanks, working to distinguish between different vegetation covers and water-saturated zones. The vegetation growing on the raised tussock mounds (*Eriophorum vaginatum*) differs from the surrounding, lower water-logged vegetation mainly comprising mosses (*Sphagnum spp.*). Isolated black spruce trees (*Picea mariana*) are widespread. Figure 4 shows the spectral reflectance characteristics of vegetation and water on 9 September 2002. Active vegetation mainly reflects the near-infrared spectrum. Water has the lowest albedo (around 0.2), while blueberry (*Vaccinium uliginosum L.*) and tussocks have the highest. Using an infrared filter (>800 nm, bandwidth B in Figure 4) thus allows distinguishing between water-logged (darker) and drier (whiter) areas (Figure 5A). Through filter arrangements, particular band patterns of the specific object can be chosen. We used a combination of yellow (> ∼520 nm) and hot mirror filter (<∼720 nm), narrowing the wavelength transmittance between 520 to 720 nm (Figure 5B; bandwidth A in Figure 4). Processing of Figure 5B consisted of subtracting the red channels minus the green channels, thus visualizing spruce trees as dark spots (Figure 5C).

OUTLOOK

In addition to being fun, kite flying is a simple and relatively inexpensive way to obtain remotely-sensed pictures. GCP or other land marks, such as transect lines and direction, are required for most of the post-image processing. Using illumination markers,

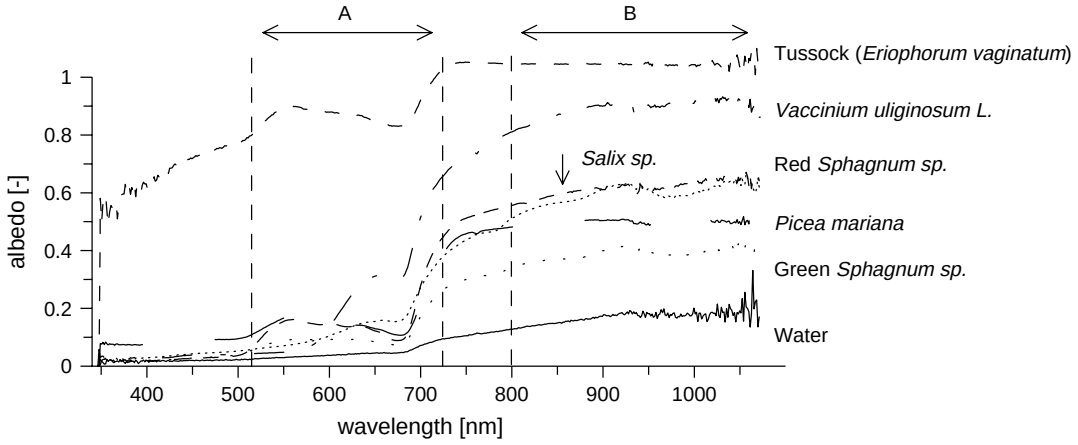

Figure 4 Major surface materials wavelength patterns (350−1050 nm) on 9 September 2002 at the Goldstream valley site, collected using a spectrometer (FieldSpec Pro, Analytical Spectral Devices, Inc). Bandwidths (A) (520−720 nm) and (B) (>800 nm) were chosen through filter arrangement and are used for the analysis in Figure 5.

Copyright © 2003 John Wiley & Sons, Ltd.

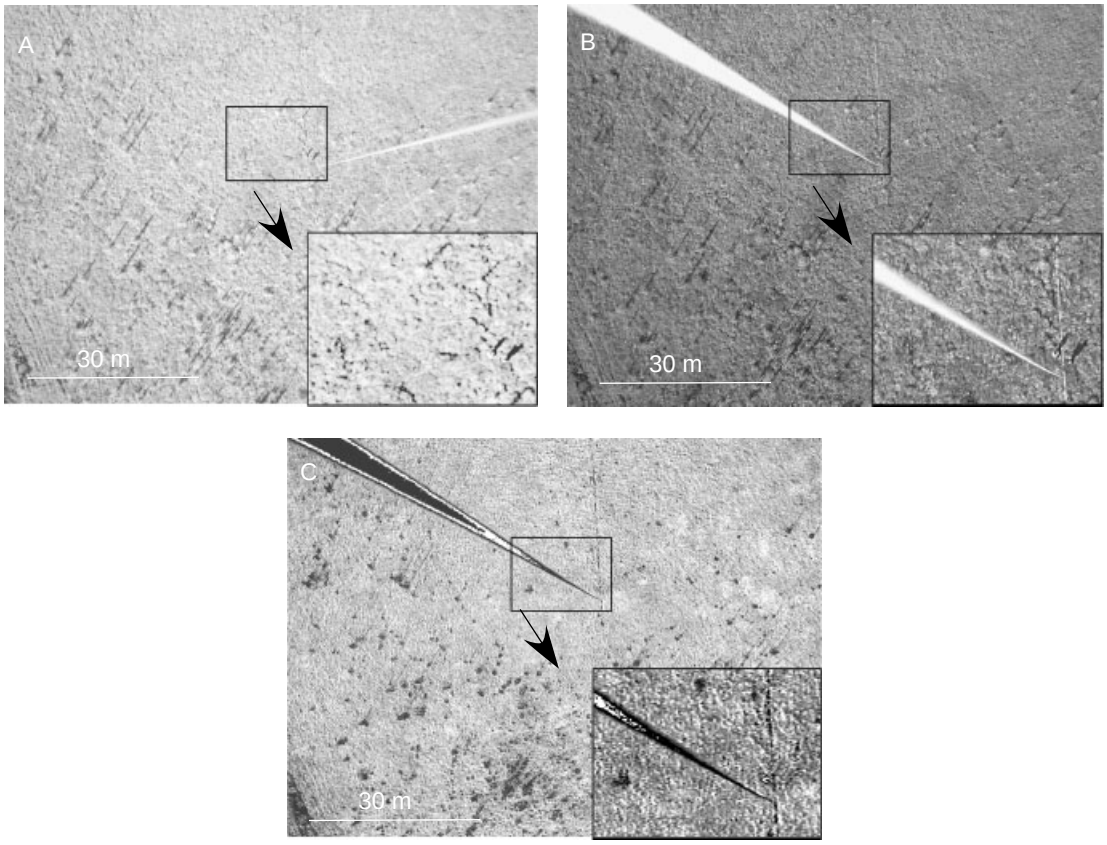

Figure 5 Balloon aerial photographs of Goldstream area taken 9 September 2002, using (A) an infrared filter (>800 nm), and (B) a yellow and hot mirror filter (520–720 nm), converted to grey scale image. (C) is processed by subtracting the red minus green channels of image (B), visualizing spruce trees as dark, isolated spots. Whiter areas are tussock mounds, partly covered with leafless branches. Enlargement of the centre box on each picture is shown in the lower right corner.

differences in light and shade could potentially be corrected. Other benefits of KAP/BAP are that wavelength transmittance can be controlled using filters, particular objects can be monitored, and high-resolution images can be compared to commercial aerial photographs. Further potential application could be stereo photography to produce digital elevation models (DEM).

ACKNOWLEDGEMENTS

We gratefully acknowledge financial support by the Deutsche Akademie der Naturforscher Leopoldina awarded to JB (BMBF-LPD 9901/8-11) and the National Weather Service in Fairbanks, Alaska, who provided the weather balloons just at the right moment.

REFERENCES

Becot C. 1998. Accurate stereo KAP. *The aerial eye* **4**(3): 8–9, 18.

Bigas C. 1997. Kite aerial photography of the Axel Heiberg Island fossil forest. In *Proceedings of the First North American. Symposium on Small Format Aerial Photography*: 147–153. American Society Remote Sensing Photogrammetry.

Mecke KR. 2000. Additivity, convexity and beyond: applications of Minkowski Functionals in statistical Physics. *Lecture Notes in Physics* **554**: 111–184.

Copyright © 2003 John Wiley & Sons, Ltd.

Chapter 4.2

Scheritz, M., Dietrich, R., Scheller, S., Schneider, W. and **Boike, J.** (2008): High Resolution Digital Elevation Model of Polygonal Patterned Ground on Samoylov Island, Siberia, Using Small-Format Photography, *Proceedings of the 9th International Conference on Permafrost*, June 29 - July 3, 2008, University of Alaska, Fairbanks, USA, 1589-1594.

Digital Elevation Model of Polygonal Patterned Ground on Samoylov Island, Siberia, Using Small-Format Aerial Photography

M. Scheritz and R. Dietrich
Dresden University of Technology, Institute of Planetary Geodesy, Dresden, Germany
S. Scheller
Dresden University of Technology, Institute of Photogrammetry, Dresden, Germany
W. Schneider and J. Boike
Alfred-Wegener-Institute for Polar- and Marine Research, Potsdam, Germany

Abstract

Accurate land cover, such as meso-scale to high-resolution digital elevation models (DEM), is needed to obtain reliable inputs for modeling the hydrology and the exchange between the surface and atmosphere. Small format aerial photography can be used to acquire high-resolution aerial images using balloons and helicopters. This method presents a low-cost, efficient method to construct a DEM of the polygonal patterned ground on Samoylov Island in the Lena Delta, Northern Siberia (72.2°N, 126.3°E). The DEM should be the foundation for modeling meso-scale hydrological processes on the island and identifying locations of discharge. The whole island could be covered with images taken from heights between 600 m and 800 m. All points of the DEM, with a resolution on the ground of 10 m, have a horizontal and vertical accuracy better than 1.0 m. This accuracy and the resolution depend on the survey height, the resolution of the camera system, the number and the quality of the images, and the algorithms used in the analysis. All listed parameters are explained and discussed in the paper.

Keywords: aerial photography; balloon; digital elevation model; polygonal patterned ground; Samoylov Island.

Introduction

The application of small format aerial photography to acquire high-resolution aerial images is still challenging. Balloons, kites, and helicopters are interesting and valuable tools for aerial photography. Several techniques with their advantages and disadvantages are briefly introduced and discussed in Bigras (1996) and Henry et al. (2002). Boike and Yoshikawa (2003) showed the successful use of balloon aerial photography for mapping snow, ice, and periglacial landforms around Fairbanks and Ny-Alesund, Svalbard. Recently, Vierling et al. (2006) successfully employed a tethered balloon with an altitude up to 2 km to acquire remotely sensed data. Further application fields are briefly explained in Aber and Aber (2002).

The goal of our work was to generate a digital elevation model (DEM, regular or irregular distributed points) of the polygonal patterned ground on Samoylov Island in the Lena Delta, Northern Siberia (72.2°N/126.3°E). The DEM should be the foundation for the modeling of meso-scale hydrological processes on the island for answering questions like: where are polygonal seas, how big are they, and where does the water drain into the Lena?

The landscape of the island is shaped by the micro topography of the wet polygonal tundra. The development of low-centered ice-wedge polygons results in a prominent micro relief with the alternation of depressed polygon centers and elevated polygon rims with elevation differences of up to 0.5 m over a few meters distance. Satellite images with resolutions between 15 m and 30m, such as Landsat (Aber & Aber 2002), do not represent this micro relief sufficiently. Difficulties of using satellite images are discussed in detail by Dare (2005). It is, however, the most important factor for small-scale differences in vegetation type and soil moisture, and is therefore a major variable when considering heat and trace gas fluxes on the meso-scale.

Depending on the general conditions, feasible equipment, cost, and available measurement time, the required horizontal and vertical accuracy of the DEM should be better than 1 m. Since remote-control-aircraft and drones are not permitted in Siberia, we used a tethered helium balloon. In addition it was also possible to take images from a helicopter. The photogrammetric equipment consists of a Nikon D200 with a 14 mm lens, 26 fabric-made targets for ground control points (GCPs), and additional geodetic equipment (tachymeter Elta C30).

This paper presents a low-cost, efficient method to acquire high-resolution aerial images using helium filled balloons. It discusses (1) different steps of obtaining aerial images from a balloon and a helicopter, (2) data analysis, (3) advantages and disadvantages of different assimilation platforms and (4) further improvements to increase the resolution of the DEM and the horizontal and vertical accuracy of the coordinates of each point.

Methods

The motivation mapping of the patterned ground on Samoylov Island was achieved using photogrammetric methods on aerial images with overlapping areas, allowing the determination of 3D coordinates (stereoscopy). There are different methods available ranging from simple stereoscopic methods with two images to a bundle block adjustment (Henry et al. 2002) over all taken images. Here

Figure 1. Camera system: Nikon D200, hanging at the tethered helium filled balloon.

Figure 2. Fabric-made targets used as ground control points with a diameter of 2.5 m.

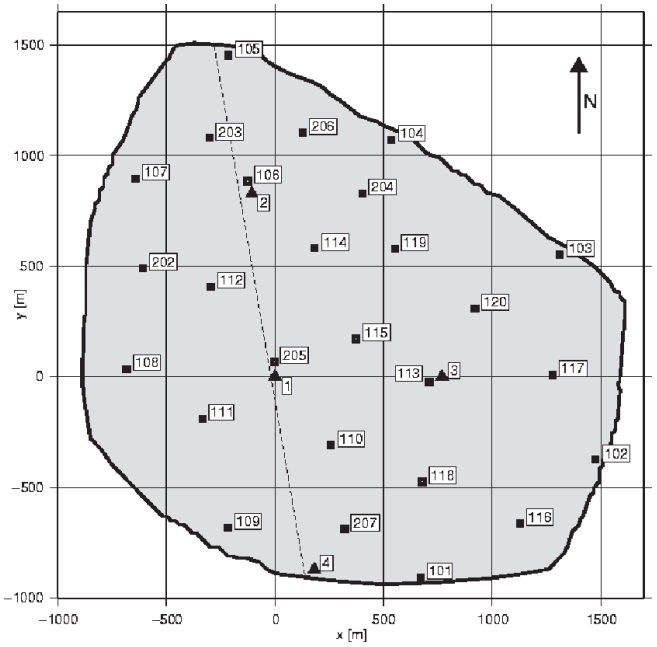

Figure 3. Schematic illustration of Samoylov Island: Network of 26 ground control points (squares); The coordinate (0,0) shows the origin of the local coordinate system with a fixed height of 100 m. The 4 datum points are displayed as triangles. The dashed line separates the flood plain (western part) and the plateau (eastern part).

the former method was used, since the flight path, height, and orientation of the balloon and thus the resulting images were somewhat unpredictable. The data analysis then consisted of two important steps: firstly a separate backward intersection for the calculation of the image orientation and secondly a forward intersection for the calculation of the 3D coordinates of the points of the DEM.

Before the fieldwork was carried out, the optimal camera system and the number of the GCPs was determined. The pre-condition for the DEM was a resolution on the ground better than 10 m with an accuracy in coordinates better than 1 m. Thus prior calculations were done on flight height, the size of the GCPs, the distance between them, and the required number of images covering the whole island. The survey height and the number and size of the GCPs finally were a compromise between the available time for measurement, the investment for the camera system, and the mentioned optimal conditions for resolution and accuracy.

Equipment

The equipment for the aerial photography consists of a Nikon D200 camera with a 14 mm lens (Fig. 1) and 26 fabric-made targets used as GCPs (Fig. 2). The Nikon D200 is a digital mirror reflex camera with a CCD sensor of 10.2 megapixel. With the calculated flight height of 800 m, one pixel maps an area of ~0.12 m² on the ground.

Depending on the flight height, the focal distance of the lens, and the condition that each GCP should represent an area of at least 6 x 6 pixels in the digital images, their diameter had to be greater than 2.0 m (Fig. 2).

To precisely calculate the image orientation, it was necessary to set up enough GCPs on the island to get a minimum of 4 points within each image. Considering the calculated flight height of 800 m, this resulted in at least 20 GCPs (called 101–120) with a spacing of about 500m to get an optimal coverage of Samoylov Island (~5 km²). Six control targets with a diameter of 1.0 m were additionally laid out to condense the point network (point IDs 202–207). The entire network of GCPs is shown in Figure 3.

A local coordinate system on Samoylov Island was fundamental to the photogrammetric fieldwork. Therefore 4 datum points (Fig. 3, point IDs 1–4) were set up, each marked with a 1m iron pipe in the permafrost soil. The distances between these points reached from 800 m to 1200 m. In Figure 3 the coordinate (0, 0) shows the origin of the local coordinate system with a fixed height of 100 m. For setting up the coordinate system we used the tachymeter Elta C30. The repeatability of the coordinates of the datum points was better than +/-2 cm.

Fieldwork

The fieldwork was divided into two parts. Firstly, GCPs were laid out, and their coordinates were surveyed in the local coordinate system. Secondly, aerial photographs were taken using a tethered balloon and a helicopter.

After laying out the GCPs, their registration was conducted

Figure 4. Tethered balloon, filled with helium, diameter 2–3 m.

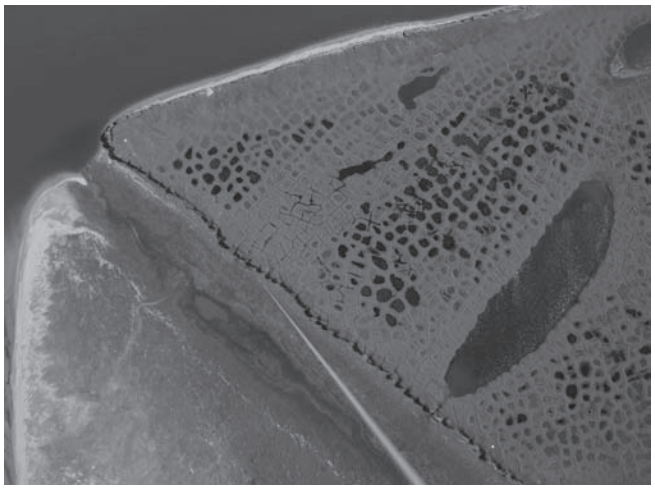

Figure 5. Polygonal patterned ground admitted from a height of ~750 m, in front the rope to the balloon.

in the local coordinate system with help of the tachymeter. The accuracy of the distances between the datum points and the GCPs was better than 1 cm. The coordinates of all GCPs had an absolute accuracy better than +/-5 cm. These accuracies depended on the determination of the center of the GCPs, the accuracy of the angle measurements with the tachymeter, and the distances to the survey points.

The balloon used in mapping the patterned ground on Samoylov Island is depicted in Figure 4, and an example image is given in Figure 5. The interval timer of the camera was adjusted to 1 minute, so the camera could take images for nearly four hours. Using the tethered balloon, one third of the entire island (western part, flood plain, Fig. 3) could be covered from a height of about 800 m.

Additionally, images were captured from a helicopter from altitudes between 600 m and 900 m. Using the helicopter, the middle part of the island could be covered with a flight height of ~600 m, the eastern part with flight heights of nearly 800–900 m.

Table 1. Nikon D200, interior parameters.

Parameter of inner orientation:	
Horizontal size Vertical size	3872 Pixel 2592 Pixel
Pixel size	0.0058mm
Principal point	x_0 = 0.10424mm y_0 = -0.19185mm
Principal distance	c = -13.32284mm
Parameter of distortion dx, dy (without units):	
Radial	a_1 = -0.000495642 a_2 = 1.65615e-006 a_3 = 0.0
Assymetric distortion Tangential distortion	b_1 = 1.72277e-005 b_2 = -1.51355e-005
Affinity Shear	c_1 = 0.000149996 c_2 = 2.72591e-005
r_0 - parameter	r_0 = 8.44

Calibration of the camera system

For the subsequent data analysis it was necessary to determine the parameters of the inner orientation of the camera system (interior parameters: principal distance c, coordinates of the principal point x_0, y_0, parameter of distortion dx, dy). The calibration of the camera system as specified in Luhmann (2000) was conducted before the fieldwork at the Institute of Photogrammetry at the Dresden University of Technology (Table 1).

To verify these camera parameters, a calibration-field was set up on Samoylov Island. Using the Elta C30, the coordinates of these points were measured with a relative accuracy of a few millimeters. The parameters of the inner orientation, that were consecutively determined, were nearly the same as in the laboratory, so the relation between the body of the camera and the objective can be assumed as stable.

Data Analysis

To analyze the collected data, a program was generated based on the algorithms of Luhmann (2000) and Schwidefsky & Ackermann (1976). The program includes the collinearity equations, which correlate the image coordinates (x,y) and the object coordinates (X,Y,Z) for each point:

$$x = x_0 - c \cdot \frac{r_{11}(X - X_0) + r_{21}(Y - Y_0) + r_{31}(Z - Z_0)}{r_{13}(X - X_0) + r_{23}(Y - Y_0) + r_{33}(Z - Z_0)} + dx \qquad (1)$$

$$y = y_0 - c \cdot \frac{r_{12}(X - X_0) + r_{22}(Y - Y_0) + r_{32}(Z - Z_0)}{r_{13}(X - X_0) + r_{23}(Y - Y_0) + r_{33}(Z - Z_0)} + dy \qquad (2)$$

First, a backward intersection was calculated for each single image to determine the outer orientation (perspective center (X_0, Y_0, Z_0) and rotation matrix $\underline{R}$). Approximated

parameters of the outer orientation were necessary and could be calculated applying a special algorithm developed by Schwidefsky and Ackermann (1976). The calculation of the outer orientation was successful for all images, which had minimized 4 GCPs.

Second, approximated coordinates for the points of the DEM were determined with help of a regular raster with a step size of 10 m based on the local coordinate system. The height of each point was set up to the average height of all GCPs. With the known outer orientation of the images a backward intersection could be determined for each preliminary point of the DEM, so the approximated positions could be found in the images. Then a search patch was defined around these locations and a matching-algorithm (with sub pixel accuracy) was implemented to locate precisely the same patch in other images. The matching algorithm was calculated with a cross-correlation:

$$k = \frac{\sum_{x'}\sum_{y'} g_1(x',y') \cdot g_2(x+x',y+y')}{\sum_{x'}\sum_{y'} g_1(x',y')^2 \cdot \sum_{x'}\sum_{y'} g_2(x+x',y+y')^2}$$
$$-1 \le k \le 1$$

At each position (x', y') a correlation coefficient k was determined depending on the gray scale value g of each pixel. The output consisted of a correlation image with all calculated values of k. Then, an algorithm was implemented which fitted an ellipsoidal paraboloid in the correlation image to find the exact position of the correlation maximum. At the end a forward intersection was calculated as a least square adjustment to get the exact 3D-coordinates for the points of the DEM.

The output dataset consists of all calculated coordinates, the standard deviation, and the correlation factor for the matching of one point between different images. If the correlation factor is greater than 0.7, and if the accuracy of the coordinates (horizontal and vertical accuracy) is better than 1 m, the point is stored as a point of the resulting DEM of Samoylov Island.

Results

Figure 6 shows the triangulated DEM. The horizontal and vertical accuracy of the coordinates of each point is better than 1.0 m (1σ, i.e., confidence interval of 68%). Polygonal lakes are easy to distinguish, because the algorithm was not able to match over the uniform water surface. Also, areas with bad data coverage are recognizable, for example in the southeastern part of Figure 6. The main reason for this is that the helicopter height changed very fast during the taking of the subsequent images, resulting in changing scaling factors of these images and smaller correlation factors. Other reasons for degraded correlation are poor illumination conditions and insufficient contours. As a result, only few points were found with a correlation larger than 0.7, whereas for most points the correlation factor was lower than 0.5. The island's center and the western and northern part have the best coverage of points. The helicopter was flying over the center

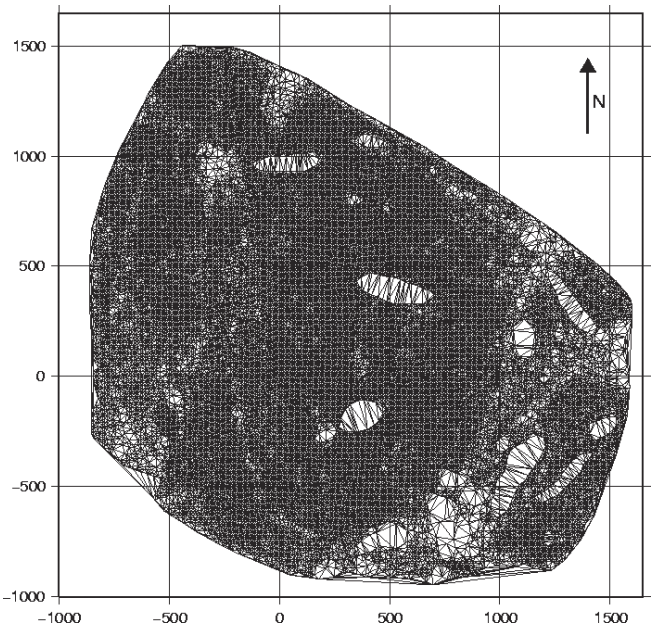

Figure 6. Triangulated irregular DEM with an approximated step size of 10 m of Samoylov Island: *x*- and *y*-coordinates are in a local coordinate-system (scale in m).

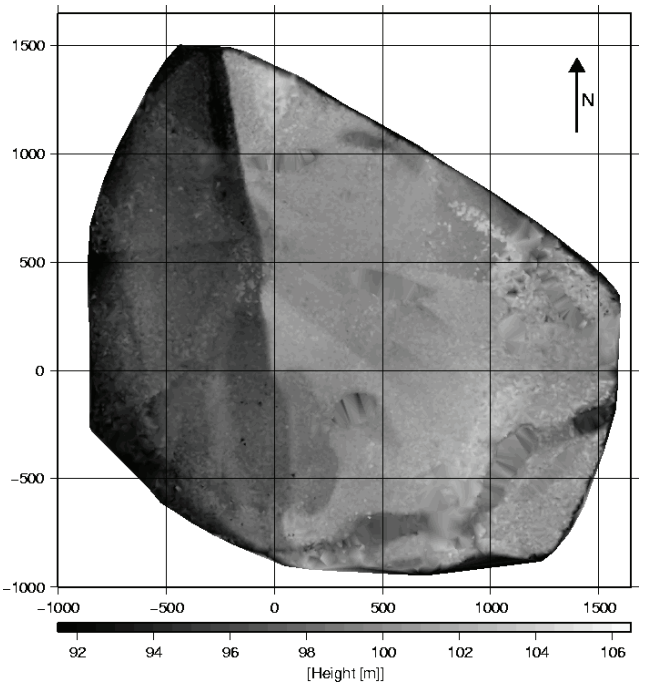

Figure 7. Surface of Samoylov Island: *x*- and *y*-coordinates are in a local coordinate system (scale in m). The heights of the points of the DEM are relative heights with respect to the origin of the local coordinate system (0.0) with a height of 100 m.

at a nearly constant height of 600 m. In addition, the height of the tethered balloon over the flood plain (western part, Fig. 6) was nearly constant, which made the calculations (in particular the matching algorithm) really successful. The estimated points from both datasets could be matched with correlation factors up to 0.99 and with horizontal and vertical accuracies partially better than 0.5 m.

In Figure 7 the triangulated network from Figure 6 is shown as a surface for the whole island. The flood plain is easy to distinguish, as well as the ridge between the flood plain and the plateau and the cliff line with height differences up to 8 m.

Discussion

The goal of this project was to generate a DEM of the whole of Samoylov Island. The short observation period and the cost of and permission for the equipment formed the boundary conditions for the field work, under which a trade-off between the resolution, accuracy, and practicable amount of work for the acquisition and evaluation of photos had to be found. We finally decided to use a tethered, helium-filled balloon and a camera with a high precision lens (Nikon D200 with 14 mm lens). On the ground, 20 fabric-made targets with a diameter of 2.5 m and 6 targets with a diameter of 1.0 m spanned a network of GCPs.

Taking aerial photographs with a balloon is a low-cost and efficient method to acquire high-resolution aerial images. However, to take images with a balloon-borne camera, a calm day with good illumination conditions is required. Especially the wind speeds limit the observation time – during the 3 weeks of the field work on Samoylov Island we had only 2 days with good weather conditions. Taking images from a helicopter is independent from wind conditions and more stable in maintaining the height and the flight path. But this application is very expensive, and it is also dependent on good illumination conditions.

A sensitive step within the data analysis is the matching algorithm, because different illumination conditions like cloud shadows and different scaling factors of the images are a disadvantage. Also the search patch has to be big enough to get sufficient correlations between different images with high correlation factors. To avoid correlations between neighboring points of the DEM (this would degrade the accuracy of coordinates) the step size has to be at least twice the size of the search patch. Depending on the survey height of 800 m and a search patch of 24 x 24 pixel, the resolution on the ground of the DEM was set to 10 m. Therefore, all points of the generated DEM should be independent from each other.

Under these terms each point of the DEM has a horizontal and vertical accuracy better than 1 m. Naturally there are improvement possibilities to retrieve the micro relief of the polygonal wet tundra, such as the use of more and smaller targets for GCPs concomitant with a lower flight height and thus a higher resolution and accuracy. Furthermore the standard deviation of the coordinates of the DEM improve, if the points can be found in more than 2 images. Therefore, a better and regular image-coverage of the whole island from the same survey heights and good stereoscopic bases (relation between survey height and image-spacing) are a requirement for high resolution DEMs.

Conclusions

The method described in this paper is, depending on the measurement time, cost, and equipment, very useful to measure typical permafrost landscapes with the desired resolution and accuracy. Depending on the survey height and conditions described above, the horizontal and vertical accuracy of each point in the generated DEM of Samoylov Island shown in Figures 6 and 7 is better than 1.0 m for nearly 70% of all triangulated points. The obtained resolution of the DEM amounts to 10 m. Additionally, the combination of images from balloon and helicopter was successful if the flight height was approximately equal.

The meso-scale DEM discussed in this paper is now utilized (at the Alfred Wegener Institute for Polar and Marine Research in Potsdam) to determine the channel routing in a spatially distributed hydrologic model for Samoylov Island. Additionally, it is also possible to generate a orthomosaic (Bitelli & Girelli 2004) with the known parameters of the outer orientation of the images. This methodology provides a good basis for quantification of fluctuating coastlines in permafrost landscapes.

Acknowledgments

This work was funded by the Alfred Wegener Institute for Polar and Marine Research in Potsdam, Germany. We are thankful for the logistical and financial support of the Russian-German research station on Samoylov that made this study possible. We also thank Günter Stoof, Moritz Langer, and Maryvonne Landolt for their assistance in the field and for data discussion and analysis.

References

Aber, J.S. & Aber, S.W. 2002. Unmanned small-format aerial photography from kites for acquiring large-scale, high-resolution, multiview-angle imagery. P*ecora 15/Land Satellite Information IV/ISPRS Commission I/FIEOS 2002 Conference Proceedings.*

Bigras, C. 1997. Kite aerial photography of the Axel Heiberg Island fossil forest. *Proceedings of the First North American Symposium on Small Format Aerial Photography.*

Bitelli, G. & Girelli, V.A. 2004. Low-height aerial imagery and digital photogrammetrical processing for archaeological mapping. *International Archives of Photogrammetry, Remote Sensing and Spatial Information Services*: 498-504.

Boike, J. & Yoshikawa, K. 2003. Mapping of periglacial geomorphology using kite/balloon aerial photography. *Permafrost and Periglacial Processes* 14:0 Wiley InterScience, DOI:10.1002/ 437 pp.

Dare, P. 2005. The use of Small Environmental Research Aircraft (SERAs) for environmental remote sensing. *International Journal of Geoinformatics* 1/3: 19-26

Henry, J.-B., Malet, J.-P., Maquaire, O. & Grussenmeyer, P. 2002. The use of small-format and low-altitude aerial photos for the realization of high-resolution DEMs in mountainous areas: Application to the super-sauze earthflow (Alpes-De-Haute-Provence, France). *Earth Surfaces and Landforms* 27: 1339-1350. DOI:10.1002/esp.411.

Luhmann, Th. 2000. *Nahbereichsphotogrammetrie, Grundlagen, Methoden und Anwendungen*. Heidelberg: Herbert Wichmann Verlag, 571 pp.

Schwidefsky, K. & Ackermann, F. 1976. *Photogrammetrie, Grundlagen, Verfahren, Anwendungen.* Stuttgart: B.G. Teubner, 384 pp.

Vierling, L.A., Fersdahl, M., Chen, X., Li, Zh. & Zimmerman, P. 2006. The Short Wave Aerostat-Mounted Imager (SWAMI): A novel platform for acquiring remotely sensed data from a tethered balloon. *Remote Sensing of Environment* 103: 255-264.

Chapter 4.3

Roth, K., **Boike, J.** and Vogel, H. -J. (2005): Quantifying permafrost patterns using Minkowski Densities, *Permafrost and Periglacial Processes* 16 (3), 277-290

PERMAFROST AND PERIGLACIAL PROCESSES
Permafrost and Periglac. Process. **16**: 277–290 (2005)
Published online in Wiley InterScience (www.interscience.wiley.com). DOI: 10.1002/ppp.531

Quantifying Permafrost Patterns using Minkowski Densities

Kurt Roth,[1]* *Julia Boike*[2] *and Hans-Jörg Vogel*[1]

[1] Institute of Environmental Physics, University of Heidelberg, Heidelberg, Germany
[2] Alfred-Wegener-Institute for Polar and Marine Research, Potsdam, Germany

ABSTRACT

Minkowski densities and density functions are measures for quantifying arbitrary binary patterns. They are employed here to describe permafrost patterns obtained from aerial photographs. We demonstrate that images taken at two neighbouring sites shown distinctly different patterns and quantify the difference. It is found that one of the sites exhibits an essentially single-scale structure while the other one has a multiscale organization. Minkowski densities and density functions are thus proposed as sensitive and objective measures to quantify the change of permafrost patterns in space or in time. Copyright © 2005 John Wiley & Sons, Ltd.

KEY WORDS: permafrost; patterned ground; density functions

INTRODUCTION

Permafrost forms like sorted circles, hummocks, polygons, and stripes are spectacular manifestations of the complex dynamics of periodically frozen soils. Their structure depends on the parent material as well as on the external forcing by the thermal and hydraulic regime (Hallet, 1990) and by possible fluxes of solid matter (Francou *et al.*, 2001). While these forms are interesting in their own right as examples of self-organized natural systems (Kessler *et al.*, 2001), they may be even more interesting as indicators of changing environmental conditions which would lead to changing patterns. These can be observed rather inexpensively and over large regions through aerial photographs. A major hurdle in this approach is the objective quantification of observed patterns. While easily recognized and categorized by eye, they are notoriously difficult to cast into numbers which is a prerequisite for quantifying changes. A popular approach to this problem is to interpret the pattern as a realization of some random space function and to estimate its statistical properties, in particular covariance functions of various order and correlation lengths (Journel and Huijbregts, 1978; van Kampen, 1981). A difficulty with this approach is that already moderately complicated patterns require higher order covariance functions which are hard to estimate for natural patterns that in general are not stationary. Alternatively, the pattern may be interpreted as a fractal object whose dimension and generator are to be determined (Mandelbrot, 1977; Bacry *et al.*, 2001). Difficulties here are that there is hardly ever a single underlying generator and that the available data do not cover sufficiently many scales. While both approaches have been demonstrated for describing various patterns they appear less attractive for quantifying patterns in permafrost soils. In this paper, we follow a different approach, interpret the patterns as arbitrary geometric objects and use Minkowski numbers and functions (Mecke, 2000) to characterize them.

THEORY

Minkowski Numbers

A quantitative geometric description aims to reduce the complexity of an object to a limited number of

* Correspondence to: Kurt Roth, Institute of Environmental Physics, INF 229, University of Heidelberg, D-69120 Heidelberg, Germany. E-mail: kurt.roth@iup.uni-heidelberg.de

Received 27 October 2003
Revised 23 March 2005
Accepted 14 April 2005

Copyright © 2005 John Wiley & Sons, Ltd.

relevant quantities. In our context, relevant means that the chosen measures distinguish between characteristic patterns. Such measures should satisfy some basic requirements so that the results obtained for different patterns and by different observers are comparable. Specifically, these requirements are:

Additivity: The results obtained for the unification of two subregions X and Y should be the same as the summation of the results obtained for the individual subregions, properly accounting for their overlap which has been counted twice. For the measure M this may be formulated as $M(X \cup Y) = M(X) + M(Y) - M(X \cap Y)$. Additivity is especially important, since we are typically not in the position to study a given pattern as a whole but are analysing limited regions.

Motion invariance: The results must not change if a given object is moved or rotated, hence are independent of the position of the observer.

Continuity: Small changes of a given object must lead to small changes of the measure. Since imaging techniques are typically afflicted with various types of noise, the measure should be robust in this context.

In the following we assume that the object of interest is the set X of black pixels of some binary structure Ω, hence $X \subset \Omega$. Specifically, the object X might represent stones, vegetation or bare soil and Ω is the image to be analysed. Given such a binary image, integral geometry provides $d+1$ basic measures, where d is the dimension of Ω. These measures are called 'Minkowski numbers' M_k and satisfy the requirements mentioned above. The first measure M_0 is simply the mass of the structural unit, which in two dimensions is its surface area A. Hence

$$M_0(X) = A(X) \tag{1}$$

The other Minkowski numbers are defined through integrals over the boundary ∂X of the object X. Notice that ∂X defines the shape of X unambiguously. In d-dimensional space there are d basic integrals related to the boundary and its $d-1$ principle radii of curvature. For $d=2$ the first integral measures the total length of the boundary,

$$M_1(X) = \int_{\partial X} \mathrm{d}s = L(X) \tag{2}$$

and the second integral measures the total curvature of the boundary,

$$M_2(X) = \int_{\partial X} \frac{1}{r}\mathrm{d}s = C(X) \tag{3}$$

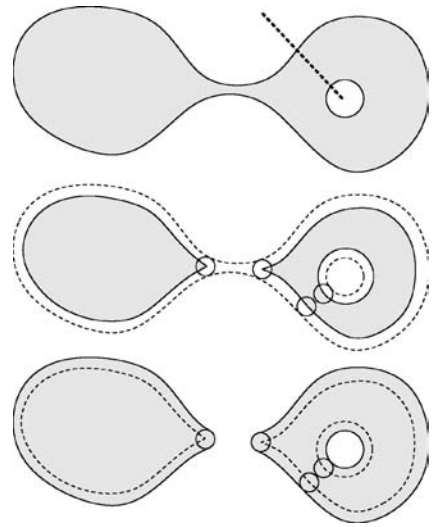

Figure 1 Sketch for Euler number defined in (4) and its change upon opening. The topmost pattern consists of one single object with one redundant connection: cutting along the dashed line removes one connection without generating a new object. Any (topologically) different cut creates a new object, the corresponding connection is thus not redundant. Hence, with (4), $\chi = 0$. The first step to opening this pattern consists of eroding it with a circular element of radius r. This leads to the grey pattern in the middle. The second step consists of dilating, adding a 'skin' of thickness r and produces the pattern at the bottom. Opening with radius r removes all smaller features, here the narrow ridge between the larger patches. For the opened pattern, $\chi = 1$.

where ds is the boundary element and r is its radius of curvature, positive for convex and negative for concave shapes. Notice that the curvature integral equals 2π for each closed convex boundary (objects) and -2π for each closed concave boundary (holes). Thus, M_2 is closely related to the Euler number χ which counts the number N_{object} of isolated objects minus the number N_{hole} of holes within the objects, which are also referred to as loops (see top of Figure 1). In particular

$$\chi(X) = N_{\mathrm{object}} - N_{\mathrm{hole}} = \frac{1}{2\pi} M_2(X) \tag{4}$$

M_2 is a dimensionless topological measure that quantifies the connectivity of the pattern while M_1 and M_0 are metric entities with units [L] and [L^2], respectively.

To compare results obtained from different images, we remove the effect of image size through normalization with respect to the total area A(Ω) of the region considered. Thus, we introduce the Minkowski densities

$$m_k(X) := \frac{M_k(X \cup \Omega)}{A(\Omega)} \tag{5}$$

Copyright © 2005 John Wiley & Sons, Ltd.

as intensive quantities and will use them throughout this paper.

Hadwiger's Theorem

At a first glance, Minkowski numbers appear to be yet another characterization of some properties of a geometric object. What makes them particularly appealing though is a theorem due to Hadwiger (1957), cited in Mecke (2000), which states that any functional $\varphi(X)$ that depends on the object's form alone and that is additive, motion invariant, and continuous may be written as a linear combination of Minkowski numbers. Hence

$$\varphi(X) = \sum_{k=0}^{d} c_k M_k(X) \tag{6}$$

where c_k are real coefficients that depend on the property $\varphi(X)$ but are independent of the object X. Minkowski numbers thus form a complete basis of the space of all these functionals. This is the motivation for using Minkowski densities and density functions for quantifying complex patterns.

Calculation of Minkowski Numbers

Given the binary image of an object where each pixel is either 1 for the object or 0 for the background, the calculation of the Minkowski numbers is straightforward (Ohser and Mücklich, 2000). They can be obtained from a local evaluation of the pixel configuration within a 2×2 neighbourhood at each location within the image. There are $n = 2^4 = 16$ possible configurations q, each of them with a specific contribution to the different Minkowski numbers: (i) the number of pixel belonging to the object is related to M_0, (ii) the number of transitions $1 \leftrightarrow 0$ leads to M_1, and (iii) the number of vertices (pixels), edges and faces, N_v, N_e, and N_f, respectively, is related to $M_2 = 2\pi\chi$ by the classical Euler formula

$$\chi = N_v - N_e + N_f \tag{7}$$

In Figure 2, all 16 configurations q together with their specific contributions $I_k(q)$ are shown. The Minkowski densities may thus be calculated from the frequencies

$$f(q) = \frac{N(q)}{\sum_{q=0}^{15} N(q)} \tag{8}$$

of the different configurations within an image, where $N(q)$ is the number of 2×2 neighbourhoods with

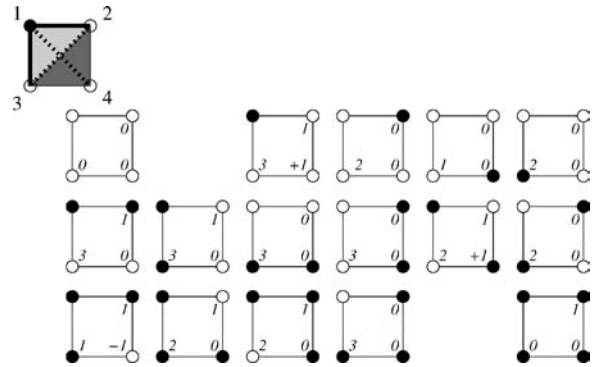

Figure 2 Complete set of the 16 possible pixel configurations in a 2×2 neighbourhood for a two-dimensional binary image. Pixels that belong to the object X are represented by a black circle. For each configuration, its contribution to M_0 (top right), M_1 (lower left), and M_2 (lower right) is given. The mode of evaluation is illustrated in the small figure at top left: For the contribution to M_0 the upper left pixel is considered. For the contribution to M_1 the transitions $1 \leftrightarrow 0$ are counted for the directions indicated by thick lines, including the two dashed ones. For M_2, the upper left vertex (pixel), the solid thick edges (provided they connect two occupied pixels), and the two grey shaded faces (provided they have three occupied vertices) are considered and evaluated according to (7).

configuration q. The Minkowski densities may thus be calculated as

$$m_k = \omega_k \sum_{q=0}^{15} I_k(q) f(q); \quad k = 0, 1, 2 \tag{9}$$

where

$$\omega_0 = \frac{1}{\sum_q f(q)} \tag{10}$$

$$\omega_1 = \frac{\pi}{4} \frac{1}{[\lambda + \sqrt{2}\lambda] \sum_q f(q)} \tag{11}$$

$$\omega_2 = \frac{2\pi}{\lambda^2 \sum_q f(q)} \tag{12}$$

and λ is the side length of 1 pixel. We comment that these weights are correct only for the special case of square pixels and must be adapted for other shapes (Ohser and Mücklich, 2000). Similarly, the pattern to be analysed must be isotropic, without preferred directions, at least microscopically. However, they may be anisotropic macroscopically.

Minkowski Density Functions

The $d+1$ Minkowski densities characterize a particular binary representation of an object. A natural extension is to consider some transformation of the

Copyright © 2005 John Wiley & Sons, Ltd.

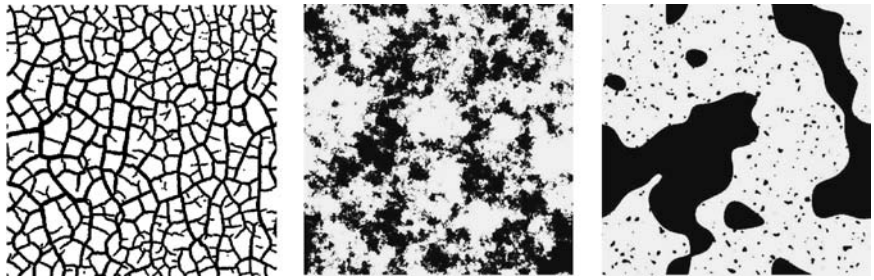

Figure 3 Exemplary 'pure' patterns—single-scale (left), fractal (middle), multiscale (right)—for which the Minkowski functions are shown in Figure 4.

original object or of its binary representation and to calculate Minkowski densities as functions of this transformation's parameter vector **p**. This leads to the Minkowski density functions $m_k(\mathbf{p})$. In this work, we will use three particularly useful transformations:

1. Given a grey-scale image, binary representations are obtained for different values of threshold g_0 and m_k is calculated for them. The resulting functions $m_k(g_0)$ for instance facilitate choosing g_0 such that an optimally and objectively segmented pattern results. The generalization to colour images is straightforward.
2. To study the spatial variability of Minkowski numbers within a given pattern, m_k is calculated locally over a circular region of radius r to obtain $m_k(\mathbf{x}, r)$ for the intersection of the original pattern with a circle of radius r located at **x**. This allows the identification of similar features within a given pattern.
3. To gain insight into the size distribution of features, the original pattern is opened with a circular element of radius r, i.e. all features of the pattern that are smaller than r are removed (Serra, 1982). This transformation is quite powerful, but may not be well-known. It is thus illustrated in the following with some artificial patterns before turning to the real application.

We choose three qualitatively different examples, (i) a single-scale pattern deduced from a cracked soil surface, (ii) a scale-free fractal pattern, and (iii) a multiscale pattern with a discrete hierarchy of scales (Figure 3). For each of these examples, we consider the black part as the pattern to be described. Opening it by radius r consists of two steps: First, it is eroded by radius r, i.e. the fraction that is within a distance r from the interface to the white part is chipped away. Some of the smaller pieces or narrow bridges between larger patches are thereby removed completely as illustrated in Figure 1. In the second step, the remaining black part is dilated, again with radius r, i.e. a 'skin' of thickness r is added. This two-step procedure effectively removes all features smaller than r and leaves the larger ones untouched. With this background, we look at the Minkowski density functions $m_k(r)$ for the three exemplary artificial patterns (Figure 4). Since we are not concerned with the real extent of the structures it is convenient to measure all distances in units of a pixel, which gives the resolution of the pattern. Notice that a 'pixel' usually refers to an area element while we will use the name for the side length of such a (quadratic) element.

First consider the single-scale pattern which essentially consists of a network of black lines that are of roughly equal thickness. Since there are many more closed loops (redundant connections) than isolated objects, the Euler number and thus m_2 is negative. The first opening step leaves the pattern practically unchanged because the surface is rather smooth. Hence, also the Minkowski numbers are practically constant. Increasing r further removes some of the bridges. Since these are roughly linear elements, the area density m_0 and the boundary density m_1 decrease by comparable factors. Removing bridges destroys loops and creates isolated patches. Hence m_2 increases and eventually becomes positive thereby indicating that isolated patches outnumber the redundant connections. We finally notice that the thickest structure in the original pattern has a diameter of 8 pixel: opening with $r = 4$ pixel removes the entire pattern since then $m_0 = 0$.

The second example, the fractal pattern, is of a completely different character. As m_2 reveals and as is quickly confirmed by looking at Figure 3, tiny isolated patches greatly outnumber loops. What is less obvious, however, is that removing these small structures by an opening with $r = 1$ pixel creates a pattern where loops outnumber patches. This swings back once more for $r > 2$ pixel. Concerning the size

Copyright © 2005 John Wiley & Sons, Ltd.

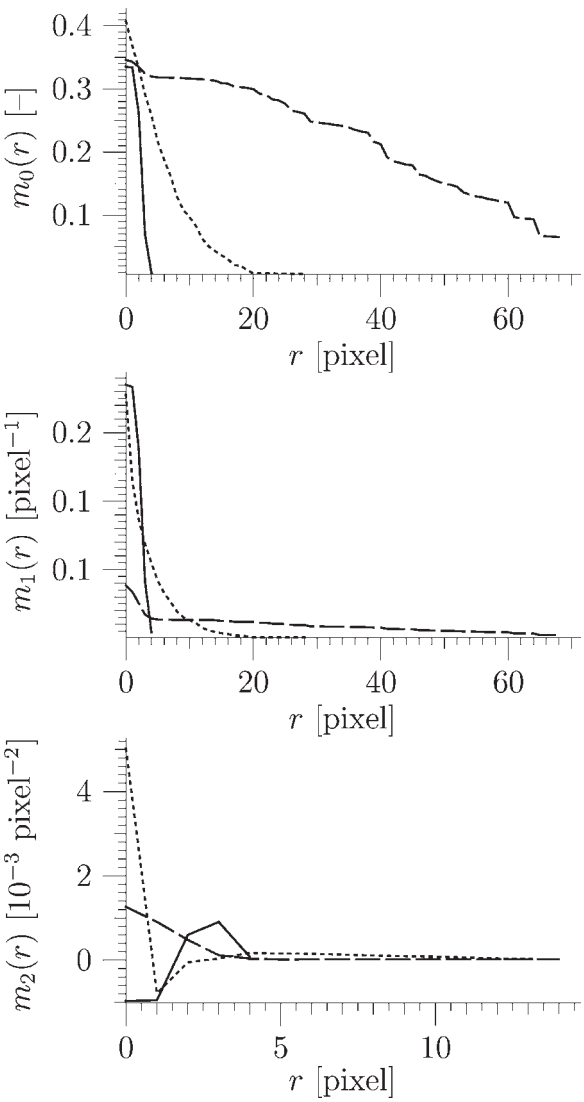

Figure 4 Minkowski density functions for the single-scale (solid), fractal (dotted), and multiscale (dashed) pattern shown in Figure 3. Notice the different scale of r for m_2 as compared to m_0 and m_1.

distribution, we conclude from the continuous decline of m_0 and m_1 with increasing r that the distribution is smooth and that the original pattern has no natural length scale beyond the trivial ones that are given by the size of a pixel and by the extent of the entire region. Plotting $\log(m_0)$ and $\log(m_1)$ versus $\log(r)$ would show if the pattern is indeed a simple fractal and would yield the respective dimensions.

Finally, the third example is revealed as a multiscale pattern by both m_0 and m_1, and m_2 shows that it essentially consists of the superposition of patches. The clearest evidence of the multiscale architecture stems from $m_1(r)$ whose slope changes abruptly at $r = 4$ pixel. The minute change of m_0 for $r < 4$ pixel shows that the areal fraction of these small-scale structures is also small. Based on the information so far, one cannot decide if they result from surface roughness or if they are small isolated patches. However, the rapid decrease of m_2 reveals that the latter is the case. Removing surface roughness would not affect the value of m_2 since no objects are created or removed.

APPLICATION

Permafrost patterns are typically not as uniform as the examples considered above and the base information is in general not in binary form. Nevertheless, Minkowski numbers and functions are a powerful tool for the quantitative analysis and interpretation of such patterns. This is demonstrated in the following for the surface patterns at two permafrost sites that are only a short distance apart. In particular, we focus on the pattern of vegetated areas.

Material

We use aerial images taken on Howe Island (N70°18′, W147°59′), located off the Alaskan Arctic coast, northeast of the Prudhoe Bay oil fields (Figure 5). The surface is loess overlaid by stabilized alluvium. Bare soil, partly encrusted with salt or cryptograms, covers 80–90% of the area. Dominant patterned ground forms are high- or flat-centred ice-wedge polygons tens of metres in size and non-sorted circles, also called mud boils or frost boils with diameters of 1–2 m. The non-sorted circles are either continuous patches of bare soil or are broken into smaller sized polygons with diameters of 0.1–0.4 m. Vegetation, mainly discontinuous prostrate shrubs, inhabits the borders of the bare ground circles and ice-wedge polygonal troughs where water content is higher. The organic layer is thin, typically less than 3 cm.

Aerial images were taken with a digital camera (Olympus C2020) suspended from a kite (Boike and Yoshikawa, 2003). The camera contains an interlaced RGB CCD with 1600×1200 square photo receptors. Images were obtained at the camera's largest focal length, 19.5 mm corresponding to 105 mm for a 35 mm camera, and stored at highest resolution. The ground resolution of the images as calculated from a few reference marks are approximately 37 mm per pixel at site H1 and 29 mm per pixel at site H2. Again, we are not concerned with the real extent of the structures and will measure all distances in units of a pixel.

Copyright © 2005 John Wiley & Sons, Ltd.

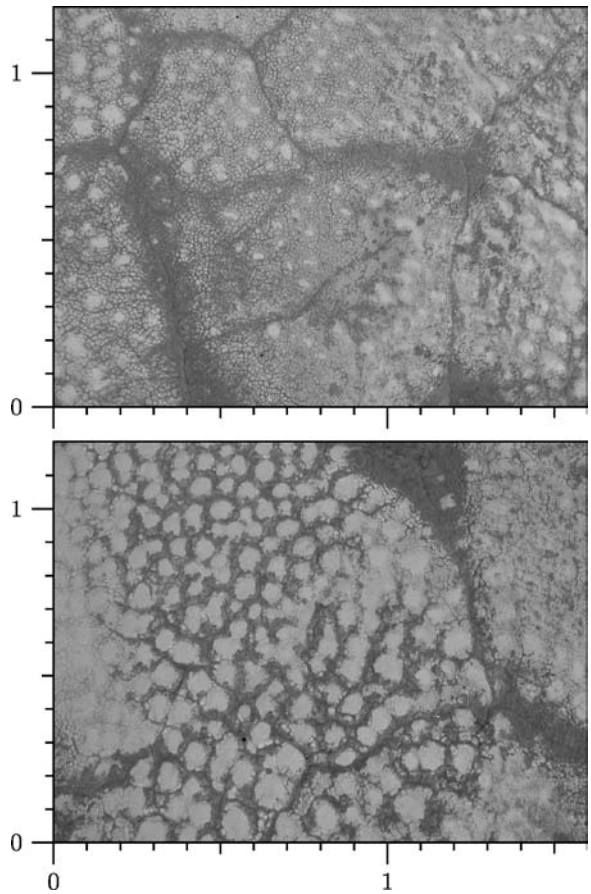

Figure 5 Original aerial images from sites H1 (top) and H2 (bottom). The discontinuous vegetation cover appears darker in contrast to the lighter bare ground, distinguishing the patterned ground features. At site H1, the polygonal ice-wedge network, non-sorted circles and small non-sorted polygons can be distinguished. Site H2 is largely dominated by non-sorted circles, each surrounded by a vegetated border. Distance units at the axes are kpixel with a resolution of some 37 m/kpixel at H1 and 29 m/kpixel at H2.

Prior to analysis, the aerial photographs were processed through the following steps: (i) Transformation of RGB colour image into an eight-bit grey scale representation (256 levels of grey) by averaging the three colour channels. (ii) Stretching contrast of the image such that the darkest 1% of the pixels turn black and the lightest 1% turn white with linear interpolation in between. (iii) The last step, inverting the image, was done only to facilitate the perception of the pattern of interest.

We comment that, for precise quantification, a few more preliminary steps would be required. These include transforming the original image into an orthonormal representation and correcting possible nonuniform illumination. Both steps require a number of reference marks on the ground that are not available for the images used here. Notice that while this renders the numbers obtained from the subsequent analysis less useful for a detailed quantitative analysis, it does not compromise the qualitative comparison of different patterns.

The most crucial step with respect to applications is the segmentation of the image, i.e. the transformation of the grey-scale image into a binary representation since this determines what features will eventually be analysed. In general this will be a rather complicated step that requires input from different colour channels of the image and possibly some ancillary information like surface topography. Since our focus is on pattern analysis, however, we will employ the most simple threshold method. We thus choose an appropriate threshold g_0 for the grey value g and assign the value 0 (white) to pixels for which $g < g_0$ (vegetated surface) and the value 1 (black) to all others (bare surface). For site H1, results of preliminary image processing and segmentation with some distinguished values of g_0 are shown in Figure 6. In the following, we will refer to the black part of the pattern, which corresponds to the bare soil, as the 'black phase'. Consequently, the vegetated soil surface is represented by the 'white phase'.

Dependence of Minkowski Densities on Segmentation Threshold

We consider the black phase of binary representations of sites H1 and H2 to study the dependence $\bar{m}_k$ on the segmentation threshold g_0 (Figure 7). The notation $\bar{m}_k$ is chosen to distinguish the Minkowski densities of the entire pattern from those of subregions which will be introduced in subsequent sections.

As expected, $\bar{m}_0$, which equals the area fraction of the black phase, increases monotonically with g_0. It actually is the probability distribution function of the grey values. Apparently, the area fraction increases more rapidly for smaller values of g_0 at site H2 than at H1. This results from the large patches of bare soil that also stand out in Figure 5.

The number $\bar{m}_1$ corresponds to the length density of the interface between the black and white phases. For the type of regular structure considered here, $\bar{m}_1$ may be expected to be small for extreme values of g_0 since the corresponding patterns consist mainly of small black or white patches. Provided the character of the interface, in particular its variation, does not depend on g_0 there will be a monotonic relation between the area of an object and its interface length. As long as the patches remain isolated, we thus expect

Copyright © 2005 John Wiley & Sons, Ltd.

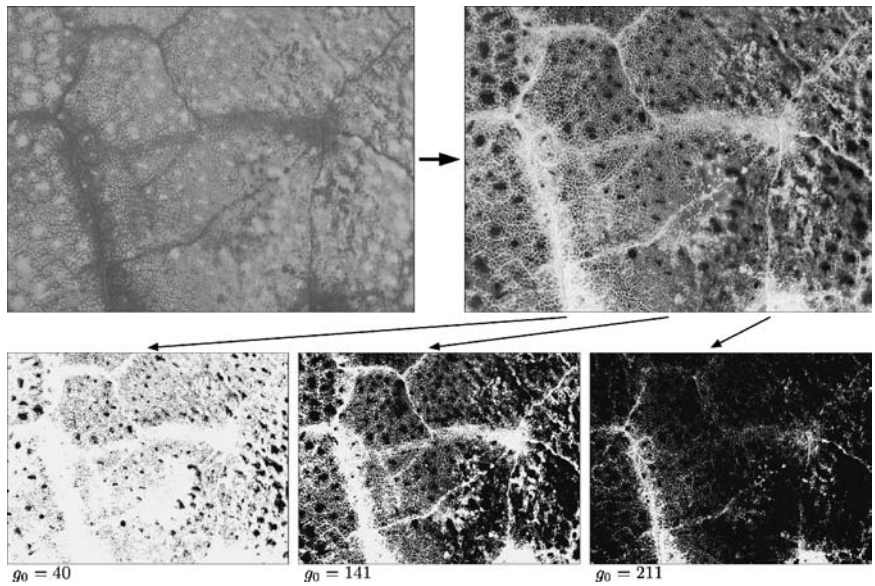

Figure 6 Preliminary image processing consists of transformation from RGB to grey scale (upper left), contrast stretching, and inversion (upper right). Segmentation with threshold g_0 then leads to a binary representation of the pattern (bottom row). The value of g_0 is chosen such that m_2 is maximal ($g_0 = 49$), zero ($g_0 = 141$), and minimal ($g_0 = 211$), respectively.

a monotonic increase of $\bar{m}_1$ as g_0 departs from the extreme value. This general behaviour is realized at both sites. For intermediate values of g_0, the shape of $\bar{m}_1(g_0)$ reflects the respective gains and losses of interfacial area as new objects occur and coalesce, respectively. The two sites show marked differences in that the two overlapping peaks for site H2 indicate the existence of two separate classes of objects with different brightnesses whereas the single-peaked shape for site H1 hints at a more uniform distribution of brightnesses.

We finally consider $\bar{m}_2$ which is proportional to the Euler number of the black phase. We recall that $\bar{m}_2$ is a topological quantity, in contrase to $\bar{m}_0$ and $\bar{m}_1$ which are metric quantities. In two dimensions, it gives the difference between the numbers of isolated objects and redundant connections, divided by the total area. As already noted in the previous paragraph, for extreme values of g_0 we expect the pattern to consist predominately of isolated patches (see Figure 6). These will be black patches for small values, representing isolated objects, and white patches for large values, corresponding to holes, hence to redundant connections. Thus, $\bar{m}_2$ is expected to be positive for small values of g_0 and negative for large ones. With g_0 departing from its extremes, the number of objects will initially increase, leading to a corresponding increase of the magnitude of $\bar{m}_2$. Eventually, with g_0 departing further, more isolated black and white objects will merge than there are created and the magnitude of $\bar{m}_2$ will decrease. We thus expect to find at least two extrema in $\bar{m}_2(g_0)$, one positive towards small values of g_0 and one negative towards large values. For both sites, this general shape is clearly discernible in the lower graph of Figure 7. For intermediate values of g_0, we may expect quite some variability for the shape of $\bar{m}_2(g_0)$ between different sites, as is already the case for the two sites considered here. Looking at H2, we find from $\bar{m}_0$ that the area fraction with grey values in the interval (100,150) is about 0.15 and that also the length of the interface as shown by $\bar{m}_1$ changes significantly in this interval. However, $\bar{m}_2$ is approximately constant in this interval which means that if the number of objects changes at all, this change is balanced by the number of redundant connections. This indicates that the topology of the black phase does not change significantly in this interval. The situation is quite different at site H1, where we find a continuous change of the metric and of the topological quantities.

As a final remark, we notice that the functions $\bar{m}_k(g_0)$ are approximately orthogonal, i.e.

$$\sum_{i=0}^{255} \left[\bar{m}_j(i) - \langle \bar{m}_j \rangle\right]\left[\bar{m}_k(i) - \langle \bar{m}_k \rangle\right] \approx 0, \quad j \neq k \quad (13)$$

where $\langle \bar{m}_j \rangle := 256^{-1} \sum_{i=0}^{255} \bar{m}_j(i)$. This means that the three functions $\bar{m}_k(g_0)$ contain approximately

Copyright © 2005 John Wiley & Sons, Ltd.

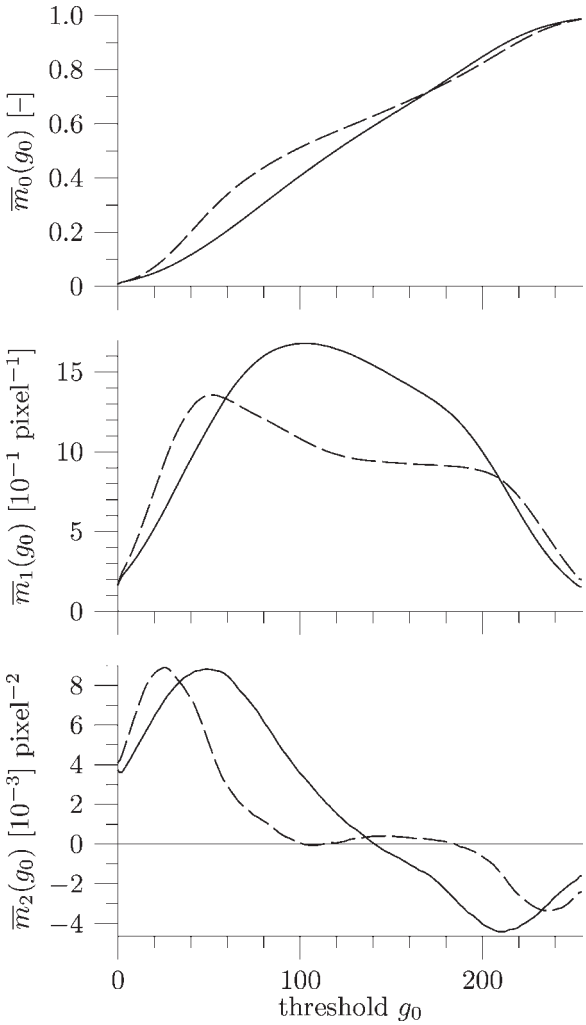

Figure 7 Global Minkowski density functions $\bar{m}_k(g_0)$ for the black phase of binary representations of H1 (solid) and H2 (dashed).

independent information on the pattern as a whole. Notice that this is a different statement from Hadwiger's theorem which only refers to the binary representation of the pattern for a particular value of g_0. Clearly, these functions cannot reveal detailed structures of the image but rather are lowest order descriptions. Their use would be analogous to that of statistical moments for characterizing probability density functions. It appears to be worthwhile to explore to what extent different patterns occurring in nature can be categorized simply by the shape of the corresponding Minkowski density functions $\bar{m}_k(g_0)$. Obviously, a quantitative exploration of this requires carefully normalized images which in turn demands a set of reference marks on the ground. However, if these are not available, as will often be the case, qualitative comparison is possible even with the type of rough normalization described in Material. We will not follow this line here, however, and proceed to analyse the spatial structure in more detail.

Spatial Variability of Minkowski Densities

Natural patterns often contain elements on different scales as is also the case for the two permafrost sites considered here. It is thus useful to calculate the Minkowski densities not only for the entire field of view but also for subregions. The first question arising concerns the size of these subregions. As a pragmatic approach, we employ the concept of the representative elementary volume (REV), choose circular subregions with radius r, calculate m_k at different locations as a function of r, and choose r such that the circle encompasses small-scale variations but is not yet affected by large-scale variations. Figure 8 shows $m_k(r)$ for a few typical locations at H1 with $g_0 = 141$. For small values of r, less than 30 say, m_k strongly depends on the immediate neighbourhood and thus fluctuates strongly with r. However, with increasing values of r, $m_k(r)$ often approaches a rather constant value that is representative for the small-scale patterns. In some instances, m_k becomes stable only for very large values of r. These typically correspond to locations that are near the boundary between some large-scale features. From Figure 8, we choose $r = 50$ as a reasonable radius for an REV.

With an REV in hand, we explore the spatial variability of the Minkowski densities by assigning to each location $\mathbf{x}$ the value of m_k in the REV centred at $\mathbf{x}$. Figure 9 shows the resulting density functions for the black phase of H1 with segmentation threshold $g_0 = 141$.

We first notice that the large-scale features of the pattern are visible in all three Minkowski densities even though the details are characteristically different. Easiest to interpret is m_0, which in two dimensions equals the areal density of the phase considered. It clearly identifies regions of extended vegetated patches (low values of m_0), of extended bare patches (high values of m_0), and of the rather wide transition regions between. Obviously, we lack the spatial resolution of the original image and thus cannot say anything about the structures of the transition regions which could be larger isolated lumps as well as finely interweaved phases. This information is to some extent contained in the Minkowski densities m_1 and m_2, however.

In regions with extreme values of m_0 either the black or the white phase dominates strongly.

Copyright © 2005 John Wiley & Sons, Ltd.

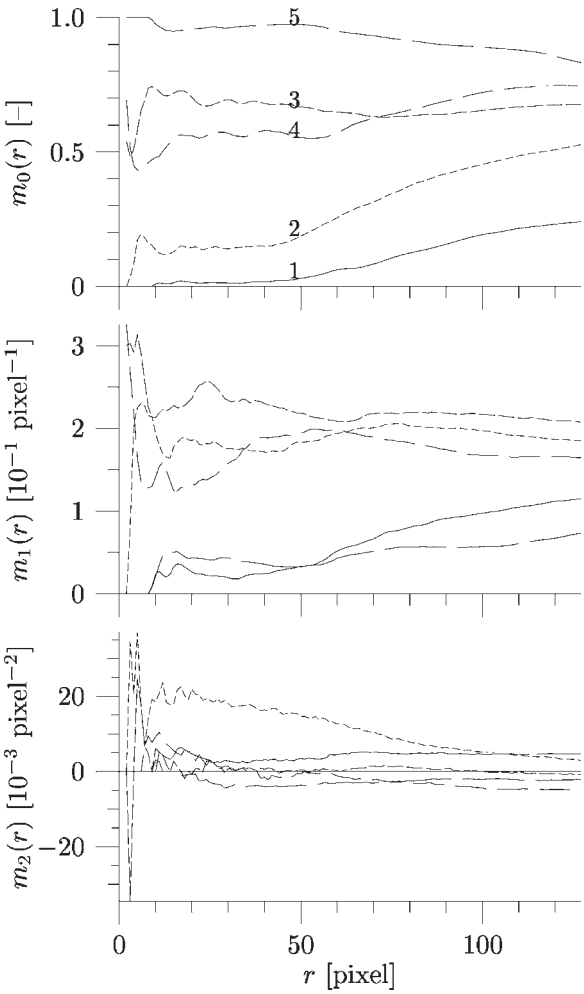

Figure 8 Typical examples for the dependence of Minkowski densities m_k *on radius* r of circular subregions (black phase of H1 for $g_0 = 141$). The numbers that identify the curves in the top graph correspond to the locations given in Figure 9.

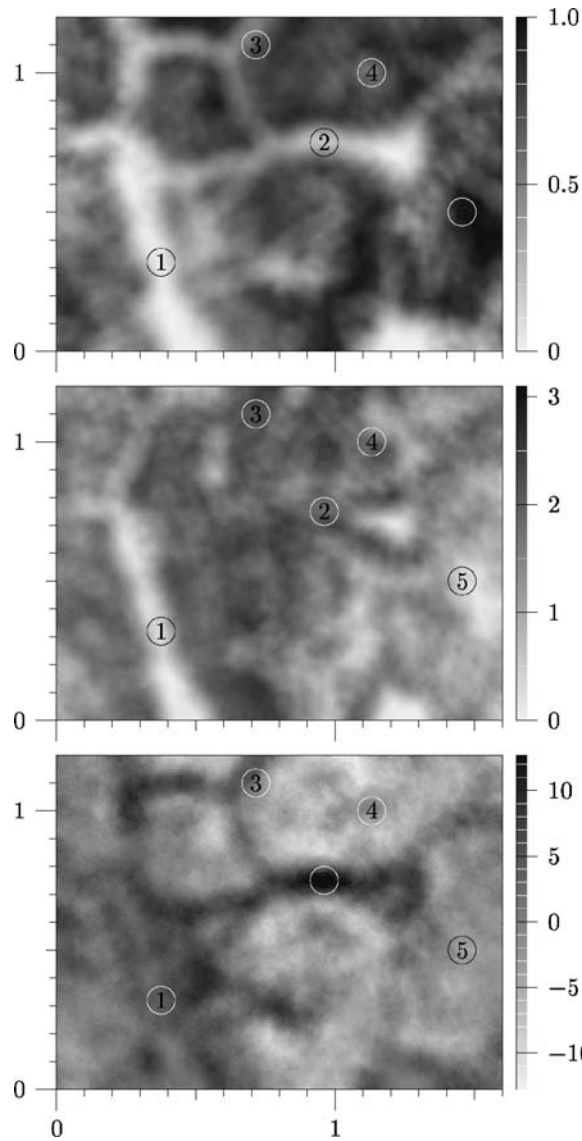

Figure 9 Spatial variability of Minkowski densities m_0 (top), m_1 [10^{-1} pixel^{-1}] (middle), and m_2 [10^{-3} pixel^{-2}] (bottom) for the black phase of H1 with threshold $g = 141$. The corresponding pattern is shown in the upper left of Figure 10. Numbers are calculated for circular areas with radius $r = 50$ pixel and plotted with a resolution of 10 pixel. Axes are labelled in kpixel. Numbered circles identify locations with radius $r = 50$ pixel used for Figure 8.

Correspondingly, the density of interfaces between them is small. Examples are the regions around $\mathbf{x} = (1.2, 0.7)$ and $\mathbf{x} = (1.5, 0.45)$ where m_0 is smaller than 0.1 and larger than 0.9, respectively. In both regions, we find values of m_1 that are more than an order of magnitude smaller than the largest values at this site. Transition regions on the other hand, with values of m_0 around 0.5, may contain high or low densities of interfaces, depending on the arrangement of the phases. Examples for regions with comparable values of m_0 but quite different values of m_1 are around $\mathbf{x} = (0.7, 0.35)$ and $\mathbf{x} = (1.3, 0.5)$.

Further information about small-scale structures, namely about their connectivity, is contained in m_2 which in two dimensions is proportional to the difference between the number of isolated objects and the number of redundant connections of the black phase. Regions with comparable values of m_0 and m_1 may thus be discriminated with respect to m_2. An example is provided by the surroundings of $\mathbf{x} = (0.45, 0.65)$

Copyright © 2005 John Wiley & Sons, Ltd.

and $\mathbf{x} = (1.1, 1.0)$. We further find that the black phase, which corresponds to the bare soil regions, consists of predominantly isolated objects near the boundaries of the large-scale features while in their interior the black phase is connected.

Of course, visual inspection also provides the information just outlined. The advantage of using Minkowski densities is that we can easily quantify such subjective impression and that inspection can be performed automatically, thereby facilitating the precise monitoring of large areas.

Comparing Sites

We compare the binary representations of H1 with $g_0 = 141$ and of H2 with $g_0 = 102$, respectively, which are shown in Figure 10. These values are chosen such that $\bar{m}_2 \approx 0$ for the global pattern at the respective site (see Figure 7). The density functions $m_0(\mathbf{x}), \ldots, m_2(\mathbf{x})$ are shown in the top rows of Figures 11–13 with the same resolution as used for Figure 9. As already mentioned, m_0 discriminates between solid patches and open transitional regions. Obviously, the forms of the transitional regions differ considerably between the two sites, with an apparent multiscale organization at H1 and dominating single scale shapes at H2. While this is reflected in considerably larger interface densities at H1 as compared to H2 (see also Figure 14 with $r = 0$) the difference is most pronounced in the spatial variation of m_2. At H1, the connectivity varies greatly in space. Regions with a highly connected black

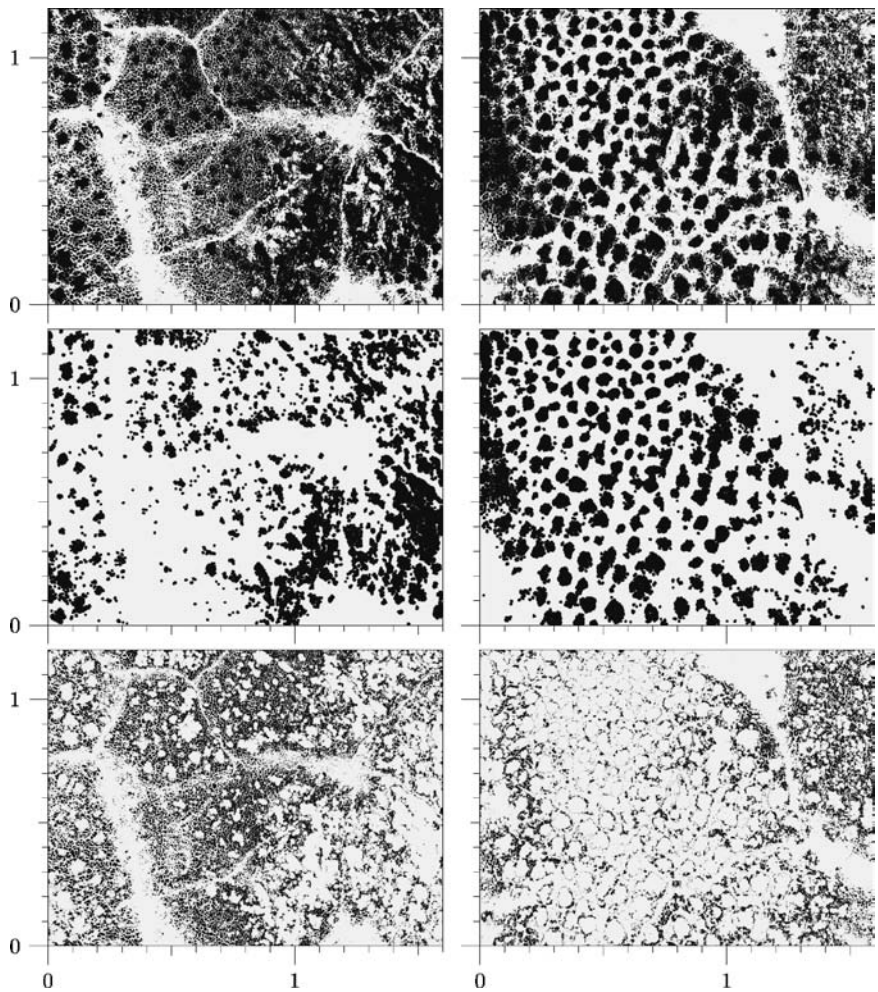

Figure 10 Binary representations of H1 with $g_0 = 141$ (left column) and of H2 with $g_0 = 102$ (right column) before (top row) and after (middle row) opening with a circular element of radius 5 pixel. The bottom row shows the difference between the original and the opened pattern, i.e. those parts of the patterns are smaller than a circle with $r = 5$ pixel. Axes are again in kpixel.

Copyright © 2005 John Wiley & Sons, Ltd.

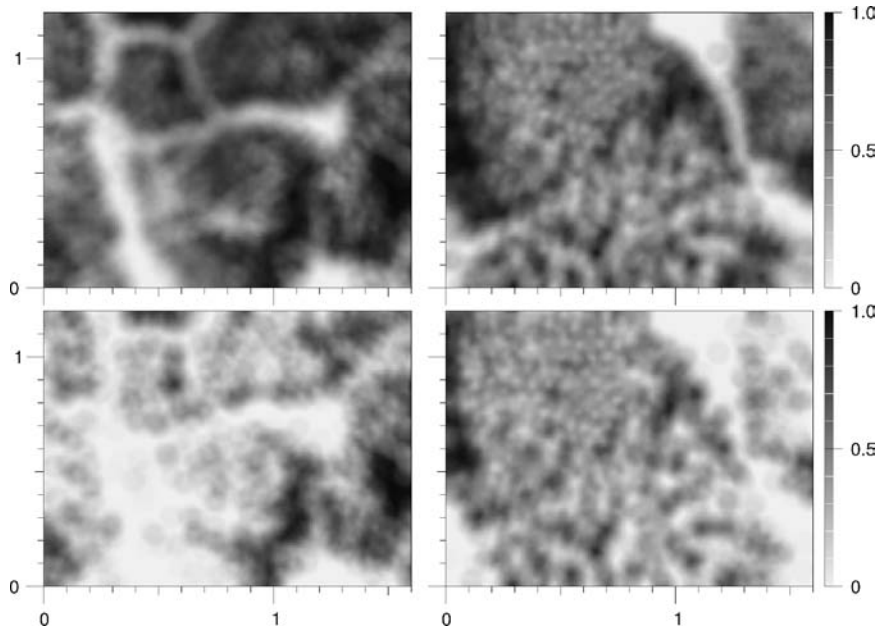

Figure 11 Minkowski density m_0—the area fraction of black phase—for the original patterns shown in the top row of Figure 10 (top row) and for the patterns opened with $r = 5$ pixel shown in the middle row of Figure 10 (bottom row). The left column is for site H1, the right one for H2. Grey-scale is dimensionless.

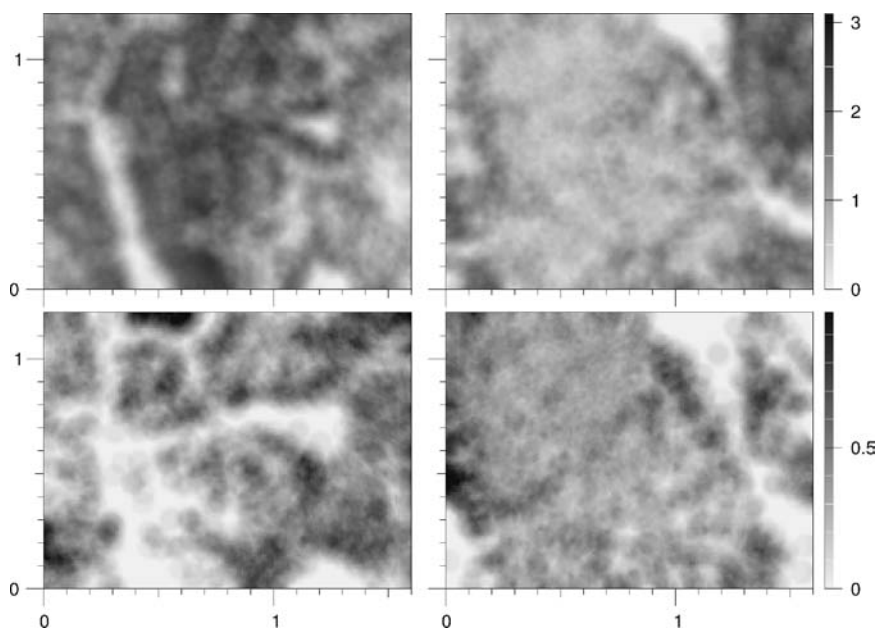

Figure 12 As Figure 11 but for Minkowski density m_1, the surface density. Notice the different grey scales. Their units are 10^{-1} pixel^{-1}.

Copyright © 2005 John Wiley & Sons, Ltd.

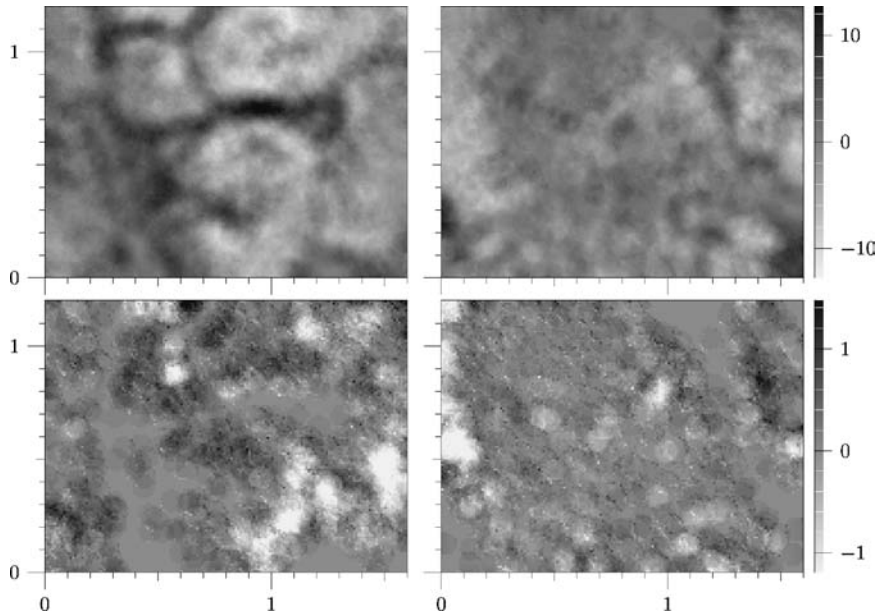

Figure 13 As Figure 11 but for Minkowski density m_2, the Euler number density. Notice the different grey scales. Their units are $10^{-3}\,\mathrm{pixel}^{-2}$.

phase, $m_2 > 10^{-2}\,\mathrm{pixel}^{-2}$, are adjacent to regions where the black phase essentially consists of isolated objects, $m_2 < -10^{-2}\,\mathrm{pixel}^{-2}$. At H2 in contrast, m_2 is rather uniform over most of the field with values between $\pm 10^{-3}\,\mathrm{pixel}^{-2}$.

As pointed out above, a more detailed analysis is possible by looking at opened patterns for which elements that are smaller than a circle with some radius r are removed. Opening has three effects on a pattern: (i) interfaces are smoothed which reduces their length, (ii) narrow bridges between larger patches are removed which tends to increase the number of isolated objects and at the same time to reduce the number of redundant connections, and (iii) small objects are removed entirely. Clearly, the impact of opening depends strongly on the organization of a pattern, as is illustrated by the bottom row of Figure 10 where those features are depicted that disappear upon opening with $r = 5$ pixel. Opening the pattern removes 55% of the black phase at H1, $\bar{m}_0$ decreases from 0.60 to 0.28, but only 36% at H2 (Table 1). Corresponding to the decrease in $\bar{m}_0$ and the interfacial smoothing, we also find a strong decrease of the interfacial length density $\bar{m}_1$ which decreases to 23% of its original value at H1 and 32% at H2. We remark that in contrast to $\bar{m}_0$, $\bar{m}_1$ need not decrease with opening, although it usually will with the type of patterns considered here. While $\bar{m}_0$ and $\bar{m}_1$ are typically found to be monotonically decreasing functions of the opening radius, $\bar{m}_2$ will in general be of a rather complicated form. The reason for this is that opening removes small isolated objects, thereby reducing $\bar{m}_2$, but also removes narrow bridges which creates new objects and reduces connections, causing $\bar{m}_2$ to increase.

More important than the different average changes of $\bar{m}_0$ at the two sites, however is that the opening at H1 removes an entire feature of the pattern, namely the small polygonal bare patches along the boundary between the largest structures (see bottom row of Figure 10). In contrast, opening at H2 leads to rather minor modifications, mostly to interface smoothing. This difference is also manifest in the spatial structure of the Minkowski densities (bottom rows of Figures 11–13). At H1, the original large regions of rather compact black phase have almost disappeared with only small patches remaining (Figure 11), the regions with negligible interfacial length density are greatly enlarged (Figure 12), and the connectivity patterns change completely with some highly connected regions transformed into ones with predominantly isolated objects, for instance near $\mathbf{x} = (0.8,1.0)$ (Figure 13). In contrast, the changes at H2 are rather moderate with the overall structure hardly affected over most of the region. An exception to this are small regions, for instance around $\mathbf{x} = (0.1,0.6)$ and $\mathbf{x} = (1.5,0.8)$, which are structurally more similar to H1. This comparison demonstrates the power of Minkowski densities to

Copyright © 2005 John Wiley & Sons, Ltd.

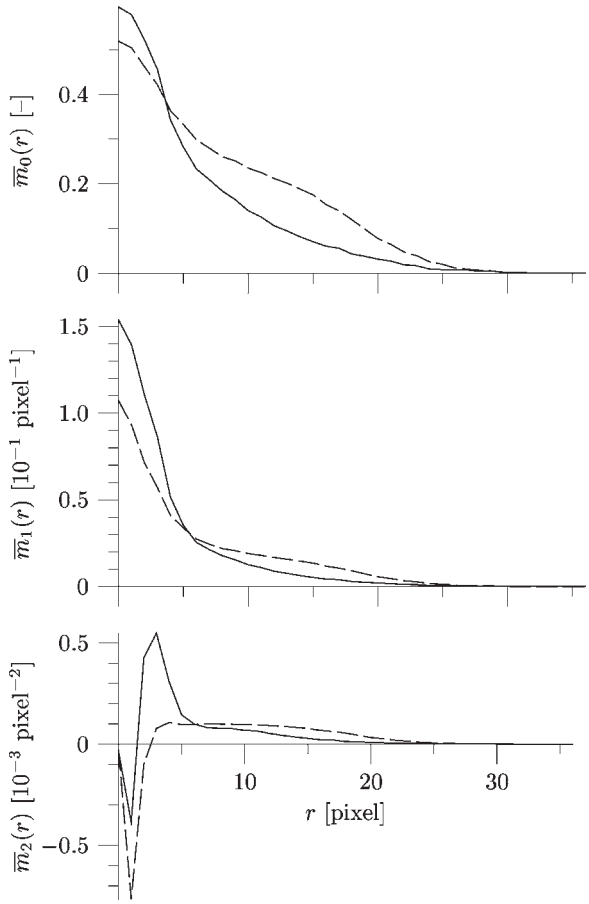

Figure 14 Minkowski densities $\bar{m}_k$ as functions of the opening radius r at sites H1 (solid) and H2 (dashed).

identify and quantify multiscale organizations of patterns as they are encountered at H1 but not at H2.

We comment that the analysis just presented could be sharpened further by discriminating between different sub-patterns and by then restricting the calculation of m_k(x) to similar sub-patterns. Figure 10 shows for instance that the top right corner at H2 is structurally more similar to the pattern found predominantly at H1 than to the rest of the pattern at H2. Such a discrimination could be readily automated since the patterns can be distinguished based on their Minkowski densities.

Table 1 Global values of Minkowski densities $\bar{m}_k$ before and after opening by a circle with radius of 5 pixel.

k	H1	H2	H1$^{\text{open}}$	H2$^{\text{open}}$	Units
0	0.60	0.52	0.28	0.33	1
1	1.54	1.07	0.35	0.34	10^{-1} pixel^{-1}
2	−0.038	0.032	0.144	0.096	10^{-3} pixel^{-2}

Minkowski Density Functions

We consider the global Minkowski densities $\bar{m}_k$ as functions of the opening radius r, again for binary representations of H1 with $g_0 = 141$ and of H2 with $g_0 = 102$ (Figure 14). The multiscale organization of the pattern at H1 postulated in the previous section becomes further manifest in that both $\bar{m}_0$ and $\bar{m}_1$ decrease rather rapidly for $r < 6$ pixel and tail off for larger values of r. In comparison, the decrease at H2 is more gradual. An even stronger discrimination between the two sites is apparent in $\bar{m}_2$. The initial opening step makes $\bar{m}_2$ more negative at both sites, although the effect is much stronger at H2 than at H1. Inspection of the images (not shown) reveals that the strong decrease of $\bar{m}_2$ results from a large number of small objects that get removed even though some redundant connections also disappear. At H2, the following opening steps let $\bar{m}_2$ jump to slightly positive values where it remains practically constant for $3 \leq r < 12$ and decreases slowly to 0 afterwards. This indicates that for a rather extended range of sizes, the topology of the pattern remains constant. At H1, in contrast, opening beyond the first step leads to a very strong increase of $\bar{m}_2$ which is caused by the creation of isolated objects by eroding away narrow necks with widths between 2 and 4 pixel. These newly formed isolated objects are rather small, however, and disappear rapidly upon further opening. With $r > 5$ pixel, $\bar{m}_2$ continues to decrease, but at a more moderate rate.

As an aside, we comment that log-log plots of $\bar{m}_0$ and $\bar{m}_1$ at the two sites show that the interfacial length density at H2 may follow a power law distribution, but that the other quantities are of a more complicated form. The underlying patterns thus cannot be described as simple fractals.

SUMMARY AND CONCLUSIONS

We have introduced Minkowski densities and density functions as tools for quantifying patterns and demonstrated them by analysing three artificial patterns. We then applied them to aerial images obtained from pattered ground at two neighbouring permafrost sites. Although these tools cannot rival our visual perception in discriminating and possibly also in categorizing natural patterns, they do have two significant advantages:

1. They can be performed automatically and thus facilitate the analysis of very large data sets as

Copyright © 2005 John Wiley & Sons, Ltd.

for instance produced by high-resolution satellite imagery. Automated analysis is typically most efficient with some initial manual adjustment of parameter ranges, most importantly for thresholds and averaging areas in case of spatially varying patterns. However, even those steps can be automated with more sophisticated algorithms that implement and combine the analyses that led to Figures 7 and 8. Exemplary visual inspection of the results will remain mandatory as with all automated procedures.

2. They are quantitative, hence allow us to monitor transitions in space and changes in time in an objective manner that does not depend on the interpreter's experience and form. This also facilitates comparisons of patterns from different sites.

We should comment in closing that the methods introduced here reduce an arbitrary pattern to a few numbers or at most to a few functions. Clearly, a huge fraction of the information contained in the pattern is thereby lost and it will, in particular, not be possible to recreate the pattern from the reduced information. Such data reductions are well known from statistical analyses where rich data sets are reduced to their first few moments, e.g. mean and variance, and the corresponding functions, e.g. the autocovariance. The power of such reductions is their focusing on just a few aspects and in eliminating all the others. They are only useful to the extent that the focused aspects are of interest. However, since areal fractions, interface densities, connectivities, and distances to interfaces are relevant for many functional aspects of a permafrost environment, Minkowski numbers and functions are proposed as a useful tool for quantifying the observed patterns.

Implementations of the tools used in this work are contained in the public domain package QuantIm which may be obtained from www.iup.uni-heidelberg.de/institut/forschung/groups/ts/tools.

ACKNOWLEDGEMENTS

Thanks to D. A. (Skip) Walker, Vladimir Romanvosky, Chien-Lu Ping, and Martha (Tako) Raynolds of the research project 'Biocomplexity on frost boil ecosystems' who supported field work and provided valuable discussion on the site. JB gratefully acknowledges financial support by the Deutsche Akademie der Naturforscher Leopoldina (BMBF-LPD 9901/8-11). An anonymous reviewer helped us greatly to improve the accessibility of the somewhat abstract concepts.

REFERENCE

Bacry E, Delour J, Muzy JF. 2001. Multifractal random walk. *Physics Review E* **64**(026103): 1–4.

Boike J, Yoshikawa K. 2003. Mapping of periglacial geomorphology using kite/balloon aerial photography. *Permafrost and Periglacial Processes* **14**(1): 81–85. DOI: 10.1002/ppp.437

Francou B, Méhauté NL, Jomelli V. 2001. Factors controlling spacing distances of sorted stripes in a low-latitude, alpine environment (Cordillera Real, 16°S, Bolivia). *Permafrost and Periglacial Processes* **12**: 367–377. DOI: 10.1002/ppp.398

Hadwiger H. 1957. *Vorlesungen über Inhalt, Oberfläche und Isoperimetre*. Springer-Verlag: Heidelberg.

Hallet B. 1990. Self-organization in freezing soils: from microscopic ice lenses to patterned ground. *Canadian Journal of Physics* **68**: 842–852.

Journel AG, Huijbregts C. 1978. *Mining Geostatistics*. Academic Press: San Diego.

Kessler MA, Murray AB, Werner BT, Hallet B. 2001. A model for sorted circles as self-organized patterns. *Journal of Geophysical Research* **106**(B7): 13287–13306.

Mandelbrot B. 1977. *The Fractal Geometry of Nature*. Freeman: New York.

Mecke KR. 2000. Additivity, convexity, and beyond: applications of Minkowski functionals in statistical physics. In *Statistical Physics and Spatial Statistics. The Art of Analyzing and Modeling Spatial Structures and Pattern Formation*, Mecke KR, Stoyan D (eds). Springer Verlag: Berlin; Lecture Notes in Physics 554, 111–184.

Ohser J, Müucklich. 2000. *Statistical Analysis of Microstructures in Materials Science*. John Wiley & Sons: New York.

Serra J. 1982. *Image Analysis and Mathematical Morphology.* Academic Press: London.

van Kampen NG. 1981. *Stochastic Processes in Physics and Chemistry.* North-Holland: Amsterdam.

Copyright © 2005 John Wiley & Sons, Ltd.

Chapter 5

Chapter 5.1

Krinner, G. and **Boike, J.** (2010): A study of the large-scale climatic effects of a possible disappearance of high-latitude inland water surfaces during the 21st century, *Boreal Environment Research* 15, 203-217.

BOREAL ENVIRONMENT RESEARCH 15: 203–217
ISSN 1239-6095 (print) ISSN 1797-2469 (online)
© 2010
Helsinki 30 April 2010

A study of the large-scale climatic effects of a possible disappearance of high-latitude inland water surfaces during the 21st century

Gerhard Krinner[1)2)] and Julia Boike[1)]

[1)] *Alfred-Wegener-Institut für Polar- und Meeresforschung, Forschungsstelle Potsdam, Postfach 60 01 49, D-14401 Potsdam, Germany*
[2)] *Laboratoire de Glaciologie et Géophysique de l'Environnement (LGGE), INSU-CNRS et UJF Grenoble, 54 rue Molière, BP 96, F-38402 St Martin d'Hères Cedex, France*

Received 25 Feb. 2009, accepted 6 May 2009 (Editor in charge of this article: Veli-Matti Kerminen)

Krinner, G. & Boike, J. 2010: A study of the large-scale climatic effects of a possible disappearance of high-latitude inland water surfaces during the 21st century. *Boreal Env. Res.* 15: 203–217.

This study evaluates the climatic impact of possible future changes in high-latitude inland water surface (IWS) area. We carried out a set of climate-change experiments with an atmospheric general circulation model in which different scenarios of future changes of IWS extent were prescribed. The simulations are based on the SRES-A1B greenhouse gas emission scenario and represent the transient climatic state at the end of the 21st century. Our results indicate that the impact of a reduction in IWS extent depends on the season considered: the total disappearance of IWS would lead to cooling during cold seasons and to warming in summer. In the annual mean, the cooling effect would be dominant. In an experiment in which the future change of prescribed IWS extent is prescribed as a function of the simulated changes of permafrost extent, we find that these changes are self-consistent in the sense that their effects on the simulated temperature and precipitation patterns would not be contradictory to the underlying scenario of changes in IWS extent. In this "best guess" simulation, the projected changes in IWS extent would reduce future near-surface warming over large parts of northern Eurasia by about 20% during the cold season, while the impact in North America and during summer is less clear. As a whole, the direct climatic impact of future IWS changes is likely to be moderate.

Introduction

Wetlands, lakes and ponds are a typical feature of northern ecosystems of Canada, Alaska and Siberia. These water bodies are under discussion as important carbon sinks or sources (e.g. Zimov *et al.* 1997, Oechel *et al.* 2000, Chapin *et al.* 2000, Walter *et al.* 2006, Walter *et al.* 2007), ecological niches (Gilg *et al.* 2000) and also play an important role in the local and regional climate and hydrology by governing the heat and water fluxes (e.g. Bonan 1995, Lofgren 1997, Krinner 2003, Gutowski *et al.* 2007). For example, Boike *et al.* (2008) found a 50% decrease of latent heat fluxes during dry summer at a Siberian wetland site due to a negative water balance and thus disappearing polygonal ponds. Despite this significance, there are few studies available on their formation and degradation processes associated with climate change. For example, using satellite

images, Smith *et al.* (2005) stated a 6% declination of lake surface area (1973–1998) in Siberia despite a concomitant precipitation increase. The deficit averages a greater loss of lakes in the discontinuous permafrost zone (13%) as compared with the gain in the continuous permafrost zone (12%). Riordan *et al.* (2006) observed an 11% decrease of closed ponds in the Alaskan subarctic for the past 50 years concomitant with an increasing air temperature and thus hypothesized enhanced evapotranspiration. Yoshikawa and Hinzman (2003) reported shrinking lakes on the Seward Peninsula in Alaska due to the loss of water through the thawing of permafrost. Jorgenson *et al.* (2006) reported a large increase of permafrost degradation (thermokarst) and pit density from 1989 to 1998 especially in ice wedge areas of northern Alaska. A study from the Canadian High Arctic on Ellesmere Island (Smol and Douglas 2007) demonstrated that ponds that existed for several millennia are now drying. The authors attributed this to changes in the evapotranspiration/precipitation ratio. Thus, an understanding of potential processes causing these changes in water surface extent is still required for local and regional scales.

Transitions between drier steppe-like surfaces and peatland-lake dominated surfaces are not uncommon throughout the Earth's history. During the last maximum (21 ky BP) the arctic landscape was characterized by arctic desert and steppe vegetation with very few lakes (Overduin *et al.* 2007). With the beginning of warming and deglaciation (starting about 15 kyr ago), the number of thermokarst lakes and the areal extent of peatlands increased exponentially to the wet conditions of the Holocene optimum (Walter *et al.* 2007). Thermokarst lake formation and expansion waned in the later Holocene. The formation of thermokarst lakes and their methane emission is currently discussed as the main factor for high methane levels at about 12 kyr ago in ice cores from Greenland and Antarctica (Walter *et al.* 2007, Petrenko *et al.* 2008).

The climatic impact of inland water surfaces (henceforth IWS) depends on the season and on the regional climate itself. In a fairly general way, it can be stated that, due to their high effective thermal inertia, IWS will tend to respond more slowly than normal continental soil to the seasonal forcing, and thus induce a lag in the surface seasonal temperature cycle and reduce its amplitude (e.g. Bonan 1995, Krinner 2003). When IWS replace normal continental soil, there will almost always be a local tendency towards a modified partitioning between sensible and latent turbulent surface fluxes (Pitman 1991). However, the impact of IWS on the hydrological cycle is much more difficult to predict and depends very much on the climate itself and on regional circulation patterns. On one hand, the presence of IWS can cause an intensification of the hydrologic cycle in dry conditions (e.g., Hostetler *et al.* 1994, Krinner *et al.* 2003). On the other hand, the cooling effect of IWS during summer can induce a stabilization of the atmosphere downstream, and thus lead to reduced precipitation rates (e.g. Lofgren 1997). In paleoclimate studies, it has been shown that ice-dammed lakes can either lead to a more positive surface mass balance of the adjacent ice sheet via reduced marginal melt rates in summer due to their cooling effect (Krinner *et al.* 2004), or to more negative ice sheet surface mass balances because of precipitation reductions as a consequence of the more stable structure of the lower atmosphere (Hostetler *et al.* 2000). It is therefore not obvious that the climatic impact of IWS, evaluated for the present in several climate model studies (e.g. Pitman 1991, Bonan 1995, Lofgren 1997, Krinner 2003), will be similar to today's in a possibly warmer future climate, particularly if one keeps in mind that the future climate change is expected to be particularly strong in the high latitudes (IPCC 2007).

Here we carry out atmospheric general circulation model simulations for the end of the 20th century and for the end of the 21st century to assess the impact of a potential future reduction of IWS extent in the boreal continental areas (in this paper, the word "boreal" refers to all ice-free continental regions polewards of the southern limit of the taiga). The simulations are based on the SRES (IPCC Special Report on Emission Scenarios: Nakicenovic *et al.* 2000) A1B greenhouse gas emission scenario. We are particularly interested in impacts on the influence of IWS on the energy and water cycle. The main question is to what degree this potential reduction of IWS could affect the expected climate change during

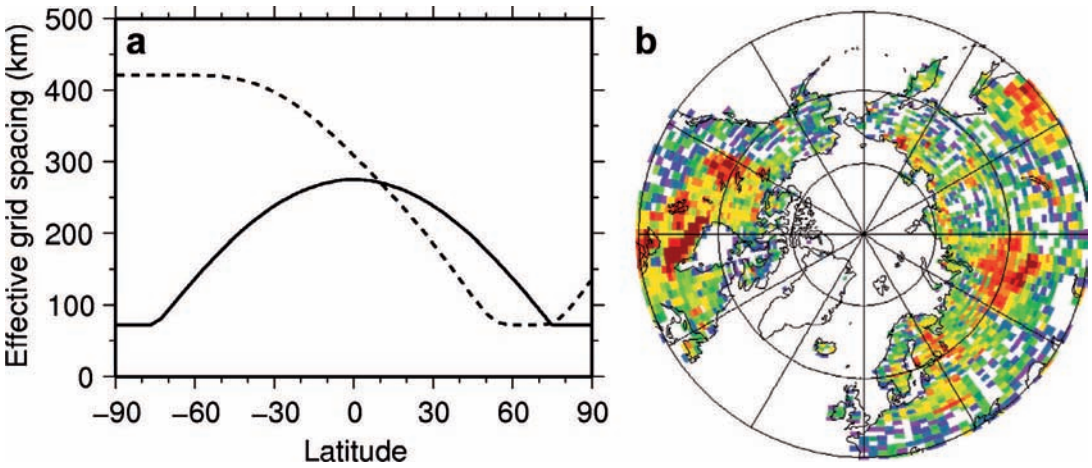

Fig. 1. (**a**) Effective meridional (dashed line) and zonal (full line) grid-point spacing (in km), taking into account the effect of zonal low-pass filtering near the poles which is necessary to ensure numerical stability. (**b**) Present-day inland water surface fraction (permanent lakes plus swamps, dimensionless) after Cogley (2003).White grid points indicate IWS below 0.003, ocean or ice cover.

the 21st century. In a first approach, we carry out sensitivity simulations in which we test the atmospheric response to a total disappearance of all IWS. This allows to compare our results for the 21st century with those of previous sensitivity tests carried out for the 20th century, and to obtain a strong signal which is easy to interpret. A second sensitivity test consists of a 50% reduction of future IWS extent. Finally, we use informed but rough estimates of the future extent of perennially frozen deep soil to produce a more realistic estimate of the future climatic impacts of a possible IWS reduction. These different sensitivity tests allow us to evaluate the dependency of the climate response on the severity of the future IWS reduction.

Methods

We used version 4 of the LMDZ (Laboratoire de Météorologie Dynamique-Zoom) atmospheric general circulation model with 144 × 108 × 19 (longitude × latitude × vertical) grid points. The model is described in detail by Hourdin *et al.* (2006). The irregular meridional grid-point spacing varies from 420 km at the South Pole to less than 75 km between 56°N and 75°N (Fig. 1a), while the convergence of the meridians near the poles automatically increases the zonal resolution. North of 75°N, zonal low-pass filtering is activated to ensure numerical stability, impeding the effective zonal grid spacing to drop below 73 km. Applications with similar grid distortions, allowing comparably high spatial resolution over the region of interest, were successfully carried out for high-latitude regions such as Antarctica and northern Eurasia (e.g. Krinner *et al.* 1997, 2004, 2006, 2007).

This version of LMDZ4 contains a lake column model described by Krinner (2003). The model takes into account molecular and wind-induced turbulent heat conduction below the lake surface, gradual absorption of sunlight, convection and water phase changes. The surface mass balance of IWS is calculated as precipitation minus evaporation minus runoff which occurs when the water column exceeds a prescribed maximum height. This maximum height is 20 m for lakes and 3 m for wetlands. We used the GGHYDRO (ver. 2.3) global hydrographic dataset (Cogley 2003) to prescribe global lake and wetland fractions in LMDZ4. GGHYDRO is a dataset covering the entire surface of the Earth and containing hydrographic data on the areal extent of different kinds of terrain, and on the distribution of mean terrestrial surface runoff. The IWS fraction on the model grid (Fig. 1b) exhibits the well-known pattern of areas of high inland water fraction such as the West Siberian Plain.

The model was run for the periods 1980–2000 and 2080–2100. For the period 1980 to 2000, the prescribed time-dependent boundary conditions are essentially observed sea-ice concentrations and sea-surface temperatures (Rayner *et al.* 2003, http://badc.nerc.ac.uk/data/hadisst/) and observed greenhouse gas (CO_2, CH_4, N_2O, CFCs), aerosol and ozone concentrations. For the period 2080 to 2100, the prescribed greenhouse gas and aerosol concentrations follow the IPCC SRES-A1B scenario (Nakicenovic *et al.* 2000). Among the different SRES scenarios of future greenhouse gas and aerosol emissions supposed to be of equal probability, SRES-A1B is a "middle of the road" estimate. The oceanic boundary conditions are obtained by using the anomalies of SST and sea-ice fraction simulated by the IPSL-CM4 (Institut Pierre-Simon Laplace coupled model ver. 4) atmosphere–ocean general circulation model under the same greenhouse gas forcing scenario (for details, *see* Krinner *et al.* 2008). Atmospheric ozone concentrations are prescribed following Meehl *et al.* (2006). The first year of each simulation is discarded as spinup. According to Simmonds (1985), this is an appropriate spin-up time for an atmosphere-only model. This leaves 20 years (periods 1981–2000 and 2081–2100) for analysis, coherent with previous applications of this model for polar climate studies (Krinner *et al.* 2007, 2008).

The setup of our simulations is summarized in Table 1. For each period (end of the 20th and end of the 21st century), we carried out one reference simulation with the present-day observed IWS extent (referred to as C20IWS and C21IWS, respectively), and one without IWS (referred to as C20 and C21, respectively). Moreover, for the end of the 21st century, we produced a simulation in which lake and wetland fractions were divided by two (C21IWS/2).

A uniform 50% or 100% reduction of IWS extent between now and the end of this century is, of course, a highly idealized scenario. Moreover, a complete IWS disappearance is rather improbable. An assessment of the influence of glacial history, permafrost, topography and peatland on the prevalence of lakes in the Arctic by Smith *et al.* (2007) has shown that spatial lake fraction statistics "are surprisingly similar across continuous, discontinuous and sporadic permafrost zones", and decrease sharply in permafrost-free areas. These authors suggest that a "permafrost-free" Arctic would see its IWS area reduced by about 40%. It is not clear how soon lake drainage occurs after a transition from a permafrost to a non-permafrost environment, although some observations (Smith *et al.* 2005) suggest that this may happen rapidly. It is not clear either whether permafrost-induced lakes require a critical minimum depth of the permafrost base, a maximum depth of the permafrost table or minimum ground ice content. The retreat of permafrost will of course occur slowly and, at least under a SRES-A1B-like scenario, the permafrost extent at the end of the 21st century will clearly be out of equilibrium with the evolving surface climate. But the annual mean temperature at a reasonable depth in the

Table 1. Overview of the simulations described in this paper.

Simulation	Period	Prescribed inland water surfaces	Note
C20IWS	1981–2000	Present-day observed IWS extent (after Cogley 2003)	Reference simulation for this period
C20	1981–2000	No IWS	
C21IWS	2081–2100	Present-day observed IWS extent (after Cogley 2003)	Reference simulation for this period
C21	2081–2100	No IWS	
C21IWS21	2081–2100	IWS reduced by 40% south of "equilibrium permafrost limit", increased by 10% in remaining "equilibrium permafrost" regions	"Best guess" simulation
C21IWS/2	2081–2100	IWS reduced by 50% as compared with present-day observed extent	Not shown

soil (such that it is approximately in equilibrium with the surface climate) can give an idea which permafrost extent would be consistent with the simulated surface climate, and it may serve as a basis for a rough estimate of large-scale changes of high latitude IWS extent during this century. Furthermore, as results by Smith *et al.* (2005, 2007) suggest, a temporary increase of IWS is possible where continuous permafrost remains in spite of the warming. These considerations led us to carry out a "best estimate" simulation (called C21IWS21) for 2081–2100 in which IWS fractions are modified in accordance to the simulated future climate change and the analysis of the dependence of IWS extent on climate as suggested by Smith *et al.* (2007). The region where the present-day annual mean temperature at the 50-cm depth ($T_{soil,50cm}$) is below 0 °C corresponds reasonably well to observed permafrost limits as given by Zhang *et al.* (2008). Therefore, this $T_{soil,50cm}$ annual mean 0 °C isotherm is referred to as the "equilibrium permafrost limit" in the following. IWS extent is reduced by 40% in regions which are north of the equilibrium permafrost limit during the period 1981–2000 (simulation C20IWS) and south of that limit at the end of the 21st century (simulation C21IWS) (green and yellow in Fig. 2). The regions remaining north of the equilibrium permafrost limit in 2081–2100 (red and brown in Fig. 2) can similarly be identified as those where an increase of IWS by about 10% might be expected according to the "thought exercise" by Smith *et al.* (2007). Consequently, the prescribed IWS fraction was increased by 10% in these areas. Except for the IWS extent, this simulation C21IWS21 is identical to the simulations C21IWS, C21IWS/2 and C21.

As the principal aim of this paper is to assess the climatic effect of a potential future decrease of the high-latitude IWS extent, and as the simulations including IWS are those in which the present surface type distribution is represented more realistically, we will present our results systematically with the "observed present inland water surfaces" case as reference simulations. In other words, our reference simulations for 1981–2000 and 2081–2100 are C20IWS and C21IWS, respectively.

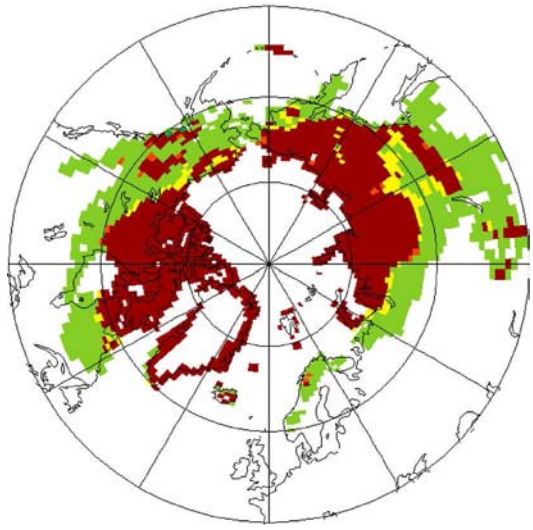

Fig. 2. Continental, ice-free areas with simulated annual mean soil temperature at 50 cm depth below 0 °C for different simulations. Green: C20IWS only; yellow: C20IWS and C21IWS21; red: C20IWS and C21IWS; brown: C20IWS, C21IWS and C21IWS21. All coloured pixels approximately correspond to the present-day simulated equilibrium permafrost extent, while pixels in red, yellow and brown indicate equilibrium permafrost in at least one of the 21st century simulations.

Results

Climate sensitivity to total IWS disappearance

If all inland water surfaces (IWS) disappeared today, warming in summer would occur (Fig. 3c). The reason is the missing large heat capacity of the IWS, which take more time to respond to seasonal forcing. For the same reason, cooling occurs in autumn (Fig. 3d). It partly extends into winter (Fig. 3a). Annual mean precipitation changes induced by IWS disappearance at the end of the 20th century (not shown) are mostly weaker than ±10%. The impact of a total disappearance of IWS on the simulated surface air temperature in the 21st century is shown in Fig. 4. Similar to the situation for the present (Fig. 3), the disappearance of IWS induces cooling during autumn and winter (Fig. 4a and d), and warming during summer (Fig. 4c). Despite justified criticism (e.g. Nicholls 2001), Student's

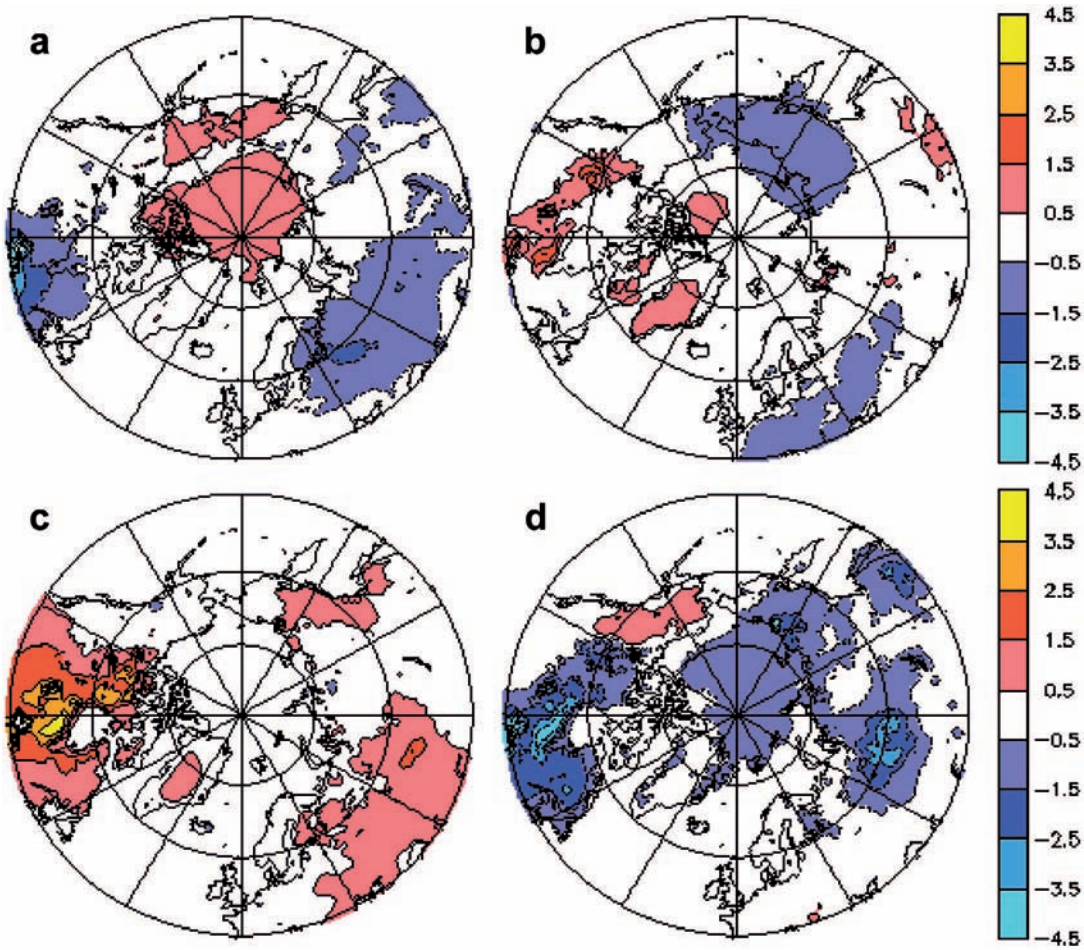

Fig. 3. Sensitivity of the simulated 1981–2000 surface air temperature (°C) to the total disappearance of inland water surfaces (IWS): $T_{2m,C20} - T_{2m,C20IWS}$. (**a**) winter (December–January–February), (**b**) spring (March–April–May), (**c**) summer (June–July–August), (**d**) autumn (September–October–November).

t-test is frequently used in atmospheric sciences to assess the likelihood of the difference between two simulations to be merely due to chance (e.g. von Storch and Zwiers 1999). A two-sided *t*-test of the temperature change signal indicates statistical significance (less than 10% probability of the signal to be due to chance) over large parts of Siberia and North America in summer and autumn, and more locally in winter. The weak spring temperature change is not significant at this 10% level.

The climatic effect of a potential future decrease of IWS has to be put into perspective with the amplitude of the expected climate change itself. On an annual mean basis (Fig. 5), the total disappearance of IWS would result in a weakening of the future warming over the largest parts of the boreal continents. The effect would be in its maximum (future warming reduced by more than 20%) over the West Siberian Plain, Karelia, Lake Baikal and western China. The largest effect in North America occurs in Québec, where the annual mean temperature increase over the 21st century is reduced by more than 15%. The opposite effect (reinforcing of the future warming) occurs over western Europe. However the absolute amplitude of this signal is weak, because the simulated annual mean climate change in that region is relatively small as a consequence of a strong projected reduction of the meridional overturning in the North Atlantic.

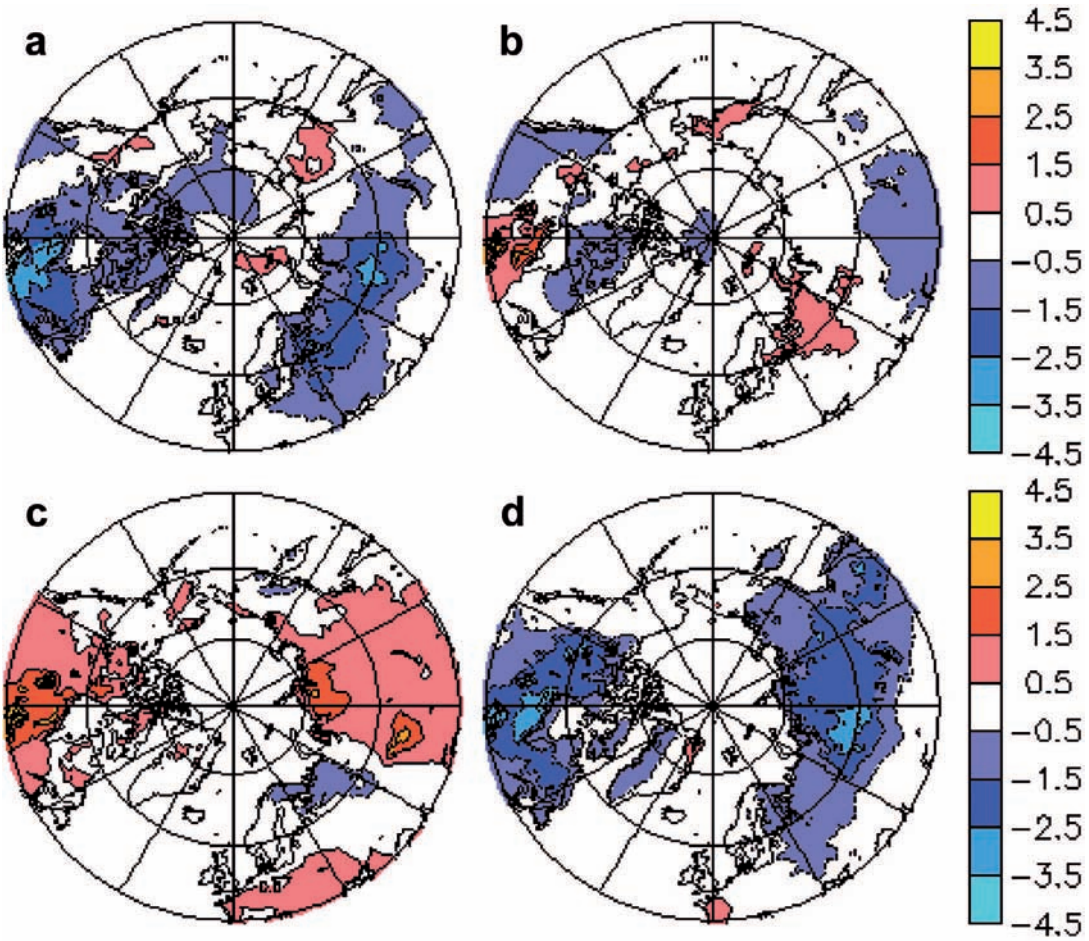

Fig. 4. Sensitivity of the simulated 2081–2100 surface air temperature (°C) to the total disappearance of inland water surfaces (IWS): $T_{2m,C21} - T_{2m,C21IWS}$: (**a**) winter (December–January–February), (**b**) spring (March–April–May), (**c**) summer (June–July–August), (**d**) autumn (September–October–November).

On a seasonal basis, the total disappearance of IWS would lead to a strong reduction of the autumn and winter warming (Figs. 6a, d and 7a, d) reaching more than 50% over the West Siberian Plain and south of the Hudson Bay in autumn. In turn, the absence of the cooling effect of the IWS in summer would lead to an increase of up to 50% of the future surface air temperature increase (Figs. 6c and 7c). Because future warming will be stronger in autumn and winter than in summer (Fig. 6), the cold season reduction of future warming dominates the annual mean signal (Fig. 5).

The simulated annual-mean boreal precipitation at the end of the 21st century is almost nowhere affected by the total disappearance of IWS and therefore not shown. Similarly, the circulation changes as illustrated by the 500-hPa height changes are weak. In terms of surface pressure, they correspond to changes of the order of 2 hPa and therefore not shown either.

Linearity of the climatic effect of IWS disappearance

How does the climatic impact of IWS vary with their extent? The surface air temperature change induced by the disappearance of 50% of all inland water surfaces (experiment C21IWS/2, not shown) is roughly half the signal we obtain with a total disappearance (experiment C21,

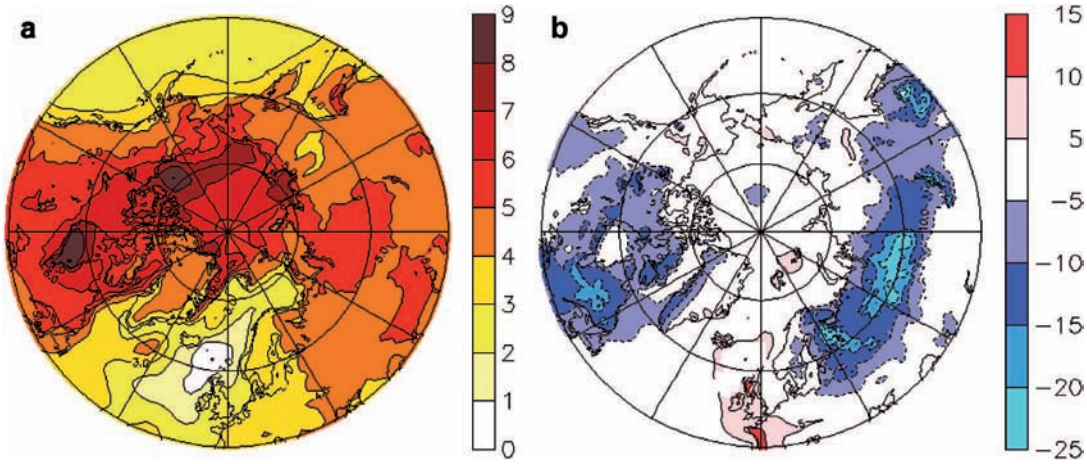

Fig. 5. (**a**) Annual mean surface air temperature change over the 21st century (from 1981–2000 to 2081–2100): $T_{2m,C21IWS} - T_{2m,C21}$ (°C). (**b**) Relative sensitivity (%) of the simulated annual mean surface air temperature change to the disappearance of inland water surfaces: $(T_{2m,C21} - T_{2m,C21IWS})/(T_{2m,C21IWS} - T_{2m,C20IWS})$.

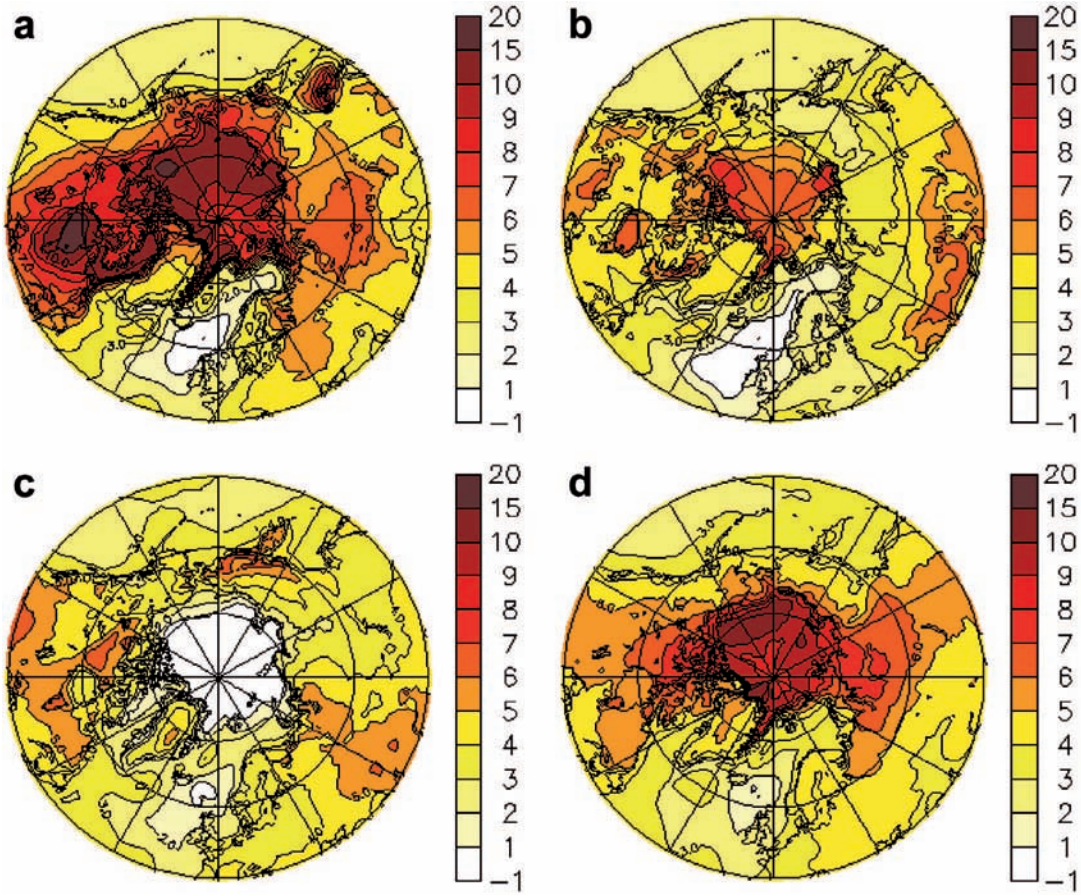

Fig. 6. Simulated seasonal surface air temperature change over the 21st century (from 1981–2000 to 2081–2100): $T_{2m,C21IWS} - T_{2m,C20IWS}$ (°C). (**a**) winter (December–January–February), (**b**) spring (March–April–May), (**c**) summer (June–July–August), (**d**) autumn (September–October–November).

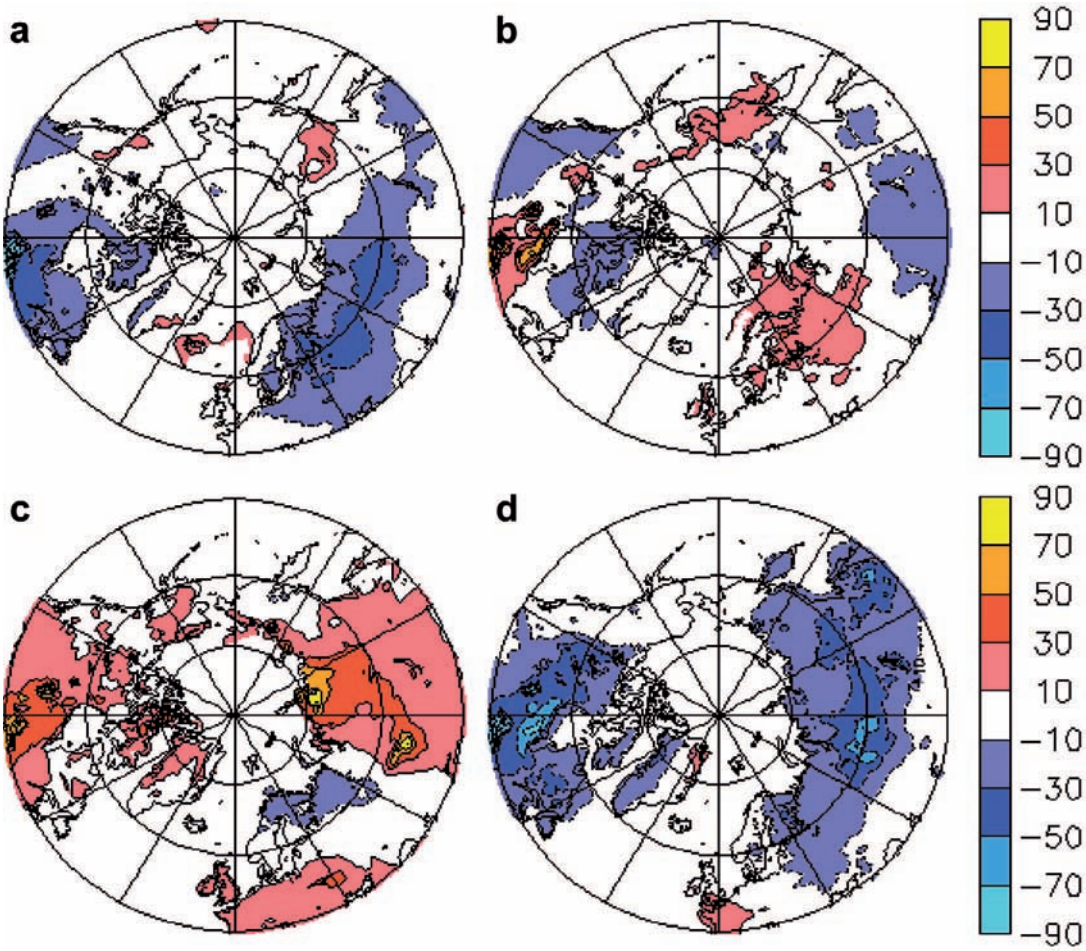

Fig. 7. Relative sensitivity (%) of the simulated seasonal surface air temperature change (from 1981–2000 to 2081–2100) to the disappearance of inland water surfaces: $(T_{2m,C21} - T_{2m,C21IWS})/(T_{2m,C21IWS} - T_{2m,C20IWS})$. (**a**) winter (December–January–February), (**b**) spring (March–April–May), (**c**) summer (June–July–August), (**d**) autumn (September–October–November).

Fig. 4). The climatic effect of IWS at the end of the 21st century therefore does appear to depend in a roughly linear manner on their extent.

With this in mind, and reminding the geographical patterns of the prescribed IWS extent changes (Fig. 2), it is fairly straightforward to interpret the temperature change signal obtained in the "best estimate" IWS extent experiment (C21IWS21: 40% IWS reduction prescribed in regions where the "equilibrium permafrost" disappears at the end of the 21st century, together with a 10% increase in the remaining "equilibrium permafrost" areas). The climatic impact of these moderate changes of IWS extent is rather weak (Fig. 8). The strongest signal appears in the northern Ural/West Siberian Plain region, where the prescribed reduced IWS leads to a clear and statistically significant cooling. Similarly, there is slight autumn cooling over central Siberia, linked to the reduced IWS and consistent with the results of experiment C21 (total disappearance of all IWS). The almost total absence of any signal south of the Hudson Bay is expected because no change of IWS is prescribed in this region in C21IWS21 (Fig. 2). In general, the statistical significance of the simulated temperature change signal is low, simply because of the weakness of the signal. However, because the signal is clearly consistent with that obtained when all IWS are removed (simulation C21),

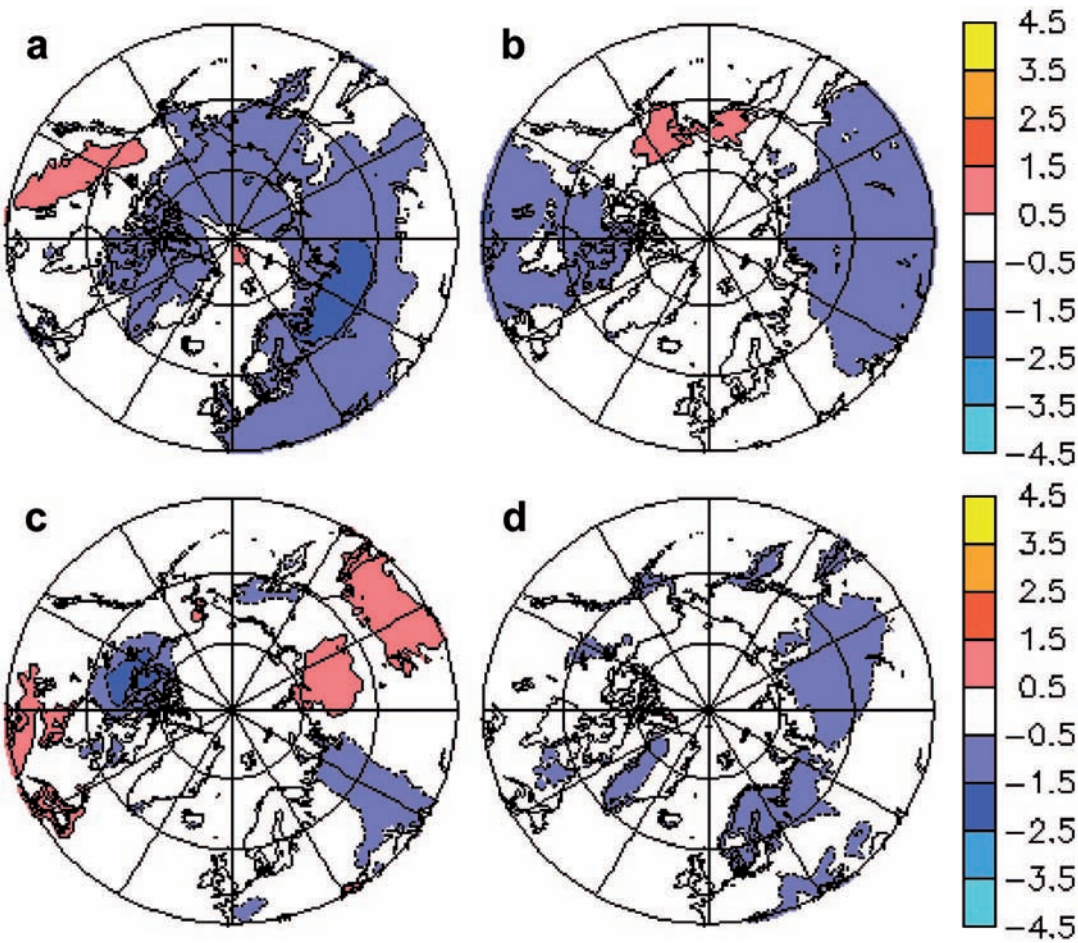

Fig. 8. Sensitivity of the simulated 2081–2100 surface air temperature (°C) to "best estimate" changes of inland water surfaces: $T_{2m,C21IWS21} - T_{2m,C21IWS}$. (**a**) winter (December–January–February), (**b**) spring (March–April–May), (**c**) summer (June–July–August), (**d**) autumn (September–October–November).

its physical significance (Nicholls 2001) is less questionable.

As compared with the anthropogenic climate change signal in absence of any changes of IWS (that is, in our case, the difference between C21IWS and C20IWS), the impact of the "best estimate" reductions of the inland water extent indeed appears fairly substantial (Fig. 9). As a consequence of the reduced thermal inertia of the surface, the future winter and spring warming is reduced by more than 15% (up to 40%) over a large part of Eurasia. A similar but weaker signal appears in autumn. Over North America the signal is not so clear. Similarly, in summer, the signal is spatially rather noisy, casting doubt about its physical significance.

Discussion

Comparison with previous work

The sensitivity of the present-day (boreal) climate to the presence of IWS has been evaluated in several previous studies (e.g. Pitman 1991, Bonan 1995, Lofgren 1997, Krinner 2003). The work by Krinner (2003) was carried out with an older version of the climate model used here and the results suggested a very strong cooling effect of IWS in summer, which was not reported by the earlier studies. It is not reproduced here, either. The sensitivity of the boreal climate obtained in the present study with the present version of LMDZ is indeed more similar to the response

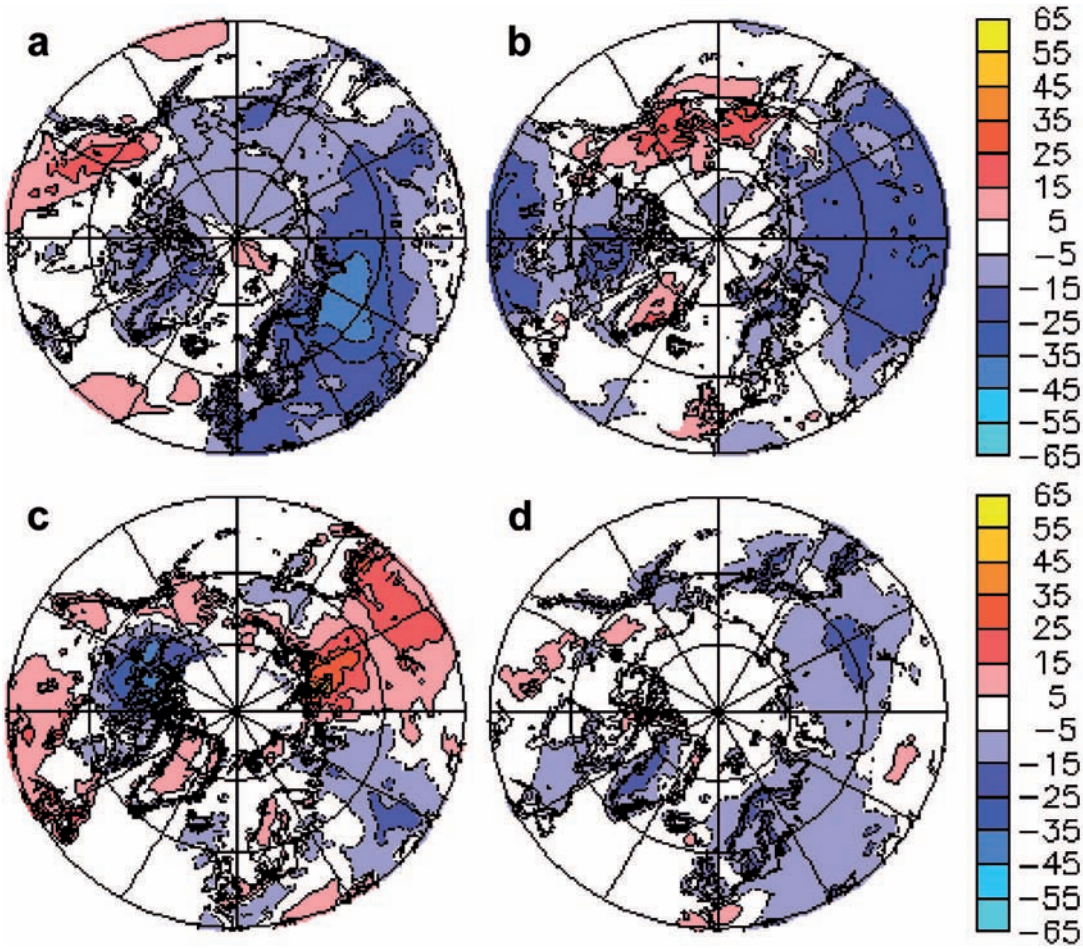

Fig. 9. Relative sensitivity of the simulated 2081–2100 minus 1981–2000 surface air temperature change (°C) to "best estimate" changes of inland water surfaces: $(T_{2m,C21IWS21} - T_{2m,C21IWS})/((T_{2m,C21IWS} - T_{2m,C20IWS})$. (**a**) winter (December–January–February), (**b**) spring (March–April–May), (**c**) summer (June–July–August), (**d**) autumn (September–October–November).

obtained by Pitman (1991) and Bonan (1995) than to the response obtained with the older version of the same model. The strong summer cooling reported by Krinner (2003) can in fact be traced back to a dry bias of the summer soil in the older version of LMDZ. This dry summer bias led to a considerable overestimate of boreal summer temperatures in the simulations without IWS, which was corrected in the simulations with IWS. The more recent version of LMDZ used here does not exhibit such a bias. The simulated boreal summer temperatures are in reasonable agreement with observations even in the version without IWS, leading to a damped thermal response of the climate model to the inclusion of IWS.

Importance of the underlying IWS map

There are several global-scale compilations of wetland and lake extents (e.g. Cogley 2003, Lehner and Döll 2004 and references therein, Prigent *et al*. 2007). For practical reasons, we used the Cogley (2003) GGHYDRO compilation in this work. A recent study by Grosse *et al*. (2008) shows a major discrepancy between these larger scale datasets and distribution and coverage of lakes obtained from high resolution remote sensing. At three study sites in eastern Siberia, they found that the extent of water bodies was underestimated by a factor of two to seven. While these differences between the vari-

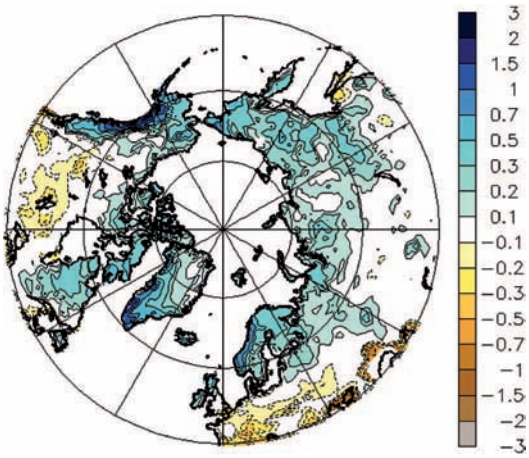

Fig. 10. Difference of annual mean precipitation minus evaporation ($P - E$, mm day^{-1}) between simulations C21IWS21 and C20IWS.

ous databases exist on small scales, the regional-scale characteristics of the distribution of IWS are similar. That is, on spatial scales represented by the climate model used here, the simulated patterns of the atmospheric response to a change in IWS extent will not be critically dependent on the underlying present-day map of IWS.

Coherence of the prescribed IWS changes with the simulated climate changes

Following Smith *et al.* (2007), we based our scenario of future changes in the IWS extent only on soil temperature changes. In reality, precipitation and evapo-transpiration contribute to determine the extent of IWS (Prigent *et al.* 2007), and will certainly continue to do so in the future. It is therefore of interest to assess the consistency of the simulated future precipitation and evaporation changes with our scenario of changes of IWS. For this to be done properly, we would have to use a detailed hydrological model, and this would be clearly beyond the scope of this work. Therefore, we base our assessment on precipitation and evaporation changes only. The simulated annual mean precipitation minus evaporation ($P - E$) changes over the 21st century (Fig. 10) indicate an increase of $P - E$ in the high northern latitudes, and a tendency to a more negative surface water balance further south. The $P - E$ changes are dominated by the precipitation changes. The evaporation changes exhibit the same spatial structure, but they are somewhat weaker. In other words, in regions where we prescribed a temperature-induced 10% increase of IWS extent in C21IWS21 because of the continuing prevalence of permafrost conditions (Fig. 2), the model tends to simulate a $P - E$ increase. In regions where the simulated annual mean soil temperature changes led us to prescribe a 40% reduction of IWS extent in C21IWS21, the annual mean $P - E$ changes tend to be more neutral. This means that our simulated $P - E$ changes do not appear in gross contradiction to the imposed scenario of changes of IWS extent.

Our results have shown that the disappearance of IWS would lead to significant, seasonally varying surface temperature changes. The scenario of IWS extent changes used in simulation C21IWS21 is based on future soil temperature changes which were simulated supposing no change of IWS extent (simulation C21IWS). Therefore it is interesting to ask whether the thermal impact of a possible future reduction of IWS would alter the future soil temperature distribution sufficiently to induce major discrepancies between the future soil temperatures simulated in C21IWS21 and those simulated in C21IWS. In our experimental setup we used the annual mean soil temperature at 50 cm depth ($T_{soil,50cm}$) as a proxy for the frost-induced changes of IWS extent. Concerning the $T_{soil,50cm}$ 0 °C isotherm, the main differences between C21IWS and C21IWS21 are a consequence of the cooling induced by the reduction of IWS extent, most pronounced in parts of central Siberia (yellow in Fig. 2). In these fairly small regions, $T_{soil,50cm}$ is below 0 °C in C21IWS21, but not in C21IWS. An iterative approach would require to carry out an additional simulation in which the prescribed IWS extent be increased by 10% (instead of being reduced by 40%) in regions which are yellow in Fig. 2 (and vice versa for the isolated regions which are red). However, such an iterative approach does not appear warranted for several reasons. First, the approach we used to prescribe future changes of IWS extent is a very rough one. Second, the absolute impact of changes of IWS extent is not extremely strong. Third, the regions concerned (yellow and red in Fig. 2) are not very large.

Indirect effects

While most studies hypothesize an increase in northern methane emission as a result of the air temperature and precipitation increase, the expected reduction of IWS will probably, at least partially, compensate for this effect. However, our study shows that the expected IWS reduction would reinforce the future summer warming. Because wetland methane emission usually peaks in summer, this means that methane emission intensity from the remaining wetlands (that is, emission per unit area of water surface) would probably be somewhat stronger than in the case without IWS reduction.

Conclusion

The aim of this work was to contribute to the ongoing discussion about possible future changes in the IWS extent in the high northern latitude by evaluating the climatic impact of such changes at the end of the 21st century (supposing greenhouse gas concentrations according to the SRES-A1B emission scenario). In an extreme (and improbable) scenario supposing the total disappearance of all IWS, our GCM simulates surface cooling locally in excess of 3 °C during winter and spring both in Eurasia and North America. Our results suggest that the climatic impact of a future reduction of the IWS extent is roughly proportional to the severity of the prescribed scenario of IWS extent changes. The impact of a potential reduction of the IWS extent on precipitation appears negligible, while the induced near-surface temperature changes are significant in large regions, and vary with season. In the annual mean, the total disappearance of IWS would reduce the expected future warming by about 10% (and locally more than 20%) over large parts of northern Eurasia and North America.

We carried out a "best guess" simulation in which we prescribed a fractional reduction of high latitude IWS extent as a function of the simulated reduction of the area of annual-mean subsurface temperatures. We insist that for several reasons detailed in the discussion, this "best guess" simulation should only be regarded as a very crude estimate of the potential climatic impact of changes of IWS extent. Taking the simulated impact of our "best guess" inland water reduction scenario at face value, we conclude that a reasonable future change of IWS would reduce future near-surface warming by up to 30% regionally and seasonally. However, in summer, future warming might be intensified due to reduced cooling induced by the decrease of IWS extent. The impact of these changes of IWS on the simulated surface water balance (precipitation minus evaporation) would not be in contradiction to the expected changes of IWS: in the most northerly regions, where our scenario would suggest an increase of IWS, the simulated annual mean $P - E$ increases. Further south, there are no systematic changes of $P - E$.

As a whole, this study suggests that the direct climatic impact of expected future IWS changes will be relatively moderate on large spatial scales. In particular, the effect on precipitation will be very weak, and circulation changes will be fairly weak. Near-surface temperature appears to be more sensitive. Future annual mean warming in the continental regions of the high northern latitudes might be reduced by about 10% by the effect of warming on the future extent of IWS. Seasonal characteristics of the future temperature changes can be more strongly affected, for example the summer surface temperature increase. This study makes no attempt to make the potential effects of these changes on the regional carbon fluxes, which could also influence the amplitude of the future climate change, not only locally, but globally (Walter *et al.* 2006). This study demonstrates, however, that the complex interactions can both amplify and counteract the predicted warming trend.

Acknowledgements: Support by the Alexander-von-Humboldt-Stiftung and CNRS for Gerhard Krinner's research stay at AWI Potsdam is gratefully acknowledged. This work is a contribution to the LEFE (EVE) project "MISSTERRE". We used computer resources at IDRIS/CNRS, AWI and the Mirage platform (UJF Grenoble).

References

Boike J., Wille C. & Abnizova A. 2008. Climatology and summer energy and water balance of polygonal tundra

in the Lena River Delta, Siberia. *J. Geophys. Res.* 113, G03025, doi:10.1029/2007JG000540.

Bonan G.B. 1995. Sensitivity of a GCM to inclusion of inland water surfaces. *J. Climate* 8: 2691– 2704.

Chapin F.S.III, McGuire A.D., Randerson J., Pielke Sr.R., Baldocchi D., Hobbie S.E., Roulet N., Eugster W., Kasischke E., Rastetter E.B., Zimov S.A. & Running S.W. 2000. Arctic and boreal ecosystems of western North America as components of the climate system. *Global Change Biology* 6: 211–223.

Cogley J.G. 2003. *GGHYDRO: Global hydrographic data, release 2.3*. Trent Tech. note 2003-1, Department of Geography, Trent Univ., Peterborough, Ontario, Canada.

Gilg O., Sané R., Solovieva D.V., Pozdnyakov V.I., Sabard B., Tsanos D., Zöckler C., Lappo E.G., Syroechkovski E.E.Jr. & Eichhorn G. 2000. Birds and mammals of the Lena Delta Nature Reserve, Siberia. *Arctic* 53: 118–133.

Grosse G., Romanovsky V., Walter K., Morgenstern A., Lantuit H. & Zimov S. 2008. Distribution of thermokarst lakes and ponds at three Yedoma sites in Siberia. In: Kane D.L. & Hinkel K.M. (eds.), *Proceedings of the 9th International Conference on Permafrost*, 29 June–3 July 2008, University of Alaska, Fairbanks, USA, pp. 551–556.

Gutowski W.J., Wei H., Vörösmarty C.J. & Fekete B.M. 2007. Influence of Arctic wetlands on Arctic atmospheric circulation. *J. Climate* 20: 4243–4254.

Hostetler S., Giorgi F., Bates G. & Bartlein P. 1994. Lake-atmosphere feedbacks associated with paleolakes Bonneville and Lahontan. *Science* 263: 665–668.

Hostetler S., Bartlein P., Clark P., Small E. & Solomon A. 2000. Simulated influence of Lake Agassiz on the climate of central North America 11 000 years ago. *Nature* 405: 334–337.

Hourdin F., Musat I., Bony S., Braconnot P., Codron F., Dufresne J.-L., Fairhead L., Filiberti M.-A., Friedlingstein P., Grandpeix J.-Y., Krinner G., LeVan P., Li Z.-X. & Lott F. 2006. The LMDZ4 general circulation model: climate performance and sensitivity to parametrized physics with emphasis on tropical convection. *Clim. Dyn.* 27: 787–813.

IPCC 2007. *Climate change 2007 — The physical science basis*. Contribution of Working Group I to the Fourth Assessment Report of the IPCC. Cambridge University Press, U.K.

Jorgenson M.T., Shur Y.L. & Pullman E.R. 2006. Abrupt increase in permafrost degradation in Arctic Alaska. *Geophys. Res. Lett.* 33, L02503, doi:10.1029/2005GL024960.

Krinner G. 2003. Impact of lakes and wetlands on boreal climate. *J. Geophys. Res.* 108, 4520, doi:10.1029/2002JD002597.

Krinner G., Boucher O. & Y. Balkanski Y. 2006. Ice-free glacial northern Asia due to dust deposition on snow. *Clim. Dyn.* 27: 613–625.

Krinner G., Genthon C., Li Z.-X. & Le Van P. 1997. Studies of the Antarctic climate with a stretched grid GCM. *J. Geophys. Res.* 102: 13731–13745.

Krinner G., Guicherd B., Ox K., Genthon C. & Magand O. 2008. Influence of oceanic boundary conditions in simulations of Antarctic climate and surface mass balance change during the coming century. *J. Climate* 21: 938–962.

Krinner G., Magand O., Simmonds I., Genthon C. & Dufresne J.-L., 2007. Simulated Antarctic precipitation and surface mass balance at the end of the 20th and 21st centuries. *Clim. Dyn.* 28: 215–230.

Krinner G., Mangerud J., Jakobsson M., Crucifix M., Ritz C. & Svendsen J.I. 2004. Enhanced ice sheet growth in Eurasia owing to adjacent ice-dammed lakes. *Nature* 427: 429–432.

Krinner G., Viovy N., de Noblet-Ducoudré N., Ogée J., Polcher J., Friedlingstein P., Ciais P., Sitch S. & Prentice I.C. 2005. A dynamic global vegetation model for studies of the coupled atmosphere-biosphere system. *Global Biogeochemical Cycles* 19, GB1015, doi:10.1029/2003GB002199.

Lehner B. & Döll P. 2004. Development and validation of a global database of lakes, reservoirs and wetlands. *J. Hydrol.* 296: 1–22.

Lofgren B.M. 1997. Simulated effects of idealized Laurentian Great Lakes on regional and large-scale climate. *J. Climate* 10: 2847–2858.

Meehl G.A., Washington W.M., Santer B.D., Collins W.D., Arblaster J.M., Hu A., Lawrence D.M., Teng H., Buja L.E. & Strand W.G. 2006. Climate change projections for the twenty-first century and climate change commitment in the CCSM3. *J. Climate* 19: 2597–2616.

Nakicenovic N., Alcamo J., Davis G., de Vries B., Fenhann J., Gaffin S., Gregory K., Grübler A., Jung T.Y., Kram T., Lebre La Rovere E., Michaelis L., Mori S., Morita T., Pepper W., Pitcher H., Price L., Riahi K., Roehrl A., Rogner H.-H., Sankovski A., Schlesinger M., Shukla P., Smith S., Swart R., van Rooijen S., Victor N. & Zhou D. 2000. *IPCC special report on emissions scenarios*. Cambridge University Press.

Nicholls N. 2001. The insignificance of significance testing. *Bull. Am. Meteorol. Soc.* 82: 981–986.

Oechel W.C., Vourlitis G., Hastings S.J., Zulueta R.C., Hinzmann L.D. & Kane D.L. 2000. Acclimation of ecosystem CO_2 exhange in the Alaskan Arctic in response ot decadal climate warming. *Nature* 406: 978–981.

Overduin P.P., Hubberten H.-W., Rachold V., Romanovskii N., Grigoriev N. & Kasymskaya M. 2007. The evolution and degradation of coastal and offshore permafrost in the Laptev and East Siberian Seas during the last climatic cycle. *The Geological Society of America*, Special Paper 426: 97–111.

Petrenko V.V., Smith A.M., Severinghaus J.P., Brook E.J., Lowe D., Riedel K., Brailsford G., Hua Q., Reeh N., Schaefer H., Weiss R.F. & Etheridge D. 2008. Measurements of carbon-14 of methane in Greenland Ice: investigating methane sources during the Last Glacial Termination. *Eos Trans. AGU* 89*:* 53.

Pitman A. 1991. A simple parameterization of sub-grid scale open water for climate models. *Clim. Dyn.* 6: 99–112.

Prigent C., Papa F., Aires F., Rossow W.B. & Matthews E. 2007. Global inundation dynamics inferred from multiple satellite observations, 1993–2000. *J. Geophys. Res.* 112, D12107, doi:10.1029/2006JD007847.

Rayner N.A., Parker D.E., Horton E.B., Folland C.K., Alexander L.V., Rowell D.P., Kent E.C. & Kaplan

A. 2003. Global analyses of sea surface temperature, sea ice, and night marine air temperature since the late nineteenth century. *J. Geophys. Res.* 108, 4407, doi:10.1029/2002JD002670.

Riordan B., Verbyla D. & McGuire A.D. 2006. Shrinking ponds in subarctic Alaska based on 1950–2002 remotely sensed images. *J. Geophys. Res.* 111, G04002, doi:10.1029/2005JG000150.

Simmonds I. 1985. Analysis of the "Spinup" of a general circulation model. *J. Geophys. Res.* 90: 5637–5660.

Smith L.C., Sheng Y., MacDonald M. & Hinzman L.D. 2005. Disappearing Arctic lakes. *Science* 308: 1429.

Smith L.C., Sheng Y. & MacDonald M. 2007. A first pan-Arctic assessment of the influence of glaciation, permafrost, topography and peatlands on northern hemisphere lake distribution. *Permafrost Periglac. Process.* 18: 201–208.

Smol J.P. & Douglas M.S.V. 2007. Crossing the final ecological threshold in high Arctic ponds. *Proc. Natl. Acad. Sci. USA* 104: 12395–12397.

von Storch H. & Zwiers F.W. 1999. *Statistical analysis in climate research*. Cambridge University Press.

Walter K.M., Zimov S.A., Chanton J.P., Verbyla D. & Chapin F.S.III 2006. Methane bubbling from Siberian thaw lakes as a positive feedback to climate warming. *Nature* 443: 71–75.

Walter K.M., Edwards M.E., Grosse G., Zimov S.A. & Chapin F.S.III 2007. Thermokarst lakes as a source of atmospheric CH_4 during the Last Deglaciation. *Science* 318: 633–636.

Yoshikawa K. & Hinzman L.D. 2003. Shrinking thermokarst ponds and groundwater dynamics in discontinuous permafrost near Council, Alaska. *Permafrost Periglac. Process.* 14: 151–160.

Zhang T., Barry R.G., Knowles K., Heginbottom J.A. & Brown J. 2008. Statistics and characteristics of permafrost and ground-ice distribution in the northern hemisphere. *Polar Geography* 31: 47–68.

Zimov S.A., Voropeav Y.V., Semelitov I.P., Davidov S.P., Prosiannikov S.F., Chapin F.S.III, Chapin M.C., Trumbore S. & Tyler S. 1997. North Siberian lakes: a methane source fueled by Pleistocene carbon. *Science* 277: 800–802.